2022

Multifunctional Organoboron Compounds and Boralactonate Salts

Randika T. Abeysinghe
West Virginia University, rta0002@mix.wvu.edu

Multifunctional Organoboron Compounds and Boralactonate Salts

Randika T. Abeysinghe

Dissertation Submitted to the
Eberly College of Arts and Sciences
at West Virginia University

In Partial Fulfillment of the Requirements for the Degree of
Doctor of Philosophy in Chemistry

Brian V. Popp, Ph.D., Chair
Jessica M. Hoover, Ph.D.
Stephen J. Valentine, Ph.D.
Blake Mertz, Ph.D.
Mark L. McLaughlin, Ph.D.

Department of Chemistry
Morgantown, West Virginia
2022

Keywords: Boracarboxylation, *bora*-ibuprofen, borafluorolactonate, NSAIDs, DABO boronates

Abstract

Multifunctional Organoboron Compounds and Boralactonate Salts

Randika T. Abeysinghe

Organoboron compounds have gathered an important significance within the chemistry community on account of their wide range of applications in synthesis, catalysis, and medicinal chemistry. Even though the uses of boron compounds in drug discovery have been overlooked until the last several decades, boronic acid containing molecules have garnered increased attention due to the unique chemical properties of the boron center. Boron-functionalized α-aryl propionic acid non-steroidal anti-inflammatory drug derivatives (*bora*-NSAIDs) can be accessed via copper(I)-catalyzed alkene boracarboxylation, using CO_2 and B_2pin_2. To explore and expand the current synthetic and future medicinal chemistry applications of these *bora*-NSAIDs, methods to derivatize the boron center need to be developed. Here, boron containing ibuprofen (*bora*-ibuprofen) synthesis via benchtop copper(I)-catalyzed alkene boracarboxylation was developed. Transesterification and transamination strategies have been employed to deprotect boron pinacol ester group in *bora*-ibuprofen, to synthesize additional *bora*-ibuprofen derivatives and subsequently isolate ibuprofen lactone boronic acid. Boracarboxylated products can be further functionalized by reacting them with potassium bifluoride under mild reaction conditions to afford air and moisture stable difluoroboralactonate salts. These Difluoroborolactonate salts exhibited remarkable stability under both acidic and basic hydrolytic conditions.

Dedicated to my mother Nalani Manike

and

my aunt Nilani Manike

Acknowledgments

First and foremost, I would like to convey my heartfelt gratitude to my advisor, Dr. Brian Popp, for his constant guidance and motivation throughout my time at the West Virginia University. I appreciate him for always giving me the right amount of push to be better and do better. He taught me many things, among which are how to answer a research problem in a logical manner and how to do a scientific research presentation in a coherent way. His kindness, patience and the understanding nature helped me through my struggles, especially as an international student. I believe his extraordinary mentorship, shaped me into a better scientist. I'm thankful to have been under the wing of Dr. Popp, who is the best advisor I could've ever asked for.

I am indebted to my committee members Dr. Jessica Hoover, Dr. Stephen Valentine, Dr. Blake Mertz and Dr. Mark McLaughlin for taking time to serve in my committee. I would also like to thank Dr. Brian Dolinar for providing the X-ray crystal structures for my substrates, Dr. Werner Geldenhuys for providing the toxicological data for my samples and Dr. Hacer Bristow for assisting me with the COX inhibitory screening assay. I would also like to express my sincere gratitude to Dr. Novruz Akhmedov, without whose NMR expertise, my project would not have been a success. Furthermore, I would like to thank all the staff members of the WVU chemistry department.

Moreover, I very much appreciate all the past and present Popp group members. Dr. Brian Nichols, Dr. Trina Perrone, Dr. Jessica Rogers, Dr. Notashia Baughman, Dr. Steven Knowlden, Dr. Alexa Martin, Stephen Long, Carly Gordon, Mason Hamilton, and Randall Koziel and Emily Heller. Their support and friendship helped me immensely. During my time at WVU, I was fortunate to work with many talented undergraduates. Thank you to Alexis Ravenscroft, Cody Tolliver, and Amanda Swistok for all the support given to me.

I sincerely thank my Fiancée Sashika Fernando for being there for me through thick and thin. I am extremely fortunate to have such an amazing person to share my life with. I love you, Sashika.

I'm beyond grateful to my aunt Nilani, my uncles Daya Sarath and Sunil Shantha as well as my grandparents for taking care of me when I was a kid. without them, I wouldn't be the person I am today. Finally, my deepest gratitude goes to my mother Nalani for everything she has done for me. As a single parent she sacrificed her whole life to raise me. Without her dedication, guidance, and encouragement none of this would have been possible. I am eternally grateful for every tear and sweat drop you shed to raise me.

Table of Contents

CHAPTER III. Synthesis of Borylated Ibuprofen Derivative through Suzuki Cross-Coupling and Alkene Boracarboxylation Reactions

CHAPTER IV. Difluoroborolactonate Salts- A New Class of Organofluoroboranes

CHAPTER V. Investigation of the Dynamic Equilibrium Between B-N Coordinated and Non-Coordinated DABO Boronate Esters in Deuterated Methanol Medium

CHAPTER V. Future Direction

List of Abbreviations

LD_{50}-	Median Lethal dose
FDA-	United states Food and Drug administration
tRNA	Transfer ribonucleic acid
PDE4	Phosphodiesterase
cAMP	Cyclic adenosine monophosphate
BNCT	Boron neutron capture therapy
BSH	Sodium borocaptate
BPA	4-dihydroxyborylphenyalanine
PMDA	Japanese Pharmaceuticals and Medical Devices Agency
ICT	Internal charge transfer
PET	Photoinduced electron transfer
BODIPY	4,4-difluoro-4-bora-3a,4a-diaza-*s*-indacene
NSAIDs	Non-Steroidal Anti-Inflammatory Drugs
COX	Cyclooxygenase
PGG_2	Prostaglandin G_2
PGH_2	Prostaglandin H_2
PGE_2	Prostaglandin E_2
$PGF_{2\alpha}$	Prostaglandin $F_{2\alpha}$
PGI_2	Prostacyclin
B_2pin_2	Bis(pinacolato)diboron
Bpin	Boronic acid pinacol ester
PPh_3	Triphenylphosphine
ICy	1,3-dicyclohexyl-imidazol-2-ylidene
IPr	1,3-bis(2,6-diisopropylphenyl)-imidazol-2-ylidene
IMe	,3-dimethyl-imidazol-2-ylidene
DEA	Diethanolamine
NHC	N-heterocyclic carbene
VT	Variable temperature
CIGAR-HMBC	Constant-time Inverse-detected Gradient Accordion Re-scaled long-range HMBC
TOCSY	Total Correlation Spectroscopy
HSQC	Heteronuclear Single Quantum Coherence

List of Figures

Chapter I:

Chapter II:

Chapter III:

Chapter IV:

Chapter V:

List of Schemes

Chapter I:

Chapter II:

Chapter III:

Chapter IV:

Chapter V:

List of Tables

Chapter I:

Chapter IV:

Chapter V:

CHAPTER I: Introduction

1.1 Elemental Boron and Organoboron Compounds

Boron is the fifth element in the periodic table and is positioned in Group 13(III A). It was first discovered and named by Sir Humphry Davy in 1807 and was first prepared by electrolyzing boric acid. It has two stable isotopes, ^{10}B and ^{11}B with natural abundances 19.10-20.31 % and 79.69- 80.90 %, respectively. By the elemental composition, it is the 51st most common element in the earth crust with a 3 ppm concentration. As a result of its electronic configuration, $1s^2 2s^2 2p^1$, it has very high first, second and third ionization energies, 8.296, 23.98 and 37.75 eV, respectively. These unique electronic properties give boron the ability to form covalent bonds and dative bonds with carbon, nitrogen, oxygen, and fluorine to form trivalent and tetravalent compounds.[1]

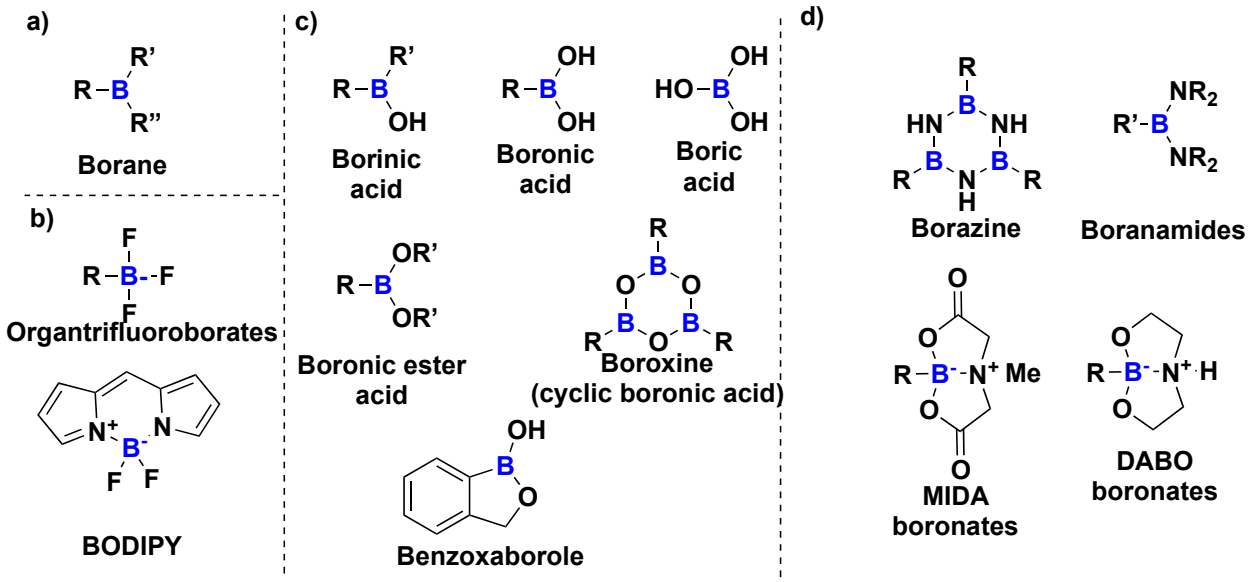

Figure 1.1 Representative examples of organoboron compounds, a) carbon containing organoboron, b) fluorine containing organoboron, c) oxygen containing organoboron d) nitrogen containing organoboron

Boron compounds have a wide range of applications in synthesis and catalysis, medicinal, sensing, material science, energy storage and polymer chemistry fields. In this chapter, applications of boron compounds in medicinal chemistry as well as sensing applications and synthesizing of boron containing molecules using boracarboxylation strategies are discussed.

1.2 Boron Compounds in Medicinal Chemistry

Boric acid ($B(OH)_3$) has been used as an anti-septic agent since the early 19th century.[2] However, the potential medicinal chemistry applications of other boron compounds were long overlooked till the early 2000s. This is mainly be due to the usage of boron compounds as insecticides.[3] Despite any conclusive evidence to suggest that boron compounds are toxic to humans. On the contrary, elemental boron, boric acid, borates and many organoboron compounds show low toxicity to mammals. The acute oral LD_{50} values for boric acid in mice is 3450 mg/kg of body weight,[4] which is similar to acute oral LD_{50} value of regular table salt in mice (3000 mg/kg of body weight).[5] At present, boron compounds and elemental boron are used for various medicinal chemistry applications such as therapeutics, boron neutron capture therapy, and sensing applications.

1.2.1 Boron Containing Therapeutics

Boron possesses unique chemical attributes that are useful in drug design. Most trivalent boron compounds are *sp*^{2} hybridized in its neutral form and has an empty *p*-orbital. Thus, they are Lewis acidic and can readily react with nucleophiles and Lewis bases such as alcohols, amines, hydroxy acids, and amino acids. Upon addition of a nucleophile, they are converted to *sp*^{3} hybridized tetravalent compounds (Figure 1.2).[6]

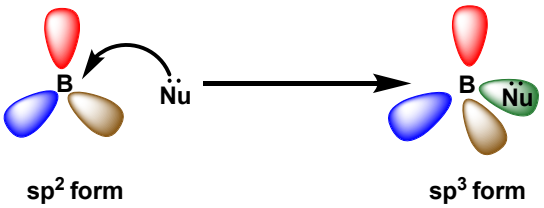

Figure 1.2 Hybridization changes on boron center upon addition of a nucleophile

Boronic acid compounds are useful in enzyme inhibition. The process of enzyme inhibition requires the conversion of sp^2 hybridized carbons into a tetrahedral sp^3 hybridized carbon. Thus, the replacement of carbonyl with bio isosteric boron would make a good transition state analog for the binding of serine protease (Scheme 1.1). The easy conversion of trigonal to tetrahedral geometry, makes boronic acid compounds an ideal candidate for enzyme inhibition. Currently, boronic acids have been used for the development of enzyme inhibitors of proteasomes, proteases, arginases, nitric oxide synthase, and transpeptidases.[7–10]

Scheme 1.1 Enzyme inhibition mechanism for boron-based compounds. (a) General mechanism of action of serine protease. (b) Boronic acid enzyme inhibition through formation of transition state analog.

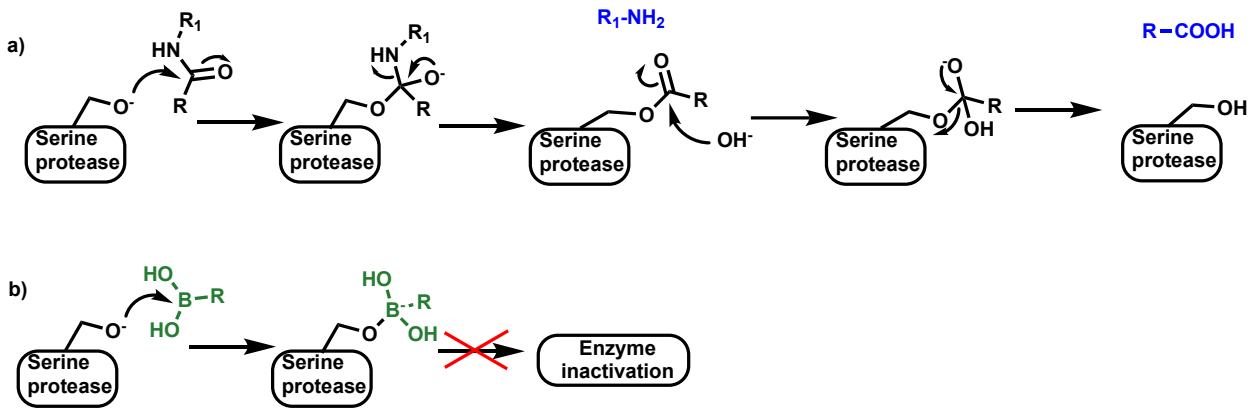

In 2003, FDA approved the first boron containing therapeutical drug, bortezomib (Velcade®). The discovery of bortezomib was a major breakthrough in cancer treatment, enabling proteasome inhibition for multiple myeloma and mantle cell lymphoma treatment.[11] Proteasomes are ubiquitous, being found in all eukaryotic cells. The tri-peptidyl aldehydes were one of the first classes of compounds that were identified as proteasome inhibitors. These peptide aldehydes (MG-132) can penetrate the cell membranes of living cells as a result of their hydrophobic nature and inhibit serine and cysteine proteases.[12] *In-vivo* usage has

been limited due to their non-selective nature towards both serine and cysteine proteases and their configurational instability.[13] The substitution of the aldehyde group with the bio-isosteric boronic acid group increased the potency of these compounds 50-100 fold. This improvement of potency is believed to be due to the greater stability of the dative bond between boron and oxygen in the threonine residue in the proteasome active site, relative to carbon oxygen bond found in the hemiacetal, which is formed by the reaction with the threonine residue in proteasome with the aldehyde inhibitor. (Figure 1.3).[14]

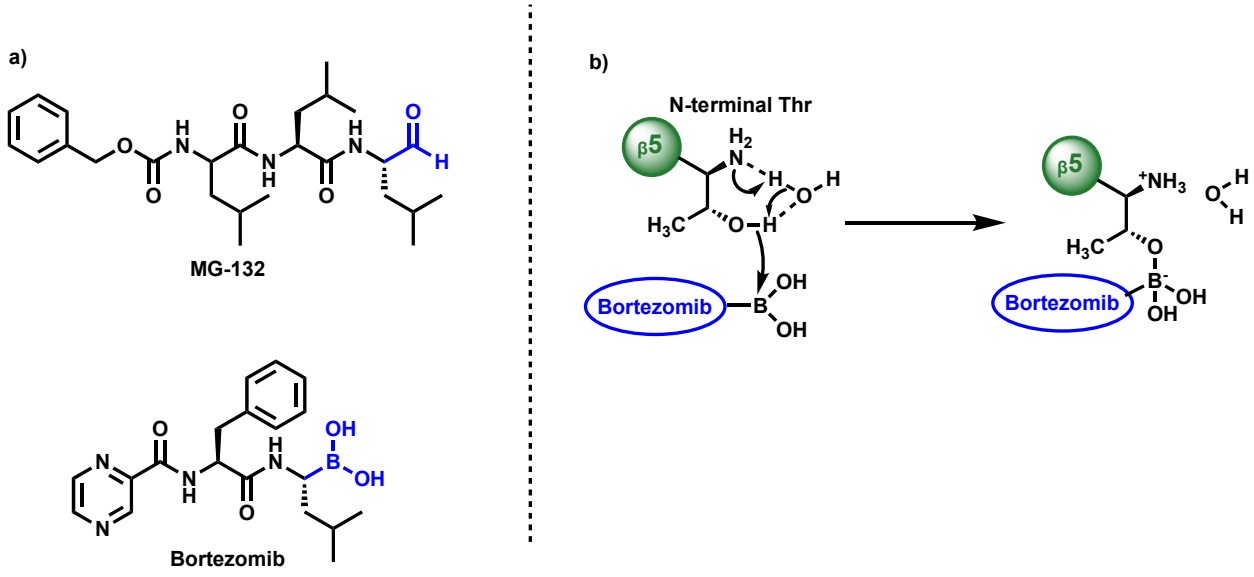

Figure 1.3 Enzyme inhibitory mechanism of bortezomib. (a) Structure of initially tested proteasome inhibitor (MG-132) and structure of bortezomib. (b) Primary mechanism of bortezomib, causing myeloma cell death.

After the approval of bortezomib, several other boron containing drugs were approved by the FDA (Figure 1.4). Tavaborole (Keryndin®), used to treat onychomycosis, inhibits yeast cytoplasmic leucyl-tRNA synthetase by the formation of a stable tRNALeu-tavaborle adduct in the editing site of the enzyme. Adduct formation is mediated through the boron atom of tavaborole and the 2′- and 3′-oxygen atoms of tRNA's 3′-terminal adenosine.[15,16] Ixazomib (Ninlaro®) is a reversible proteasome inhibitor that is used to treat

multiple myeloma. Ixazomib binds to the β-5 subunit of the 20S proteasome and inhibits its chymotrypsin-like activity.[17] In 2016, FDA approved crisaborole (Eucrisa®), which is used to treat mild to moderate atopic dermatitis (Eczema). The boron group in the benzoxaborole functionality in crisaborole, enables it to target and inhibit PDE4 by acting as a mimic of the phosphate of cAMP.[18] Vabrobactum (Vabomere®) is a cyclic boronic acid β-lactamase inhibitor that was approved in the United States for treatment of complicated urinary tract infections.[19] The cyclic boronic acid group inhibits serine β-lactamase by forming a stable covalent bond between the boron moiety and active site serine residue. This eventually results in inhibition of serine β-lactamase enzymatic activity.[20]

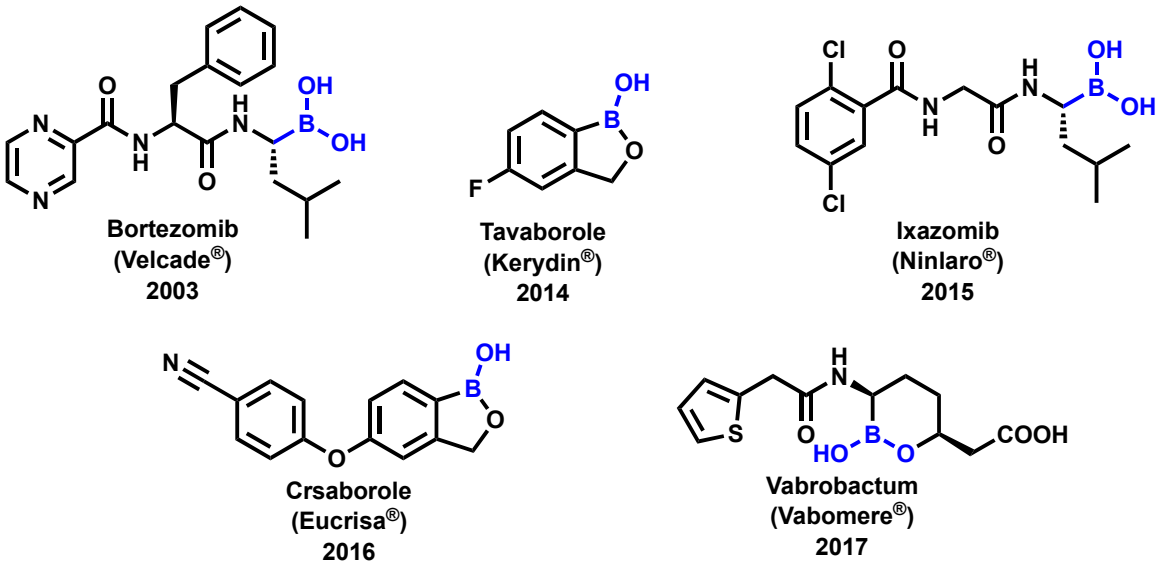

Figure 1.4 FDA approved boron containing drugs.

1.2.2 Boron Neutron Capture Therapy (BNCT)

BNCT is a potentially useful radiotherapy treatment, that can be used clinically for the management of various cancers. In BNCT, the low energy (<0.5 eV) thermal neutrons are absorbed by non-radioactive ^{10}B

atoms, which then undergoes a fission reaction to generate an alpha (^{4}He) particle and a recoil ^{7}Li nucleus. During this process, the consequent ^{11}B isotope undergoes nuclear fission to produce an alpha particle, a ^{7}Li nucleus and gamma radiation equal to 2.31 MeV (94 %) or 2.79 MeV (6 %) **(**Figure 1.5 a**).**[21]

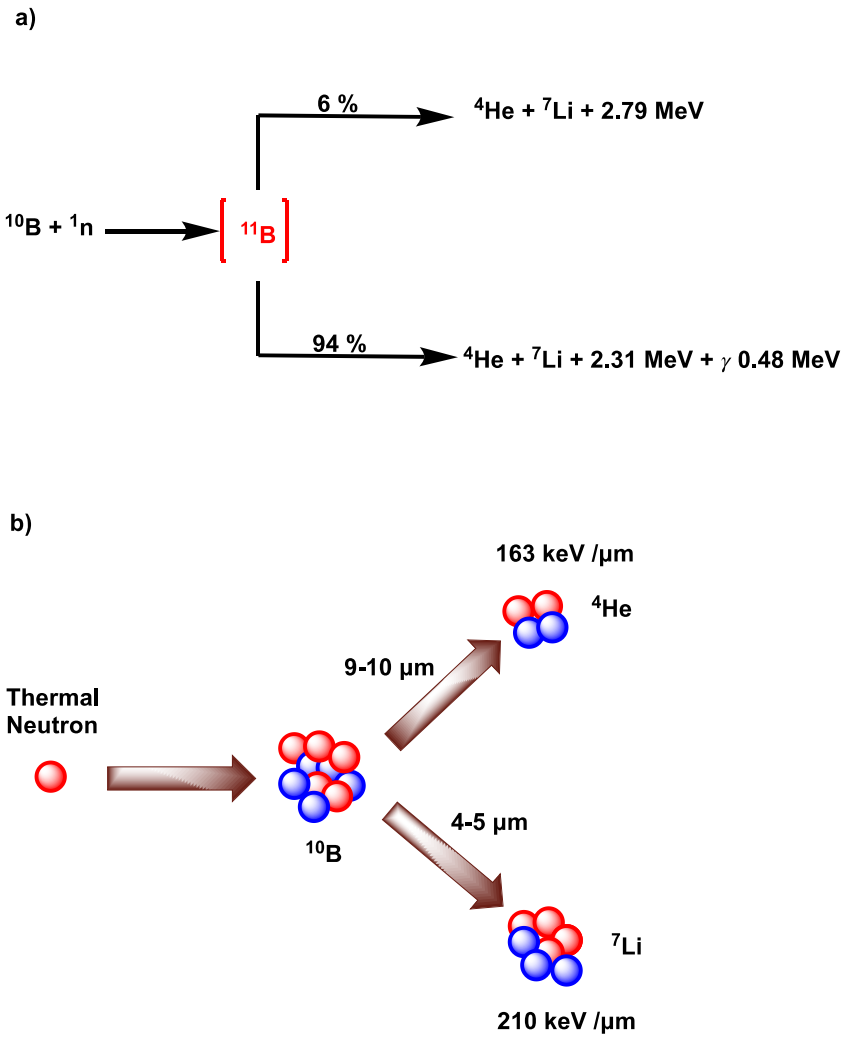

Figure 1.5 a) The nuclear fission reaction of ^{10}B atom b) Boron Neutron Capture Therapy mechanism

A couple of factors are needed for this method to be successful. First, enough thermal neutrons must be absorbed to cause lethal damage from ^{10}B fission. These high energy particles release energy over a short wavelength range (<10 µm), similar to the size of a single cell. Therefore, in theory, only boron containing tumor cells are destroyed, while adjacent normal cells are spared **(**Figure 1.5 b**).**[22]

The other factor is selective delivering of an adequate amount of ^{10}B atoms to all tumor cells (10^9 atoms/cell). These ^{10}B delivering agents can be categorized into three types, depending on their nature, boron containing small molecules, boron compound conjugates and targeted boron delivery nanoparticles. Sodium borocaptate (BSH, $Na_2B_{12}H_{11}SH$), and 4-dihydroxyborylphenyalanine (BPA) are currently used as BNCT carriers in clinical trials. BSH enter tumor cells by passive diffusion through the plasma membrane. BSH is used to treat certain types of cancers as it improves the 2- and 5-year survival rate of glioblastoma patients by 31.8% and 9.1% respectively.[23] Even though BSH has more ^{10}B atoms compared to BPA, its clinical applications are limited due to the low accumulation in tumors and poor blood brain barrier penetration.[24]

However, BPA was found to collect selectively in tumor cells because L-amino acid transporters (LAT-1) readily transport BPA into tumor cells. After the initial success of BPA, several other BPA derivatives were developed. The coupling of fructose with BPA (F-BPA) improved solubility and increased delivery of boron to tumor cells.[25] In March 2020, the first boron containing BNCT drug p-borono-L-phenylalanine (L-BPA, generic name: Boropharan [10B] Steboronine®) was approved by the Japanese Pharmaceuticals and Medical Devices Agency (PMDA) for clinical use.[26] L-BPA selectively targets amino acid transporters and delivers high concentrations of ^{10}B atoms into tumor cells.[27] Currently, L-BPA is used to treat locally unresectable recurrent or advanced unresectable head and neck cancers.[28] Even though some progress has been made in BNCT over the years, its usage is still limited due to the requirement of novel instrumental techniques to investigate quantitively ^{10}B in cancer cells after its administration. Additionally, the lack of methods to deliver high concentrations of ^{10}B selectively to cancer cells represents an unmet challenge in BNCT. Therefore, the discovery of novel BNCT carriers is necessary for the advancement of BNCT.

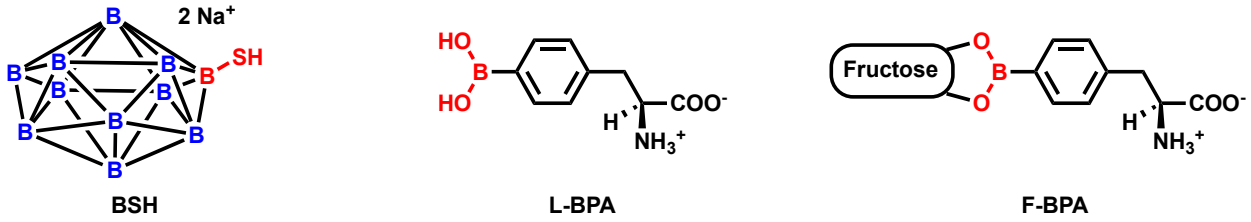

Figure 1.6 ^{10}B delivering agents used in BNCT

1.2.3 Boronic Acid Containing Molecular Sensors

The Lewis acidic nature of boronic acid compounds, allows them to form complexes with Lewis bases such as fluoride, hydroxide anions, or electron donating centers, such as nitrogen or oxygen. This Lewis acidic nature also allows boronic acid to form esters with biologically important diol species such as saccharides, glycoproteins, and dopamine. The pKa of boronic acids is similar to that of carboxylic acids and can range from 4.0 to 10.5,[29] while the pKa of boronic esters is slightly lower than that of boronic acids. Consequently, the binding of diols to boronic acids shift the equilibrium between neutral boronic acid and boronate ester towards boronate ester (scheme 1.2). This can cause changes in solubility, fluorescent intensity, and cross-linking density in boron compounds. The driving force of the development of boron-based sensors and anion receptors is the ability of boron compounds to form reversible bonds with diols and Lewis bases.

Scheme 1.2 Esterification equilibrium between boronic acid or boronate anion in aqueous solution with 1,2- or 1,3-diols. $pK_{a,BA}$ - pKa value for boronic acid, $pK_{a,BE}$ - pK_a value for boronate ester

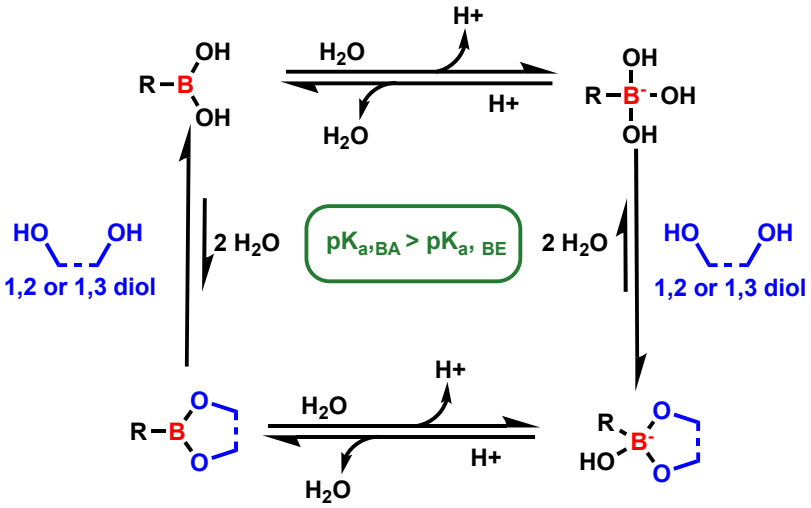

1.2.3.1 Saccharide Sensors

The initial work of Lorand and Edwards laid the foundation for boronic acid based receptor design.[30] They observed that the pH of a solution decreased when a saccharide complexed with a boronic acid. This pH drop was used to determine the saccharide affinity. Boronic acids react with 1,2-1,3- or 1,4-diols to form cyclic boronic esters in aqueous medium, and the acidity of the medium was found to increase. [31]

In 1992, Yoon and Czarnik developed the first fluorescent-based saccharide sensor using boronic acids.[32] They were internal charge transfer(ICT) sensors with the boronic acid group directly attached to a fluorescent unit (anthracene). Once the heteroatom of the saccharide was bound to the boronic acid, it could cause a variation in the fluorescent emission resulting from the changes in its electronic properties that accompany the rehybridization at the boron from sp^2 to sp^3. This led to a 30% decrease in the fluorescent emission in the 2-anthrylboronic acid molecule. In contrast, isomeric 9-anthrylboronic acid was found to exhibit only small changes in the fluorescent emission. These ICT sensors have high sensitivities towards pH changes and as a result, their real-world applications have been limited.

In 1994, the first photoinduced-electron-transfer (PET) fluorescent saccharide sensor was developed. This o-(aminomethyl)phenyl boronic acid receptor unit contains both a tertiary amine group (Lewis base) and a boronic acid group (Lewis acid). The inclusion of the two functional groups allows the sensor to function over a broad pH range.[33] The PET process can be explained using the pKa switch mechanism. In polar protic solvents, boronic ester formation, followed by water complexation/deprotonation at the boron ester, results in the formation of a tetracoordinate boronate ester. This process leads to a simultaneous protonation of the amine and end to the PET quenching pathway (Scheme 1.3).[34] This receptor is selective for D-fructose over D-glucose.

Scheme 1.3 *o*-(Aminomethyl)phenyl boronic acid receptor photoinduced electron transfer (PET) ON/OFF mechanism in polar protic solvents

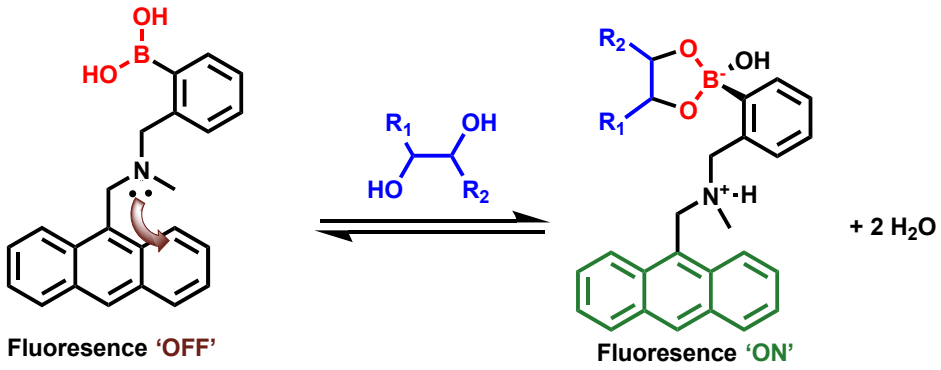

The following molecules are representative examples of different boronic acid containing saccharide sensors (Figure 1.7). The squarilium cyanine-based fluorescent sensor (Neu5Ac) is a selective chemo sensor, used to identify sialic acid in cancer cells.[35] As sialic acid is expressed in high concentrations in cancer cells, it is associated with the increase in tumor growth and metathesis.[36] The boronic acid functionalized Aza-BODIPY is used in fluorescence optodes to analyze glucose levels in blood.[37] A mono-boronic acid tricarbocyanine molecular sensor is used for *in vitro* live cell labeling. These tricarbocyanin molecular sensors are sensitive towards saccharides, which are components of glycoproteins, and glycoconjugates in live cells.[38]

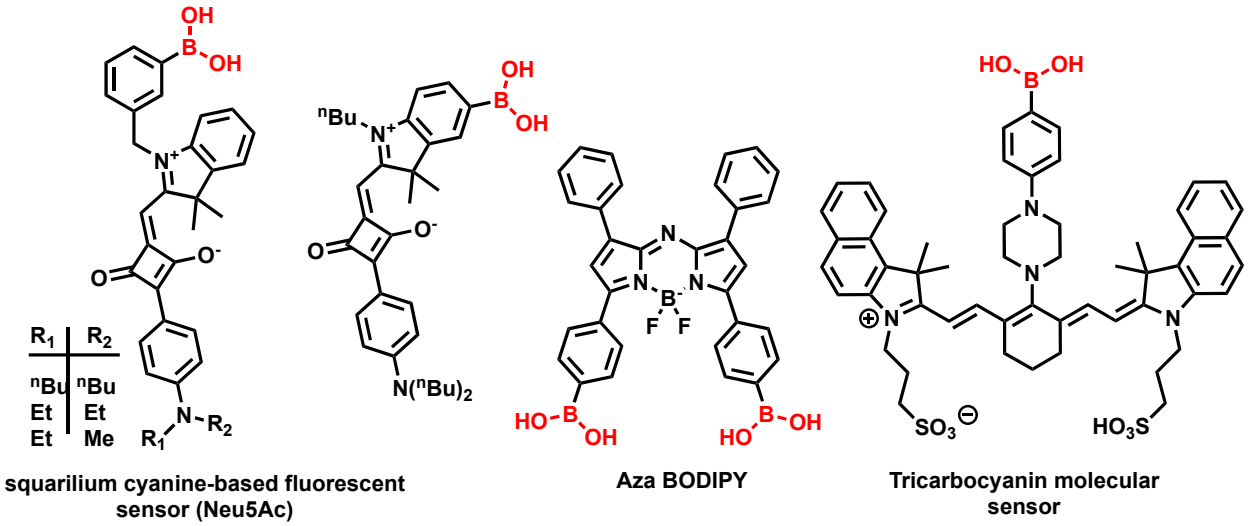

squarilium cyanine-based fluorescent sensor (Neu5Ac)

Aza BODIPY

Tricarbocyanin molecular sensor

Figure 1.7 Representative examples for boronic acid containing saccharide sensors

1.2.3.2 Anion Sensors

The characteristic Lewis acidic nature of boronic acids provides further possibilities to detect strong Lewis bases such as fluoride and cyanide ions. These sensors show fluorescence quenching or enhancement with respect to anion binding. Sequential addition of anions to boronic acid leads to decreasing fluorescence emission from the fluorophore (Scheme 1.4).[39]

Scheme 1.4 Boronic acid anion recognition general mechanism

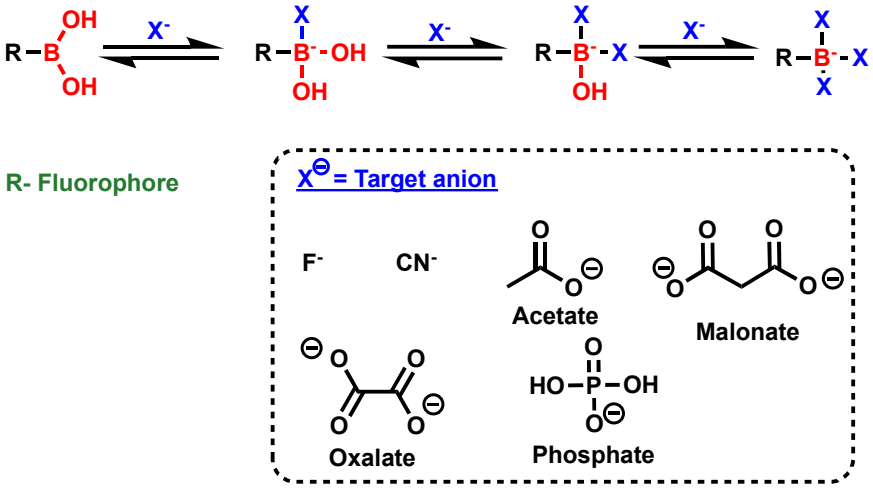

In 1998, James and coworkers reported the first boron based fluorescent anionic sensor for fluoride recognition. At pH 5.5, fluorescent quenching was observed with the addition of fluoride ions. The partially protonated nitrogen formed a hydrogen bond interaction with a bound fluoride, leading to further stabilization of the fluoride bound molecule.[40] Similarly, the tridentate napthylimidazolium receptor **(1)** was developed as an anion sensor. This utilized the formation of a B-F complex, which stabilized the interaction between fluoride and imidazolium, and subsequently produced a fluorescence response.[41] Moreover, a pyrene based boronic acid bound molecular sensor (**2**) was developed to measure fluoride levels (0.1 and 1.5 ppm) in water.[42]

Phenyl boronic acid and methylpyridinium cation containing molecular sensors **(3)** were used to quantify cyanide concentrations in solutions. So far, two chemosensors have been developed that can target cyanide anions. These sensors were based on incorporation of N-methylpyridinium cation and the boronic acid moieties into a single compound. Both absorption and fluorescence emission wavelength ratiometric and colorimetric sensing can be performed with these sensors. In acetonitrile. The sensors employ two different methods to recognize cyanide anions through: 1) color change and 2) fluorescence emission reaction that results from the sensor binding to cyanide anion through the boronic acid functional group.

This method has proved to be more effective compared to other currently available cyanide detection methods such as potentiometric, spectrophotometric, chromatographic, and electrochemical analysis methods that involve advanced instrumentation and extended time periods.[43] However, a major limitation of boronic acid-based anion sensors is that these sensors lack the ability to distinguish multiple anions simultaneously.

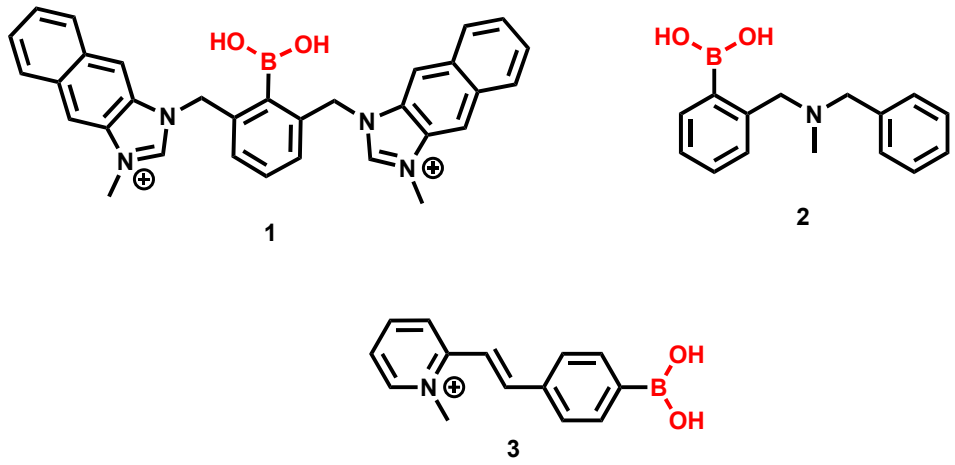

Figure 1.8 Representative examples for boronic acid containing fluoride and cyanide sensors

1.3.1 Non-Steroidal Anti-Inflammatory Drugs (NSAIDs)

NSAIDs are used in pain management due to their analgesic, anti-inflammatory, antipyretic effects, and platelet inhibitory actions. The first NSAID, acetyl salicylic acid (Aspirin), was discovered in 1897.[44] Since then, many NSAIDs have been developed to treat various medical conditions. NSAIDS are one of the most prescribed drug classes worldwide. It is estimated that globally 30 million people take a type of NSAID daily to manage various conditions.[45] NSAIDs have been classified based on their selective inhibition of cyclooxygenase enzymes, the major biological targets of these drugs. The NSAIDs that inhibit both COX-1 and COX-2 enzymes, are known as non-selective NSAIDs, whereas the NSAIDs that only inhibit COX-2 are known as COX-2 selective NSAIDs (Table 1.1). [46]

Table 1.1 Commonly used COX-2 selective and non-selective NSAIDs

Non-selective NSAIDs	COX-2 Selective NSAIDS
Ibuprofen, Fenoprofen, Ketoprofen, Naproxen, Flurbiprofen, Diclofenac, Diflunisal, Ketorolac, Indomethacin, Oxaprozin, Sulindac, Tolmetin, Meloxicam, Nabumetone, Mefanamic acid	Celecoxib Rofecoxib Valdecoxib

Although effectiveness of NSAIDs was well known in the 19th century, its inhibitory mechanism was unknown until 1971. Vane published his groundbreaking observations proposing that the ability of NSAIDs to reduce inflammation was dependent primarily on their ability to inhibit cyclooxygenase enzymes. This cyclooxygenase inhibition leads to diminished production of proinflammatory prostaglandins at the place of injury.[47]

There is evidence that major complications and adverse side effects can arise with NSAIDs that are prescribed for long term chronic pain management. Non-selective NSAIDs can cause perforations, ulcers, and bleeding in upper gastrointestinal tract.[48,49] This happens because of the inhibition of COX-1 by NSAIDs, leading to a decrease in the prostaglandin production in gastric mucosa and thromboxane production in platelets. The prostaglandin in intestine stimulates the secretion of mucin and surface-active phospholipids to protect gastroduodenal mucosa against gastric acids.[50] The inhibition of prostaglandin synthesis in kidneys cause renal toxicity due to interstitial nephritis and acute tubular necrosis.[50] Relative to non-selective NSAIDs, COX-2 selective NSAIDs, cause less adverse effects on the gastrointestinal tract. Moreover, COX-2 selective inhibitors may also prevent colorectal cancer.[51] One of the drawbacks of COX-2 inhibitors is that they cause adverse cardiovascular effects. Rofecoxib, which was introduced in 1999, was withdrawn from the market just 5 years later due to an linked increase in cardiovascular events such as

myocardial infarctions and strokes in humans.[52] To understand effects of NSAIDs, it is important to understand the role COX enzymes play in the prostaglandin biosynthetic pathway.

1.3.2 Cyclooxygenase (COX)

COX enzymes can be found membrane-bound on the luminal surfaces of the endoplasmic reticulum and on the inner and outer membranes of the nuclear envelope. COX-1 is constitutively expressed and has a functional role in the production of prostaglandins that are required to maintain basic functions of the body. Some tissues such as the brain and kidney do contain the ability to constitutively express COX-2. Despite this fact, COX-2 is mainly considered as an inducible enzyme, which is an enzyme that gets its expression activated by cytokines, mitogens, endotoxin, and tumor promoters in different cells.[53]

COX-1 and COX-2 are both bifunctional enzymes that perform two consecutive reactions in two active sites that are topologically different, yet mechanistically coupled. These are called the COX active site and the peroxidase active site, and are both located in the catalytic domain of the COX enzymes.[54] Cyclooxygenase catalyzes first two steps of the Prostaglandin biosynthesis pathway (Scheme 1.5). In the first step, COX convert arachidonic acid into a prostaglandin (PGG_2) by oxidative cyclization of the central five carbons in the arachidonic acid chain. Then, PGG_2 is converted into PGH_2 by peroxidase activity of COX enzyme. Finally, PGH_2 is metabolized to various types of prostaglandins including PGE_2, $PGF_{2\alpha}$, PGI_2 and thromboxane A_2 by isomerase enzymes (Scheme 1.5).[55]

Scheme 1.5 Prostaglandin biosynthesis pathway

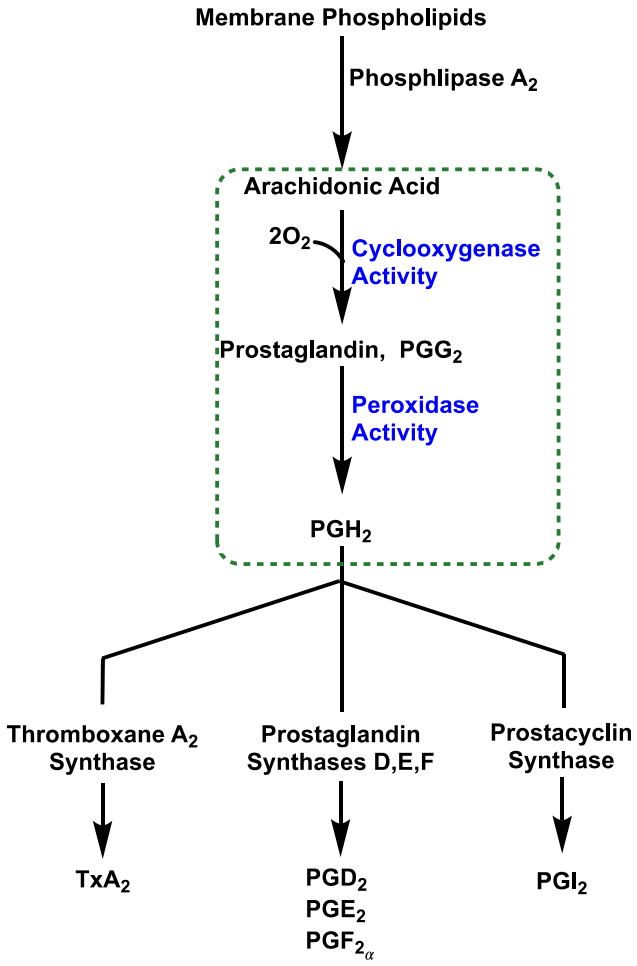

NSAIDs can inhibit COX enzymes by both covalent and non-covalent modifications. The only inhibitor that is currently clinically used and can irreversibly inactivate COX-1 and COX-2 is Aspirin (2-(acetyloxy)benzoic acid). It carries out this irreversible inactivation through a covalent modification of the COX active site in a time dependent manner. Every other known NSAID only possesses the ability to couple with the protein in a non-covalent manner. [56]

NSAIDs can be categorized into several different groups based on their chemical structure. Most of the common NSAIDs such as ibuprofen, naproxen, ketoprofen, fenoprofen and flurbiprofen contain an α-aryl propionic acid skeleton in their chemical structures.

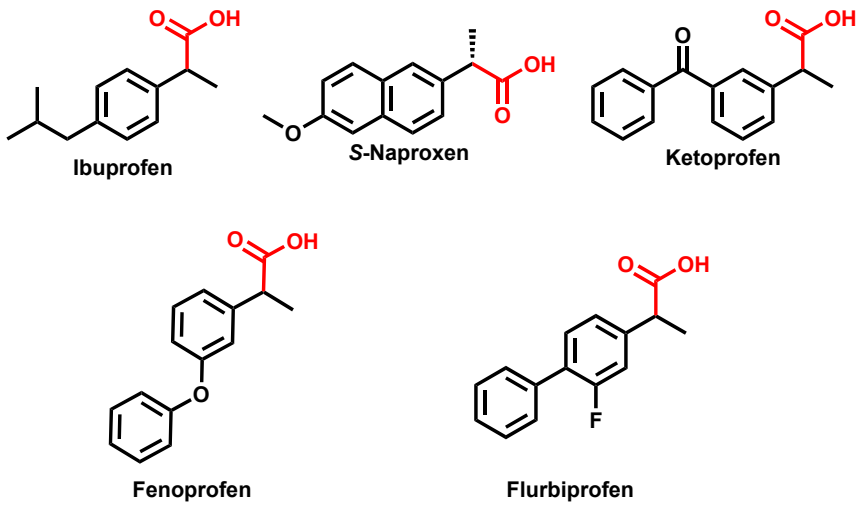

Figure 1.9 FDA approved α-aryl propionic acid non-steroidal anti-inflammatory drugs (NSAIDS)

1.4 Ibuprofen Synthesis Strategies

In 1961, the Boots Pure Drug company first synthesized ibuprofen using a 6-step synthetic procedure (Scheme 1.6).[57] Later in 1992, the Hoechst Company improved and optimized this synthetic procedure to 3 steps. Here, they used palladium-mediated carbon monoxide insertion to a benzylic alcohol to introduce the carboxylic acid group.[58] In 2009, McQuade and coworkers developed an efficient three step continuous flow method to synthesize ibuprofen. This method does not require the isolation of intermediates and yields the desired product in a shorter reaction time. However, scaling up of this method has been challenging due to the high temperatures utilized and the requirement of precise temperature controls between steps.[59]

Scheme 1.6 Synthesis of Ibuprofen by conventional methods

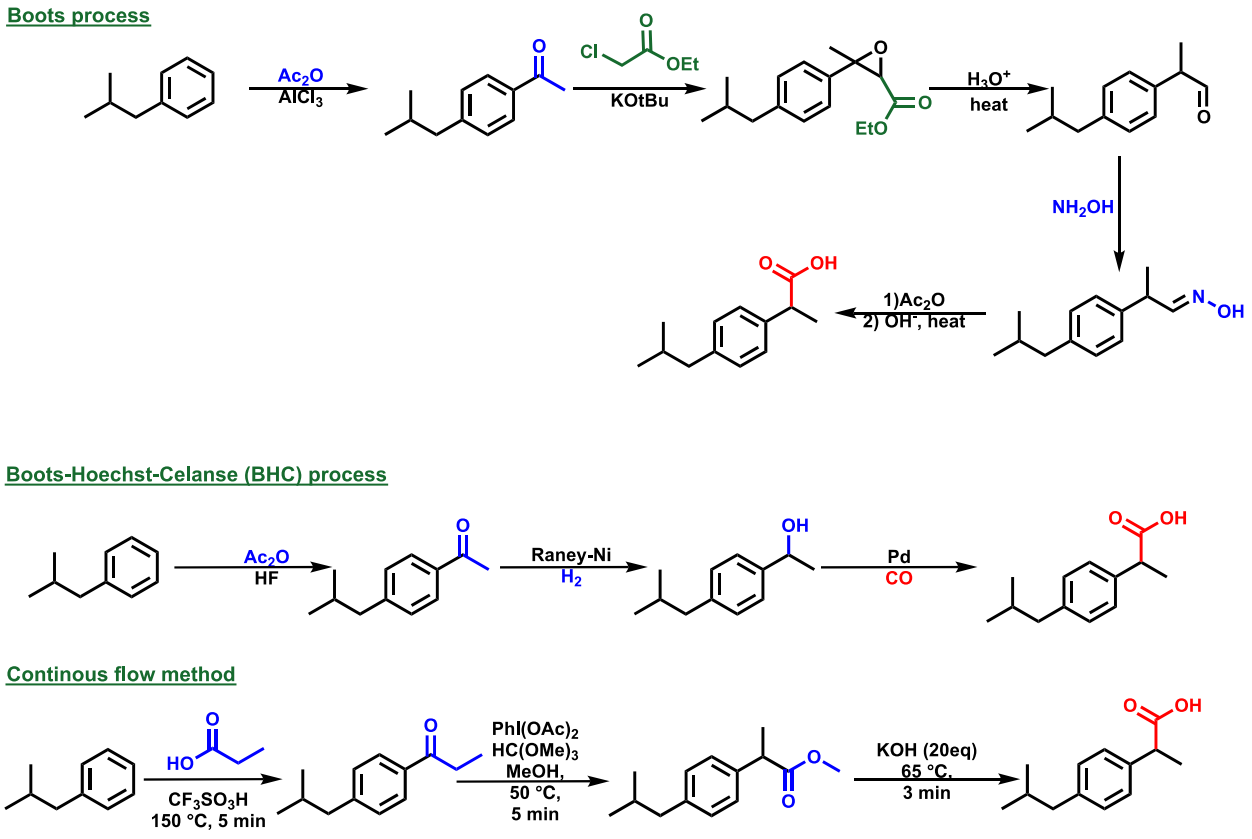

Ibuprofen can be directly synthesized from isobutyl vinyl styrene using transition metal-catalyzed hydrocarboxylation methods (Scheme 1.7). In 2012, Thomas reported an iron-catalyzed hydrocarboxylation of vinyl arenes using atmospheric CO_2 as C1 feedstock. Using this method, ibuprofen was synthesized in excellent yield with high regioselectivity. Further mechanistic studies demonstrated that the reaction is composed of two steps, a highly regioselective and reversible iron-catalyzed hydrometallation followed by transmetalation that provides an α-aryl Grignard reagent. This α-aryl Grignard reagent goes onto react with CO_2.[60] Cp_2TiCl_2-catalyzed regioselective hydrocarboxylation, reported by the Xi group, also used CO_2 as the carbon source. This proved to hydrocarboxylate vinyl arenes efficiently with high regioselectivity in excellent yield. In this method, iPrMgCl was used as the hydride source.[61] Dual visible-light-Ni-catalyzed ligand-controlled Markovnikov and anti-Markovnikov

hydrocarboxyaltion of styrene was reported in 2018 by the König group.[62] They developed a simple, mild and highly regioselective aryl alkene hydrocarboxylation method using CO_2 as the C1 source.

Scheme 1.7 Ibuprofen synthesis by hydrocarboxylation methods

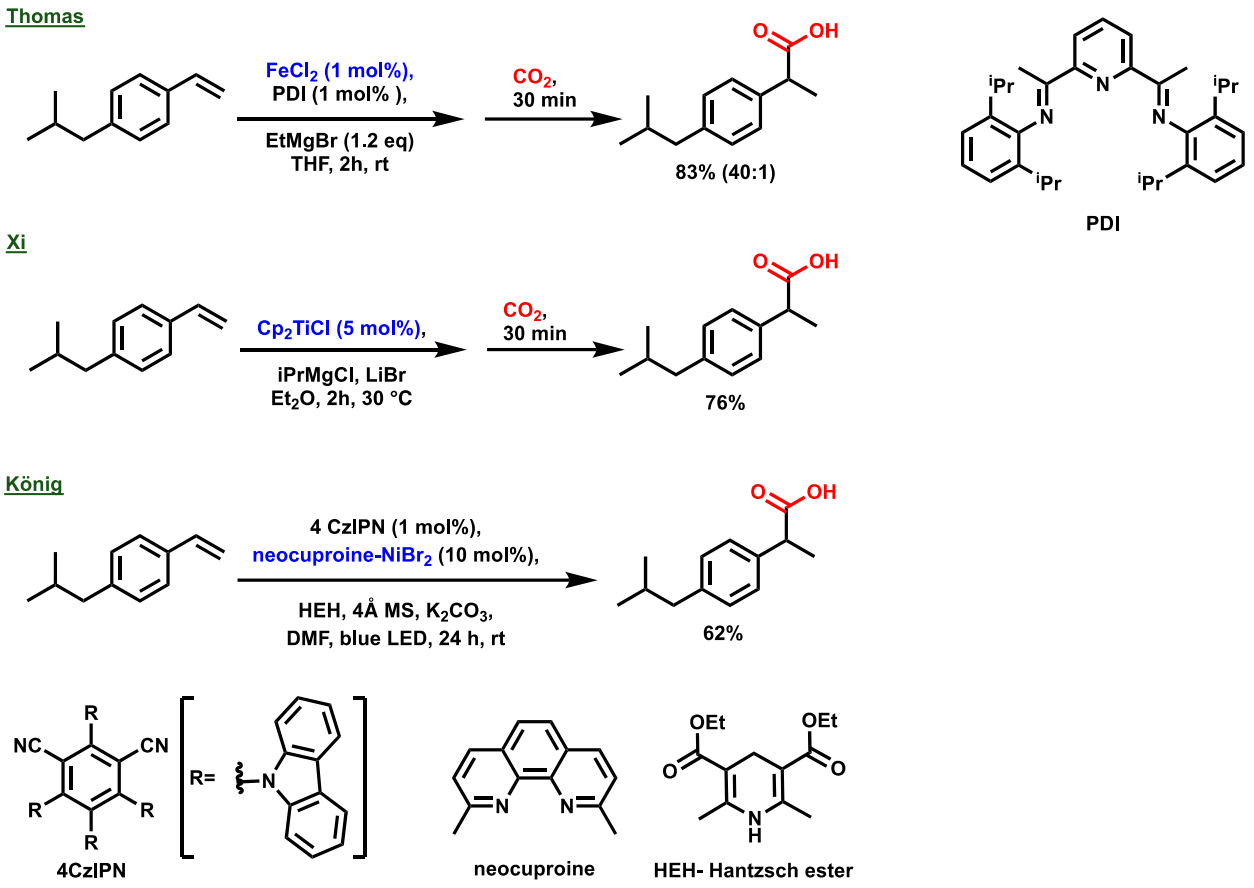

1.5 Copper-Catalyzed Boracarboxylation of Vinyl Arenes

In 2016, the Popp group reported a new reaction method to access boron containing ibuprofen and naproxen derivatives by using redox neutral copper catalysis.[63] Using this boracarboxylation strategy, the Popp group was able to install a carboxylic acid group and a boronic ester group into vinyl arenes. This difunctionalization chemistry is significant because it can directly make boron containing α-phenyl propionic acids. Since boron has taken on a lead role in the field of therapeutics recently, there is potential for boracarboxylative difunctionalization chemistry to be performed as discussed in earlier sections in this

chapter. A proposed catalytic cycle for this transformation is shown below (Scheme 1.8). In step I of the catalytic cycle, active catalyst [Cu]-O^{t}Bu undergoes transmetalation with B_2pin_2 to generate copper-boryl intermediate [Cu]Bpin. Subsequently, step II, vinyl styrene inserts into copper boryl to generate a copper-alkyl intermediate. By overcoming two side reactions of protonation and beta-hydride elimination, CO_2 is inserted into the copper-alkyl bond. This leads to the generation of a carboxylated-copper product in step III. Lastly, it undergoes salt metathesis to generate the carboxylated product in step IV.

Scheme 1.8 Popp group proposed boracarboxylation catalytic cycle

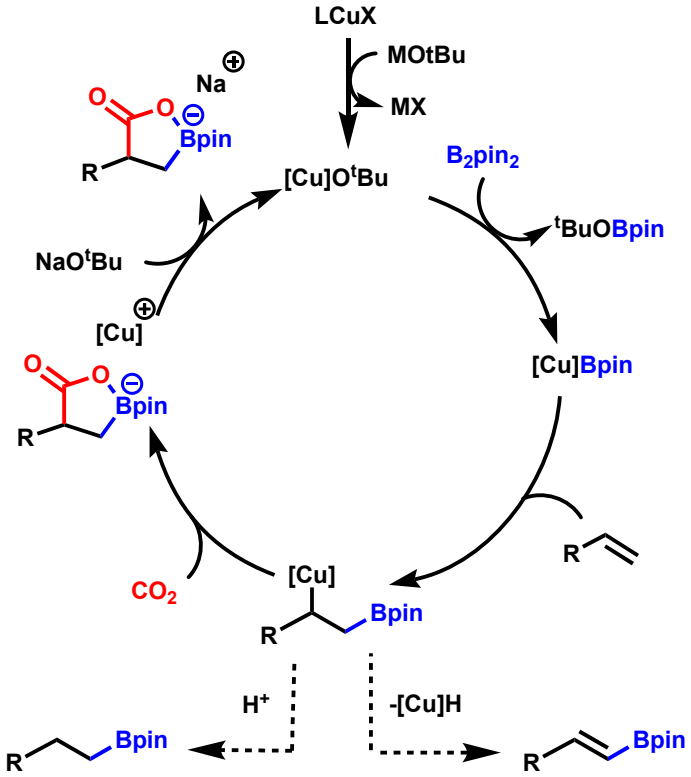

With the understanding of this mechanism, the Popp group started the process of reaction optimization (Table 1.2). Two side products were observed during the reaction: a hydroboration product (**2**), resulting from copper-alkyl intermediate proto-demetallation, and dehydrogenative borylation product (**3**), resulting from copper-alkyl intermediate β-hydride elimination. The boracarboxylated product (1) yield was increased with the electron donating nature of the ligand. (Entry 1-4). When bisphosphine ligands were used in the reaction, boracarboxylated product yield was reduced significantly (Entry 5-7). ICyCuCl gave

the boracarboxylated product in a 92% yield when strong σ-donating N-heterocyclic carbene (NHC) ligands were used. Except for IPrCuCl, NHC ligands such as IMesCuCl, SIMesCuCl and ICyCuCl gave product in good yield with less side product formation. Strongly sigma donating NHC ligands proved to be the most efficient for boracarboxylation of styrene (Entries 8-11) with ICyCuCl giving the product in an excellent yield (92%). In the absence of the ligand, CuCl did not give boracarboxylation product.

Table 1.2 Catalyst optimization for boracarboxylation of styrene

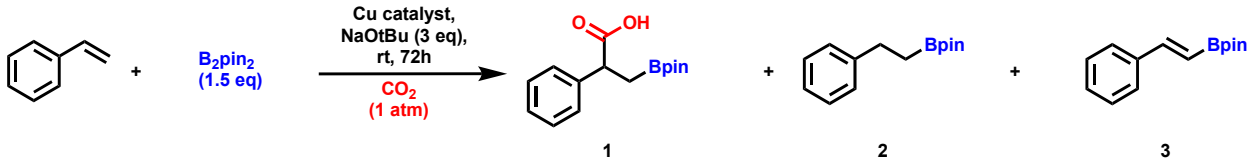

Entry	Catalyst[a]	% Yield (NMR)			Convn (%)
		1	2	3	styrene
1	PPh_3 + CuCl	1	22	13	99
2	$PMePh_2$ + CuCl	21	11	17	98
3	PEt_3 + CuCl	58	14	11	100
4	PCy_3 + CuCl	79	5	14	99
5	(R)-DTBM-SEGPHOS + CuCl	0	6	2	94
6	(R,R)-Me-BPE + CuCl	11	41	12	100
7	Xanthphos + CuCl	20	8	17	98
8	IPrCuCl	17	<1	<1	99
9	IMesCuCl	85	8	<1	100
10	SIMesCuCl	<70	<1	4	100
11	ICyCuCl	92	<1	3	100
12	CuCl	0	1	2	92

[a] CuCl (12 mol %) and phosphine ligand (13 mol %) or (NHC) CuCl (12 mol %). Yield and conversion were determined by ^{1}H NMR spectroscopy by using mesitylene as internal standard.

Next, the substrate scope was investigated by using optimized catalytic conditions. This set of catalytic conditions worked well with electron neutral and electron donating substrates such as methyl, tert-butyl, isobutyl, methoxy, phenoxy and naphthyl substrates, containing electron donating groups in *meta*- and *para*- positions. Substrates with sterically hindered groups at ortho positions gave diminished yields compared to meta and para substrates, such as o-methyl styrene. 2,4,6- trimethyl styrene only gave a 14% yield, even after the reaction was heated. Remarkably, steric hinderance on the arene ring had no effect on the regioselectivity. Reactions that occurred with slightly less electron rich substrates such as *p*-fluorostyrene and fused aromatic system 2-vinylnaphthalene resulted in the products and in 63% and 69% yields, respectively. Styrenes that contained moderate and strong electron withdrawing substituents such as chloro, bromo, cyano and trifluoromethyl did not provide boracarboxylation products, even when the reactions were heated. The main limitation of this catalytic system is that it does not grant access to the electron deficient styrenes, and the method requires high catalyst loading.

Scheme 1.9 Vinyl styrene boracarboxylation substrate scope

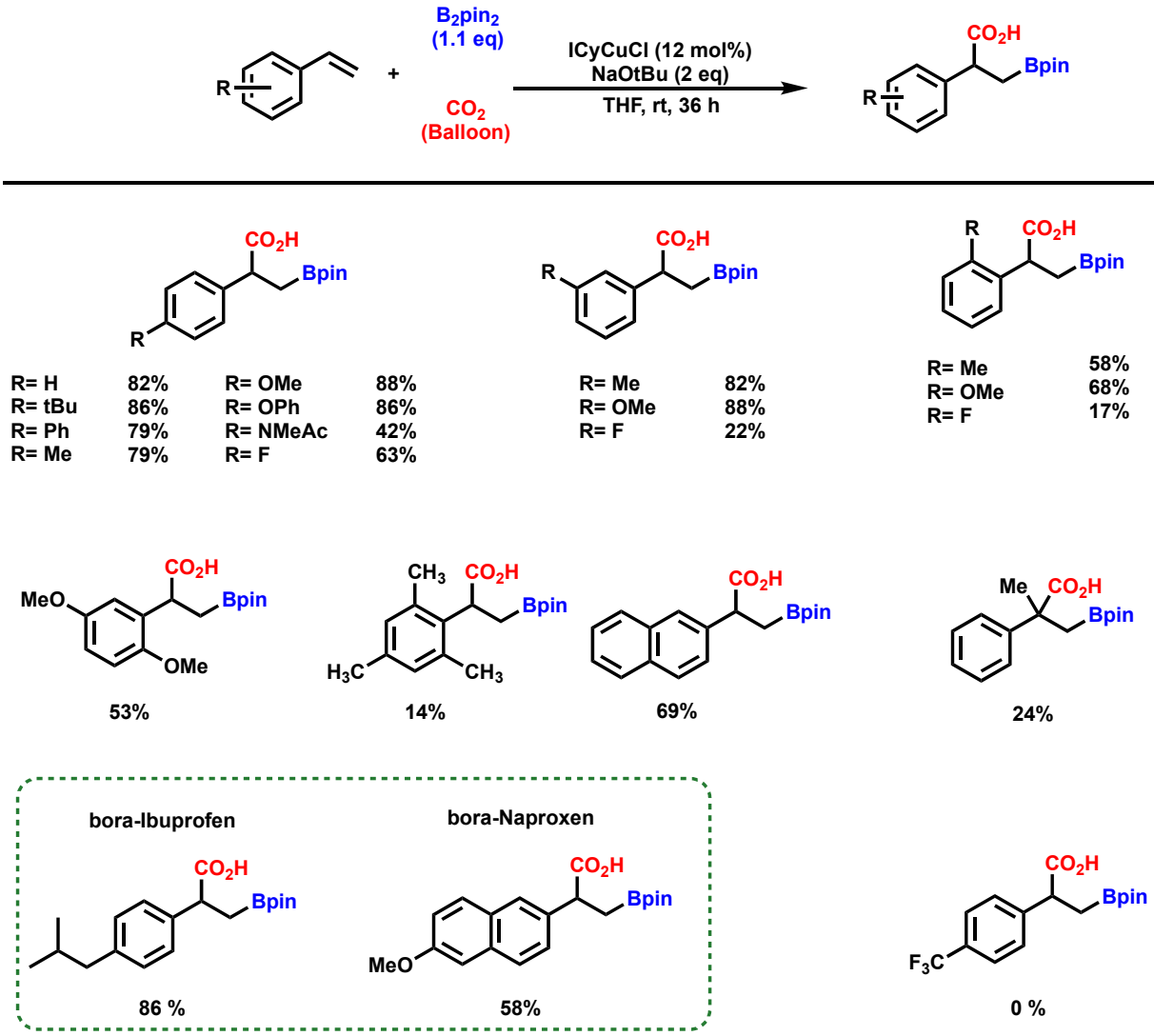

In this study, the Popp group reported that the synthesis of a novel boron functionalized Ibuprofen and Naproxen derivatives (*bora*-NSAIDs) resulted in 86% and 58% yields, respectively. These boracarboxylated compounds can be further derivatized to provide beneficial compounds under different reaction conditions (Scheme 1.10). Under oxidation conditions, the boron pinacol ester group was oxidized to a hydroxyl group, providing tropic acid. Silver-catalyzed fluorination, using Selectfluor as the fluorinating agent, resulted in the generation of fluorinated α-phenyl propionic acids. When

boracarboxylated product was reacted with KHF_2, a new example of organodifluoroboryl compound (borafluorolactonate salts) was obtained.

Scheme 1.10 Derivatization of boracarboxylated products

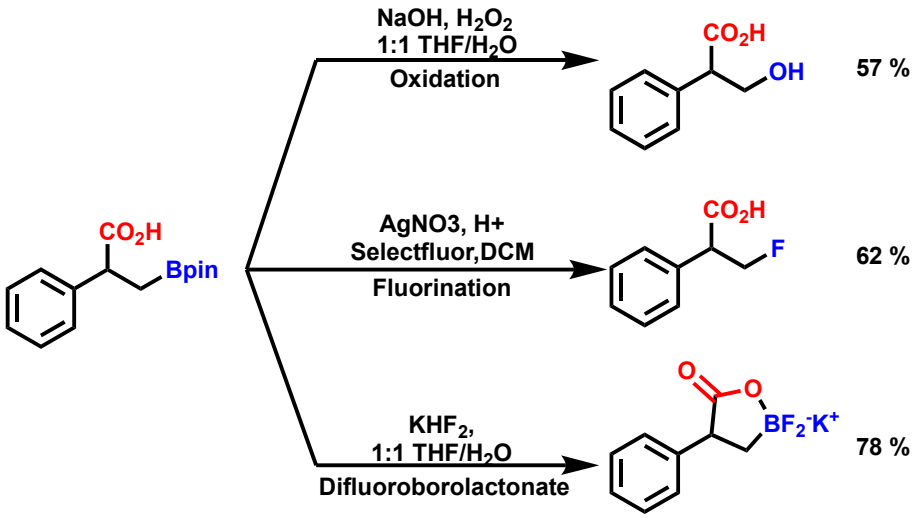

In 2019, the Popp group developed a catalytic system using a secondary PPh_3 ligand to overcome the limitations of the original redox-neutral copper catalytic system.[64] Electron deficient vinyl arenes substrates were inaccessible while using the initial boracarboxylation catalytic conditions.[63] According to literature, in reductive copper catalyst processes, addition of secondary ligands such as PPh_3 is believed to deactivate the decomposition of the catalyst while improving the reaction yield. [65,66] With the addition of 5-10 mol% PPh_3, the catalyst loading could be reduced from 12 mol% to 5 mol%. With these new catalytic conditions, they compared the vinyl arene boracarboxylation substrate scope for the initial catalytic conditions and the new catalytic conditions. This comparison was done using the product yields for each catalytic condition (Scheme 1.11).

For electron neutral substrates such as styrene, *p*-tertbutyl, *p*-methyl and *p*-isobutyl, slightly lower isolated yields were observed. The lower yields were attributed to the difficulty of removing the PPh_3 during product isolation. Heteroatom-group-substituted vinyl arenes were tolerated well under new catalytic conditions. A slightly lower yield compared to the initial conditions was observed with *p*-OMe. An improved yield was observed with *p*-*N*-methylamidostyrene. Using reaction condition B, electron deficient

vinyl arenes such as *p*-CN could be boracarboxylated in moderate yields and *p*-CF_3, *p*-Cl, *p*-AcO, and -C_6F_5 in lower yields (Scheme 1.11). These boracarboxylation products could not be obtained using the initial conditions (Condition A). Further, synthesis of two new boron containing NSAID derivatives in moderate yields was reported.

Scheme 1.11 Substrate scope for boracarboxylation of vinyl styrene using ICyCuCl catalytic system (Condition A) and ICyCuCl+ PPh_3 catalytic system (Condition B)

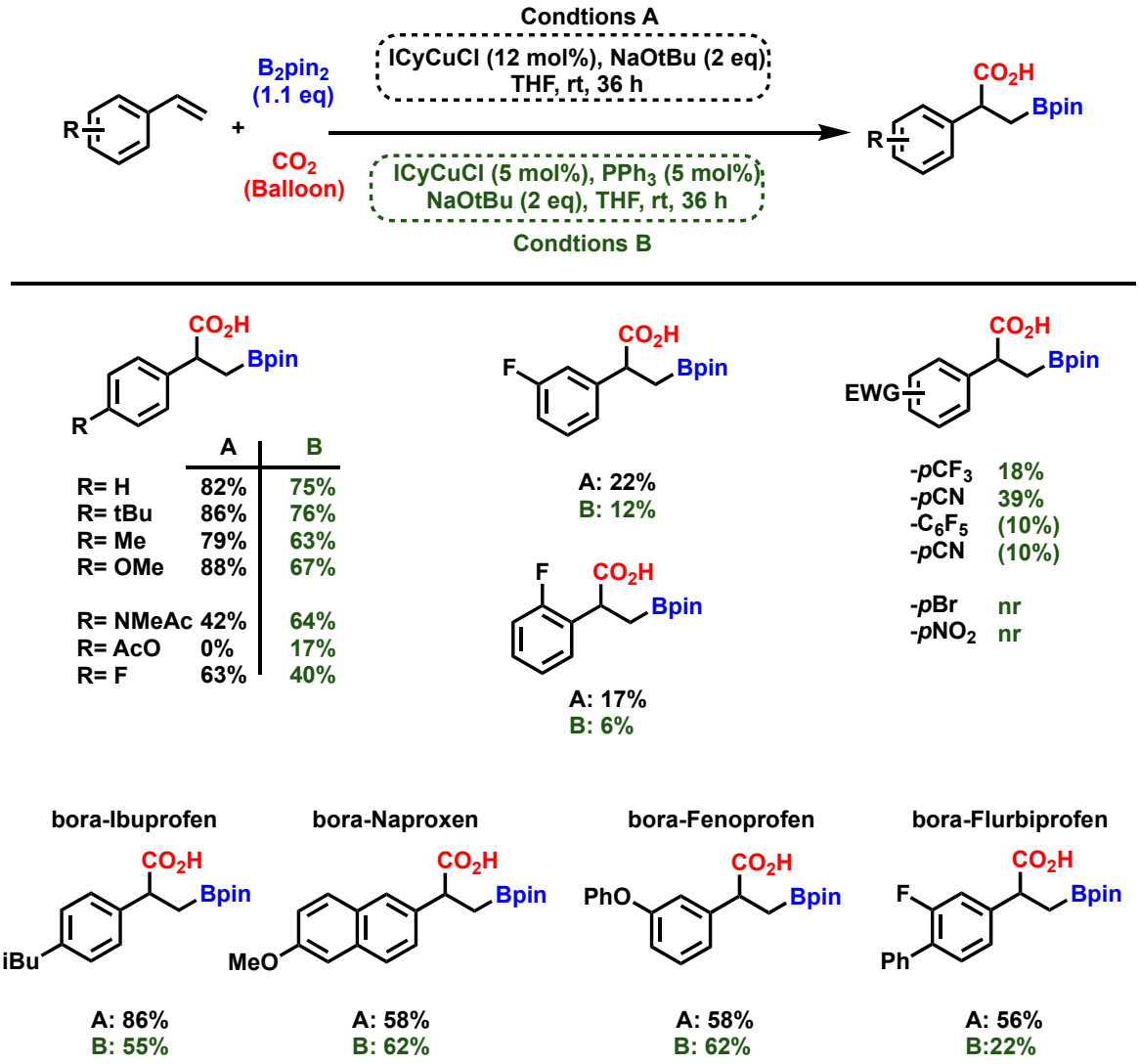

In 2022, the Popp group reported regioselective boracarboxylation of α-substituted vinyl arenes.[67] Using newly discovered conditions, they were able to synthesize α-quaternary carboxylic acids. Synthesis of quaternary centers via boracarboxylation is important because it provides direct access to synthetically and medicinally important carboxylic acids. In their initial boracarboxylation work, boracarboxylation of α-methylstyrene was reported in only an 11% yield. With optimized SIMesCuCl (13 mol%) catalytic system, they were able to boracarboxylate α-methylstyrene derivatives in good to moderate yields.

Scheme 1.12 α-Methylstyrene boracarboxylation substrate scope

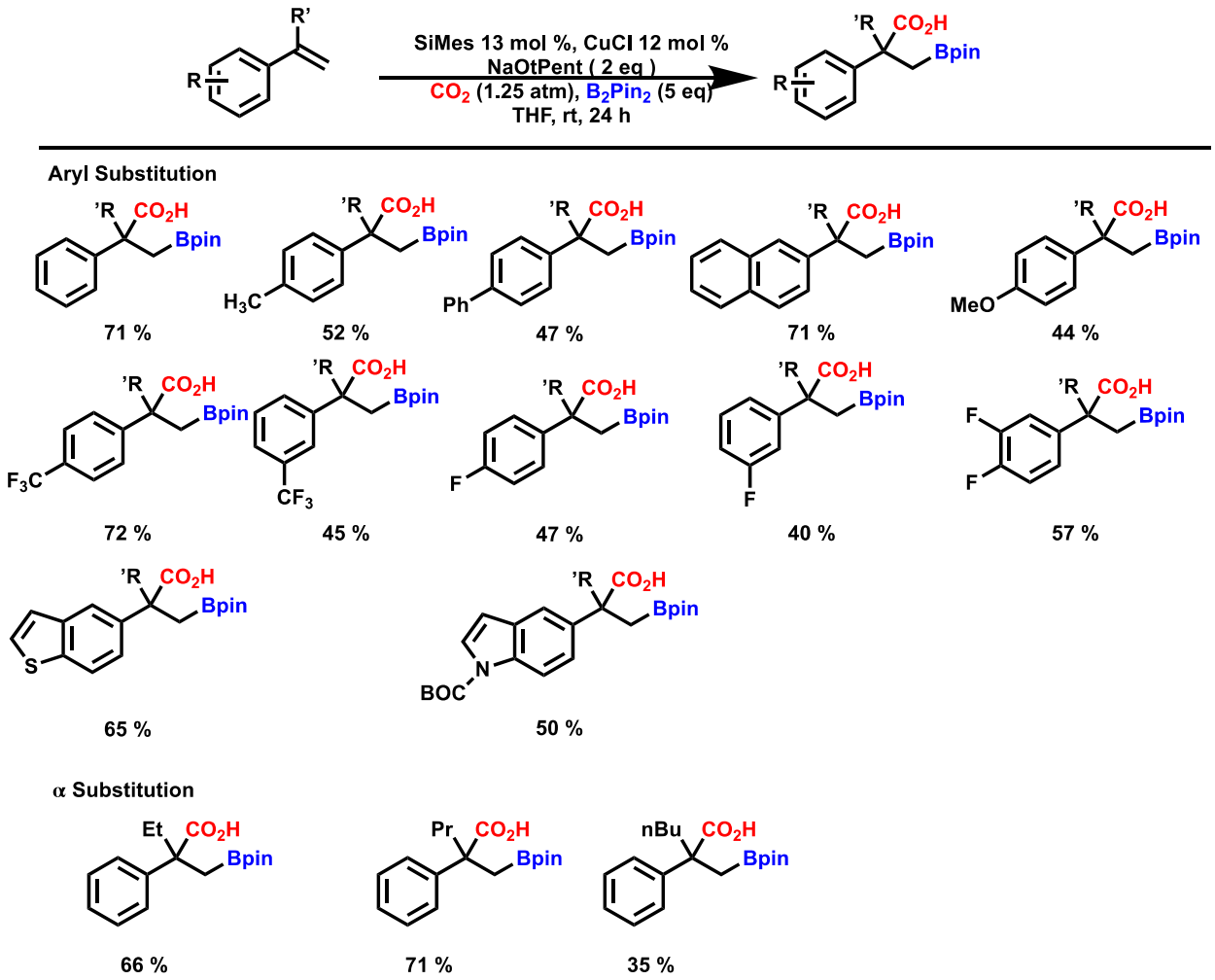

A broad substrate scope was established for the boracarboxylation of α-substituted vinyl arenes. For α-methyl substituted vinyl arenes, electron-neutral (styrene, *p*-methyl, *p*-phenyl, naphthyl) and electron-rich *p*-OMe vinyl arene substrates, products were obtained in good to moderate yields. Electron-rich heteroarenes (benzothiophene and indole) were boracarboxylated successfully to obtain products in moderate yields. Similarly, electron deficient *p*-CF_3, *o*-CF_3, *p*-F, *o*-F and 3,4-difluoro α-methyl vinyl arene substrates were boracarboxylated in good to moderate yields. This catalytic system tolerated other α-substituents well, if the substituent group was small, such as ethyl and propyl substrates. If the substituent group was bulkier, such as *n*-butyl, product yield decreased. SiMesCuCl catalyzed boracarboxylation of α-substituted vinyl arenes provided access to diverse group quaternary α-carboxylic acid products containing a β-boronic ester functional group.

1.6 Summary

In this chapter, the properties of organoboron compounds as related to their applications to medicinal chemistry have been discussed. Medicinal applications include therapeutic agents, boron neutron capture therapy, and their applications as saccharides and anion sensors. Under physiological conditions, boronic acids and boron esters can convert from trivalent sp^2 hybridization to tetravalent sp^3 hybridization with the addition of nucleophiles. This is useful in enzyme inhibition processes. Copper-catalyzed boracarboxylation methodology reported by the Popp group, has given direct access to boron functionalized non-steroidal anti-inflammatory drugs (*bora*-NSAIDs). These *bora*-NSAIDs and related compounds may have interesting pharmacological properties.

In the following chapters, the derivatization of boracarboxylated products toward future efforts to expand their medicinal chemistry and synthetic applications will be discussed. Chapter 2 examines the isolation of lactone boronic acid/ester substrates and further derivatization of *bora*-ibuprofen by using transesterification and transamination strategies. Chapter 3 discusses the synthesis of bora-ibuprofen using Suzuki cross coupling and newly discovered benchtop boracarboxylation catalytic method. Chapter 4 examines the synthesis of air and moisture stable organo difluoroboronates using milder reaction

conditions. Lastly in chapter 5, the dynamic equilibrium of DABO boronates in methanol medium is discussed.

1.7 References

(1) Johnson, G. T. Boron. In *Hamilton & Hardy's Industrial Toxicology*; Harbison, R. D., Bourgeois, M. M., Johnson, G. T., Eds.; John Wiley & Sons, Inc.: Hoboken, New Jersey, 2015; pp 79–84. https://doi.org/10.1002/9781118834015.ch11.

(2) Pennington, T. H. Listerism, Its Decline and Its Persistence: The Introduction of Aseptic Surgical Techniques in Three British Teaching Hospitals, 1890–99. *Med. Hist.* **1995**, *39* (1), 35–60. https://doi.org/10.1017/S0025727300059470.

(3) Gentz, M. C.; Grace, J. K. A Review of Boron Toxicity in Insects With an Emphasis on Termites. **2006**, *23*, 7.

(4) Pfeiffer, C. C. BORIC ACID OINTMENT: A STUDY OF POSSIBLE INTOXICATION IN THE TREATMENT OF BURNS. *J. Am. Med. Assoc.* **1945**, *128* (4), 266. https://doi.org/10.1001/jama.1945.02860210022006.

(5) Baker, S. J.; Ding, C. Z.; Akama, T.; Zhang, Y.-K.; Hernandez, V.; Xia, Y. Therapeutic Potential of Boron-Containing Compounds. *Future Med. Chem.* **2009**, *1* (7), 1275–1288. https://doi.org/10.4155/fmc.09.71.

(6) Das, B. C.; Thapa, P.; Karki, R.; Schinke, C.; Das, S.; Kambhampati, S.; Banerjee, S. K.; Van Veldhuizen, P.; Verma, A.; Weiss, L. M.; Evans, T. Boron Chemicals in Diagnosis and Therapeutics. *Future Med. Chem.* **2013**, *5* (6), 653–676. https://doi.org/10.4155/fmc.13.38.

(7) Bouza, A. A.; Swanson, H. C.; Smolen, K. A.; VanDine, A. L.; Taracila, M. A.; Romagnoli, C.; Caselli, E.; Prati, F.; Bonomo, R. A.; Powers, R. A.; Wallar, B. J. Structure-Based Analysis of Boronic Acids as Inhibitors of *Acinetobacter* -Derived Cephalosporinase-7, a Unique Class C β-Lactamase. *ACS Infect. Dis.* **2018**, *4* (3), 325–336. https://doi.org/10.1021/acsinfecdis.7b00152.

(8) Connolly, B. A.; Sanford, D. G.; Chiluwal, A. K.; Healey, S. E.; Peters, D. E.; Dimare, M. T.; Wu, W.; Liu, Y.; Maw, H.; Zhou, Y.; Li, Y.; Jin, Z.; Sudmeier, J. L.; Lai, J. H.; Bachovchin, W. W. Dipeptide Boronic Acid Inhibitors of Dipeptidyl Peptidase IV: Determinants of Potency and in Vivo Efficacy and Safety. *J. Med. Chem.* **2008**, *51* (19), 6005–6013. https://doi.org/10.1021/jm800390n.

(9) Borek, B.; Gajda, T.; Golebiowski, A.; Blaszczyk, R. Boronic Acid-Based Arginase Inhibitors in Cancer Immunotherapy. *Bioorg. Med. Chem.* **2020**, *28* (18), 115658. https://doi.org/10.1016/j.bmc.2020.115658.

(10) Yang, W.; Gao, X.; Wang, B. Boronic Acid Compounds as Potential Pharmaceutical Agents. *Med. Res. Rev.* **2003**, *23* (3), 346–368. https://doi.org/10.1002/med.10043.

(11) Field-Smith, A.; Morgan, G. J.; Davies, F. E. Bortezomib (Velcade?) In the Treatment of Multiple Myeloma. *Ther. Clin. Risk Manag.* **2006**, *2* (3), 271–279. https://doi.org/10.2147/tcrm.2006.2.3.271.

(12) Rock, K. L.; Gramm, C.; Rothstein, L.; Clark, K.; Stein, R.; Dick, L.; Hwang, D.; Goldberg, A. L. Inhibitors of the Proteasome Block the Degradation of Most Cell Proteins and the Generation of Peptides Presented on MHC Class I Molecules. *Cell* **1994**, *78* (5), 761–771. https://doi.org/10.1016/S0092-8674(94)90462-6.

(13) Adams, J.; Stein, R. Chapter 28. Novel Inhibitors of the Proteasome and Their Therapeutic Use in Inflammation. In *Annual Reports in Medicinal Chemistry*; Elsevier, 1996; Vol. 31, pp 279–288. https://doi.org/10.1016/S0065-7743(08)60467-4.

(14) Adams, J.; Palombella, V. J.; Sausville, E. A.; Johnson, J.; Destree, A.; Lazarus, D. D.; Maas, J.; Pien, C. S.; Prakash, S.; Elliott, P. J. Proteasome Inhibitors: A Novel Class of Potent and Effective Antitumor Agents. *Cancer Res.* **1999**, *59* (11), 2615–2622.

(15) Baker, S. J.; Zhang, Y.-K.; Akama, T.; Lau, A.; Zhou, H.; Hernandez, V.; Mao, W.; Alley, M. R. K.; Sanders, V.; Plattner, J. J. Discovery of a New Boron-Containing Antifungal Agent, 5-Fluoro-1,3-Dihydro-1-Hydroxy-2,1- Benzoxaborole (AN2690), for the Potential Treatment of Onychomycosis. *J. Med. Chem.* **2006**, *49* (15), 4447–4450. https://doi.org/10.1021/jm0603724.
(16) Rock, F. L.; Mao, W.; Yaremchuk, A.; Tukalo, M.; Crépin, T.; Zhou, H.; Zhang, Y.-K.; Hernandez, V.; Akama, T.; Baker, S. J.; Plattner, J. J.; Shapiro, L.; Martinis, S. A.; Benkovic, S. J.; Cusack, S.; Alley, M. R. K. An Antifungal Agent Inhibits an Aminoacyl-TRNA Synthetase by Trapping TRNA in the Editing Site. *Science* **2007**, *316* (5832), 1759–1761. https://doi.org/10.1126/science.1142189.
(17) Raedler, L. A. Ninlaro (Ixazomib): First Oral Proteasome Inhibitor Approved for the Treatment of Patients with Relapsed or Refractory Multiple Myeloma. **2016**, *9*, 4.
(18) Zane, L.; Chanda, S.; Jarnagin, K.; Nelson, D.; Spelman, L.; Gold, L. S. Crisaborole and Its Potential Role in Treating Atopic Dermatitis: Overview of Early Clinical Studies. *Immunotherapy* **2016**, *8* (8), 853–866. https://doi.org/10.2217/imt-2016-0023.
(19) Dhillon, S. Meropenem/Vaborbactam: A Review in Complicated Urinary Tract Infections. *Drugs* **2018**, *78* (12), 1259–1270. https://doi.org/10.1007/s40265-018-0966-7.
(20) Weston, G. S.; Blázquez, J.; Baquero, F.; Shoichet, B. K. Structure-Based Enhancement of Boronic Acid-Based Inhibitors of AmpC β-Lactamase. *J. Med. Chem.* **1998**, *41* (23), 4577–4586. https://doi.org/10.1021/jm980343w.
(21) Barth, R. F.; Coderre, J. A.; Vicente, M. G. H.; Blue, T. E. Boron Neutron Capture Therapy of Cancer: Current Status and Future Prospects. *Clin. Cancer Res.* **2005**, *11* (11), 3987–4002. https://doi.org/10.1158/1078-0432.CCR-05-0035.
(22) He, H.; Li, J.; Jiang, P.; Tian, S.; Wang, H.; Fan, R.; Liu, J.; Yang, Y.; Liu, Z.; Wang, J. The Basis and Advances in Clinical Application of Boron Neutron Capture Therapy. *Radiat. Oncol.* **2021**, *16* (1), 216. https://doi.org/10.1186/s13014-021-01939-7.
(23) Kageji, T.; Nagahiro, S.; Mizobuchi, Y.; Matsuzaki, K.; Nakagawa, Y.; Kumada, H. Boron Neutron Capture Therapy (BNCT) for Newly-Diagnosed Glioblastoma: Comparison of Clinical Results Obtained with BNCT and Conventional Treatment. *J. Med. Invest.* **2014**, *61* (3.4), 254–263. https://doi.org/10.2152/jmi.61.254.
(24) Yang, W.; Barth, R. F.; Rotaru, J. H.; Boesel, C. P.; Wilkie, D. A.; Bresnahan, J. C.; Hadjiconstantinou, M.; Goettl, V. M.; Joel, D. D.; Nawrocky, M. M. Boron Neutron Capture Therapy of Brain Tumors: Functional and Neuropathologic Effects of Blood–Brain Barrier Disruption and Intracarotid Injection of Sodium Borocaptate and Boronophenylalanine. 12.
(25) Heikkinen, S.; Kangasm ki, A.; Timonen, M.; Kankaanranta, L.; H kkinen, A.-M.; Lundbom, N.; V h talo, J.; Savolainen, S. ^{1}H MRS of a Boron Neutron Capture Therapy ^{10}B-Carrier, L-*p*-Boronophenylalanine Fructose Complex, BPA F: Phantom Studies at 1.5 and 3.0 T. *Phys. Med. Biol.* **2003**, *48* (8), 1027–1039. https://doi.org/10.1088/0031-9155/48/8/305.
(26) Nakashima H. The New Generation of Particle Therapy Focused on Boron Element (Boron Neutron Capture Therapy; BNCT) —The World's First Approved BNCT Drug—. *YAKUGAKU ZASSHI* **2022**, *142* (2), 155–164. https://doi.org/10.1248/yakushi.21-00173-4.
(27) Coderre, J. A.; Glass, J. D.; Fairchild, R. G.; Roy, U.; Cohen, S.; Fand, I. Selective Targeting of Boronophenylalanine to Melanoma in BALB/c Mice for Neutron Capture Therapy. 7.
(28) Hirose, K.; Konno, A.; Hiratsuka, J.; Yoshimoto, S.; Kato, T.; Ono, K.; Otsuki, N.; Hatazawa, J.; Tanaka, H.; Takayama, K.; Wada, H.; Suzuki, M.; Sato, M.; Yamaguchi, H.; Seto, I.; Ueki, Y.; Iketani, S.; Imai, S.; Nakamura, T.; Ono, T.; Endo, H.; Azami, Y.; Kikuchi, Y.; Murakami, M.; Takai, Y. Boron Neutron Capture Therapy Using Cyclotron-Based Epithermal Neutron Source and Borofalan (10B) for Recurrent or Locally Advanced Head and Neck Cancer (JHN002): An Open-Label Phase II Trial. *Radiother. Oncol.* **2021**, *155*, 182–187. https://doi.org/10.1016/j.radonc.2020.11.001.
(29) Hall, D. G. 1 Structure, Properties, and Preparation of Boronic Acid Derivatives. 134.
(30) Lorand, J. P.; Edwards, J. O. Polyol Complexes and Structure of the Benzeneboronate Ion. *J. Org. Chem.* **1959**, *24* (6), 769–774. https://doi.org/10.1021/jo01088a011.

(31) Conner, J. M.; Bulgrin, V. C. Equilibria between Borate Ion and Some Polyols in Aqueous Solution. *J. Inorg. Nucl. Chem.* **1967**, *29* (8), 1953–1961. https://doi.org/10.1016/0022-1902(67)80455-X.
(32) Yoon, J.; Czarnik, A. W. Fluorescent Chemosensors of Carbohydrates. A Means of Chemically Communicating the Binding of Polyols in Water Based on Chelation-Enhanced Quenching. *J. Am. Chem. Soc.* **1992**, *114* (14), 5874–5875. https://doi.org/10.1021/ja00040a067.
(33) James, T. D.; Sandanayake, K. R. A. S.; Shinkai, S. Novel Photoinduced Electron-Transfer Sensor for Saccharides Based on the Interaction of Boronic Acid and Amine. *J. Chem. Soc. Chem. Commun.* **1994**, No. 4, 477. https://doi.org/10.1039/c39940000477.
(34) Ni, W.; Kaur, G.; Springsteen, G.; Wang, B.; Franzen, S. Regulating the Fluorescence Intensity of an Anthracene Boronic Acid System: A B–N Bond or a Hydrolysis Mechanism? *Bioorganic Chem.* **2004**, *32* (6), 571–581. https://doi.org/10.1016/j.bioorg.2004.06.004.
(35) Ouchi, K.; Colyer, C. L.; Sebaiy, M.; Zhou, J.; Maeda, T.; Nakazumi, H.; Shibukawa, M.; Saito, S. Molecular Design of Boronic Acid-Functionalized Squarylium Cyanine Dyes for Multiple Discriminant Analysis of Sialic Acid in Biological Samples: Selectivity toward Monosaccharides Controlled by Different Alkyl Side Chain Lengths. *Anal. Chem.* **2015**, *87* (3), 1933–1940. https://doi.org/10.1021/ac504201b.
(36) Scott, E.; Munkley, J. Glycans as Biomarkers in Prostate Cancer. *Int. J. Mol. Sci.* **2019**, *20* (6), 1389. https://doi.org/10.3390/ijms20061389.
(37) Liu, Y.; Zhu, J.; Xu, Y.; Qin, Y.; Jiang, D. Boronic Acid Functionalized Aza-Bodipy (AzaBDPBA) Based Fluorescence Optodes for the Analysis of Glucose in Whole Blood. *ACS Appl. Mater. Interfaces* **2015**, *7* (21), 11141–11145. https://doi.org/10.1021/acsami.5b00265.
(38) Samaniego Lopez, C.; Lago Huvelle, M. A.; Uhrig, M. L.; Coluccio Leskow, F.; Spagnuolo, C. C. Recognition of Saccharides in the NIR Region with a Novel Fluorogenic Boronolectin: In Vitro and Live Cell Labeling. *Chem. Commun.* **2015**, *51* (23), 4895–4898. https://doi.org/10.1039/C4CC10425K.
(39) Cao, Z.; Cao, Y.; Kubota, R.; Sasaki, Y.; Asano, K.; Lyu, X.; Zhang, Z.; Zhou, Q.; Zhao, X.; Xu, X.; Wu, S.; Minami, T.; Liu, Y. Fluorescence Anion Chemosensor Array Based on Pyrenylboronic Acid. *Front. Chem.* **2020**, *8*, 414. https://doi.org/10.3389/fchem.2020.00414.
(40) Cooper, C. R. Selective Fluorescence Detection of Fluoride Using Boronic Acids. *Chem. Commun.* **1998**, No. 13, 1365–1366. https://doi.org/10.1039/a801693c.
(41) Jun, E. J.; Xu, Z.; Lee, M.; Yoon, J. A Ratiometric Fluorescent Probe for Fluoride Ions with a Tridentate Receptor of Boronic Acid and Imidazolium. *Tetrahedron Lett.* **2013**, *54* (22), 2755–2758. https://doi.org/10.1016/j.tetlet.2013.02.112.
(42) Nishimura, T.; Xu, S.-Y.; Jiang, Y.-B.; Fossey, J. S.; Sakurai, K.; Bull, S. D.; James, T. D. A Simple Visual Sensor with the Potential for Determining the Concentration of Fluoride in Water at Environmentally Significant Levels. *Chem Commun* **2013**, *49* (5), 478–480. https://doi.org/10.1039/C2CC36107H.
(43) Guan, R.; Chen, H.; Cao, F.; Cao, D.; Deng, Y. Two Fluorescence Turn-on Chemosensors for Cyanide Anions Based on Pyridine Cation and the Boronic Acid Moiety. *Inorg. Chem. Commun.* **2013**, *38*, 112–114. https://doi.org/10.1016/j.inoche.2013.10.024.
(44) Desborough, M. J. R.; Keeling, D. M. The Aspirin Story - from Willow to Wonder Drug. *Br. J. Haematol.* **2017**, *177* (5), 674–683. https://doi.org/10.1111/bjh.14520.
(45) Department of Pharmacology, Ondokuz Mayıs University School of Medicine, Samsun, Turkey; Gunaydin, C.; Bilge, S. S.; Department of Pharmacology, Ondokuz Mayıs University School of Medicine, Samsun, Turkey. Effects of Nonsteroidal Anti-Inflammatory Drugs at the Molecular Level. *Eurasian J. Med.* **2018**, *50* (2). https://doi.org/10.5152/eurasianjmed.2018.0010.
(46) Cashman, J. N. The Mechanisms of Action of NSAIDs in Analgesia: *Drugs* **1996**, *52* (Supplement 5), 13–23. https://doi.org/10.2165/00003495-199600525-00004.
(47) VANE, J. R. Inhibition of Prostaglandin Synthesis as a Mechanism of Action for Aspirin-like Drugs. *Nature. New Biol.* **1971**, *231* (25), 232–235. https://doi.org/10.1038/newbio231232a0.

(48) Coxib and Traditional NSAID Trialists' (CNT) Collaboration, Bhala N, Emberson J, Merhi A, Abramson S, Arber N, Baron JA, Bombardier C, Cannon C, Farkouh ME, FitzGerald GA, Goss P, Halls H, Hawk E, Hawkey C, Hennekens C, Hochberg M, Holland LE, Kearney PM, Laine L, Lanas A, Lance P, Laupacis A, Oates J, Patrono C, Schnitzer TJ, Solomon S, Tugwell P, Wilson K, Wittes J, Baigent C. Vascular and Upper Gastrointestinal Effects of Non-Steroidal Anti-Inflammatory Drugs: Meta-Analyses of Individual Participant Data from Randomised Trials. Lancet. 2013 Aug 31;382(9894):769-79. Doi: 10.1016/S0140-6736(13)60900-9. Epub 2013 May 30. PMID: 23726390; PMCID: PMC3778977.

(49) Lichtenstein, D. R.; Syngal, S.; Wolfe, M. M. Nonsteroidal Antiinflammatory Drugs and the Gastrointestinal Tract the Double-Edged Sword. *Arthritis Rheum.* **1995**, *38* (1), 5–18. https://doi.org/10.1002/art.1780380103.

(50) Peng, S.; Duggan, A. Gastrointestinal Adverse Effects of Non-Steroidal Anti-Inflammatory Drugs. *Expert Opin. Drug Saf.* **2005**, *4* (2), 157–169. https://doi.org/10.1517/14740338.4.2.157.

(51) Koehne, C.-H.; Dubois, R. N. COX-2 Inhibition and Colorectal Cancer. *Semin. Oncol.* **2004**, *31*, 12–21. https://doi.org/10.1053/j.seminoncol.2004.03.041.

(52) Topol, E. J. Failing the Public Health — Rofecoxib, Merck, and the FDA. *N. Engl. J. Med.* **2004**, *351* (17), 1707–1709. https://doi.org/10.1056/NEJMp048286.

(53) Vane, J. R.; Bakhle, Y. S.; Botting, R. M. CYCLOOXYGENASES 1 AND 2. *Annu. Rev. Pharmacol. Toxicol.* **1998**, *38* (1), 97–120. https://doi.org/10.1146/annurev.pharmtox.38.1.97.

(54) Mengle-Gaw, L. J.; Schwartz, B. D. Cyclooxygenase-2 Inhibitors: Promise or Peril? *Mediators Inflamm.* **2002**, *11* (5), 275–286. https://doi.org/10.1080/09629350290000041.

(55) Schildknecht, S.; Daiber, A.; Ghisla, S.; Cohen, R. A.; Bachschmid, M. M. Acetaminophen Inhibits Prostanoid Synthesis by Scavenging the PGHS-activator Peroxynitrite. *FASEB J.* **2008**, *22* (1), 215–224. https://doi.org/10.1096/fj.06-8015com.

(56) Blobaum, A. L.; Marnett, L. J. Structural and Functional Basis of Cyclooxygenase Inhibition. *J. Med. Chem.* **2007**, *50* (7), 1425–1441. https://doi.org/10.1021/jm0613166.

(57) Acetti, D.; Brenna, E.; Fronza, G.; Fuganti, C. Monitoring the Synthetic Procedures of Commercial Drugs by 2H NMR Spectroscopy: The Case of Ibuprofen and Naproxen. *Talanta* **2008**, *76* (3), 651–655. https://doi.org/10.1016/j.talanta.2008.04.009.

(58) Montes, F.; Gernaey, K. V.; Sin, G. Uncertainty and Sensitivity Analysis for an Ibuprofen Synthesis Model Based on Hoechst Path. In *Computer Aided Chemical Engineering*; Elsevier, 2017; Vol. 40, pp 163–168. https://doi.org/10.1016/B978-0-444-63965-3.50029-5.

(59) Bogdan, A. R.; Poe, S. L.; Kubis, D. C.; Broadwater, S. J.; McQuade, D. T. The Continuous-Flow Synthesis of Ibuprofen. *Angew. Chem.* **2009**, *121* (45), 8699–8702. https://doi.org/10.1002/ange.200903055.

(60) Greenhalgh, M. D.; Thomas, S. P. Iron-Catalyzed, Highly Regioselective Synthesis of α-Aryl Carboxylic Acids from Styrene Derivatives and CO_2. *J. Am. Chem. Soc.* **2012**, *134* (29), 11900–11903. https://doi.org/10.1021/ja3045053.

(61) Shao, P.; Wang, S.; Chen, C.; Xi, C. Cp_2TiCl_2-Catalyzed Regioselective Hydrocarboxylation of Alkenes with CO_2. *Org. Lett.* **2016**, *18* (9), 2050–2053. https://doi.org/10.1021/acs.orglett.6b00665.

(62) Meng, Q.-Y.; Wang, S.; Huff, G. S.; König, B. Ligand-Controlled Regioselective Hydrocarboxylation of Styrenes with CO_2 by Combining Visible Light and Nickel Catalysis. *J. Am. Chem. Soc.* **2018**, *140* (9), 3198–3201. https://doi.org/10.1021/jacs.7b13448.

(63) Butcher, T. W.; McClain, E. J.; Hamilton, T. G.; Perrone, T. M.; Kroner, K. M.; Donohoe, G. C.; Akhmedov, N. G.; Petersen, J. L.; Popp, B. V. Regioselective Copper-Catalyzed Boracarboxylation of Vinyl Arenes. *Org. Lett.* **2016**, *18* (24), 6428–6431. https://doi.org/10.1021/acs.orglett.6b03326.

(64) Perrone, T. M.; Gregory, A. S.; Knowlden, S. W.; Ziemer, N. R.; Alsulami, R. N.; Petersen, J. L.; Popp, B. V. Beneficial Effect of a Secondary Ligand on the Catalytic Difunctionalization of Vinyl Arenes with Boron and CO_2. *ChemCatChem* **2019**, *11* (23), 5814–5820. https://doi.org/10.1002/cctc.201901197.

(65) Ascic, E.; Buchwald, S. L. Highly Diastereo- and Enantioselective CuH-Catalyzed Synthesis of 2,3-Disubstituted Indolines. *J. Am. Chem. Soc.* **2015**, *137* (14), 4666–4669. https://doi.org/10.1021/jacs.5b02316.
(66) Bandar, J. S.; Ascic, E.; Buchwald, S. L. Enantioselective CuH-Catalyzed Reductive Coupling of Aryl Alkenes and Activated Carboxylic Acids. *J. Am. Chem. Soc.* **2016**, *138* (18), 5821–5824. https://doi.org/10.1021/jacs.6b03086.
(67) Knowlden, S. W.; Popp, B. V. Regioselective Boracarboxylation of α-Substituted Vinyl Arenes. *Organometallics* **2022**, *41* (14), 1883–1891. https://doi.org/10.1021/acs.organomet.2c00184.

Chapter II

Synthesis of Novel Multifunctional *bora*-Ibuprofen Derivatives

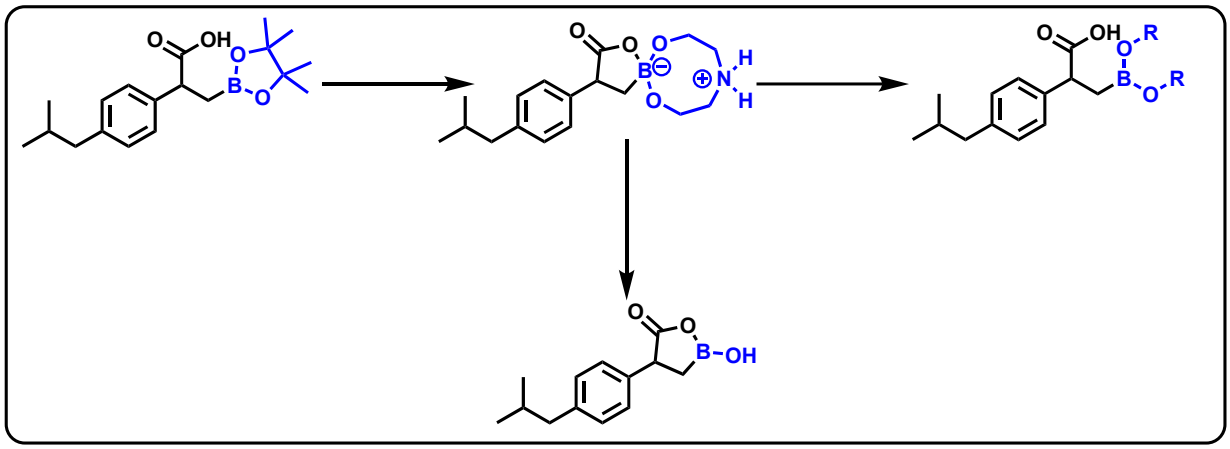

2.1. Abstract

Boronic acid containing molecules have garnered increased attention in drug discovery research due to the unique chemical properties of the boron center. A boron functionalized ibuprofen (*bora*-NSAIDs) can be accessed via copper catalyzed boracarboxylation of 4-isobutylstyrene, by using CO_2 and B_2pin_2 reagents. An alkylpinacolyl ester deprotection was carried out by transesterification with diethanolamine followed by hydrolysis. By using subsequent transesterification/transamination strategies, *bora*-ibuprofen was further functionalized to make a more diverse substrate scope in good to excellent yield. Similarly, ibuprofen lactone boronic acid was isolated and used for transesterification of substrates with acid sensitive groups.

2.2 Introduction

Boronic acids and boron esters are important synthons in organic synthesis. This is due to their usage as synthetic intermediates in the transition metal catalyzed cross coupling reactions, such as Suzuki-Miyaura,[1] Chan-Lam[2] and C-X bond forming reactions.[3] Most boron compounds are strongly Lewis acidic and contain an empty *p*-orbital. Therefore, they can react with strong nucleophiles/Lewis bases such as alcohols, amines, hydroxy acids, and amino acids. Under physiological conditions, they have an ability to convert from trivalent sp^2 hybridized form to tetravalent sp^3 hybridized form with addition of Lewis bases. This changing nature of hybridization with addition of Lewis bases is useful in the process of enzyme inhibition. In 2003, FDA approved first boron containing therapeutic agent Bortezomib to treat multiple myeloma and cell lymphoma. After that, several other boron containing drugs were approved by FDA to treat various conditions (figure 2.1a**)**.[4–6]

Non-steroidal anti-inflammatory drugs (NSAIDs) are used for pain management due to their analgesic and anti-inflammatory actions. NSAIDs limit the production of prostaglandin on the inflammatory site by inhibiting the cyclooxygenase enzyme.[7] The usage of NSAIDs for chronic pain management have adverse effects such as, bleeding in upper gastrointestinal tract,[8] renal toxicity, and myocardial infarctions.[9] NSAIDs can be categorized based on their chemical structure. Ibuprofen, naproxen, ketoprofen, fenoprofen and flurbiprofen are examples for some of the most used NSAIDs. They all have α-aryl propionic acid skeletons in their chemical structures (figure 2.1b).[10]

In 2016, Popp and co-workers reported a redox neutral copper catalytic boracarboxylation method to insert a carboxylic acid group and boron ester group into vinyl styrene.[11] This work reported the first synthesis of boron containing NSAID (*bora*-NSAIDs) analogs of ibuprofen and naproxen. Later in 2019, synthesis of *bora*-fenoprofen and *bora*-flurbiprofen using secondary ligand, triphenyl phosphine (PPh_3) with redox neutral copper catalytic system were reported (figure 2.1c).[12] To improve the utility of these *bora*-NSAIDs, it is necessary to further derivatize the boron center of these molecules. In this work, the deprotection of boron ester group of *bora*-ibuprofen using transesterification/transamination methods have

been examined. Thereafter, *bora*-ibuprofen was further functionalized with diols and diamines to expand their medicinal and synthetic applications.

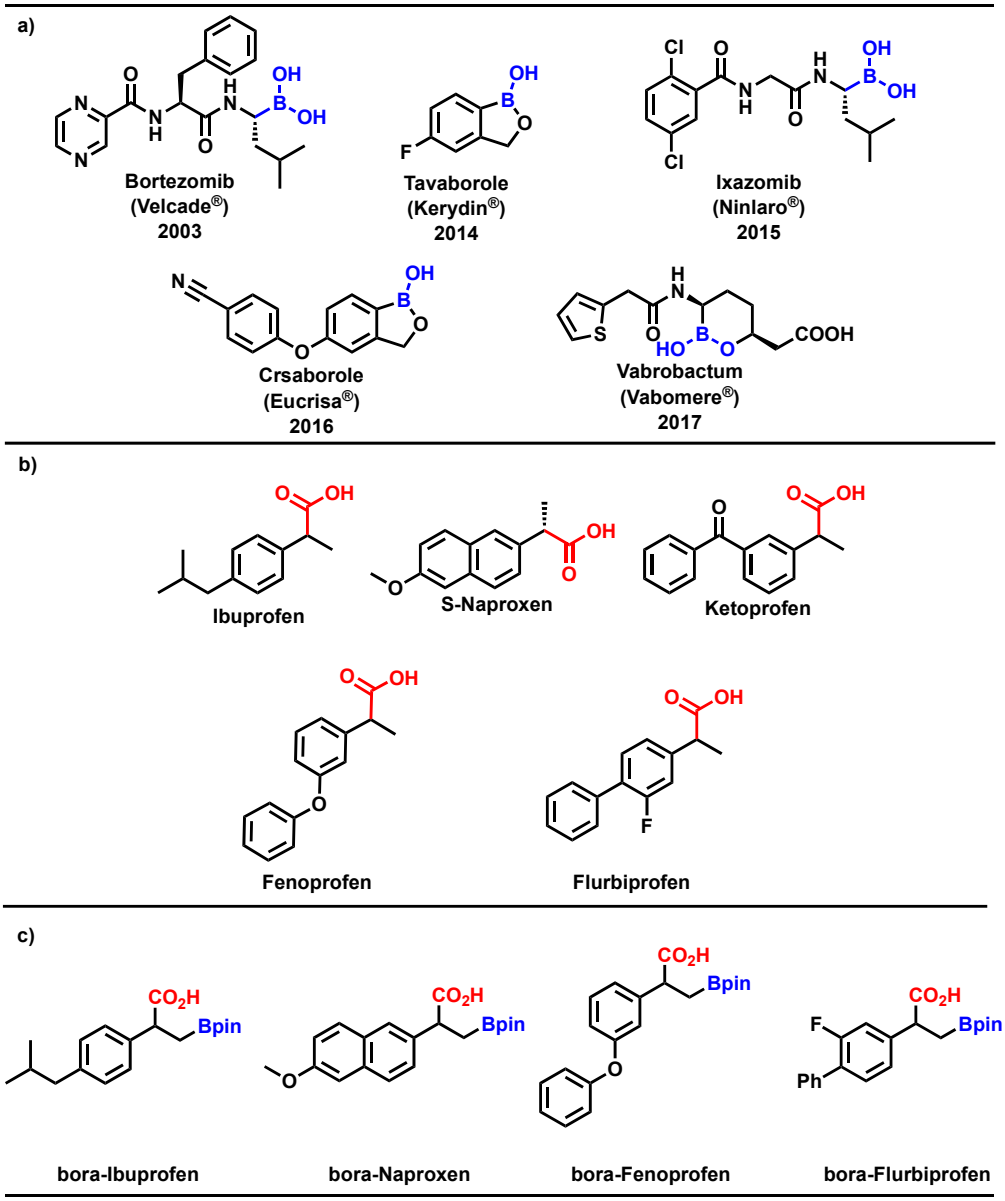

Figure 2.1 a) FDA approved boron containing therapeutic drugs. b) Common α-aryl propionic acid NSAIDs. c) boron containing α-aryl propionic acid NSAID derivatives (*bora*-NSAIDs)

Several deprotection methods have been reported to deprotect cyclic boron esters. These methods can be classified into two groups based on the deprotection reaction conditions. One of the deprotection methods require harsh reaction conditions. Following deprotection methods are examples for such harsh reaction conditions. Transborylation with boron trichloride,[13,14] oxidative cleavage with sodium periodate,[15] reductive cleavage with lithium aluminum hydride, [16,17] and hydrolysis with potassium hydrogen fluoride.[18–21] The main problems with these reaction conditions are their less tolerance for substrates with sp^3 C-sp^2 B bonds and difficulties in the product purification.

The second deprotection method includes transesterification with different regents such as boronic acids and ethanol amines. Biphasic transesterification with phenyl boronic acid and isobutyl boronic acid is limited due to the difficulty of product isolation. Under biphasic reaction conditions, boronic acid should be water soluble and should separate from phenyl/isobutyl boronic acids.[15,22] This method was surpassed by the usage of solid phase transesterification with phenyl boronic acid.[23] But this method was limited to aromatic boronic esters. Recently, Klein and co-workers reported a monophasic transesterification method using methyl boronic acid. In this method resultant methyl pinacol ester was removed by evaporation at 40 °C.[24]

Transesterification with diethanolamine was also used to deprotect cyclic boronic esters.[25–28] During this reaction, sp^3 hybridized tetracoordinated zwitterionic diethanolamine boronate adduct (DEA adduct) was formed. Then with acid hydrolysis, DEA adduct can easily be converted into boronic acid. This DEA adduct was precipitated in the etherate medium. The ease of purification, high functional group tolerance, and air and moisture stability of the DEA adduct make this method ideal for boron ester deprotection. This deprotection strategy via DEA adduct has potential applications in academic and pharmaceutical research. This was highlighted in the recently reported kilogram scale (5,50 and 100 kg) synthesis of DEA boronate ester.[29] In this work we have used modified diethanolamine transesterification method to deprotect boron pinacol ester (Bpin) group in *bora*-ibuprofen.

Scheme 2.1 Cyclic boron ester deprotection methods.

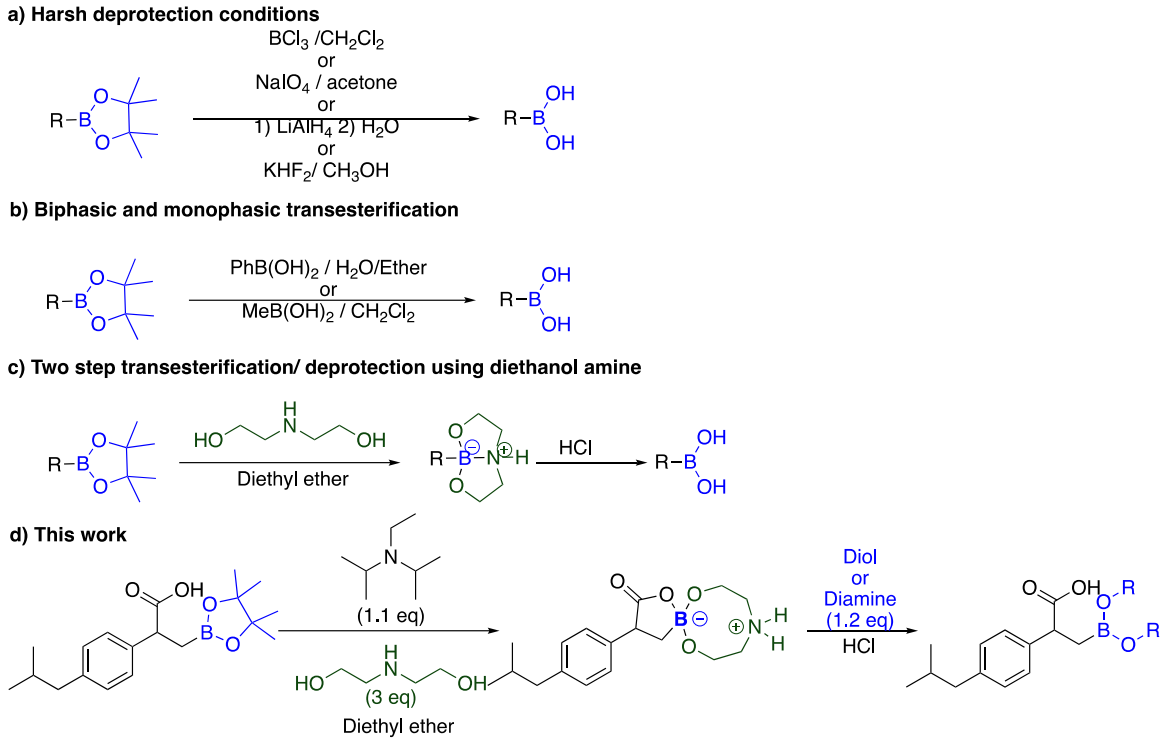

2.3 Results and Discussion

We started our deprotection process by directly reacting *bora*-ibuprofen with diethanolamine in diethyl ether medium at room temperature. Due to the presence of carboxylic acid group in *bora*-ibuprofen, the direct reaction of *bora*-ibuprofen with diethanolamine did not generate the desired product. Therefore, carboxylic acid group was neutralized using 1.1 equivalence of organic base (*N*,*N*-diisopropylethyl amine). Once carboxylic acid group was neutralized with the base, it formed a carboxylate. The resulting negatively charged oxygen atom in the carboxylate group, then bound to boron atom to form a new tetracoordinated boron spiro structure **1** (Scheme 2.2).

Scheme 2.2 Neutralization of carboxylic acid group in *bora*-ibuprofen with *N*,*N*-diisopropylethyl amine (1.1 eq)

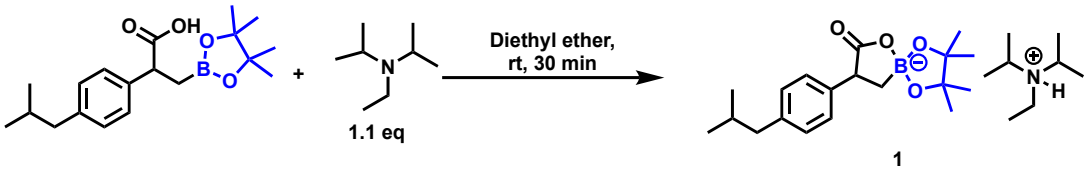

This formation of boron spiro structure was observed using ^{11}B NMR spectroscopy in $CDCl_3$. ^{11}B NMR signal for boron pinacol ester showed up at δ 33.50 ppm, with the formation of tetracoordinated boronspiro structure ^{11}B NMR signal was shifted upfield to δ 15.8 ppm (Figure 2.2).

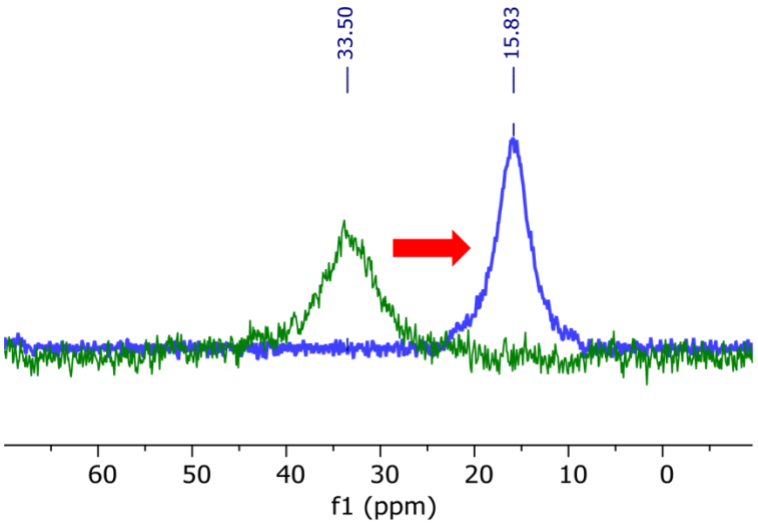

Figure 2.2 ^{11}B NMR spectral changes with the formation of boron-spirostructure **1**.

Next, tetracoordinated boronspiro structure **1** was reacted with 3 equivalences of diethanolamine to obtain *bora*-ibuprofen diethanolamine adduct **2** with an **80**% yield (scheme 2.3). Diethanolamine transesterified the pinacol ester group to form a new tetracoordinated sp^3 hybridized *bora*-ibuprofen diethanolamine boronate product **2**. This *bora*-ibuprofen diethanolamine boronate product **2** was easily purified by simple filtration since it precipitated in the ethereal solution.

Scheme 2.3 Synthesis of *bora*-ibuprofen diethanolamine adduct **2**

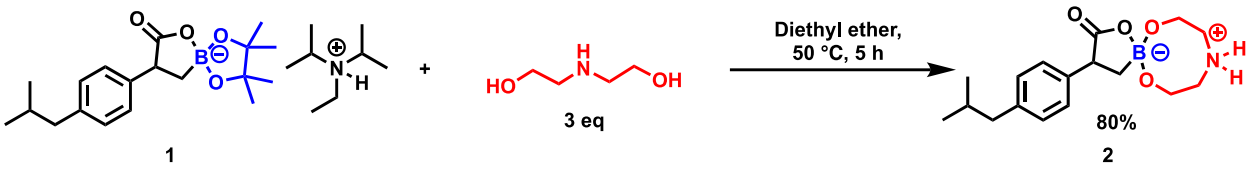

The formation of *bora*-ibuprofen diethanolamine boronate product **2** from boron spiro structure **1** can be observed by the changes in the ^{11}B NMR spectral signals. The ^{11}B NMR spectral chemical shift for spirostructure **1** was shifted further upfield into δ 9.84 ppm with the formation *bora*-ibuprofen diethanolamine boronate product **2** (Figure 2.3).

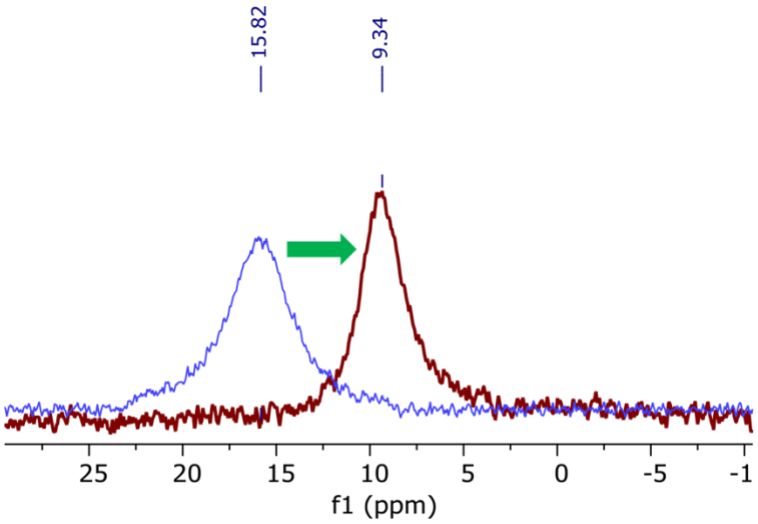

Figure 2.3 ^{11}B NMR spectral shift change with the formation of *bora*-ibuprofen diethanolamine boronate product **2.**

One of the questions we had regarding structure **2** was, whether nitrogen from diethanolamine coordinated to the boron center or oxygen from carboxylate bind to the boron. To deduce the correct structure, constant time inverse-detection accordion rescaled heteronuclear multiple bond correlation spectroscopy (CIGAR-HMBC) experiment was performed (Figure 2.4). In CIGAR-HMBC spectra, no

correlation was observed between methylene protons and nitrogen. Nitrogen was only observed to be correlated to O-CH_2 protons and N-CH_2 protons. This provides evidence that the oxygen from the carboxylate group binds to the boron center.

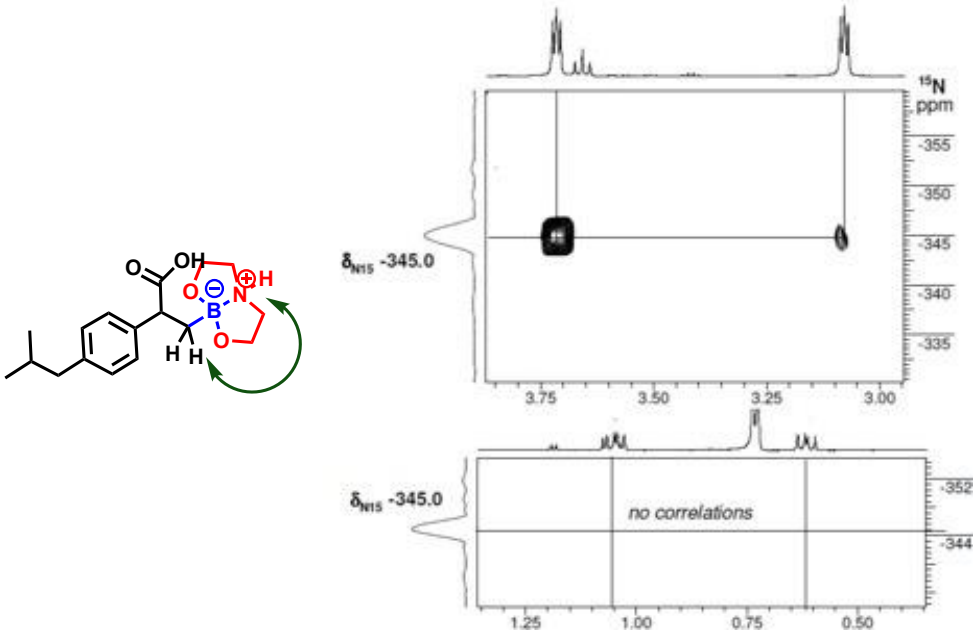

Figure 2.4 CIGAR-HMBC spectra of diethanolamine boronate product 2.

Next, *bora*-ibuprofen diethanolamine boronate product **2** was hydrolyzed into the corresponding lactone boronic acid, using a biphasic solution of 0.1 M HCl and diethyl ether (scheme 2.4). Corresponding boronic acid product was isolated at 81% yield.

Scheme 2.4 Hydrolysis of *bora*-ibuprofen diethanolamine boronate product **2** to form ibuprofen lactone boronic acid.

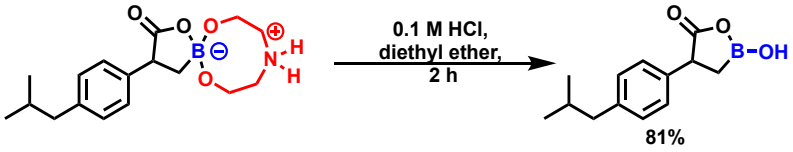

This novel lactone boronic acid was characterized using ^{1}H, ^{13}C and ^{11}B NMR spectroscopic methods. In non protic deuterated solvents, this boronic acid product exhibit a dynamic nature. Therefore, the formation of several boron species was observed in ^{11}B NMR spectrums (Appendix A6 spectra). In

deuterated methanol, due to the hydrogen bond stabilization only ^{11}B NMR signal was observed at δ 29.36 ppm (Figure 2.4).

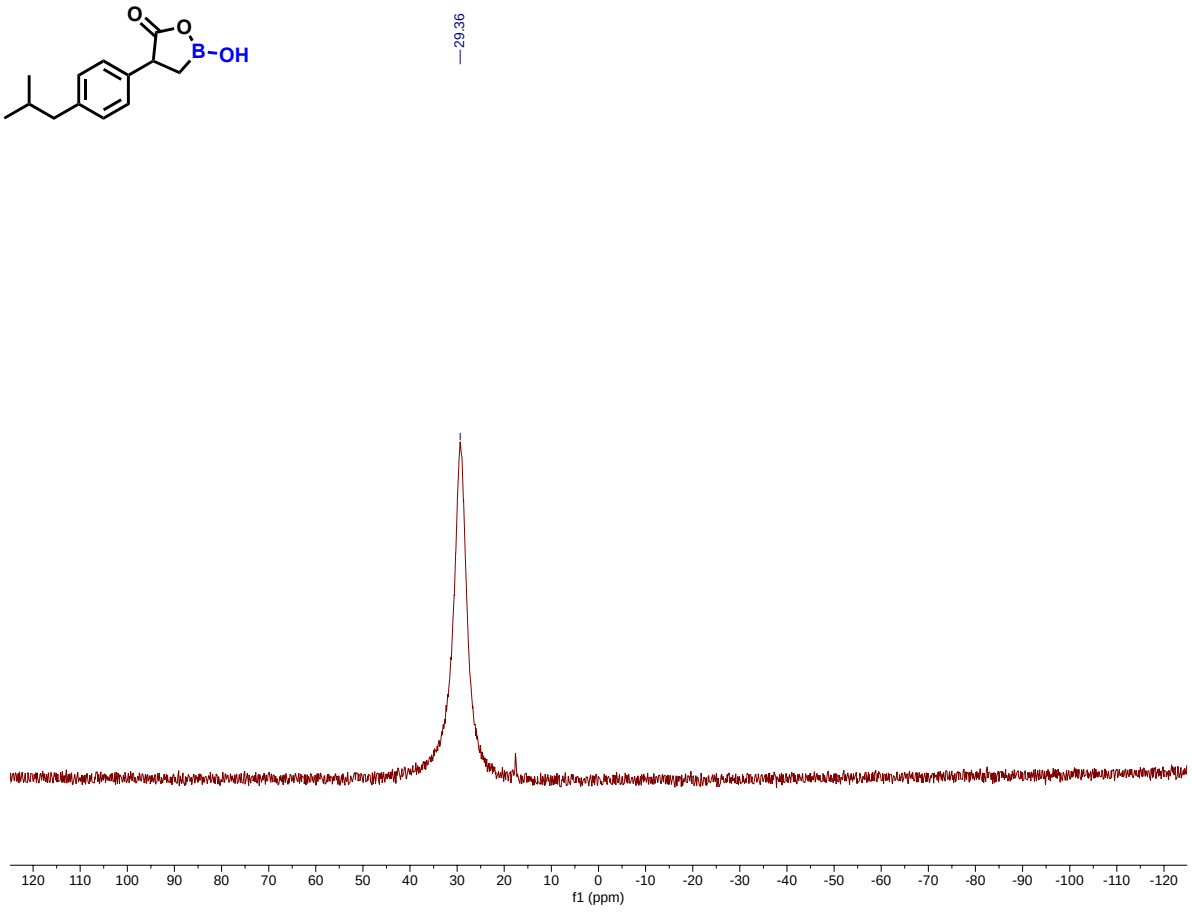

Figure 2.5 ^{11}B NMR spectrum of ibuprofen lactone boronic acid.

Spectral data were in good agreement with the structure of ibuprofen lactone boronic acid. The ^{1}H NMR obtained in deuterated methanol (Figure 2.5) shows an ABX splitting pattern. This pattern is observed due to diastereotopic methylene protons (H_a and $H_{b)}$, arising from the benzylic stereogenic center.

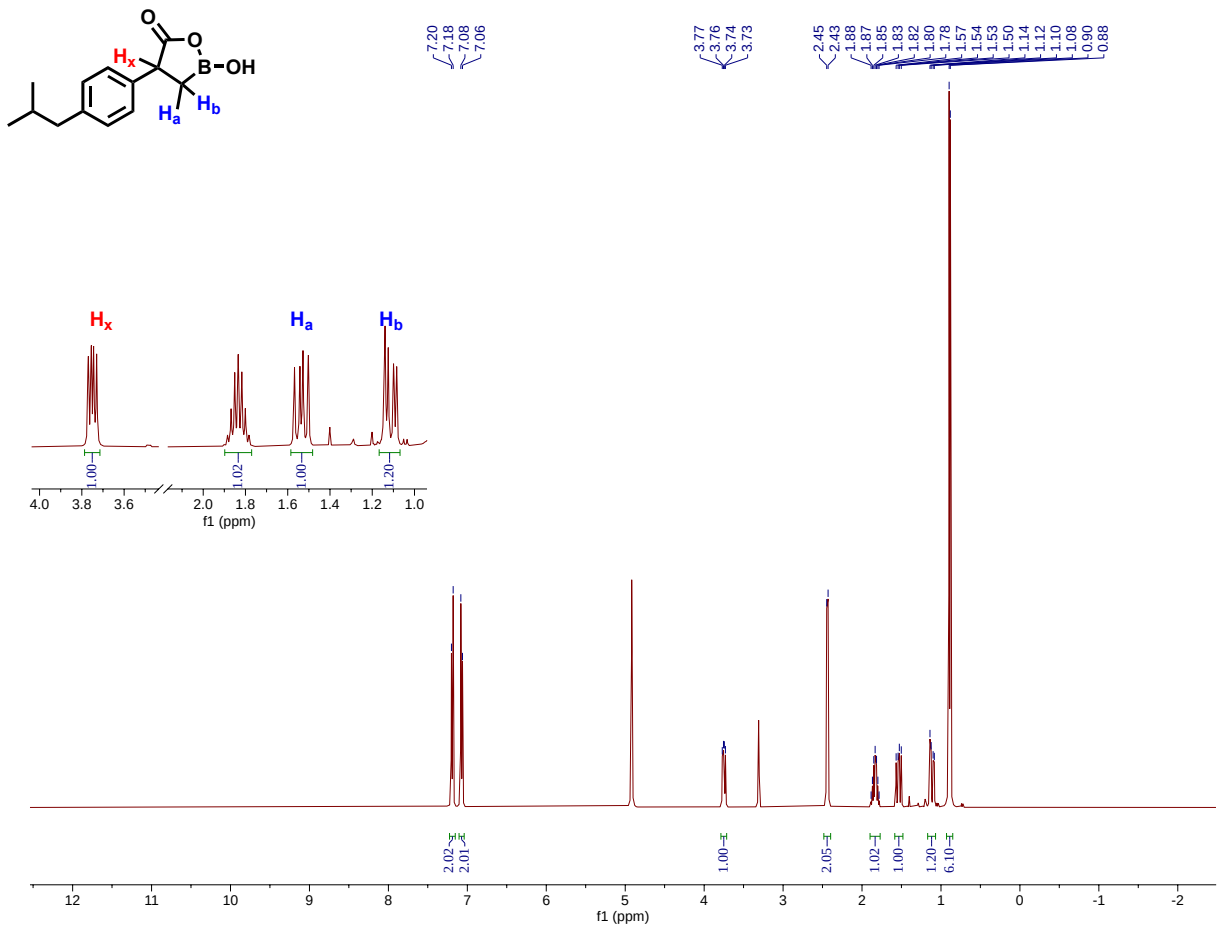

Figure 2.6 ^{1}H NMR spectrum of ibuprofen lactone boronic acid.

Next, a series of novel bora-ibuprofen substrates were prepared using *bora*-ibuprofen diethanol amine boronate **2.** *bora*-ibuprofen diethanol amine boronate product **2** was subjected to a biphasic solution of 0.1M HCl and diethyl ether in the presence of 1.2 equivalence of respective diol or diamine. During this this reaction, bora-ibuprofen diethanol amine boronate product **2** undergoes rapid hydrolysis to generate ibuprofen lactone boronic acid in solution in situ. Thereafter, it undergoes esterification with diol or diamine to generate respective boronic ester product (Scheme 2.5).

Scheme 2.5 Substrate scope for *bora*-ibuprofen derivatives

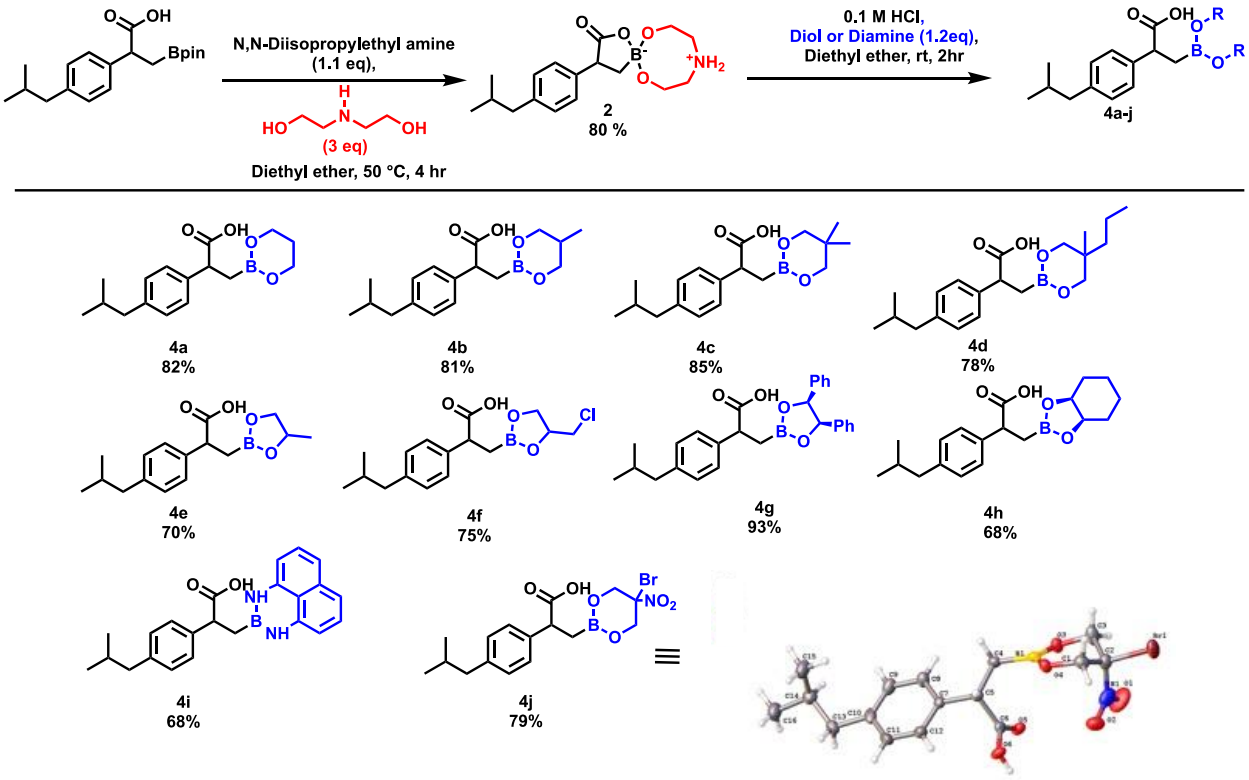

[a] *bora*-ibuprofen diethanolamine boronate 2 (0.1 mmol) and diol or diamine (0.12 mmol) in 0.1 M HCl (2 ml), diethyl ether (2 ml). [b] Isolated yield.

Using biphasic hydrolysis conditions, 1,3-diol boron ester derivatives (4a, 4b, 4c,4d and 4j) were succesfully synthesized in good to excellent yields from *bora*-ibuprofen diethanol amine boronate **2**. X-ray crystal structure for 4j was obtained, while *n*-heptane was used as the recrystalization solvent.1,2-diols boron esters 4e,4f,4g and 4h were synthesized in good yeilds. When chiral diols were used as starting diol for the synthesis of 4e,4f and 4g products, the resulting 4e,4f and 4g products were obtained as racemic mixtures. *bora*-ibuprofen diaminonaphthalene derivative 4i was synthesized in a moderate yield using 1,8-diaminonapthalene. However, substartes with acid sensitive groups such as ethers and monosacarides were not tolerated under these reaction conditions.

Scheme 2.6 Substrate scope for *bora*-ibuprofen derivative with acid sensitive groups[a,b]

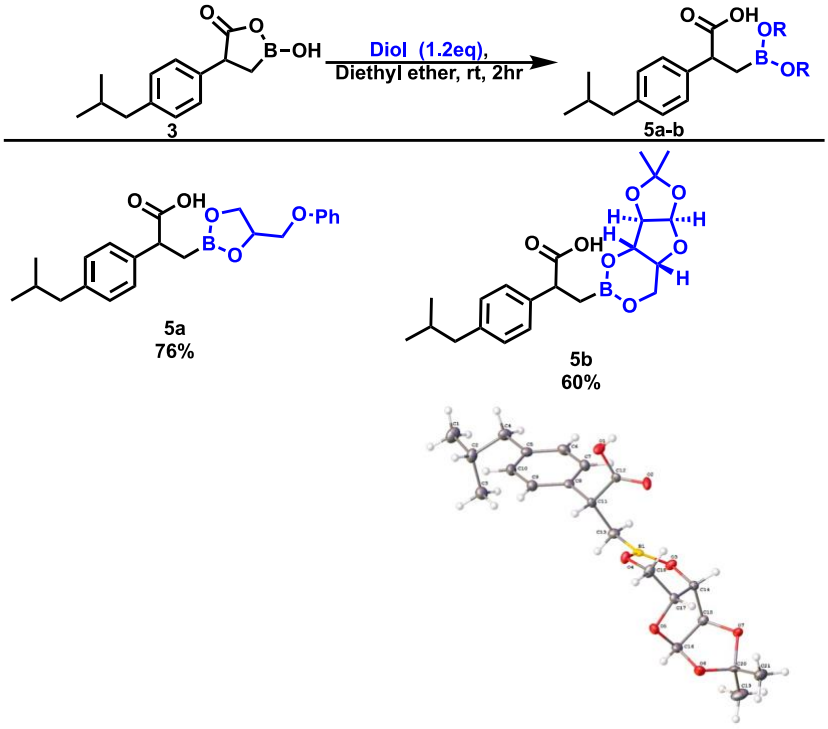

[a] ibuprofen lactone boronic acid (0.1 mmol) and diol (0.12 mmol) in H_2O (2 ml), diethyl ether (2 ml). [b] Isolated yield.

To access substrates with acid sensitive groups, ibuprofen lactone boronic acid was reacted with respective diol substrates under biphasic reaction conditions. *Bora*-ibuprofen esters with ether groups 5a,5b were successfully synthesized in good yields. The complexation between boronic acids and monosaccharides with cis diol motifs was used in functionalization of carbohydrate derivatives.[30,31] When ibuprofen lactone boronic acid was reacted with xylofuranose substrate under biphasic conditions, 5c product was produced in a 60% yield. This could be a pro-drug to deliver ibuprofen lactone boronic acid into cells. Furthermore, boronic acids have been extensively exploited as a catalyst in regioselective glycosylation reactions.[32–34] Due to its unique chemical structure, ibuprofen lactone boronic acid can be a good catalyst for glycosylation reactions. Biological activities of these substrates will be investigated in the future.

2.4 Conclusion

In this chapter, we have outlined a methodology to achieve pinacol deprotection in *bora*-ibuprofen via transesterification with diethanolamine. By using subsequent transesterification/transamination strategies, *bora*-ibuprofen was further functionalized to make a more versatile substrate scope. *Bora*-ibuprofen with 1,2-diol and 1,3-diol motifs were synthesized in good to moderate yields. Similarly, a *bora*-ibuprofen diamino naphthalene derivative was synthesized in a good yield. Under these conditions, a new ibuprofen lactone boron acid was prepared in an excellent yield. Using that as a starting substrate, diol with acid sensitive substrates such as monosaccharide and ethers were installed into boron center in *bora*-ibuprofen.

2.5 Experimental Methods

General information

All commercially available compounds were used as received, and all were purchased from either Oakwood chemicals, Alfa Aesar, or Fisher chemicals.

^{1}H, ^{13}C, and ^{11}B NMR spectra were recorded on JEOL 400 MHz and Varian INOVA 600 MHz NMR spectrometers, and all deuterated solvents were purchased from Cambridge Isotope Laboratories, Inc. The chemical shifts (δ) are given in parts per million and referenced relative to residual proteo solvent (1.94 or 3.31 ppm for d3-CD_3CN and d4-CD_3OD, respectively), d3-CD_3CN or d4-CD_3OD (1.30 or 49.30 ppm for ^{13}C), and internal (capillary) BF_3•OEt_2 (32.1 ppm). ^{11}B NMR spectra recorded using quartz NMR tubes. High-resolution mass spectra were recorded on a Thermofisher Scientific Q Exactive Mass Spectrometer using MeOH (Fisher Optima grade).

General procedures for preparing tetracoordinated boron spiro structure 1

A 20 mL scintillation vial was charged with compound *bora*-ibuprofen (1 eq, 0.1 mmol, 33.1 mg), and *N,N*-diisopropylethylamine (1.1 eq, 0.11 mmol, 19 μl). A 2 mL of diethyl ether solution was added, and the resulting suspension was stirred at ambient temperature for 1 hour. The resulting solution was concentrated under vacuum to obtained yellow color oily layer. The mixture was then dissolved in 1 mL of $CDCl_3$ and analyzed by ^{1}H NMR and ^{11}B spectroscopy.

General procedures for synthesis of *bora*-ibuprofen diethanolamine adduct 2

A 20 mL scintillation vial was charged with compound *bora*-ibuprofen (1 eq, 0.1 mmol, 33.1 mg), *N,N*-diisopropylethylamine (1.1 eq, 0.11 mmol, 19 μl) and diethanolamine (3eq, 0.3mmol, 31.5 mg). A 2 mL of diethyl ether solution was added, and the resulting suspension was stirred at 50℃ for 4 hours. After 4 hours white fine powdered product was vacuum filtered to provide the *bora*-ibuprofen diethanolamine adduct. The resulting white powdered solid was washed with excess diethyl ether to remove impurities.

General procedures for preparing ibuprofen lactone boronic acid

A 20 mL scintillation vial was charged with *bora*-ibuprofen diethanolamine adduct 2 (1 eq, 0.1 mmol, 31.9 mg). A 2 mL of 0.1 M HCl and 2 ml of diethyl ether solutions were added, and the resulting suspension was stirred at ambient temperature for 2 hours. Upon completion, the crude mixture was added to a 15 mL separatory funnel and then extracted with diethyl ether (3 × 4 mL) and collected in a 20 mL scintillation vial. The combined organic extracts were washed with saturated sodium chloride (4 ml), and dried with sodium sulfate, and the organic solvent was removed under reduced pressure. Evaporation of residual solvent provided the analytically pure product as white solid.

General procedures for preparing ibuprofen derivatives

A 20 mL scintillation vial was charged with *bora*-ibuprofen diethanolamine adduct 2 (1 eq, 0.1 mmol, 31.9 mg) and diol/diamine (1.1 eq, 0.11mmol). A 2 mL of 0.1 M HCl and 2 ml of diethyl ether solutions were added, and the resulting suspension was stirred at ambient temperature for 2 hours. Upon completion, the crude mixture was added to a 15 mL separatory funnel and then extracted with diethyl ether (3 × 4 mL) and collected in a 20 mL scintillation vial. The combined organic extracts were washed with saturated sodium chloride (4 ml), and dried with sodium sulfate, and the organic solvent was removed under reduced pressure to obtain desired product, further purified by recrystallization in *n*-heptane

General procedures for preparing ibuprofen derivatives with acid sensitive groups

A 20 mL scintillation vial was charged with ibuprofen lactone boronic acid (1 eq, 0.1 mmol, 31.9 mg) and diol/diamine (1.1 eq, 0.11mmol). A 2 mL of distilled water and 2 ml of diethyl ether solutions were added, and the resulting suspension was stirred at ambient temperature for 2 hours. Upon completion, the crude mixture was added to a 15 mL separatory funnel and then extracted with diethyl ether (3 × 4 mL) and collected in a 20 mL scintillation vial. The combined organic extracts were washed with saturated sodium chloride (4 ml), and dried with sodium sulfate, and the organic solvent was removed under reduced pressure to obtain desired product, further purified by recrystallization in *n*-heptane

Characterization data

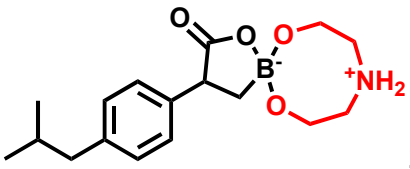

2: White solid, 80% **yield** (25.6 mg).

^{1}H NMR (600 MHz, CD_3OD-d4) δ 7.15 – 7.11 (m, 2H), 7.03 (d, *J* = 7.8 Hz, 2H), 3.81 – 3.76 (m, 4H), 3.65 (t, *J* = 9.5 Hz, 1H), 3.13 (t, *J* = 5.3 Hz, 4H), 2.42 (d, *J* = 7.2 Hz, 2H), 1.82 (hept, *J* = 6.7 Hz, 1H), 1.13 (dd, *J* = 13.7, 10.0 Hz, 1H), 0.88 (d, *J* = 6.7 Hz, 6H), 0.69 (dd, *J* = 13.7, 8.9 Hz, 1H). **^{13}C NMR** (101 MHz, CD_3OD-d4) δ 186.66, 142.93, 140.23, 129.98, 128.94, 57.69, 51.75, 50.30, 46.11, 31.51, 22.74.**^{11}B NMR** (128 MHz, CD_3OD-d3) δ 9.37. HRMS (ESI) m/z 320.2021 [$C_{17}H_{26}BNO_4$- (M+H)- requires 320.2028].

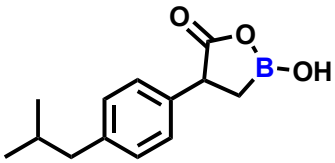

3: White solid, 81% **yield** (18.8 mg).

^{1}H NMR (400 MHz, CD_3OD-d4) 7.22 – 7.16 (2 H, m), 7.10 – 7.04 (2 H, m), 3.75 (1 H, dd, *J* 10.1, 5.8), 2.44 (2 H, d, *J* 7.2), 1.83 (1 H, dp, *J* 13.6, 6.7), 1.53 (1 H, dd, *J* 16.0, 10.2), 1.17 – 1.06 (1 H, m), 0.89 (6 H, d, *J* 6.6).**^{13}C NMR** (101 MHz, CD_3OD-d4) δ 178.71, 140.64, 140.17, 129.56, 127.68, 49.00, 48.79, 48.64, 48.57, 48.36, 48.15, 47.93, 47.72, 47.48, 45.37, 30.80, 22.05. **^{11}B NMR** (128 MHz, CD_3OD-d4) δ 29.36. HRMS (ESI) m/z 231.1192 [$C_{13}H_{17}BO_3$- (M-H)- requires 231.1198].

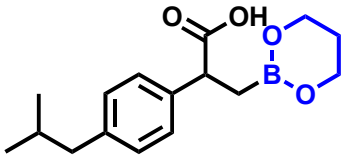

4a: White solid, 82% **yield** (23.8 mg).

^{1}H NMR (600 MHz, $CDCl_3$-d) δ 7.19 (d, *J* = 7.7 Hz, 2H), 7.06 (d, *J* = 7.7 Hz, 2H), 3.95 – 3.86 (m, 4H), 3.76 (dd, *J* = 10.1, 6.0 Hz, 1H), 2.42 (d, *J* = 7.2 Hz, 2H), 1.88 – 1.77 (m, 2H), 1.49 (dd, *J* = 16.0, 10.2 Hz, 1H), 1.16 – 1.09 (m, 1H), 0.87 (dd, *J* = 6.6, 1.0 Hz, 7H). **^{13}C NMR** (101 MHz, $CDCl_3$-d) δ 180.10, 140.43, 138.13, 129.25, 127.45, 77.34, 77.22, 77.02, 76.70, 61.70, 46.26, 45.05, 30.16, 27.22, 22.40. **^{11}B NMR** (128 MHz, $CDCl_3$-d) δ 31.70. **HRMS (ESI) m/z** 289.1622 [$C_{16}H_{23}BO_4$- (M-H)- requires 289.1617].

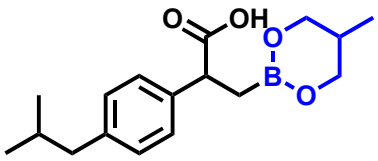

4b: White solid, 81% **yield** (24.5 mg).

^{1}H NMR (600 MHz, $CDCl_3$-d) δ 7.24 – 7.18 (m, 2H), 7.09 – 7.04 (m, 2H), 3.88 (dddd, *J* = 11.0, 6.5, 4.4, 2.1 Hz, 2H), 3.77 (dd, *J* = 10.0, 6.2 Hz, 1H), 3.47 (dt, *J* = 11.0, 9.4 Hz, 2H), 2.43 (d, *J* = 7.2 Hz, 2H), 2.03 – 1.94 (m, 1H), 1.83 (hept, *J* = 6.7 Hz, 1H), 1.50 (dd, *J* = 15.9, 10.0 Hz, 1H), 1.18 – 1.09 (m, 1H), 0.88 (dd, *J* = 6.6, 1.0 Hz, 6H), 0.80 (d, *J* = 6.8 Hz, 3H). **^{13}C NMR** (101 MHz, $CDCl_3$-d) δ 207.23, 181.12, 140.39, 138.14, 129.22, 127.61, 127.49, 83.35, 77.35, 77.24, 77.04, 76.72, 67.59, 46.42, 45.05, 31.15, 30.94, 30.16, 29.71, 24.63, 24.50, 22.39, 19.46, 12.62. **^{11}B NMR** (128 MHz, $CDCl_3$-d) δ 28.65. **HRMS (ESI) m/z** 303.1777 [$C_{17}H_{25}BO_4$- (M-H)- requires 303.1773].

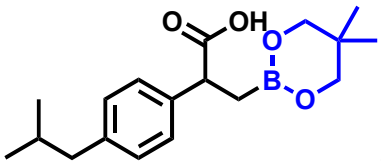

4c: White solid, 85% **yield** (27.1 mg).

^{1}H NMR (400 MHz, $CDCl_3$-d) δ 7.22 – 7.18 (m, 2H), 7.08 – 7.03 (m, 2H), 3.79 (dd, *J* = 9.6, 6.6 Hz, 1H), 3.52 (s, 4H), 2.42 (s, 2H), 1.82 (hept, *J* = 6.7 Hz, 1H), 1.52 (dd, *J* = 16.0, 9.6 Hz, 1H), 1.19 (dd, *J* = 16.0, 6.7 Hz, 1H), 0.87 (d, *J* = 6.6 Hz, 6H), 0.83 (s, 6H). **^{13}C NMR** (101 MHz, $CDCl_3$-d) δ 179.54, 140.42, 137.99, 129.22, 127.48, 77.30, 76.98, 76.66, 71.99, 46.15, 45.03, 31.61, 30.14, 22.35, 22.34, 21.67.
^{11}B NMR (128 MHz, $CDCl_3$-d) δ 30.19.

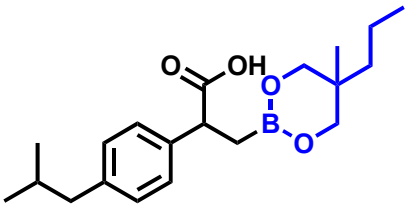

4d: White solid, 78% **yield** (27.1 mg).

^{1}H NMR (600 MHz, $CDCl_3$-d) δ 7.23 – 7.19 (m, 2H), 7.08 – 7.03 (m, 2H), 3.78 (dd, *J* = 9.5, 6.7 Hz, 1H), 3.59 (ddd, *J* = 11.1, 4.4, 1.5 Hz, 2H), 3.51 (ddd, *J* = 11.3, 7.6, 1.5 Hz, 2H), 2.42 (d, *J* = 7.1 Hz, 2H), 1.82 (dp, *J* = 13.5, 6.8 Hz, 1H), 1.51 (dd, *J* = 16.0, 9.5 Hz, 1H), 1.20 (tdd, *J* = 11.0, 8.4, 5.4 Hz, 3H), 1.16 – 1.10 (m, 2H), 0.88 (d, *J* = 6.6 Hz, 7H), 0.85 (t, *J* = 7.1 Hz, 4H), 0.78 (s, 3H). **^{13}C NMR** (101 MHz, $CDCl_3$-d) δ 180.93, 140.50, 138.09, 129.31, 129.30, 127.61, 77.43, 77.11, 76.79, 70.94, 70.92, 46.39, 45.15, 37.14, 34.33, 30.24, 22.49, 18.90, 16.43, 14.85. **^{11}B NMR** (128 MHz, $CDCl_3$-d) δ 28.31. **HRMS (ESI) m/z** 345.2244 [$C_{20}H_{31}BO_4$- (M-H)- requires 345.2243].

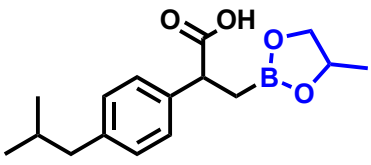

4e: White solid, 70% **yield** (20.4 mg).

^{1}H NMR (400 MHz, $CDCl_3$-d) 7.19 (2 H, d, *J* 7.9), 7.05 (2 H, dd, *J* 7.8, 5.2), 4.19 (1 H, t, *J* 8.3), 3.82 (1 H, dt, *J* 9.0, 6.8), 3.63 (1 H, q, *J* 7.5), 2.41 (2 H, dd, *J* 7.2, 2.9), 1.82 (1 H, dp, *J* 12.9, 6.3), 1.56 (1 H, ddd, *J* 32.5, 16.0, 9.4), 1.28 (1 H, dd, *J* 16.0, 7.6), 1.20 (2 H, t, *J* 6.6), 1.11 (4 H, d, *J* 5.0), 0.86 (6 H, dd, *J* 6.7, 4.4). **^{13}C NMR** (101 MHz, $CDCl_3$-d) δ 179.57, 140.61, 137.45, 129.31, 129.22, 127.54, 127.35, 83.32,

73.22, 72.06, 46.28, 45.01, 30.13, 30.11, 24.60, 24.50, 22.35, 22.32, 22.29, 21.57, -0.04. **^{11}B NMR** (128 MHz, $CDCl_3$-d) δ 34.57.

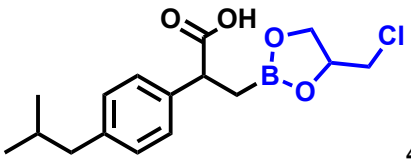

4f: White solid, 75% **yield** (24.3 mg).

^{1}H NMR (400 MHz, $CDCl_3$-d) δ 7.20 (d, *J* = 7.8 Hz, 2H), 7.08 (d, *J* = 7.8 Hz, 2H), 4.64 – 4.52 (m, 1H), 4.27 – 4.18 (m, 1H), 4.01 (ddd, *J* = 9.2, 7.5, 5.7 Hz, 1H), 3.85 (dd, *J* = 9.6, 6.6 Hz, 1H), 3.55 – 3.38 (m, 2H), 2.44 (d, *J* = 7.2 Hz, 2H), 1.84 (dp, *J* = 13.5, 6.8 Hz, 1H), 1.64 (ddd, *J* = 16.2, 9.8, 2.3 Hz, 1H), 1.39 – 1.23 (m, 1H), 0.89 (d, *J* = 6.6 Hz, 6H). **^{13}C NMR** (101 MHz, $CDCl_3$-d) δ 180.42, 141.01, 137.50, 129.57, 127.62, 127.58, 68.72, 46.50, 46.48, 46.18, 45.23, 30.33, 22.57, 15.30. **^{11}B NMR** (128 MHz, $CDCl_3$-d) δ 32.98. **HRMS (ESI) m/z** 323.1230 [$C_{16}H_{22}BClO$ - (M-H)- requires 323.1227].

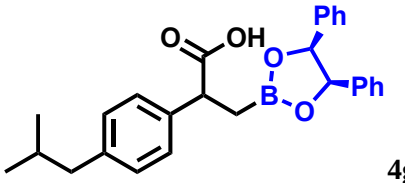

4g: White solid, 93% yield (39.8 mg).

^{1}H NMR (400 MHz, $CDCl_3$-d) 7.30 (8 H, tdd, *J* 9.1, 4.8, 2.2), 7.24 – 7.05 (7 H, m), 5.07 (2 H, s), 4.11 – 3.97 (1 H, m), 2.50 (2 H, dd, *J* 7.2, 3.0), 2.00 – 1.76 (2 H, m), 1.61 (1 H, ddd, *J* 15.9, 14.2, 7.5), 1.01 – 0.87 (6 H, m).**^{13}C NMR** (101 MHz, $CDCl_3$-d) δ 179.63, 140.80, 140.26, 137.51, 129.44, 128.69, 128.22, 128.12, 127.93, 127.69, 127.60, 126.92, 125.77, 125.72, 86.53, 79.11, 46.49, 45.10, 30.19, 22.42. **^{11}B NMR** (128 MHz, $CDCl_3$-d) δ 33.67. **HRMS (ESI) m/z** 427.2084 [$C_{27}H_{29}BO_4$ -(M-H)- requires 427.2086]. **Melting point:** 149-152 ℃.

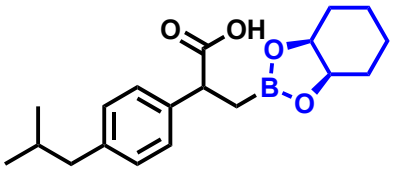

4h: White solid, 78% **yield** (22.5 mg). **^{1}H NMR** (600 MHz, $CDCl_3$-d) δ 7.24 – 7.20 (m, 2H), 7.10 – 7.05 (m, 2H), 4.31 – 4.25 (m, 2H), 3.86 (dd, *J* = 9.2, 7.3 Hz, 1H), 2.43 (d, *J* = 7.1 Hz, 2H), 1.83 (dp, *J* = 13.5, 6.7 Hz, 1H), 1.68 (ddd, *J* = 13.8, 9.2, 4.5 Hz, 2H), 1.61 (dd, *J* = 16.1, 9.2

Hz, 1H), 1.52 (s, 2H), 1.41 – 1.32 (m, 3H), 1.29 – 1.19 (m, 2H), 0.90 – 0.86 (m, 6H). **^{13}C NMR** (101 MHz, $CDCl_3$-d) δ 180.32, 140.70, 137.48, 129.32, 127.52, 77.34, 77.23, 77.02, 76.71, 75.19, 46.40, 45.04, 30.18, 28.27, 22.35, 18.98. **^{11}B NMR** (128 MHz, $CDCl_3$-d) δ 33.35. **HRMS (ESI) m/z** 329.1936 [$C_{19}H_{27}BO_4$ -(M-H)- requires 329.1930]. **Melting point:** 136-140 ℃

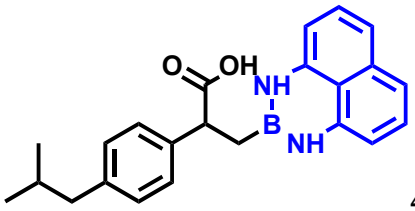

4i: 0range oil, 68% **yield** (25.4 mg).

0range oil, 68% **yield** (25.4 mg). **^{1}H NMR** (400 MHz, $CDCl_3$-d) 7.28 – 7.24 (2 H, m), 7.22 – 7.18 (1 H, m), 7.17 – 7.09 (3 H, m), 7.03 (2 H, dd, *J* 8.3, 7.2), 6.96 (2 H, d, *J* 8.2), 6.47 (1 H, dd, *J* 7.2, 1.1), 6.14 (2 H, d, *J* 7.2), 5.47 (2 H, s), 3.76 (1 H, t, *J* 7.9), 2.45 (2 H, d, *J* 7.2), 1.83 (1 H, dq, *J* 13.4, 6.7), 1.59 (1 H, dd, *J* 15.3, 7.5), 1.48 – 1.40 (1 H, m), 0.89 (7 H, d, *J* 6.6). **^{13}C NMR** (101 MHz, CHLOROFORM-*D*) δ 179.73, 141.35, 140.90, 140.33, 137.09, 136.28, 134.73, 129.75, 129.16, 128.35, 127.64, 127.60, 127.13, 119.68, 117.63, 117.31, 113.12, 106.14, 105.75, 64.70, 47.22, 45.12, 32.00, 30.30, 28.96, 22.82, 22.50, 14.25.**^{11}B NMR** (128 MHz, $CDCl_3$-d) δ 31.62

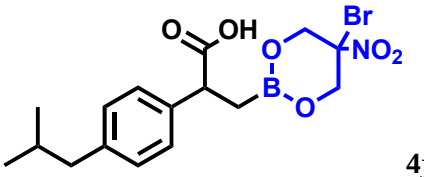

4j: White solid, 79% **yield** (32.7 mg).

^{1}H NMR (600 MHz, $CDCl_3$-d) δ 7.25 (s, 1H), 7.13 (2 H, d, *J* 8.0), 7.06 (2 H, d, *J* 8.0), 4.84 (2 H, dd, *J* 13.2, 2.9), 4.31 (2 H, t, *J* 12.3), 3.76 (1 H, dd, *J* 10.5, 6.0), 2.42 (2 H, d, *J* 7.2), 1.82 (1 H, hept, *J* 6.7), 1.48 (1 H, dd, *J* 16.1, 10.4), 1.17 (1 H, dd, *J* 16.1, 6.0), 0.88 (6 H, d, *J* 6.6). **^{13}C NMR** (101 MHz, $CDCl_3$-d) δ 180.56, 140.87, 137.42, 129.75, 129.50, 128.09, 127.46, 127.27, 83.35, 66.97, 46.27, 45.13, 30.24, 22.49, 18.97. **^{11}B NMR** (128 MHz, $CDCl_3$-d) δ 33.75. **HRMS (ESI) m/z** 412.0571 [$C_{16}H_{21}BBrNO_6$- (M-H)- requires 412.0573]. **Melting point:** 141-148 ℃

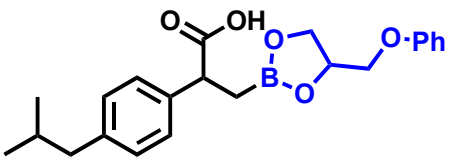

5a: White solid, 76% **yield** (29.1 mg).

^{1}H NMR (600 MHz, $CDCl_3$-d) 7.26 (2 H, ddd, *J* 11.5, 6.0, 3.1), 7.19 (2 H, dd, *J* 7.9, 5.7), 7.06 (1 H, d, *J* 7.9), 7.04 (1 H, d, *J* 7.9), 6.95 (1 H, td, *J* 7.2, 4.5), 6.86 (2 H, dd, *J* 8.3, 3.6), 4.68 (1 H, dt, *J* 8.1, 5.1), 4.26 (1 H, td, *J* 8.6, 2.5), 4.05 (1 H, ddd, *J* 11.6, 9.2, 6.0), 3.94 (1 H, ddd, *J* 9.8, 8.2, 4.8), 3.85 (2 H, qd, *J* 6.6, 3.4), 2.41 (2 H, t, *J* 6.4), 1.87 – 1.76 (1 H, m), 1.64 (1 H, dd, *J* 16.1, 9.5), 1.34 (1 H, ddd, *J* 16.0, 6.8, 1.9), 0.87 (6 H, dd, *J* 6.7, 2.1). **^{13}C NMR** (400 MHz, $CDCl_3$-d) ^{13}C NMR (101 MHz, CHLOROFORM-*D*) δ 180.33, 180.27, 158.41, 140.74, 137.47, 137.45, 129.50, 129.36, 129.35, 127.45, 127.43, 121.26, 114.57, 114.55, 74.86, 69.26, 67.99, 67.94, 46.38, 45.04, 30.14, 29.71, 22.40, 15.22.**^{11}B NMR** (400 MHz, $CDCl_3$-d) δ 33.62.

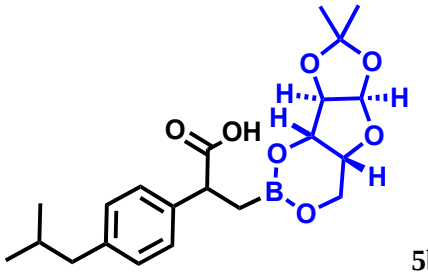

5b: White solid, 60% **yield** (27.5 mg).

^{1}H NMR (600 MHz, $CDCl_3$-d) 7.22 – 7.16 (2 H, m), 7.09 – 7.05 (2 H, m), 5.74 (1 H, d, *J* 3.7), 4.46 (1 H, d, *J* 3.7), 4.36 (1 H, q, *J* 2.0), 4.31 (1 H, d, *J* 2.7), 4.19 (1 H, d, *J* 13.1), 4.02 (1 H, dd, *J* 13.2, 2.1), 3.77 (1 H, dd, *J* 10.1, 6.1), 2.43 (2 H, d, *J* 7.2), 1.83 (1 H, dp, *J* 13.5, 6.7), 1.52 (1 H, dd, *J* 16.1, 10.2), 1.48 (3 H, s), 1.29 (3 H, s), 1.15 (1 H, dd, *J* 16.1, 6.1), 0.89 (6 H, d, *J* 6.6). **^{13}C NMR** (101 MHz, $CDCl_3$-d) δ 180.50, 140.70, 137.74, 129.39, 127.52, 112.06, 105.03, 84.84, 74.54, 74.31, 60.35, 46.21, 45.12, 30.24, 26.79, 26.19, 22.50. **^{11}B NMR** (128 MHz, $CDCl_3$-d) δ 28.72. **HRMS (ESI) m/z** 403.1932 [: $C_{21}H_{29}BO_7$ -(M-H)- requires 403.1934]. **Melting point: 163-171** ℃

2.6 References

(1) Miyaura, Norio.; Suzuki, Akira. Palladium-Catalyzed Cross-Coupling Reactions of Organoboron Compounds. *Chem. Rev.* **1995**, *95* (7), 2457–2483. https://doi.org/10.1021/cr00039a007.

(2) Chen, J.; Li, J.; Dong, Z. A Review on the Latest Progress of Chan-Lam Coupling Reaction. *Adv. Synth. Catal.* **2020**, *362* (16), 3311–3331. https://doi.org/10.1002/adsc.202000495.

(3) Pattison, G. Fluorination of Organoboron Compounds. *Org. Biomol. Chem.* **2019**, *17* (23), 5651–5660. https://doi.org/10.1039/C9OB00832B.

(4) Song, S.; Gao, P.; Sun, L.; Kang, D.; Kongsted, J.; Poongavanam, V.; Zhan, P.; Liu, X. Recent Developments in the Medicinal Chemistry of Single Boron Atom-Containing Compounds. *Acta Pharm. Sin. B* **2021**, *11* (10), 3035–3059. https://doi.org/10.1016/j.apsb.2021.01.010.

(5) Baker, S. J.; Ding, C. Z.; Akama, T.; Zhang, Y.-K.; Hernandez, V.; Xia, Y. Therapeutic Potential of Boron-Containing Compounds. *Future Med. Chem.* **2009**, *1* (7), 1275–1288. https://doi.org/10.4155/fmc.09.71.

(6) Fernandes, G. F. S.; Denny, W. A.; Dos Santos, J. L. Boron in Drug Design: Recent Advances in the Development of New Therapeutic Agents. *Eur. J. Med. Chem.* **2019**, *179*, 791–804. https://doi.org/10.1016/j.ejmech.2019.06.092.

(7) Cashman, J. N. The Mechanisms of Action of NSAIDs in Analgesia: *Drugs* **1996**, *52* (Supplement 5), 13–23. https://doi.org/10.2165/00003495-199600525-00004.

(8) Wolfe, M. M.; Singh, G. Gastrointestinal Toxicity of Nonsteroidal Antiinflammatory Drugs. *N. Engl. J. Med.* **1999**, 12.

(9) Bally, M.; Dendukuri, N.; Rich, B.; Nadeau, L.; Helin-Salmivaara, A.; Garbe, E.; Brophy, J. M. Risk of Acute Myocardial Infarction with NSAIDs in Real World Use: Bayesian Meta-Analysis of Individual Patient Data. *BMJ* **2017**, j1909. https://doi.org/10.1136/bmj.j1909.

(10) RajanBabu, T. V.; Smith, C. R. 5.16 Reduction: Enantioselective Hydrovinylation of Alkenes. In *Comprehensive Chirality*; Elsevier, 2012; pp 355–398. https://doi.org/10.1016/B978-0-08-095167-6.00518-8.

(11) Butcher, T. W.; McClain, E. J.; Hamilton, T. G.; Perrone, T. M.; Kroner, K. M.; Donohoe, G. C.; Akhmedov, N. G.; Petersen, J. L.; Popp, B. V. Regioselective Copper-Catalyzed Boracarboxylation of Vinyl Arenes. *Org. Lett.* **2016**, *18* (24), 6428–6431. https://doi.org/10.1021/acs.orglett.6b03326.

(12) Perrone, T. M.; Gregory, A. S.; Knowlden, S. W.; Ziemer, N. R.; Alsulami, R. N.; Petersen, J. L.; Popp, B. V. Beneficial Effect of a Secondary Ligand on the Catalytic Difunctionalization of Vinyl Arenes with Boron and CO_2. *ChemCatChem* **2019**, *11* (23), 5814–5820. https://doi.org/10.1002/cctc.201901197.

(13) Kinder, D. H.; Katzenellenbogen, J. A. Acylamido Boronic Acids and Difluoroborane Analogs of Amino Acids: Potent Inhibitors of Chymotrypsin and Elastase. *J. Med. Chem.* **1985**, *28* (12), 1917–1925. https://doi.org/10.1021/jm00150a027.

(14) Martichonok, V.; Jones, J. B. Probing the Specificity of the Serine Proteases Subtilisin Carlsberg and R-Chymotrypsin with Enantiomeric 1-Acetamido Boronic Acids. An Unexpected Reversal of the Normal "L"-Stereoselectivity Preference. 9.

(15) Coutts, S. J.; Adams, J.; Krolikowski, D.; Snow, R. J. Two Efficient Methods for the Cleavage of Pinanediol Boronate Esters Yielding the Free Boronic Acids. *Tetrahedron Lett.* **1994**, *35* (29), 5109–5112. https://doi.org/10.1016/S0040-4039(00)77040-7.

(16) Brown, H. C.; Rangaishenvi, M. V. LI *. Convenientproceduresfor the Recovery of Pinanediol in Asymmetricsynthesisvia One-Carbon Homologation of Boronic Esters. 16.

(17) Diemer, V.; Chaumeil, H.; Defoin, A.; Carré, C. Syntheses of Extreme Sterically Hindered 4-Methoxyboronic Acids. *Tetrahedron* **2010**, *66* (4), 918–929. https://doi.org/10.1016/j.tet.2009.11.103.

(18) Molander, G. A.; Ito, T. Cross-Coupling Reactions of Potassium Alkyltrifluoroborates with Aryl and 1-Alkenyl Trifluoromethanesulfonates. *Org. Lett.* **2001**, *3* (3), 393–396. https://doi.org/10.1021/ol006896u.

(19) Yuen, A. K. L.; Hutton, C. A. Deprotection of Pinacolyl Boronate Esters via Hydrolysis of Intermediate Potassium Trifluoroborates. *Tetrahedron Lett.* **2005**, *46* (46), 7899–7903. https://doi.org/10.1016/j.tetlet.2005.09.101.
(20) Inglis, S. R.; Woon, E. C. Y.; Thompson, A. L.; Schofield, C. J. Observations on the Deprotection of Pinanediol and Pinacol Boronate Esters via Fluorinated Intermediates. *J. Org. Chem.* **2010**, *75* (2), 468–471. https://doi.org/10.1021/jo901930v.
(21) Murphy, J. M.; Tzschucke, C. C.; Hartwig, J. F. One-Pot Synthesis of Arylboronic Acids and Aryl Trifluoroborates by Ir-Catalyzed Borylation of Arenes. *Org. Lett.* **2007**, *9* (5), 757–760. https://doi.org/10.1021/ol062903o.
(22) Snow, R. J.; Bachovchin, W. W.; Barton, R. W.; Campbell, S. J.; Coutts, S. J.; Freeman, D. M.; Gutheil, W. G.; Kelly, T. A.; Kennedy, C. A. Studies on Proline Boronic Acid Dipeptide Inhibitors of Dipeptidyl Peptidase IV: Identification of a Cyclic Species Containing a B-N Bond. *J. Am. Chem. Soc.* **1994**, *116* (24), 10860–10869. https://doi.org/10.1021/ja00103a002.
(23) Pennington, T. E.; Kardiman, C.; Hutton, C. A. Deprotection of Pinacolyl Boronate Esters by Transesterification with Polystyrene–Boronic Acid. *Tetrahedron Lett.* **2004**, *45* (35), 6657–6660. https://doi.org/10.1016/j.tetlet.2004.07.014.
(24) Hinkes, S. P. A.; Klein, C. D. P. Virtues of Volatility: A Facile Transesterification Approach to Boronic Acids. *Org. Lett.* **2019**, *21* (9), 3048–3052. https://doi.org/10.1021/acs.orglett.9b00584.
(25) Song, Y.-L.; Morin, C. Cedranediolborane as a Borylating Agent for the Preparation of Boronic Acids: Synthesis of a Boronated Nucleoside Analogue. *Synlett* **2001**, *2001* (02), 0266–0268. https://doi.org/10.1055/s-2001-10762.
(26) Jung, M. E.; Lazarova, T. I. New Efficient Method for the Total Synthesis of (*S* , *S*)-Isodityrosine from Natural Amino Acids. *J. Org. Chem.* **1999**, *64* (9), 2976–2977. https://doi.org/10.1021/jo9902751.
(27) Perttu, E. K.; Arnold, M.; Iovine, P. M. The Synthesis and Characterization of Phenylacetylene Tripodal Compounds Containing Boroxine Cores. *Tetrahedron Lett.* **2005**, *46* (50), 8753–8756. https://doi.org/10.1016/j.tetlet.2005.10.033.
(28) Sun, J.; Perfetti, M. T.; Santos, W. L. A Method for the Deprotection of Alkylpinacolyl Boronate Esters. *J. Org. Chem.* **2011**, *76* (9), 3571–3575. https://doi.org/10.1021/jo200250y.
(29) Inglesby, P. A.; Agnew, L. R.; Carter, H. L.; Ring, O. T. Diethanolamine Boronic Esters: Development of a Simple and Standard Process for Boronic Ester Synthesis. *Org. Process Res. Dev.* **2020**, *24* (9), 1683–1689. https://doi.org/10.1021/acs.oprd.0c00296.
(30) Mancini, R. S.; Lee, J. B.; Taylor, M. S. Boronic Esters as Protective Groups in Carbohydrate Chemistry: Processes for Acylation, Silylation and Alkylation of Glycoside-Derived Boronates. *Org. Biomol. Chem.* **2017**, *15* (1), 132–143. https://doi.org/10.1039/C6OB02278B.
(31) Taylor, M. S. Catalysis Based on Reversible Covalent Interactions of Organoboron Compounds. *Acc. Chem. Res.* **2015**, *48* (2), 295–305. https://doi.org/10.1021/ar500371z.
(32) Tanaka, M.; Nakagawa, A.; Nishi, N.; Iijima, K.; Sawa, R.; Takahashi, D.; Toshima, K. Boronic-Acid-Catalyzed Regioselective and 1,2- *Cis* -Stereoselective Glycosylation of Unprotected Sugar Acceptors via S_Ni-Type Mechanism. *J. Am. Chem. Soc.* **2018**, *140* (10), 3644–3651. https://doi.org/10.1021/jacs.7b12108.
(33) Shimada, N.; Sugimoto, T.; Noguchi, M.; Ohira, C.; Kuwashima, Y.; Takahashi, N.; Sato, N.; Makino, K. Boronic Acid-Catalyzed Regioselective Koenigs–Knorr-Type Glycosylation. *J. Org. Chem.* **2021**, *86* (8), 5973–5982. https://doi.org/10.1021/acs.joc.1c00130.
(34) D'Angelo, K. A.; Taylor, M. S. Borinic Acid Catalyzed Stereo- and Regioselective Couplings of Glycosyl Methanesulfonates. *J. Am. Chem. Soc.* **2016**, *138* (34), 11058–11066. https://doi.org/10.1021/jacs.6b06943.

Chapter III

Synthesis of Borylated Ibuprofen Derivative through Suzuki Cross-Coupling and Alkene Boracarboxylation Reactions

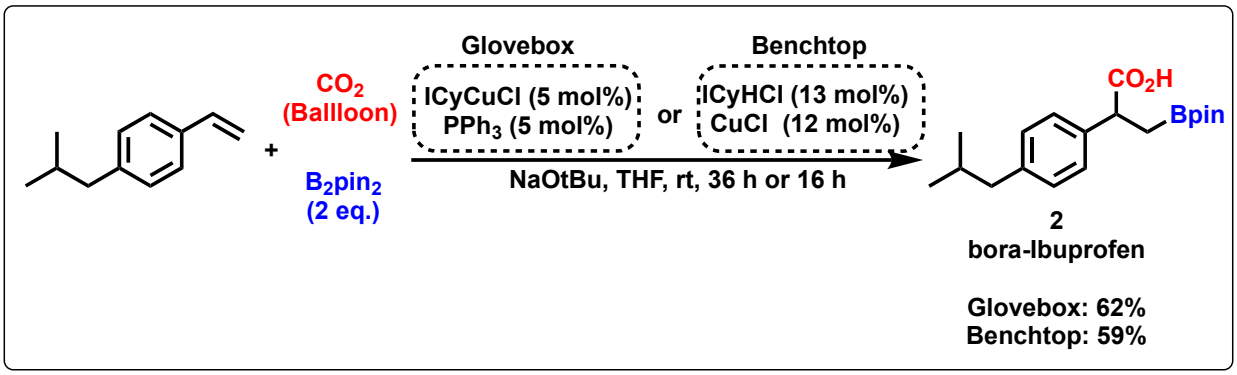

3.1 Abstract

Non-steroidal anti-inflammatory drugs (NSAIDs) are among the most common drugs used to manage and treat pain and inflammation. A new class of boron functionalized NSAID (*bora* NSAID) was accessed under mild conditions *via* copper-catalyzed regioselective boracarboxylation of vinyl arenes using carbon dioxide (balloon) and a diboron reductant at room temperature in 2016. This original method was performed primarily in a glovebox or with a Schlenk manifold under rigorous air and moisture free conditions, leading often to irreproducible reaction outcomes due to trace impurities. Here, a simpler and more convenient benchtop method for synthesizing a representative *bora*-NSAID, *bora*-ibuprofen, is disclosed. A Suzuki-Miyaura cross-coupling reaction between 4-bromo-isobutylbenzene and vinylboronic acid pinacol ester, provides access to 4-isobutylstyrene. The styrene is subsequently boracarboxylated regioselectively to provide *bora* ibuprofen, an a-aryl-b-boryl-propionic acid, in good yield on multi-gram scale. This procedure allows for the broader utilization of copper-catalyzed boracarboxylation in synthetic laboratories, enabling research to ensue on *bora*-NSAIDs and other unique boron-functionalized drug-like molecules

3.2 Introduction

Organoboron compounds have been employed strategically in chemical synthesis for more than 50 years.[1–6] Reactions such as hydroboration-oxidation,[7–10] halogenation,[11, 12] amination,[13, 14] and Suzuki-Miyaura cross-coupling[15–17] have led to significant multidisciplinary innovations in chemistry and related-disciplines. The Suzuki-Miyaura reactions, for example, account for 40% of all carbon-carbon bond forming reactions in the pursuit of pharmaceutical drug candidates.[18]The Suzuki-Miyaura cross-coupling reaction allows direct access to vinyl arenes in one step from the halogenated arene precursor.[19] This greener catalytic strategy is valuable relative to traditional poorly atom economical Wittig syntheses from aldehydes that produce stoichiometric triphenylphosphine oxide byproduct.

A regioselective hetero(element)carboxylation of vinyl arenes was envisaged to allow for direct access to novel hetero(element)-containing non-steroidal anti-inflammatory drugs (NSAIDs) utilizing CO_2 directly in the synthesis. However, hetero(element)carboxylation reactions were exceedingly rare, and limited to alkynyl and allenyl substrates prior to 2016.[20–22] Extension of the boracarboxylation reaction to vinyl arenes would provide boron-functionalized NSAIDs, and boron-based pharmaceutical candidates (Figure 1) have been gaining popularity marked by recent decisions by the FDA to approve the chemotherapeutic bortezomib, antifungal tavaborole, and anti-inflammatory crisaborole. The Lewis acidity of boron is interesting from a drug design standpoint due to the capability to readily bind Lewis bases such as diols, hydroxyl groups on carbohydrates, or nitrogen-bases in RNA and DNA since these Lewis bases play important roles in physiological and pathological processes.[23]

This catalytic approach to boracarboxylation relies upon borylcupration of the alkene by a Cu-boryl intermediate, followed by CO_2 insertion into the resulting Cu-alkyl intermediate. Sadeghi and coworkers reported the borylcupration of styrene derivatives through use of (NHC)Cu-boryl,[24] and carboxylation of Cu-alkyl species has also been observed.[25] In 2016, the Popp lab developed a new synthetic approach to

achieve mild difunctionalization, of vinyl arenes using a (NHC)Cu-boryl catalyst and only a single atmosphere of gaseous CO_2.[26] Using this method, the α-aryl propionic acid pharmacophore is accessed in a single step, and a novel unexplored class of boron-modified NSAID can be prepared in excellent yields. In 2019, catalytic additives improved catalyst efficiency and broadening of substrate scope, including the preparation of an additional two novel borylated NSAIDs (Figure 3.1).[27]

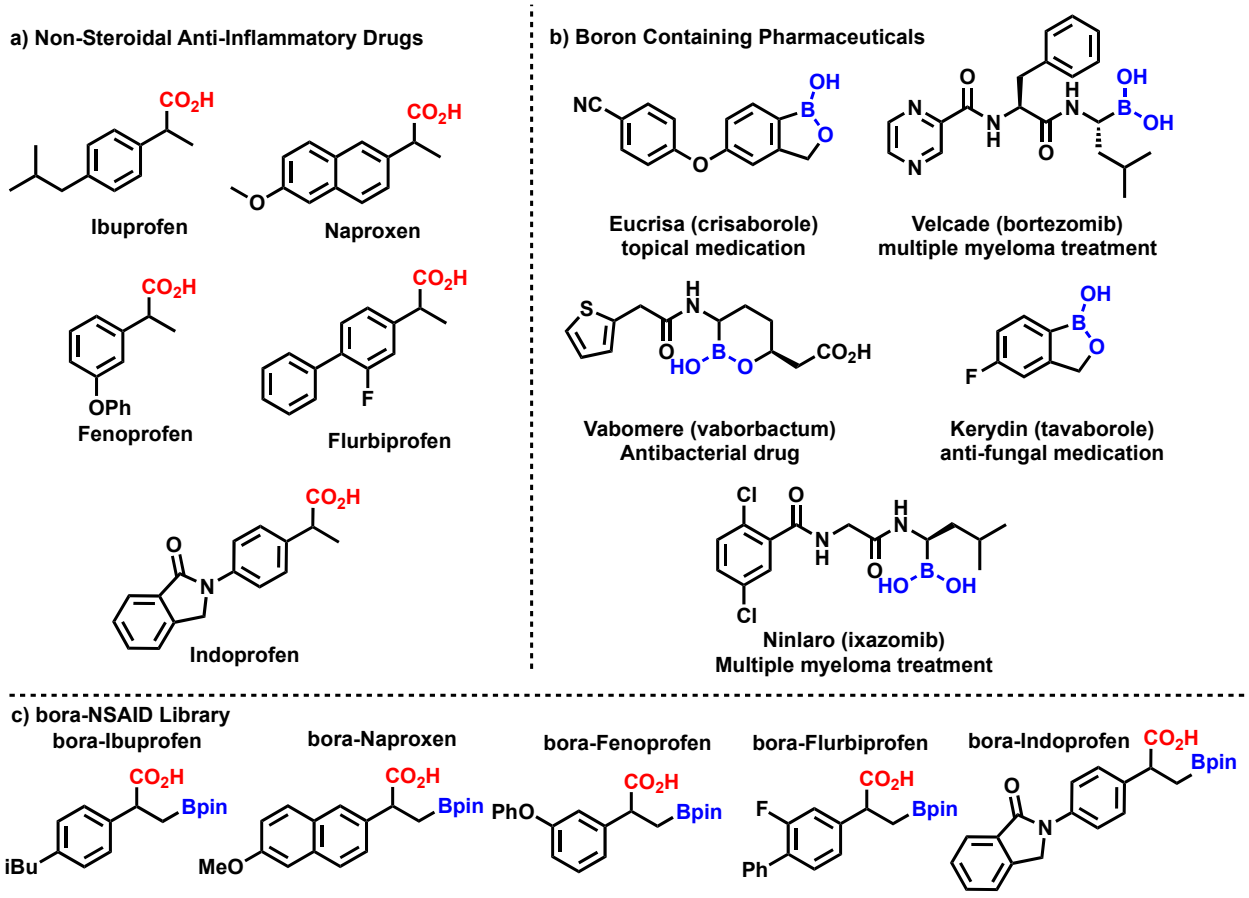

Figure 3.1 Medicinal relevance of organoboron compound. a) Carboxylic acid group containing non-steroidal anti inflammatory drugs. b) FDA approved Boron containing pharmaceuticals. c) boron containing NSAID analouges (*bora*-NSAIDs).

Previous boracarboxylation reactions of alkenes could only be achieved under stringent air and moisture free conditions with use of an isolated N-heterocyclic-carbene ligated copper(I) precatalyst (NHC-

Cu; NHC = 1,3-bis(cyclohexyl)-1,3-dihydro-2*H*-imidazol-2-ylidene, ICy). A benchtop method wherein borylated Ibuprofen can be synthesized using simple reagents would be more desirable to the synthetic community, prompting us to develop reaction conditions that allowed for boracarboxylation of vinyl arenes, particularly 4-isobutylstyrene, to proceed from the *in-situ* generation of NHC-Cu precatalyst, and without the need of a glovebox. Recently, a boracarboxylation protocol was reported using imidazolium salts and copper(I)-chloride to generate in-situ active NHC-ligated copper(I) catalyst.[28] Using this method, α-methyl styrene was boracarboxylated to afford 71% isolated yield of the desired product, albeit with use of a glovebox. Inspired by this result, a modified procedure to boracarboxylate tert-butylstyrene without using a nitrogen-filled glovebox was devised. The desired boracarboxylated tert-butyl styrene product was afforded in 90% yield on a 1.5-gram scale. Gratifyingly, this method could be applied to 4-isobutylstyrene to afford *bora*-Ibuprofen NSAID derivative in moderate yield. The α-aryl propionic acid pharmacophore is the core motif amongst NSAIDs, therefore synthetic strategies that allow direct access to this motif are highly desirable chemical transformations. Herein, a synthetic pathway to access a novel *bora*-Ibuprofen NSAID derivative from an abundant, inexpensive 1-bromo-4-isobutylbenzene starting material (~$2.50/1 g) in moderate yield in two steps, without the need for a glovebox, is presented.

3.3 Reaction Protocols

3.3.1 Synthesis of 4-isobutylstyrene through Suzuki Cross Coupling of 1-bromo-4-isobutylbenzene with vinylboronic acid pinacol ester

Scheme 3.1 Synthesis of 4-Isobutylstyrene (1) via Suzuki Cross Coupling reaction

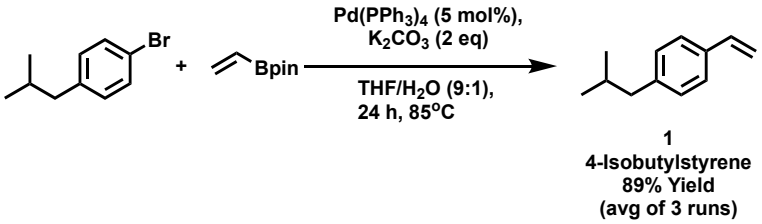

1.1. Add 144 mg of palladium(0) tetrakistriphenylphosphine (5 mol%), 1.04 g of anhydrous potassium carbonate (2 equiv), and a magnetic stir bar (0.5 x 0.125 in.) to a 40 mL scintillation vial then seal with a pressure relief cap. Completely encapsulate the vial seal with electrical tape.

1.1.1. Purge the reaction mixture with argon for 2 min. After the 2 min, add 1.07 g of 1-bromo-4-isobutylbenzene (1 equiv), then add 13 mL of anhydrous THF obtained from a solvent purification system (or still pot) with continuous argon flow, then commence magnetic stirring.

Note: Argon gas can be replaced with dry nitrogen gas.

1.1.2. Add 1.5 mL of argon-sparged deionized water to the solution, followed by 0.72 mL of vinylboronic acid pinacol ester (1.5 equiv), then purge the reaction mixture with argon for an additional 5 min.

1.1.3. Once the purge has finished, heated at 85 ^{o}C for 24 h on an IKA stirring hot plate.

1.1.4. After 24 h, remove a small aliquot from the reaction and dilute it with 2 mL of dichloromethane, then perform TLC (UV visualization) using hexane to ensure reaction completion (R_f = 0.9 reactant, R_f = 0.91 product).

1.2. Upon confirmation of 1-bromo-4-isobutylbenzene consumption, add the reaction mixture to a 125 mL separatory funnel and then add 30 mL of deionized water.

1.2.1. Extract 3x with 5 mL dichloromethane, adding the organic extracts to a 125 mL Erlenmeyer flask, then discard the aqueous layer.

1.2.2. Transfer the organic extracts into a 125 mL separatory funnel, wash with 30 mL of brine, an aqueous saturated sodium chloride solution and discard the brine.

1.2.3. Transfer the organic layer to a 125 mL Erlenmeyer flask, then add 5 g of sodium sulfate and swirl the flask for at least 20 s.

1.2.4. Vacuum filter, using a Buchner funnel, the solution into a 125 mL filter flask.

1.2.5. Transfer the organic layer to a 100 mL round-bottom flask, then concentrate the reaction in vacuum for 15-30 minutes, pending vacuum strength, to provide a pale-yellow viscous oil.

1.3. Subject the crude reaction mixture to column chromatography using 50 g of SilicaFlash P60 silica gel and pure hexane as the eluent to obtain pure 4-isobutylstyrene (**1**).

NOTE: For the present study, the yield was 89% (average of 3 reactions).

NOTE: 4-isobutylstyrene is subjected to polymerization at room temperature under light, so once isolated, the product must be stored in the dark at or below -20 ºC until needed. If necessary, a small amount of butylated hydroxytoluene (BHT) can be added to inhibit polymerization. BHT does not impact the efficiency of copper-catalyzed boracarboxylation.

3.3.2 Glovebox large-scale synthesis of *bora*-Ibuprofen

Scheme 3.2 Synthesis of *bora*-Ibuprofen (**2**) via glovebox and benchtop boracarboxylation methods.

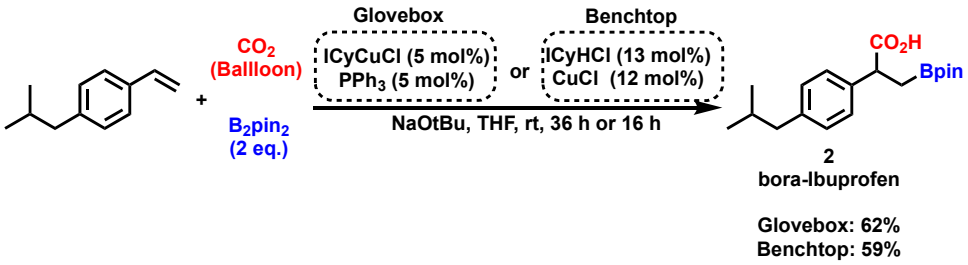

1.1. Add 160 mg of ICyCuCl (5 mol%), 131 mg of triphenylphosphine (5 mol%), 1.92 g of sodium tert-butoxide (2 equiv), 20 mL of anhydrous, degassed THF, and a 0.5 x 0.125 in. magnetic stir bar to a 20 mL scintillation vial, then seal with an air-tight septum, and stir the resulting solution for 20 min.

1.1.1. After 20 min, the catalyst solution was transferred to a 60 mL syringe, and the needle was plugged into a septum.

1.1.2. Add 2.79 g of bis(pinacolato)diboron (1.1 equiv), 1.87 mL of 4-isobutylstyrene (1 equiv), 140 mL of THF, and a 2 x 0.3125 in. magnetic stir bar to a 500 mL round-bottom flask, seal with a septum, then tape around the septum until the seal is encapsulated.

1.2. Remove the 500 mL round-bottom flask containing the styrene solution and the 60 mL syringe containing the catalyst solution from the glovebox and move to a fume hood.

NOTE: After preparation, the 500 mL round-bottom flask and catalyst solution syringe must be removed immediately from the glovebox. The styrene substrate is subjected to polymerization in THF, and the catalyst solution decomposes upon standing for a long period of time or upon exposure to air.

1.2.1. While purging the 500 mL round-bottom flask with dry carbon dioxide, add the catalyst solution over 30 s, then stir the reaction at ambient temperature for 3 h.

1.2.2. After 3 h, again purge the round-bottom flask with dry carbon dioxide (bone dry) for 15 min, then stir at ambient temperature for 33 h.

1.3. Upon reaction completion, concentrate the reaction mixture in vacuum then acidify with 30 mL of aqueous HCl (1.0 M).

1.3.1. Add 50 mL of diethyl ether to the round-bottom flask containing the acidified reaction solution, swirl the solution for at least 10 s, transfer the solution to a 500 mL separatory funnel, separate organic and aqueous layers adding the aqueous layer to a 1000 mL Erlenmeyer flask.

1.3.2. Extract the organic layer 8x with 50 mL saturated $NaHCO_3$, and transfer aqueous extracts to a 1000 mL Erlenmeyer flask.

1.3.3. Acidify combined aqueous layers in 1000 mL Erlenmeyer flask with 12 M HCl (to pH $\leq$ 1.0 by litmus paper), transfer solution to clean 1000 mL separatory funnel.

1.3.4. Extract aqueous solution 8x with 50 mL of dichloromethane and transfer the organic extracts to a clean 1000 mL Erlenmeyer flask.

1.3.5. Add 50 g of sodium sulfate to the organic extraction solution, and swirl the flask for at least 20 s.

1.3.6. Filter the organic extraction solution through a Buchner funnel and collect in a clean 1000 mL filtration flask.

1.3.7. Concentrate the solution in vacuum

1.4. Dissolve the residue in 10 mL of HPLC-grade heptane, then store it in a freezer (-20 ^{o}C) overnight to afford pure recrystallized *bora*-Ibuprofen.

NOTE: The present study, the yield of *bora*-Ibuprofen was 62% (average of 2 reactions).

3.3.3 Benchtop large-scale synthesis of *bora*-Ibuprofen

NOTE: This reaction procedure described below was carried out without using a nitrogen-filled glovebox. All chemicals were used as received or synthesized without further purification (drying, distilling, etc.). All vials and glassware were dried and heated in an oven (180 ^{o}C) for at least 24 h prior to use and cooled under argon to room temperature immediately before reaction setup.

1.1. Add 334 mg of ICyH•Cl (13 mol%), 2.92 g of sodium tert-butoxide (3 equiv), and a 0.5 x 0.125 in. magnetic stir bar to a 20 mL scintillation vial, then seal with an air-tight septum and immediately purge with argon for 5 min.

1.1.1. Add 20 mL of anhydrous, degassed THF *via* syringe to the 20 mL scintillation vial containing the ligand and base mixture, purge the resulting solution for 5 min with argon, then stir for an additional 30 min.

1.1.2. Add 119 mg of CuCl (12 mol%) and a 0.5 x 0.125 in. magnetic stir bar to a 20 mL scintillation

vial, then seal with an air-tight septum and immediately purge with argon for 5 min. After stirring the ligand solution (from step 3.1.1) for 30 min, add it to the CuCl scintillation vial under a positive argon flow, then stir the resulting solution for 1 h.

NOTE: When weighing out CuCl, take care to place it directly in the center of the bottom of the scintillation vial, as it tends to get stuck around the inside corner edges of the vial, resulting in poor dissolution in the ligand solution.

1.2. Add 5.08 g of bis(pinacolato)diboron (2 equiv) and a 2 x 0.3125 in. magnetic stir bar to a 500 mL round-bottom flask and seal with a septum, then encapsulate the septum seal with black electrical tape. Once sealed, add 140 mL of THF, and 1.78 mL of 4-isobutylstyrene (1 equiv) to the flask, then purge with argon for 5 min.

1.2.1. Purge the 500 mL round-bottom flask with dry carbon dioxide immediately following the argon purge. Then add the catalyst solution (from step 3.1.2) for 30 s, continue purging with dry carbon dioxide for 15 min, then stir the reaction at ambient temperature for 16 h.

1.3. Concentrate the reaction mixture for 15-30 minutes in vacuum upon reaction completion, then acidify with 30 mL of aqueous HCl (1.0 M).

1.3.1. Add 50 mL of diethyl ether to the round-bottom flask containing the acidified reaction solution, swirl the solution for at least 10 s, transfer the solution to a 500 mL separatory funnel, separate organic and aqueous layers, and add the aqueous layer to a 1000 mL Erlenmeyer flask.

1.3.2. Extract the organic layer 8x with 50 mL of saturated $NaHCO_3$, and transfer aqueous extracts to a 1000 mL Erlenmeyer flask.

1.3.3. Acidify combined aqueous layers in 1000 mL of Erlenmeyer flask with 12 M HCl (to pH ≤ 1.0 by litmus paper), transfer solution to clean 1000 mL separatory funnel.

1.3.4. Extract aqueous solution 8x with 50 mL dichloromethane, and transfer the organic extracts to a clean 1000 mL Erlenmeyer flask.

1.3.5. Add 50 g of sodium sulfate to the organic extraction solution, and swirl the flask for at least 20 s.

1.3.6. Filter the organic extraction solution through a Buchner funnel, and collect in a clean 1000 mL filtration flask.

1.3.7. Transfer the filtrate to a round bottom flask

1.3.8. Concentrate the filtrate in vacuo.

1.4. Dissolve the residue in 10 mL of HPLC-grade heptane, then store it in a freezer (-20 ^{o}C) overnight to afford pure recrystallized *bora*-Ibuprofen.

NOTE: For the present study, the yield of *bora*-Ibuprofen was 59%.

3.4 Representative Results

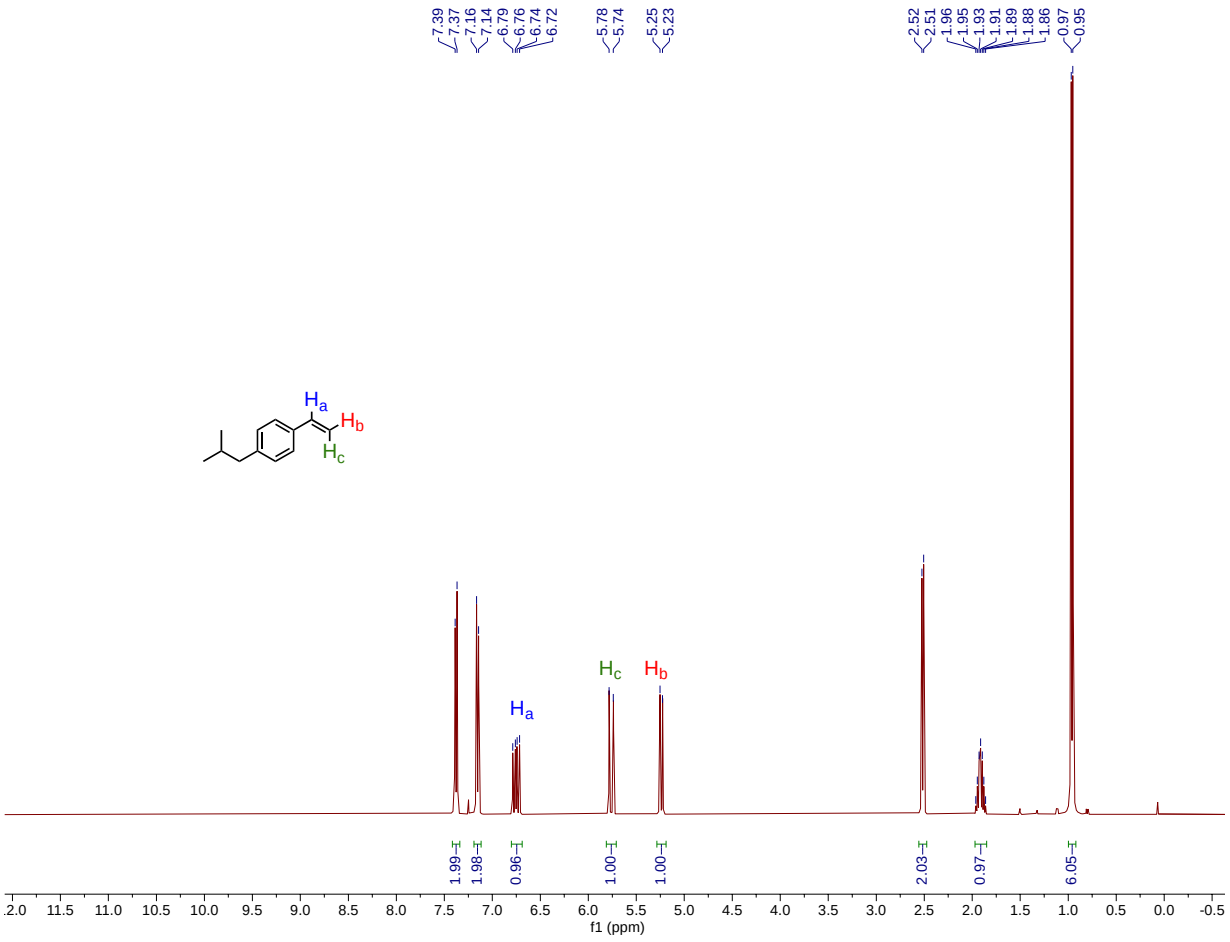

Figure 3.2 ^{1}H NMR spectrum of 4-Isobutyl styrene (**1**)

4-Isobutylstyrene was characterized by ^{1}H and ^{13}C NMR spectroscopy. *bora*-Ibuprofen was characterized by ^{1}H, ^{13}C, and ^{11}B NMR spectroscopy to confirm the product structure and assess purity. Key data for these compounds are described in this section.

Spectral data are in good agreement with the structure of 4-isobutylstyrene **1** (Figure 3.2). The ^{1}H NMR spectrum obtained in $CDCl_3$ (Figure 3.2) shows the characteristic AMX splitting pattern seen for monosubstituted styrene derivatives. These resonances are observed as a doublet at 5.17 (d, J = 10.9 Hz,

1H), a doublet at 5.69 (d, J = 17.6 Hz, 1H), and a doublet of doublets at 6.62 – 6.78 (dd, J = 10.9, 17.6 Hz 1H). A second characteristic feature is the iso-butyl methine proton, appearing as a nonet at 2.37–2.52 (m, 2H) with corresponding methyl groups at 0.89 (d, J = 6.6 Hz, 6H).[30] The nine resonances observed in the ^{13}C NMR spectrum agree with literature values (Figure 3.3).[30]

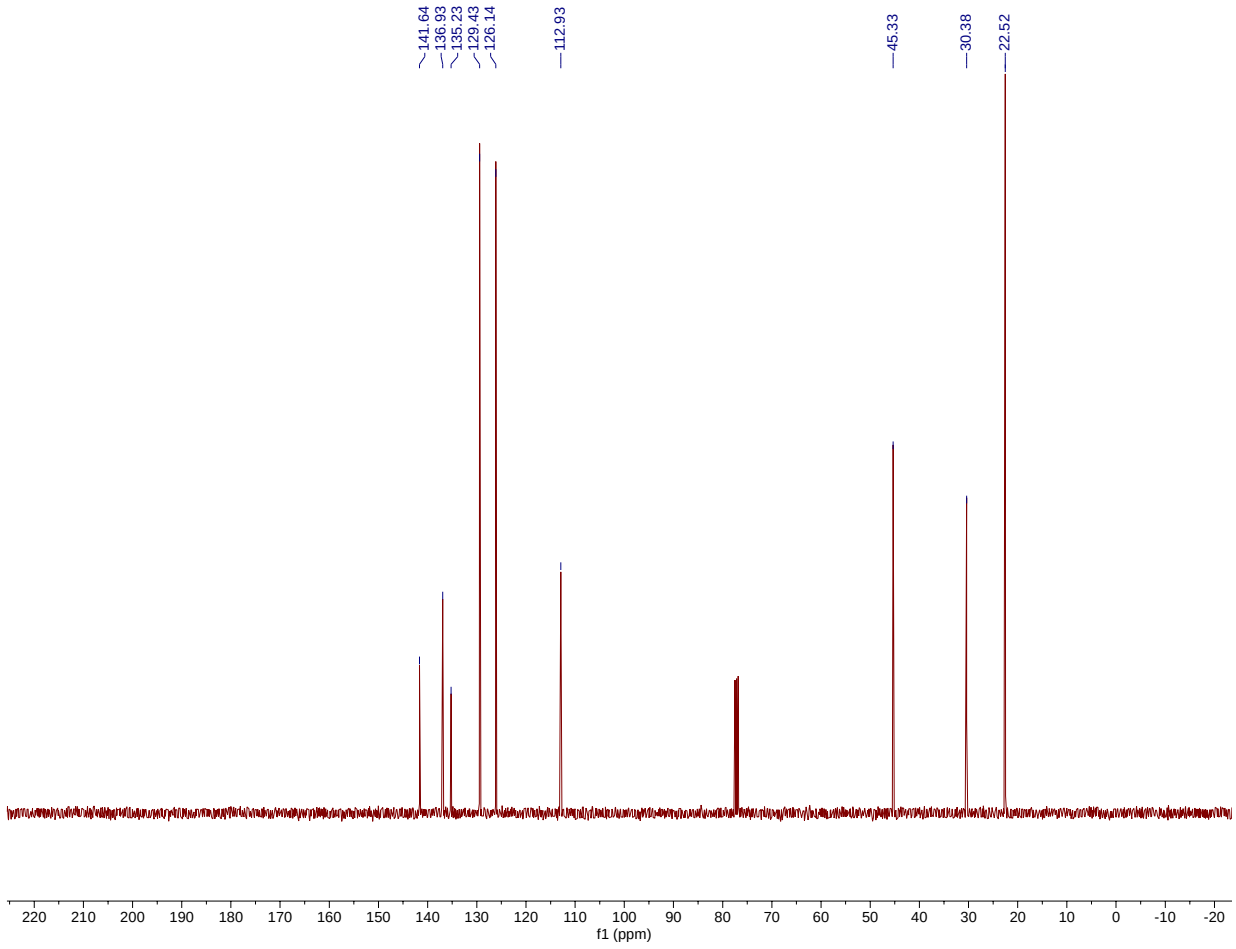

Figure 3.3 ^{13}C NMR spectrum of 4-Isobutyl styrene (**1**)

Synthesis of 4-isobutylstyrene *via* this protocol reliably provides direct access to the product in 89% yield (average of 3 reactions, 5 mmol scale); however, deviation from any of the key reaction conditions such as temperature and time significantly impact the efficiency of the reaction. It is important that the reaction be heated at no less than 85 ^{o}C. Reaction completion should be verified by TLC at or after 24 hours.

Spectral data are in good agreement with the structure of boracarboxylated product **2** (Figure 3.5). As with the previous substrate the ^{1}H NMR spectrum obtained in $CDCl_3$ (Figure 6) shows an ABX splitting pattern, but this pattern occurs due to diastereotopic methylene protons, arising from the newly generated benzylic stereogenic center. The AB resonances are observed as a pair of doublets of doublets at 1.53 (dd, J = 16.0, 9.1 Hz, 1H) and 1.29 (dd, J = 16.0, 7.6 Hz, 1H) while the X resonance is observed at 3.82 (dd, J = 9.1, 7.6 Hz, 1H). The latter resonance is deshielded, which is consistent with a methine proton alpha to two sp^2 carbons. Another set of significant resonances are at 1.12 (s, 6H) and 1.11 (s, 6H), corresponding to magnetically inequivalent methyl groups on the two sides of the pinacolato boron moiety.[26]

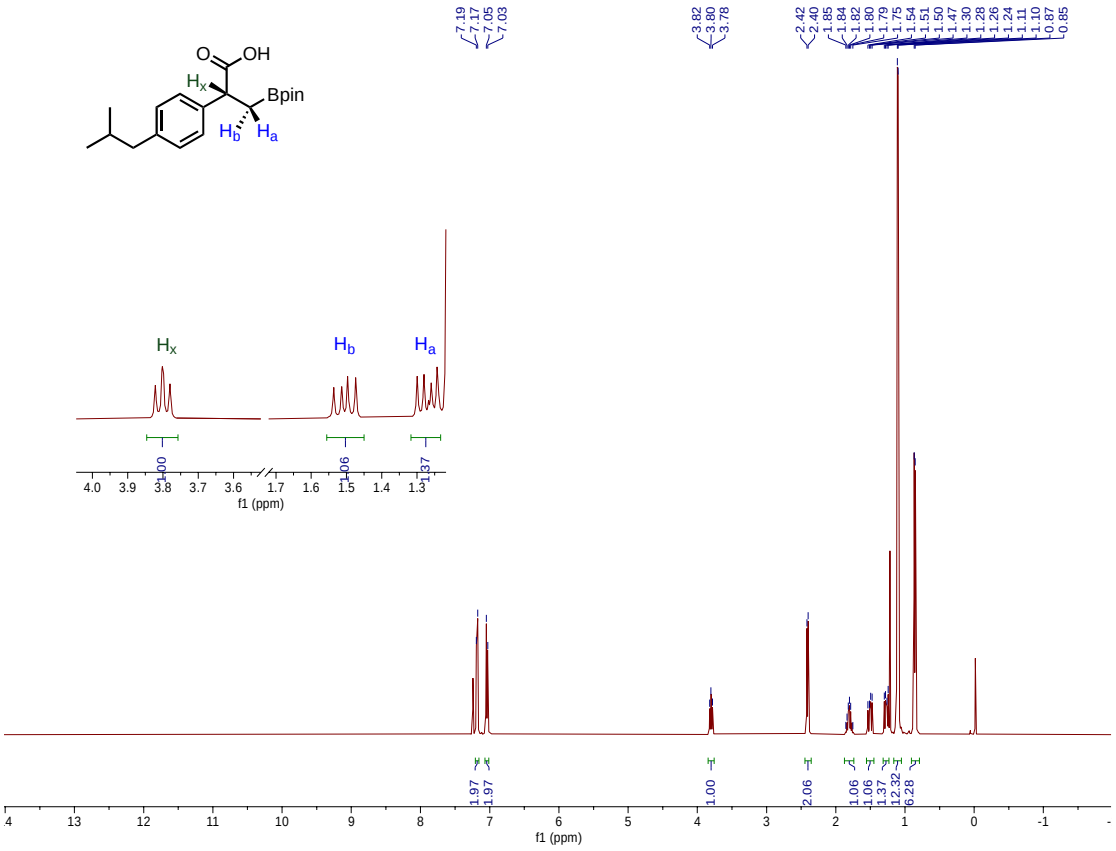

Figure 3.4 ^{1}H NMR spectrum of *bora*-Ibuprofen (**2**)

The ^{13}C NMR spectrum of boracarboxylated product **2** (Figure 3.5) shows a very broad signal at 16 ppm, which is characteristic of a quadrupolar-broadened carbon bound to the boron. Another significant resonance is at 180.8 ppm corresponding to the carbonyl carbon of the free carboxylic acid group.

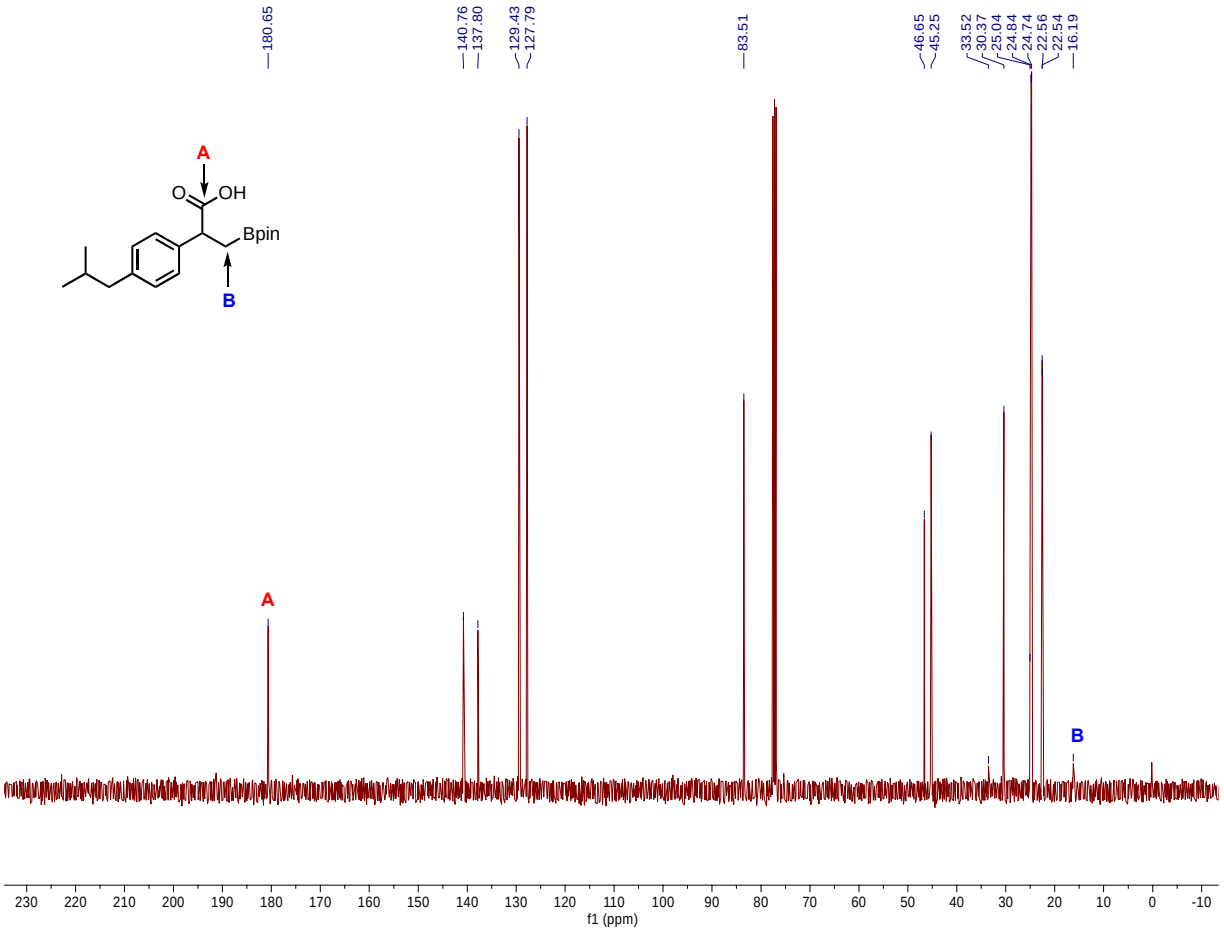

Figure 3.5 ^{13}C NMR spectrum of *bora*-Ibuprofen (**2**)

The ^{11}B NMR spectrum (Figure 3.6) shows a single broad resonance at 33.4 ppm that is characteristic of a trivalent boronic ester.

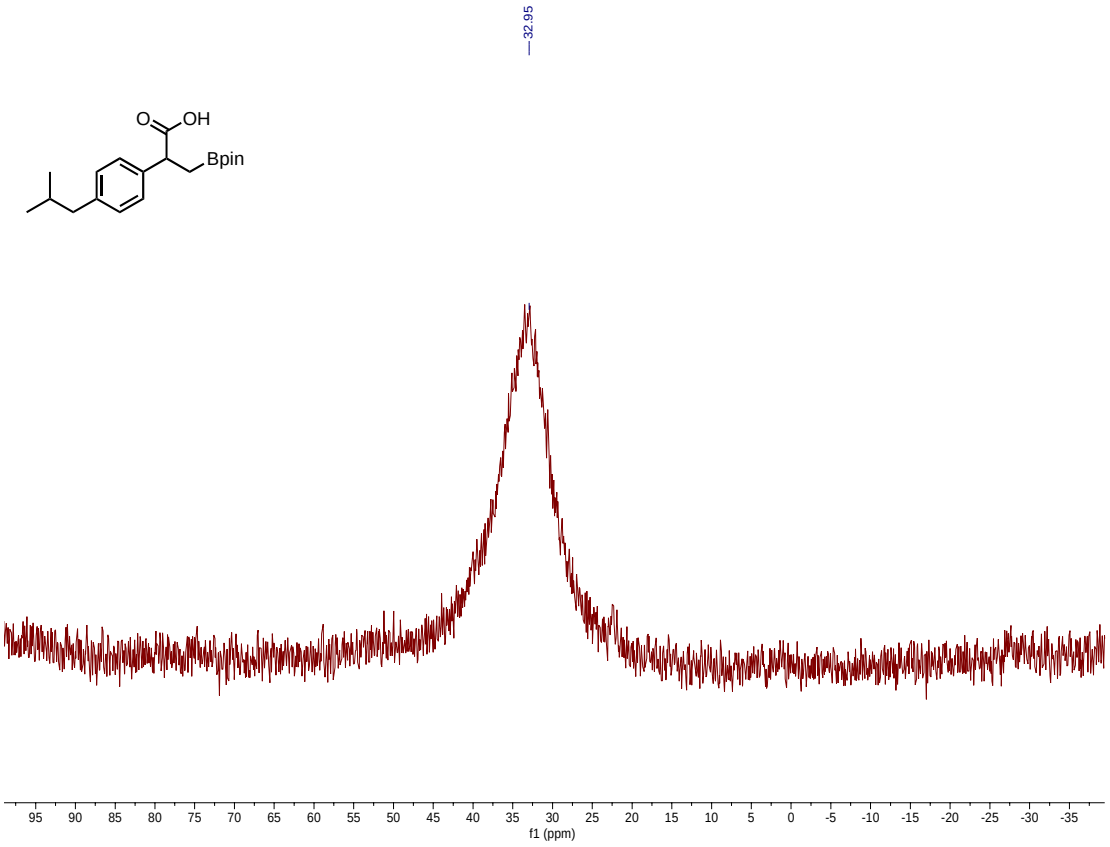

Figure 3.6 ^{11}B NMR spectrum of *bora*-Ibuprofen (**2**)

The synthesis of *bora*-Ibuprofen via this protocol reliably provides direct access to the product in 62% yield (average of 2 reactions, 2.05 g isolated), however, this reaction is far more sensitive than the previous Suzuki cross-coupling reaction. Any deviation that occurs from the reported protocol will result in significantly diminished yields. Particular attention needs to be paid to the air sensitive nature of this reaction. Using the benchtop protocol, the large-scale synthesis of *bora*-Ibuprofen provides the desired product in 59% yield (1.95 g isolated) which is comparable to the glovebox method.

3.5 Discussion

4-Isobutylstyrene (**1**) was obtained efficiently via a Suzuki Cross Coupling reaction from inexpensive, commercially available 4-bromoIsobutylbenzene, and vinylboronic acid pinacol ester. This allows for access to the desired styrene in a greener, more atom economical manner than the conventional Wittig approach. Reaction monitoring via TLC was crucial to ensure full conversion of the 1-bromo-4-isobutylbenzene substrate, because reactions not proceeding to full conversion led to difficult flash chromatographic separation of the substrate and products.

Boracarboxylation of 4-isobutylstyrene with an NHC-copper(I) catalyst at ambient temperature using a pincolato diboron reductant under an atmosphere of gaseous CO_2 provides *bora*-Ibuprofen (**2**) in high yield. It is important to note that the styrene must be rigorously freeze- pump-thawed[31] to ensure no dioxygen remains in the solution, presumably due to copper(I)-aerobic decomposition[32] that leads to diminished reactivity and unwanted side products such as formal hydroboration of the styrene. The catalyst must be added to the reaction mixture quickly due the air sensitive nature of the catalyst. A tell-tale sign that dioxygen has contaminated the reaction is the evolution of a sky-blue reaction color. Reactions that progress appropriately to high yield will appear cloudy white with a slight pink tint after addition of the catalyst solution then will turn to brown and ultimately light green after the reaction is exposed to CO_2 for 3 or more hours. The boracarboxylation reaction can tolerate gentle heating up to 45 ^{o}C but higher temperatures lead to diminished yields.[27]

The reaction cannot be stored for any amount of time and must be immediately purified. The resulting end color of a successful boracarboxylation reaction is either brown or light green. Reactions not immediately purified will turn sky blue, owing to copper oxidation with concomitant product decomposition. Product isolation is still possible but diminished yields will result. *bora*-Ibuprofen cannot be isolated by column chromatography of any type (e.g., silica gel, Florisil) and must be isolated following

the acid-base workup protocol described above. Once isolated *bora*-ibuprofen, as well as many other similar a-aryl-b-boryl propionic acid derivatives studied thus far, is an air stable white solid. Trace amounts of diboron reductant often remain after the first acid-base workup. A second acid-base workup followed by a second recrystallization in heptane often satisfactorily removes trace impurities to provide analytically pure products.

The benchtop boracarboxylation method is more convenient and easier to execute that the glovebox method, while still producing similar reaction outcomes. Nevertheless, there are some known limitations associated with the benchtop method. The reaction must be performed under moisture and air-free conditions. To further understand moisture sensitivity, a boracarboxylation reaction was performed using the benchtop method with "wet" THF (a high purity 4 L bottle that was previously opened) for both the *in situ* catalyst preparation and reaction steps. In this case, only 2% NMR yield of the desired product was obtained. Next, a reaction was performed in which the catalyst solution was prepared using anhydrous THF (solvent system dried) while the remaining THF used in the reaction was "wet". A modest increase to 13% NMR yield of boracarboxylated product was observed. It is clear that trace, adventitious water impacts the reaction negatively, especially during pre-/active-catalyst formation. Using the benchtop protocol without an Ar purge (or N_2 purge) of the reaction solution prior to the introduction of CO_2 gas, an NMR yield of 46% (vs. 66% with Ar purge) was obtained. However, a second identical reaction setup provided an NMR yield of only 17%, suggesting that adventitious oxygen/air impacts the reaction in various, irreproducible ways.

In the future, the Popp Group expect that *bora*-Ibuprofen, and other boracarboxylated compounds, will provide access to a host of other functionalized-ibuprofen derivatives (Figure 3.7), thus allowing for their study as potential therapeutic agents for pain management[33–37] or other pharmaceutical applications.

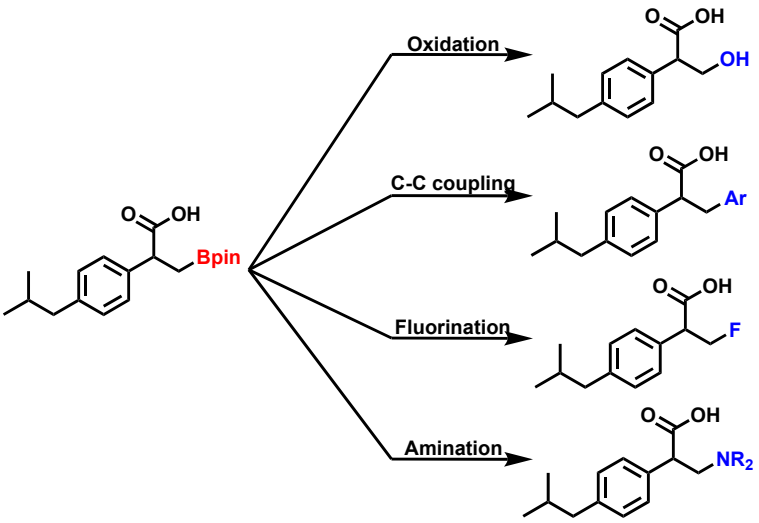

Figure 3.7 Derivatization of *bora*-Ibuprofen

3.6 Experimental Methods

General information

All the air and moisture sensitive experiments were set up in a nitrogen filled MBraun 200B dual port glove box. The cross coupling and boracarboxylation reactions were performed in 500 mL round bottom flasks purchased from ChemGlass and were dried in an oven at 180 ℃ for at least 24 hours prior to use. All glassware used in the glovebox was dried for at least 24 h in the 180 ℃ oven prior to use. The dry solvent used for all experiments was dried on a Glass Contour solvent purification system, and further dried over 4 Å mol sieves. The liquid reagents used in the glovebox were degassed using a freeze/pump/thaw method on a Schlenk line prior to use. $CDCl_3$ was purchased from Cambridge Isotope Laboratories, Inc. NMR spectra were recorded on either a 400 MHz Agilent or 600 MHz Agilent NMR spectrometer. ^{1}H, ^{13}C, and ^{11}B, and 19F NMR experiments were acquired in CDCl3 using tetramethylsilane as a reference in quartz NMR tubes. 11B NMR was referenced to an external BF3·OEt2 standard.

Compound characterization

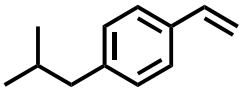

4-Isobutylstyrene

^{1}H NMR (400 MHz, CHLOROFORM-*D*) δ 7.39, 7.38, 7.37, 7.37, 7.36, 7.25, 7.16, 7.16, 7.15, 7.14, 6.79, 6.76, 6.74, 6.72, 5.78, 5.78, 5.74, 5.74, 5.25, 5.25, 5.23, 5.22, 2.52, 2.51, 1.96, 1.95, 1.93, 1.91, 1.90, 1.88, 1.86, 1.33, 0.97, 0.95, 0.07. ^{13}C NMR (101 MHz, CHLOROFORM-*D*) δ 141.64, 136.93, 135.23, 129.43, 126.14, 112.93, 112.91, 45.33, 30.38, 22.52.

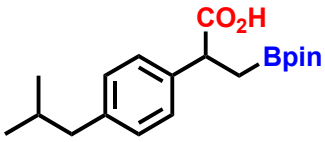

3-boronic acid pinacol ester-2-phenyl propionic acid

^{1}H NMR (400 MHz, CHLOROFORM-*D*) 7.22 – 7.15 (2 H, m), 7.07 – 7.01 (2 H, m), 3.80 (1 H, dd, *J* 9.1, 7.6), 2.41 (2 H, d, *J* 7.2), 1.79 (1 H, dq, *J* 13.5, 6.8), 1.50 (1 H, dd, *J* 15.9, 9.1), 1.32 – 1.23 (1 H, m), 1.22 (1 H, s), 1.10 (12 H, d, *J* 4.9), 0.86 (6 H, dd, *J* 6.6, 1.3). ^{13}C NMR (101 MHz, CHLOROFORM-*D*) δ 180.65, 140.76, 137.80, 129.43, 127.79, 83.51, 46.65, 45.25, 33.52, 30.37, 25.04, 24.84, 24.74, 22.56, 22.54, 16.19. ^{11}B NMR (128 MHz, CHLOROFORM-*D*) δ 32.95.

3.7 References

1. Bose, S.K. *et al.* First-Row d-Block Element-Catalyzed Carbon–Boron Bond Formation and Related Processes. *Chemical Reviews*. **121** (21), 13238–13341, doi: 10.1021/acs.chemrev.1c00255 (2021).
2. Hemming, D., Fritzemeier, R., Westcott, S.A., Santos, W.L., Steel, P.G. Copper-boryl mediated organic synthesis. *Chemical Society Reviews*. **47** (19), 7477–7494, doi: 10.1039/C7CS00816C (2018).
3. Taniguchi, T. Boryl Radical Addition to Multiple Bonds in Organic Synthesis: Boryl Radical Addition to Multiple Bonds in Organic Synthesis. *European Journal of Organic Chemistry*. **2019** (37), 6308–6319, doi: 10.1002/ejoc.201901010 (2019).
4. Budiman, Y.P., Westcott, S.A., Radius, U., Marder, T.B. Fluorinated Aryl Boronates as Building Blocks in Organic Synthesis. *Advanced Synthesis & Catalysis*. **363** (9), 2224–2255, doi: 10.1002/adsc.202001291 (2021).
5. Wang, M., Shi, Z. Methodologies and Strategies for Selective Borylation of C–Het and C–C Bonds. *Chemical Reviews*. **120** (15), 7348–7398, doi: 10.1021/acs.chemrev.9b00384 (2020).

6. Tian, Y.-M., Guo, X.-N., Braunschweig, H., Radius, U., Marder, T.B. Photoinduced Borylation for the Synthesis of Organoboron Compounds: Focus Review. *Chemical Reviews*. **121** (7), 3561–3597, doi: 10.1021/acs.chemrev.0c01236 (2021).
7. Brown, H.C., Rathke, M.W., RogiC´, M.M., De Lue, N.R. Organoboranes for synthesis. 9. Rapid reaction of organoboranes with iodine under the influence of base. a convenient procedure for the conversion of alkenes into iodides via hydroboration. *Tetrahedron*. **44** (10), 2751–2762, doi: 10.1016/S0040-4020(88)90010-5 (1988).
8. Shegavi, M.L., Bose, S.K. Recent advances in the catalytic hydroboration of carbonyl compounds. *Catalysis Science and Technology* **9** (13), 3307–3336, doi: 10.1039/C9CY00807A (2019).
9. Clay, J.M., Vedejs, E. Hydroboration with Pyridine Borane at Room Temperature. *Journal of the American Chemical Society*. **127** (16), 5766–5767, doi: 10.1021/ja043743j (2005).
10. Mao, L., Bose, S.K. Hydroboration of Enynes and Mechanistic Insights. *Advanced Synthesis & Catalysis*. **362** (20), 4174–4188, doi: 10.1002/adsc.202000603 (2020).
11. Pattison, G. Fluorination of organoboron compounds. *Organic & Biomolecular Chemistry*. **17** (23), 5651–5660, doi: 10.1039/C9OB00832B (2019).
12. Zhu, C., Falck, J.R. Transition Metal-Free *ipso* -Functionalization of Arylboronic Acids and Derivatives. *Advanced Synthesis & Catalysis*. **356** (11–12), 2395–2410, doi: 10.1002/adsc.201400305 (2014).
13. Chen, J., Li, J., Dong, Z. A Review on the Latest Progress of Chan-Lam Coupling Reaction. *Advanced Synthesis & Catalysis*. **362** (16), 3311–3331, doi: 10.1002/adsc.202000495 (2020).
14. Rucker, R.P., Whittaker, A.M., Dang, H., Lalic, G. Synthesis of Tertiary Alkyl Amines from Terminal Alkenes: Copper-Catalyzed Amination of Alkyl Boranes. *Journal of the American Chemical Society*. **134** (15), 6571–6574, doi: 10.1021/ja3023829 (2012).
15. Miyaura, Norio., Suzuki, Akira. Palladium-Catalyzed Cross-Coupling Reactions of Organoboron Compounds. *Chemical Reviews*. **95** (7), 2457–2483, doi: 10.1021/cr00039a007 (1995).
16. Lennox, A.J.J., Lloyd-Jones, G.C. Selection of boron reagents for Suzuki–Miyaura coupling. *Chemical Society Reviews*. **43** (1), 412–443, doi: 10.1039/C3CS60197H (2014).
17. Osakada, K., Nishihara, Y. Transmetalation of boronic acids and their derivatives: mechanistic elucidation and relevance to catalysis. *Dalton Transactions*. **51** (3), 777–796, doi: 10.1039/D1DT02986J (2022).
18. Sharma, S., Das, J., Braje, W.M., Dash, A.K., Handa, S. A Glimpse into Green Chemistry Practices in the Pharmaceutical Industry. *ChemSusChem*. **13** (11), 2859–2875, doi: 10.1002/cssc.202000317 (2020).
19. Bhaskaran, S., Padusha, M.S.A., Sajith, A.M. Application of Palladium Based Precatalytic Systems in the Suzuki-Miyaura Cross-Coupling Reactions of Chloro- Heterocycles. *ChemistrySelect*. **5** (29), 9005–9016, doi: 10.1002/slct.202002357 (2020).
20. Fujihara, T., Tani, Y., Semba, K., Terao, J., Tsuji, Y. Copper-Catalyzed Silacarboxylation of Internal Alkynes by Employing Carbon Dioxide and Silylboranes. *Angewandte Chemie International Edition*. **51** (46), 11487–11490, doi: 10.1002/anie.201207148 (2012).
21. Tani, Y., Fujihara, T., Terao, J., Tsuji, Y. Copper-Catalyzed Regiodivergent Silacarboxylation of Allenes with Carbon Dioxide and a Silylborane. *Journal of the American Chemical Society*. **136** (51), 17706–17709, doi: 10.1021/ja512040c (2014).
22. Zhang, L., Cheng, J., Carry, B., Hou, Z. Catalytic Boracarboxylation of Alkynes with Diborane and Carbon Dioxide by an N-Heterocyclic Carbene Copper Catalyst. *Journal of the American Chemical Society*. **134** (35), 14314–14317, doi: 10.1021/ja3063474 (2012).
23. *Atypical Elements in Drug Design*. **17**, doi: 10.1007/978-3-319-27742-4. Springer International Publishing. Cham. (2016).
24. Laitar, D.S., Tsui, E.Y., Sadighi, J.P. Copper(I) β-Boroalkyls from Alkene Insertion: Isolation and Rearrangement. *Organometallics*. **25** (10), 2405–2408, doi: 10.1021/om060131u (2006).

25. Mankad, N.P., Laitar, D.S., Sadighi, J.P. Synthesis, Structure, and Alkyne Reactivity of a Dimeric (Carbene)copper(I) Hydride. *Organometallics*. **23** (14), 3369–3371, doi: 10.1021/om0496380 (2004).
26. Butcher, T.W. *et al.* Regioselective Copper-Catalyzed Boracarboxylation of Vinyl Arenes. *Organic Letters*. **18** (24), 6428–6431, doi: 10.1021/acs.orglett.6b03326 (2016).
27. Perrone, T.M. *et al.* Beneficial Effect of a Secondary Ligand on the Catalytic Difunctionalization of Vinyl Arenes with Boron and CO_2. *ChemCatChem*. **11** (23), 5814–5820, doi: 10.1002/cctc.201901197 (2019).
28. Knowlden, S.W., Popp, B.V. Regioselective Boracarboxylation of α-Substituted Vinyl Arenes. *Organometallics*. **41** (14), 1883–1891, doi: 10.1021/acs.organomet.2c00184 (2022).
29. Santoro, O., Collado, A., Slawin, A.M.Z., Nolan, S.P., Cazin, C.S.J. A general synthetic route to [Cu(X)(NHC)] (NHC = N-heterocyclic carbene, X = Cl, Br, I) complexes. *Chemical Communications*. **49** (89), 10483, doi: 10.1039/c3cc45488f (2013).
30. Su, M., Huang, X., Lei, C., Jin, J. Nickel-Catalyzed Reductive Cross-Coupling of Aryl Bromides with Vinyl Acetate in Dimethyl Isosorbide as a Sustainable Solvent. *Organic Letters*. **24** (1), 354–358, doi: 10.1021/acs.orglett.1c04018 (2022).
31. JoVE Science Education Database. Organic Chemistry. Degassing Liquids with Freeze-Pump-Thaw Cycling. *Journal of Visual Experimentation*, Cambridge, MA, (2022).
32. . Li, D., Ollevier, T. Mechanism studies of oxidation and hydrolysis of Cu(I)-NHC and Ag-NHC in solution under air. *Journal of Organometallic Chemistry*. **906**, 121025-121035, doi:10.1016/j.jorganchem.2019.121025 (2018).
33. Hernández-Díaz, S., Rodríguez, L.A.G. Association Between Nonsteroidal Anti-inflammatory Drugs and Upper Gastrointestinal Tract Bleeding/Perforation: An Overview of Epidemiologic Studies Published in the 1990s. *Archives of Internal Medicine*. **160** (14), 2093, doi: 10.1001/archinte.160.14.2093 (2000).
34. Wolfe, M.M., Singh, G. Gastrointestinal Toxicity of Nonsteroidal Antiinflammatory Drugs. *The New England Journal of Medicine*. 12 (1999).
35. Singh, G. Gastrointestinal tract complications of nonsteroidal anti-inflammatory drug treatment in rheumatoid arthritis. A prospective observational cohort study. *Archives of Internal Medicine*. **156** (14), 1530–1536, doi: 10.1001/archinte.156.14.1530 (1996).
36. Lichtenstein, D.R., Syngal, S., Wolfe, M.M. Nonsteroidal antiinflammatory drugs and the gastrointestinal tract the double-edged sword. *Arthritis & Rheumatism*. **38** (1), 5–18, doi: 10.1002/art.1780380103 (1995).
37. Singh, G., & Triadafilopoulos, G. (1999). Epidemiology of NSAID induced gastrointestinal complications. The Journal of rheumatology. Supplement, 56, 18–24.

Chapter IV

Difluoroborolactonate Salts- A New Class of Organofluoroboranes

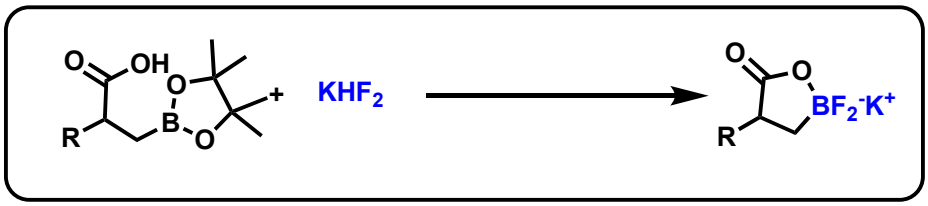

4.1 Abstract

Organofluoroborates are excellent alternative to boronic acids and boron esters, for use in transition metal-catalyzed cross-coupling reactions. Organofluoroborates have a significant advantage over other derivatives due to its ease of preparation. A method to synthesize a of new class of organodifluoroboryl compounds using mild reaction conditions is reported. Difluoroborolactonate compounds are unique due to the nature of $C(sp^3)$-$B(sp^3)$ bond. Stability of these compounds have been tested under air, aqueous, acidic, and basic conditions.

4.2 Introduction

Organoboranes have transformed organic synthesis in the last several decades. They have been widely used as preferred nucleophilic partners in transition metal catalyzed C-C,[1] C-X,[2] and C-N[3] bond forming reactions, due to their low toxicity, relative stability, and ease of preparation. Boronic acid and boronic esters are the most commonly used nucleophilic partners among organoboranes. However, boronic acids and boronic esters are far from ideal due to their physical properties and reactivity patterns. The trivalent boronic acids are prone to undergo protodeboration under cross-coupling conditions.[4] Though boronic esters (e.g., pinacolboronates) improve these issues, they are less reactive and much less atom economical than boronic acids.

In their first groundbreaking contribution, the Vedejs group reported a synthesis of organotrifluoroborate potassium salt using potassium bifluoride.[5] This method has shown to be effective against all types of organoboron moieties (aryl, heteroaryl, alkynyl, alkyl) and any type boronic acid derivative RBY_2(Y= OH, OR, NR_2, halide and allyl). This reaction gives a high yield of easily isolated, air and moisture stable monomeric product within hours at room temperature. These compounds react well under cross coupling conditions to give desired products. In contrast to tetravalent organotrifluoroborate salts, trivalent organodifluoroboryls are lesser studied due to their reactivity and known to undergo protodeboroation.[6] Because of this reactivity, the see less use in organic transformations. However, tetracoordinated difluoroborates are extensively used as dyes, chelators, and sensing applications[7] (Figure 1). Introduction of difluoroboryl group into a chromophore will enhance the properties of the dyes by improving their quantum yields. As examples, difluoroboryl fluorescent protein chromopores,[8] BODIPY,[9] boron containing Π-extended trans stilbenes[10] and curcumin-BF2 have been used as dyes for imaging applications.

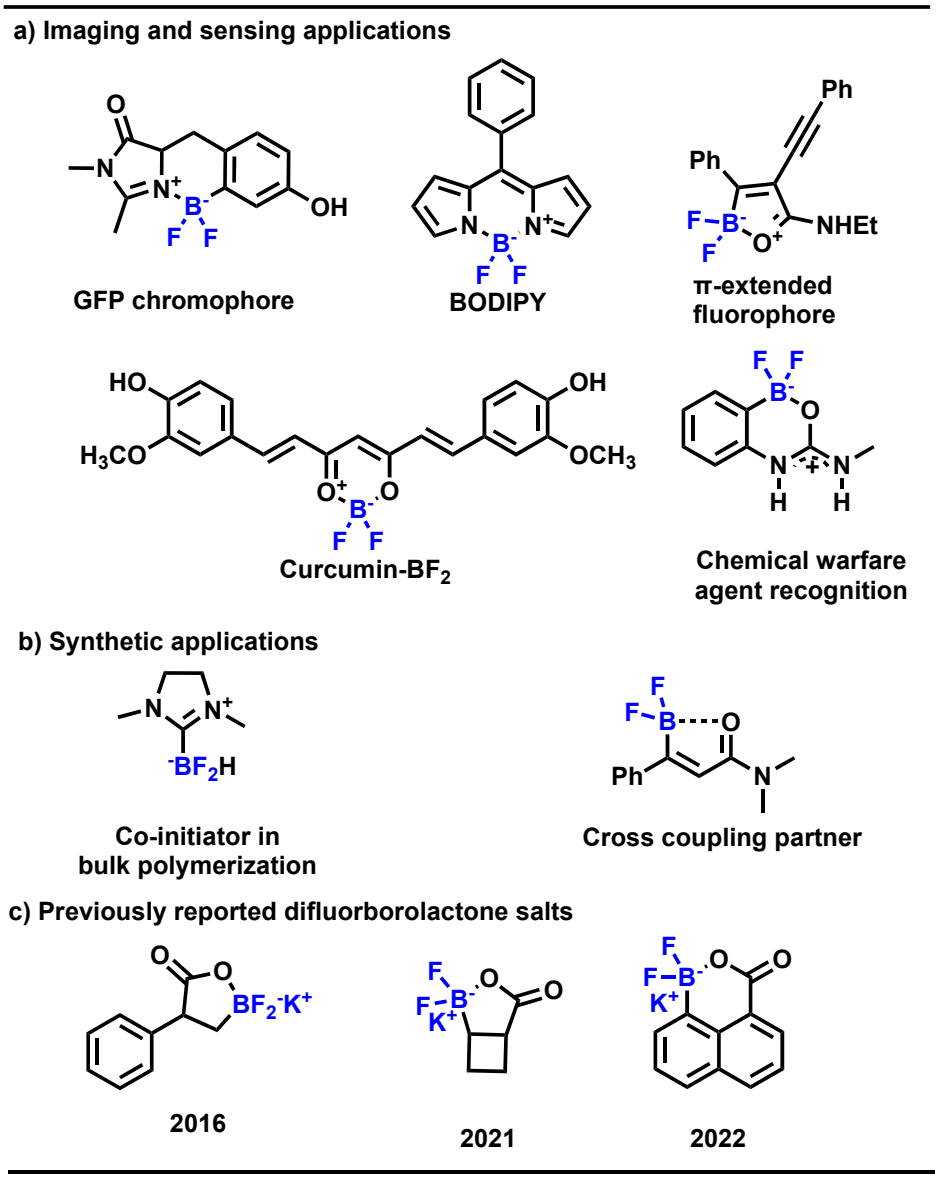

Figure 4.1 Selected examples of difluoroboryl molecules.

The Difluoroboryl urea analogues have been used as a sensor to identify anions and organophosphorus nerve agents.[11] Furthermore, some organodifluoroborates are used in synthesis and catalysis. N-heterocyclic carbene bound difluoroborates are used as a co-initiator in bulk photopolymerization.[12] β-difluoroboryl acrylamides are efficient cross coupling substrates which give moderate to excellent yields.[13] They have also functioned as frustrated Lewis's pair catalysts in C-H borylation and conjugate addition reactions.[14] In 2016, we reported the first synthesis of difluoroboralactonate salts.[15] According to our

knowledge, this was the first reported example of a C-sp^3-B bound difluoroboronate species. More recently, Hall and co-workers reported the synthesis of difluoroboralactonate using a palladium catalyst and potassium bifluoride.[16] In 2022, Luliński and co-workers reported an example of the synthesis of aryldifluoroboronolactone **.**[17]

During our previous synthetic and mechanistic work in regioselective Copper catalyzed boracarboxylation of vinyl arenes, we synthesized new boron functionalized α-aryl carboxylic acid substrates.[18] Through further derivatization of the boron center in these products, we were able to expand their synthetic effectiveness. Inspired by our previous boracarboxylation work, here in we report the synthesis of air and moisture stable difluoroboralactone potassium salts using milder reaction conditions and a shorter reaction time.

4.3 Results and Discussion

Table 4.1 Reaction optimization for synthesis of borafluorolactonate salts.

Entry	KHF_2	Solvent	Time, h	% Yield
1	5	THF/H_2O (1:1)	3	43
2	5	THF/H_2O (1:1), Polyethylene bottle	3	55
3	5	THF	3	15
4	5	Dioxane/H_2O (1:1)	3	26
5	5	Dioxane	3	28
6	5	MeOH/H_2O (1:1)	3	77
7	5	MeOH	3	70
8	5	EtOH/H_2O (1:1)	3	71
9	5	EtOH	3	74
10	5	MeCN/H_2O (1:1)	3	57
11	5	MeCN	3	82
12	3	MeCN	3	80
13	1.5	MeCN	1.5	53
14	3	MeCN	1.5	81
15	3	EtOH	1.5	77
16	2	EtOH	1.5	66

We started reaction optimization by using our previously used conditions (Table 4.1, entry 1).[15] Next the reaction was carried out in a polyethylene bottle due to the possibility of KHF_2 reacting with borosilicate's glass.[19] The reaction yield was slightly increased up to 55% when using the polyethylene bottle. Different solvents were screened at room temperature (Table 4.1, entry 4-15). It turned out that acetonitrile and ethanol were the most efficient solvents for this reaction and yields were 81 % and 77% respectively.

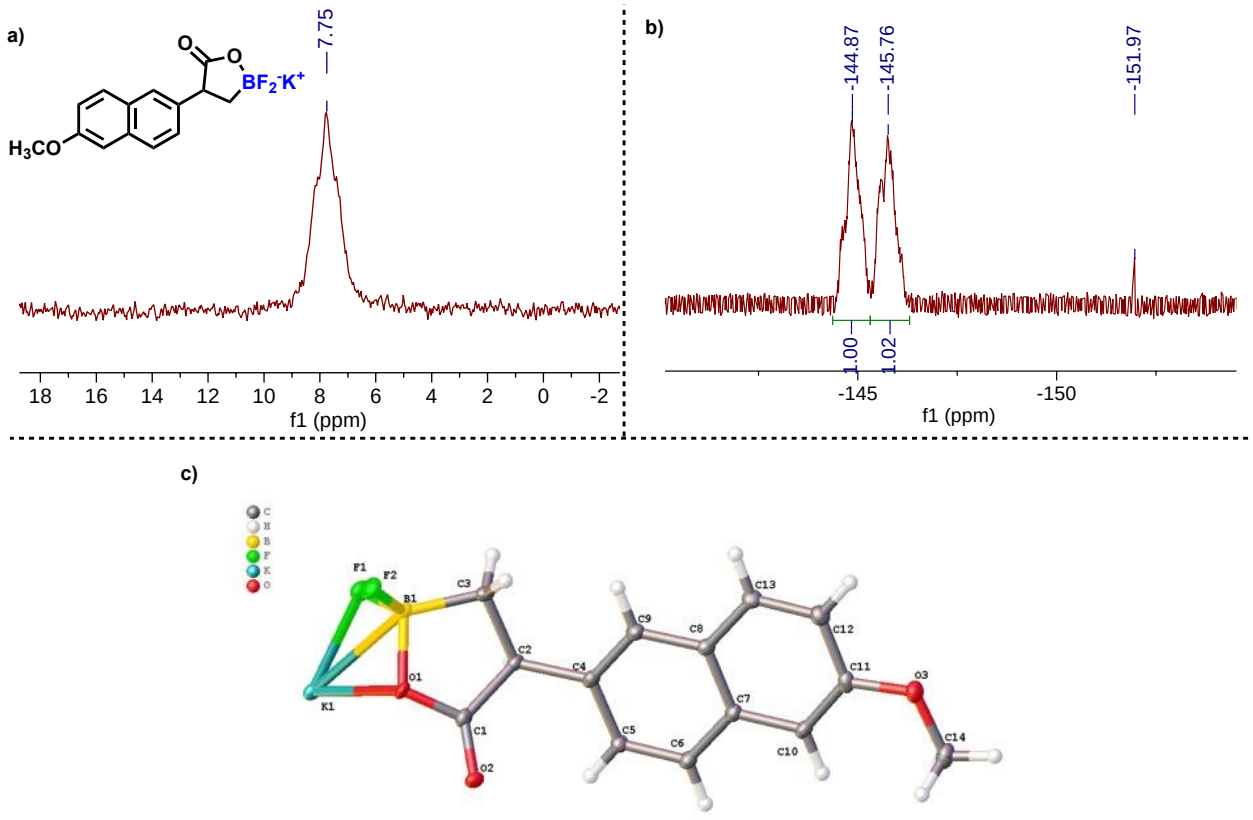

Figure 4.2 a) ^{11}B NMR, b) ^{19}F NMR and c) X-ray crystal structure for 2g

.

^{11}B, ^{19}F NMR spectroscopy and X-ray crystallographic data were used to confirm the product structure and assess the purity. ^{11}B NMR indicated a O-B coordination as suggested by a single peak at 7.75 ppm, which is characteristic for a tetrahedral geometry on boron (Figure 2a). Due to the diastereotopic nature of two fluorine atoms, two ^{19}F NMR signals were observed at -144.87 ppm and -145.76 ppm respectively. The smaller ^{19}F NMR peak was observed at -151.97 ppm and is believed to result from the formation of $[BF_4]^-$. which is less than 1% from the overall yield (Figure 2b). An X-ray crystal structure of 2g further confirmed the formation of difluoroboryl lactone structure.

Using optimized mild reaction conditions, difluoroboralactonate salts 2a-2t were efficiently synthesized, using potassium bifluoride in ethanol (Scheme 4.1). Difluoroboralactonate salts containing alkyl groups (2a-2f) and electron donating substrates such as naproxen (2g), *p*-methoxy (2h), o-methoxy (2i), *o,p*-dimethoxy (2j) and m-phenoxy were synthesized from their corresponding *bora*-carboxylated products in good to excellent yields, with no noteworthy change with respect to electronics or sterics of the substrates. Difluoroboralactonate salts bearing electron withdrawing groups such as acetoxy (2l) and fluorine (2o, 2p) were also synthesized in excellent yields. In the case of *p*-cyano substrate (2m), the reaction gave a slightly diminished yield. Moreover, for the *p*-trifluoromethyl substrate (2n) crude yield was reported, due to the difficulty in purification. The heterocycles such as thiophene (2q, 2r), indole (2s) and benzofuran (2t) were also efficiently transformed into difluoroboralactonate salts in excellent yields. Using these conditions, difluoroboryl derivatives of nonsteroidal anti-inflammatory drugs ibuprofen (2e), naproxen (2g) and fenoprofen (2k) were successfully synthesized in excellent yields.

Scheme 4.1 Substrate scope of Difluoroboralactonate salts

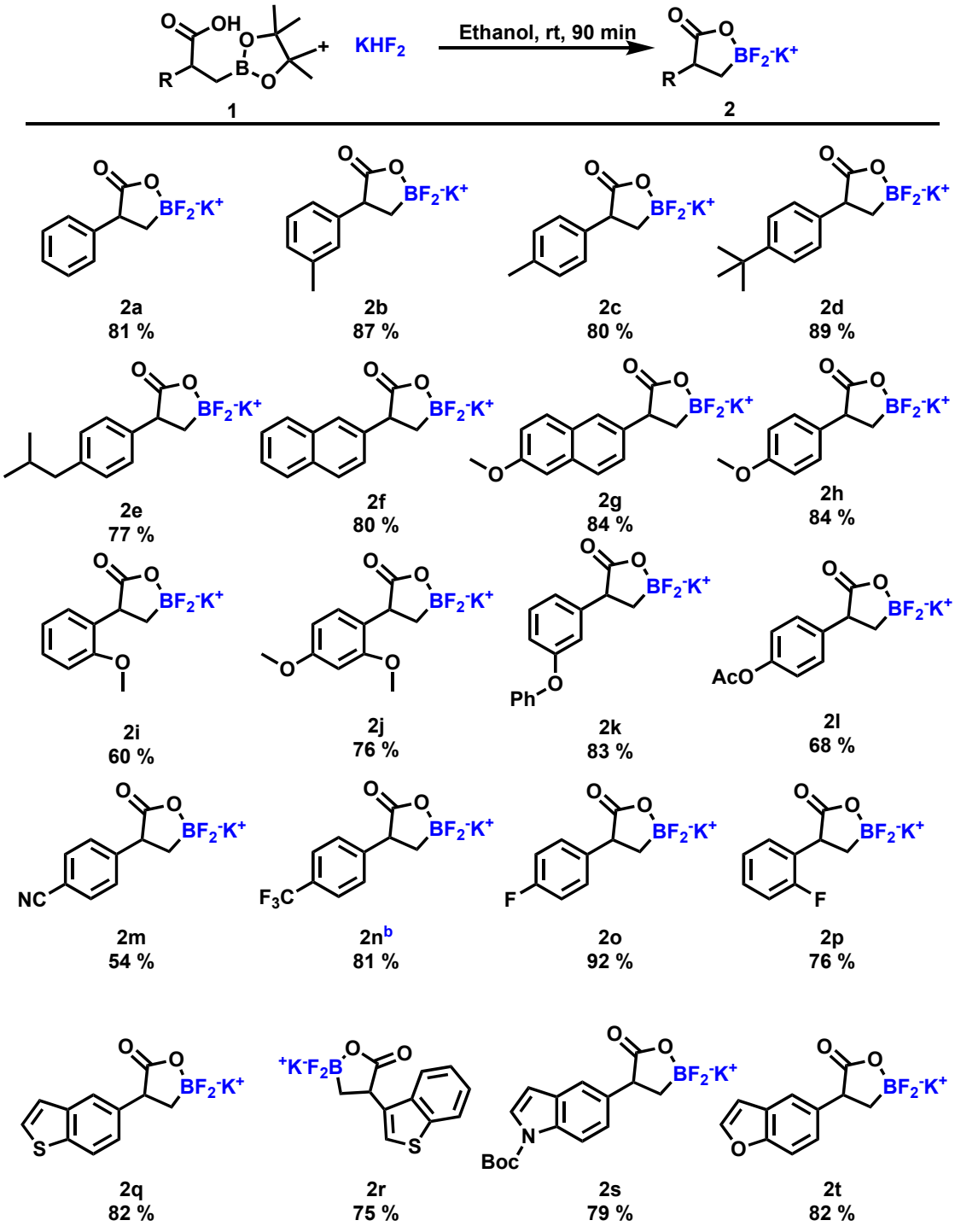

[a]Reaction conditions : 1 (0.1 mmol) and KHF_2 (0.3 mmol) were dissilved in 95 % ethanol (2 ml) at room temperature for 1.5. Isolated yieldss are shown. [b]Crude yield.

Next, hydrolytic stability of difluoroboralactonate salts (2e) in deuterated water was tested using ^{11}B and ^{19}F NMR spectroscopic methods (Figure 3). After 24 hours, in D_2O, a new ^{11}B peak appeared between -0.4 to -0.9 ppm due to the formation of BF_3OH^- in D_2O Correspondingly, in the ^{19}F spectrum, a new fluorine peak for BF_3OH^- appeared at -143.6 ppm. Also, several other low intensity ^{19}F NMR peaks were observed at -130 ppm and -139.5 ppm due to the formation of BF_3 and $BF_2(OH)_2^-$ respectively.[20] After 12days, intensity of the 0.4 to -0.9 ppm ^{11}B NMR peak was decreased, and intensity of the -130 ppm ^{19}F NMR peak was increased.

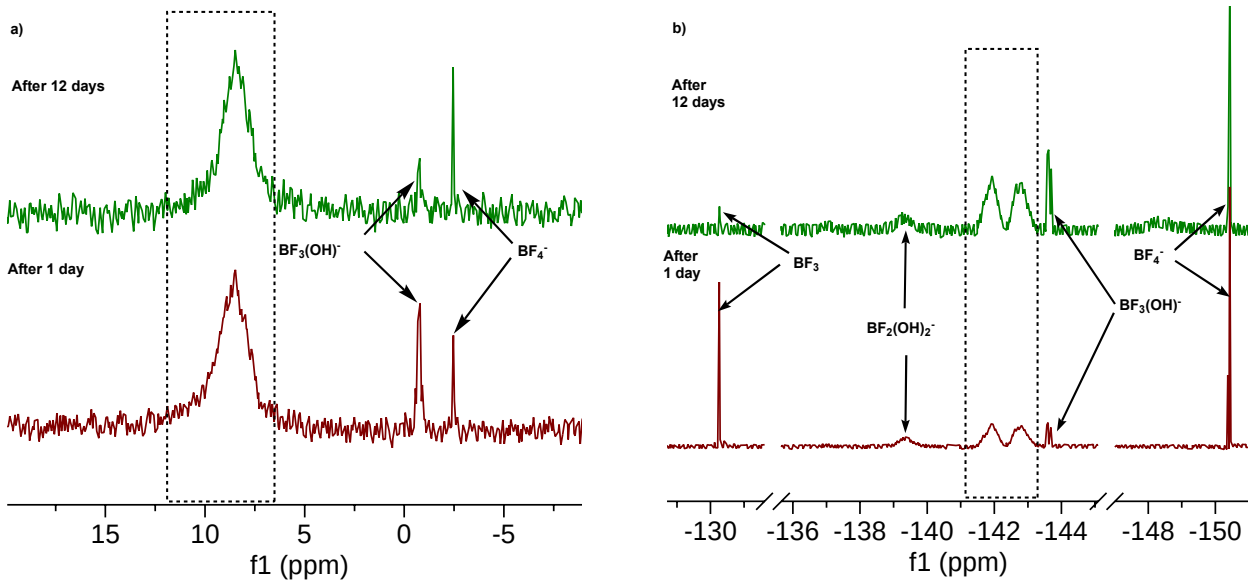

Figure 4.3 Hydrolytic stability of 2e in D_2O monitored using ^{11}B NMR (a) and ^{19}F NMR (b) spectroscopic methods.

Similarly, stability of borafluorolactonate salts (2e) were tested in 0.1 M HCl, 0.01 M HCl, 0.01 M KOH and 0.1 M KOH after 24 hours and 12 days by using ^{11}B NMR and ^{19}F NMR spectroscopic methods. In ^{11}B NMR spectrum after 24 hours (Figure 4.5), we observed the formation of BF_3OH^- in in 0.1 M HCl, 0.01 M HCl and 0.01 M KOH. After 12 days, no significant changes were observed in ^{11}B NMR in 0.1 M HCl, 0.01 M HCl and 0.01 M KOH solutions. In 0.1 M KOH solution new peak were formed at 1.97 ppm due to the formation of $B(OH)_4^-$ in solution.[21] In ^{19}F NMR spectrums after 24 hours (Figure 4.6), the 1:1:1:1 splitting near -143 ppm and a peak near -130 ppm were observed in 0.1 M HCl, 0.01 M HCl and 0.01 M KOH samples, due to the formation of BF_3OH^- (J_{FB}~13 Hz) and BF_3 respectively. In 0.01 M KOH,

additional peak was observed at 124 ppm, due to the formation of $BF(OH)_3^-$. In 0.1 M KOH, the product was totally decomposed. Two ^{19}F NMR peaks were observed at -120 ppm and -150 ppm resulting from the formation of KF and $[BF_4]^-$. No significant changes were observed from the spectra between day 1 to day 12.

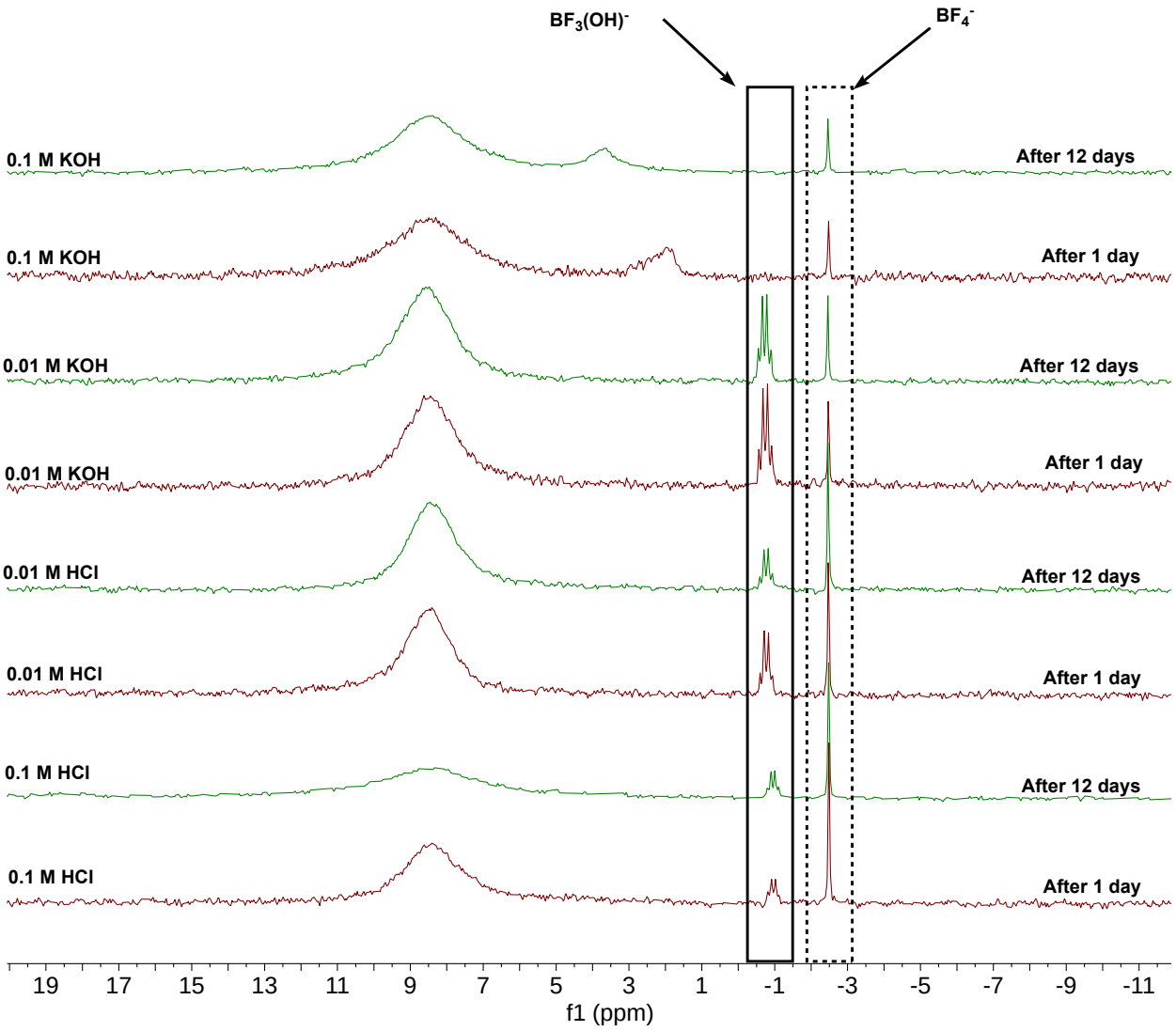

Figure 4.4 Stability of 2e in 0.1 M HCl, 0.01 M HCl, 0.01 M KOH and 0.1 M KOH after 24 hours and 12 days monitored using ^{11}B NMR spectroscopy

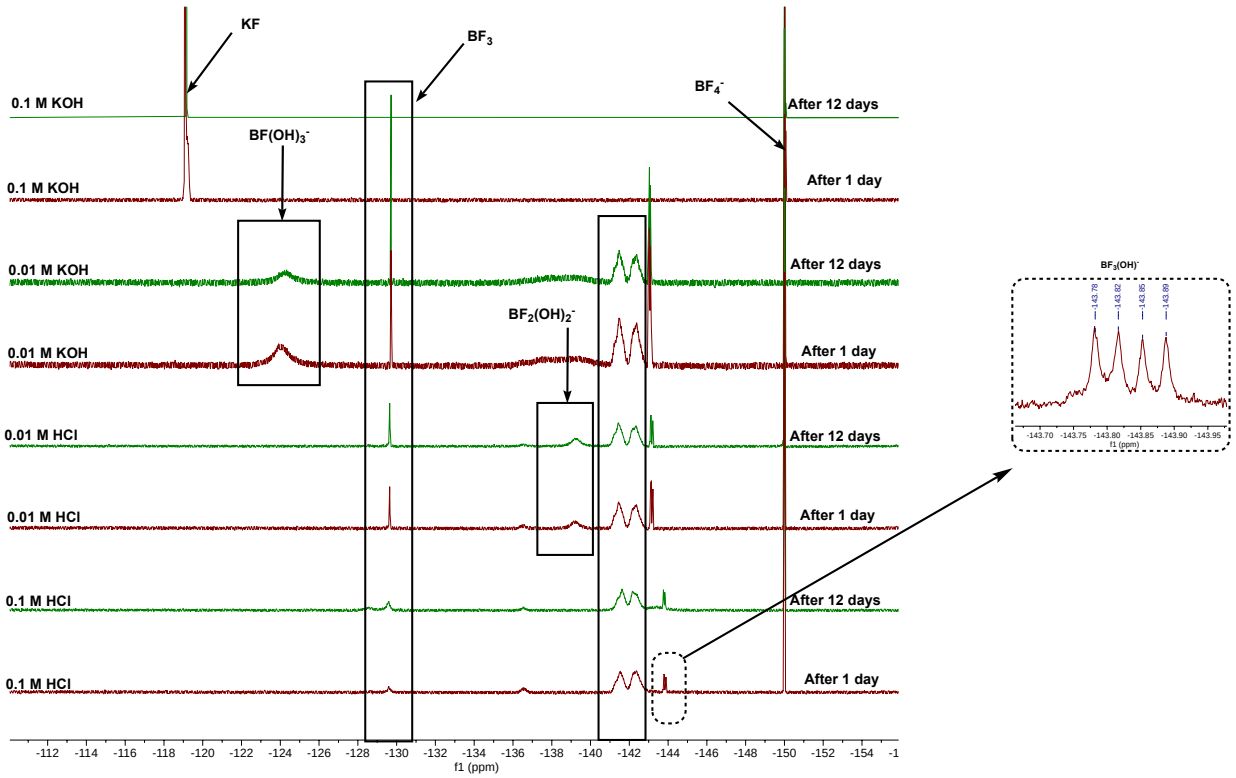

Figure 4.5 Stability of 2e in 0.1 M HCl, 0.01 M HCl, 0.01 M KOH and 0.1 M KOH after 24 hours and 12 days monitored using ^{19}F NMR spectroscopy

4.4 Conclusion

In summary, we have synthesized a new class of readily accessible organodifluoroboryl compounds by using mild reaction conditions. This method has given access to difluoroboryl derivatives of nonsteroidal anti-inflammatory drugs. The stability of the compound 2e was tested under different hydrolytic, acidic, and basic conditions. Evaluation of the synthetic applicability of these compounds are currently under progress.

4.5 Experimental Methods

General information

All commercially available compounds were used as received, and all were purchased from either Oakwood chemicals, ACROS Organics, Alfa Aesar, or Fisher chemicals. Solvents were purchased from Fisher The manipulation of air- and moisture-sensitive compounds was conducted and performed under a nitrogen atmosphere utilizing glove box techniques.

^{1}H, ^{13}C, and ^{11}B NMR spectra were recorded on Agilent 400 MHz, JEOL 400 MHz and Varian INOVA 600 MHz NMR spectrometers, and all deuterated solvents were purchased from Cambridge Isotope Laboratories, Inc. The chemical shifts (δ) are given in parts per million and referenced relative to residual proteo solvent (1.94, 2.05 or 2.50 ppm for ACETONITRILE-D_3, ACETONE-D_6 and DMSO-D_6, respectively), ACETONITRILE-D_3, ACETONE-D_6 and DMSO-D_6 (1.3, 29.8 and 39.7 ppm for ^{13}C), internal (capillary) CF_3CO_2H (-76.5 ppm for F), and internal (capillary) BF_3•OEt_2 (32.1 ppm). ^{11}B NMR spectra recorded using quartz NMR tubes. The ^{13}C NMR resonance for methylene carbon signal has very low intensity due to ^{11}B quadrupolar broadening.

General Procedures for Preparing Borafluorolactonate Potassium Salts

A 20 mL scintillation vial was charged with compound **1a-1t** (1 eq, 0.1 mmol) and KHF_2 (23.4mg, 0.3 mmol, 3 eq.). A 2 mL of ethanol solution was added, and the resulting suspension was stirred at ambient temperature for 90 minutes. The solution was transferred to a round bottom flask and the volatiles were removed in vacuo to provide a crude white powder. The product was taken up in acetone (3 mL) and filtered through cotton. The insoluble material was washed with acetone (3 x 3 mL), the combined acetone filtrates were dried in vacuo, and the resulting solid was washed with ether (2 x 5 mL) to provide as a white, microcrystalline solid.

General procedures for stability studies on borafluorolactonate potassium salts

Six NMR quartz tubes were charged with compound **2e** (10 mg) and 0.5 mL of D_2O, 0.1 M HCl, 0.01 M HCl, 0.01 M KOH and 0.1 M KOH were added to each NMR tube separately, 50 μL of D2O added to each HCl and KOH sample. After 24 hours, ^{11}B and ^{19}F NMR spectrums were obtained for each sample. Again after 12 days, ^{11}B and ^{19}F NMR spectrums were obtained for each sample.

Note- Product **2a,2b,2d,2f** and **2h** were recrystallized using 200-500 μL acetonitrile to obtain crystal structures. Product **2o** and **2p** were recrystallized using 100-500 μL of ethanol.

Characterization data

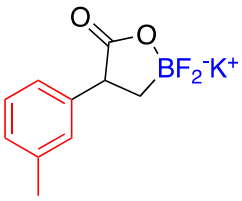

2a: White solid, 81 % **yield** (19 mg). **Melting point:** 224-228 °C

^{1}H NMR (400 MHz, ACETONE-D_6) δ 7.35 – 7.25 (m, 2H), 7.21 (dd, J = 8.5, 6.7 Hz, 2H), 7.15 – 7.06 (m, 1H), 3.60 – 3.50 (m, 1H), 1.04 (ddd, J = 18.3, 9.8, 3.9 Hz, 1H), 0.69 – 0.61 (m, 1H). **^{13}C NMR** (101 MHz, ACETONE-D_6) δ 146.03, 128.99, 128.66, 126.18, 51.59, 51.56, **^{11}B NMR** (128 MHz, ACETONE-D_6) δ 8.17, 7.75, 7.34. **^{19}F NMR** (376 MHz, ACETONE-D_6) δ -145.01, -146.05. **HRMS (ESI) m/z** calc for **$C_9H_8BF_2O_2^-$ (M-K)$^-$**, 197.0591, observed 197.0586

The ^{13}C NMR resonance at 23.79 (methylene carbon signal) has very low intensity due to ^{11}B quadrupolar broadening.

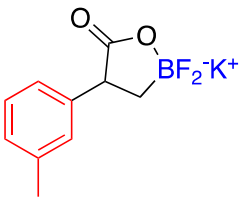

2b: White solid, 87 % **yield** (21.5 mg). **Melting point:** 238-242 °C

^{1}H NMR (400 MHz, ACETONE-D_6) δ 7.13 – 7.01 (m, 3H), 6.96 – 6.86 (m, 1H), 3.51 (ddd, J = 9.8, 8.1, 1.3 Hz, 1H), 2.26 (s, 3H), 1.01 (ddt, J = 14.3, 9.8, 4.7 Hz, 1H), 0.64 (tt, J = 12.0, 5.5 Hz, 1H). **^{13}C NMR** (101 MHz, ACETONE-D_6) δ 145.16, 136.92, 128.89, 127.71, 125.98, 125.19, 50.70, 50.68, 20.65. **^{11}B NMR** (128 MHz, ACETONE-D_6) δ 8.17, 7.75, 7.33. **^{19}F NMR** (376 MHz, ACETONE-D_6) δ -144.78, -145.98. **HRMS (ESI) m/z** calc for **$C_{10}H_{10}BF_2O_2^-$ (M-K)$^-$**, 211.0747, observed 211.0744.

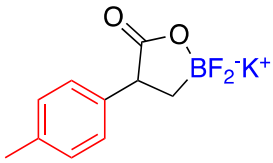

2c: White solid, 80 % **yield** (21.5 mg). **Melting point:** 199-206 °C

^{1}H NMR (600 MHz,) δ 7.14 (d, *J* = 8.1 Hz, 2H), 7.09 (d, *J* = 7.8 Hz, 2H), 3.57 (dd, *J* = 10.0, 8.2 Hz, 1H), 1.01 (td, *J* = 9.7, 5.3 Hz, 1H), 0.66 – 0.56 (m, 1H). **^{13}C NMR** (151 MHz, ACETONITRILE-*D*$_3$) δ 181.20, 23.13. **^{11}B NMR** (128 MHz, ACETONITRILE-*D*$_3$) δ 8.15, 7.72, 7.29. **^{19}F NMR** (376 MHz, ACETONITRILE-*D*$_3$) δ -144.85, -145.90. **HRMS (ESI) m/z** calc for **$C_{10}H_{10}BF_2O_2^-$ (M-K)$^-$**, 211.0747, observed 211.0745.

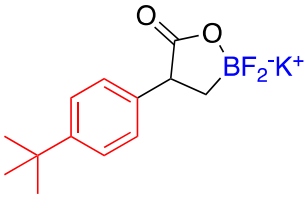

2d: White solid, 89 % **yield** (26 mg). **Melting point:** 232-242 °C

^{1}H NMR (600 MHz, ACETONE-*D*$_6$) δ 7.27 – 7.22 (m, 2H), 7.22 – 7.17 (m, 2H), 3.51 (t, *J* = 8.8 Hz, 1H), 1.27 (s, 8H), 1.02 – 0.96 (m, 1H), 0.65 (s, 1H). **^{13}C NMR** (101 MHz, ACETONE-*D*$_6$) δ 180.95, 147.88, 141.81, 127.79, 124.66, 50.12, 50.10, 33.96, 30.93. **^{11}B NMR** (128 MHz, ACETONE-*D*$_6$) δ 7.81. **^{19}F NMR** (376 MHz, ACETONE-*D*$_6$) δ -145.04, -146.06. **HRMS (ESI) m/z** calc for **$C_{13}H_{16}BF_2O_2^-$ (M-K)$^-$**, 253.1217, observed 253.1217

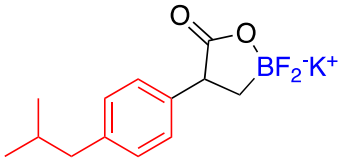

2e: White solid, 77 % **yield** (22.4 mg). **Melting point:** 233-242 °C

^{1}H NMR (400 MHz, ACETONE-*D*$_6$) δ 7.22 – 7.16 (m, 2H), 7.05 – 6.99 (m, 2H), 3.57 (ddd, *J* = 9.7, 8.0, 1.3 Hz, 1H), 2.42 (d, *J* = 7.1 Hz, 2H), 1.82 (dh, *J* = 13.4, 6.7 Hz, 1H), 1.03 (ddt, *J* = 14.5, 9.9, 4.9 Hz, 1H), 0.92 – 0.83 (m, 7H), 0.68 (dtd, *J* = 15.9, 7.9, 5.7 Hz, 1H). **^{13}C NMR** (101 MHz, ACETONE-*D*$_6$) δ 181.63, 143.23, 139.26, 129.40, 128.75, 51.15, 51.13, 45.72, 31.07, 22.72. **^{11}B NMR** (128 MHz, ACETONE-*D*$_6$) δ 8.76. **^{19}F NMR** (376 MHz, ACETONE-*D*$_6$) δ -145.17, -146.20. **HRMS (ESI) m/z** calc for **$C_{13}H_{16}BF_2O_2^-$ (M-K)$^-$**, 253.1217, observed 253.1217.

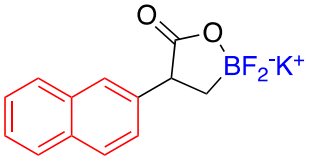

2f: White solid, 80 % **yield** (23 mg). **Melting point:** 259-265 °C

^{1}H NMR (400 MHz, ACETONE-*D*$_6$)7.84 – 7.78 (2 H, m), 7.78 – 7.72 (2 H, m), 7.48 (1 H, dd, *J* 8.5, 1.8), 7.41 (2 H, dddd, *J* 14.8, 8.2, 6.9, 1.5), 3.74 (1 H, t, *J* 9.0), 1.16 – 1.04 (1 H, m), 0.82 – 0.69 (1 H, m). **^{13}C**

NMR (101 MHz, DMSO-D_6) δ 180.09, 142.57, 133.44, 131.92, 127.81, 127.77, 127.29, 126.21, 126.18, 125.48, 50.73, 50.71, 40.58, 40.38, 40.17, 39.96, 39.75, 39.54, 39.33, 23.85. **^{11}B NMR** (128 MHz, ACETONE-D_6) δ 7.78. **^{19}F NMR** (376 MHz, ACETONE-D_6) δ -145.16, -145.24. **HRMS (ESI) m/z** calc for **$C_{13}H_{10}BF_2O_2^-$ (M-K)$^-$**, 247.0747, observed 247.0748.

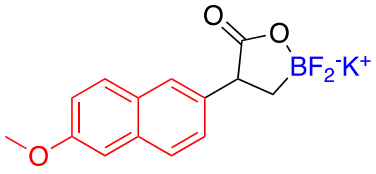

2g: White solid, 84 % **yield** (26.5 mg). **Melting point:** 172-179 °C

^{1}H NMR (400 MHz, ACETONE-D_6) δ 7.79 – 7.59 (m, 3H), 7.43 (dd, J = 8.5, 1.8 Hz, 1H), 7.21 (d, J = 2.5 Hz, 1H), 7.08 (dd, J = 8.9, 2.5 Hz, 1H), 3.89 (s, 3H), 3.70 (t, J = 9.0 Hz, 1H), 1.07 (d, J = 12.5 Hz, 1H), 0.75 (s, 1H). **^{13}C NMR** (101 MHz, ACETONITRILE-D_3) δ 207.59, 158.20, 141.05, 134.10, 129.94, 129.88, 128.41, 127.52, 126.80, 119.30, 106.70, 55.93, 51.51, 51.49, 30.90. **^{11}B NMR** (128 MHz, ACETONE-D_6) δ 7.75. **^{19}F NMR** (376 MHz, ACETONE-D_6) δ -144.87, -145.76.

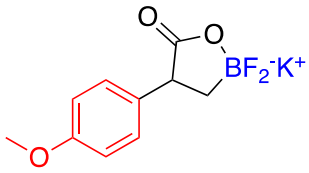

2h: White solid, 84 % **yield** (30.75 mg). **Melting point:** 238-242 °C

^{1}H NMR (400 MHz, ACETONE-D_6) δ 7.24 – 7.14 (m, 2H), 6.83 – 6.73 (m, 2H), 3.74 (s, 3H), 3.50 (t, J = 8.9 Hz, 1H), 0.99 (td, J = 9.5, 4.9 Hz, 1H), 0.69 – 0.55 (m, 1H). **^{13}C NMR** (101 MHz, ACETONE-D_6) δ 205.36, 157.80, 137.14, 128.95, 113.19, 54.54, 49.77. **^{11}B NMR** (128 MHz, ACETONE-D_6) δ 7.71. **^{19}F NMR** (376 MHz, ACETONE-D_6) δ -145.06, -146.18. **HRMS (ESI) m/z** calc for **$C_{10}H_{10}BF_2O_3^-$ (M-K)$^-$**, 227.0697, observed 227.0695.

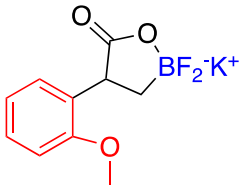

2i: White solid, 60 % **yield** (26.5 mg).

^{1}H NMR (400 MHz, ACETONE-D_6) δ 7.14 (dd, J = 7.5, 1.8 Hz, 1H), 7.09 (ddd, J = 8.2, 7.4, 1.8 Hz, 1H), 6.87 (dd, J = 8.2, 1.2 Hz, 1H), 6.81 (td, J = 7.4, 1.2 Hz, 1H), 3.94 (t, J = 9.5 Hz, 1H), 3.77 (s, 3H), 1.04 – 0.93 (m, 1H), 0.62 – 0.48 (m, 1H). **^{13}C NMR** (101 MHz, ACETONITRILE-D_3) δ 185.74, 139.93, 137.08, 126.69, 125.15, 122.70, 122.02, 50.55. **^{11}B NMR** (128 MHz, ACETONITRILE-D_3) δ 7.64. **^{19}F NMR** (376 MHz, ACETONE-D_6) δ -145.53, -145.71. **HRMS (ESI) m/z** calc for **$C_{10}H_{10}BF_2O_3^-$ (M-K)$^-$**, 227.0697, observed 227.0695

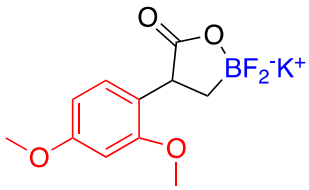

2j: White solid, 76 % **yield** (23.81 mg).

^{1}H NMR (400 MHz, ACETONE-D_6) δ 7.04 (d, J = 8.3 Hz, 1H), 6.46 (d, J = 2.5 Hz, 1H), 6.40 (dd, J = 8.3, 2.5 Hz, 1H), 3.86 (t, J = 9.5 Hz, 1H), 3.75 (d, J = 6.1 Hz, 7H), 0.96 (dddt, J = 14.4, 10.3, 6.6, 3.4 Hz, 1H), 0.56 (p, J = 9.0 Hz, 1H). **^{13}C NMR** (101 MHz, ACETONE-D_6) δ 182.59, 159.98, 158.94, 130.02, 127.00, 105.37, 99.22, 55.95, 55.54, 44.79, 30.50, 30.31. **^{11}B NMR** (128 MHz, ACETONE-D_6) δ 7.76, -2.01. **^{19}F NMR** (376 MHz, ACETONE-D_6) δ -145.47, -145.65. **HRMS (ESI) m/z** calc for **$C_{11}H_{12}BF_2O_4^-$ (M-K)$^-$**, 257.0802, observed 257.0803.

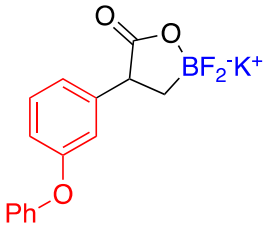

2k: White solid, 79 % **yield** (26.5 mg). **Melting point:** 135-141 °C

^{1}H NMR (400 MHz, ACETONE-D_6) δ 7.35 (t, J = 7.8 Hz, 2H), 7.23 (t, J = 7.9 Hz, 1H), 7.09 (t, J = 7.9 Hz, 2H), 7.04 – 6.93 (m, 3H), 6.76 (dd, J = 8.0, 2.5 Hz, 1H), 3.61 (t, J = 9.1 Hz, 1H), 1.05 (ddt, J = 14.4, 10.0, 4.7 Hz, 1H), 0.67 (qd, J = 10.4, 6.0 Hz, 1H). **^{13}C NMR** (101 MHz, ACETONE-D_6) δ 180.85, 158.62, 157.63, 148.32, 130.69, 130.00, 124.34, 123.80, 119.85, 119.32, 116.71, 51.43, 51.41, 25.28. **^{11}B NMR** (128 MHz, ACETONE-D_6) δ 7.77. **^{19}F NMR** (376 MHz, ACETONE-D_6) δ -145.07, -146.18. **HRMS (ESI) m/z** calc for **$C_{15}H_{12}BF_2O_3^-$ (M-K)$^-$**, 289.0853, observed 289.0854.

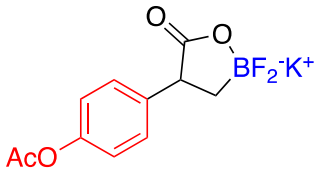

2l: White solid, 68 % **yield** (20.0 mg). **Melting point:** 174-185 °C

^{1}H NMR (400 MHz, ACETONE-D_6) δ 7.34 – 7.27 (m, 2H), 7.00 – 6.93 (m, 2H), 3.59 (t, J = 9.0 Hz, 1H), 2.23 (s, 4H), 1.12 – 0.97 (m, 1H), 0.66 (s, 1H). **^{13}C NMR** (101 MHz, ACETONE-D_6) δ 180.43, 169.03, 149.00, 142.32, 128.89, 121.06, 50.00, 20.17. **^{11}B NMR** (128 MHz, ACETONE-D_6) δ 7.74. **^{19}F NMR** (376 MHz, ACETONE-D_6) δ -144.96, -146.18. **HRMS (ESI) m/z** calc for **$C_{11}H_{10}BF_2O_4^-$ (M-K)$^-$**, 255.0646, observed 255.0647.

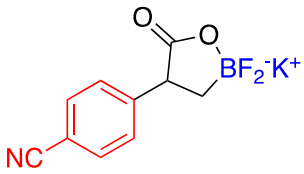

2m: White solid, 54 % **yield** (142 mg). (1 mmol scale) **Melting point:** 241-251°C **^{1}H NMR** (400 MHz, DMSO-D_6) δ 7.71 (d, J = 8.0 Hz, 2H), 7.40 (d, J = 8.0 Hz, 2H), 3.65 (t, J = 9.0 Hz, 1H), 0.95 (ddt, J = 14.2, 9.5, 4.4 Hz, 1H), 0.58 – 0.44 (m, 1H). **^{13}C NMR** (101 MHz, ACETONE-D_6) δ 179.67, 150.52, 131.83, 131.79, 129.18, 118.93, 109.24, 50.69, 50.67, 50.45. **^{11}B NMR** (128 MHz, ACETONE-D_6) δ 8.15, 7.72, 7.29. **^{19}F NMR** (376 MHz, ACETONE-D_6) δ -145.05, -145.16. **HRMS (ESI) m/z** calc for **$C_{10}H_7BF_2NO_2^-$ (M-K)$^-$**, 222.0543, observed 222.0542.

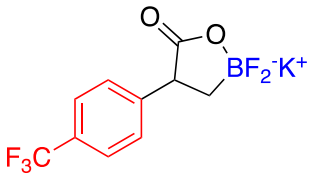

2n: White solid, 81 % **crude yield** (20.4 mg).

^{1}H NMR (400 MHz, ACETONE-D_6) δ 7.54 (d, J = 8.2 Hz, 2H), 7.46 (d, J = 8.3 Hz, 2H), 3.66 (t, J = 9.0 Hz, 1H), 1.04 (ddt, J = 13.9, 9.1, 4.5 Hz, 1H), 0.64 (tq, J = 13.1, 6.4 Hz, 1H). **^{13}C NMR** (101 MHz, ACETONE-D_6) δ 205.58, 179.78, 149.74, 130.03, 129.61, 128.96, 128.78, 127.30, 126.80, 124.72, 124.68, 50.52, 24.83. **^{11}B NMR** (128 MHz, ACETONE-D_6) δ 7.79. **^{19}F NMR** (376 MHz, ACETONE-D_6) δ -62.51, -62.52, -145.06, -146.33. **HRMS (ESI) m/z** calc for **$C_{10}H_7BF_5O_2^-$ (M-K)$^-$**, 265.0465, observed 265.0468.

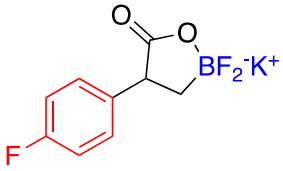

2o: White solid, 92 % **yield** (234 mg). (1 mmol scale) **Melting point:** 241-244.5 °C. **^{1}H NMR** (400 MHz, ACETONE-D_6) δ 7.32 – 7.22 (m, 2H), 7.00 – 6.89 (m, 2H), 3.61 – 3.52 (m, 1H), 2.08 – 1.99 (m, 1H), 1.00 (ddt, J = 14.2, 9.7, 4.7 Hz, 1H), 0.61 (ddt, J = 18.2, 13.3, 8.0 Hz, 1H). **^{13}C NMR** (101 MHz, ACETONE-D_6) δ 180.61, 162.33, 159.93, 140.80, 129.74, 129.66, 114.43, 114.22, 49.72, 49.70. **^{11}B NMR** (128 MHz, ACETONE-D_6) δ 8.16, 7.74, 7.33. **19F NMR** (376 MHz, ACETONE-D_6) δ -119.99, -120.19, -120.20, -120.21, -120.23, -144.76, -146.08. **HRMS (ESI) m/z** calc for **$C_9H_7BF_3O_2^-$ (M-K)$^-$**, 215.0497, observed 215.0495.

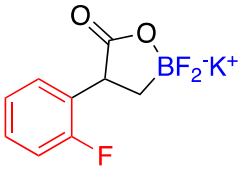

2p: White solid, 76 % **yield** (19.3 mg). **Melting point:** 214-220 °C

^{1}H NMR (400 MHz, ACETONE-D_6) δ 7.26 (td, J = 7.7, 1.9 Hz, 1H), 7.12 (tdd, J = 7.4, 5.1, 1.8 Hz, 1H), 7.02 (td, J = 7.5, 1.3 Hz, 1H), 6.95 (ddd, J = 9.6, 8.1, 1.4 Hz, 1H), 3.79 (t, J = 9.5 Hz, 1H), 1.06 – 0.93 (m, 1H), 0.59 (s, 1H). **^{13}C NMR** (101 MHz, ACETONE-D_6) δ 159.68, 129.95, 129.90, 127.19, 127.11, 123.89, 123.86, 114.83, 114.60, 44.12. **^{11}B NMR** (128 MHz, ACETONE-D_6) δ 8.00, 7.58, 7.17. **^{19}F NMR** (376 MHz, ACETONE-D_6) δ -119.50, -119.51, -119.52, -119.53, -119.53, -119.54, -119.55, -119.56, -145.78, -145.90. **HRMS (ESI) m/z** calc for **$C_9H_7BF_3O_2^-$ (M-K)$^-$**, 215.0497, observed 215.0494.

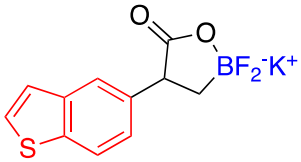

2q: Yellow solid, 82 % **yield** (22.34 mg).

^{1}H NMR (400 MHz, ACETONE-D_6) δ 7.83 – 7.75 (m, 2H), 7.55 (d, J = 5.4 Hz, 1H), 7.37 – 7.30 (m, 2H), 3.73 – 3.65 (m, 1H), 1.15 – 1.02 (m, 1H), 0.80 – 0.65 (m, 1H).**^{13}C NMR** (101 MHz, ACETONE-D_6) δ 180.40, 141.74, 139.93, 136.88, 126.13, 125.37, 123.90, 122.84, 121.59, 50.68. **^{11}B NMR** (128 MHz, ACETONE-D_6) δ 7.70. **^{19}F NMR** (376 MHz, ACETONE-D_6) δ -144.64, -146.09. **HRMS (ESI) m/z** calc for **$C_{11}H_8BF_2O_2S^-$ (M-K)$^-$**, 253.0312, observed 253.0313.

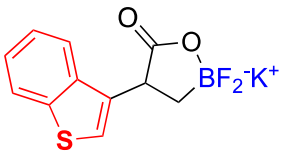

2r: Yellow solid, 75 % **yield** (22.55 mg).

^{1}H NMR (400 MHz, ACETONITRILE-D_3) δ 7.89 (d, J = 7.6 Hz, 1H), 7.85 – 7.78 (m, 1H), 7.45 – 7.31 (m, 2H), 7.29 (s, 1H), 4.04 (t, J = 9.4 Hz, 1H), 1.10 (ddt, J = 14.6, 10.0, 4.6 Hz, 1H), 0.85 – 0.66 (m, 1H). **^{13}C NMR** (101 MHz, DMSO-D_6) δ 179.42, 140.39, 139.16, 138.76, 124.43, 124.12, 123.32, 123.21, 122.25, 44.68, 44.67, 31.24. **^{11}B NMR** (128 MHz, ACETONITRILE-D_3) δ 7.93. **^{19}F NMR** (376 MHz, ACETONITRILE-D_3) δ -144.90, -145.23. **HRMS (ESI) m/z** calc for **$C_{11}H_8BF_2O_2S^-$ (M-K)$^-$**, 253.0312, observed 253.0313.

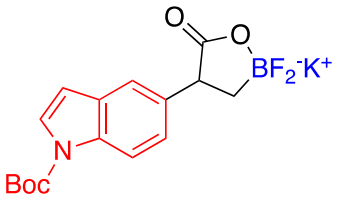

2s: Orange oil, 79 % **yield** (24.0 mg).

^{1}H NMR (400 MHz, ACETONE-D_6) δ 7.98 (d, J = 8.6 Hz, 1H), 7.58 (d, J = 3.7 Hz, 1H), 7.48 (d, J = 1.7 Hz, 1H), 7.26 (dd, J = 8.6, 1.7 Hz, 1H), 6.57 (d, J = 3.7 Hz, 1H), 3.66 (t, J = 9.0 Hz, 1H), 1.67 (s, 9H), 1.07 (ddt, J = 14.3, 9.7, 4.8 Hz, 1H), 0.81 – 0.65 (m, 1H). **^{13}C NMR** (101 MHz, ACETONE-D_6) δ 180.75, 149.63, 139.75, 133.53, 130.57, 125.60, 124.87, 120.11, 114.32, 107.34, 83.20, 50.56, 27.43. **^{11}B NMR** (128 MHz, ACETONE-D_6) δ 7.88. **^{19}F NMR** (376 MHz, ACETONE-D_6) δ -144.84, -146.01. **HRMS (ESI) m/z** calc for **$C_{16}H_{17}BF_2NO_4^-$ (M-K)$^-$**, 336.1224, observed 336.1228.

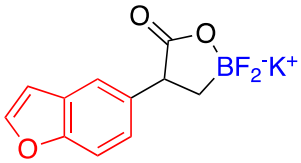

2t: Colorless oil, 82 % **yield** (7.89 mg) (0.033 mmol scale).

^{1}H NMR (400 MHz, ACETONE-D_6) δ 7.71 (d, J = 2.2 Hz, 1H), 7.50 (d, J = 1.8 Hz, 1H), 7.33 (dt, J = 8.5, 0.9 Hz, 1H), 7.22 (dd, J = 8.6, 1.8 Hz, 1H), 6.78 (dd, J = 2.2, 1.0 Hz, 1H), 3.63 (ddd, J = 9.5, 7.8, 1.3 Hz, 1H), 1.10 – 0.98 (m, 1H), 0.74 – 0.61 (m, 1H). **^{13}C NMR** (101 MHz, ACETONE-D_6) δ 179.78, 149.74, 130.03, 129.61, 128.96, 128.78, 127.30, 126.80, 124.72, 124.68, 50.52. **^{11}B NMR** (128 MHz, ACETONE-D_6) δ 7.75. **^{19}F NMR** (376 MHz, ACETONE-D_6) δ -144.79, -146.13. **HRMS (ESI) m/z** calc for **$C_{11}H_8BF_2O_3^-$ (M-K)$^-$**, 237.0540, observed 237.0540.

4.6 References

(1) Bhaskaran, S.; Padusha, M. S. A.; Sajith, A. M. Application of Palladium Based Precatalytic Systems in the Suzuki-Miyaura Cross-Coupling Reactions of Chloro- Heterocycles. *ChemistrySelect* **2020**, *5* (29), 9005–9016. https://doi.org/10.1002/slct.202002357.

(2) Furuya, T.; Kaiser, H. M.; Ritter, T. Palladium-Mediated Fluorination of Arylboronic Acids. *Angew. Chem. Int. Ed.* **2008**, *47* (32), 5993–5996. https://doi.org/10.1002/anie.200802164.

(3) Campbell, M. G.; Ritter, T. Modern Carbon–Fluorine Bond Forming Reactions for Aryl Fluoride Synthesis. *Chem. Rev.* **2015**, *115* (2), 612–633. https://doi.org/10.1021/cr500366b.

(4) Chen, J.; Li, J.; Dong, Z. A Review on the Latest Progress of Chan-Lam Coupling Reaction. *Adv. Synth. Catal.* **2020**, *362* (16), 3311–3331. https://doi.org/10.1002/adsc.202000495.

(5) Lozada, J.; Liu, Z.; Perrin, D. M. Base-Promoted Protodeboronation of 2,6-Disubstituted Arylboronic Acids. *J. Org. Chem.* **2014**, *79* (11), 5365–5368. https://doi.org/10.1021/jo500734z.

(6) Vedejs, E.; Chapman, R. W.; Fields, S. C.; Lin, S.; Schrimpf, M. R. Conversion of Arylboronic Acids into Potassium Aryltrifluoroborates: Convenient Precursors of Arylboron Difluoride Lewis Acids. *J. Org. Chem.* **1995**, *60* (10), 3020–3027. https://doi.org/10.1021/jo00115a016.

(7) Iashin, V.; Berta, D.; Chernichenko, K.; Nieger, M.; Moslova, K.; Pápai, I.; Repo, T. Metal-Free C−H Borylation of N-Heteroarenes by Boron Trifluoride. *Chem. – Eur. J.* **2020**, *26* (61), 13873–13879. https://doi.org/10.1002/chem.202001436.

(8) Taguchi, J.; Matsuura, S.; Seki, T.; Ito, H. Synthesis and Tunable Optical Properties of C,N-Chelated Borate Luminophores Derived from Potassium Acyltrifluoroborates. *Chem. – Eur. J.* **2020**, *26* (11), 2450–2455. https://doi.org/10.1002/chem.201904983.

(9) Baleeva, N. S.; Myannik, K. A.; Yampolsky, I. V.; Baranov, M. S. Bioinspired Fluorescent Dyes Based on a Conformationally Locked Chromophore of the Fluorescent Protein Kaede: Bioinspired Fluorescent Dyes. *Eur. J. Org. Chem.* **2015**, *2015* (26), 5716–5721. https://doi.org/10.1002/ejoc.201500721.

(10) Baruah, M.; Qin, W.; Vallée, R. A. L.; Beljonne, D.; Rohand, T.; Dehaen, W.; Boens, N. A Highly Potassium-Selective Ratiometric Fluorescent Indicator Based on BODIPY Azacrown Ether Excitable with Visible Light. *Org. Lett.* **2005**, *7* (20), 4377–4380. https://doi.org/10.1021/ol051603o.

(11) Coskun, A.; Akkaya, E. U. Ion Sensing Coupled to Resonance Energy Transfer: A Highly Selective and Sensitive Ratiometric Fluorescent Chemosensor for Ag(I) by a Modular Approach. *J. Am. Chem. Soc.* **2005**, *127* (30), 10464–10465. https://doi.org/10.1021/ja052574f.

(12) Nogami, M.; Hirano, K.; Morimoto, K.; Tanioka, M.; Miyamoto, K.; Muranaka, A.; Uchiyama, M. Alkynylboration Reaction Leading to Boron-Containing π-Extended *Cis* -Stilbenes as a Highly Tunable Fluorophore. *Org. Lett.* **2019**, *21* (9), 3392–3395. https://doi.org/10.1021/acs.orglett.9b01132.

(13) Hiscock, J. R.; Wells, N. J.; Ede, J. A.; Gale, P. A.; Sambrook, M. R. Biasing Hydrogen Bond Donating Host Systems towards Chemical Warfare Agent Recognition. *Org. Biomol. Chem.* **2016**, *14* (40), 9560–9567. https://doi.org/10.1039/C6OB01210H.

(14) Hughes, M. P.; Smith, B. D. Enhanced Carboxylate Binding Using Urea and Amide-Based Receptors with Internal Lewis Acid Coordination: A Cooperative Polarization Effect. *J. Org. Chem.* **1997**, *62* (13), 4492–4499. https://doi.org/10.1021/jo9702249.

(15) Subervie, D.; Graff, B.; Nerkar, S.; Curran, D. P.; Lalevée, J.; Lacôte, E. Difluorination at Boron Leads to the First Electrophilic Ligated Boryl Radical (NHC-BF_2·). *Angew. Chem. Int. Ed.* **2018**, *57* (32), 10251–10256. https://doi.org/10.1002/anie.201806476.

(16) Fritzemeier, R. G.; Medici, E. J.; Szwetkowski, C.; Wonilowicz, L. G.; Sibley, C. D.; Slebodnick, C.; Santos, W. L. Route to Air and Moisture Stable β-Difluoroboryl Acrylamides. *Org. Lett.* **2019**, *21* (19), 8053–8057. https://doi.org/10.1021/acs.orglett.9b03031.

(17) Légaré, M.-A.; Rochette, É.; Légaré Lavergne, J.; Bouchard, N.; Fontaine, F.-G. Bench-Stable Frustrated Lewis Pair Chemistry: Fluoroborate Salts as Precatalysts for the C–H Borylation of Heteroarenes. *Chem. Commun.* **2016**, *52* (31), 5387–5390. https://doi.org/10.1039/C6CC01267A.
(18) Butcher, T. W.; McClain, E. J.; Hamilton, T. G.; Perrone, T. M.; Kroner, K. M.; Donohoe, G. C.; Akhmedov, N. G.; Petersen, J. L.; Popp, B. V. Regioselective Copper-Catalyzed Boracarboxylation of Vinyl Arenes. *Org. Lett.* **2016**, *18* (24), 6428–6431. https://doi.org/10.1021/acs.orglett.6b03326.
(19) Nguyen, K.; Clement, H. A.; Bernier, L.; Coe, J. W.; Farrell, W.; Helal, C. J.; Reese, M. R.; Sach, N. W.; Lee, J. C.; Hall, D. G. Catalytic Enantioselective Synthesis of a *Cis* -β-Boronyl Cyclobutylcarboxyester Scaffold and Its Highly Diastereoselective Nickel/Photoredox Dual-Catalyzed Csp^3 –Csp^2 Cross-Coupling to Access Elusive *Trans* -β-Aryl/Heteroaryl Cyclobutylcarboxyesters. *ACS Catal.* **2021**, *11* (1), 404–413. https://doi.org/10.1021/acscatal.0c04520.
(20) Durka, K.; Marek-Urban, P. H.; Nowicki, K.; Drapała, J.; Jarzembska, K. N.; Łaski, P.; Grzelak, A.; Dąbrowski, M.; Woźniak, K.; Luliński, S. Expedient Synthesis of Oxaboracyclic Compounds Based on Naphthalene and Biphenyl Backbone and Phase-Dependent Luminescence of Their Chelate Complexes. *Chem. – Eur. J.* **2022**, *28* (14). https://doi.org/10.1002/chem.202104492.
(21) Perrone, T. M.; Gregory, A. S.; Knowlden, S. W.; Ziemer, N. R.; Alsulami, R. N.; Petersen, J. L.; Popp, B. V. Beneficial Effect of a Secondary Ligand on the Catalytic Difunctionalization of Vinyl Arenes with Boron and CO_2. *ChemCatChem* **2019**, *11* (23), 5814–5820. https://doi.org/10.1002/cctc.201901197.
(22) Knowlden, S. W.; Popp, B. V. Regioselective Boracarboxylation of α-Substituted Vinyl Arenes. *Organometallics* **2022**, acs.organomet.2c00184. https://doi.org/10.1021/acs.organomet.2c00184.
(23) Baughman, N. N.; Akhmedov, N. G.; Petersen, J. L.; Popp, B. V. Experimental and Computational Analysis of CO_2 Addition Reactions Relevant to Copper-Catalyzed Boracarboxylation of Vinyl Arenes: Evidence for a Phosphine-Promoted Mechanism. *Organometallics* **2021**, *40* (1), 23–37. https://doi.org/10.1021/acs.organomet.0c00488.
(24) Lennox, A. J. J.; Lloyd-Jones, G. C. Selection of Boron Reagents for Suzuki–Miyaura Coupling. *Chem Soc Rev* **2014**, *43* (1), 412–443. https://doi.org/10.1039/C3CS60197H.
(25) Ochoa, G.; Pilgrim, C. D.; Kerr, J.; Augustine, M. P.; Casey, W. H. Aqueous Geochemistry at Gigapascal Pressures: NMR Spectroscopy of Fluoroborate Solutions. *Geochim. Cosmochim. Acta* **2019**, *244*, 173–181. https://doi.org/10.1016/j.gca.2018.09.033.
(26) Hiraishi, N.; Sayed, M.; Hill, R.; Tagami, J.; Hayashi, F. Interactions of Boron Released from Surface Pre-Reacted Glass Ionomer with Enamel/Dentin and Its Effect on PH. *Sci. Rep.* **2021**, *11* (1), 15734. https://doi.org/10.1038/s41598-021-95279-x.

Chapter V

Investigation of the Dynamic Equilibrium Between B-N Coordinated and Non-Coordinated DABO Boronate Esters in Deuterated Methanol Medium

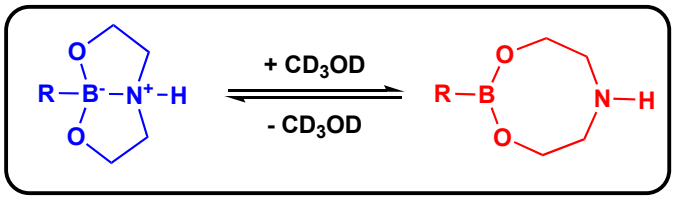

5.1. Abstract

Diethanolamine complexed boronic esters (DABO boronates) are air and moisture stable tetracoordinated boronic adducts synthesized by condensation of diethanolamine with boronic compounds. In non protic organic solvents DABO boronate exist in a stable [3,3,0]-bicyclic structure due to the formation of intramolecular B-N dative bond. In polar protic mediums, B-N bond weakened and form another 8-membered ring containing tricoordinate boron ester species. These two species exist in a dynamic equilibrium. This equilibrium was studied using the VT-NMR spectroscopic method in deuterated methanol medium. Using that the equilibrium constant, Keq were calculated in different temperature 298.15 K to 333.15 K. The Van't Hoff plot was constructed to calculate the enthalpy change ($\Delta H°$), entropy change ($\Delta S°$), and free energy change ($\Delta G°$) for given equilibrium. The enthalpy change values for all substrates at the given equilibrium is endothermic. The DABO boronate esters with less sterically hindered boron centers, such as methyl, n-butyl and isobutyl have high entropy values relative to the sterically hindered ones. This high entropy value offset high positive enthalpy. Therefore, methyl, n-butyl, and isobutyl DABO boronates have negative values for free energy change and favored the formation of 8-member boron ester at 298.15 K.

5.2. Introduction

In the past several decades, boron compounds have gained an important position in the scientific community, due to their wide range of applications. They are used as therapeutic agents,[1,2] sensors,[3] synthesis and catalysis[4] as well as in Boron Neutron Capture Therapy (BNCT).[5,6] Most of the common organoboron compounds such as boronic esters and boronic acids are trivalent and exist in a sp^2 hybridized form. Because of the vacant *p*-orbital, boronic acids are susceptible to reactions with oxidants and nucleophiles. On the contrary, tetravalent sp^3 hybridized organoboron compounds are more stable towards oxidants and nucleophiles. Trifluoroborates,[7] borafluorolactonate potassium salts,[8] N-methylimidodiacetic boronic esters (MIDA boronates)[9] and diethanolamine complexed boronic esters (DABO boronates)[10] are some examples for tetravalent organoboron compounds (Figure 5.1). These tetracoordinated organoboron compounds have exceptional stability towards air and moisture.

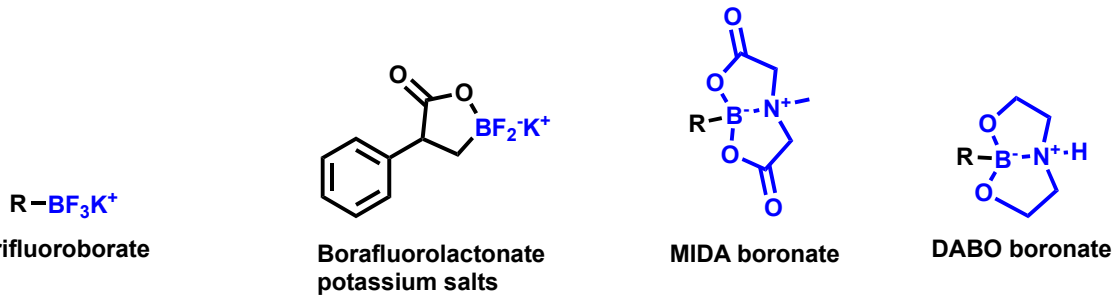

Figure 5.1 Representative examples for tetracoordinated organoboron compounds.

DABO boronates have a significant advantage over other derivatives due to its ease of preparation. They can be easily isolated by simple filtration of ethereal media. This is due to them precipitating in the ethereal medium because of their high polarity. DABO boronate exists in a stable [3,3,0]-bicyclic structure owing to the formation of an intramolecular B-N dative bond. X-Ray crystallographic data of reported examples confirm the formation of two trans annular five membered rings and the tetrahedral geometry of

the boron center.[11] In non protic organic solvents, ^{11}B NMR spectra show a single peak in the region between 7-12 ppm.[12]

In chapter 2, a CIGAR-HMBC experiment was carried out to identify the correct structure for diethanolamine complexed bora-ibuprofen structure (Figure 2.4). Any previous examples were not found in literature for ^{1}H-^{15}N correlation through B-N bond. Therefore, we have synthesized model compound methyl-DABO boronate ester to observe a correlation between methyl protons and nitrogen through B-N bond. When we tried to run the CIGAR-HMBC experiment on methyl-DABO boronate ester in deuterated methanol medium, the appearance of this new boron signal was observed around 30 ppm. This change in the ^{11}B chemical shift suggests a formation of another boron species in the medium with weakening or disappearance of the B-N bond. Additionally, in deuterated methanol medium, a complex 1H NMR spectra was observed for methyl DABO- boronate ester.

In literature, two mechanisms were used to explain this dynamic behavior. First mechanism, DABO boronates get decomposed in polar protic conditions to generate boronic acid and diethanolamine in the solution (Scheme 2a). Prusoff et al., 1985, made a similar observation and suggested the mechanism 2a.[13] However, there are no conclusive evidence to suggest that in polar protic mediums such as water, DABO boronate undergoes hydrolysis to form boronic and diethanol amine. Due to the lack of evidence, there has been a long debate ongoing about the cause of the new species formation.

In the second mechanism, in polar protic mediums, B-N bond gets weakened by the formation of a hydrogen bond between the reaction medium and the nitrogen atom. This leads to the creation of a dynamic equilibrium between a closed bicyclic ring structure and an open 8-membered ring structure (Scheme 2b). Gras et al. , 2011 mentioned that further structural investigations are required to explain these observations in the presence of polar protic solvents.[14] Another important observation is that, when polar protic solvents get evaporated, DABO boronate gets regenerated and can be observable by ^{11}B NMR chemical shifts. We hypothesized that DABO boronate exists in a dynamic equilibrium between open and closed forms due to

the labile nature of the B-N bond. Furthermore, the dynamic equilibria between [3,3,0] bicyclic and 8-membered ring structures was investigated by variable-temperature NMR spectroscopy (VT-NMR). The enthalpy change (△H), entropy change (△S) and Gibbs free energy change (△G) for this equilibrium were calculated using the Van't Hoff equation.

Scheme 5.1 Plausible mechanism for DABO boronates dissociation in polar protic solvents.

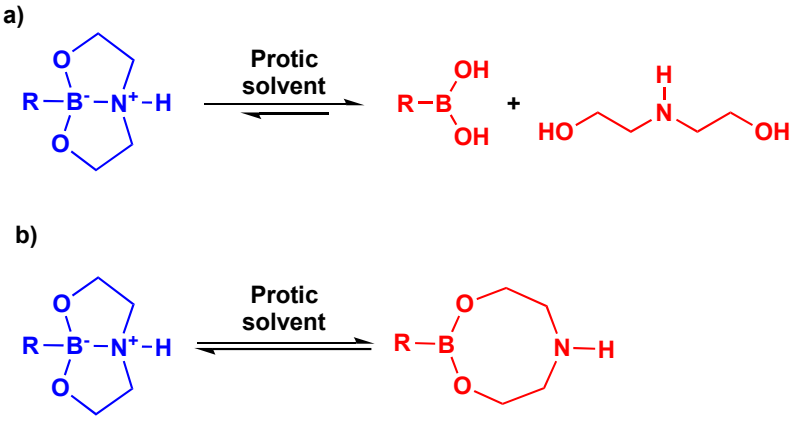

5.3 Results and Discussion

First, we have synthesized series of DABO boronates, using condensation between diethanolamine and boronic acid in non-polar solvents such as diethyl ether or dichloromethane. Using these reaction conditions, DABO boronate (**3a-3g**) was synthesized in good to excellent yields (Scheme 5.2).[15]

Scheme 5.2 Synthesis of DABO boronate model compounds.

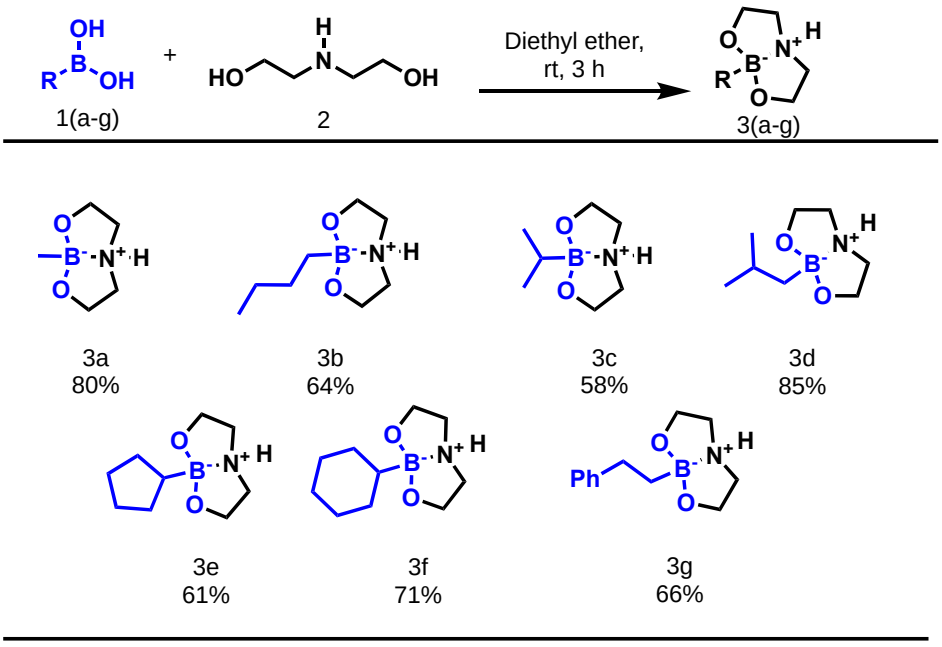

[a]1a-1g (1 eq, 0.5 mmol) and 2 diethanol amine (157.5 mg, 1.5 mmol, 3 eq.), 3 mL of diethyl ether was added.

These compounds were characterized using NMR spectroscopic methods. Due to the formation of transannular rings, methylene protons in the two rings are diastereotopic and exhibit a AA'BB' second order splitting pattern in proton NMR for compound 3a (Figure 5.2). Because of the formation of the B-N dative bond, the tetracoordinated boron center showed up at 11.24 ppm in the boron NMR spectra for compound **3a** (Figure 5.3).

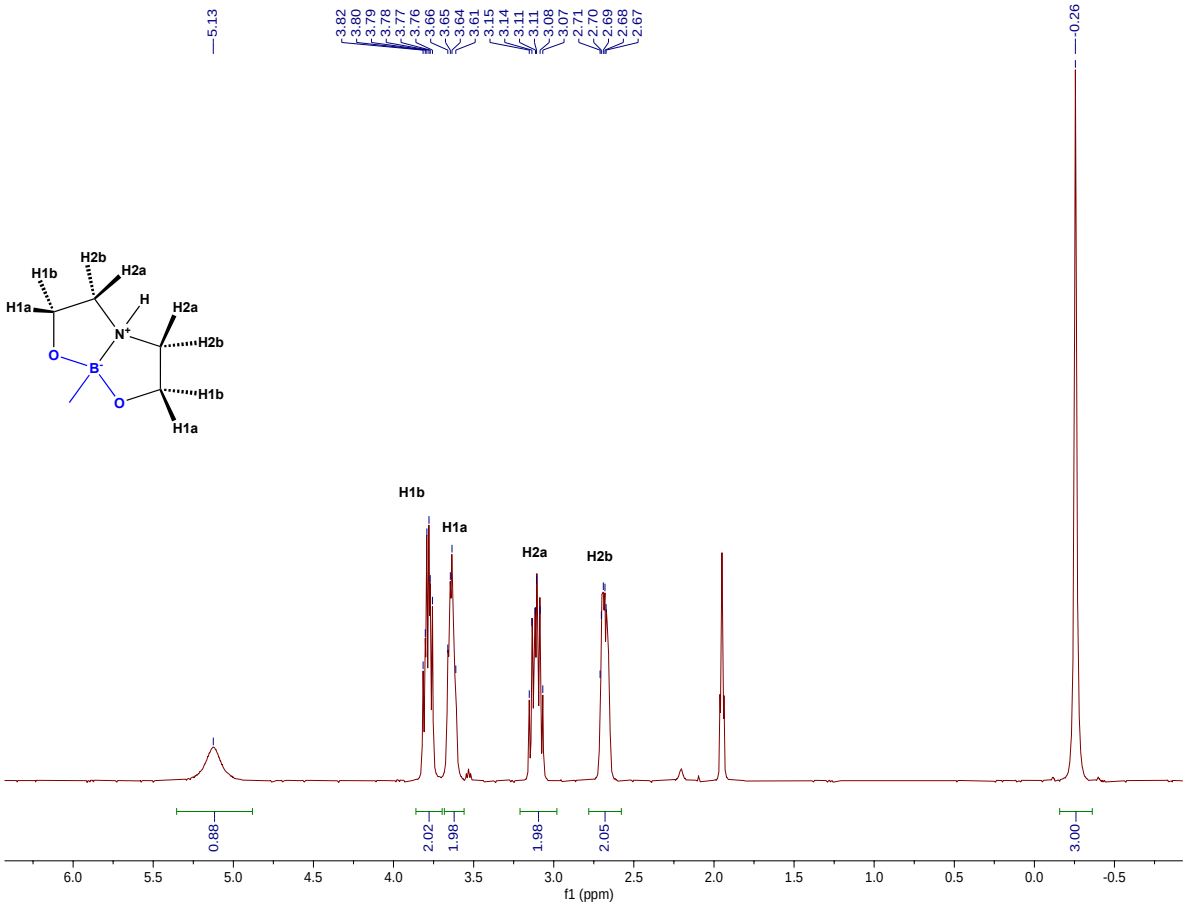

Figure 5.2 ^{1}H NMR spectra of **3a** in CD_3CN-*d3*

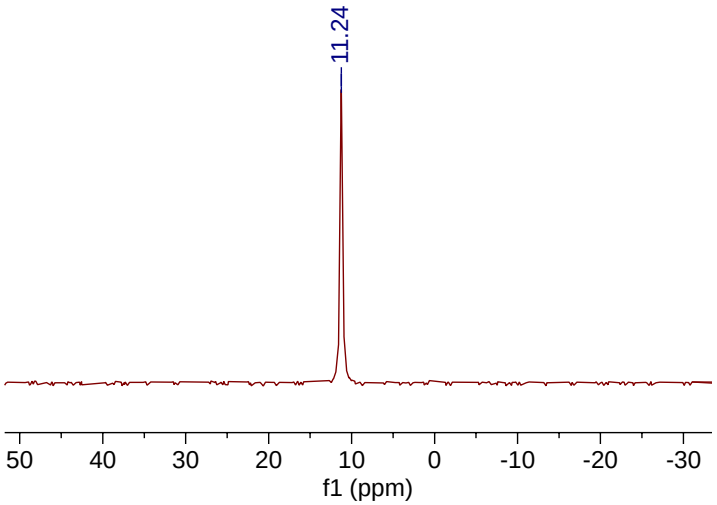

Figure 5.3 ^{11}B NMR spectra of **3a** in CD_3CN-*d3*

Furthermore, **3a** was characterized using the CIGAR-HMBC 2D NMR spectroscopic method (Figure 5.4).[16] Methyl group protons correlate to nitrogen at -332.0 ppm and to our understanding this is the first example for this observation of ^{1}H-^{15}N correlation through a B-N dative bond. Also, methylene group protons (H1a and H1b) show correlation to the nitrogen atom. For acetonitrile, reference ^{15}N peak showed up at -137.6 ppm.

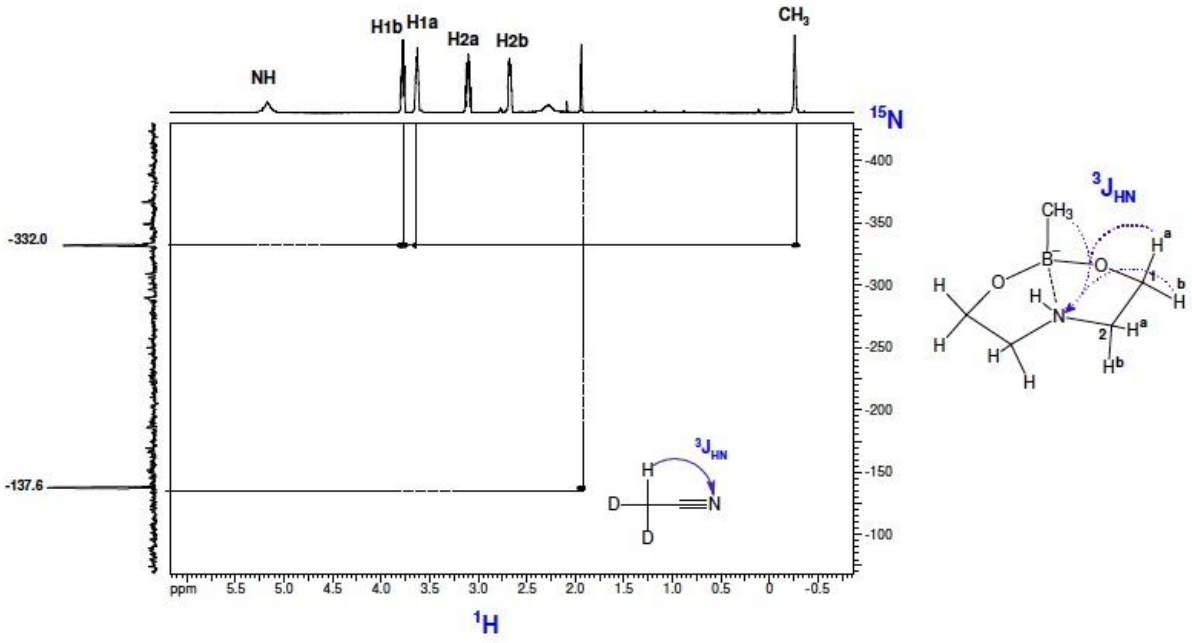

Figure 5.4 2D CIGAR-HMBC spectrum of **3a** CD_3CN-*d3*

When DABO boronates were added into deuterated methanol, a new chemical species was formed. A hydrogen bond was formed between nitrogen and methanol in the medium. Because of this hydrogen bond formation, the B-N bond become weakened and reversible. Therefore, in methanol solution DABO boronates exist in a dynamic equilibrium between tetracoordinate bicyclic structure and tricoordinate 8-membered structure. In ^{11}B NMR, two peaks were observed (Figure 5.5). The peak at 10.6 ppm represents the tetracoordinated [3,3,0]-bicyclic structure and the peak at 30.3 ppm represents the tricoordinate boron ester.

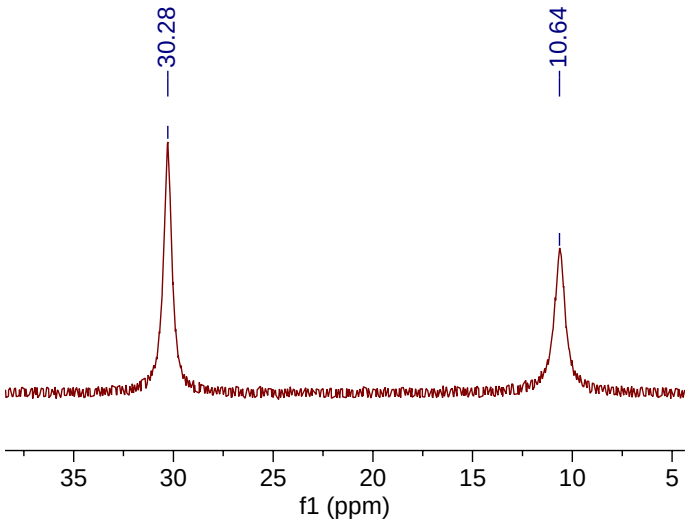

Figure 5.5 ^{11}B NMR spectrum of 3a in CD_3OD-*d4* at 298.15 K

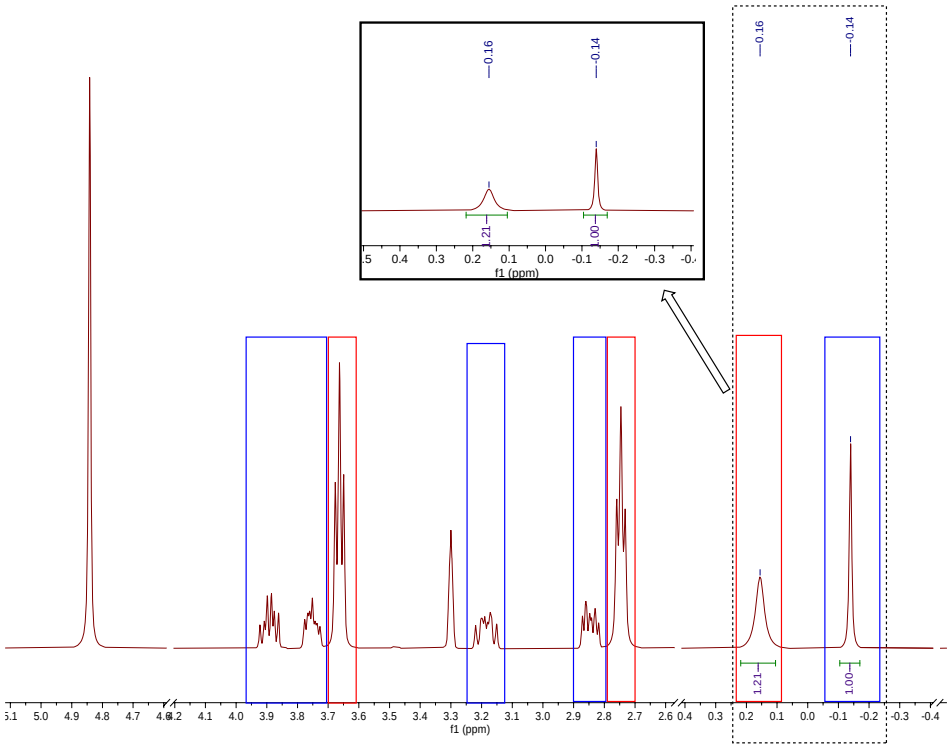

Figure 5.6 ^{1}H NMR spectrum of 3a in CD_3OD-*d4* at 298.15 K

In the ^{1}H spectrum, two sets of NMR peaks were observed (Figure 5.6). The peaks encircled in blue represents the tetracoordinated [3,3,0]-bicyclic methyl DABO boronate ester. The peaks encircled in red represent tricoordinate 8-membered ring boron ester. The equilibrium constant for the dynamic between

[3,3,0]-bicyclic structure and 8-membered ring structure can be determined by using the ratio between the integral value of the methyl groups in the ^{1}H NMR spectrum (Figure 5.7).

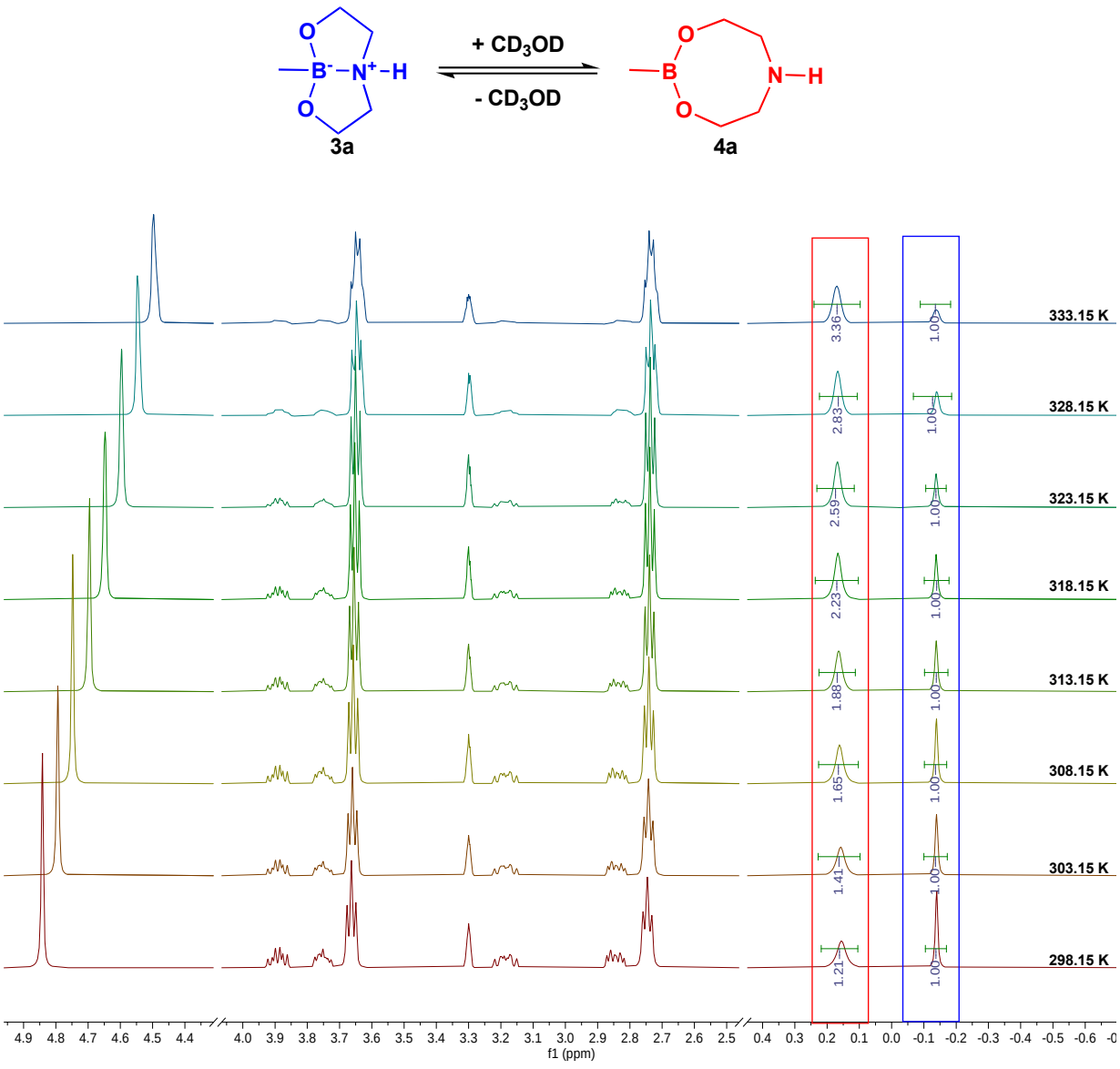

Figure 5.7 VT ^{1}H NMR experimental data collected from 298.15 K to 333.15 K in CD_3OD-*d4* for the dynamic equilibrium between **3a** and **4a.** (At each temperature samples were equilibrated for 15 minutes prior to getting the readings)

Afterwards, the equilibrium constant (K_{eq}) for the dynamic equilibria between [3,3,0] bicyclic structure (3a) and 8-membered ring from (4a) at different temperatures, were determined by variable-temperature NMR spectroscopy. When temperature increased, the equilibrium favored the 8-membered ring structure (4a) more. Therefore, the integral ratio for 4a increased with the increasing temperature. Using the integral ratio between 3a and 4a, Keq for each temperature were determined.

In an equilibrium reaction, the equilibrium constant changes with the change in temperature in the equilibrium system. Using the Van't Hoff equation (equation 5.1), the equilibrium constants can be related to the thermodynamic parameters in the system.[17] The Van't Hoff equation is used to determine thermodynamic parameters for various equilibrium reactions, such as, biological systems,[18] organic reactions,[19] and separation science.[20]

$$\ln Keq = -\frac{\Delta H^{\circ}}{RT} + \frac{\Delta S^{\circ}}{R} \qquad (5.1)$$

Using the equilibrium ratios of **3a** and **4a** obtained from VT-NMR experiments, equilibrium constant K_{eq} was calculated for each temperature (Table 5.1). Next, a Van't Hoff plot was constructed to calculate the thermodynamic parameters for the dynamic equilibrium between 3**a** and 4**a.**

Table 5.1. Dynamic equilibria data for **3a** and **4a** in CD_3OD-*d4* at different temperatures.

Temperature (K)	1/K x10^{-3}	Equilibrium ratio of [3,3,0] bicyclic ring structure (**3a**)	Equilibrium ratio of 8 membered ring structure (**4a**)	K_{eq}	ln K_{eq}
298.15	3.35	1.00	1.22	1.22	0.20
303.15	3.30	1.00	1.41	1.41	0.34
308.15	3.25	1.00	1.65	1.65	0.50
313.15	3.19	1.00	1.90	1.90	0.64
318.15	3.14	1.00	2.22	2.22	0.80
323.15	3.09	1.00	2.55	2.55	0.94
328.15	3.05.	1.00	2.90	2.90	1.06
333.15	3.00	1.00	3.35	3.35	1.21

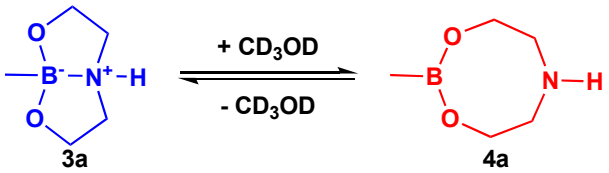

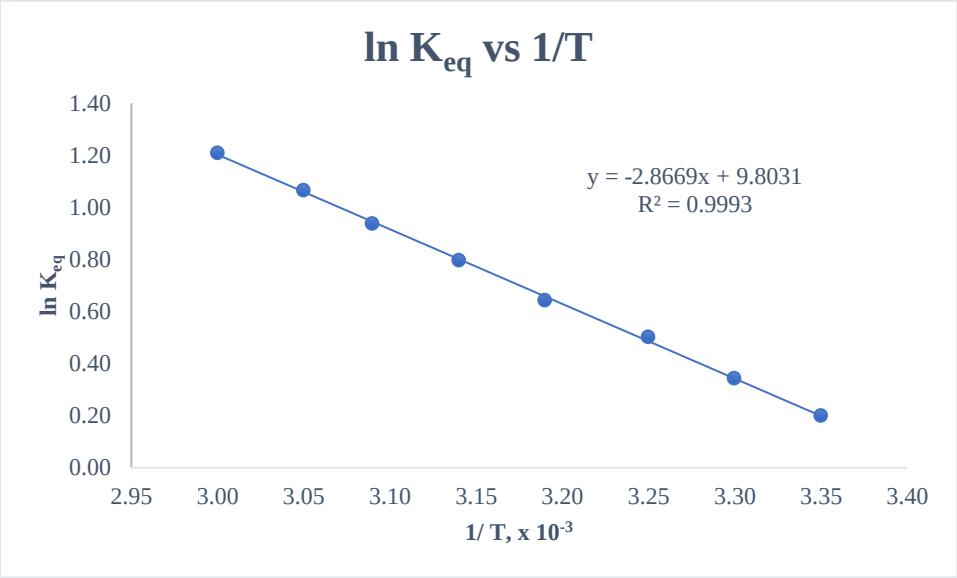

Slope is $-\frac{\Delta H^\circ}{R}$

Intercept is $\frac{\Delta S^\circ}{R}$

Figure 5.8 Van't Hoff plot of ln K_{eq} vs. 1/T for equilibrium constants obtained for dynamic equilibria between **3a** and **4a** by VT ^{1}H NMR experiments at temperatures between 298.15 K to 333.15 K in CD_3OD-*d4*.

<u>ΔH° calculated using gradient</u>

$-\frac{\Delta H^\circ}{R}$ = -2.8669

R = 1.987 cal K^{-1} mol^{-1}

ΔH° = 5.70 kcal mol^{-1}

<u>ΔS° calculated using intercept</u>

$\frac{\Delta S^\circ}{R}$ = 9.8031

R = 1.987 cal K^{-1} mol^{-1}

ΔS° = 19.5 cal K^{-1} mol^{-1}

<u>ΔG° calculated at 298.15,</u>

$\Delta G^\circ = \Delta H^\circ - T\Delta S$ (5.2)

ΔG° = - 114 cal mol^{-1}

The standard enthalpy change ($\Delta H°$) for the dynamic equilibrium between **3a** and **4a**, was determined using the gradient of the Van't Hoff plot (Figure 5.8). The enthalpy change was 5.70 kcal mol^{-1} . This positive enthalpy change suggests that the equilibrium is endothermic and is favored in the forward direction. Similarly, the standard entropy change ($\Delta S°$) was determined using the intercept of the Van't Hoff plot. The positive entropy change was 19.48 cal K^{-1} mol^{-1}, which means that the release of B-N bond entropically favored the formation of **4b.** Lastly, the free energy change ($\Delta G°$) was calculated using the enthalpy and entropy changes obtained from the Van't Hoff plot (equation 5.2). The calculated free energy change value was -108 cal mol^{-1}, suggesting that this equilibrium was favored in the forward direction at 298.15 K.

Table 5.2. Standard enthalpy ($\Delta H°$), entropy ($\Delta S°$), and free energy ($\Delta G°$) values at 298.15 K for dynamic equilibria between **3a-g** and **4a-g** in CD_3OD-*d4*.

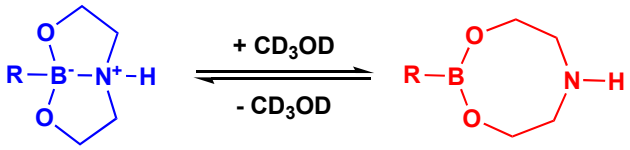

3a-g **4a-g**

Substrate, R	$\Delta H°$ kcal mol^{-1}	$\Delta S°$ cal K^{-1} mol^{-1}	$\Delta G°$ **(298.15K)** kcal mol^{-1}
H_3C-	5.70	19.5	-0.114
$CH_2CH_2CH_2CH_2-$	5.72	20.4	-0.362
	5.21	15.7	0.529
	4.91	16.8	-0.099
	4.30	12.8	0.484
	4.92	12.9	1.07
	5.18	15.3	0.618

Similarly, thermodynamic parameters were calculated for the dynamic equilibrium between **3a-g** and **4a-g** using the Van't Hoff plot (Table 5.2). For all the equilibriums, the enthalpy changes were positive, suggesting that the equilibrium between 3 and 4 was endothermic in the forward direction. The substrates with more sterically hindered boron centers have had relatively lower standard positive enthalpy values than less hindered substrates. The standard entropy has also been positive for all the equilibriums. The breaking of B-N bond has increased the randomness of the molecule. Thus, the positive standard entropy changes had been observed. Likewise, in the standard enthalpy change, the substrates with more sterically hindered boron centers have showed lower standard entropy values relative to the less hindered ones.

The standard free energy change was calculated for the given equilibria using the standard enthalpy and entropy values. The methyl, n-butyl, and isobutyl substrates have had negative free energy values for the given equilibria at 298.15 K and favored the formation of the 8-membered structures. This is mainly due to the comparatively high entropy changes in these three equilibriums. This can offset large positive enthalpy changes. The n-butyl substrate has had the highest degree of freedom; thus, it has had the highest entropy change value and the highest negative free energy change value. The formation of the 8-membered structures was not favorable for the substrates with larger steric hindrance around the boron center such as, isopropyl, cyclopentyl, cyclohexyl, and 2-phenylethyl. They all have had positive free energy change values at 298.15 K. They all have had relatively smaller entropy values, which is not sufficient to offset the positive enthalpy value. The cyclopentyl and cyclohexyl substrates have had lowest entropy values because of the ring being constrained.

5.4 Conclusion

Presented in this chapter was the study of the dynamic equilibria between the B-N coordinated [3,3,0] bicyclic structures and B-N non coordinated 8-membered ring containing DABO boronates in deuterated methanol mediums. The VT-NMR spectroscopic method was used to determine equilibrium constants for each equilibrium in given temperatures. By constructing a Van't Hoff plot, the standard enthalpy changes and standard entropy changes were calculated for each equilibrium. The standard free energy change for

each equilibrium was calculated using the standard enthalpy and entropy changes. The substrates with less sterically hindered boron centers have showed higher entropy change values relative to the more hindered ones. This high entropy change values are enough to offset positive enthalpy changes. Therefore, less sterically hindered substrates more favored the 8-membered structure at 298.15 K.

Overall, this study, which was carried out on the dynamic equilibrium between B-N coordinated and B-N non coordinated DABO boronates in polar protic mediums, provides a clear answer to a long ongoing debate about DABOboronates dissociation mechanism in polar protic mediums. This understanding would further enhance its synthetic capabilities in different solvent mediums.

5.5 Experimental Methods

General information

All commercially available compounds were used as received, and all were purchased from either Oakwood chemicals, Alfa Aesar, or Fisher chemicals.

^{1}H, ^{13}C, and ^{11}B NMR spectra were recorded on JEOL 400 MHz and Varian INOVA 600 MHz NMR spectrometers, and all deuterated solvents were purchased from Cambridge Isotope Laboratories, Inc. The chemical shifts (δ) are given in parts per million and referenced relative to residual proteo solvent (1.94 or 3.31 ppm for d3-CD_3CN and d4-CD_3OD, respectively), d3-CD_3CN or d4-CD_3OD (1.30 or 49.30 ppm for ^{13}C), and internal (capillary) BF_3•OEt_2 (32.1 ppm). ^{11}B NMR spectra recorded using quartz NMR tubes. For variable temperature NMR (VT-NMR) experiments, temperature varied in the following order 25 °C, 35 °C, 45 °C, 55 °C, 60 °C, 50 °C, 40 °C, 30 °C and prior to spectral reading sample was equilibrate for 15 minutes at each temperature. High-resolution mass spectra were recorded on a Thermofisher Scientific Q Exactive Mass Spectrometer using MeOH (Fisher Optima grade).

Van't Hoff plots were constructed to determine enthalpy change (ΔH) and entropy change (ΔS) for each equilibrium. Graphs were plotted using Microsoft Excel and standard errors were calculated using LINEST functions in Microsoft Excel.

General procedures for preparing diethanolamine complexed heterocyclic boronic acids (DABO boronates)

A 20 mL scintillation vial was charged with compound **1a-1g** (1 eq, 0.5 mmol) and diethanol amine (157.5 mg, 1.5 mmol, 3 eq.). A 3 mL of ethanol solution was added, and the resulting suspension was stirred at ambient temperature for 3 hours. After 3 hours white fine powdered product was vacuum filtered to provide the DABO boronate desired product. The resulting white powdered solid was washed with excess diethyl ether to remove impurities.

DABO boronates product characterization

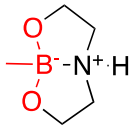

3a: White microcrystalline solid 80 % **yield** (51.70 mg isolated).

^{1}H (400 MHz, ACETONITRILE-*D*$_3$) 5.13 (1 H, s), 3.79 (2 H, td, *J* 9.0, 5.4), 3.64 (2 H, ddd, *J* 9.9, 6.3, 4.0), 3.11 (2 H, dq, *J* 11.7, 7.2), 2.68 (2 H, ddt, *J* 12.1, 8.2, 3.4), -0.26 (3 H, s). **^{13}C NMR (101 MHz, ACETONITRILE-*D*$_3$)** δ 62.13, 51.00. **^{11}B NMR (128 MHz, ACETONITRILE-*D*$_3$)** δ 11.24. **HRMS (ESI) m/z** calc for **$C_5H_{12}BNO_2$+H: $C_5H_{11}BNO_2$ pa Chrg -1,** 128.0888, observed 128.0879.

The ^{13}C NMR resonance at 14.73 (methylene carbon signal) has very low intensity due to 11B quadrupolar broadening.

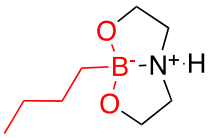

3b: White microcrystalline solid, 64 % **yield** (55.0 mg isolated).

^{1}H NMR (400 MHz, ACETONITRILE-*D*$_3$) δ 5.15 (1 H, s), 3.80 (2 H, td, *J* 9.1, 5.3), 3.66 (2 H, ddd, *J* 9.8, 6.4, 3.8), 3.09 (2 H, ddt, *J* 11.7, 8.5, 6.7), 2.76 – 2.66 (2 H, m), 1.36 – 1.12 (4 H, m), 0.89 (3 H, t, *J* 7.2), 0.34 – 0.26 (2 H, m). **^{13}C NMR** (101 MHz, ACETONITRILE-*D*$_3$) δ 63.24, 52.10, 29.09, 14.56.

^{11}B NMR (128 MHz, ACETONITRILE-*D*$_3$) δ 11.59. **HRMS (ESI) m/z** calc for **$C_8H_{18}BNO_2$+H: $C_8H_{17}BNO_2$ pa Chrg -1,** 170.1358, observed 170.1352.

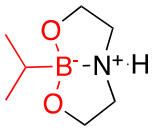

3c: White microcrystalline solid, 58 % **yield** (44.0 mg isolated). **Melting point:** 151-159 °C

^{1}H NMR (600 MHz, ACETONITRILE-*D*$_3$) δ 5.09 (1 H, s), 3.81 (2 H, td, *J* 9.3, 5.4), 3.68 (2 H, ddd, *J* 9.8, 6.6, 3.5), 3.07 (2 H, ddt, *J* 11.8, 9.1, 6.9), 2.74 (2 H, dddd, *J* 11.6, 5.7, 3.5, 2.5), 0.80 (6 H, d, *J* 7.3), 0.54 (1 H, p, *J* 7.2).**^{13}C NMR** (101 MHz, ACETONITRILE-*D*$_3$) δ 62.59, 51.45, 18.80. **^{11}B NMR (**128 MHz, ACETONITRILE-*D*$_3$) δ 12.16. **HRMS (ESI) m/z** calc for **$C_7H_{16}BNO_2$+H: $C_7H_{15}BNO_2$ pa Chrg -1,** 156.1201, observed 156.1194.

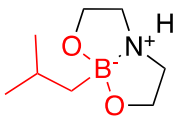

3d: White microcrystalline solid, 85 % **yield** (73.0 mg isolated). **Melting point:** 128-132 °C

^{1}H NMR (400 MHz, ACETONITRILE-*D*$_3$) δ 4.96 (1 H, s), 3.79 (2 H, td, *J* 9.3, 5.3), 3.70 – 3.59 (2 H, m), 3.16 – 3.01 (2 H, m), 2.75 – 2.61 (2 H, m), 1.61 (1 H, dp, *J* 13.2, 6.6), 0.88 (6 H, d, *J* 6.6), 0.26 (2 H, d, *J*

6.9). **^{13}C NMR** (101 MHz, ACETONITRILE-D_3) δ 63.21, 52.01, 26.55, 26.41. **^{11}B NMR** (128 MHz, ACETONITRILE-D_3) δ 11.46. **HRMS (ESI) m/z** calc for **$C_8H_{18}BNO_2$+H: $C_8H_{17}BNO_2$ pa Chrg -1,** 170.1358, observed 170.1351.

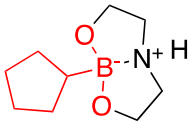

3e: White microcrystalline solid, 61 % **yield** (56.0 mg isolated). **Melting point:** 198-207 °C

^{1}H NMR (400 MHz, ACETONITRILE-D_3) δ 4.99 (1 H, s), 3.81 (2 H, td, *J* 9.3, 5.3), 3.67 (2 H, ddd, *J* 10.0, 6.7, 3.5), 3.08 (2 H, ddt, *J* 12.1, 9.0, 7.0), 2.73 (2 H, ddt, *J* 11.6, 5.7, 3.0), 1.64 – 1.49 (5 H, m), 1.49 – 1.37 (2 H, m), 1.17 (2 H, h, *J* 8.8), 0.80 – 0.69 (1 H, m).**^{13}C NMR** (101 MHz, ACETONE-D_6) δ 62.63, 51.53, 29.32, 26.88. **^{11}B NMR** (128 MHz, ACETONE-D_6) δ 12.11. **HRMS (ESI) m/z** calc for **$C_9H_{18}BNO_2$+H: $C_9H_{17}BNO_2$ pa Chrg -1,** 182.1358, observed 182.1352.

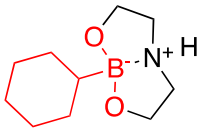

3e: White microcrystalline solid, 71 % **yield** (60.57 mg isolated). **Melting point:** 230-235 °C

^{1}H NMR (400 MHz, ACETONITRILE-D_3) δ 5.00 (1 H, s), 3.79 (2 H, td, *J* 9.3, 5.3), 3.65 (2 H, ddd, *J* 9.8, 6.6, 3.5), 3.09 – 2.97 (2 H, m), 2.72 (2 H, dddd, *J* 11.6, 5.6, 3.5, 2.5), 1.75 – 1.63 (3 H, m), 1.62 – 1.54 (2 H, m), 1.25 – 1.09 (3 H, m), 0.97 (2 H, qd, *J* 12.1, 2.8), 0.34 (1 H, t, *J* 12.5). **^{13}C NMR** (101 MHz, ACETONITRILE-D_3) δ 62.56, 51.33, 29.27, 28.32, 27.41. **^{11}B NMR** (128 MHz, ACETONITRILE-D_3) δ 11.73. **HRMS (ESI) m/z** calc for **$C_{10}H_{20}BNO_2$+H: $C_{10}H_{19}BNO_2$ pa Chrg -1,** 196.1514, observed 196.1511.

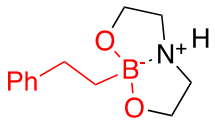

3e: White microcrystalline solid, 66% **yield** (72.00 mg isolated). **Melting point:** 109-113 °C

^{1}H NMR (400 MHz, ACETONITRILE-D_3) δ 7.20 (4 H, h, *J* 5.9), 7.07 (1 H, ddt, *J* 7.2, 5.8, 2.2), 5.15 (1 H, s), 3.80 (2 H, td, *J* 9.2, 5.4), 3.66 (2 H, ddd, *J* 9.9, 6.5, 3.8), 3.07 (2 H, ddt, *J* 11.8, 8.7, 6.8), 2.75 – 2.61 (2 H, m), 2.52 – 2.43 (2 H, m), 0.65 – 0.56 (2 H, m). **^{13}C NMR** (101 MHz, ACETONITRILE-D_3) δ 147.47, 128.27, 128.14, 127.91, 125.39, 124.86, 62.46, 51.23, 32.00. **^{11}B NMR** (128 MHz, ACETONITRILE-D_3) δ 11.32. **HRMS (ESI) m/z** calc for **$C_{12}H_{18}BNO_2$+H: $C_{12}H_{17}BNO_2$ pa Chrg -1,** 218.1358, observed 218.1356.

5.6 References

(1) Ali, F.; S Hosmane, N.; Zhu, Y. Boron Chemistry for Medical Applications. *Molecules* **2020**, *25* (4), 828. https://doi.org/10.3390/molecules25040828.

(2) Fernandes, G. F. S.; Denny, W. A.; Dos Santos, J. L. Boron in Drug Design: Recent Advances in the Development of New Therapeutic Agents. *Eur. J. Med. Chem.* **2019**, *179*, 791–804. https://doi.org/10.1016/j.ejmech.2019.06.092.

(3) Zhai, J.; Pan, T.; Zhu, J.; Xu, Y.; Chen, J.; Xie, Y.; Qin, Y. Boronic Acid Functionalized Boron Dipyrromethene Fluorescent Probes: Preparation, Characterization, and Saccharides Sensing Applications. *Anal. Chem.* **2012**, *84* (23), 10214–10220. https://doi.org/10.1021/ac301456s.

(4) Lennox, A. J. J.; Lloyd-Jones, G. C. Selection of Boron Reagents for Suzuki–Miyaura Coupling. *Chem Soc Rev* **2014**, *43* (1), 412–443. https://doi.org/10.1039/C3CS60197H.

(5) Hirose, K.; Konno, A.; Hiratsuka, J.; Yoshimoto, S.; Kato, T.; Ono, K.; Otsuki, N.; Hatazawa, J.; Tanaka, H.; Takayama, K.; Wada, H.; Suzuki, M.; Sato, M.; Yamaguchi, H.; Seto, I.; Ueki, Y.; Iketani, S.; Imai, S.; Nakamura, T.; Ono, T.; Endo, H.; Azami, Y.; Kikuchi, Y.; Murakami, M.; Takai, Y. Boron Neutron Capture Therapy Using Cyclotron-Based Epithermal Neutron Source and Borofalan (10B) for Recurrent or Locally Advanced Head and Neck Cancer (JHN002): An Open-Label Phase II Trial. *Radiother. Oncol.* **2021**, *155*, 182–187. https://doi.org/10.1016/j.radonc.2020.11.001.

(6) Barth, R. F.; H Vicente, Mg.; Harling, O. K.; Kiger, W.; Riley, K. J.; Binns, P. J.; Wagner, F. M.; Suzuki, M.; Aihara, T.; Kato, I.; Kawabata, S. Current Status of Boron Neutron Capture Therapy of High Grade Gliomas and Recurrent Head and Neck Cancer. *Radiat. Oncol.* **2012**, *7* (1), 146. https://doi.org/10.1186/1748-717X-7-146.

(7) Molander, G. A.; Ellis, N. Organotrifluoroborates: Protected Boronic Acids That Expand the Versatility of the Suzuki Coupling Reaction. *Acc. Chem. Res.* **2007**, *40* (4), 275–286. https://doi.org/10.1021/ar050199q.
(8) Butcher, T. W.; McClain, E. J.; Hamilton, T. G.; Perrone, T. M.; Kroner, K. M.; Donohoe, G. C.; Akhmedov, N. G.; Petersen, J. L.; Popp, B. V. Regioselective Copper-Catalyzed Boracarboxylation of Vinyl Arenes. *Org. Lett.* **2016**, *18* (24), 6428–6431. https://doi.org/10.1021/acs.orglett.6b03326.
(9) Gillis, E. P.; Burke, M. D. Iterative Cross-Couplng with MIDA Boronates: Towards a General Platform for Small Molecule Synthesis. **2012**, 35.
(10) Reilly, M.; Rychnovsky, S. DABO Boronates: Stable Heterocyclic Boronic Acid Complexes for Use in Suzuki-Miyaura Cross-Coupling Reactions. *Synlett* **2011**, *2011* (16), 2392–2396. https://doi.org/10.1055/s-0030-1261218.
(11) Thadani, A. N.; Batey, R. A.; Lough, A. J. 2-(2-Cyclohex-1-Enylvinyl)[1,3,6,2]Dioxazaborocane. *Acta Crystallogr. Sect. E Struct. Rep. Online* **2001**, *57* (11), o1010–o1011. https://doi.org/10.1107/S1600536801015136.
(12) Doidge-Harrison, S. M. S. V.; Musgrave, O. C.; Wardell, J. L. Structure of Tetrahydro-2-Naphthyl-4H-1,3,6,2-Dioxazaboracine. *J. Chem. Crystallogr.* **1998**, *28* (5), 361–366. https://doi.org/10.1023/A:1022460124784.
(13) Schinazi, R. F.; Prusoff, W. H. Synthesis of 5-(Dihydroxyboryl)-2'-Deoxyuridine and Related Boron-Containing Pyrimidines. *J. Org. Chem.* **1985**, *50* (6), 841–847. https://doi.org/10.1021/jo00206a024.
(14) Bonin, H.; Delacroix, T.; Gras, E. Dioxazaborocanes: Old Adducts, New Tricks. *Org. Biomol. Chem.* **2011**, *9* (13), 4714. https://doi.org/10.1039/c1ob05330b.
(15) Sun, J.; Perfetti, M. T.; Santos, W. L. A Method for the Deprotection of Alkylpinacolyl Boronate Esters. *J. Org. Chem.* **2011**, *76* (9), 3571–3575. https://doi.org/10.1021/jo200250y.
(16) Kline, M.; Cheatham, S. A Robust Method for Determining1H-15N Long-Range Correlations:15N Optimized CIGAR-HMBC Experiments. *Magn. Reson. Chem.* **2003**, *41* (5), 307–314. https://doi.org/10.1002/mrc.1180.
(17) Tellinghuisen, J. Van't Hoff Analysis of K°(T): How Good…or Bad? *Biophys. Chem.* **2006**, *120* (2), 114–120. https://doi.org/10.1016/j.bpc.2005.10.012.
(18) Sharma, G.; First, E. A. Thermodynamic Analysis Reveals a Temperature-Dependent Change in the Catalytic Mechanism of Bacillus Stearothermophilus Tyrosyl-TRNA Synthetase. *J. Biol. Chem.* **2009**, *284* (7), 4179–4190. https://doi.org/10.1074/jbc.M808500200.
(19) Yang, Z.; Houk, K. N. The Dynamics of Chemical Reactions: Atomistic Visualizations of Organic Reactions, and Homage to van 't Hoff. *Chem. - Eur. J.* **2018**, *24* (16), 3916–3924. https://doi.org/10.1002/chem.201706032.
(20) Asnin, L. D.; Stepanova, M. V. Van't Hoff Analysis in Chiral Chromatography. *J. Sep. Sci.* **2018**, *41* (6), 1319–1337. https://doi.org/10.1002/jssc.201701264.

Chapter VI

Future Directions

In chapter 2, the synthesis of new boron-functionalized ibuprofen derivatives were reported. Inhibitory activity of these substrates should be evaluated using a cyclooxygenase inhibitory screening assay. Similarly, pharmacological properties such as solubility, permeability, cell toxicity and metabolic stability of these substrates should be evaluated. Also, p*K*a and oxidative stability of these compound should be evaluated. During this work, synthesis of novel lactone boronic acid was reported. Boronic acids were used as a catalyst in regioselective glycosylation reactions.[1–3] Due to its unique structure, ibuprofen lactone boronic acid could be explored as a catalyst in regioselective glycosylation.

The benchtop boracarboxylation catalytic system could be further optimized to reduce catalyst loading and different styrene substrates would need to be screened. In this study, we established the reactivity of borafluorolactonate under reducing conditions and Suzuki cross coupling conditions. Further reaction optimizations are required to establish a reactivity profile for borafluorolactonate under nucleophilic, electrophilic, and oxidizing reaction conditions.

6.2 References

(1) Lee, D.; Taylor, M. S. Regioselective Silylation of Pyranosides Using a Boronic Acid/Lewis Base Co-Catalyst System. *Org. Biomol. Chem.* **2013**, *11* (33), 5409. https://doi.org/10.1039/c3ob40981c.

(2) D'Angelo, K. A.; Taylor, M. S. Borinic Acid Catalyzed Stereo- and Regioselective Couplings of Glycosyl Methanesulfonates. *J. Am. Chem. Soc.* **2016**, *138* (34), 11058–11066. https://doi.org/10.1021/jacs.6b06943.

(3) Dimakos, V.; Gorelik, D.; Su, H. Y.; Garrett, G. E.; Hughes, G.; Shibayama, H.; Taylor, M. S. Site-Selective Redox Isomerizations of Furanosides Using a Combined Arylboronic Acid/Photoredox Catalyst System. *Chem. Sci.* **2020**, *11* (6), 1531–1537. https://doi.org/10.1039/C9SC05173B.

Appendix I NMR Characterization Data and Equilibrium Calculation Data

^{1}H, ^{13}C and ^{11}B NMR Spectra-Compounds in Chapter II

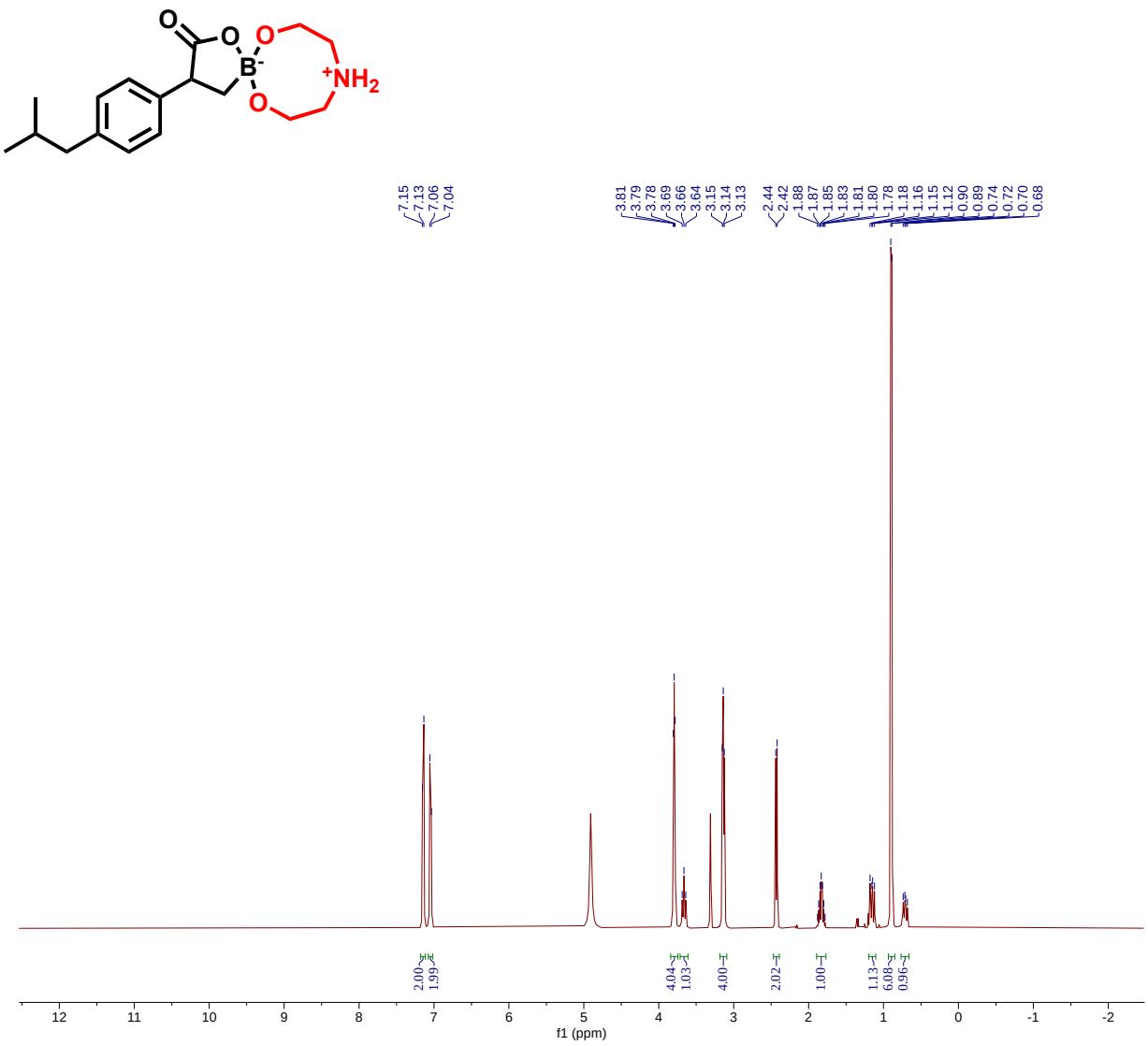

Figure A-1. ^{1}H NMR Spectrum of 2 in CD_3OD-d_3.

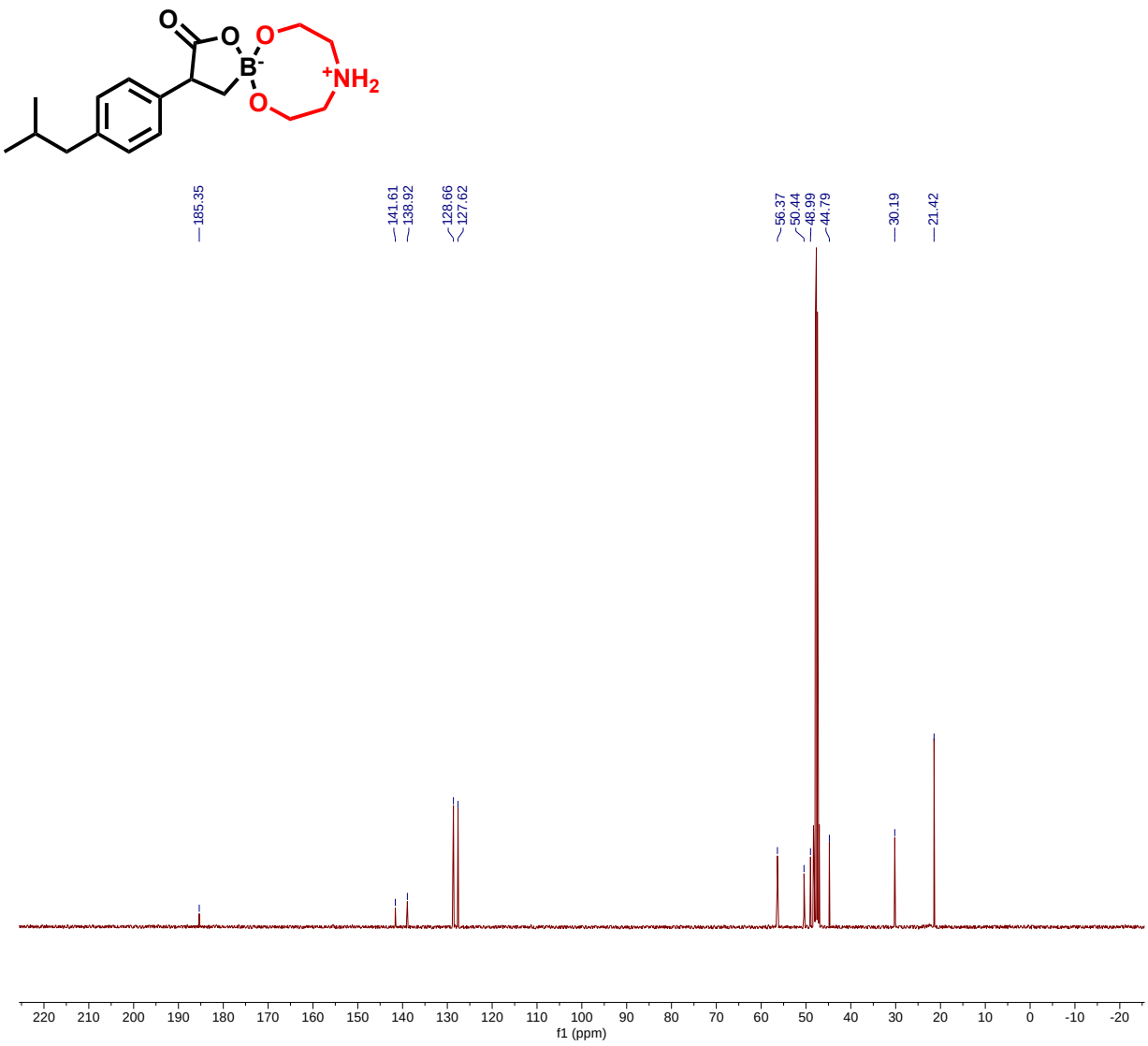

Figure A-2. ^{13}C NMR Spectrum of 2 in CD_3OD-d_3.

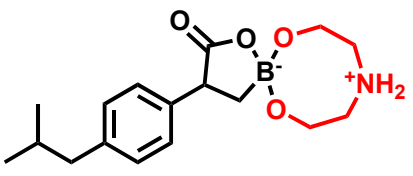

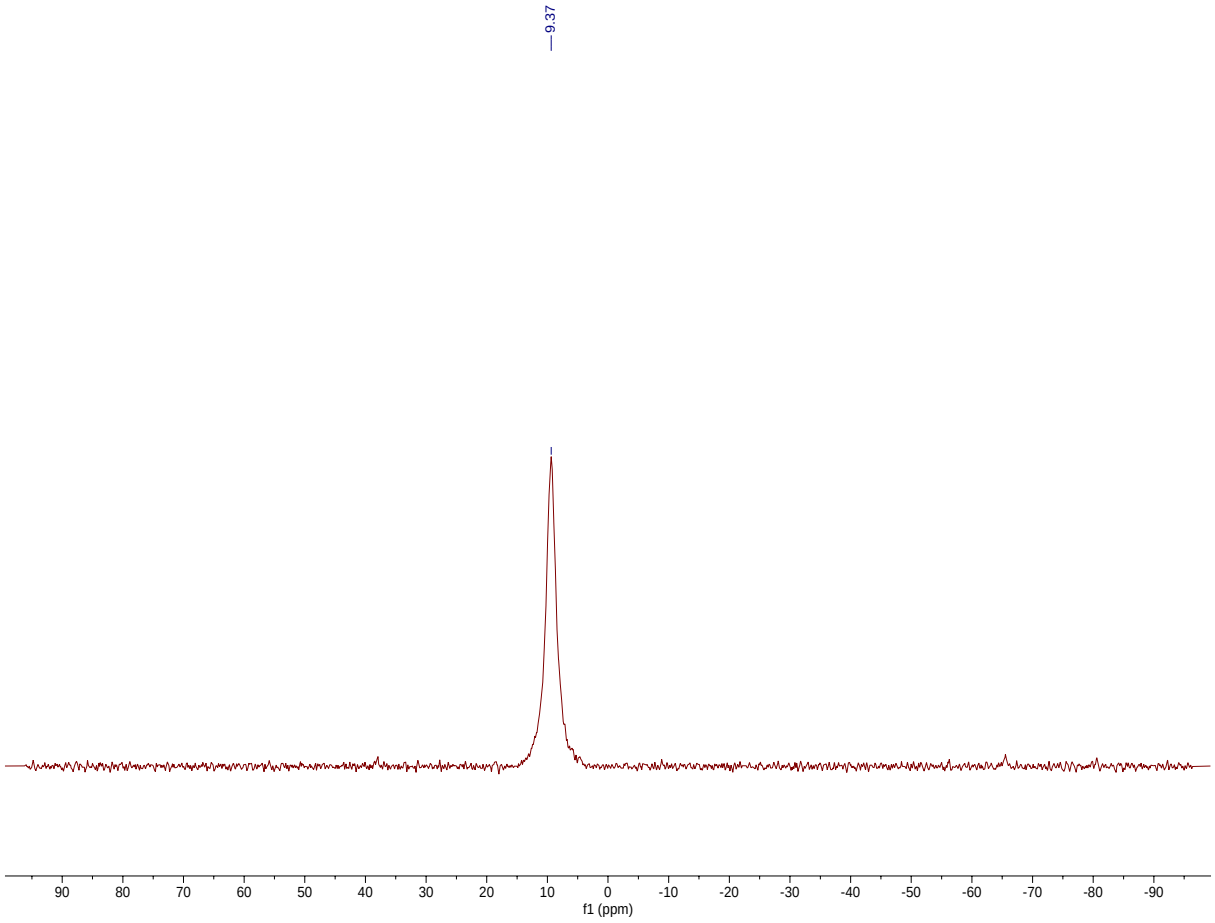

Figure A-3. ^{11}B NMR Spectrum of 2 in CD_3OD-d_3.

Constant time inverse-detection gradient accordion rescaled heteronuclear multiple bond correlation spectroscopy: ^{1}H - ^{15}N CIGARAD spectrum

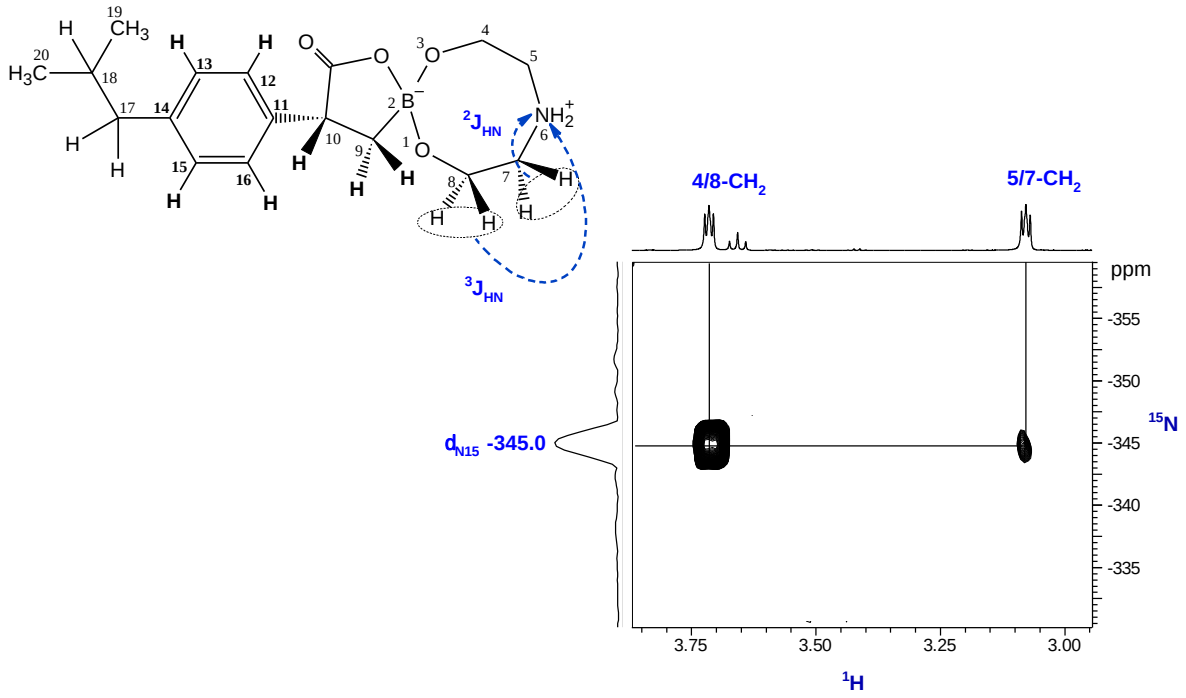

ABX spin system

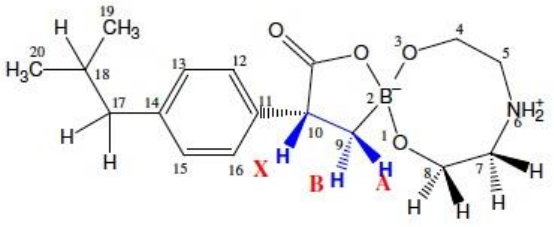

Coupling constants

J_{AB} = 13.7 Hz

J_{AX} = 9.6 Hz

J_{BX} = 10.0 Hz

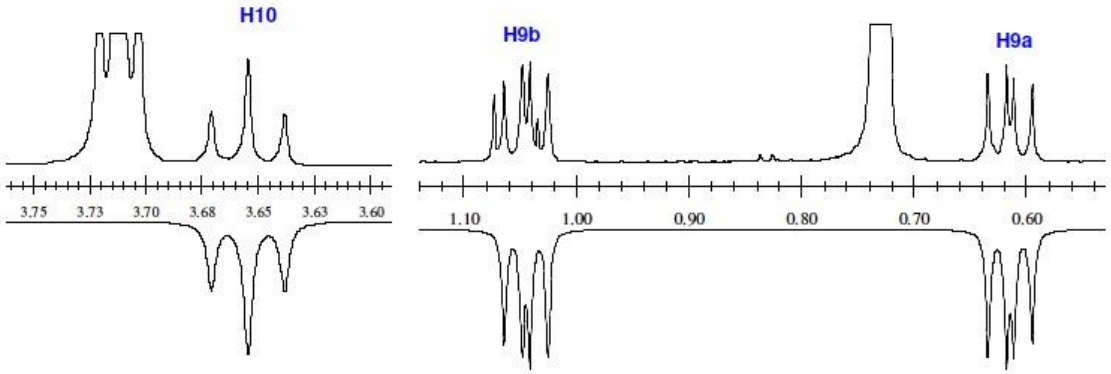

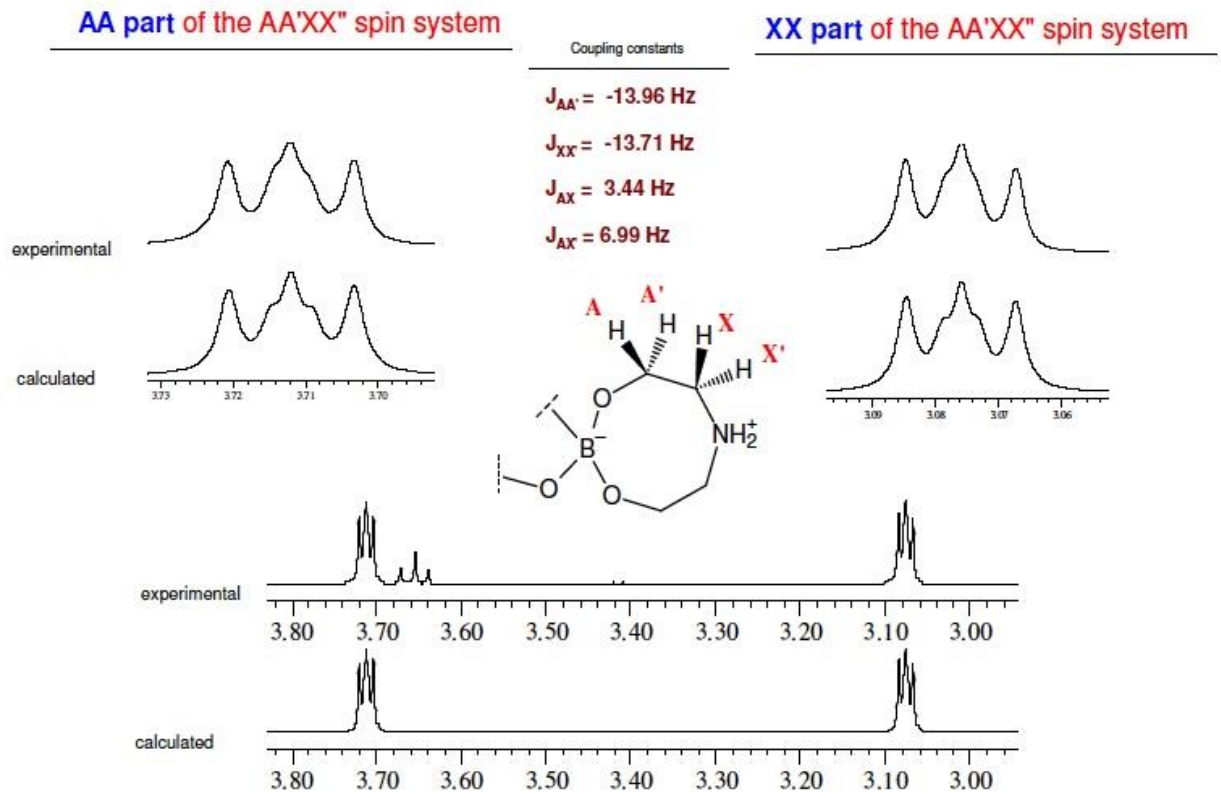
AA part of the AA'XX" spin system
XX part of the AA'XX" spin system
Coupling constants
$J_{AA'}$ = -13.96 Hz
$J_{XX'}$ = -13.71 Hz
J_{AX} = 3.44 Hz
$J_{AX'}$ = 6.99 Hz
experimental
calculated
A
A'
X
X'
H
O
B⁻
NH₂⁺
3.80 3.70 3.60 3.50 3.40 3.30 3.20 3.10 3.00

A6BX2 spin system

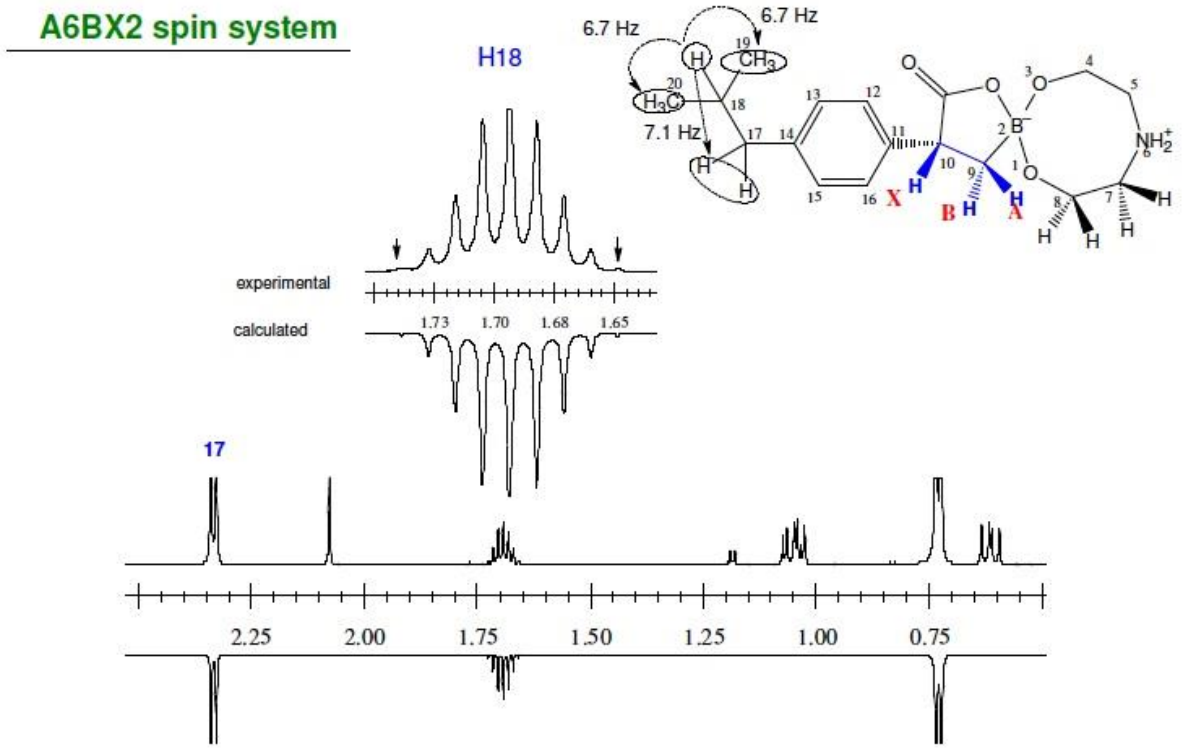

AA'BB' spin system

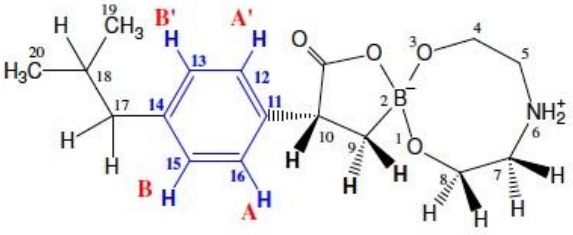

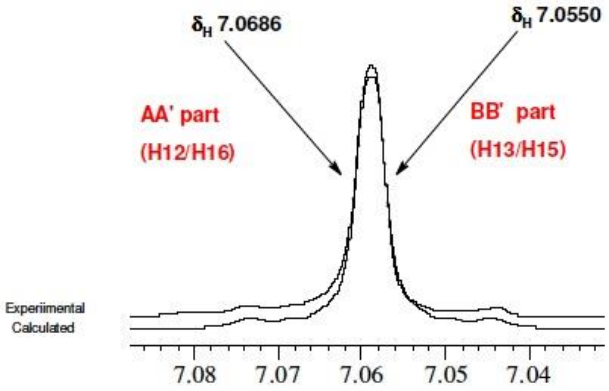

Coupling constants (Hz)

$J_{AA'}$ = 2.0 Hz

$J_{BB'}$ = 2.2 Hz

J_{AB} = 7.7 Hz

$J_{AB'}$ = 0.4 Hz

^{1}H NMR spectrum in D_2O

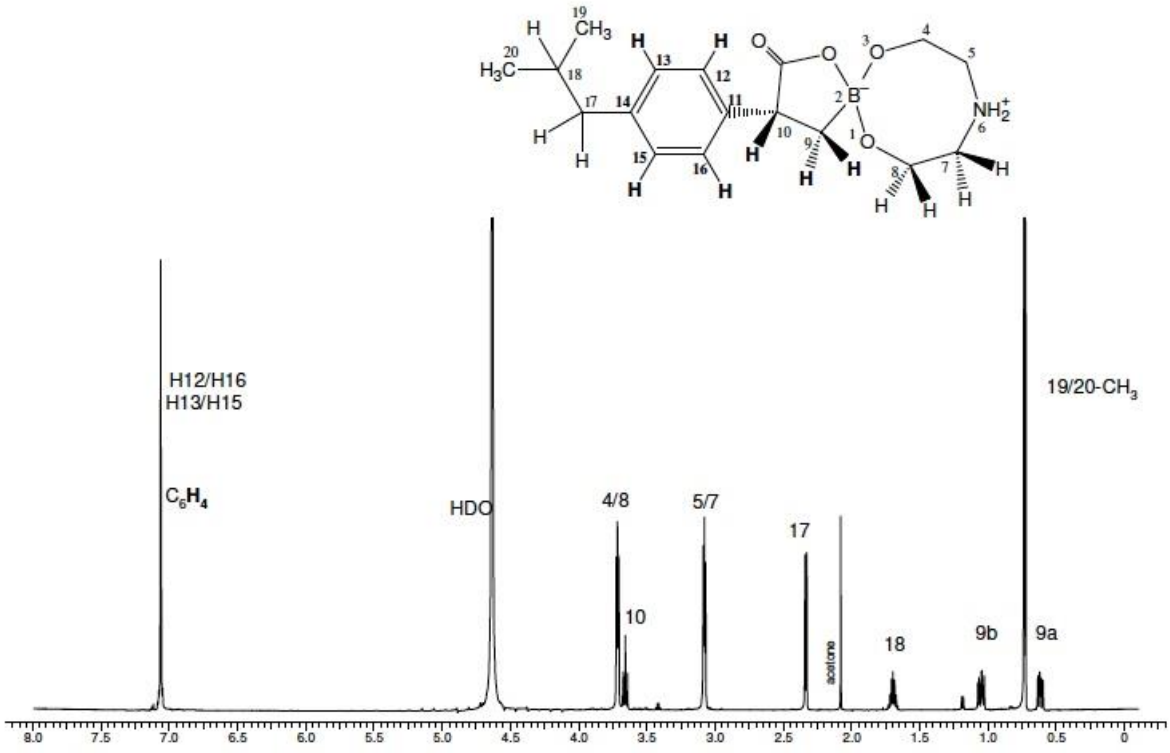

Multiplicity edited gHSQCAD spectrum

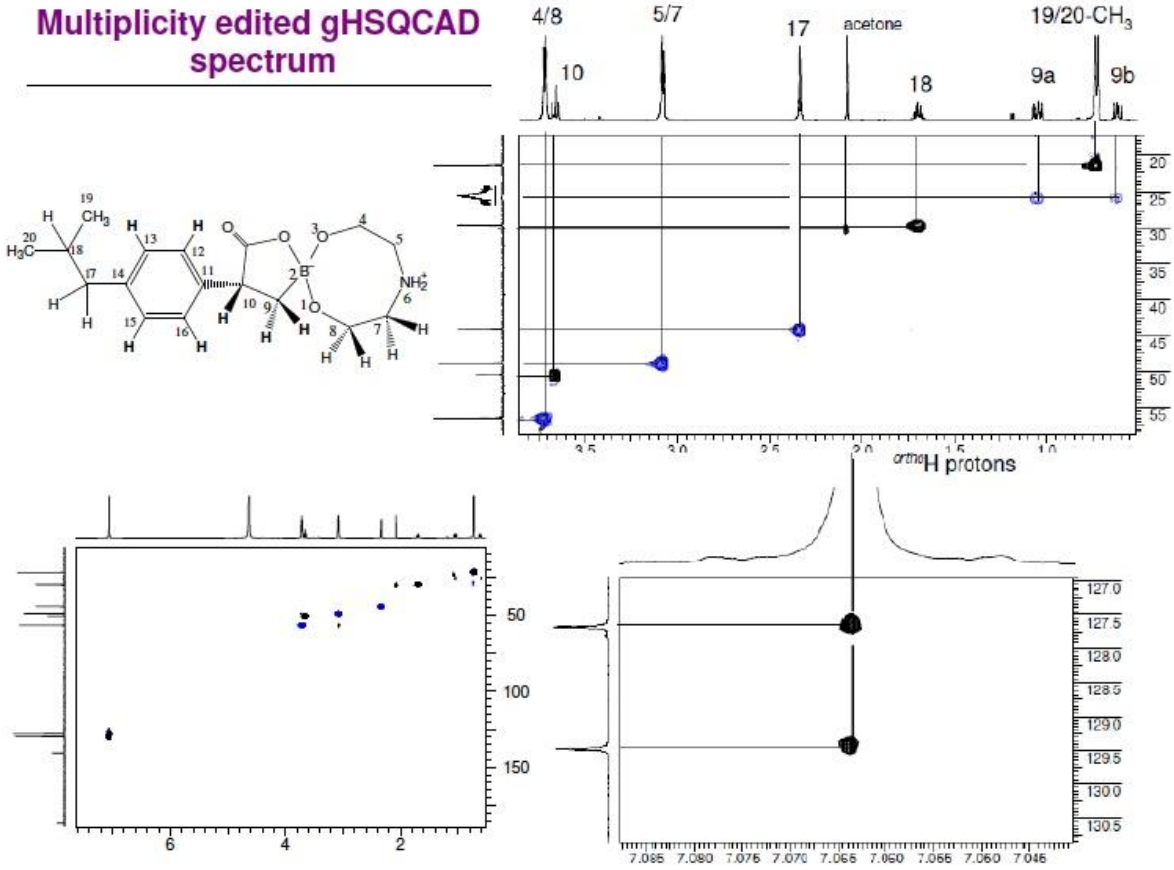

Long-range HMBC correlations

(expanded regions)

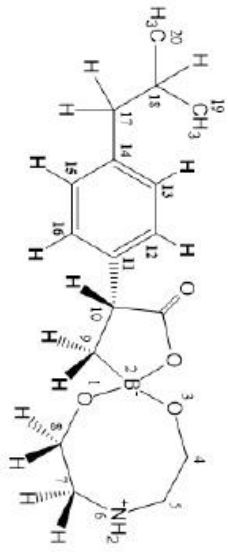

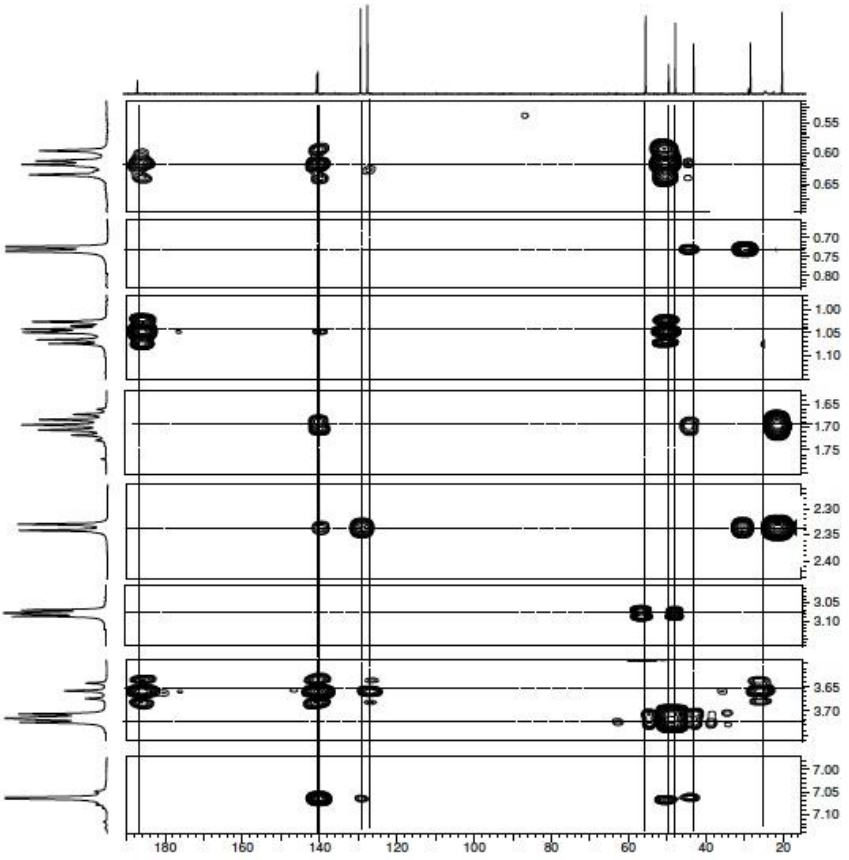

Relative stereochemistry

H10 and H9a shares a syn relationship

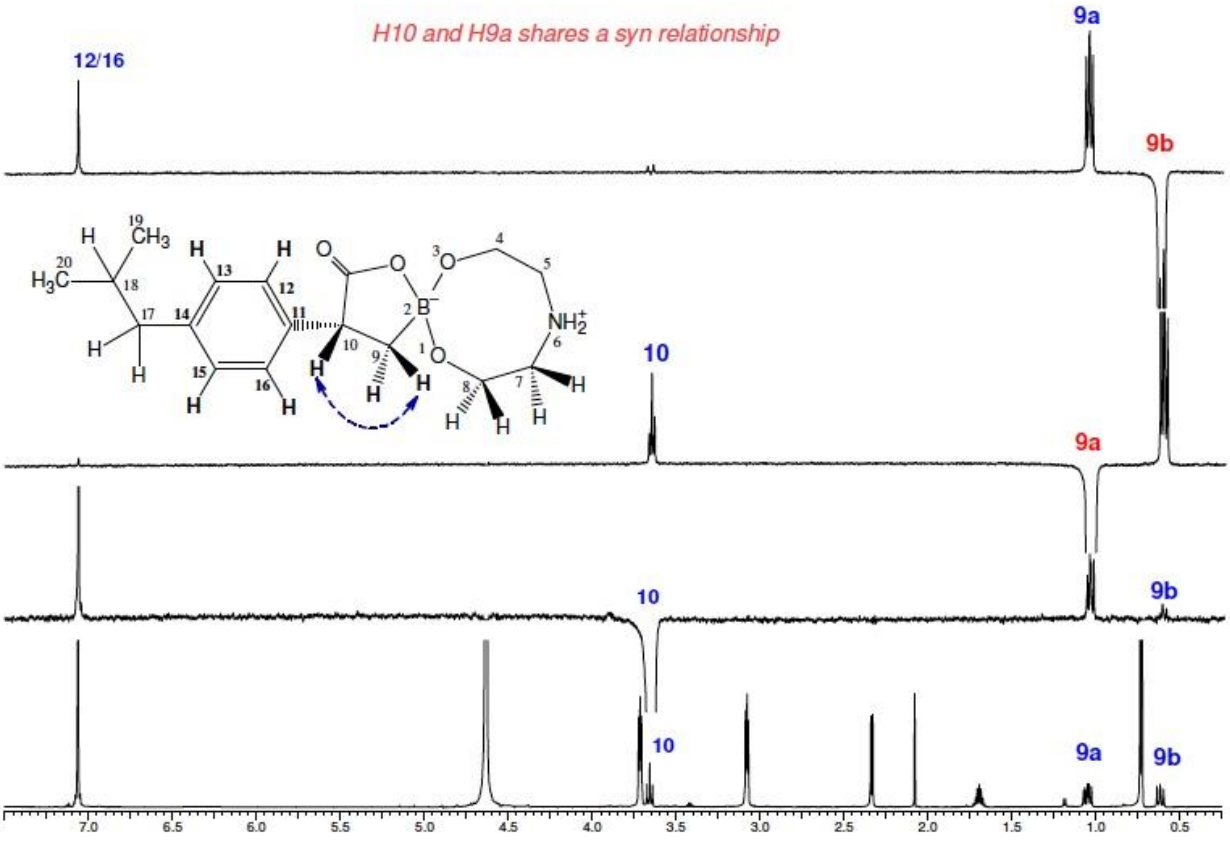

DPFGSENOE

subspectrum

H9b in space is close to the ortho protons of the Phenyl group

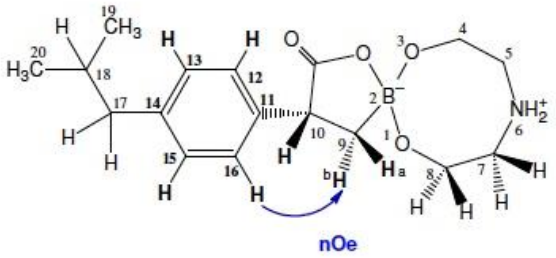

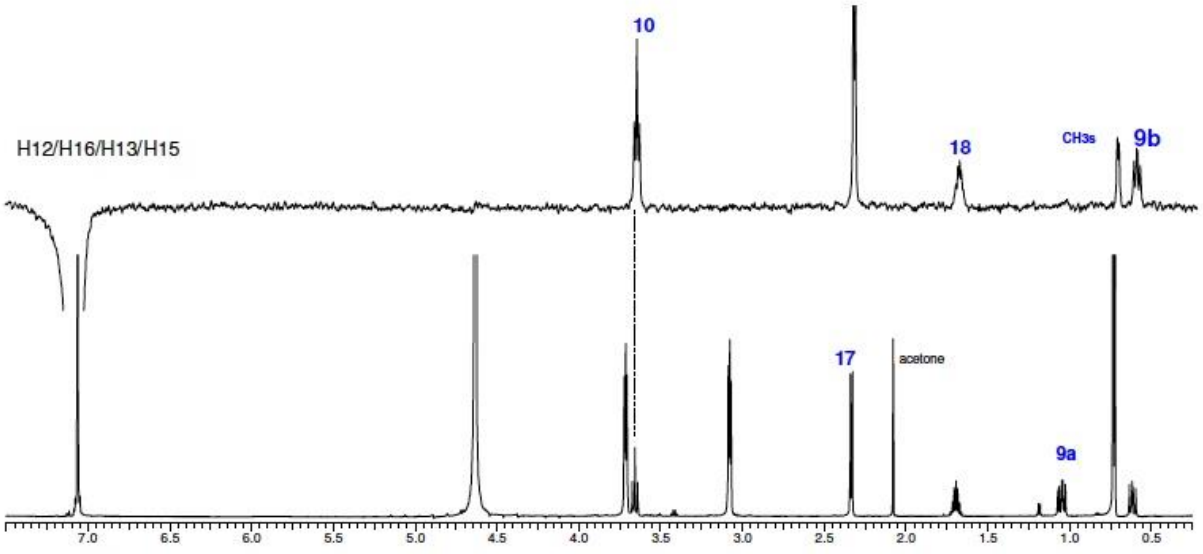

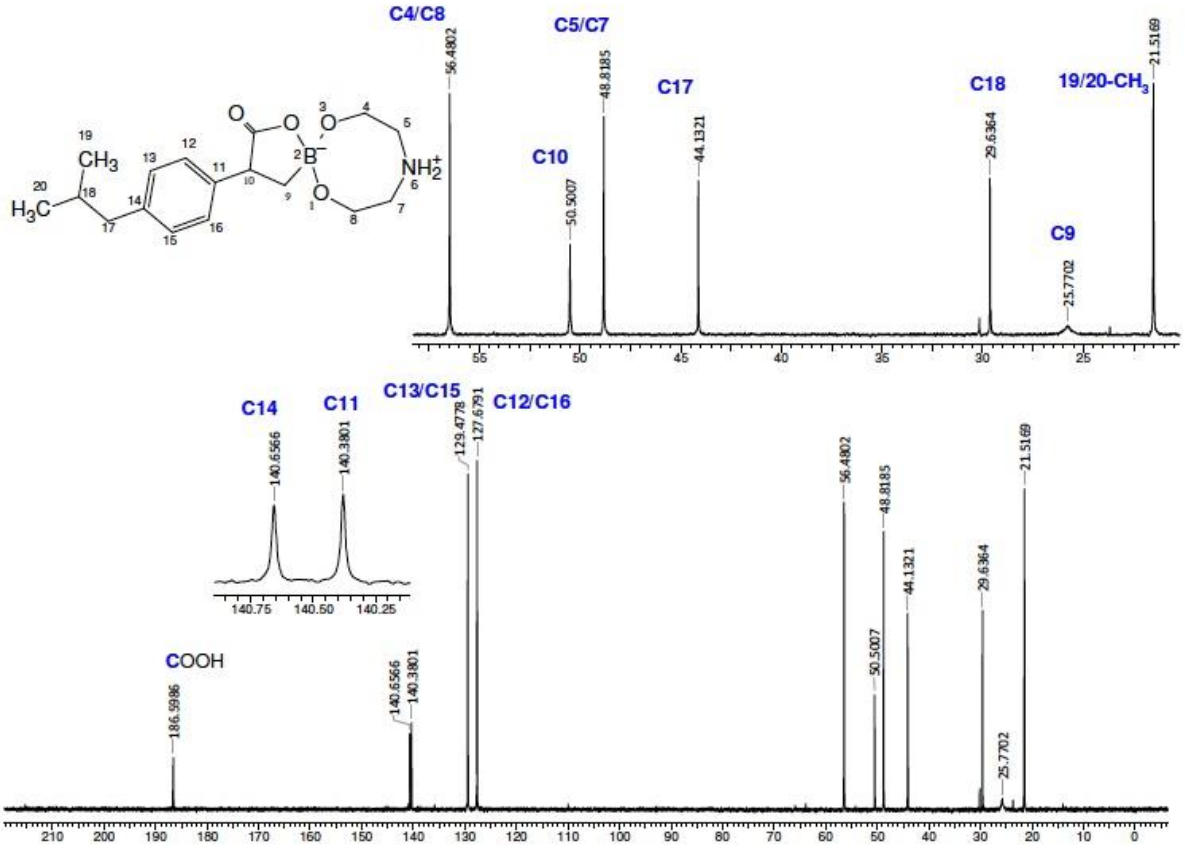
C4/C8
C5/C7
C17
C18
19/20-CH3
C10
C9
C14
C11
C13/C15
C12/C16
COOH
56.4802
48.8185
44.1321
29.6364
21.5169
50.5007
25.7702
140.6566
140.3801
129.4778
127.6791
186.5986

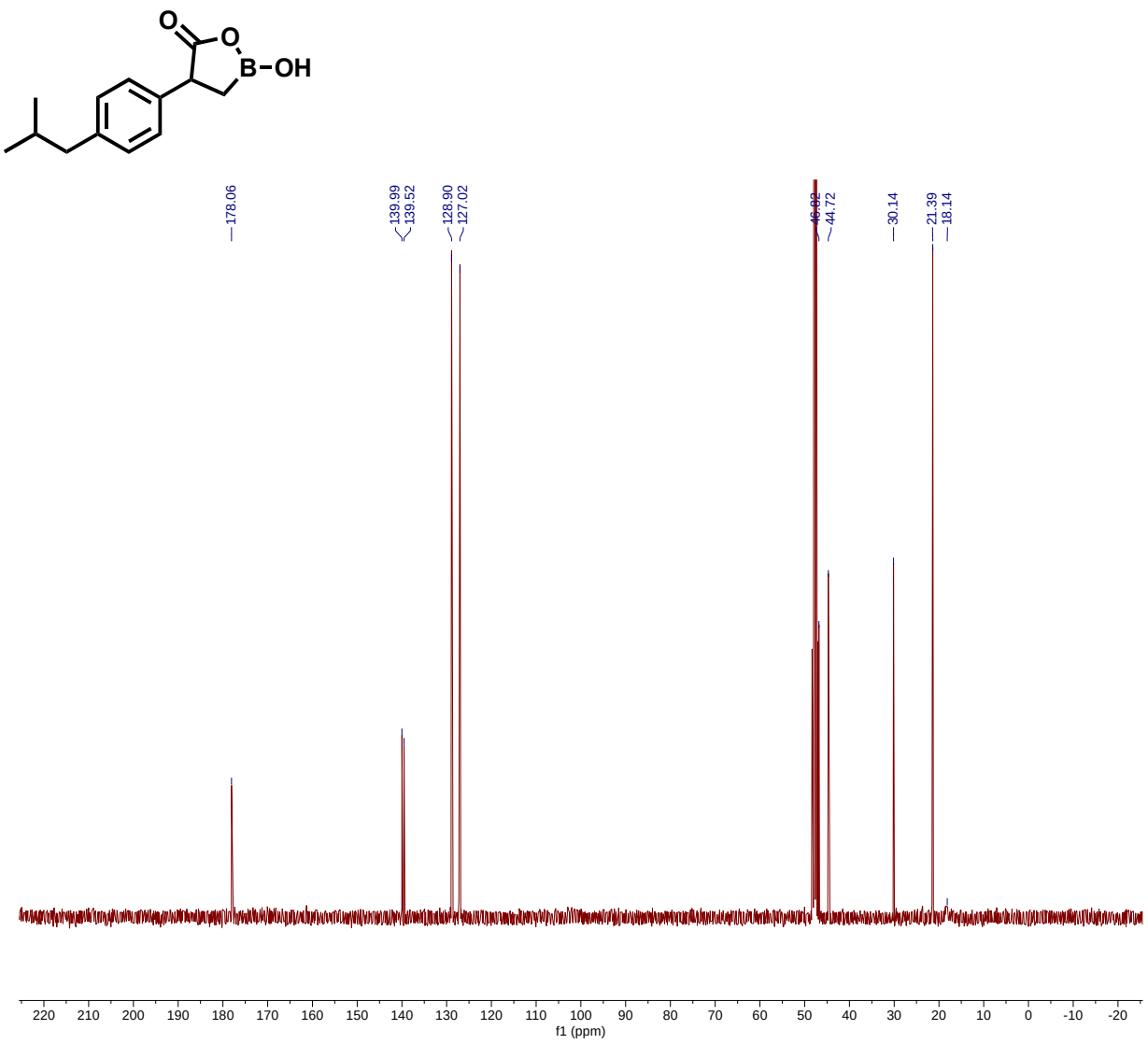

Figure A-4. ^{13}C NMR Spectrum of 3 in CD_3OD-d_3.

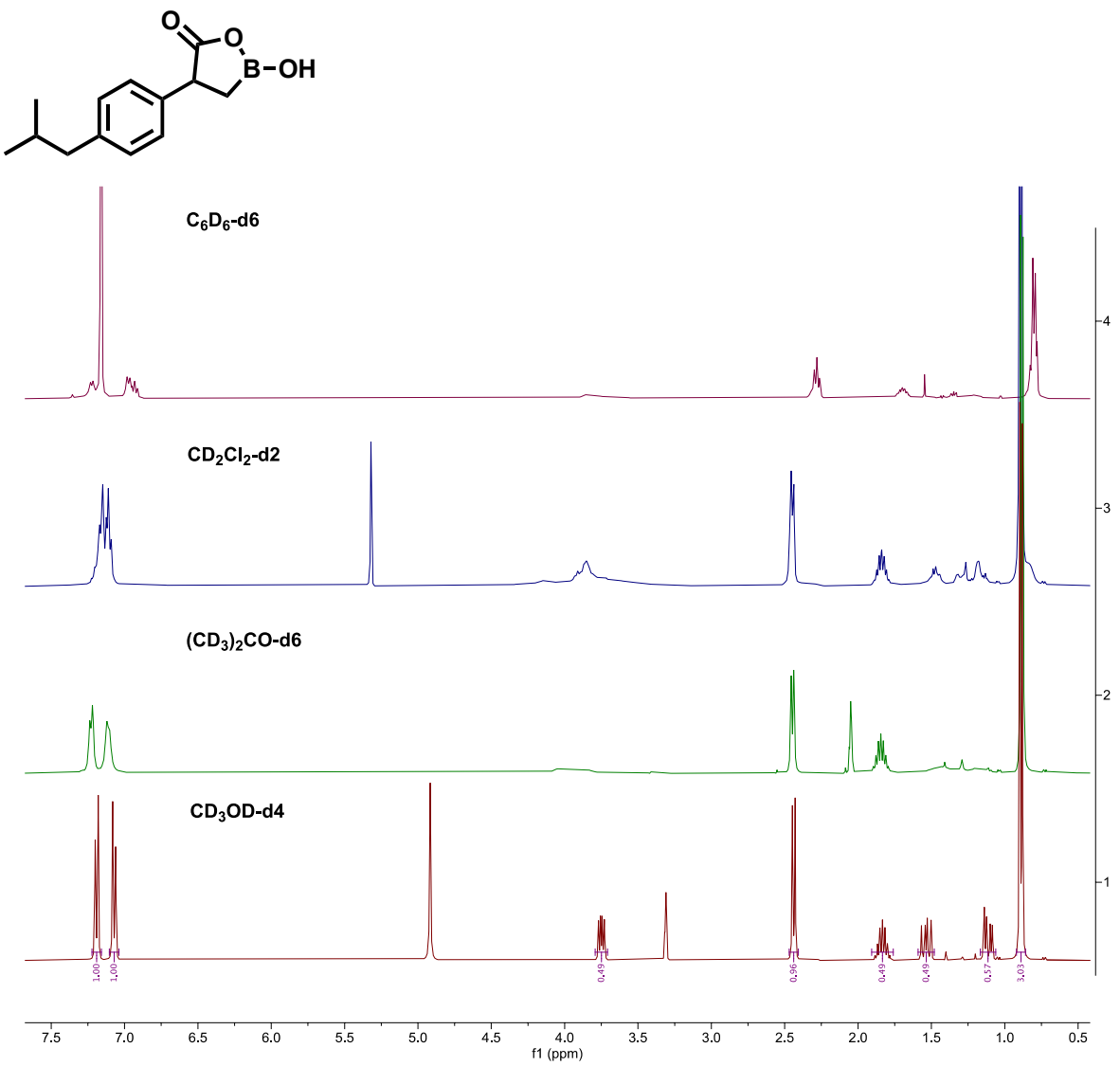

Figure A-5. ^{1}H NMR Spectrum of 3 in different deuterated solvents.

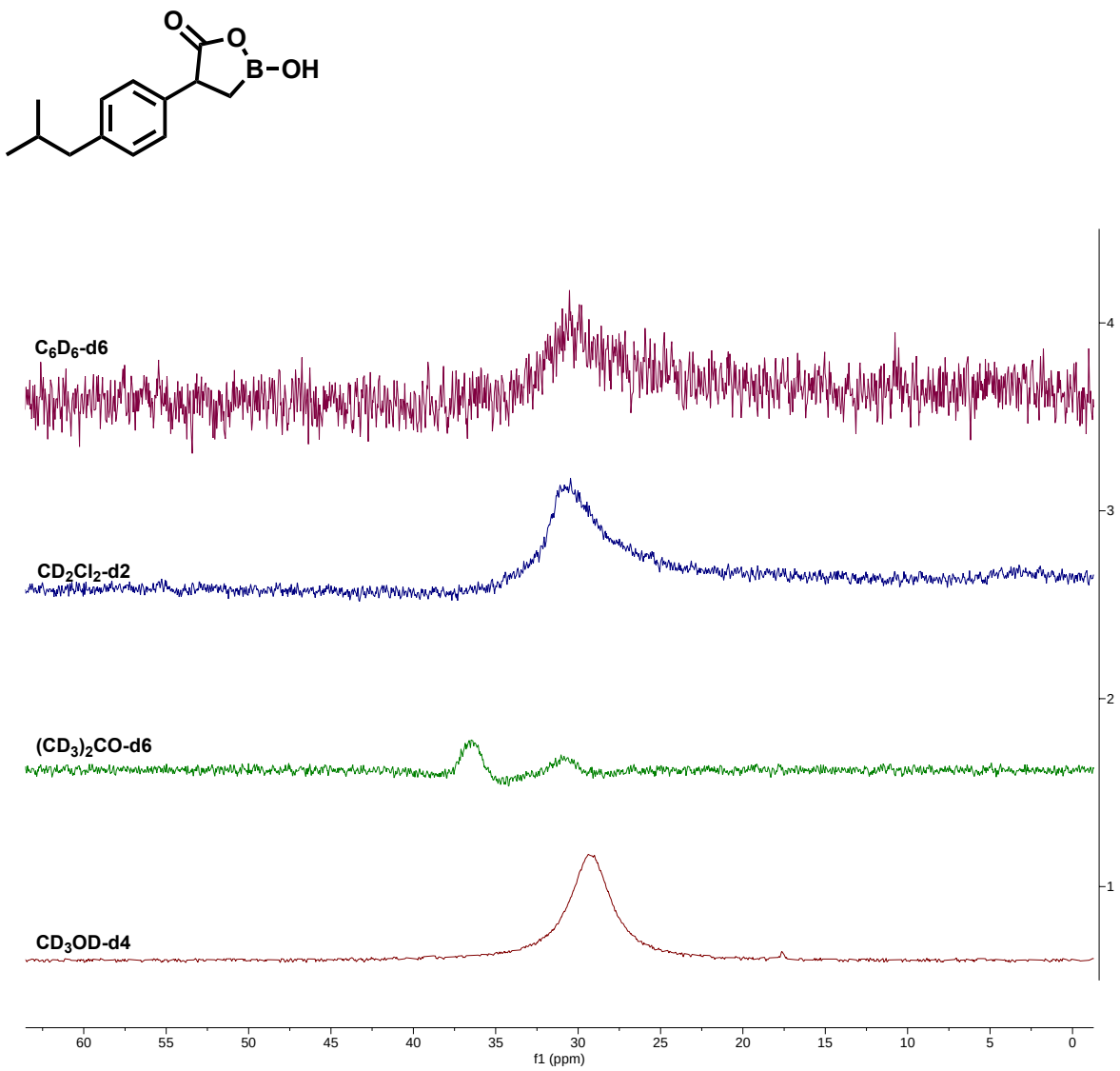

Figure A-6. ^{11}B NMR Spectrum of 3 in different deuterated solvents.

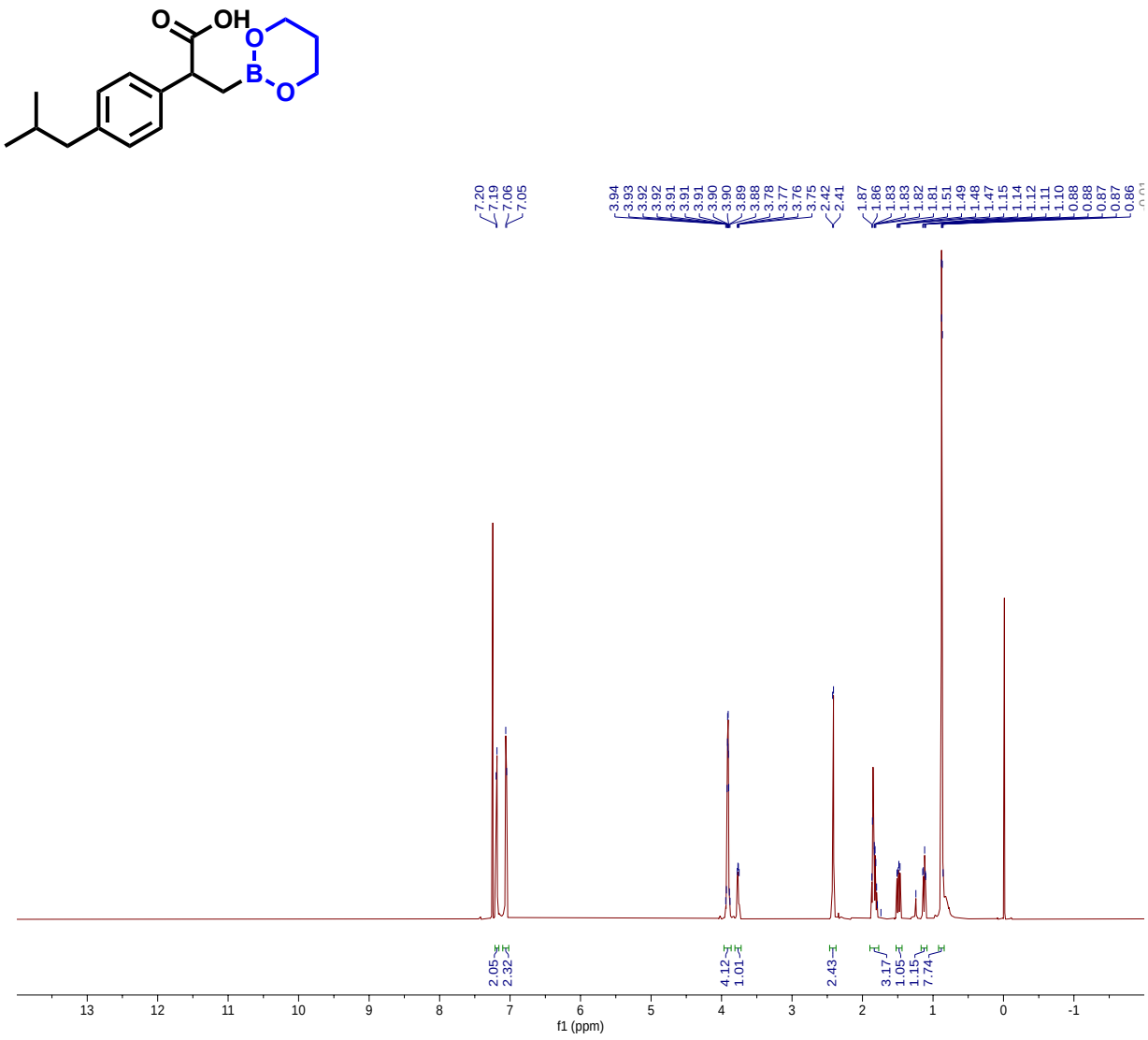

Figure A-7. ^{1}H NMR Spectrum of 4a in $CDCl_3$.

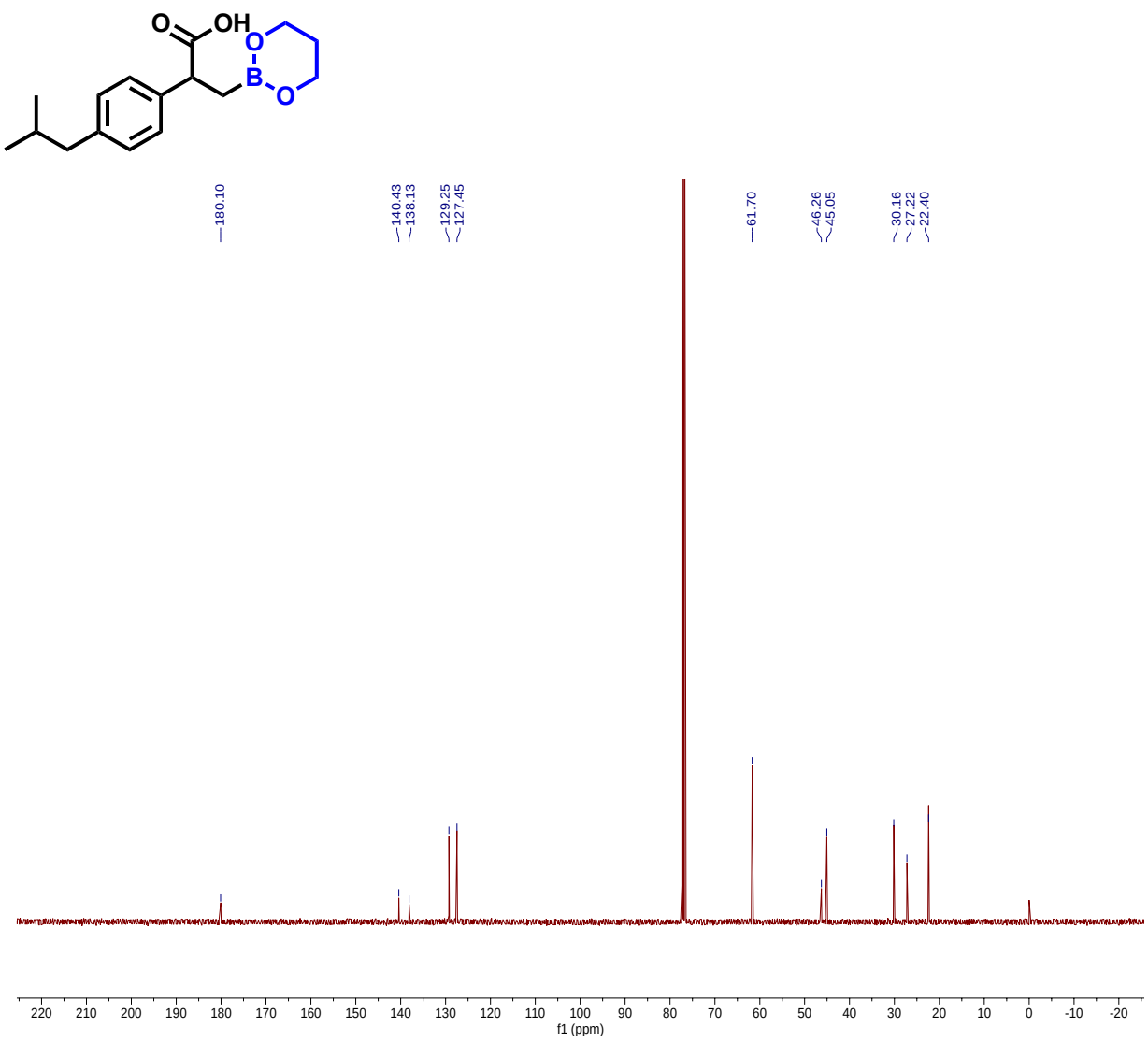

Figure A-8. ^{13}C NMR Spectrum of 4a in $CDCl_3$.

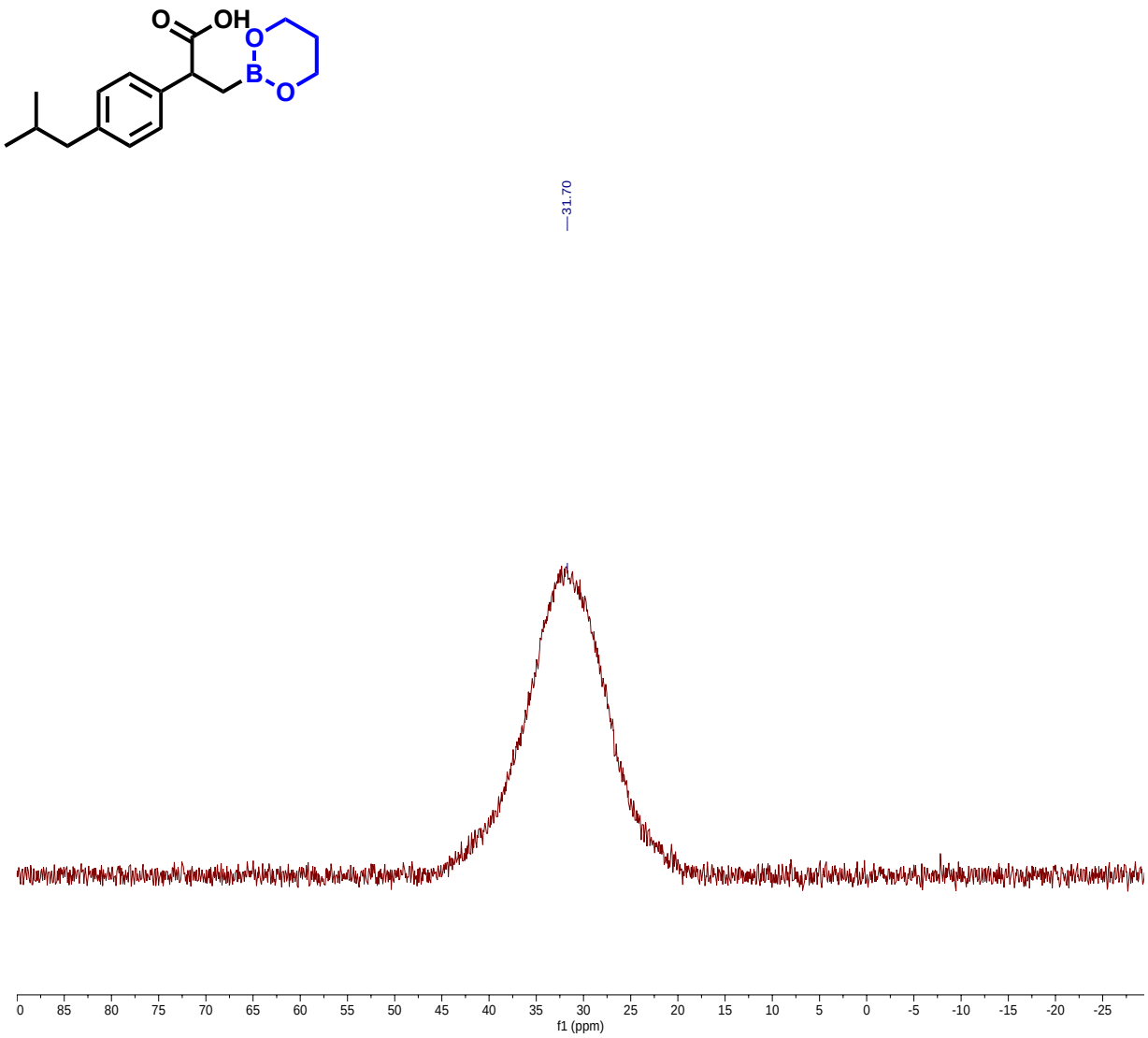

Figure A-9. ^{11}B NMR Spectrum of 4a in $CDCl_3$.

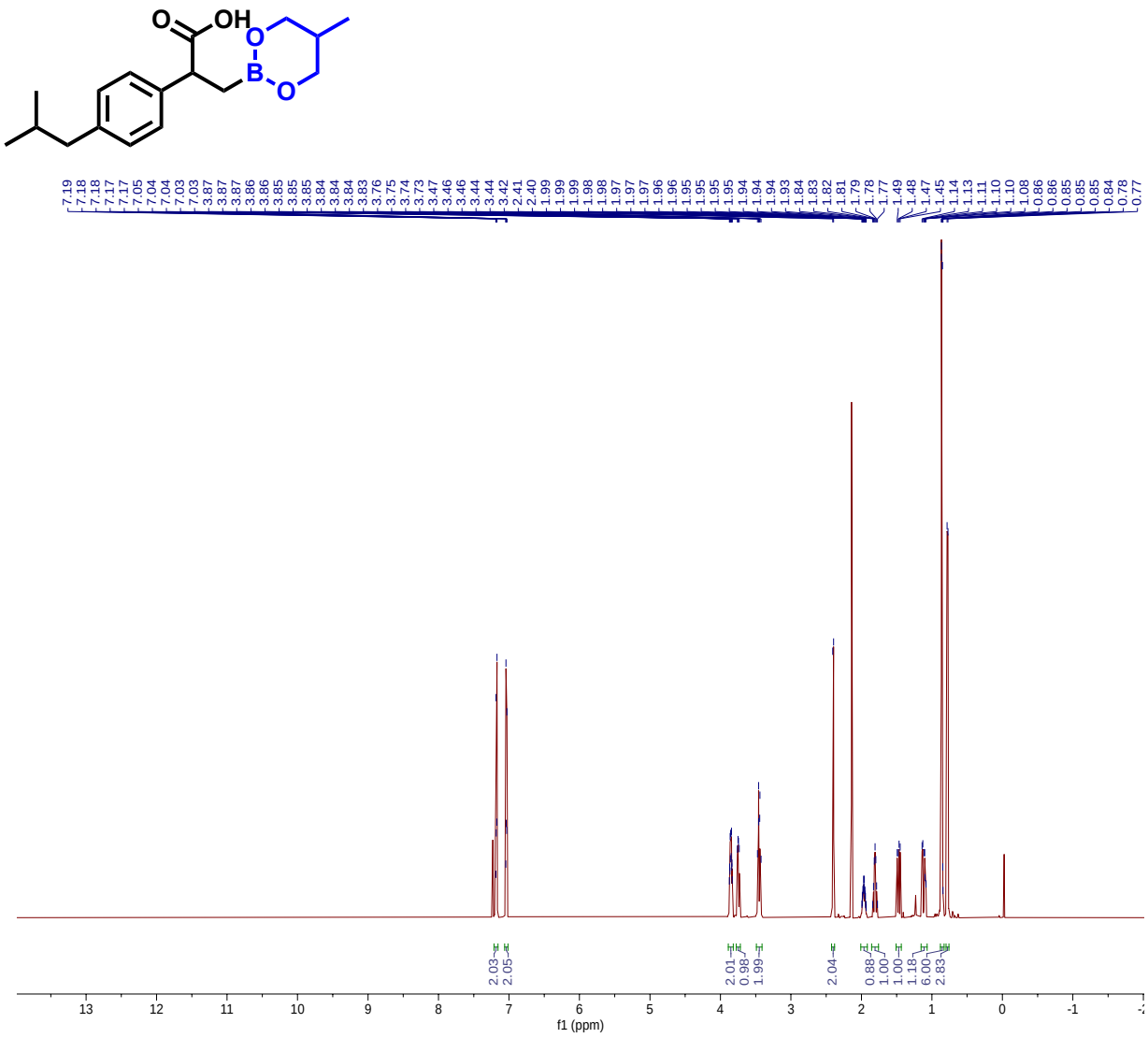

Figure A-10. ^{1}H NMR Spectrum of 4b in $CDCl_3$.

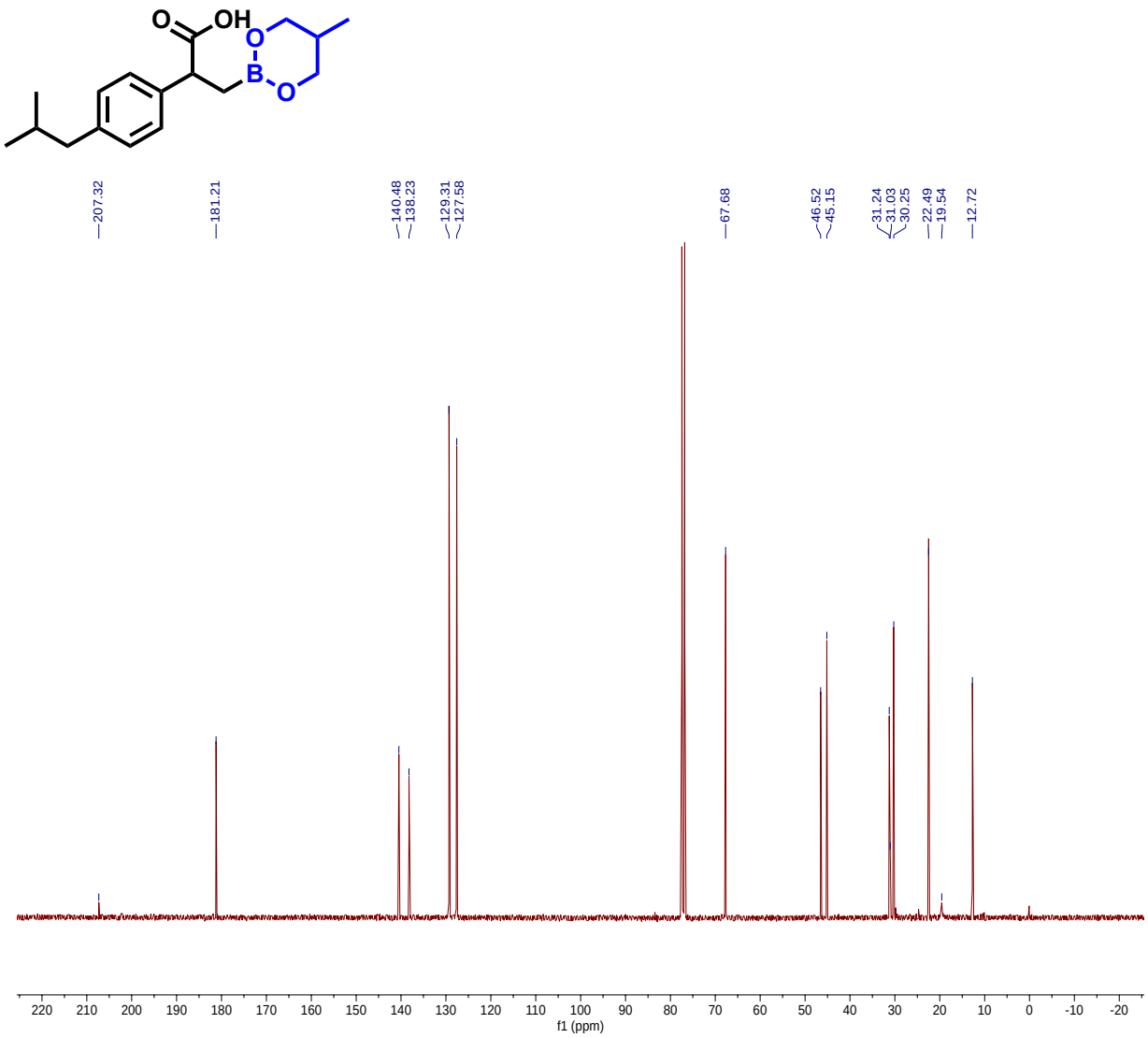

Figure A-11. ^{13}C NMR Spectrum of 4b in $CDCl_3$.

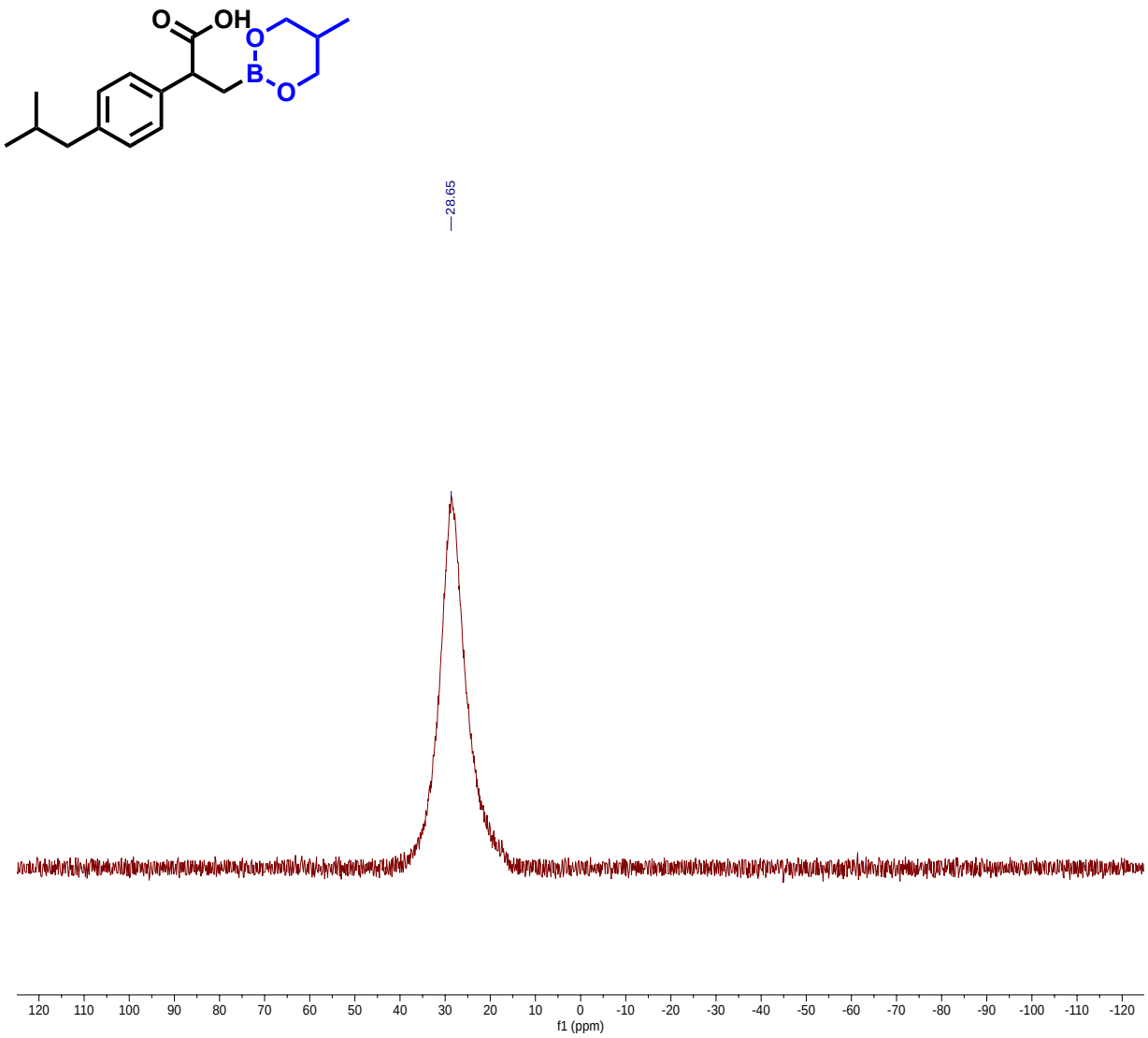

Figure A-12. ^{11}B NMR Spectrum of 4b in $CDCl_3$.

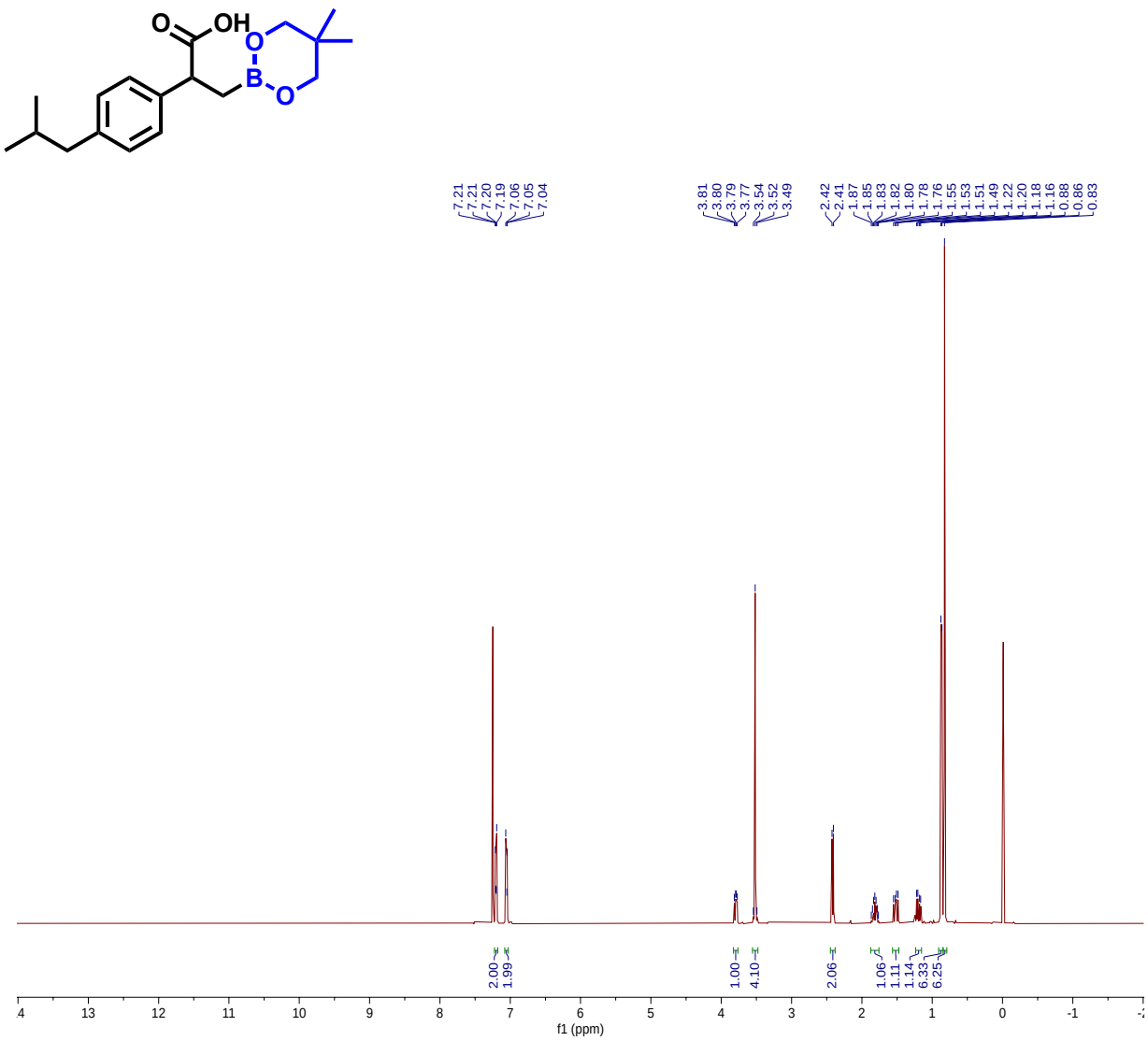

Figure A-13. ^{1}H NMR Spectrum of 4c in $CDCl_3$.

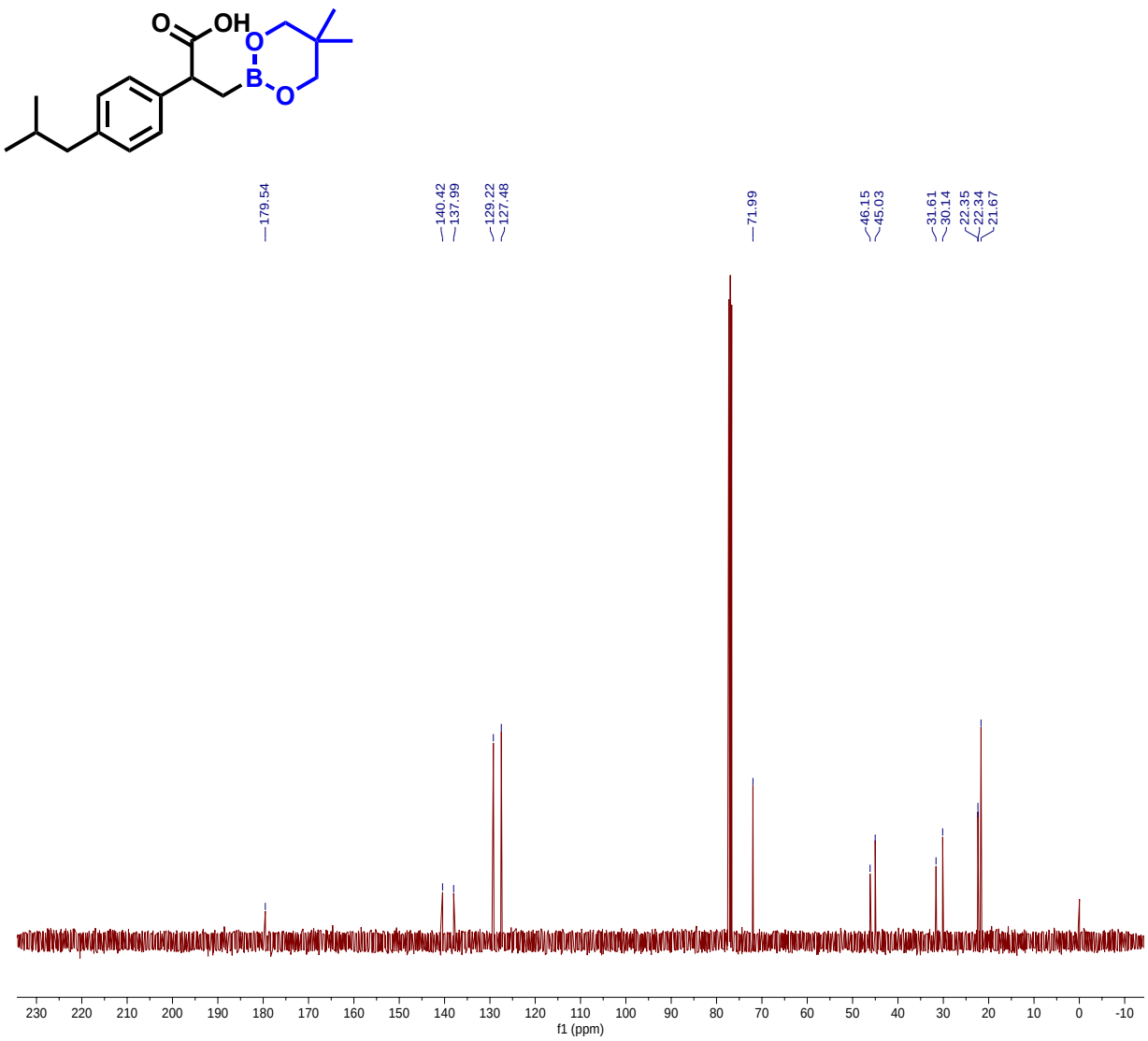

Figure A-14. ^{13}C NMR Spectrum of 4c in $CDCl_3$.

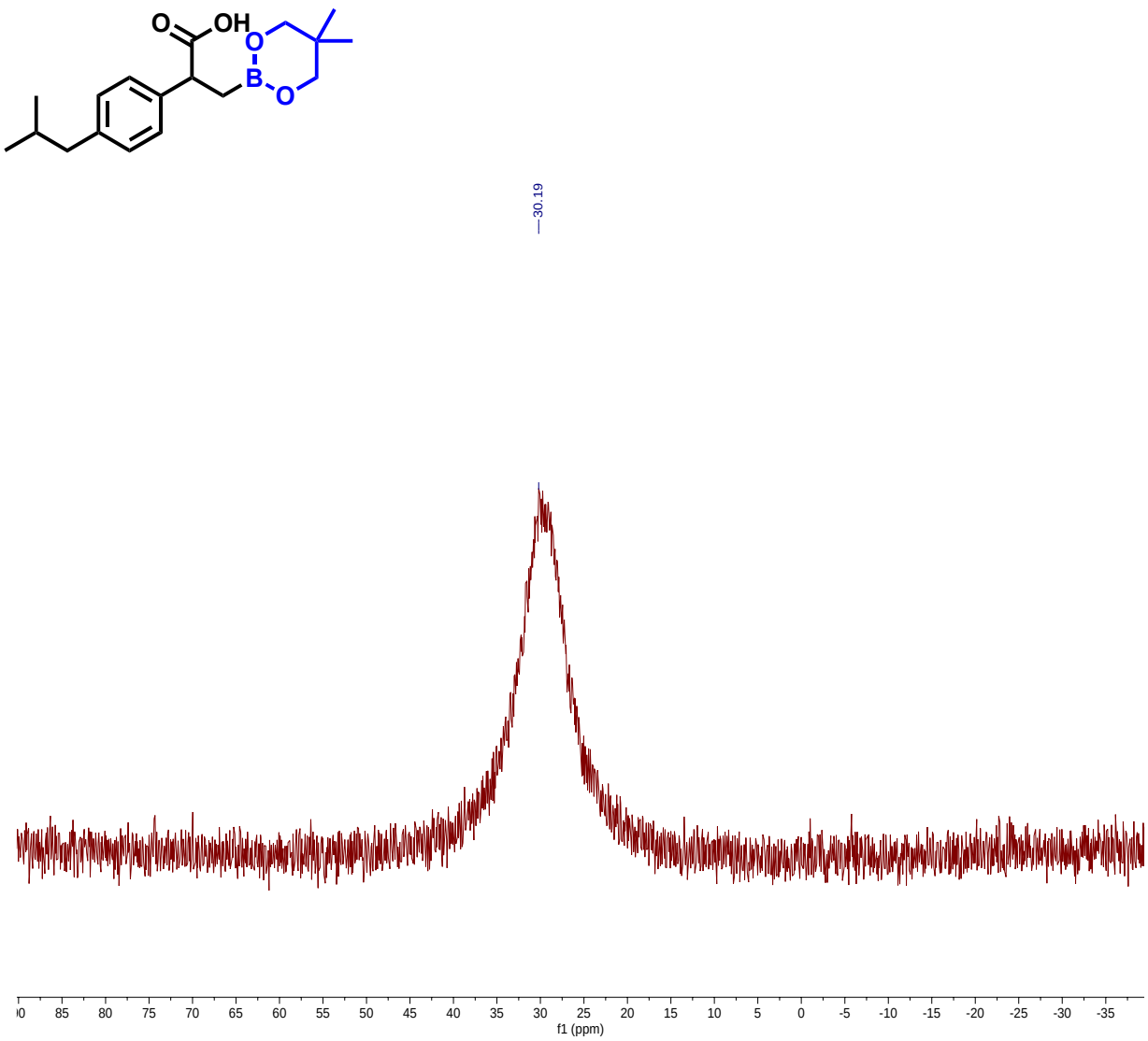

Figure A-15. ^{11}B NMR Spectrum of 4c in $CDCl_3$.

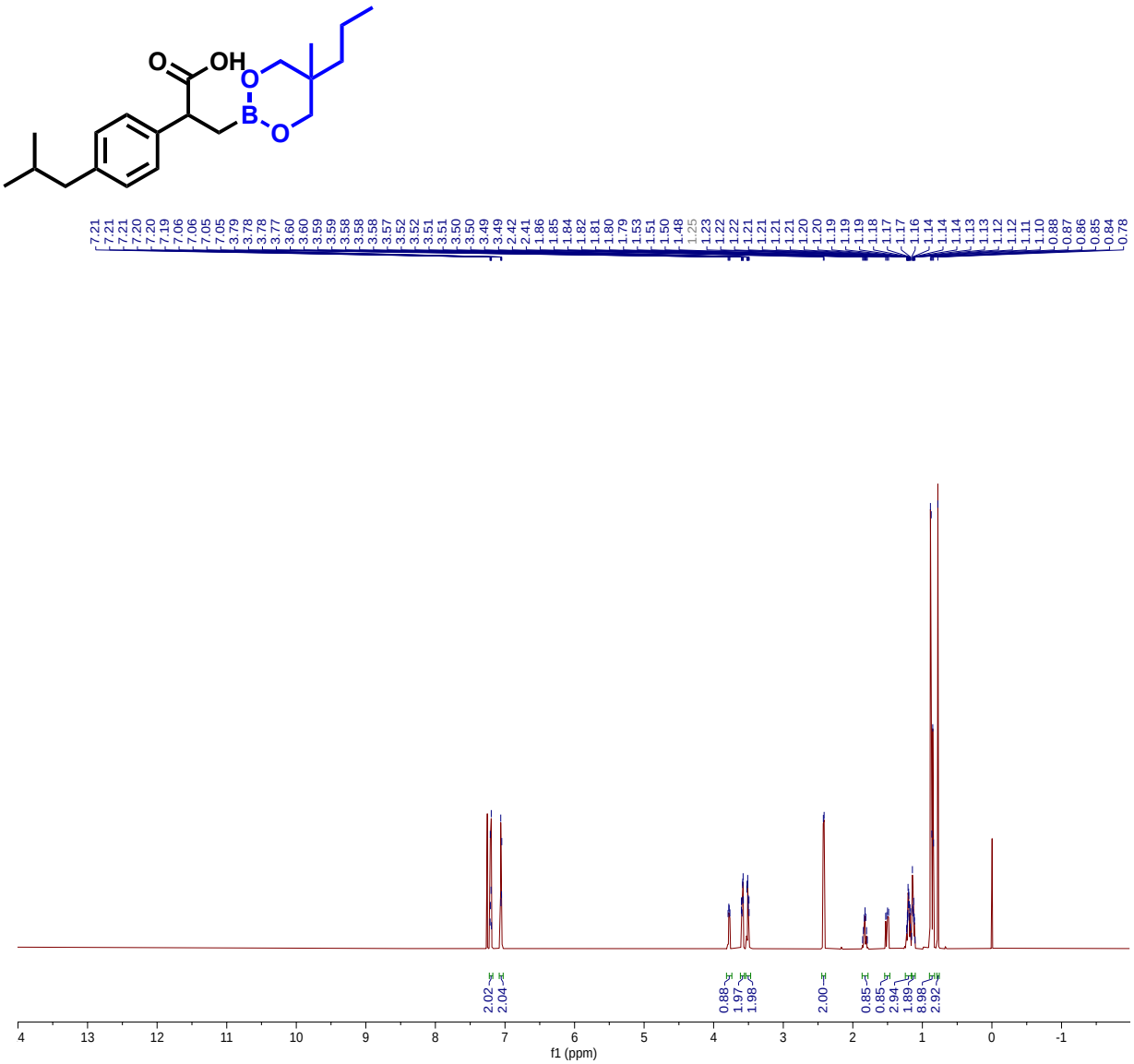

Figure A-16. ^{1}H NMR Spectrum of 4d in $CDCl_3$.

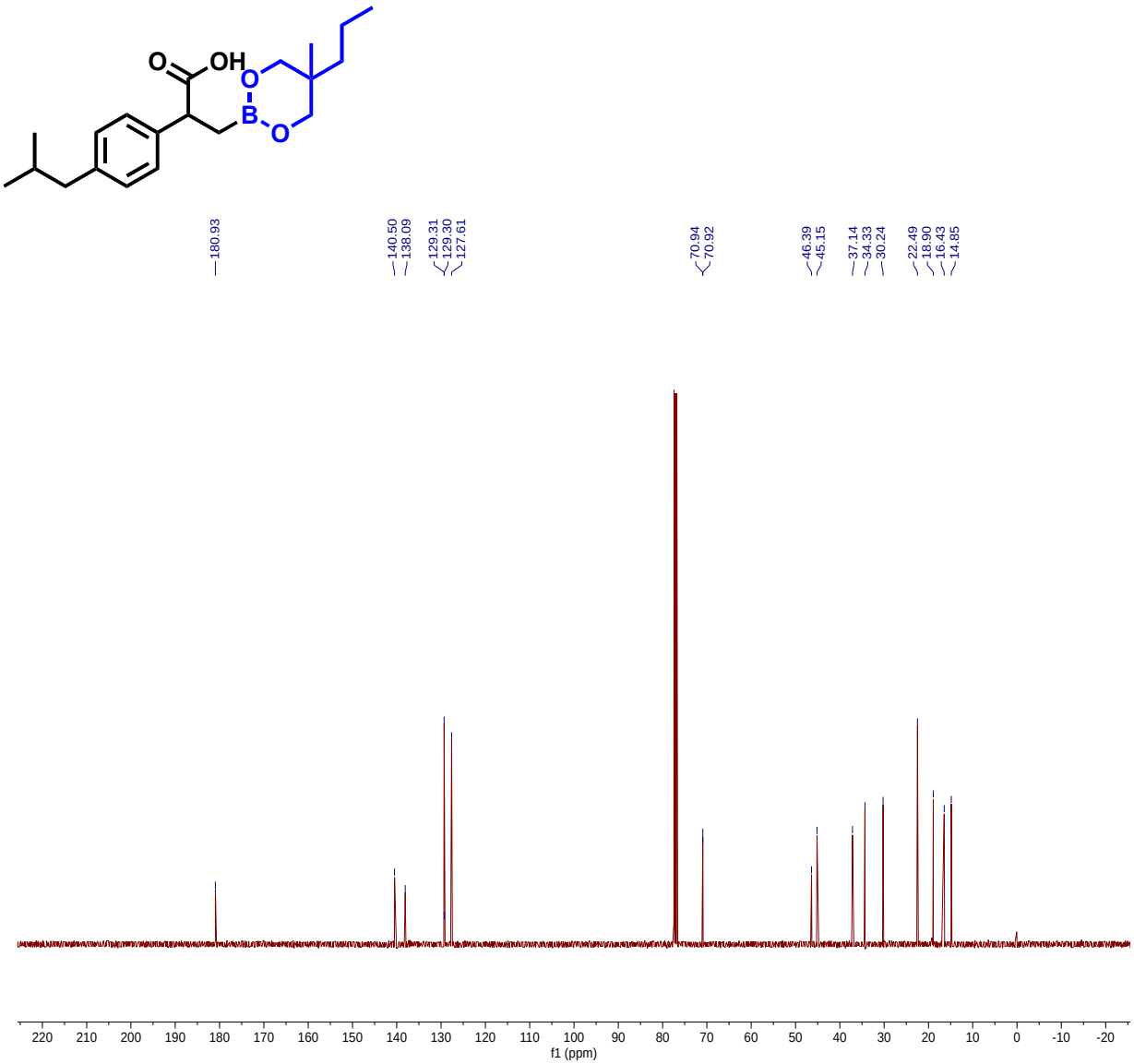

Figure A-17. ^{13}C NMR Spectrum of 4d in $CDCl_3$.

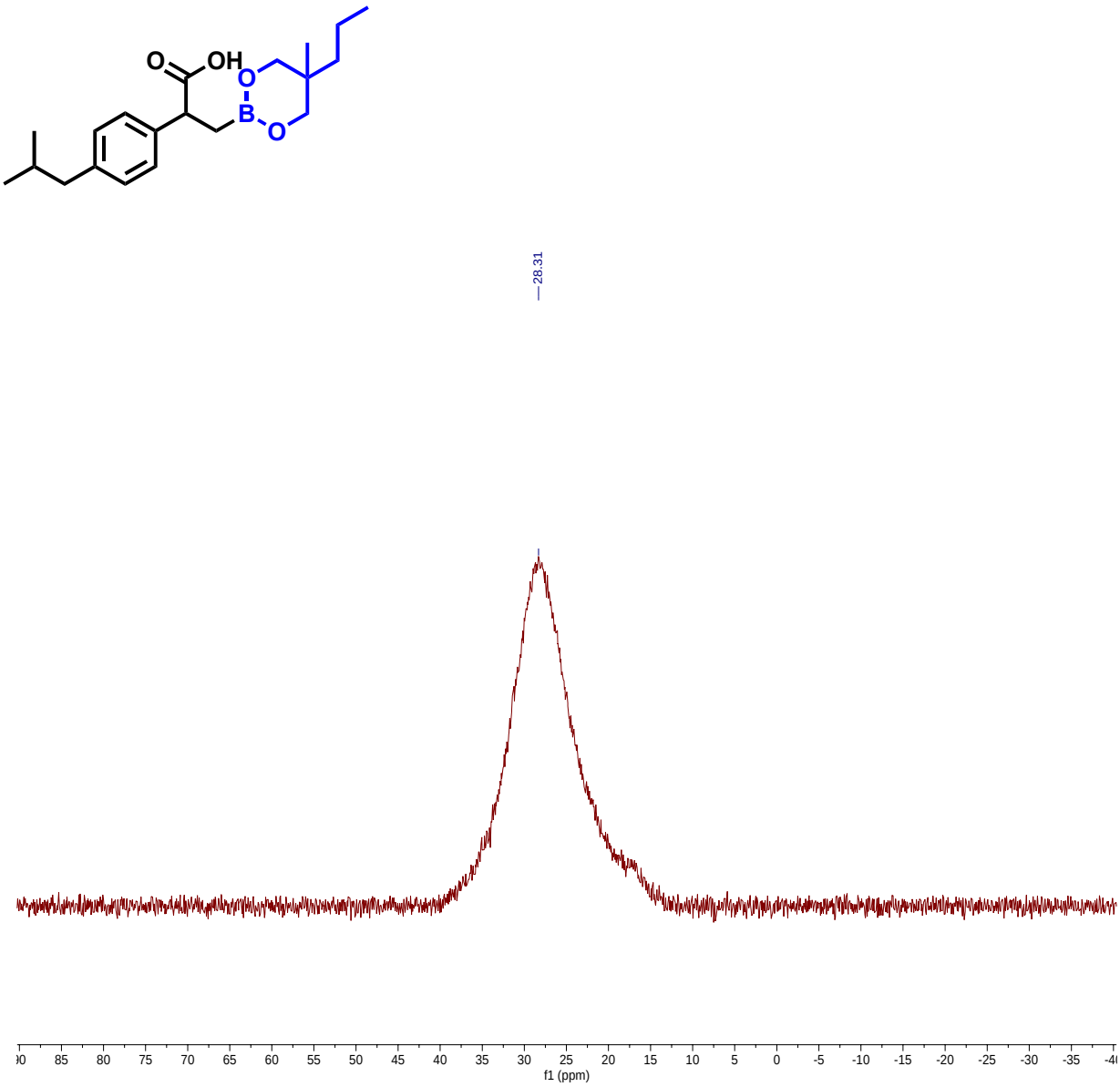

Figure A-18. ^{11}B NMR Spectrum of 4d in $CDCl_3$.

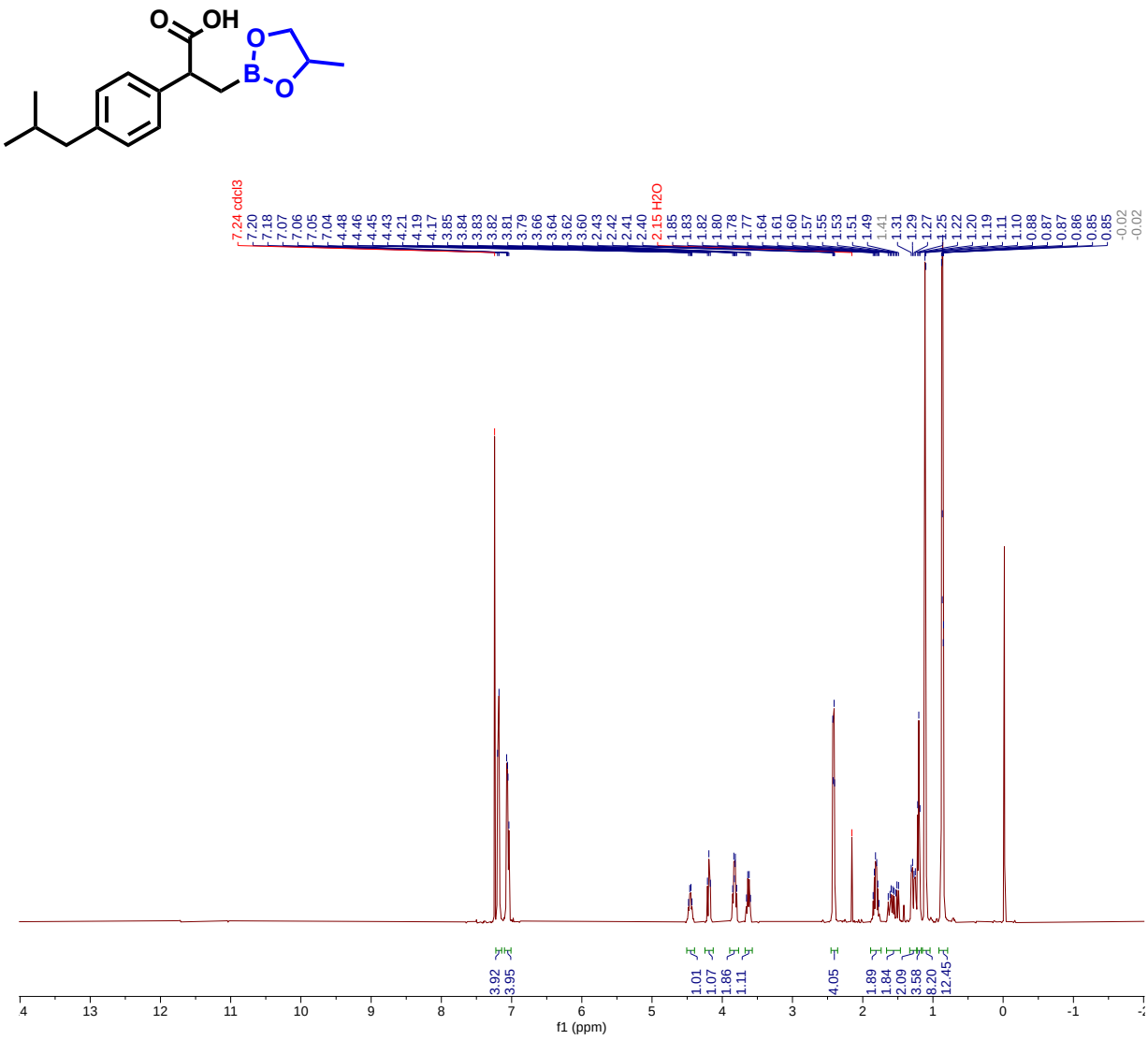

Figure A-19. ^{1}H NMR Spectrum of 4e in $CDCl_3$.

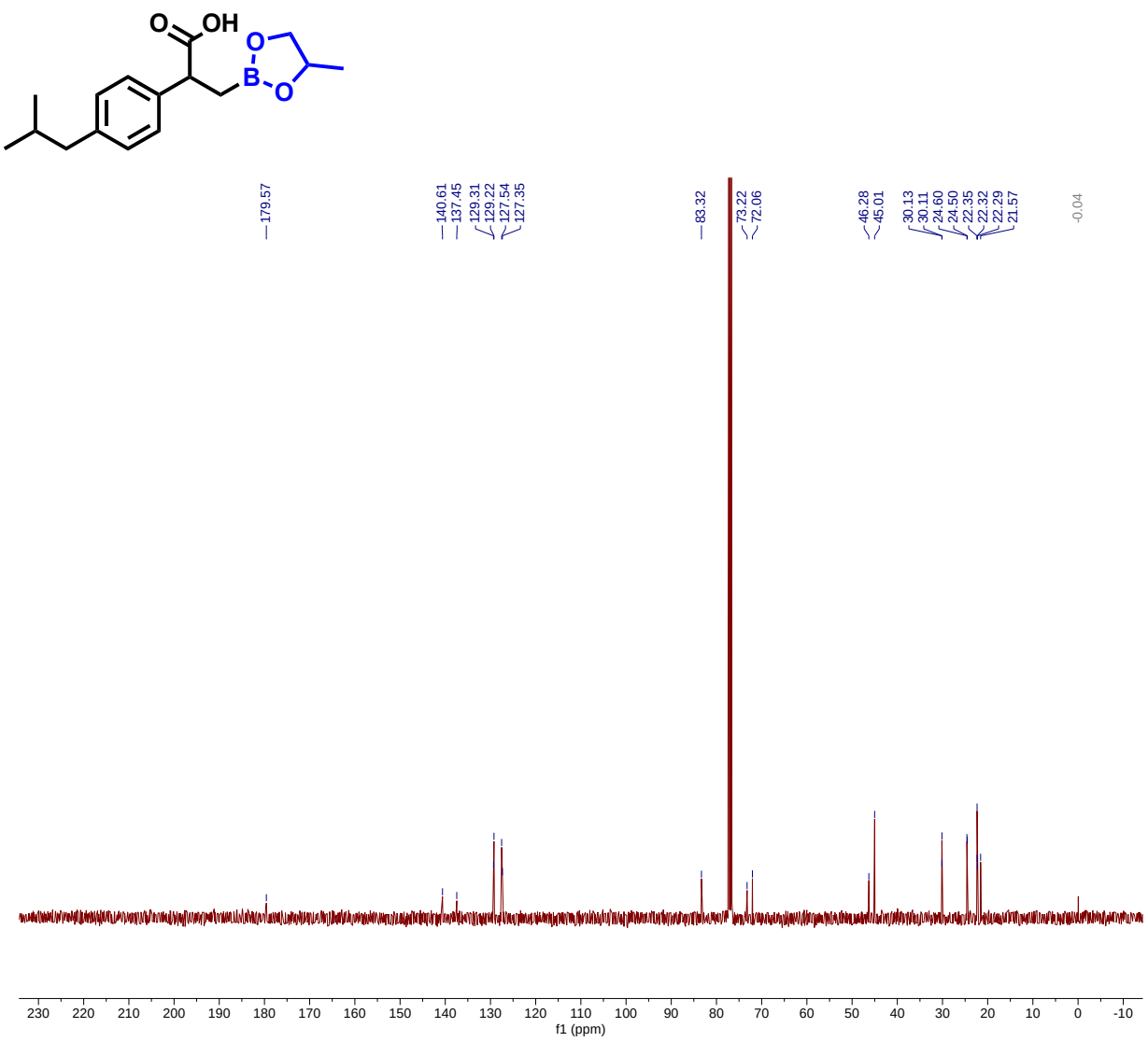

Figure A-20. ^{13}C NMR Spectrum of 4e in $CDCl_3$.

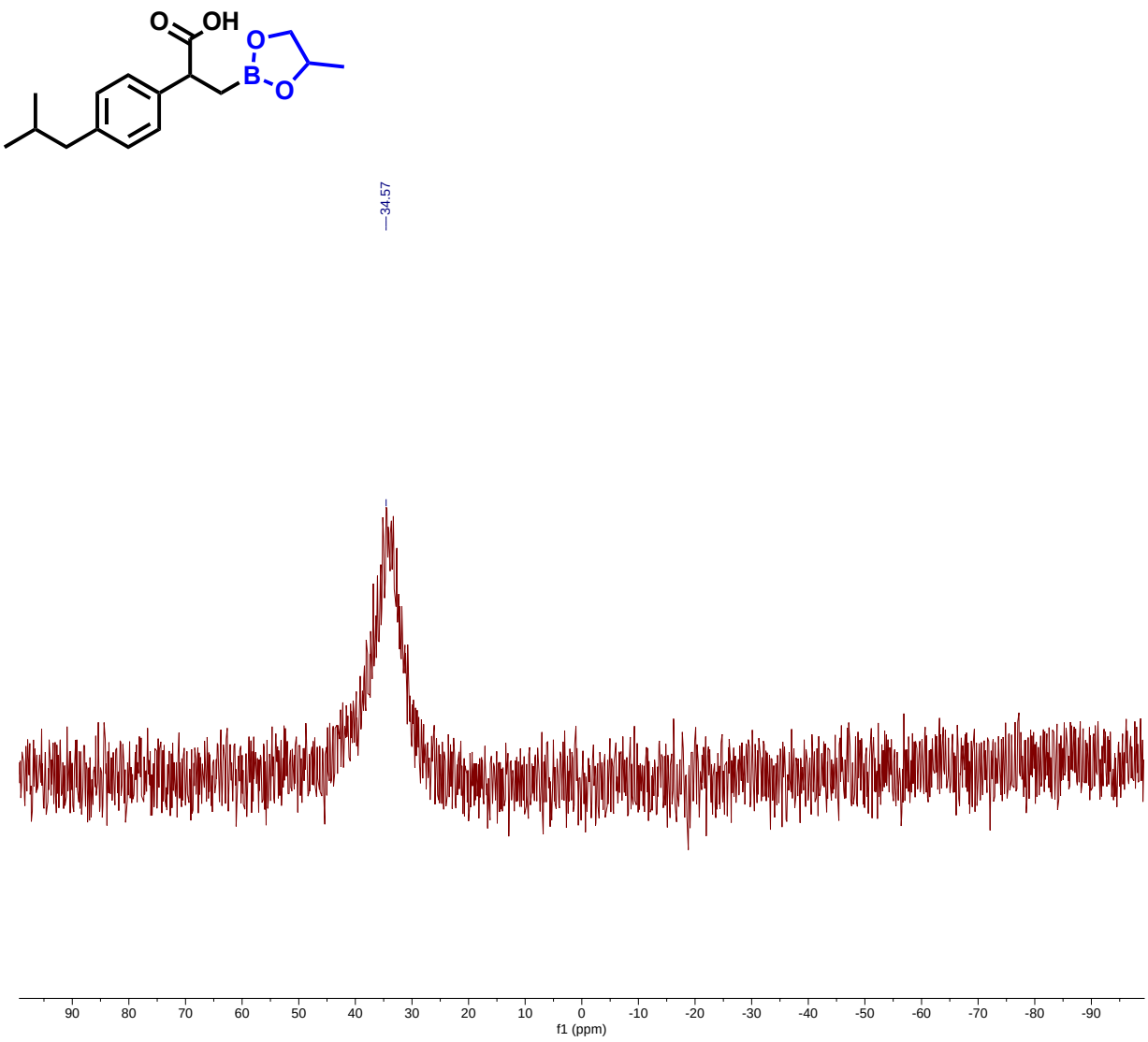

Figure A-21. ^{11}B NMR Spectrum of 4e in $CDCl_3$.

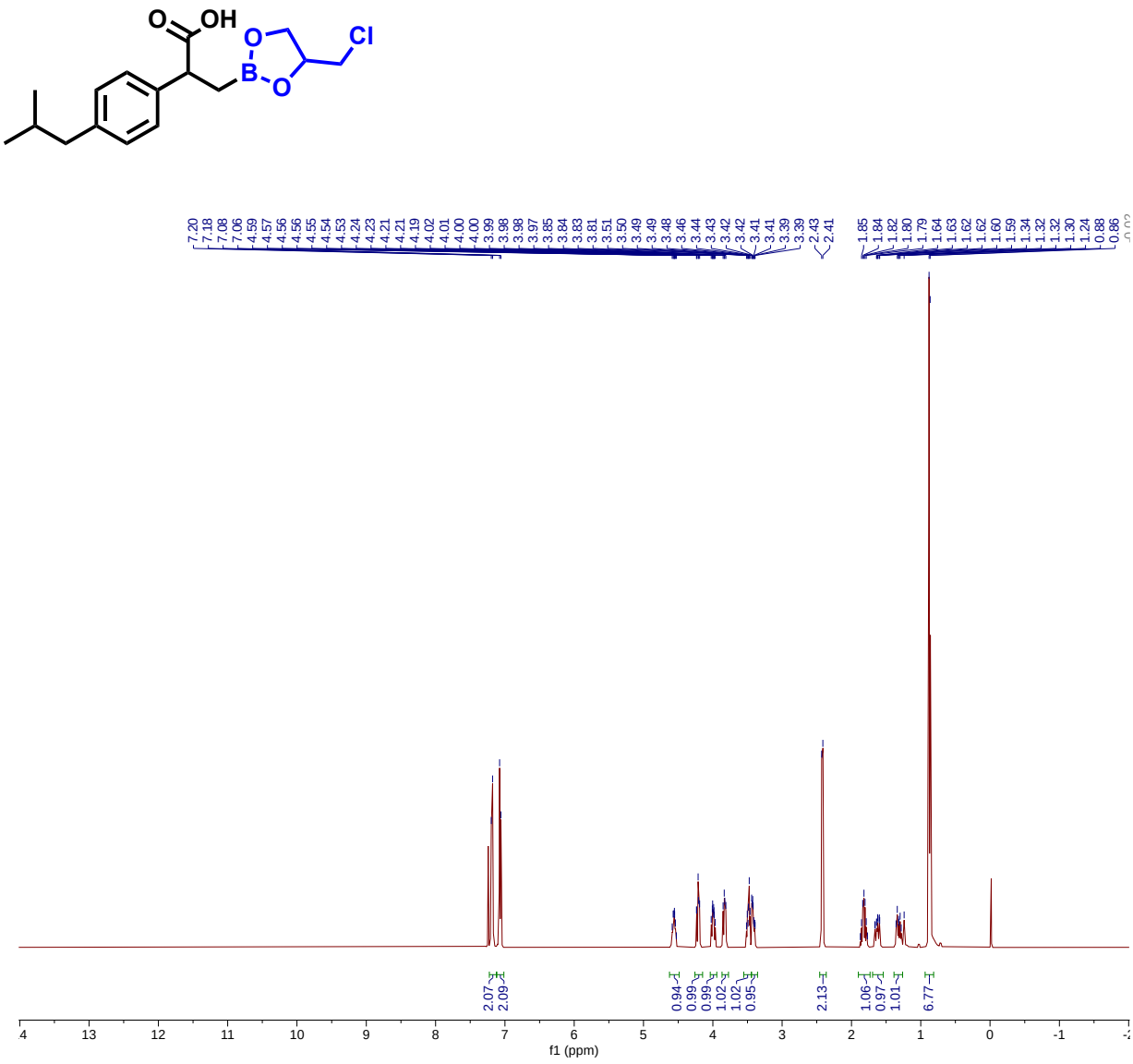

Figure A-22. ^{1}H NMR Spectrum of 4f in $CDCl_3$.

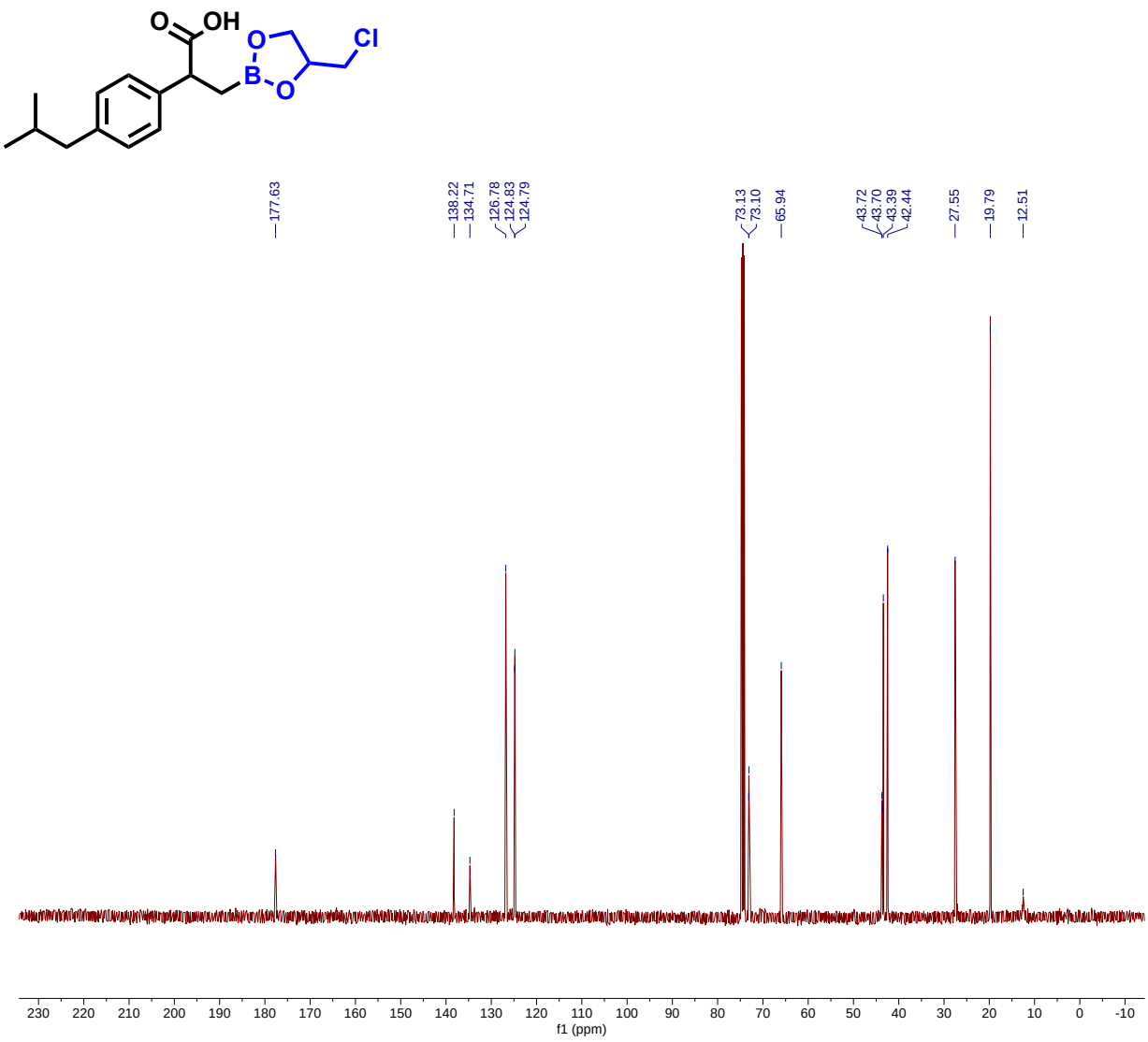

Figure A-23. ^{13}C NMR Spectrum of 4f in $CDCl_3$.

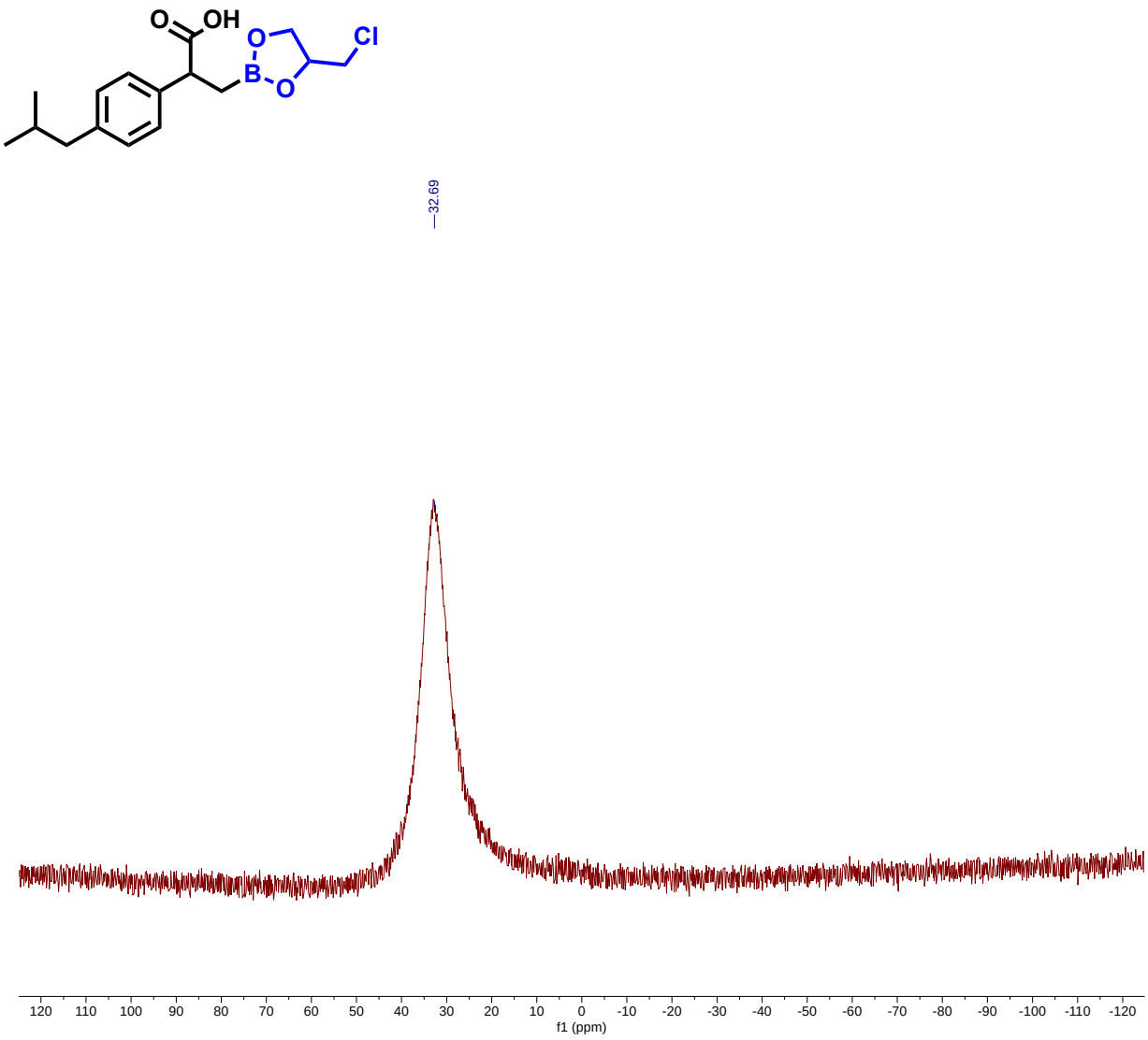

Figure A-24. ^{11}B NMR Spectrum of 4f in $CDCl_3$.

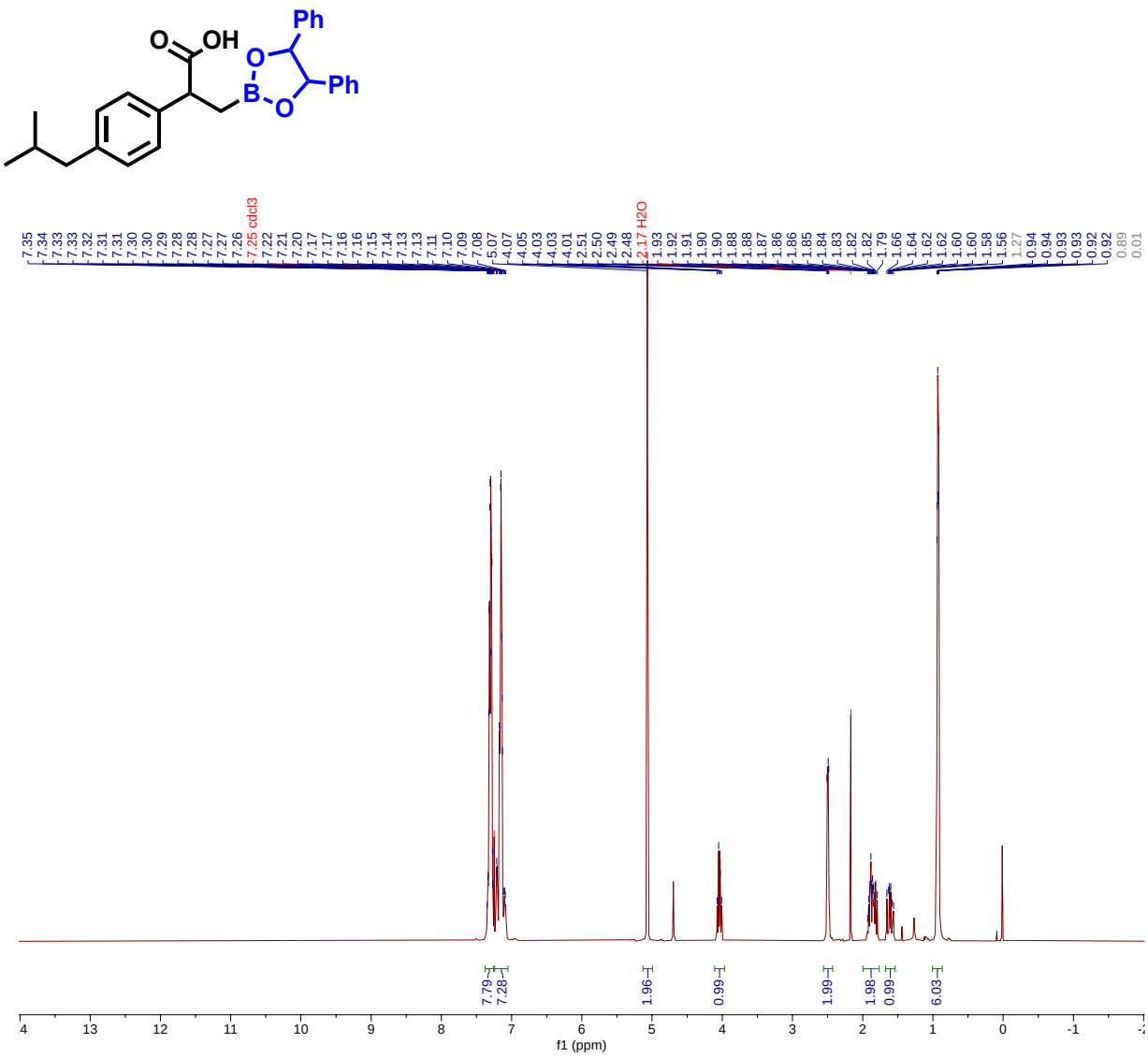

Figure A-25. ^{1}H NMR Spectrum of 4g in $CDCl_3$.

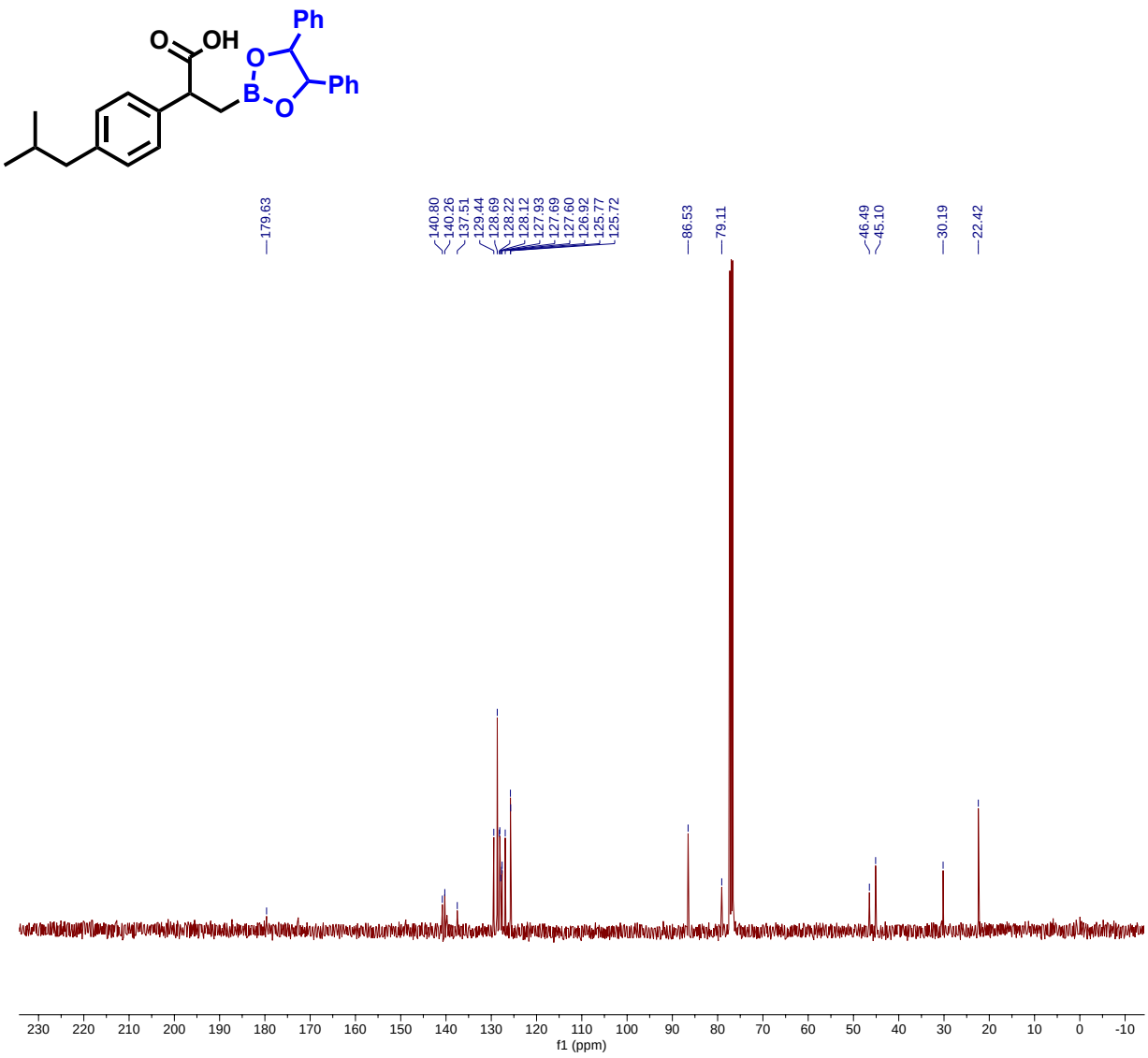

Figure A-26. ^{13}C NMR Spectrum of 4g in $CDCl_3$.

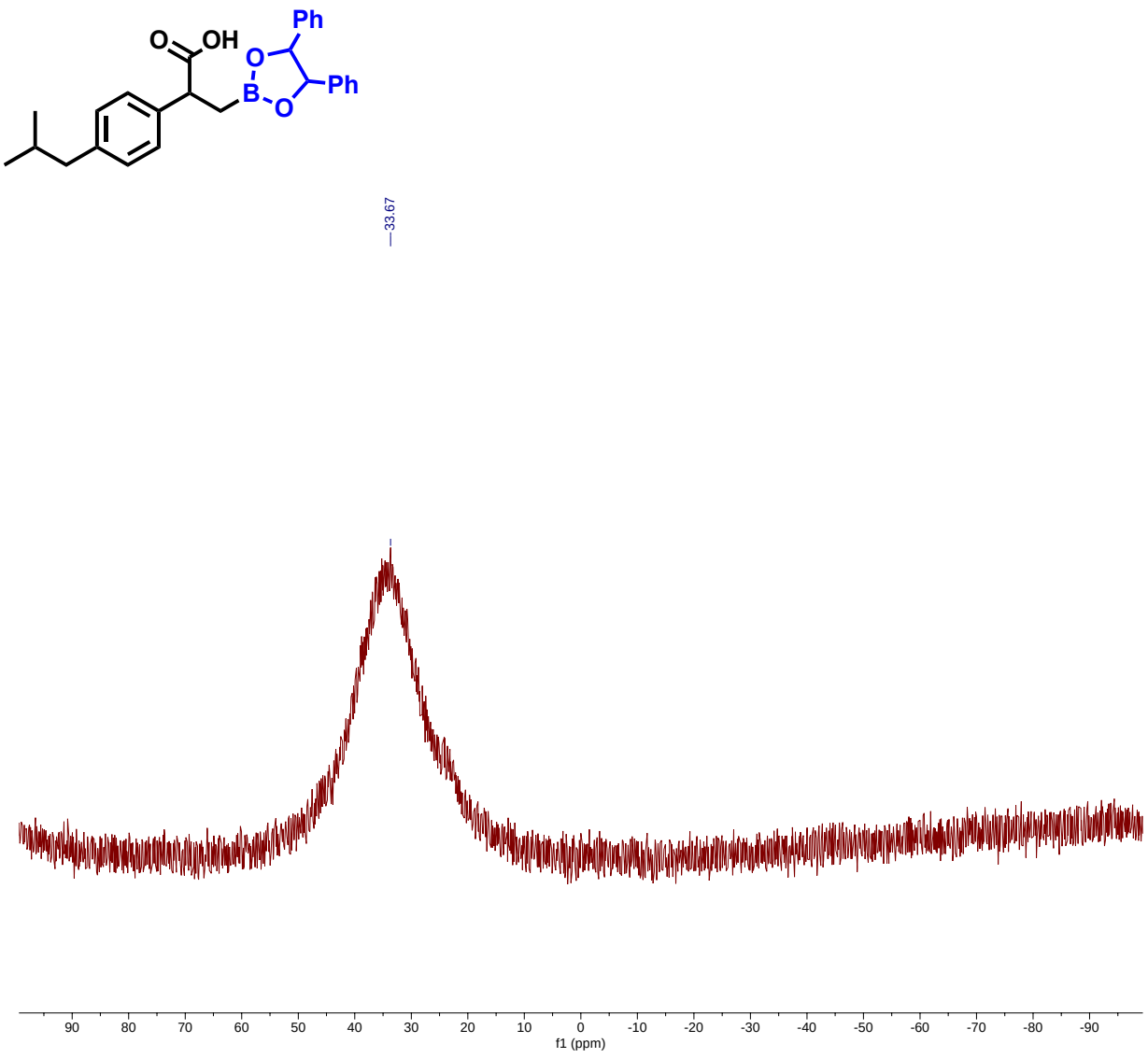

Figure A-27. ^{11}B NMR Spectrum of 4g in $CDCl_3$.

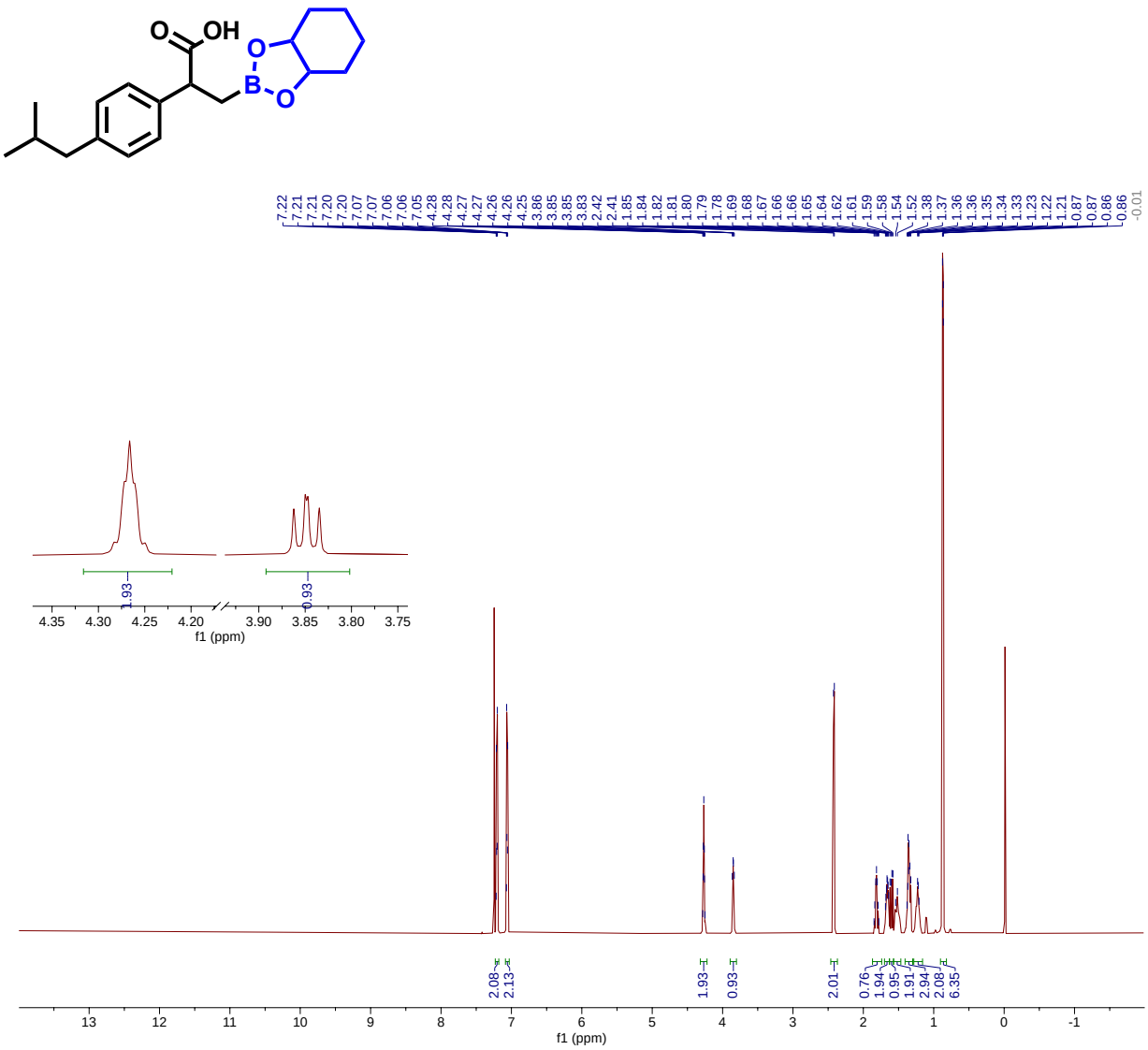

Figure A-28. ^{1}H NMR Spectrum of 4h in $CDCl_3$.

A series of selective decoupled ^{1}H NMR spectra (b-d)

400 MHz JEOL NMR

Simultaneously irradiation of two different frequencies---c and d subspectra

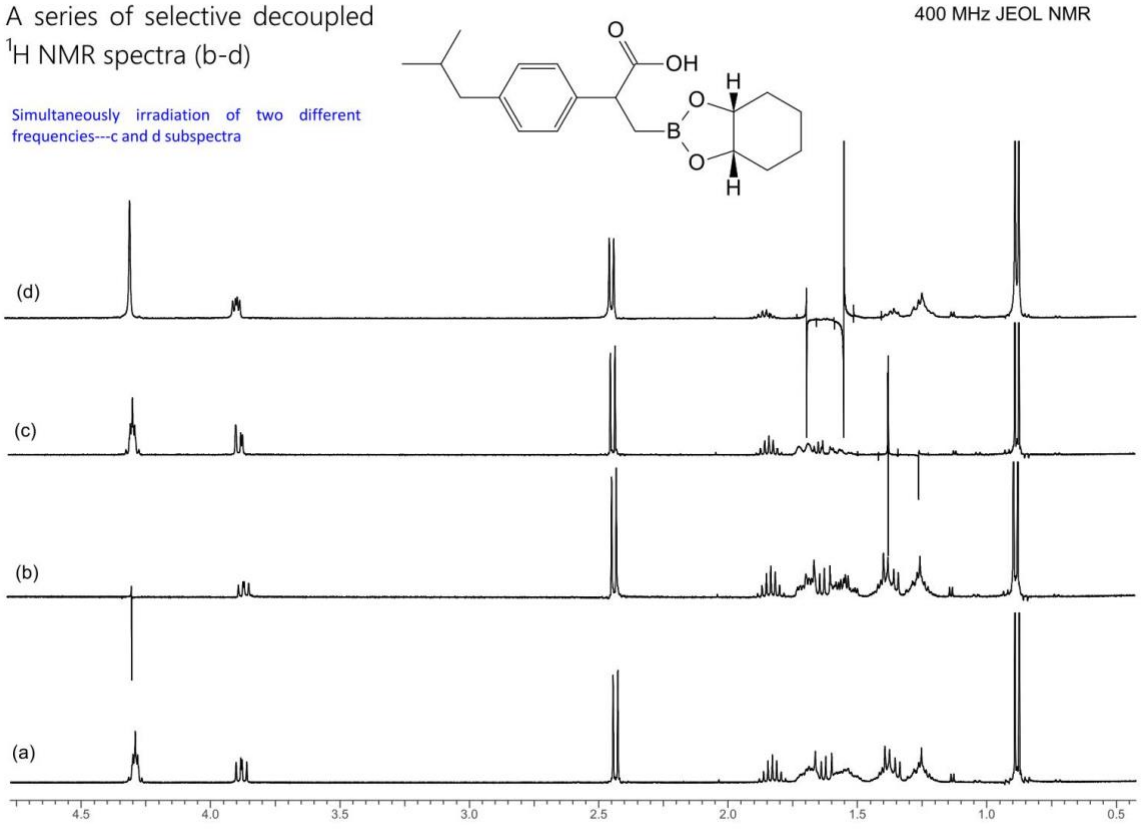

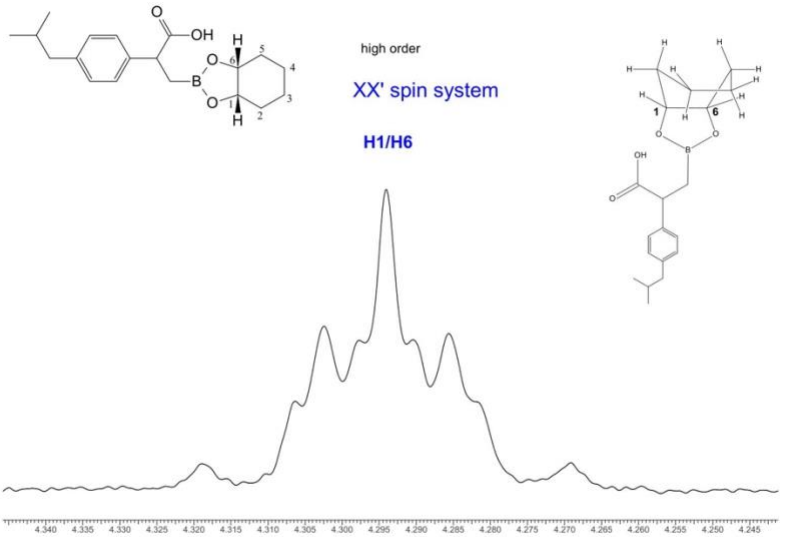
high order
XX' spin system
H1/H6

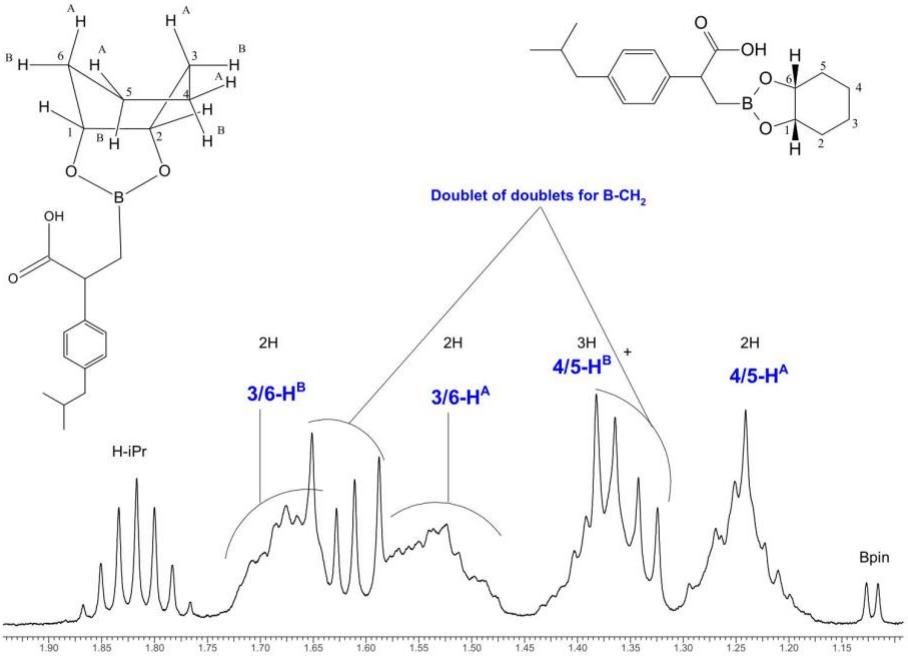
Doublet of doublets for B-CH2
2H
3/6-HB
2H
3/6-HA
3H
4/5-HB
+
2H
4/5-HA
H-iPr
Bpin

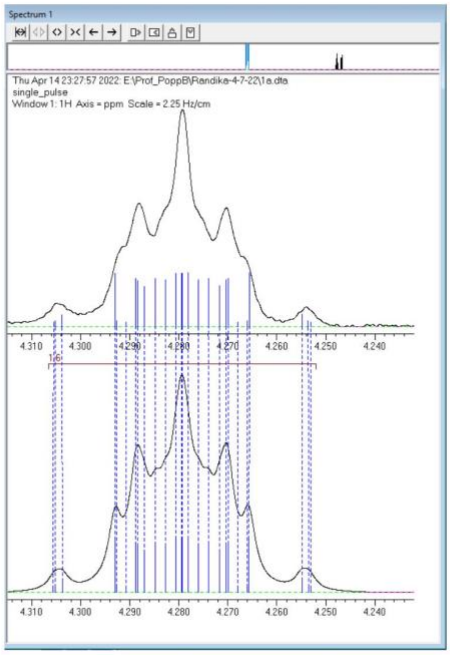

Simulation of the multiplicity patterns of OCH protons (bridge)

Coupling constants in Hz

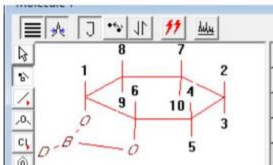

#	n	Shift	Width	J[1]	J[2]	J[3]	J[4]	J[5]	J[6]	J[7]	J[8]	J[9]
1	1	4.279										
		x	-									
2	*1*	*1.360*		*0.00*								
		c	-	-								
3	*1*	*1.230*		*0.00*	*-12.00*							
		d	-	-	-							
4	1	1.539		0.00	*7.00*	*7.00*						
		a	-	-	-	-						
5	1	1.679		0.00	*7.00*	*7.00*	-13.60					
		b	-	-	-	-	ab					
6	1	4.279		6.70	*0.00*	*0.00*	4.97	5.98				
		x	-	xx'	-	-	ax	bx				
7	*1*	*1.360*		*0.00*	*7.00*	*7.00*	*0.00*	*0.00*	*0.00*			
		c	-	-	-	-	-	-	-			
8	1	1.539		4.97	*0.00*	*0.00*	0.00	0.00	0.00	*7.00*		
		a	-	ax	-	-	-	-	-	-		
9	1	1.679		5.98	*0.00*	*0.00*	0.00	0.00	0.00	*7.00*	-13.60	
		b	-	bx	-	-	-	-	-	-	ab	
10	*1*	*1.230*		*0.00*	*7.00*	*7.00*	*0.00*	*0.00*	*0.00*	*-16.00*	*7.00*	*7.00*
		d	-	-	-	-	-	-	-	-	-	-

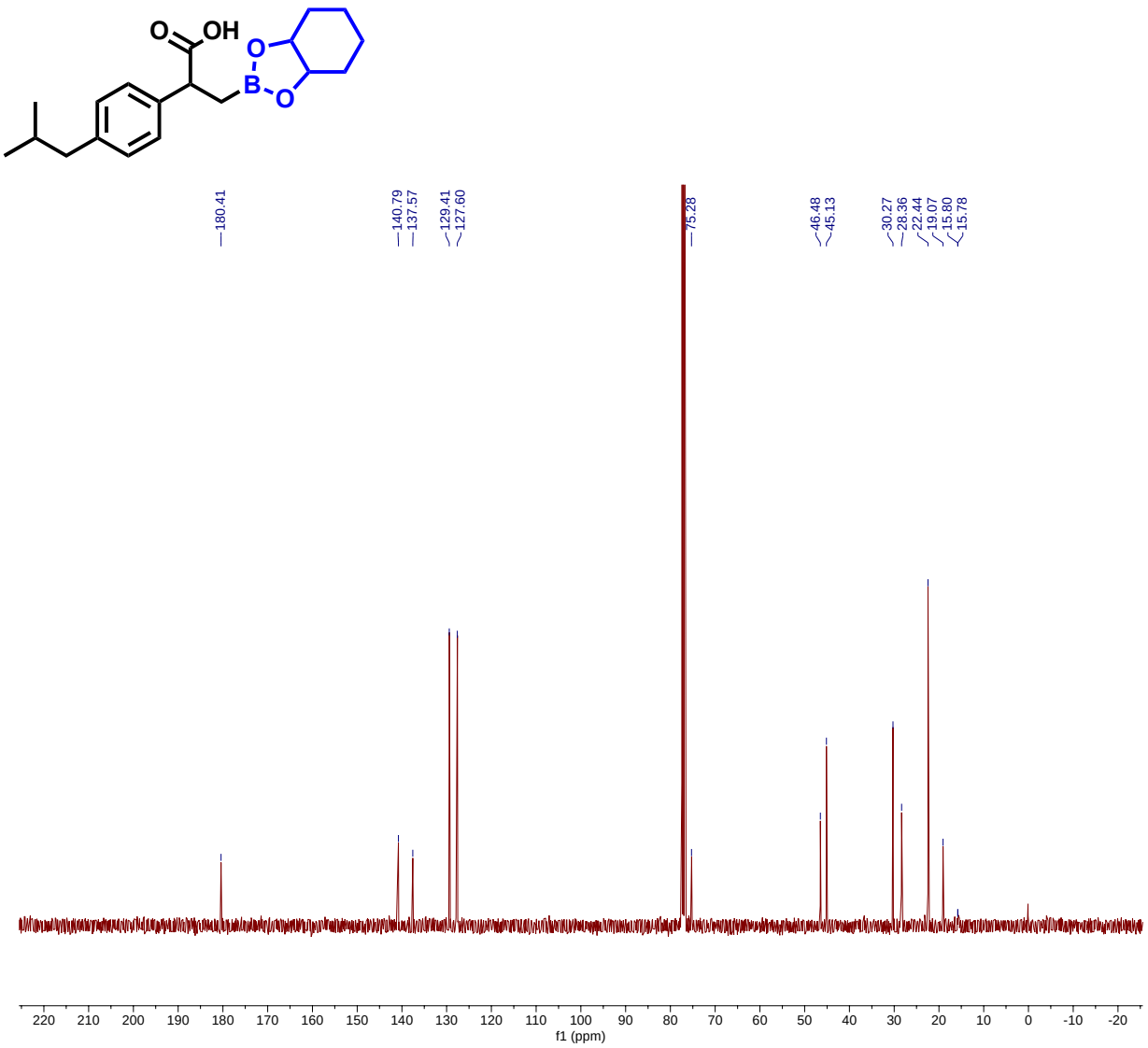

Figure A-29. ^{13}C NMR Spectrum of 4h in $CDCl_3$.

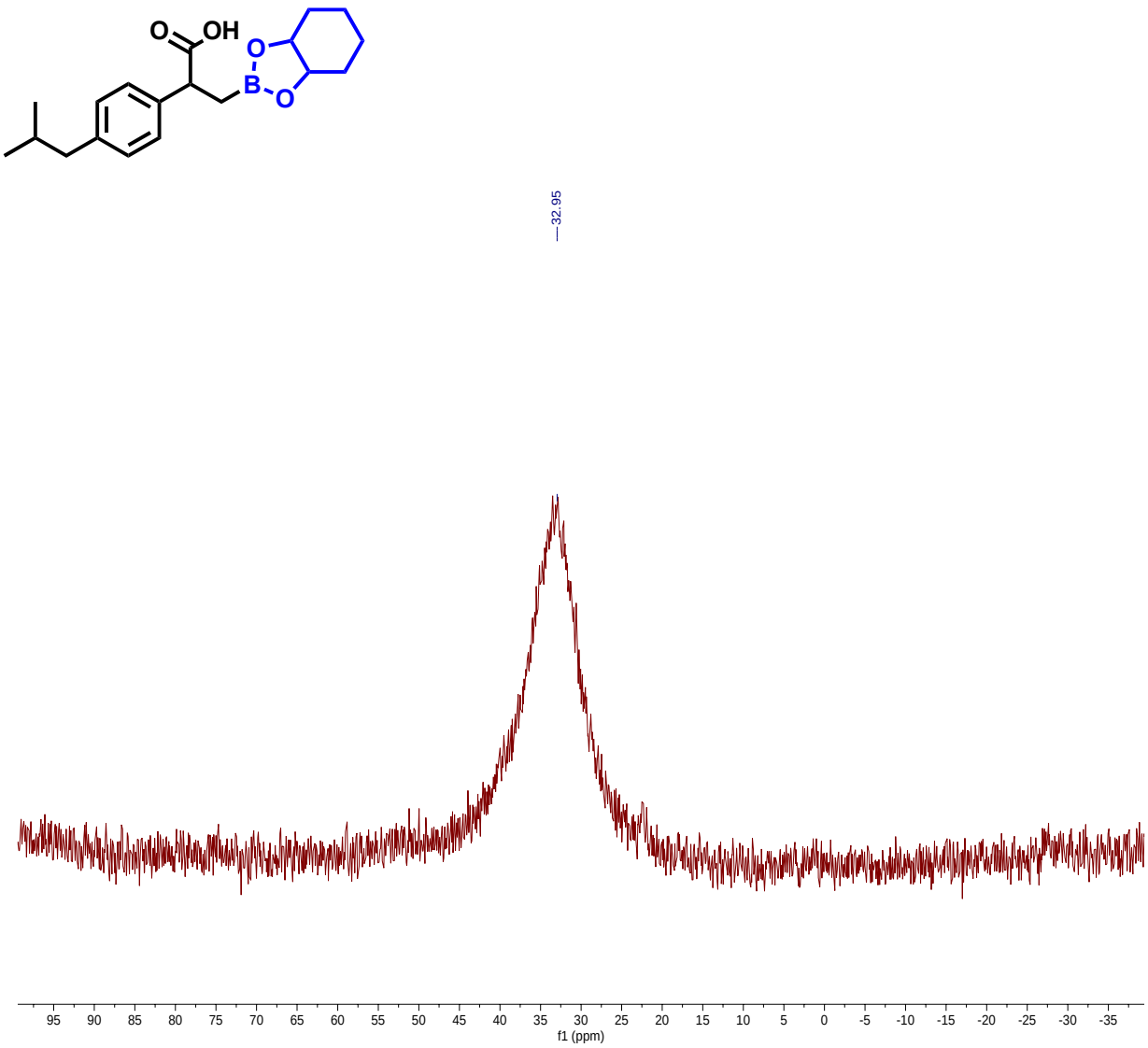

Figure A-30. ^{11}B NMR Spectrum of 4h in $CDCl_3$.

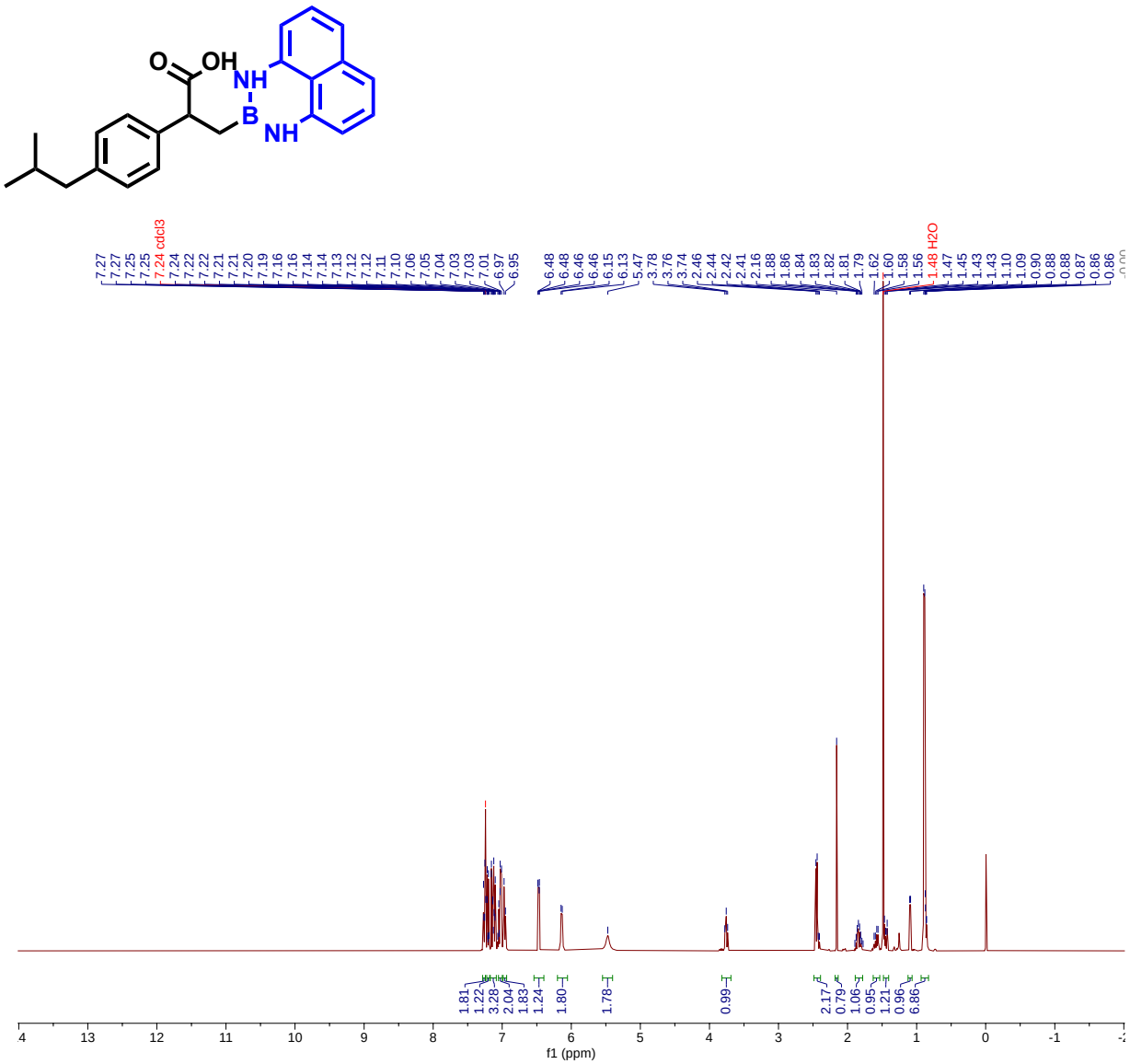

Figure A-31. ^{1}H NMR Spectrum of 4i in $CDCl_3$.

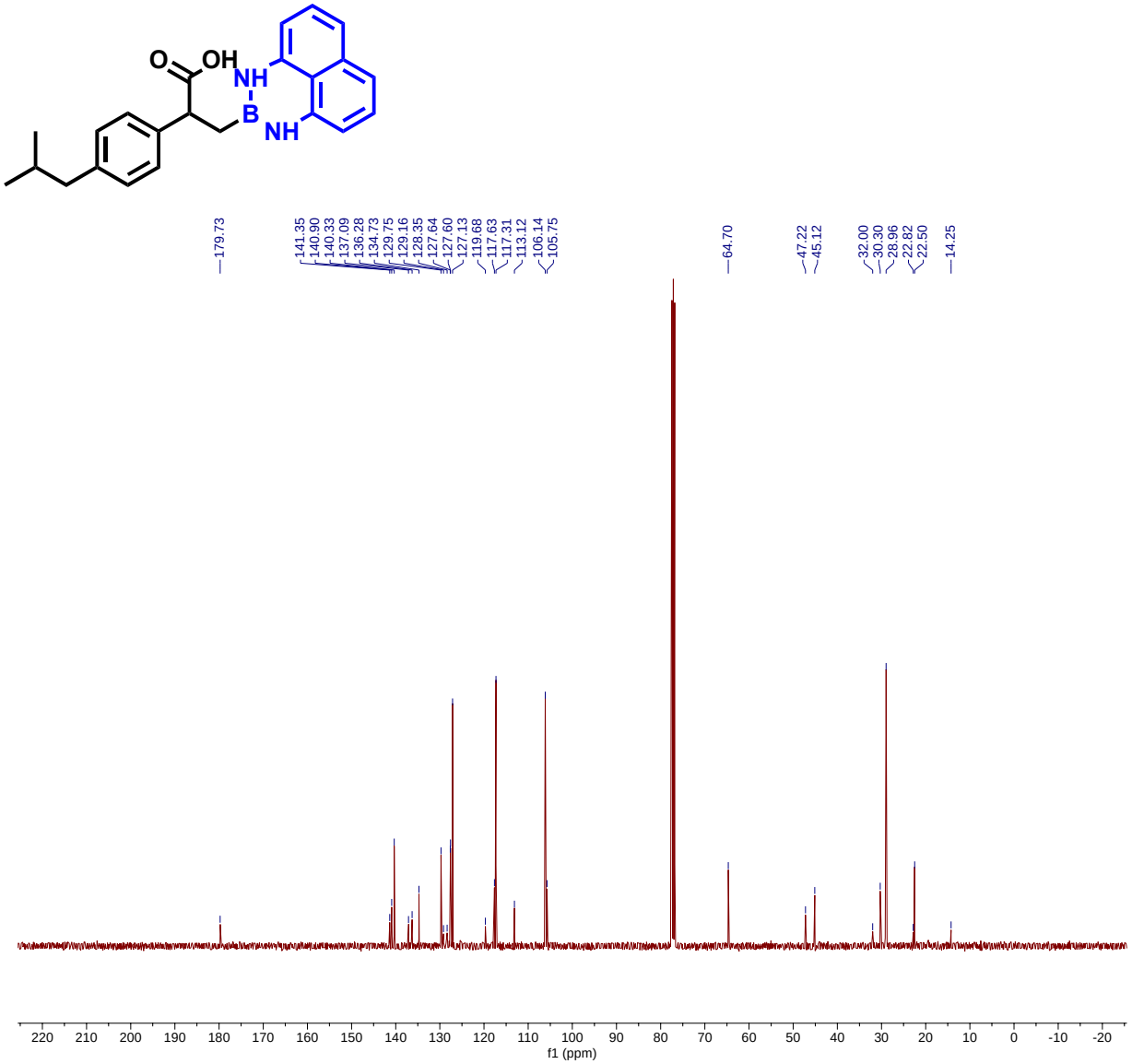

Figure A-32. ^{13}C NMR Spectrum of 4i in $CDCl_3$.

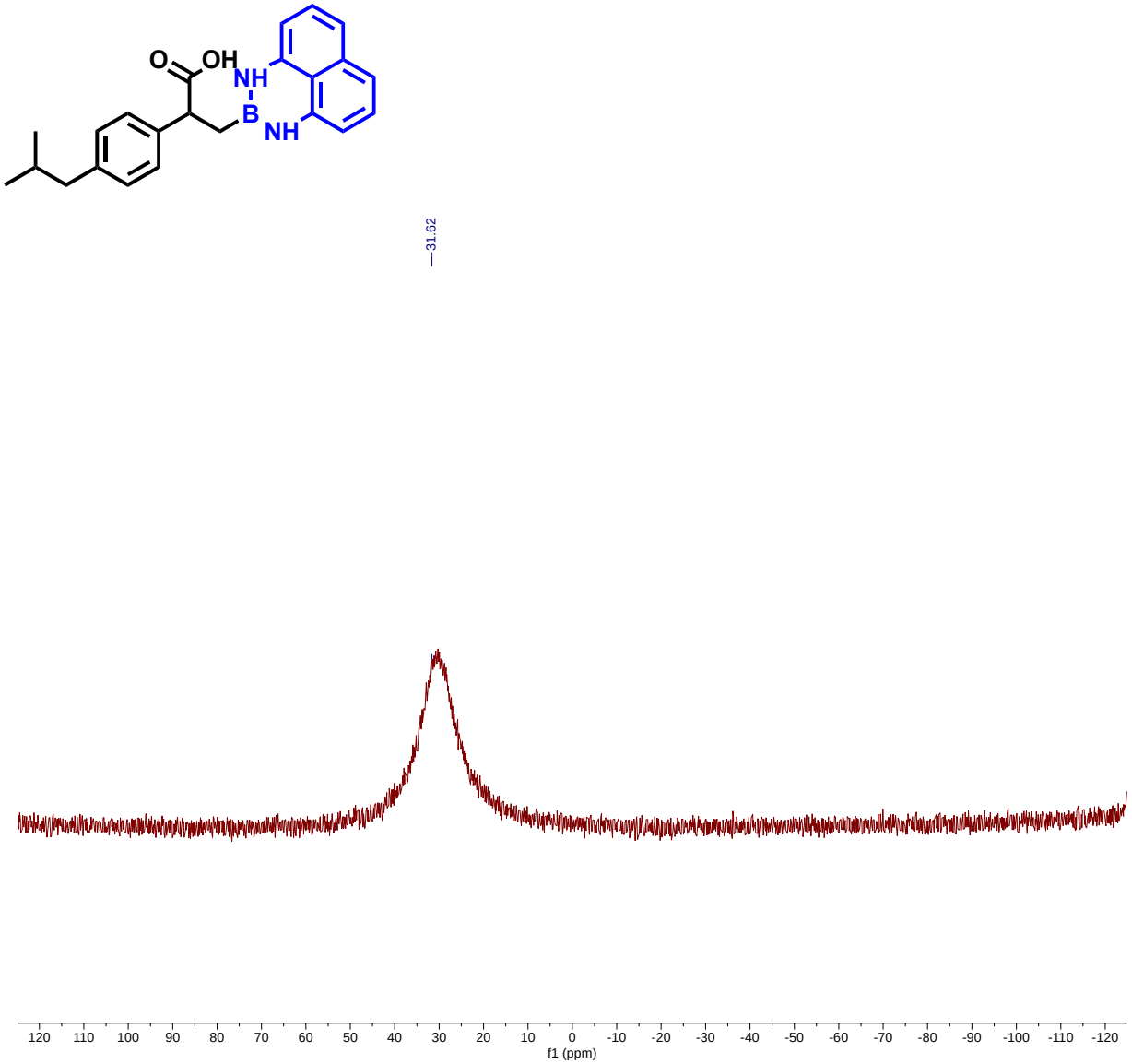

Figure A-33. ^{13}C NMR Spectrum of 4i in $CDCl_3$.

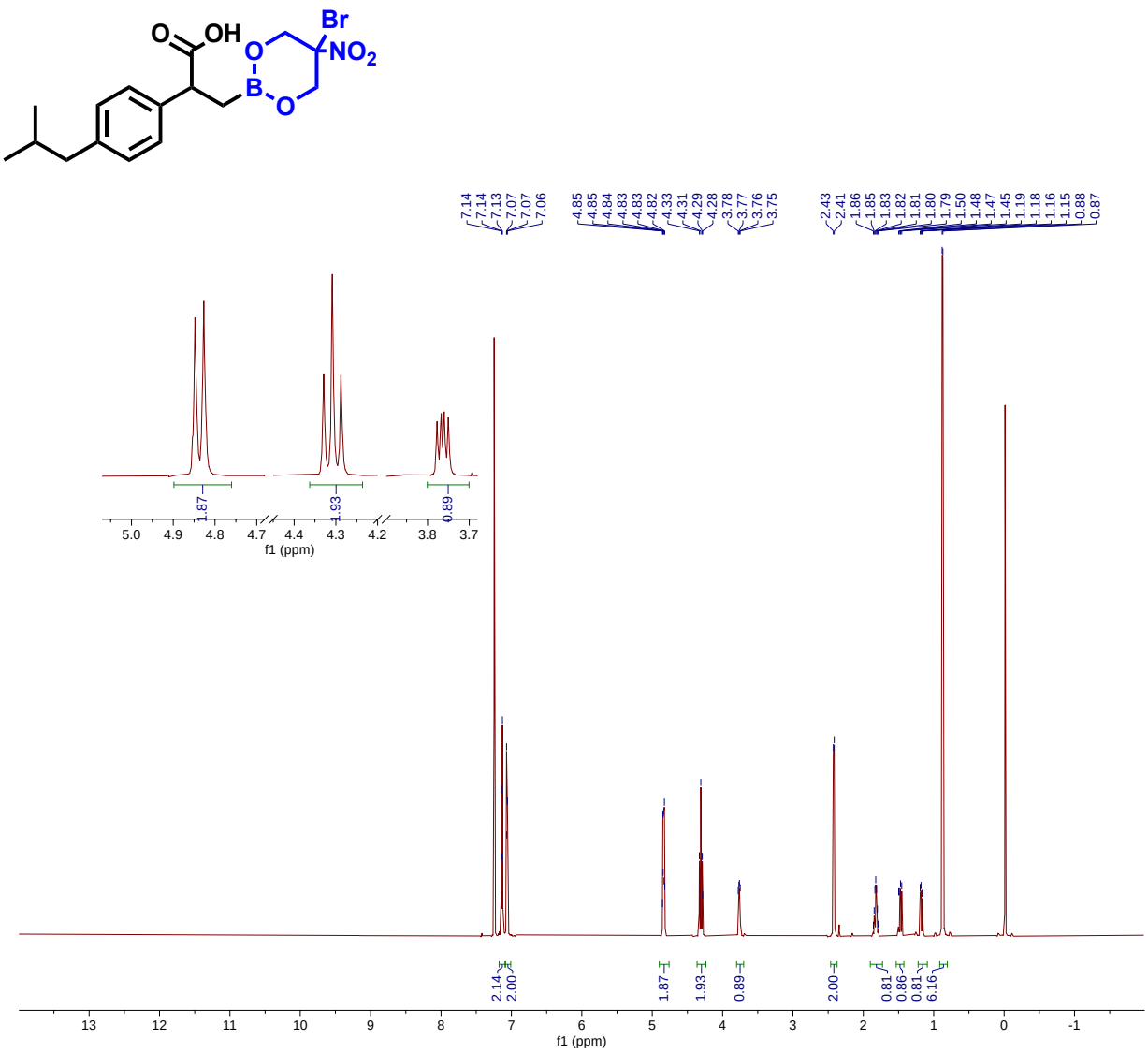

Figure A-34. ^{1}H NMR Spectrum of 4j in $CDCl_3$.

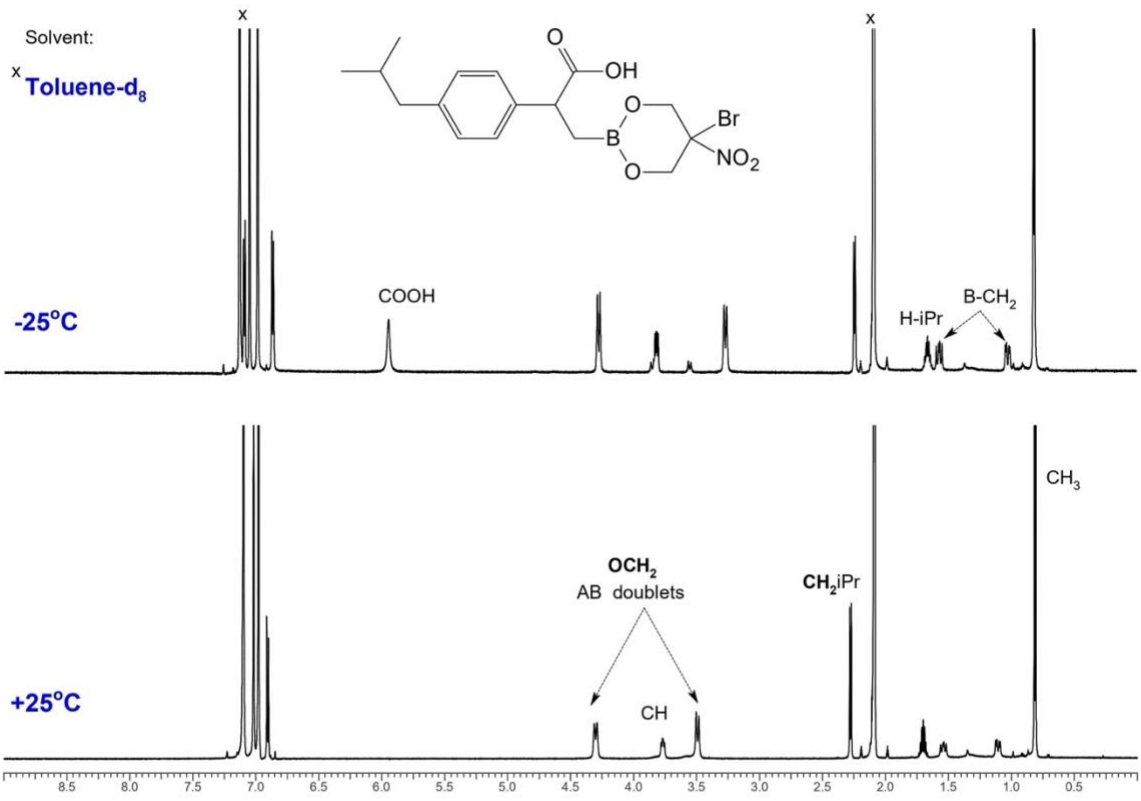

Figure A-35. VT-^{1}H NMR Spectrum of 4j in Toluene-d_8.

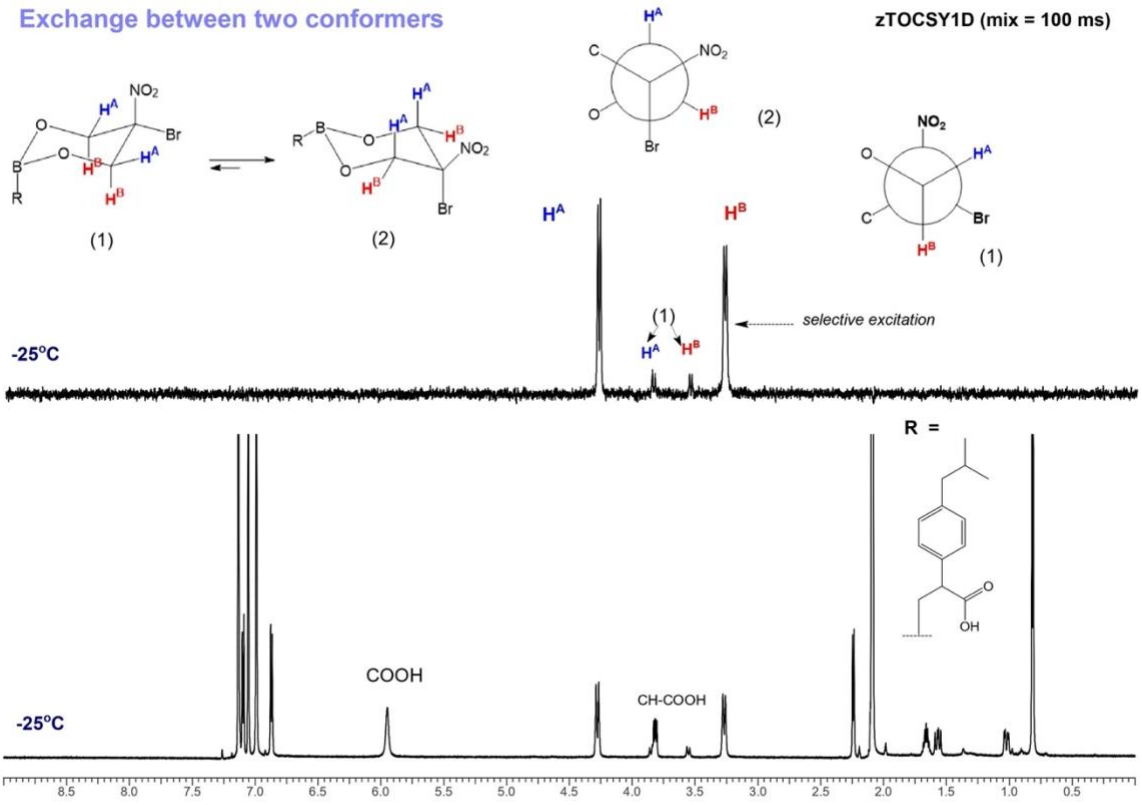

Figure A-36. zTOCSY 1D ^{1}H NMR Spectrum of 4j in Toluene-d_8.

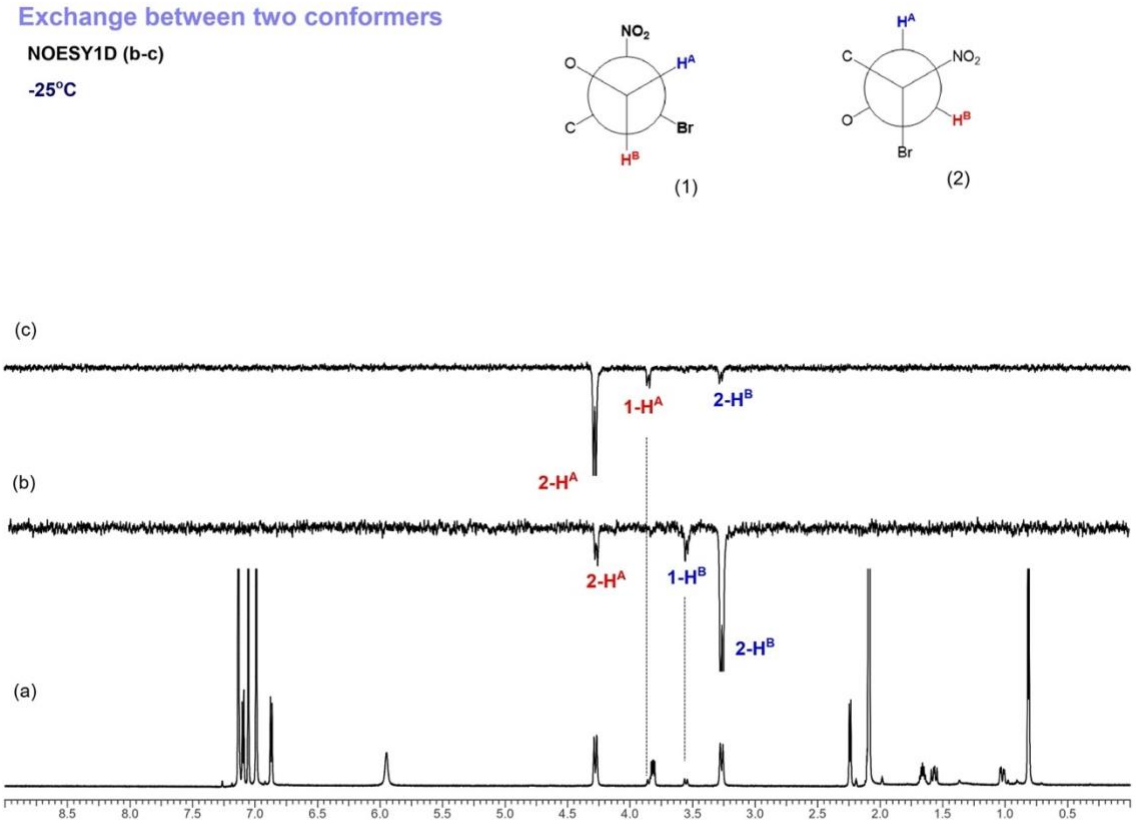

Figure A-37. NOESY 1D ^{1}H NMR Spectrum of 4j in Toluene-d_8.

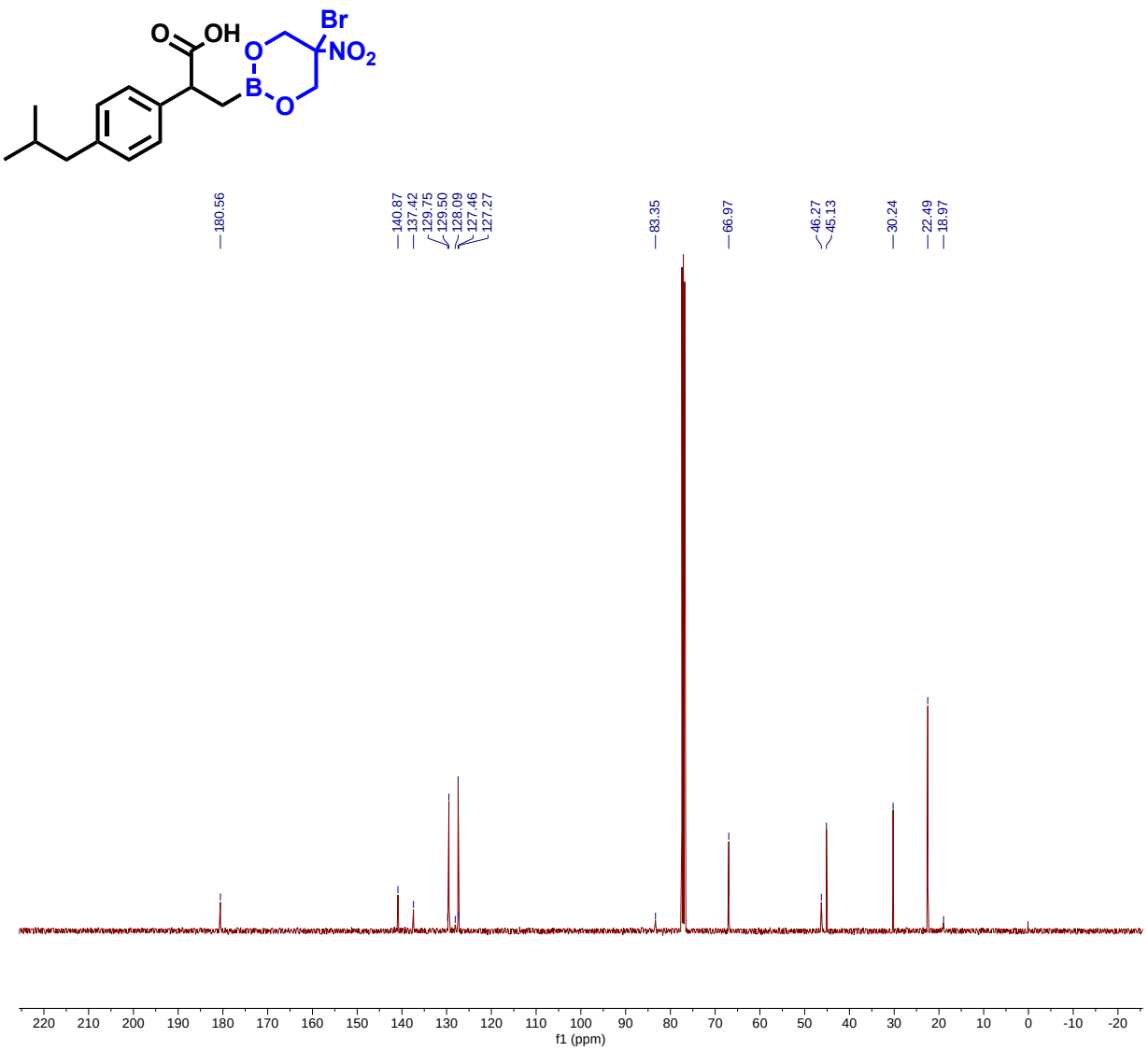

Figure A-38. ^{13}C NMR Spectrum of 4j in $CDCl_3$.

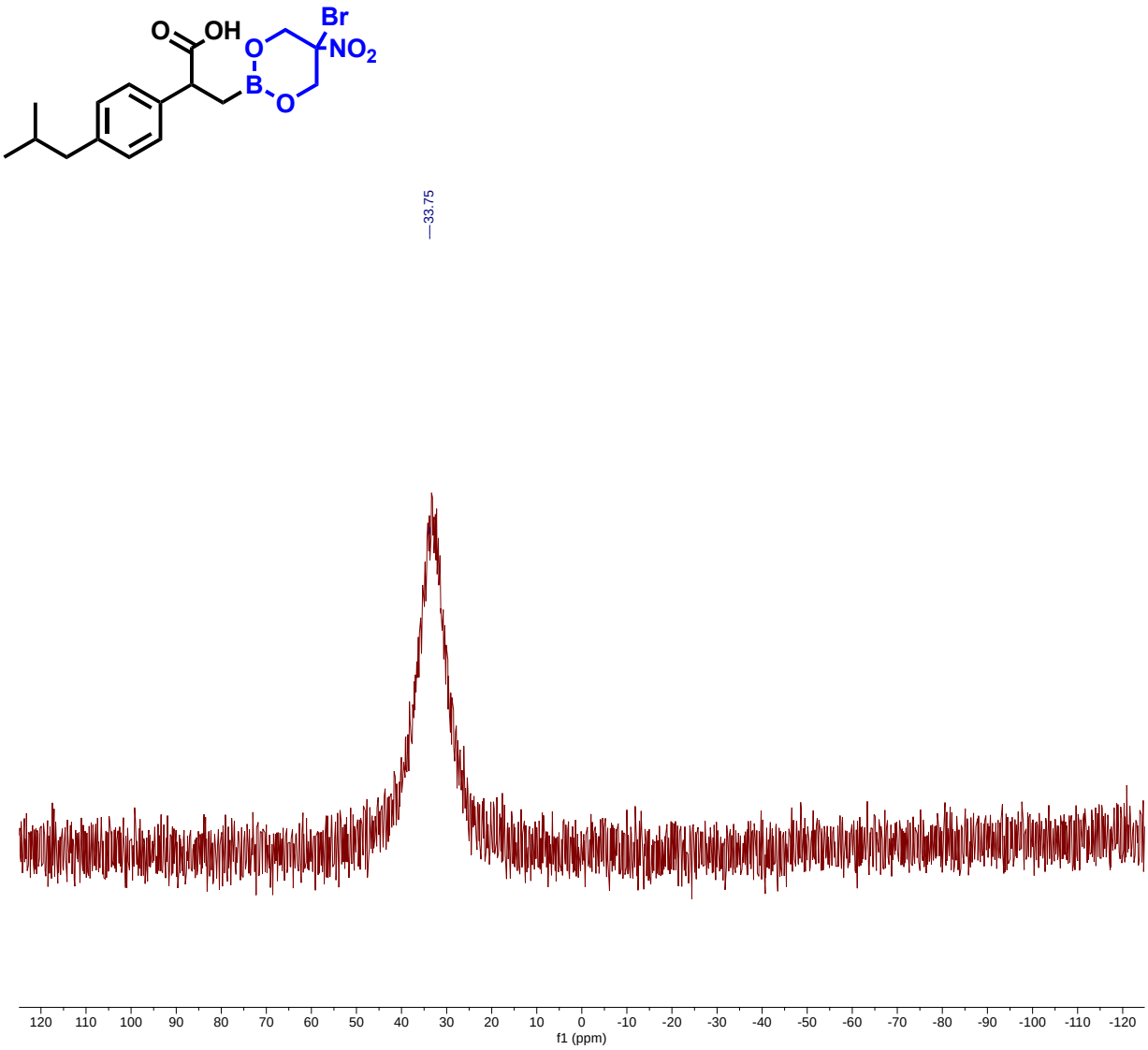

Figure A-39. ^{11}B NMR Spectrum of 4j in $CDCl_3$.

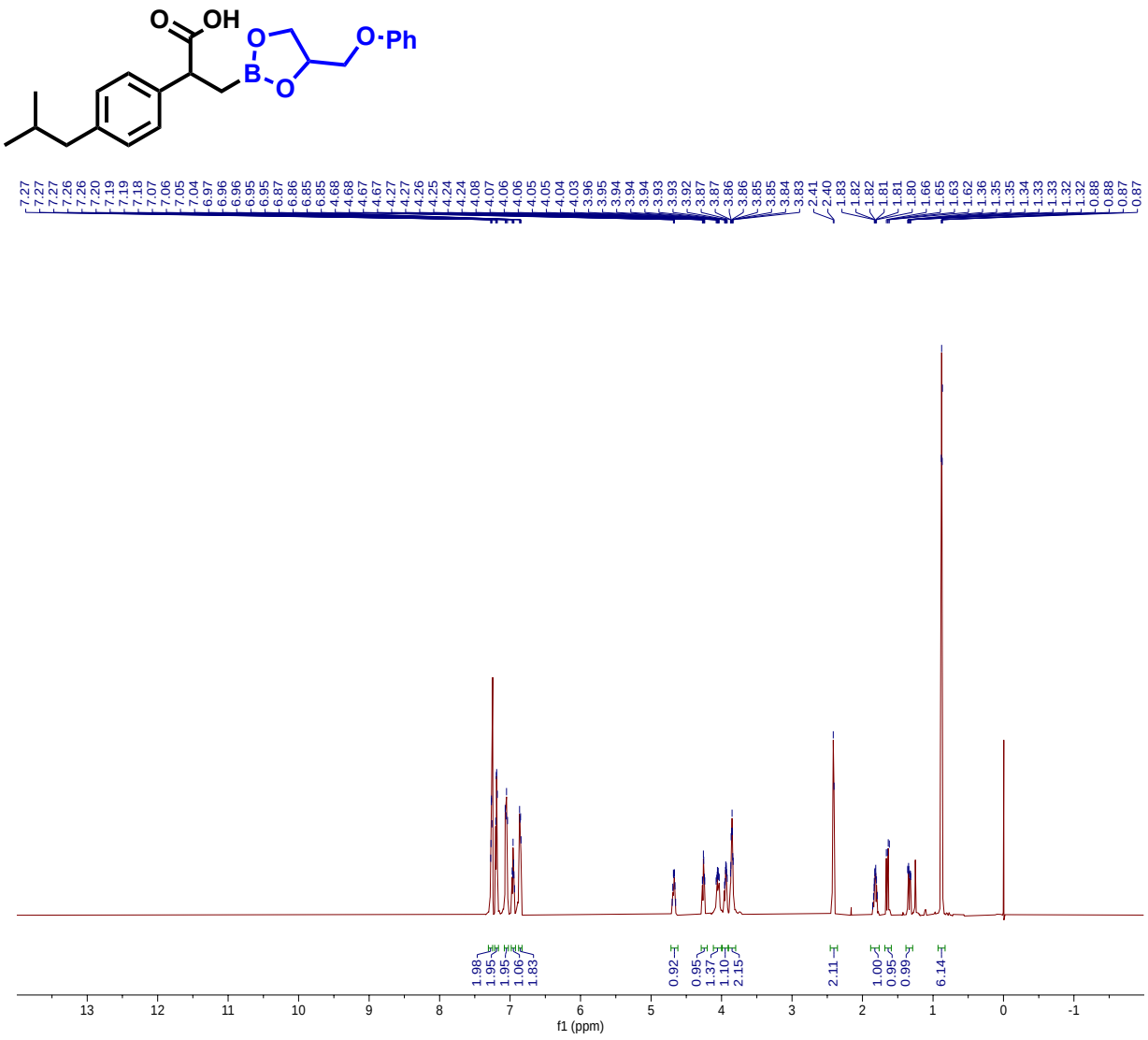

Figure A-40. ^{1}H NMR Spectrum of 5a in $CDCl_3$.

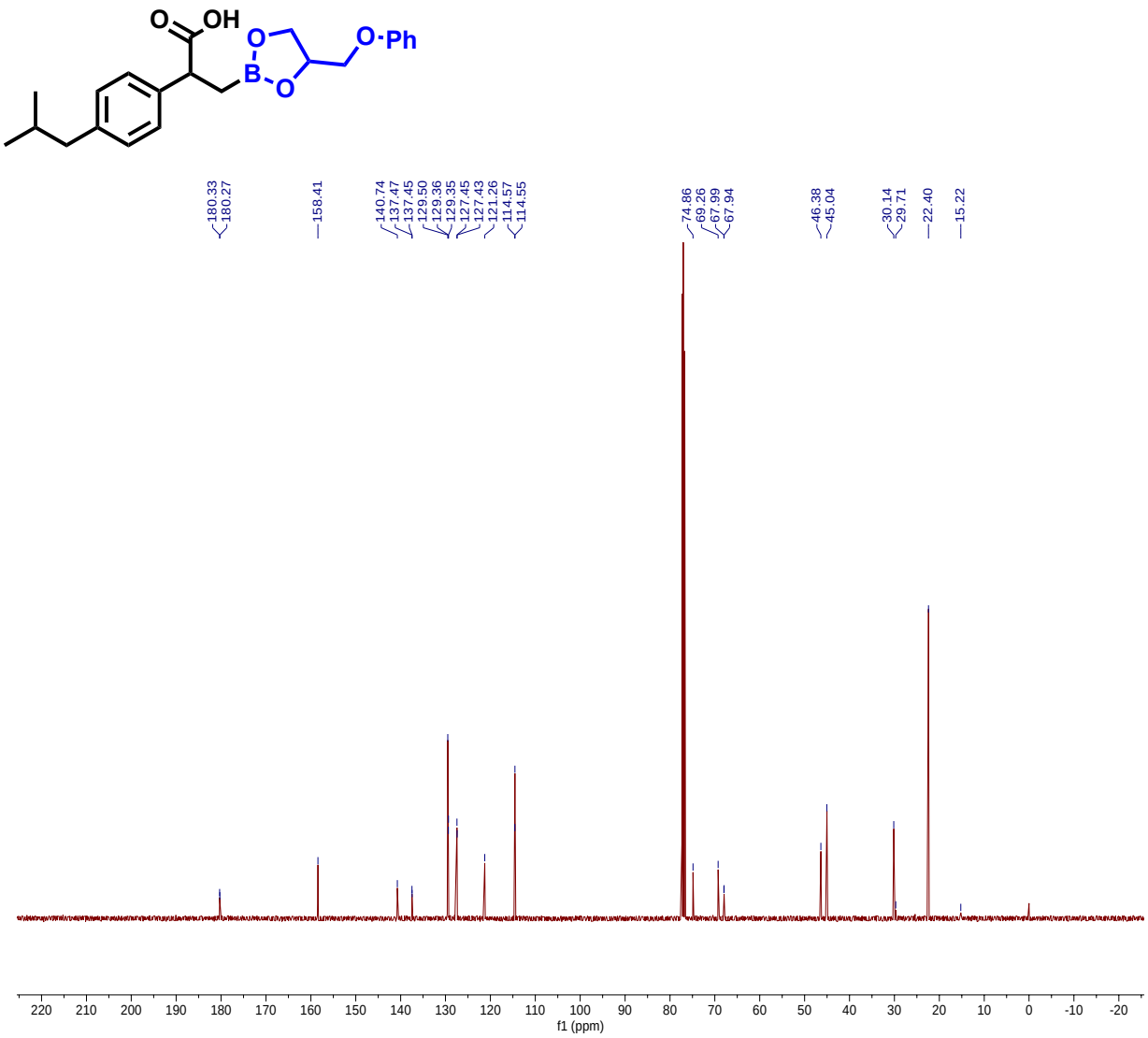

Figure A-41. ^{13}C NMR Spectrum of 5a in $CDCl_3$.

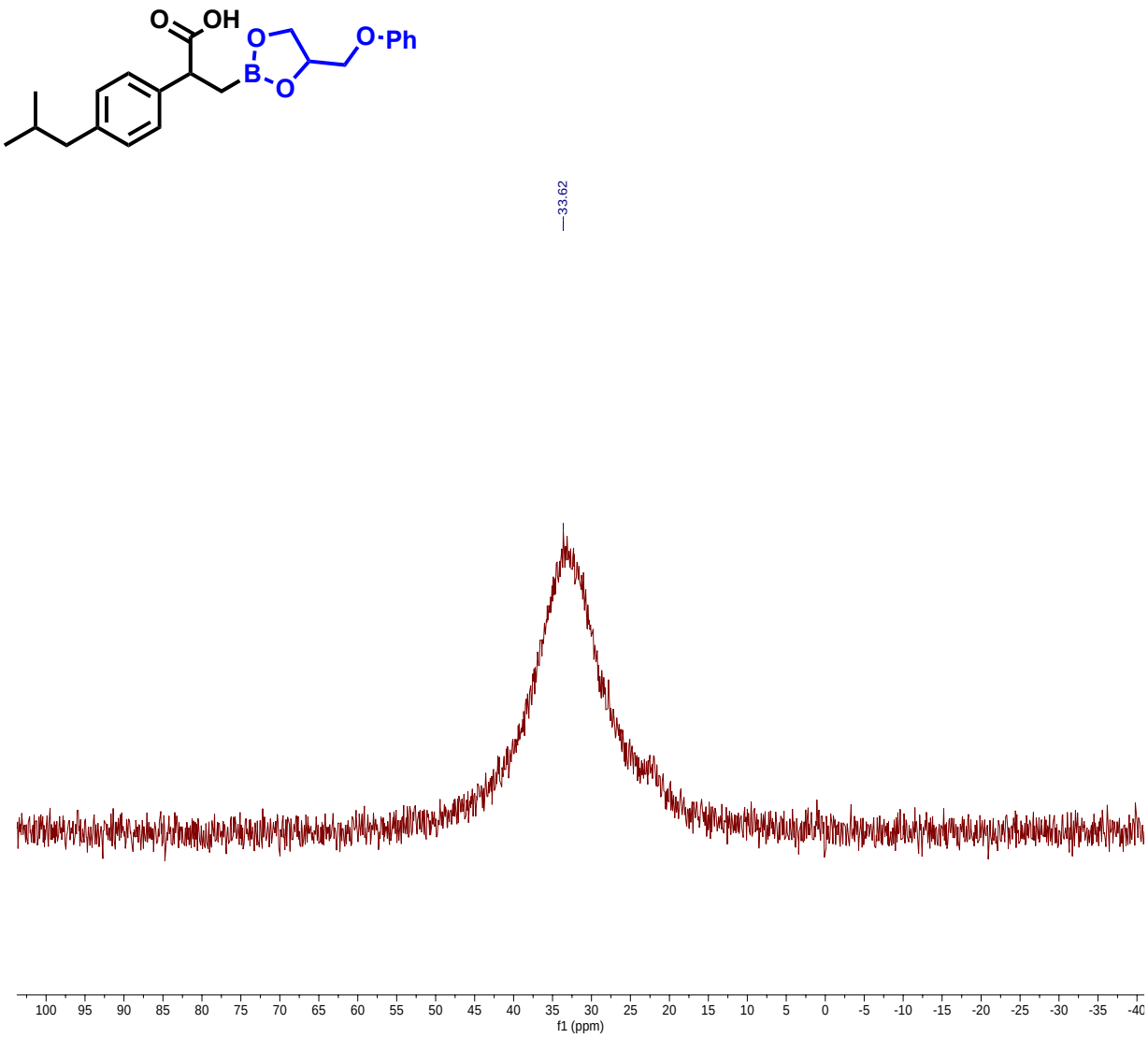

Figure A-42. ^{11}B NMR Spectrum of 5a in $CDCl_3$.

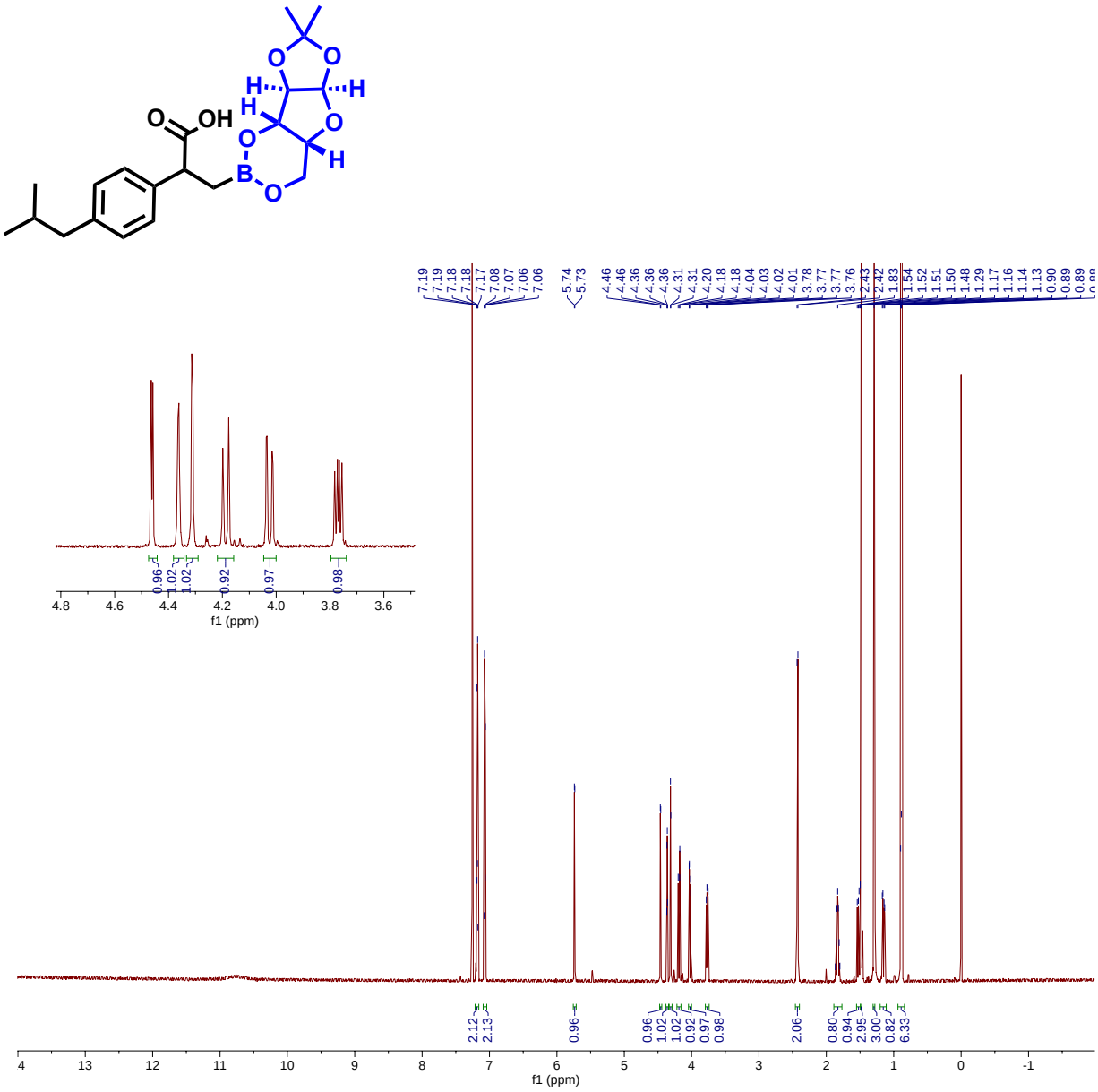

Figure A-43. ^{1}H NMR Spectrum of 5b in $CDCl_3$.

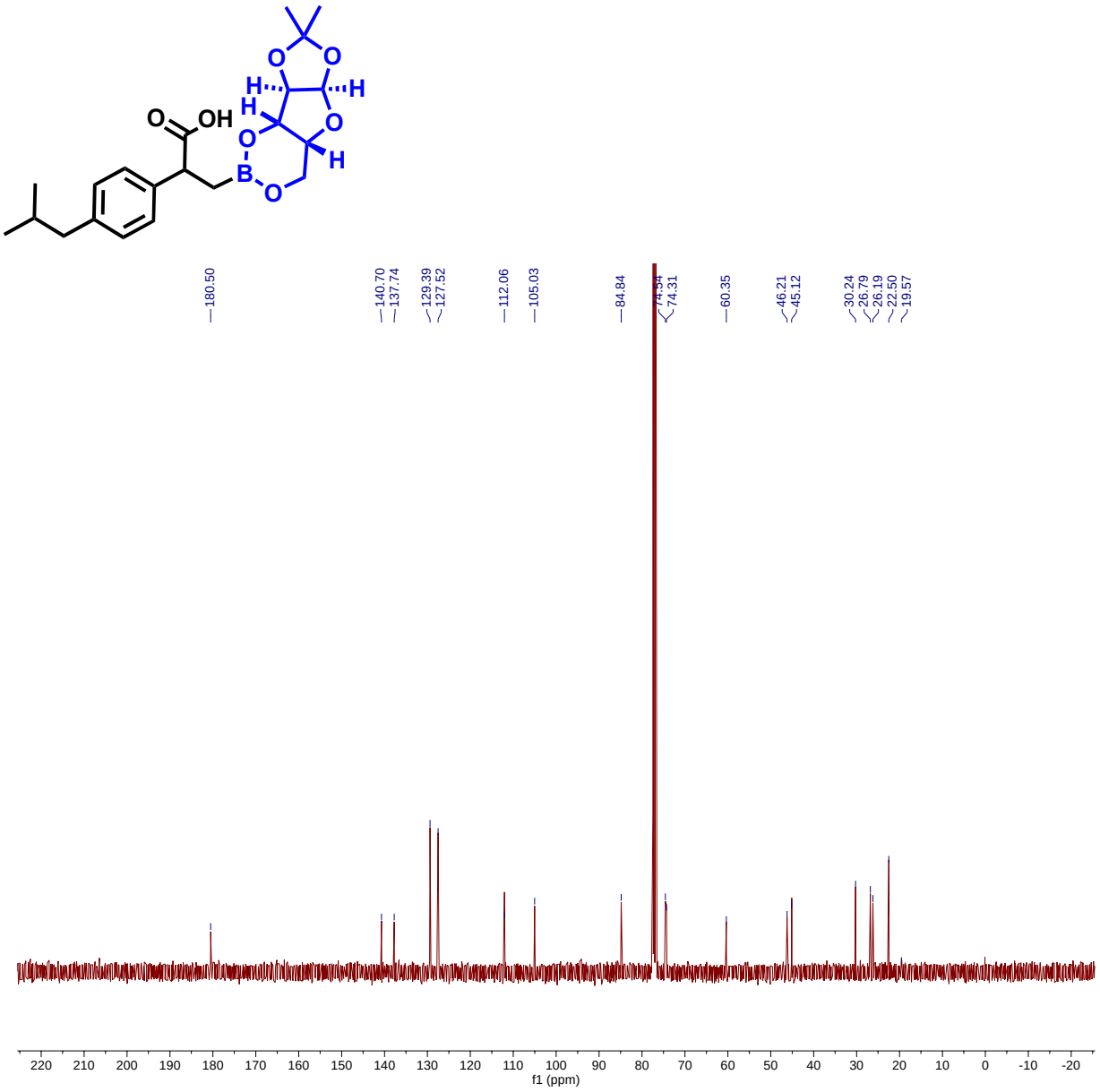

Figure A-44. ^{13}C NMR Spectrum of 5b in $CDCl_3$.

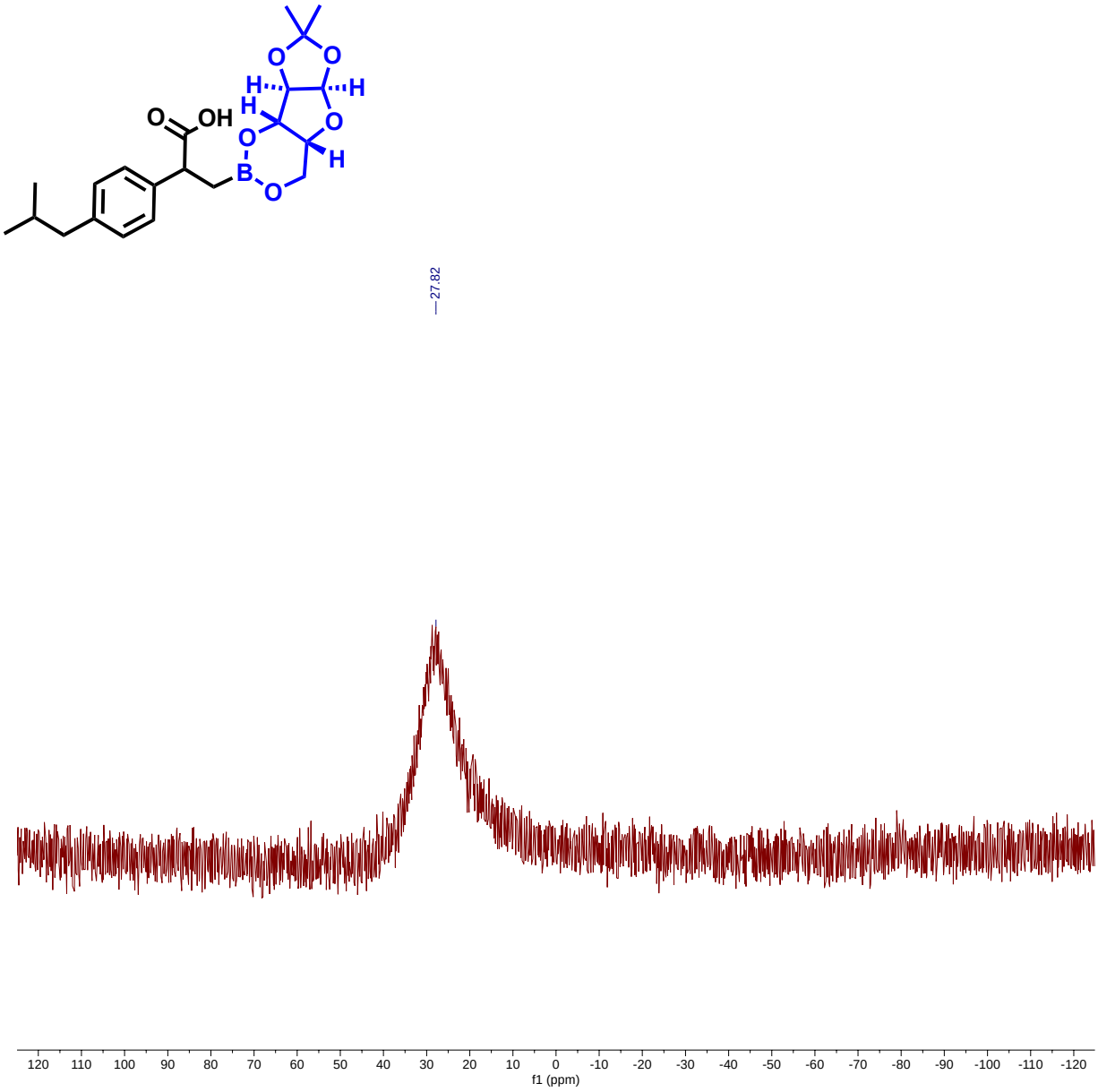

Figure A-45. ^{11}B NMR Spectrum of 5b in $CDCl_3$.

^{1}H, ^{13}C, ^{11}B and ^{19}F NMR Spectra-Compounds in Chapter IV

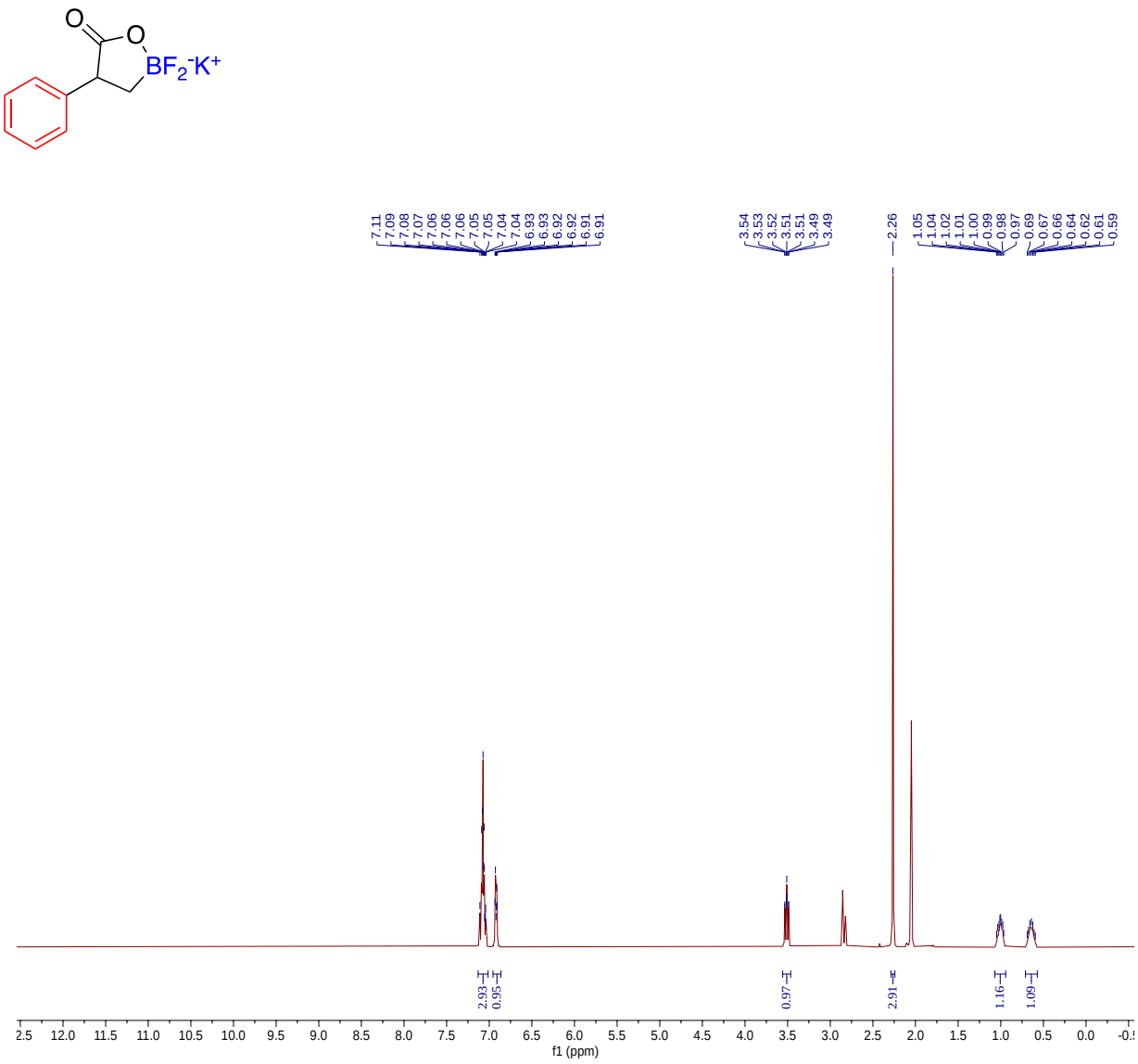

Figure A-46. ^{1}H NMR Spectrum of 2a in Acetone-d_6.

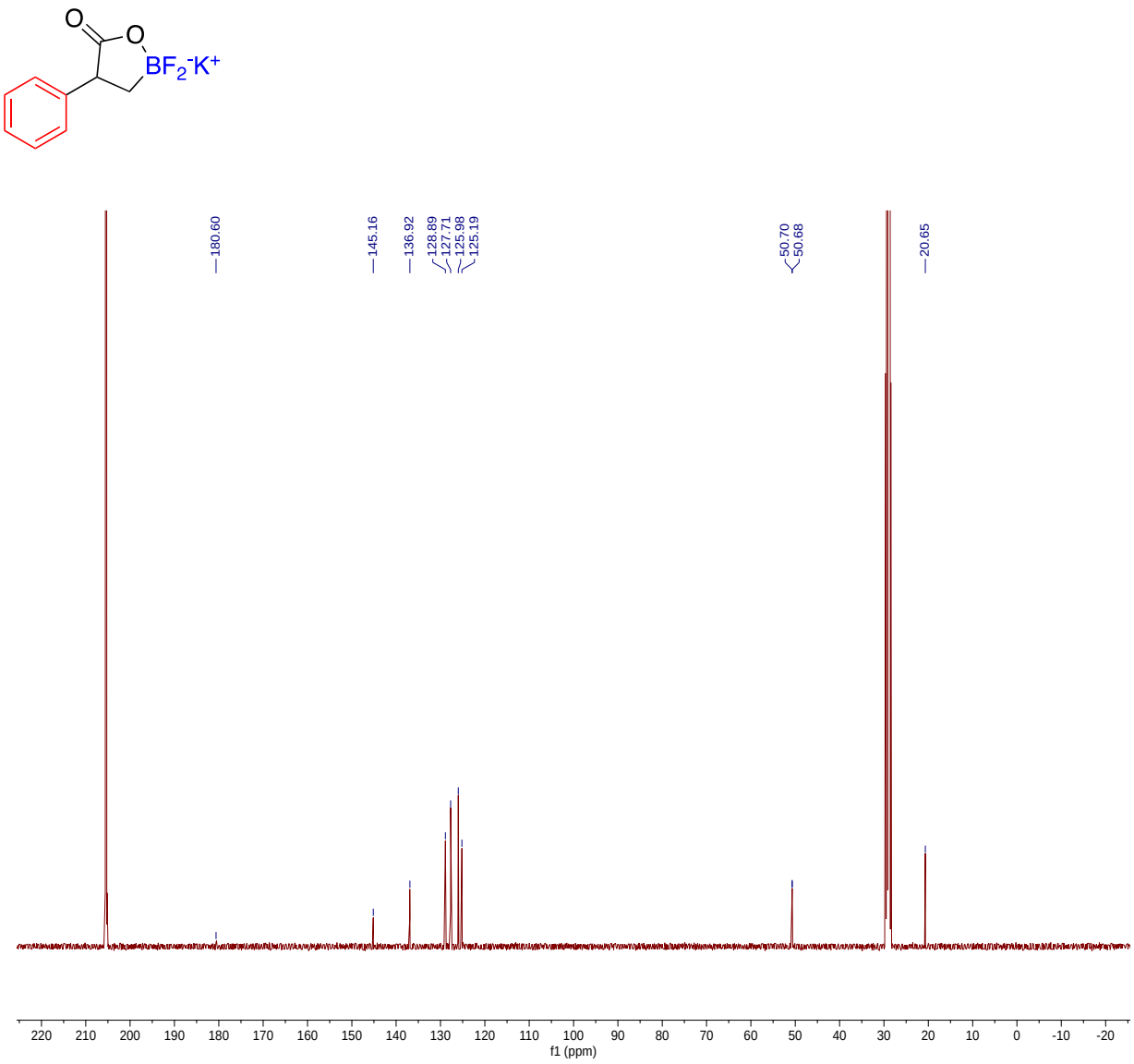

Figure A-47. ^{13}C NMR Spectrum of 2a in Acetone-d_6.

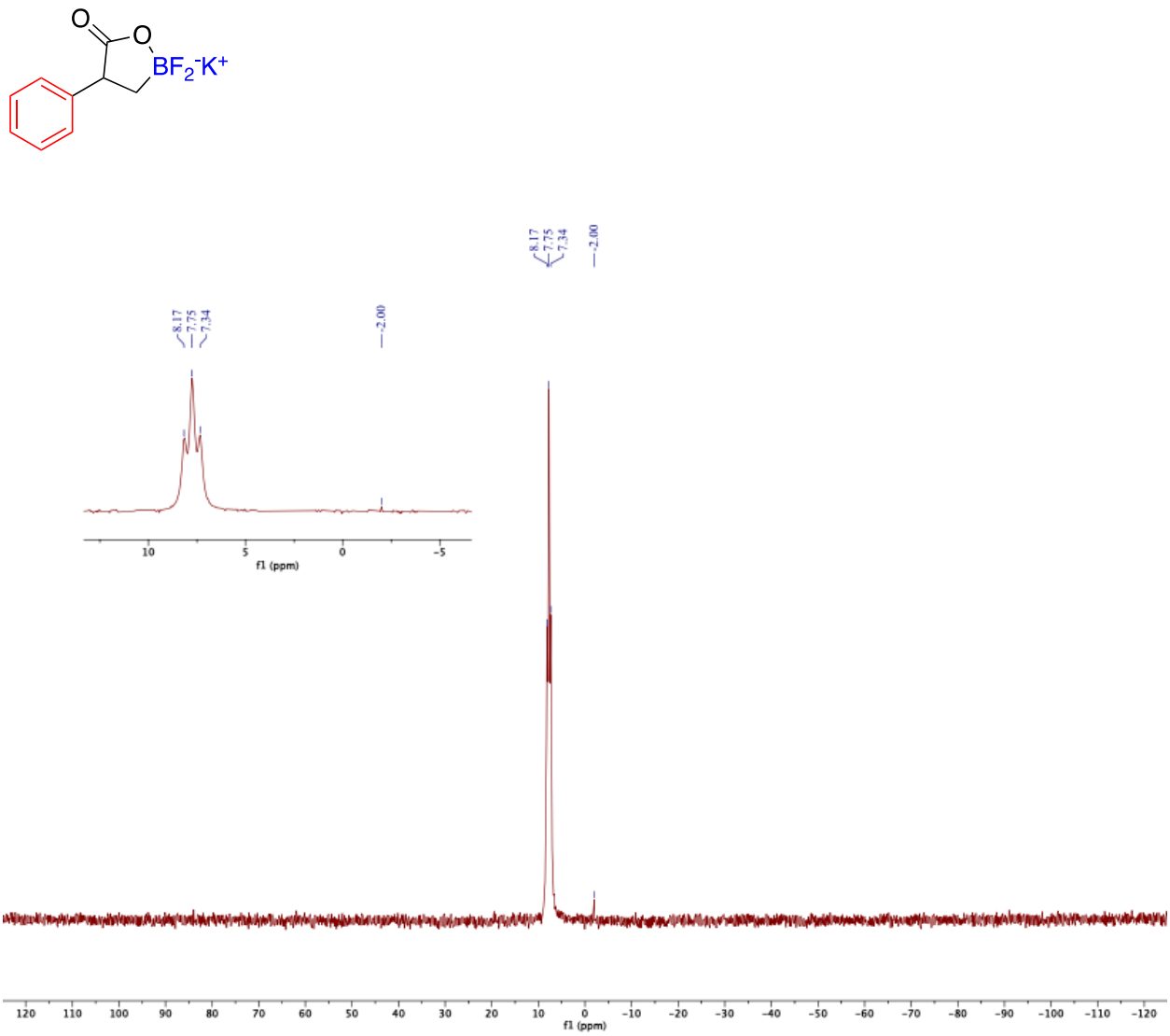

Figure A-48. ^{11}B NMR Spectrum of 2a in Acetone-d_6.

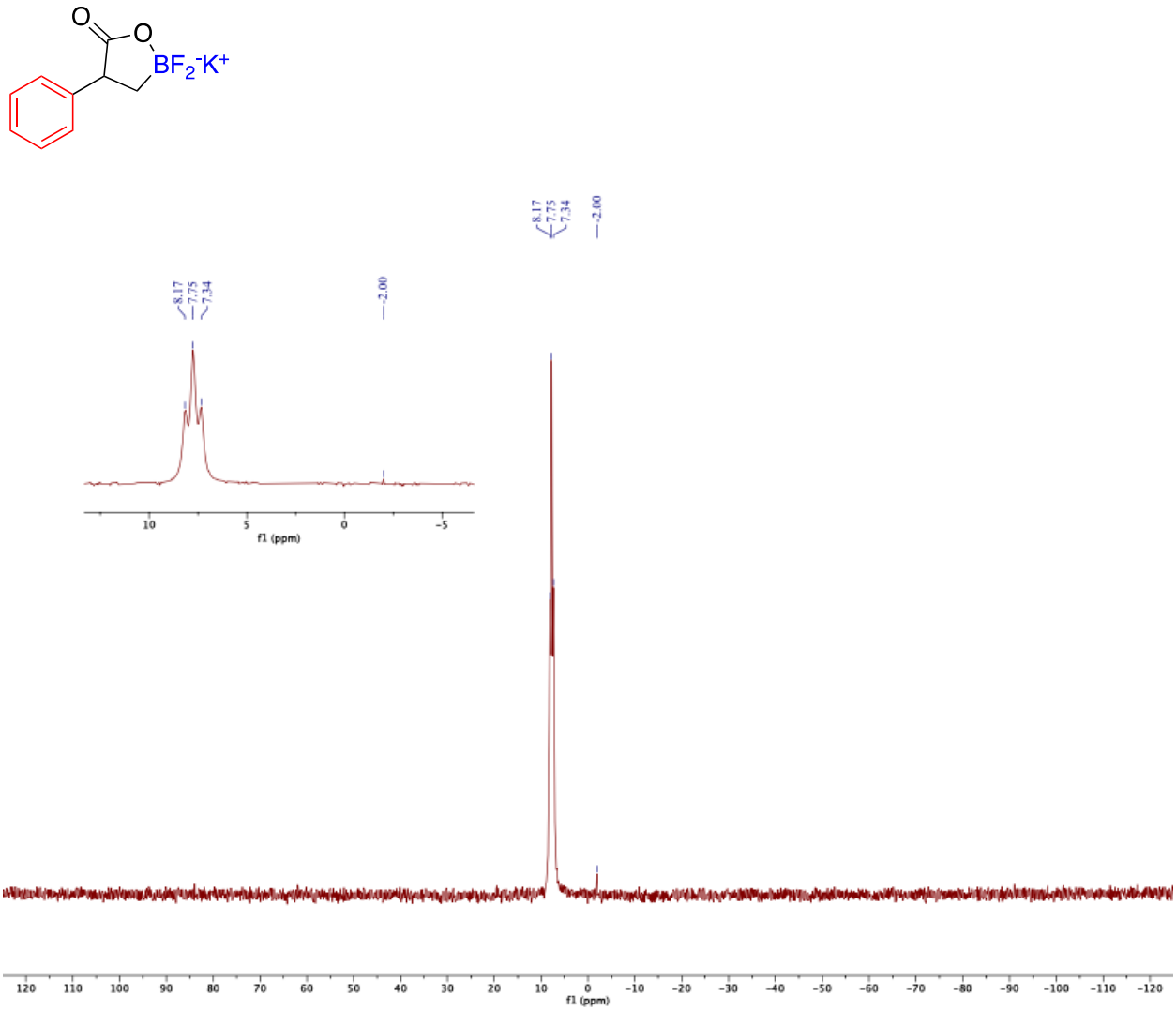

Figure A-49. ^{19}F NMR Spectrum of 2a in Acetone-d_6.

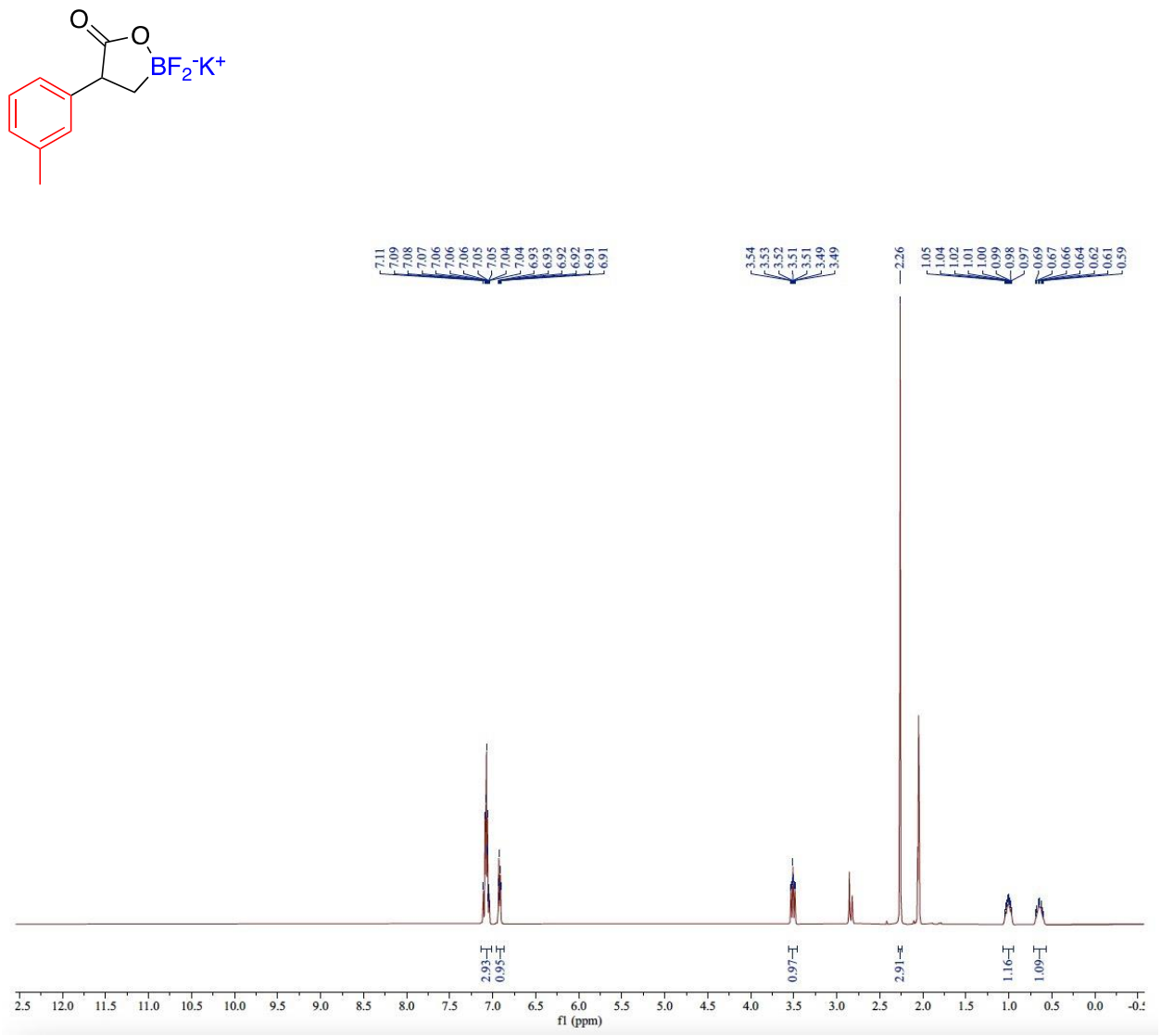

Figure A-50. ^{1}H NMR Spectrum of 2b in Acetone-d_6.

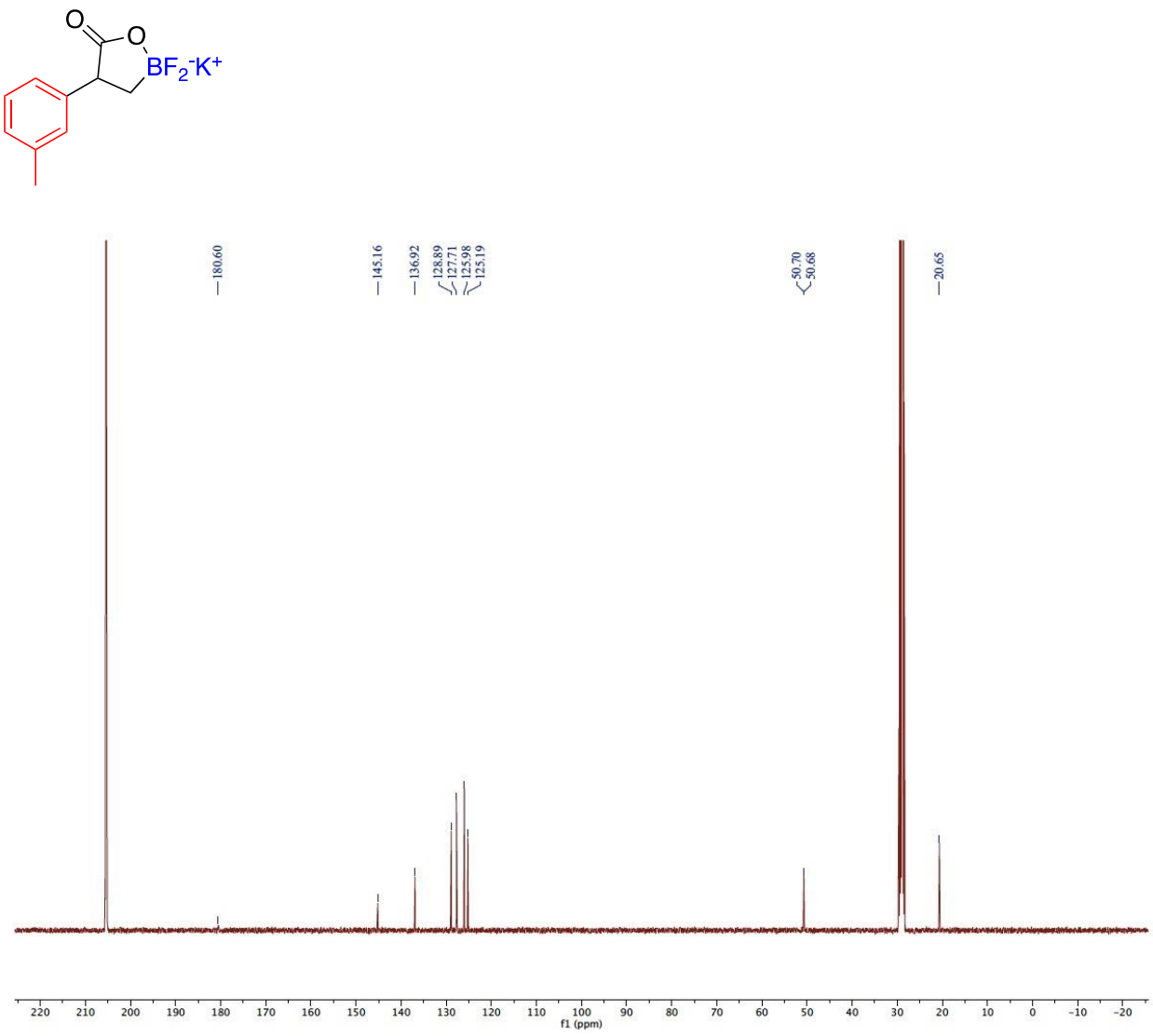

Figure A-51. ^{13}C NMR Spectrum of 2b in Acetone-d_6.

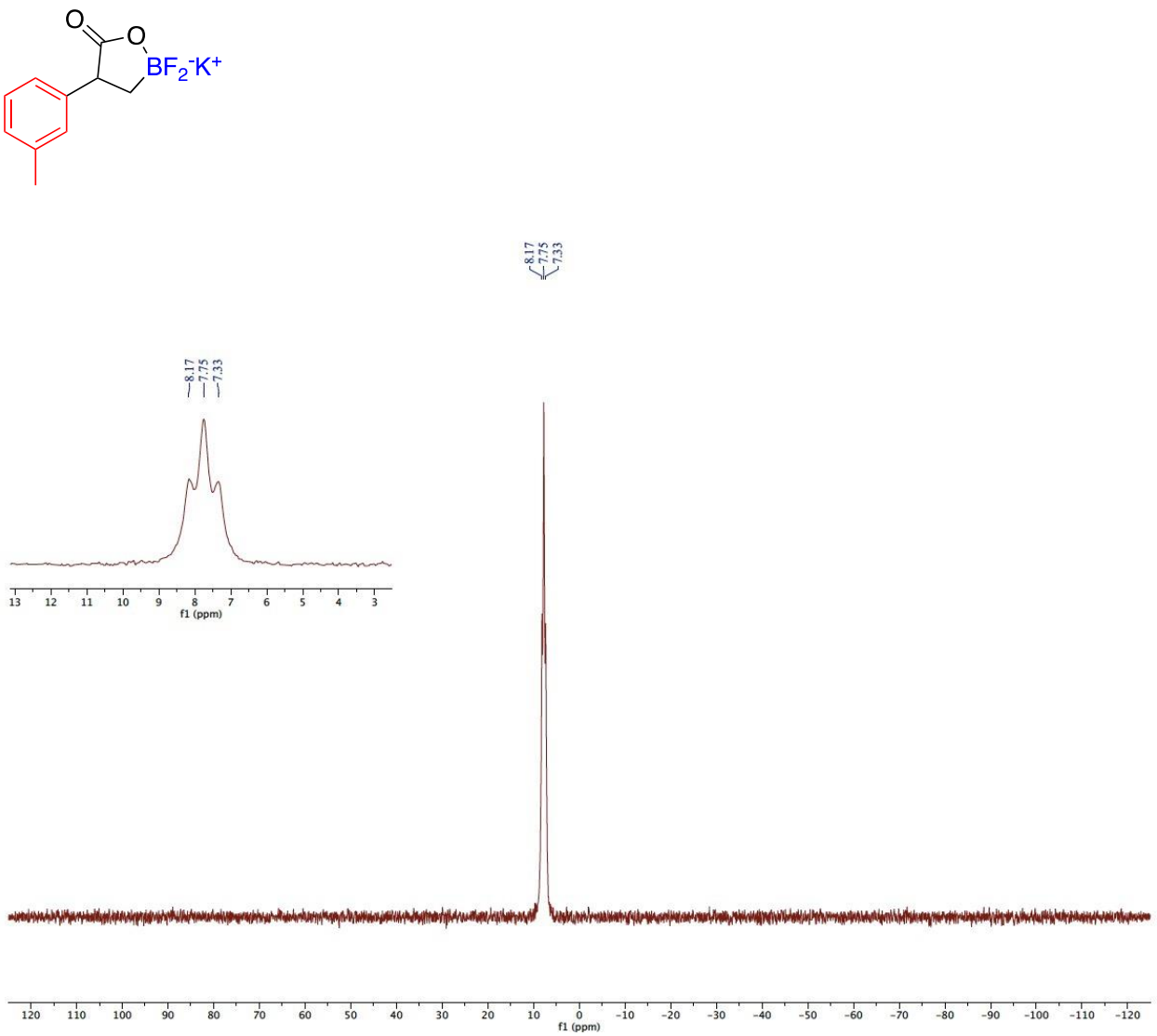

Figure A-52. ^{11}B NMR Spectrum of 2b in Acetone-d_6.

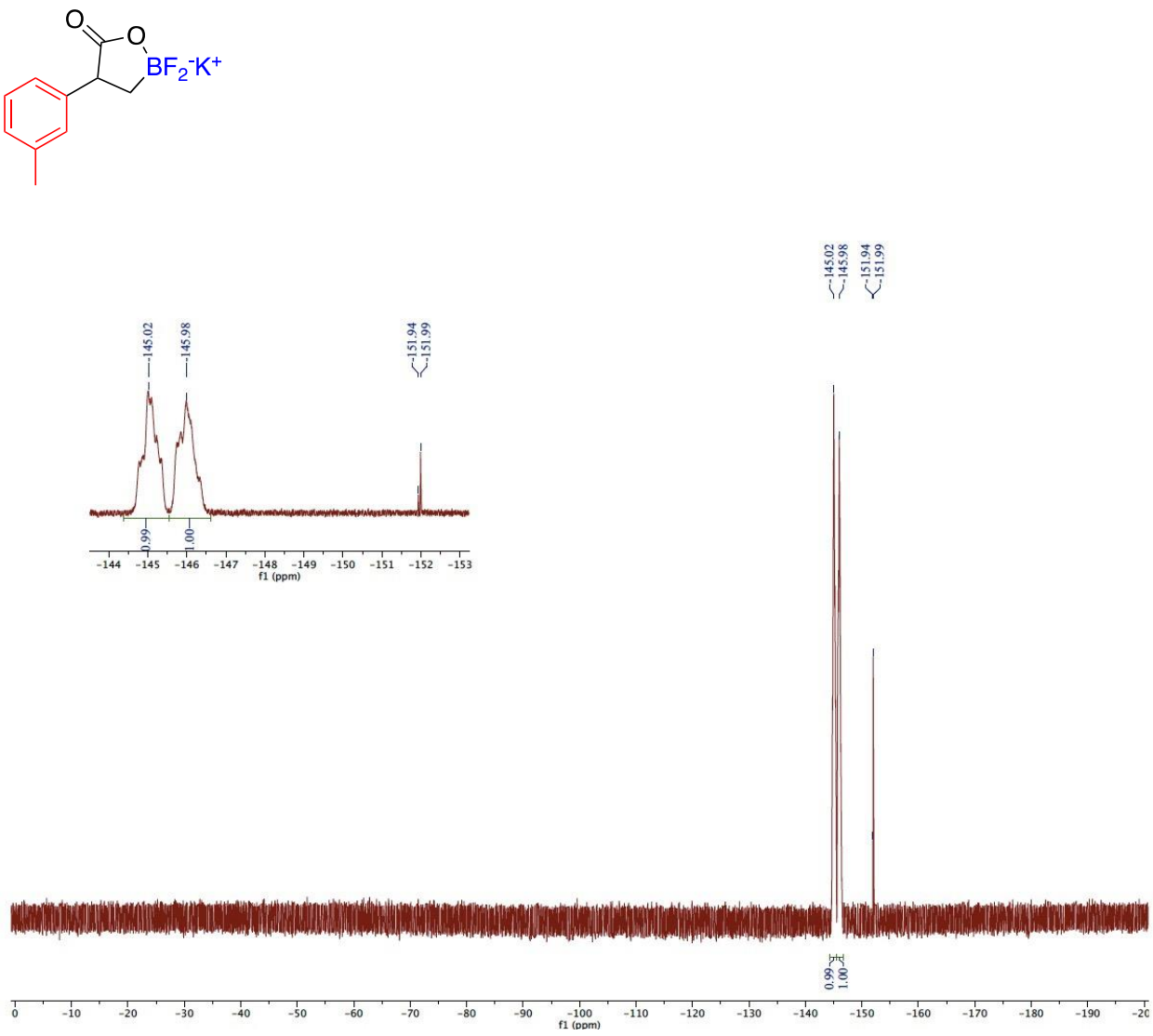

Figure A-53. ^{19}F NMR Spectrum of 2b in Acetone-d_6.

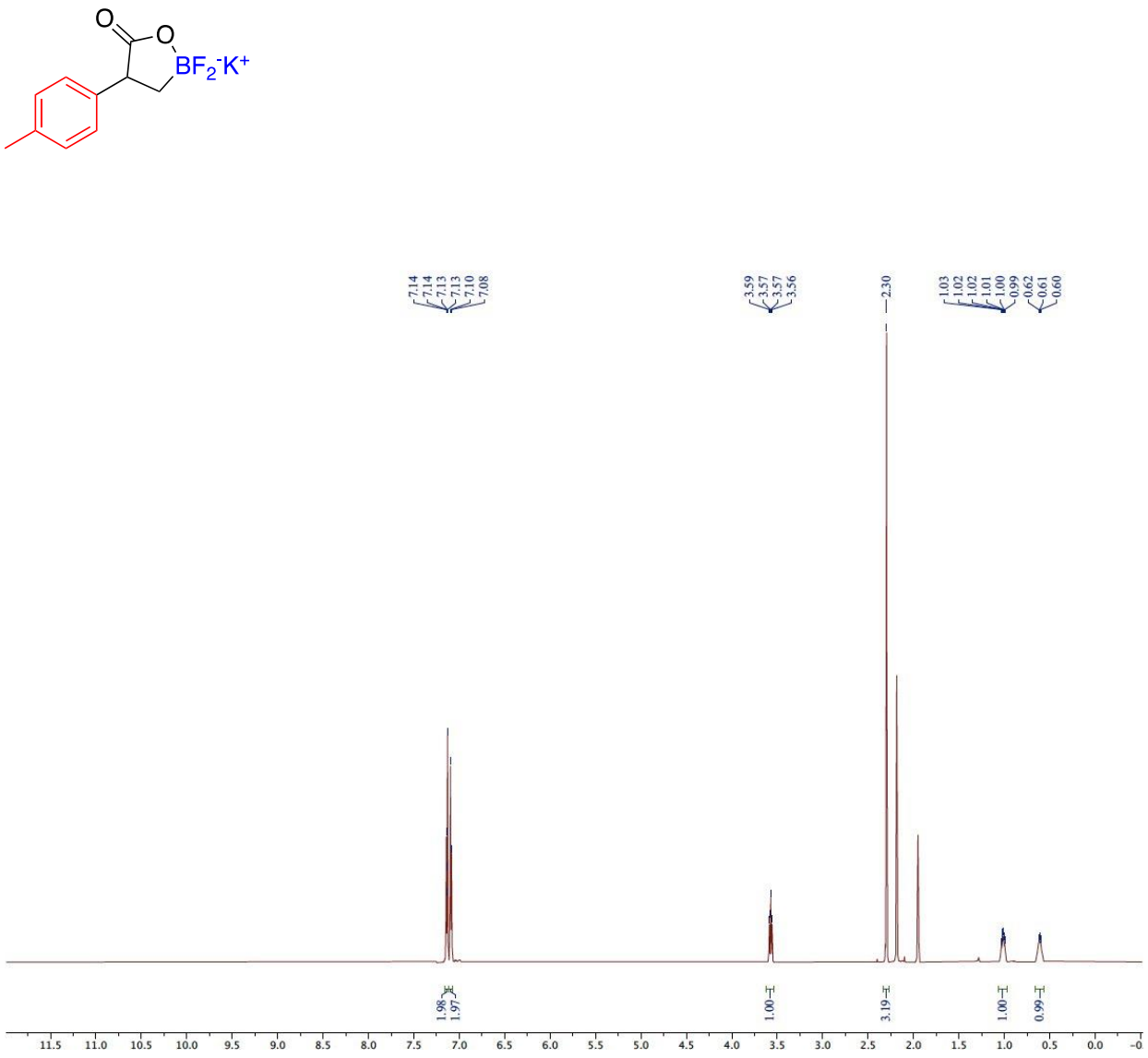

Figure A-54. ^{1}H NMR Spectrum of 2c in Acetone-d_6.

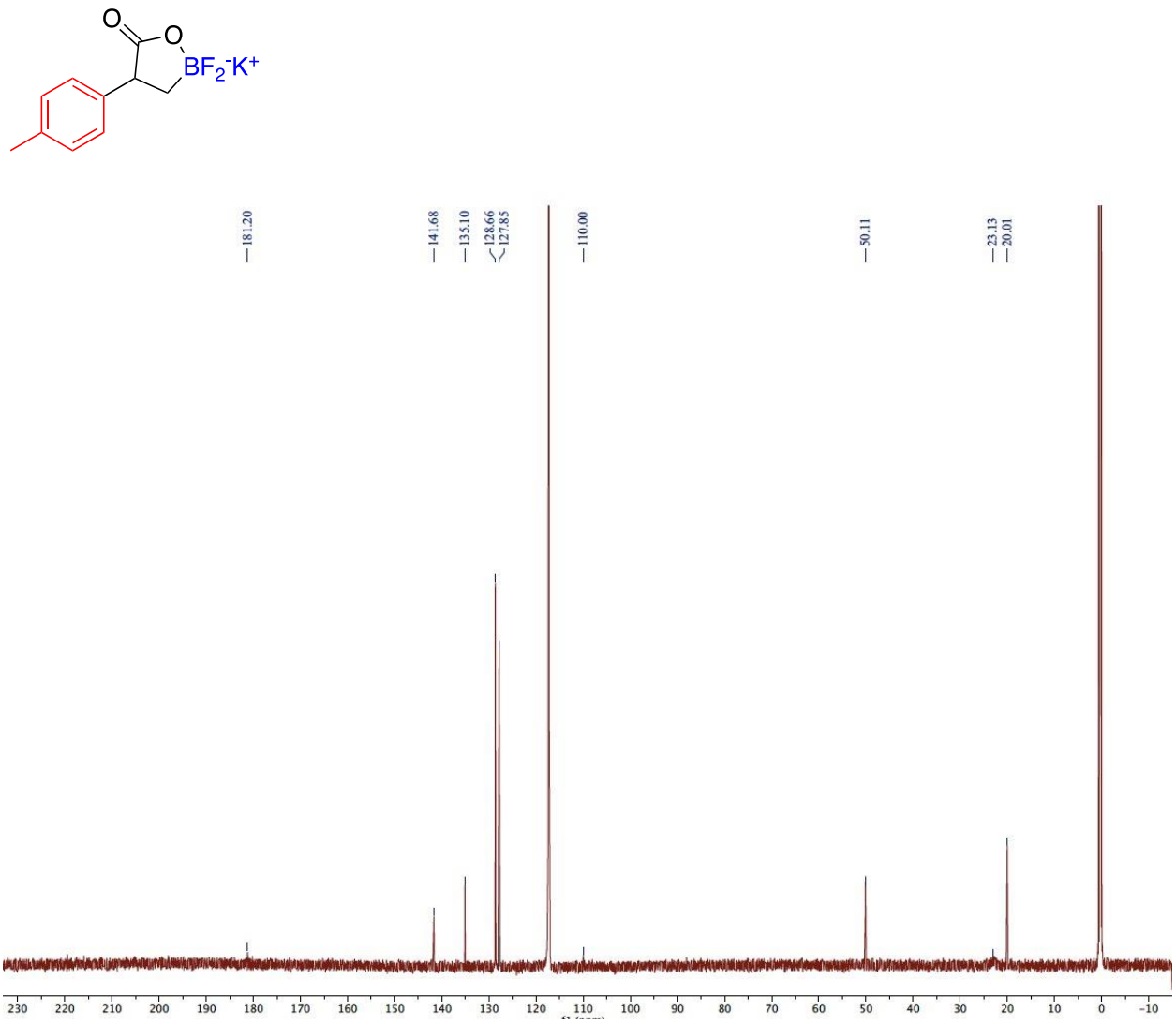

Figure A-55. ^{13}C NMR Spectrum of 2c in Acetone-d_6.

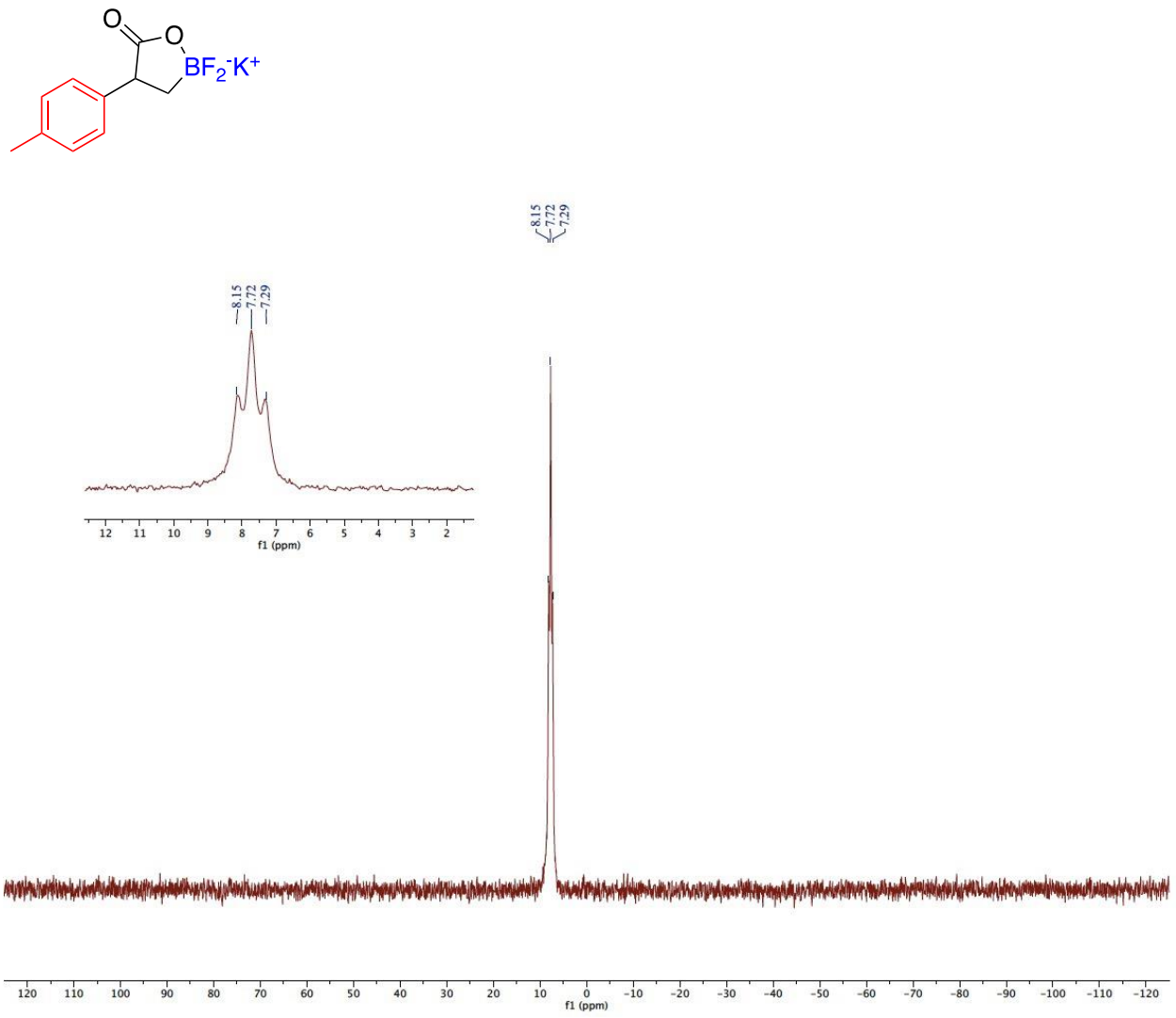

Figure A-56. ^{11}B NMR Spectrum of 2c in Acetone-d_6.

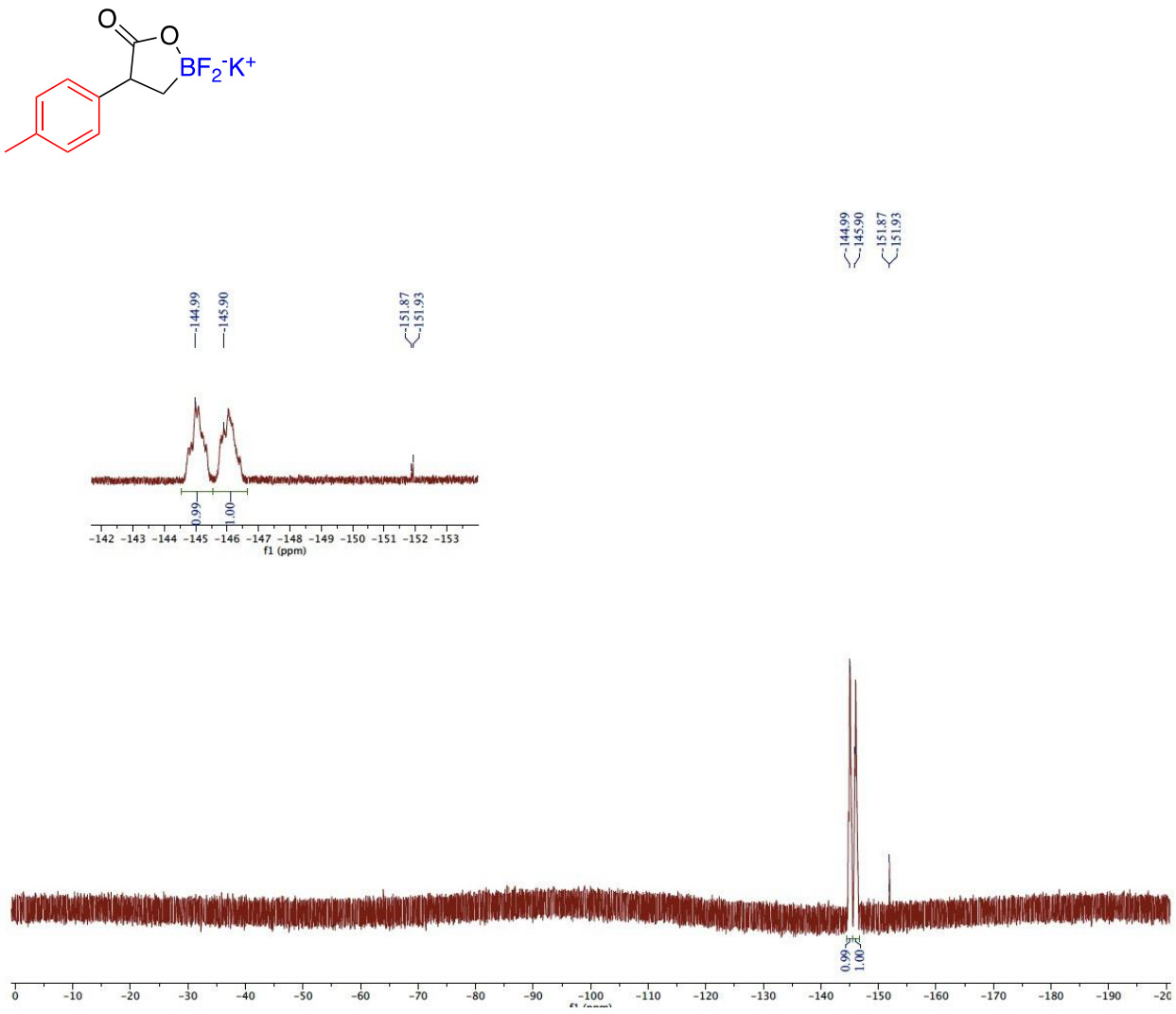

Figure A-57. ^{19}F NMR Spectrum of 2c in Acetone-d_6.

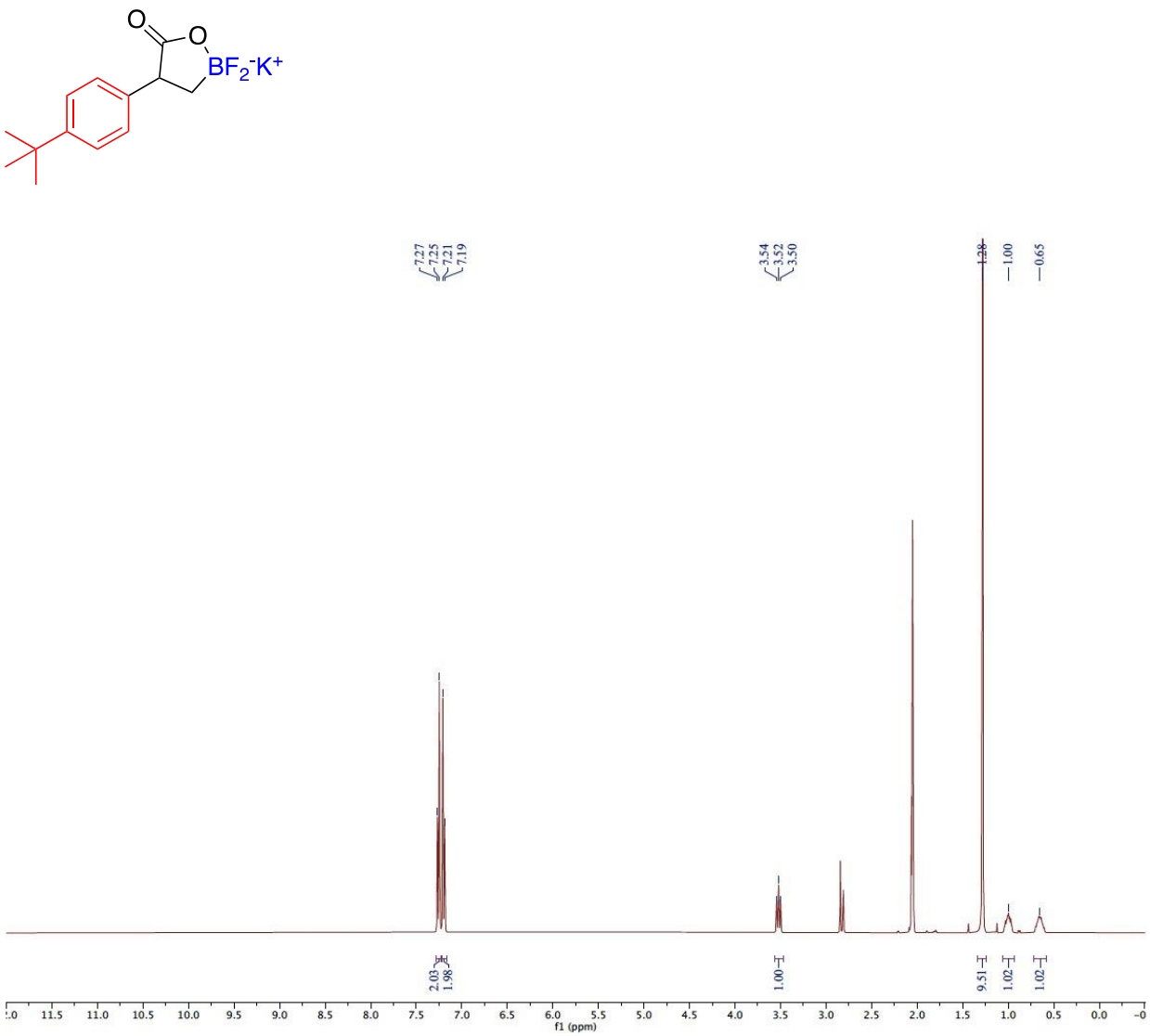

Figure A-58. ^{1}H NMR Spectrum of 2d in Acetone-d_6.

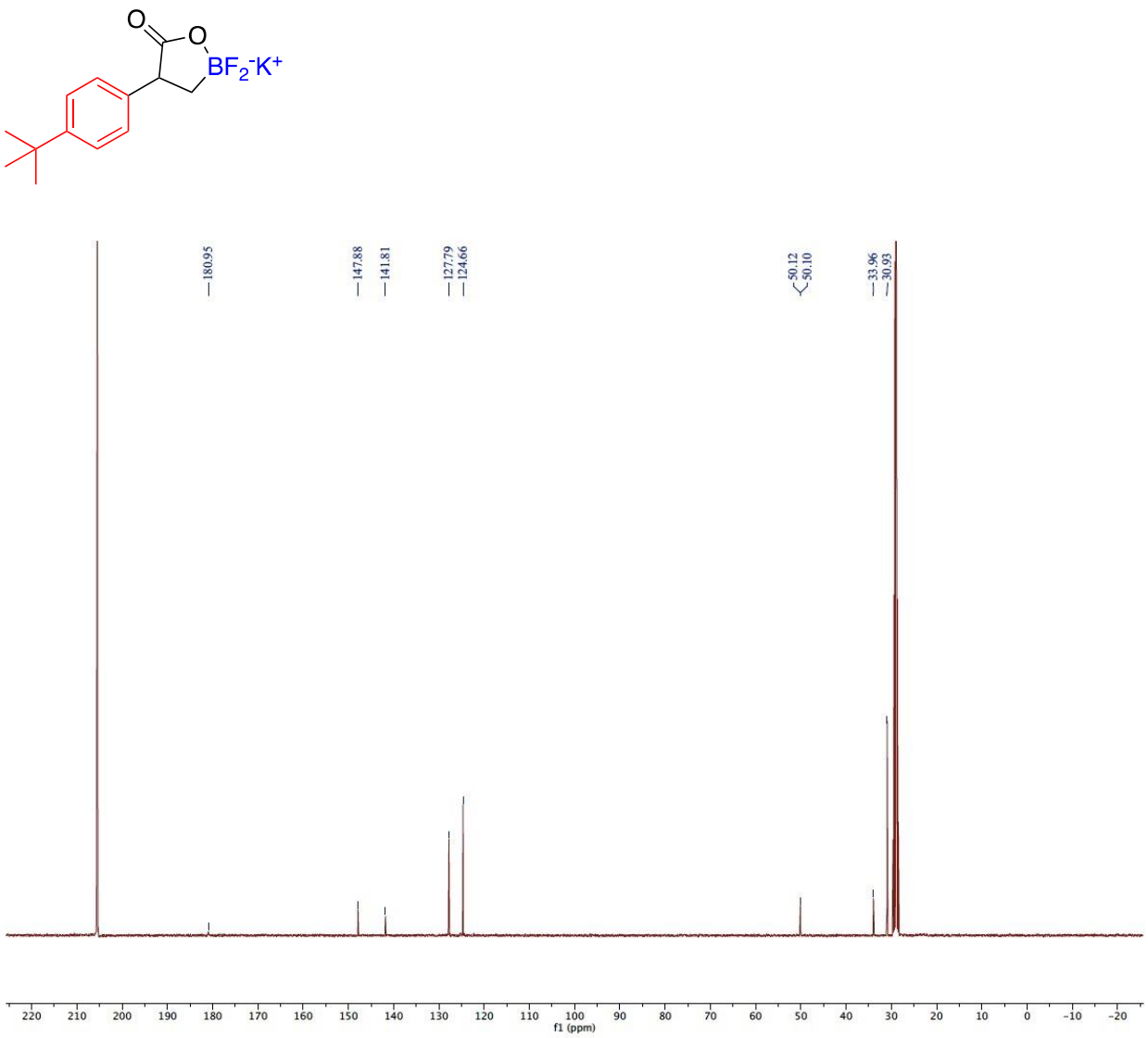

Figure A-59. ^{13}C NMR Spectrum of 2d in Acetone-d_6.

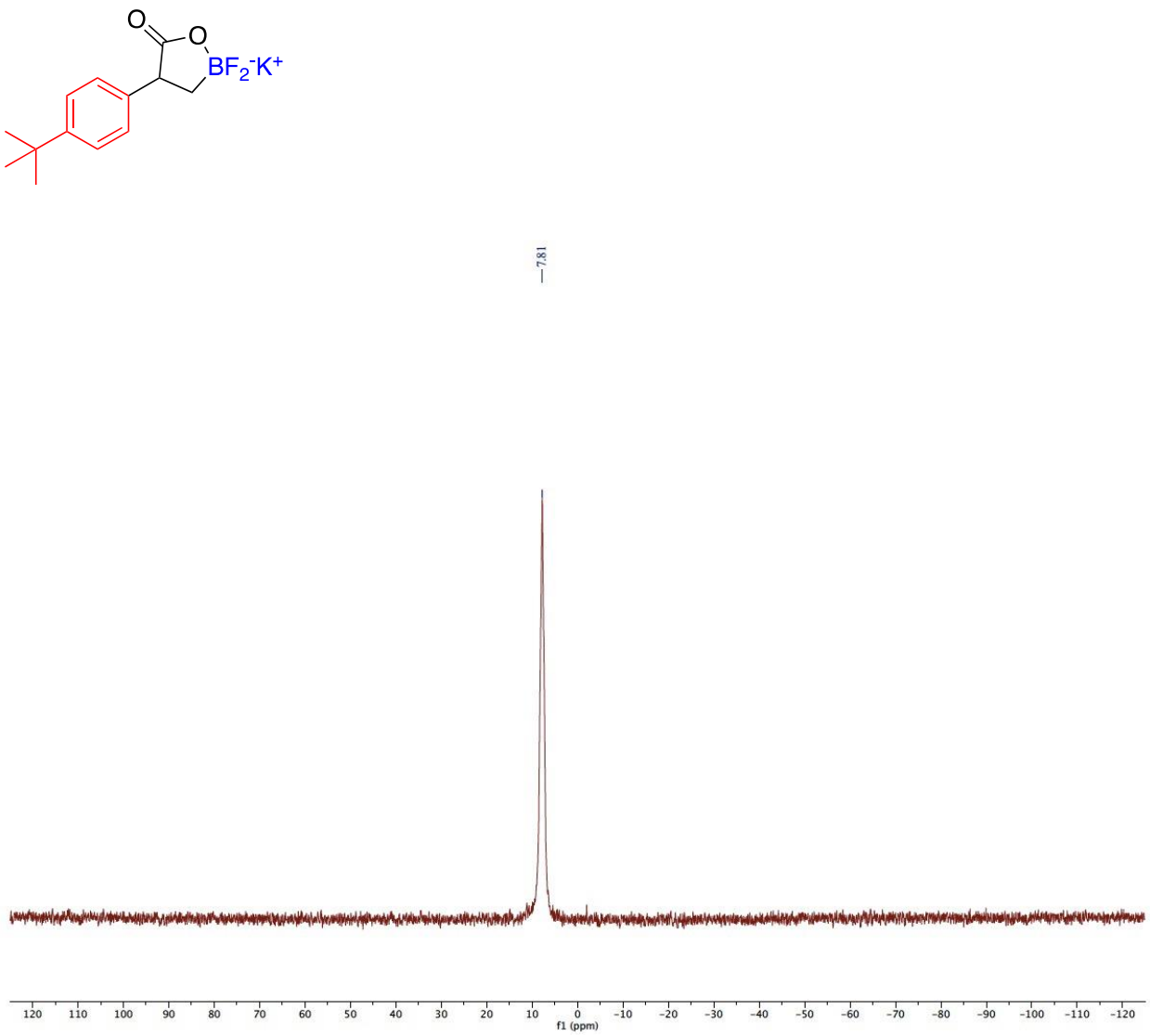

Figure A-60. ^{11}B NMR Spectrum of 2d in Acetone-d_6.

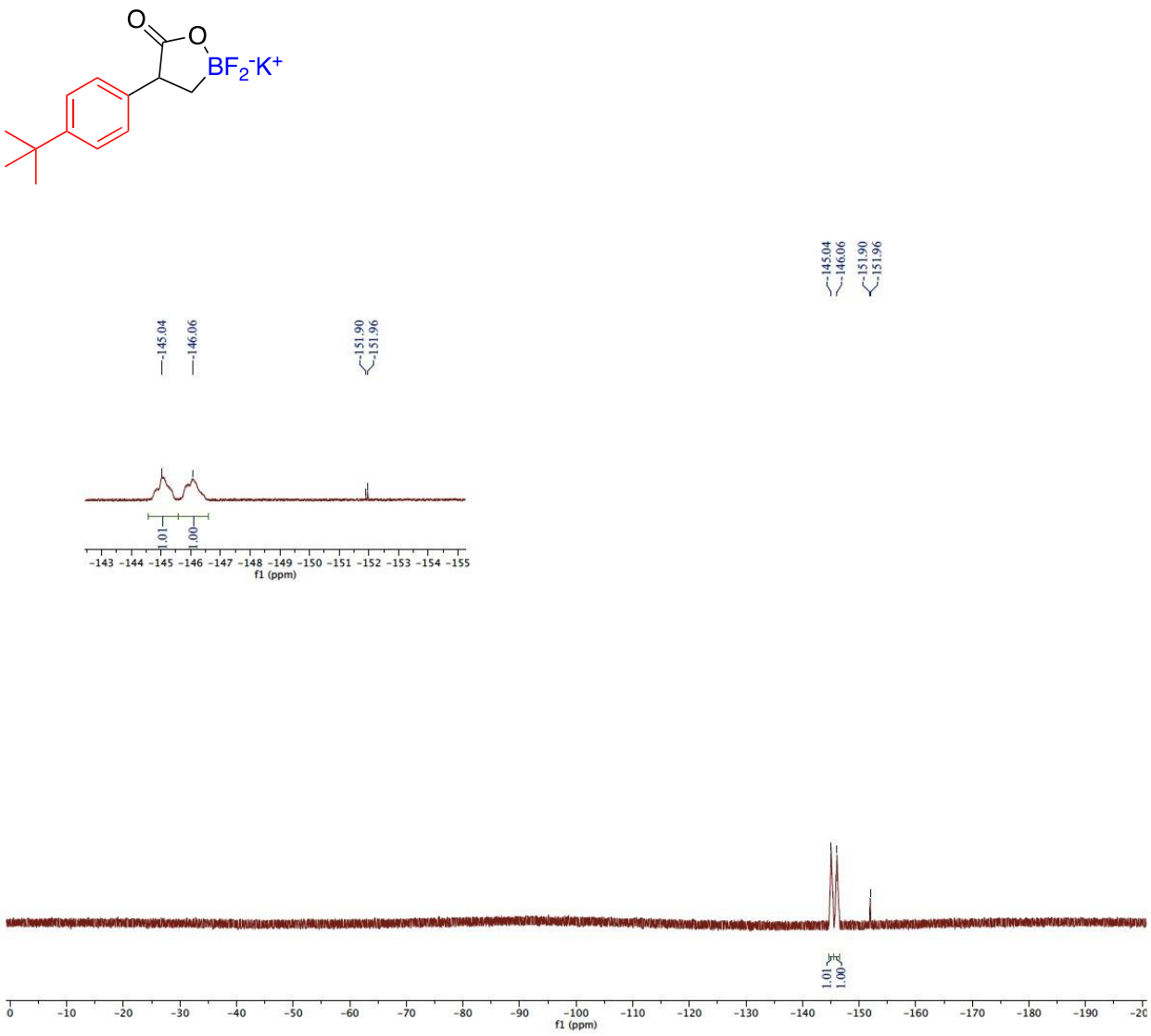

Figure A-61. ^{19}F NMR Spectrum of 2d in Acetone-d_6.

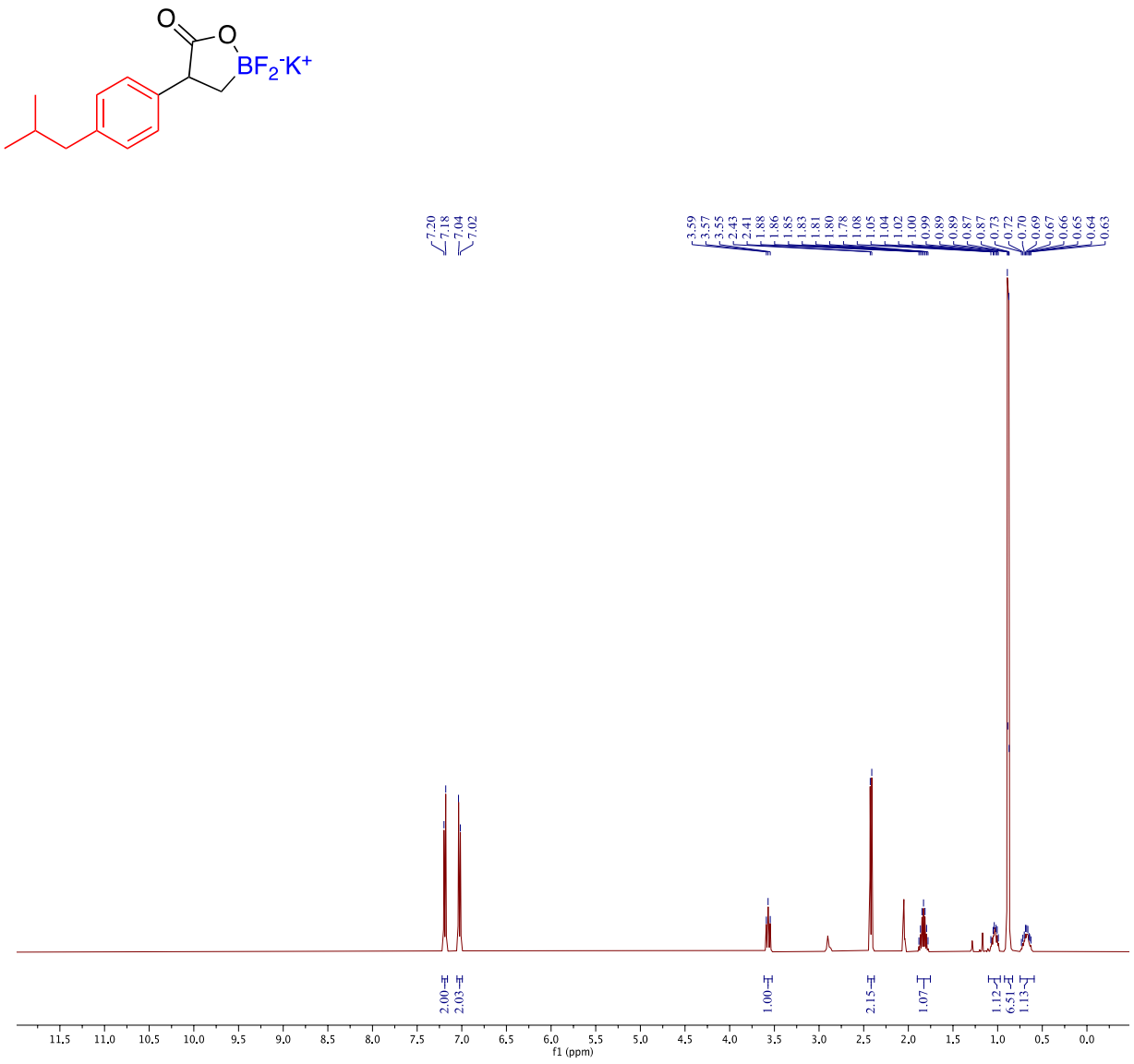

Figure A-62. ^{1}H NMR Spectrum of 2e in Acetone-d_6.

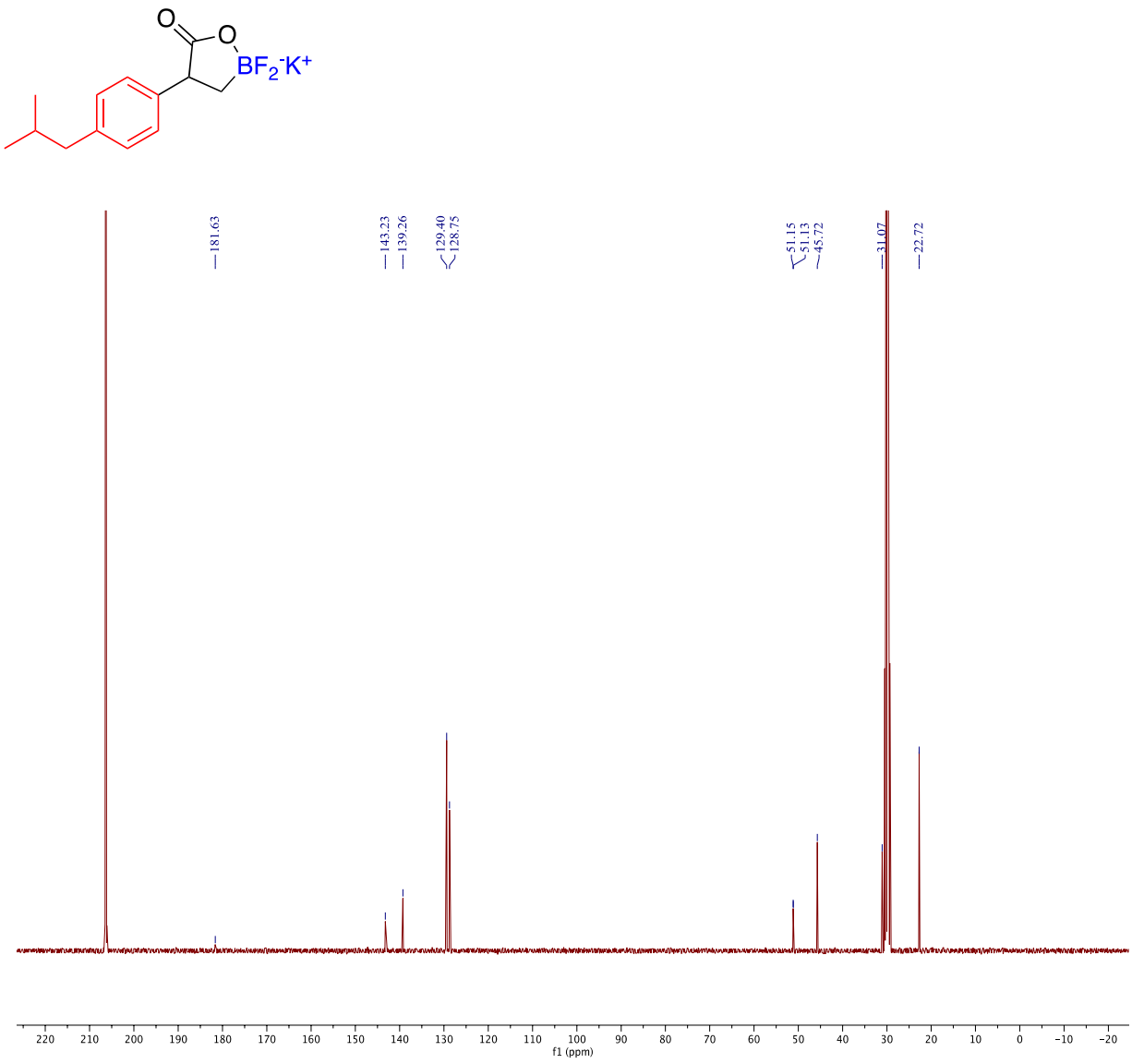

Figure A-63. ^{13}C NMR Spectrum of 2e in Acetone-d_6.

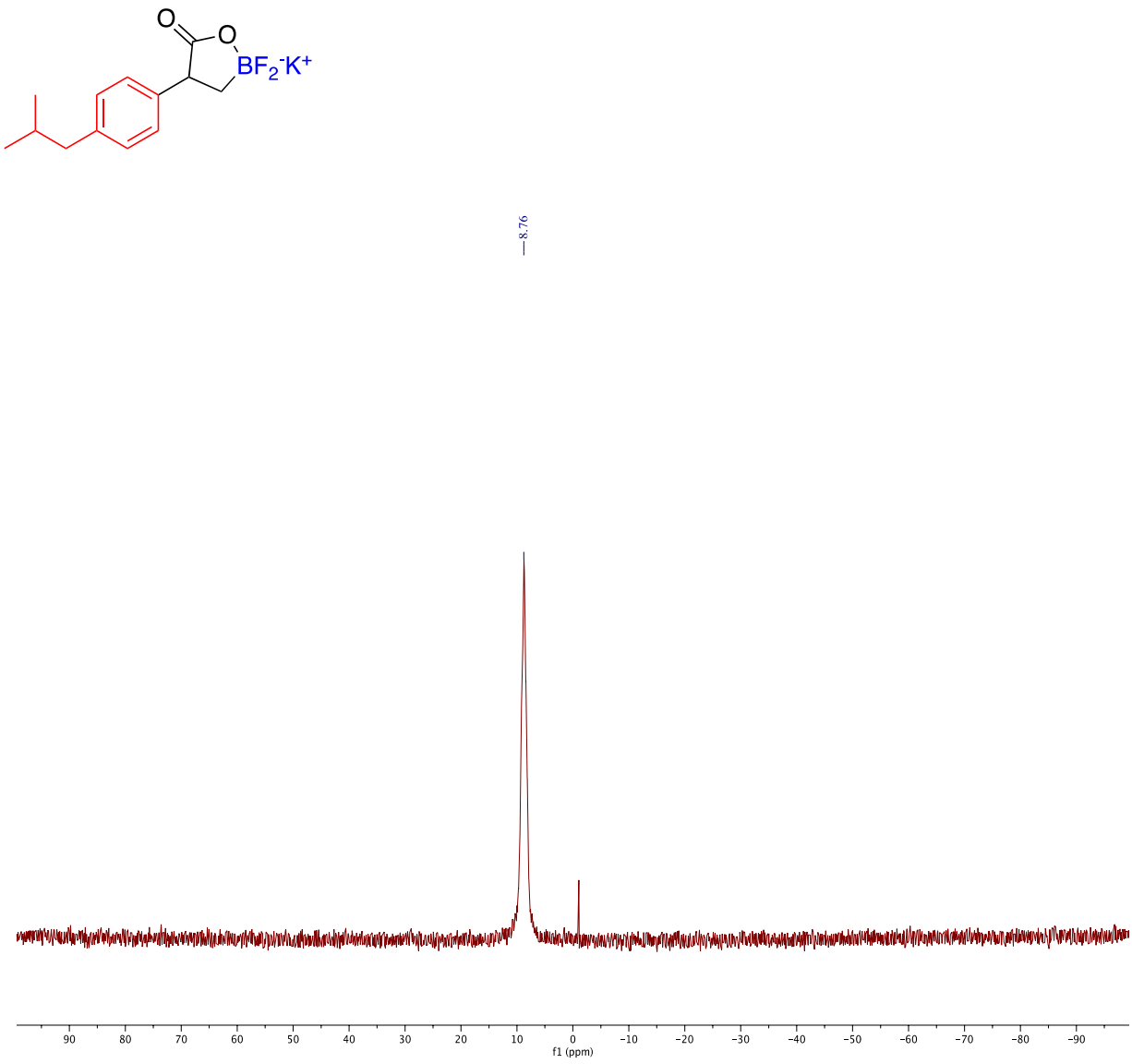

Figure A-64. ^{11}B NMR Spectrum of 2e in Acetone-d_6.

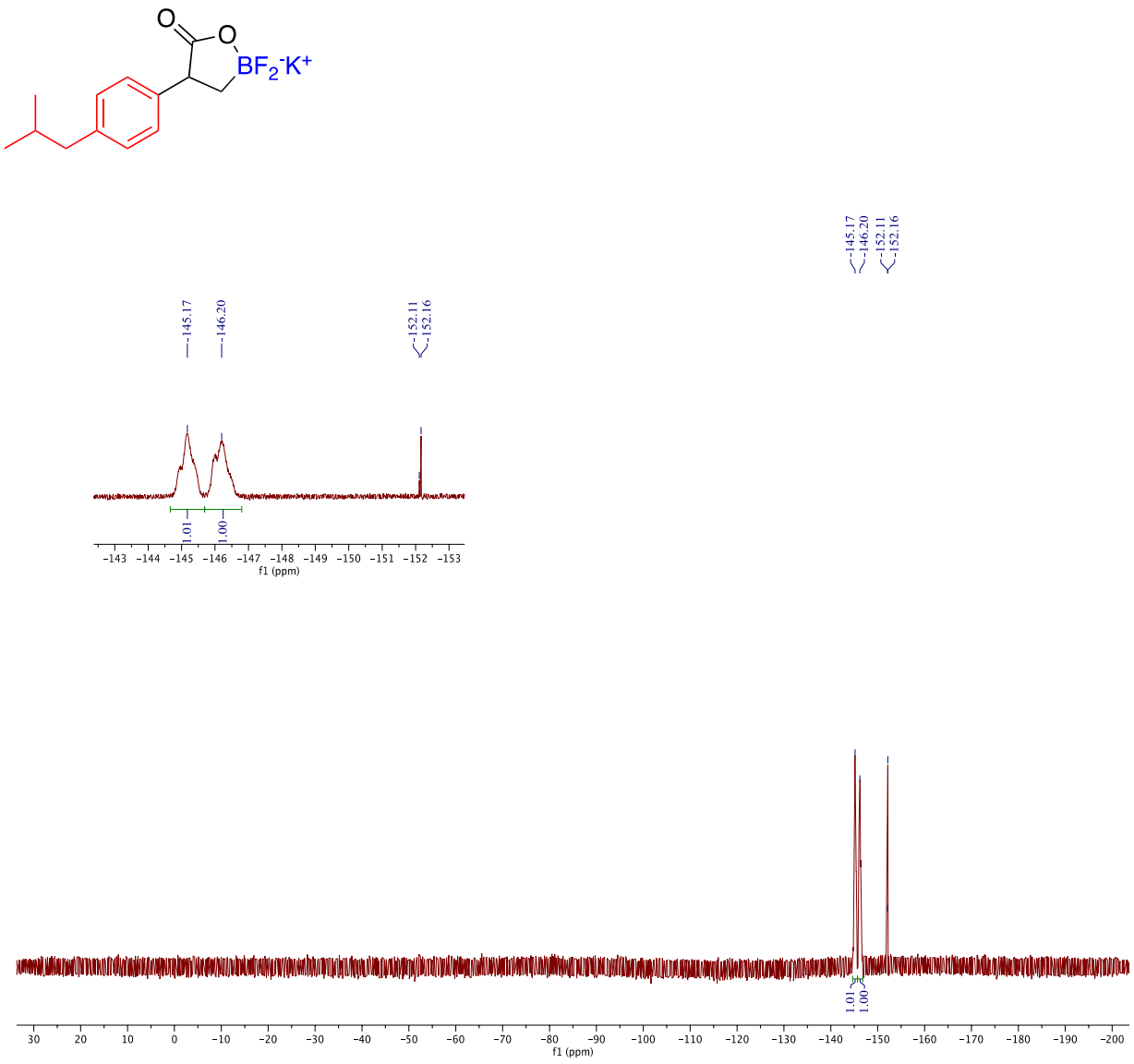

Figure A-65. ^{19}F NMR Spectrum of 2e in Acetone-d_6.

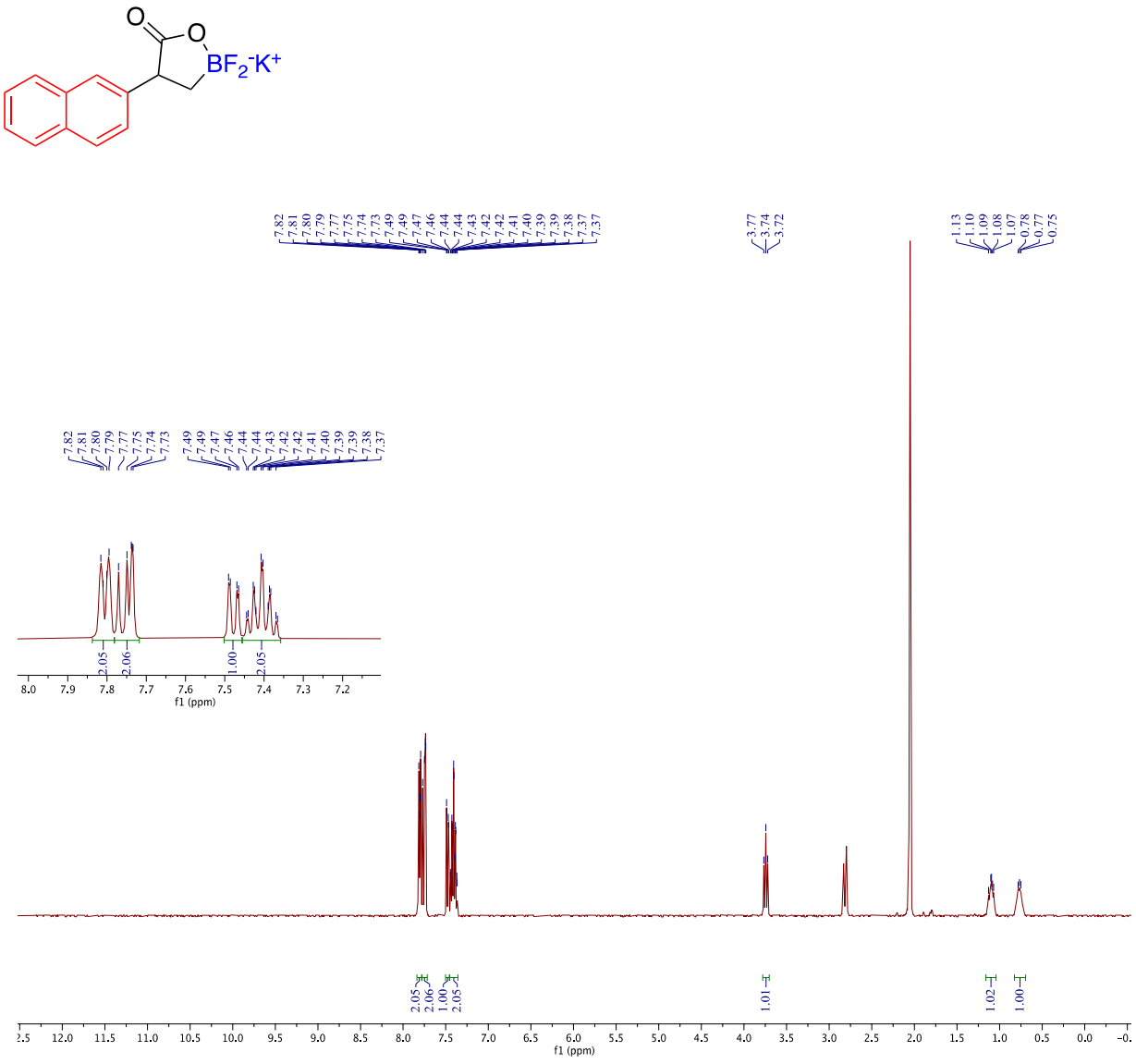

Figure A-66. ^{1}H NMR Spectrum of 2f in Acetone-d_6.

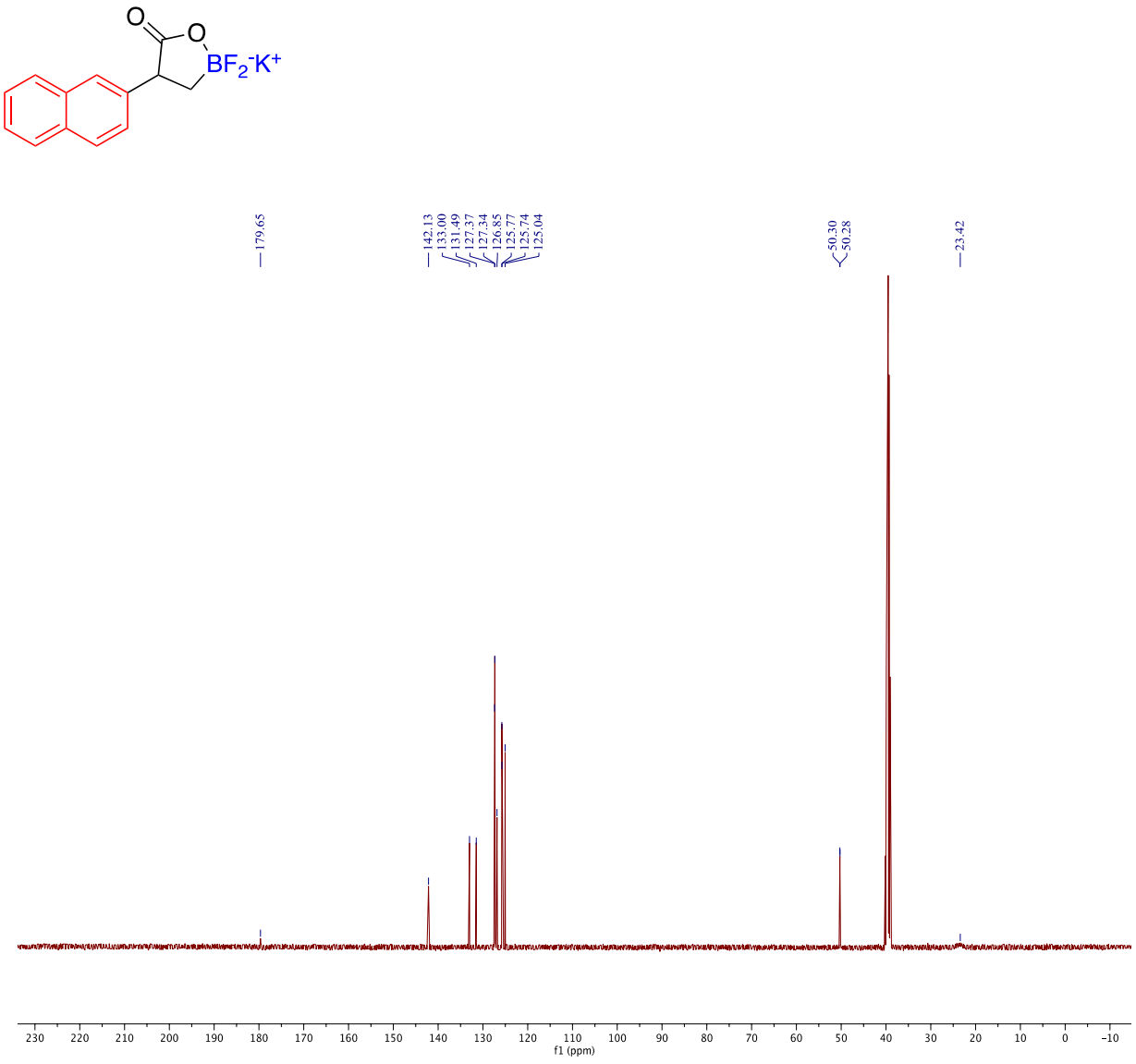

Figure A-67. ^{13}C NMR Spectrum of 2f in DMSO-d_6.

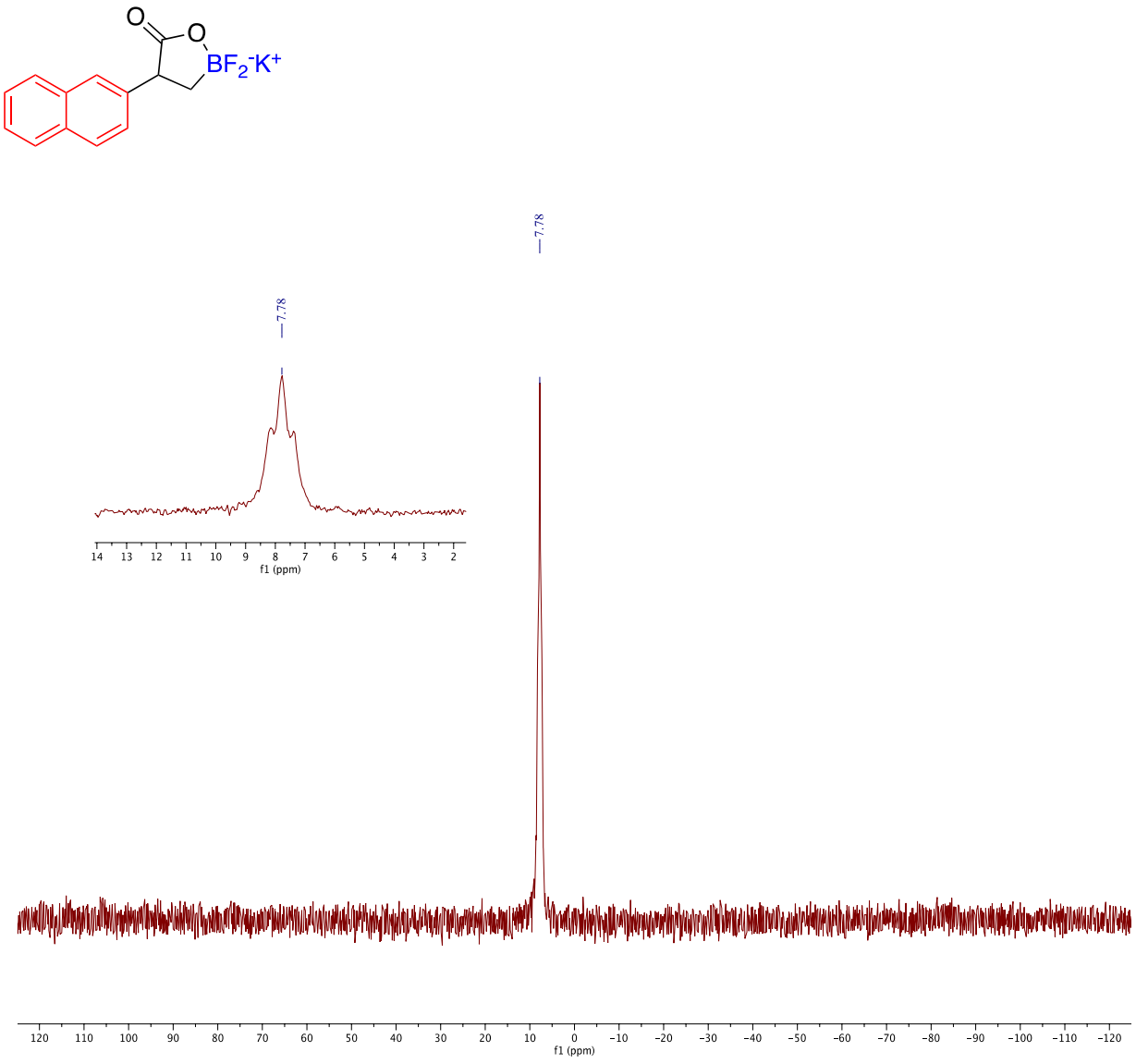

Figure A-68. ^{11}B NMR Spectrum of 2f in Acetone-d_6.

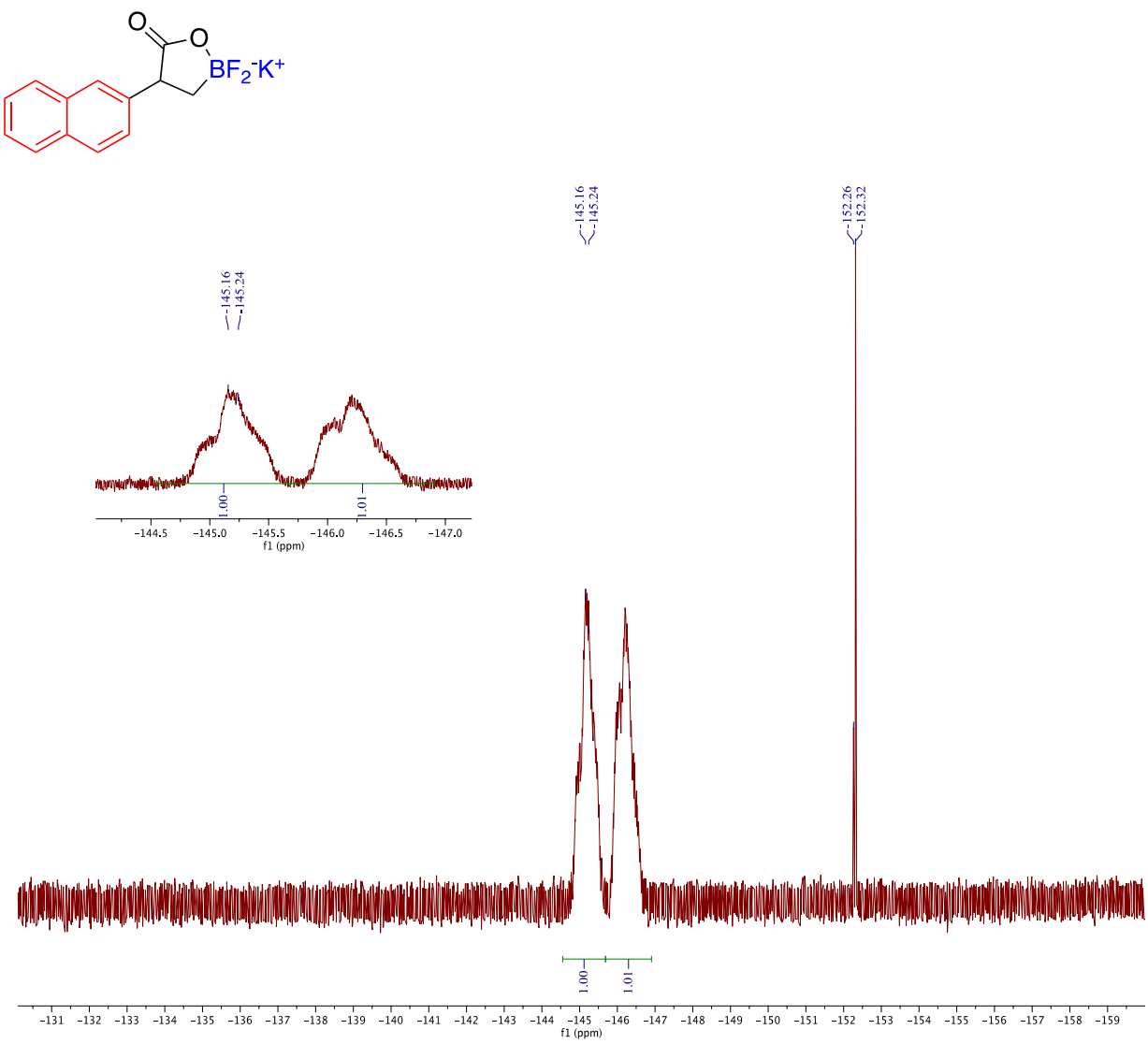

Figure A-69. ^{19}F NMR Spectrum of 2f in Acetone-d_6.

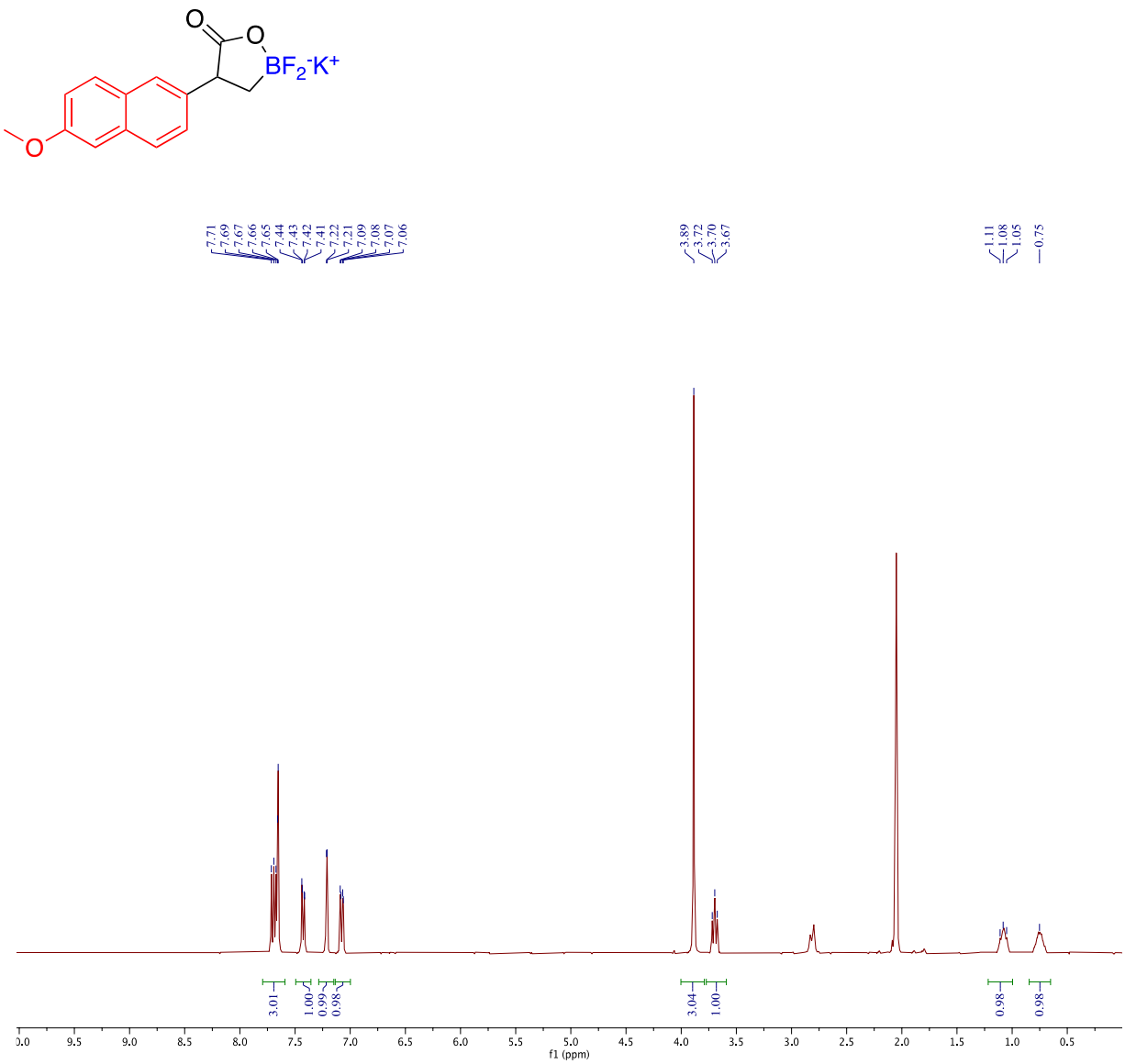

Figure A-70. ^{1}H NMR Spectrum of 2g in Acetone-d_6.

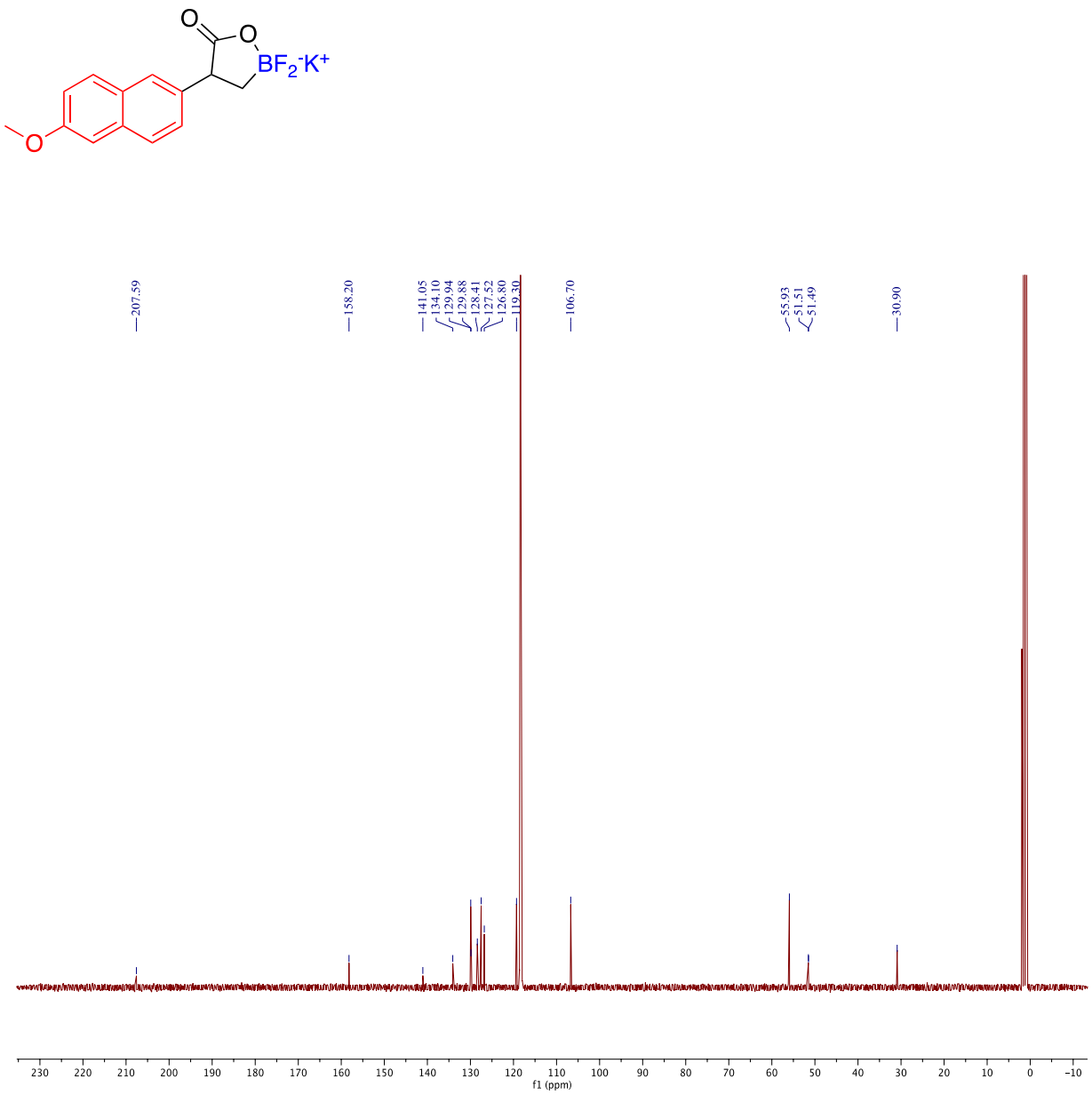

Figure A-71. ^{13}C NMR Spectrum of 2g in Acetonitrile-d_3.

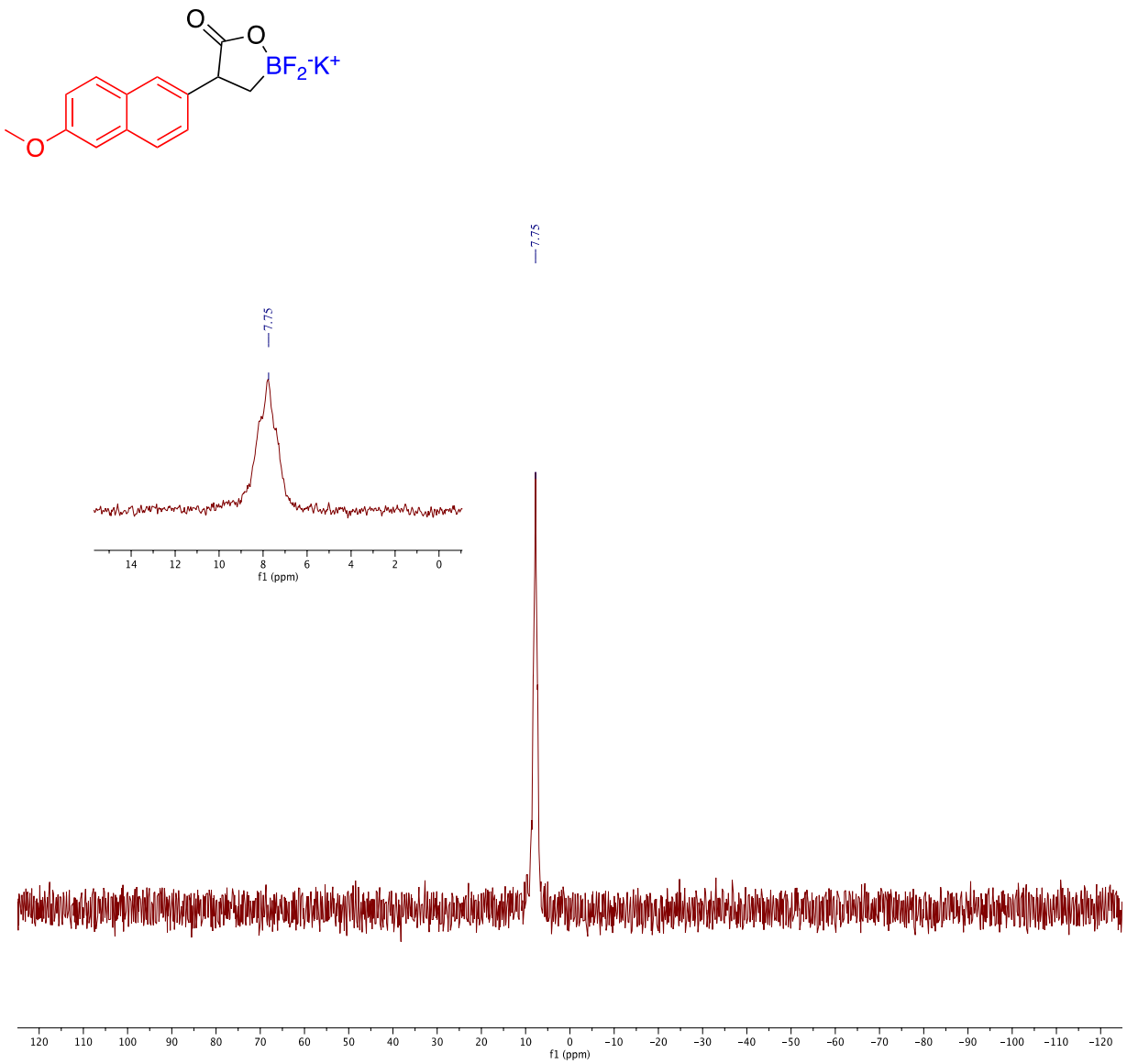

Figure A-72. ^{11}B NMR Spectrum of 2g in Acetone-d_6.

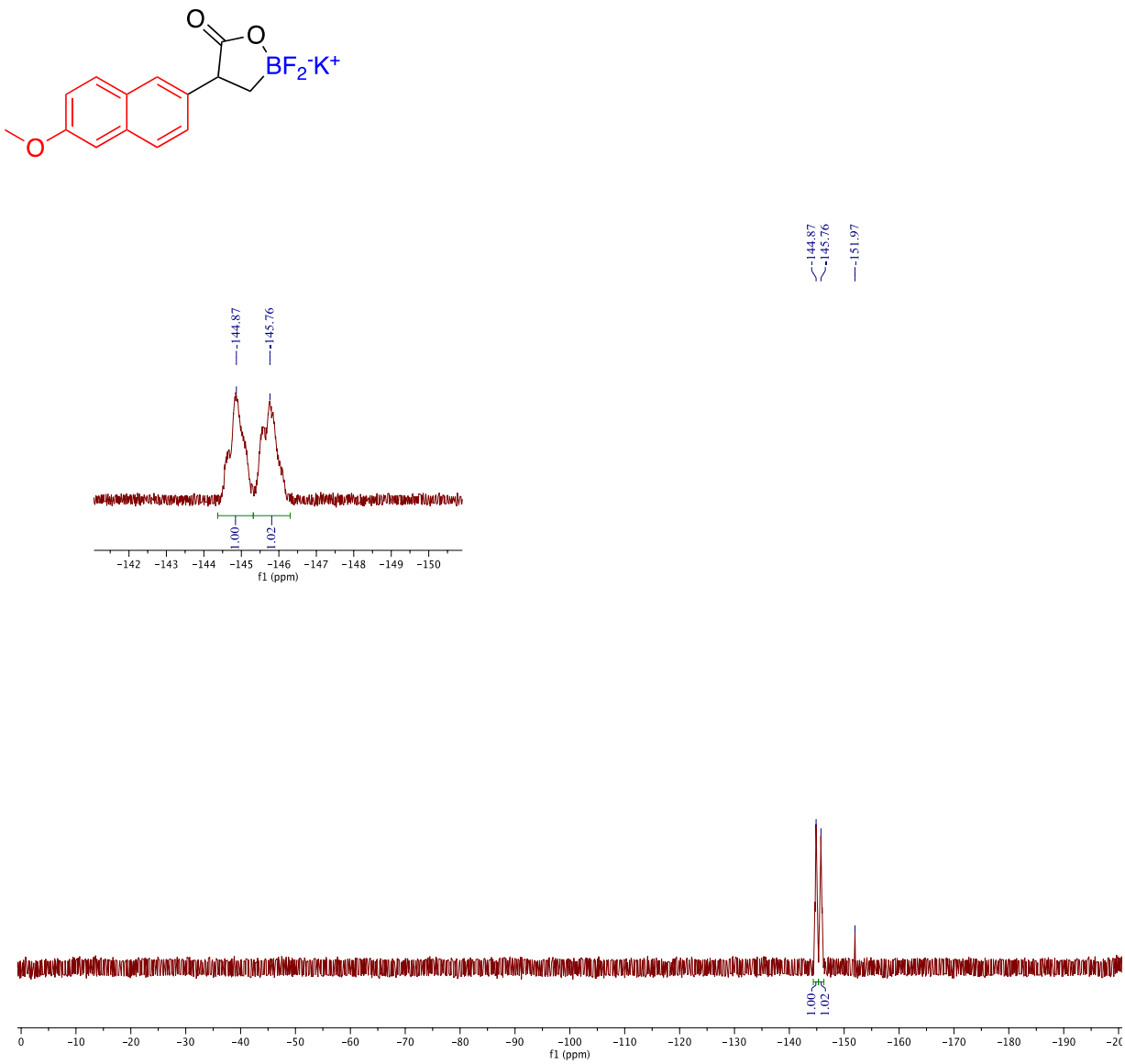

Figure A-73. ^{19}F NMR Spectrum of 2g in Acetone-d_6.

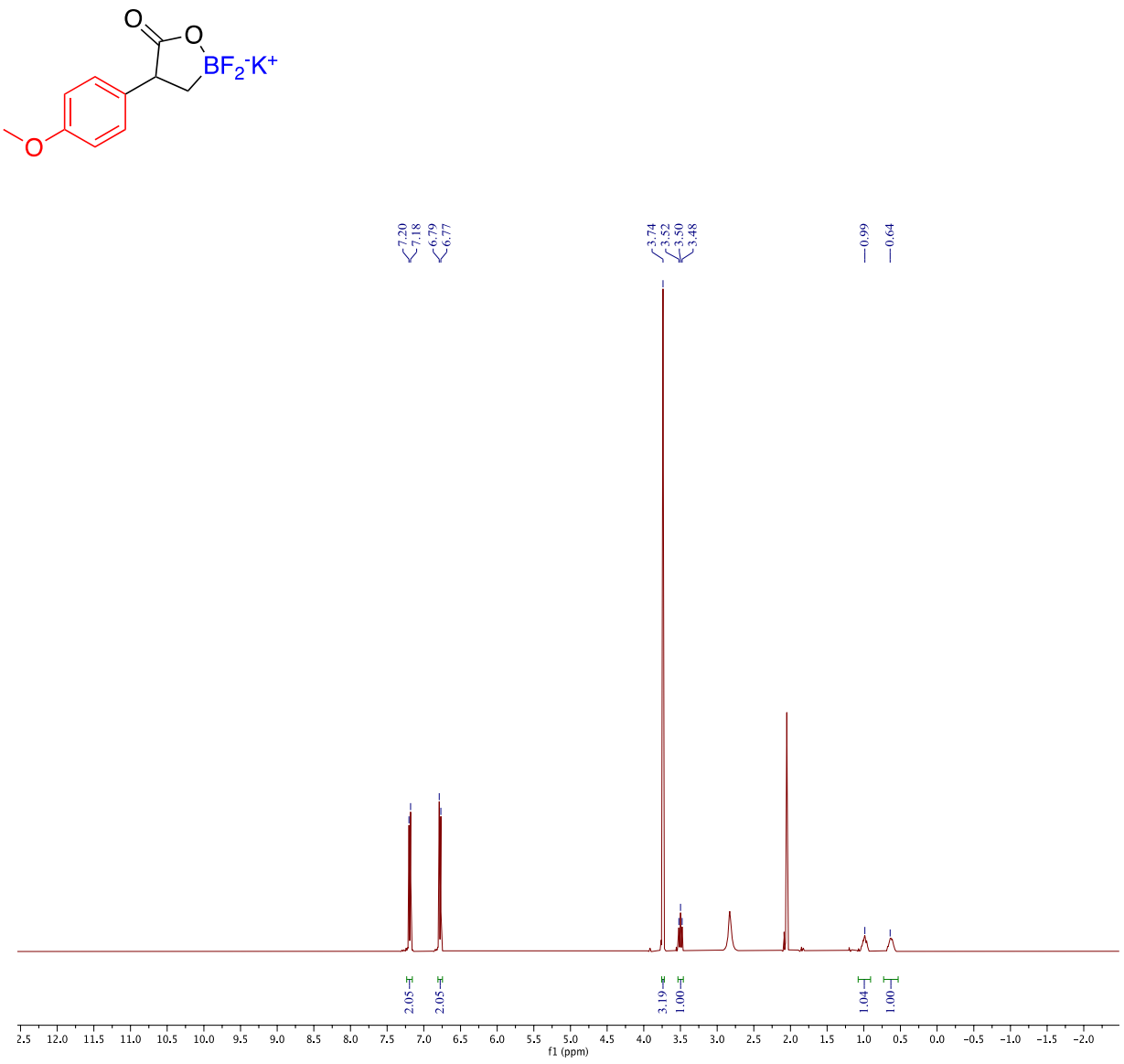

Figure A-74. ^{1}H NMR Spectrum of 2h in Acetone-d_6.

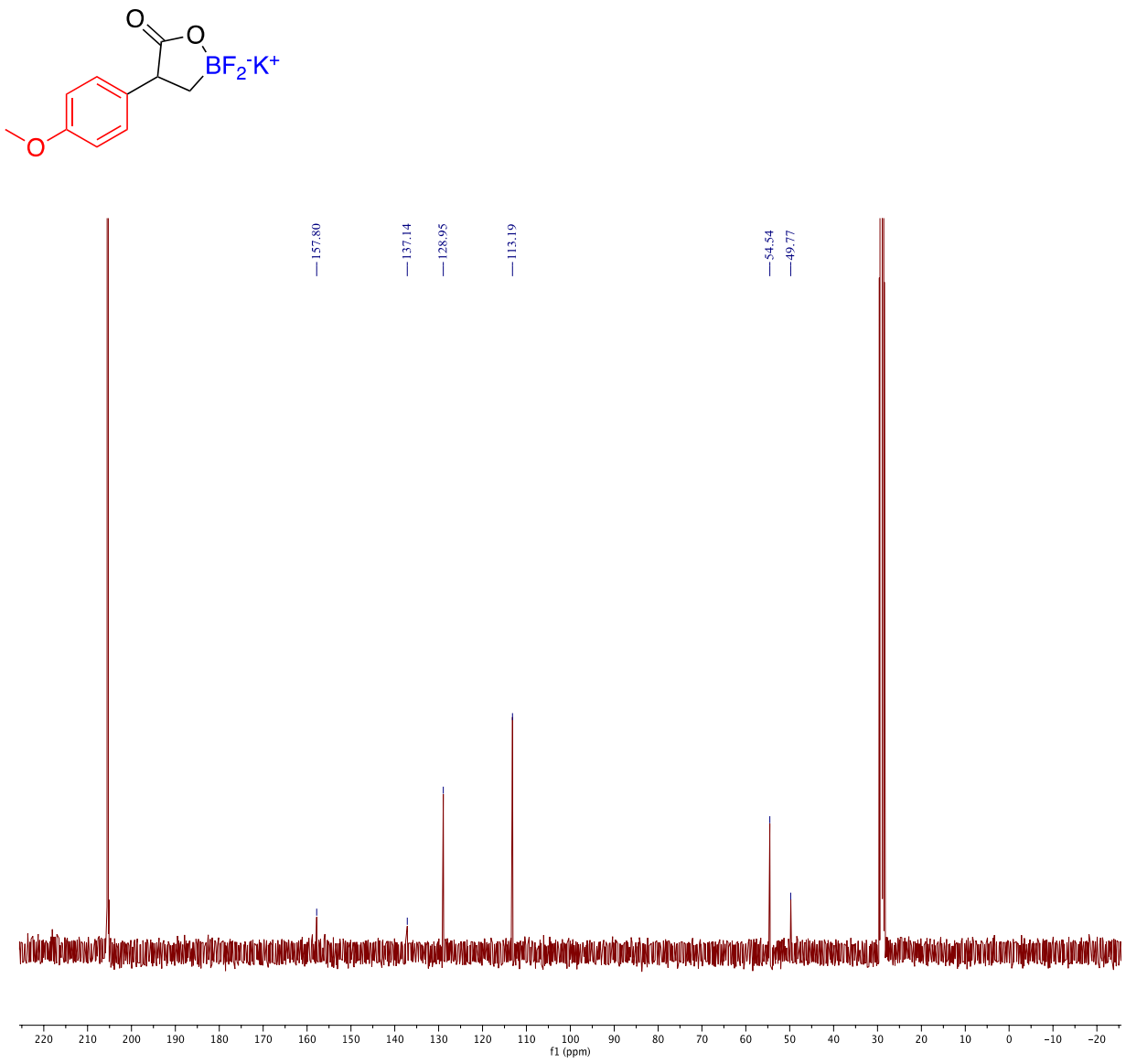

Figure A-75. ^{13}C NMR Spectrum of 2h in Acetone-d_6.

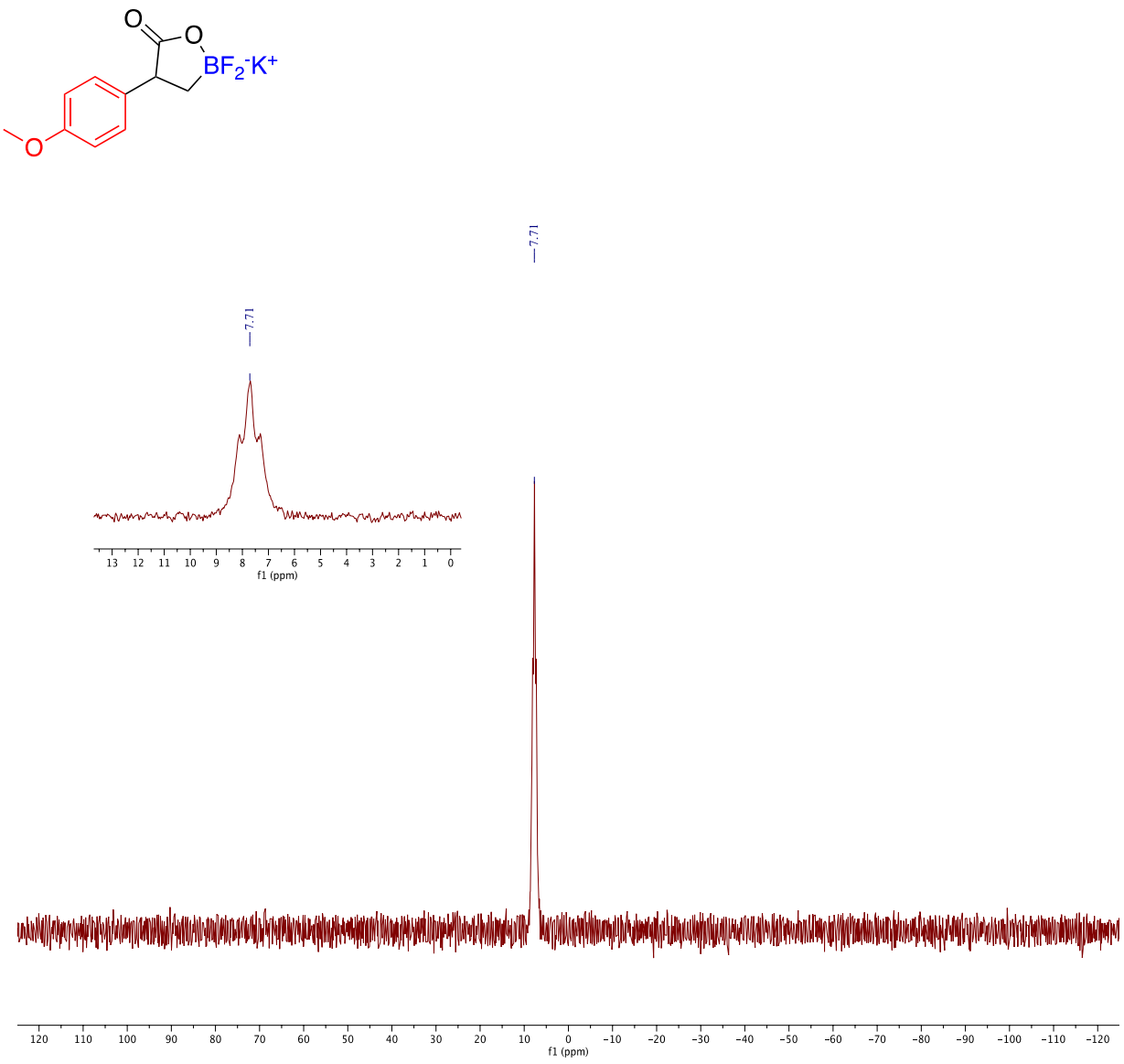

Figure A-76. ^{11}B NMR Spectrum of 2h in Acetone-d_6.

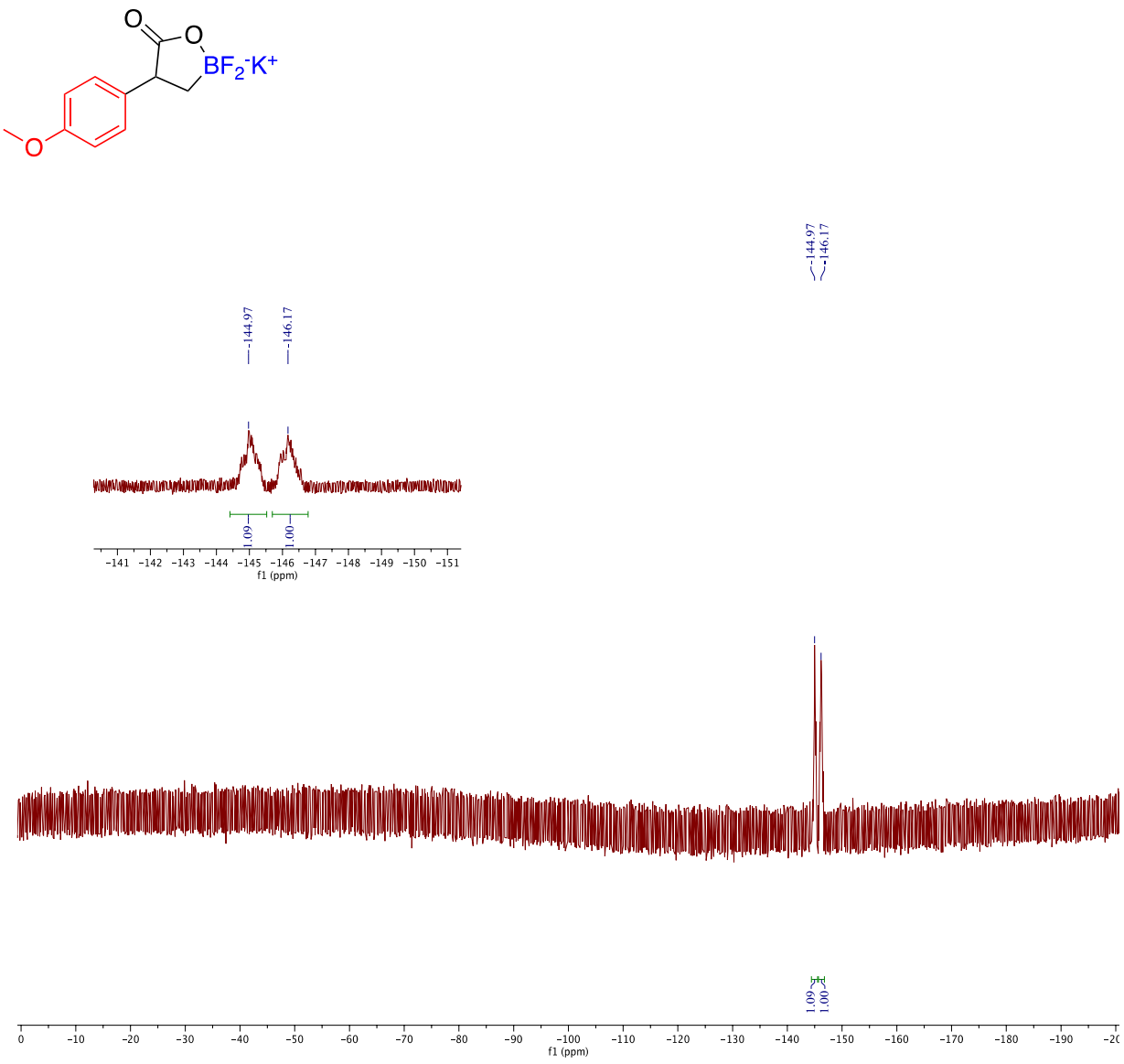

Figure A-77. ^{19}F NMR Spectrum of 2h in Acetone-d_6.

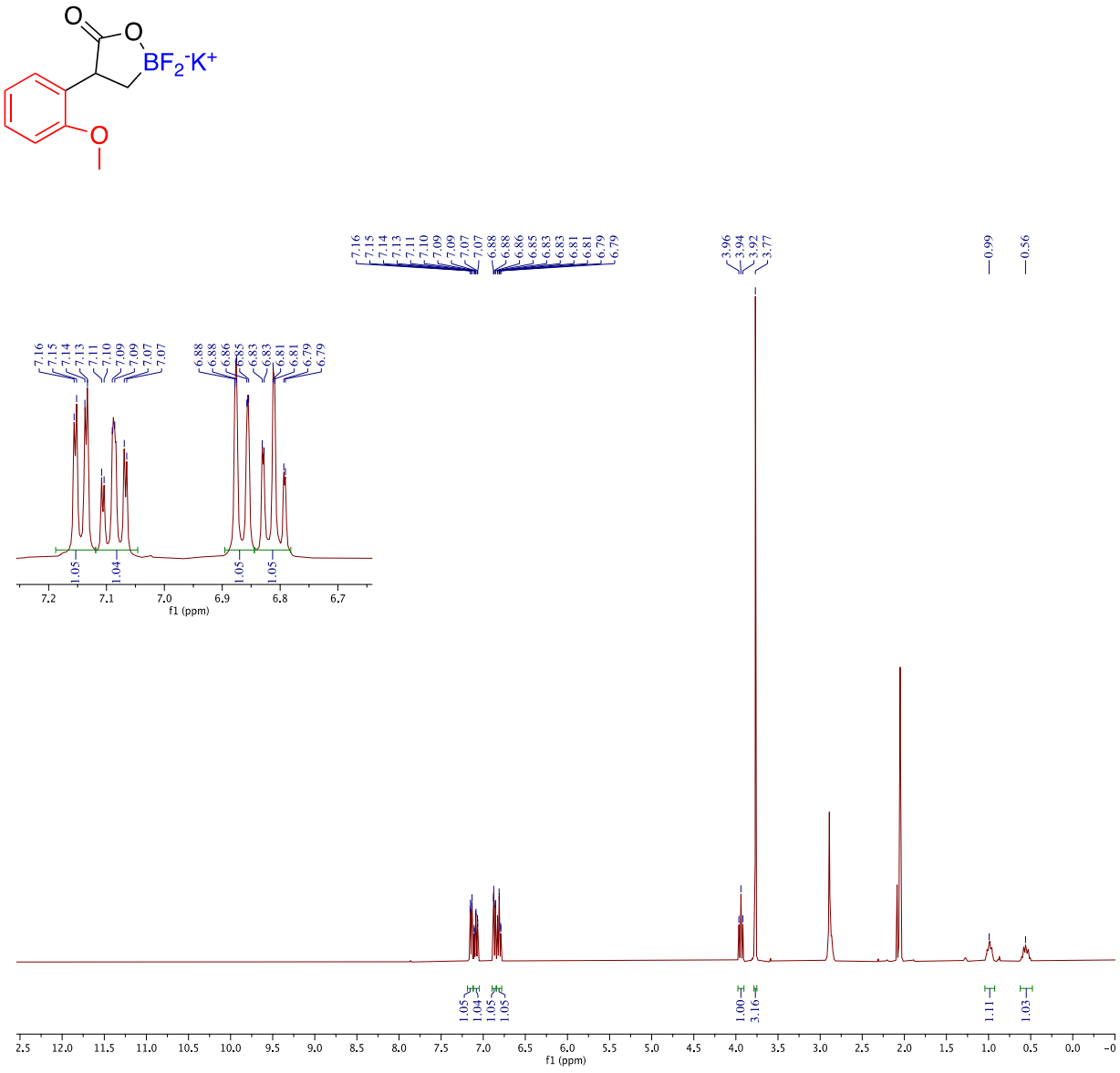

Figure A-78. ^{1}H NMR Spectrum of 2i in Acetone-d_6.

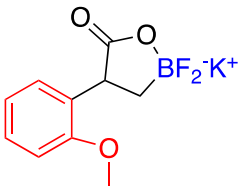

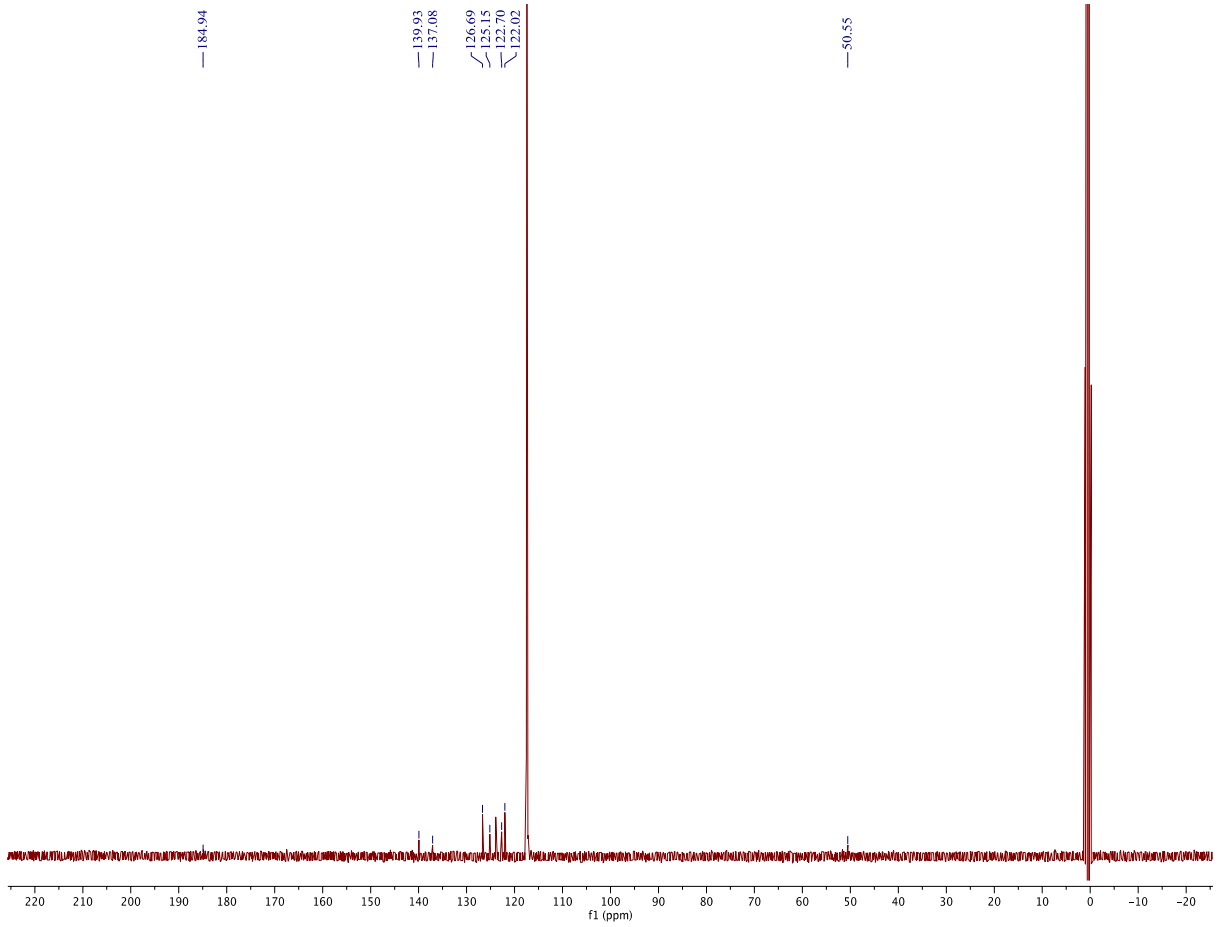

Figure A-79. ^{13}C NMR Spectrum of 2i in Acetone-d_6.

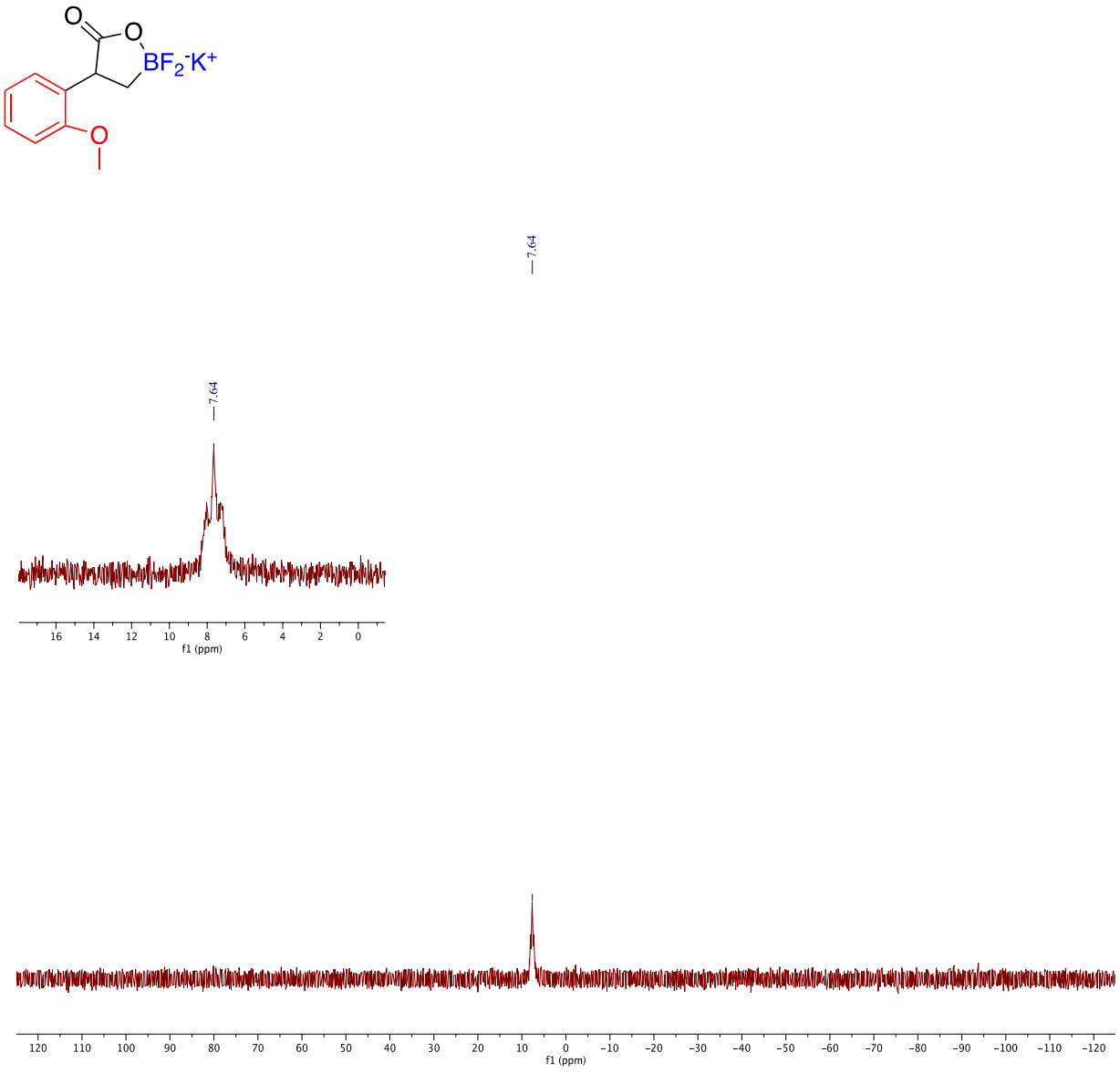

Figure A-80. ^{11}B NMR Spectrum of 2i in Acetone-d_6.

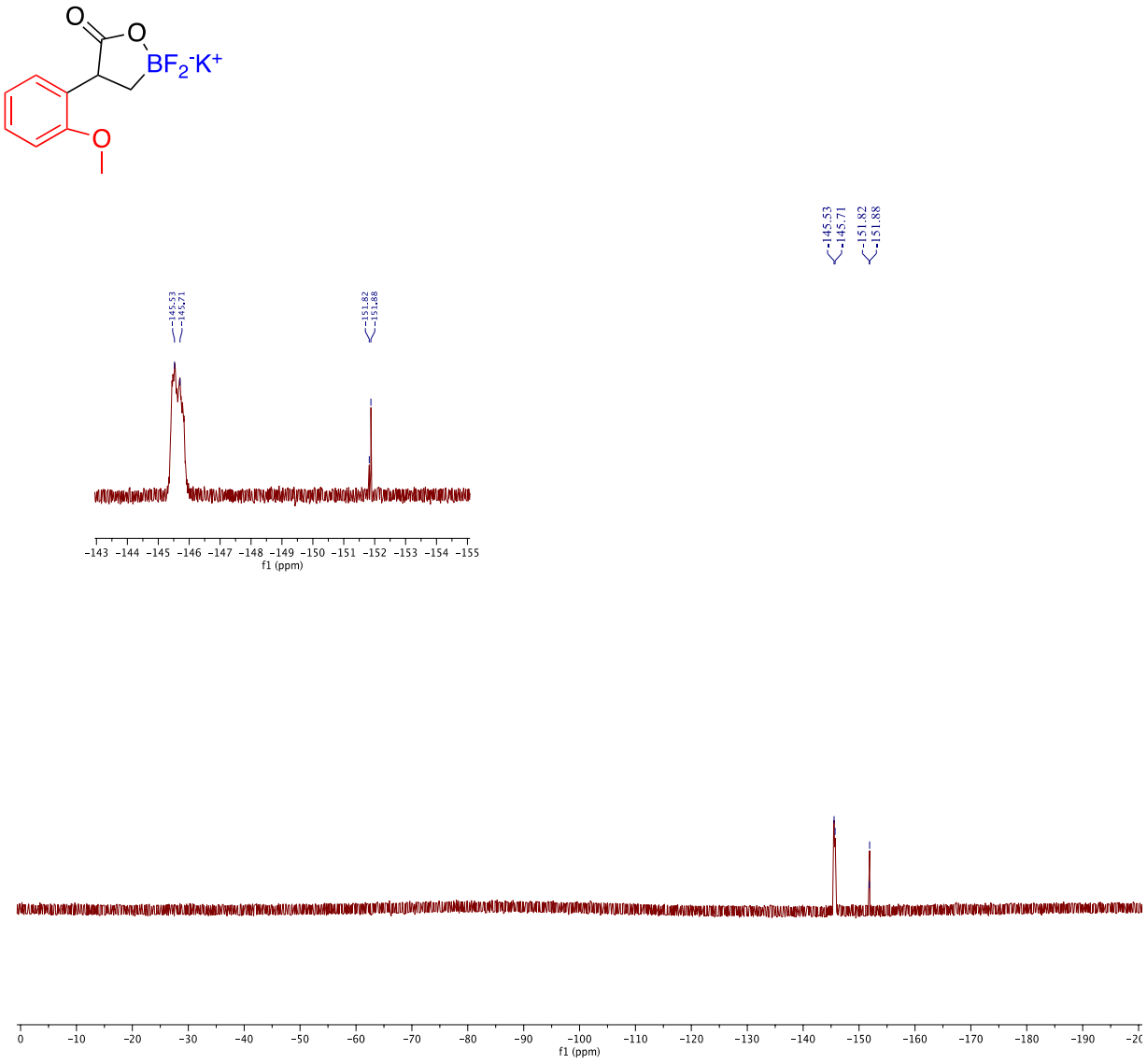

Figure A-81. ^{19}F NMR Spectrum of 2i in Acetone-d_6.

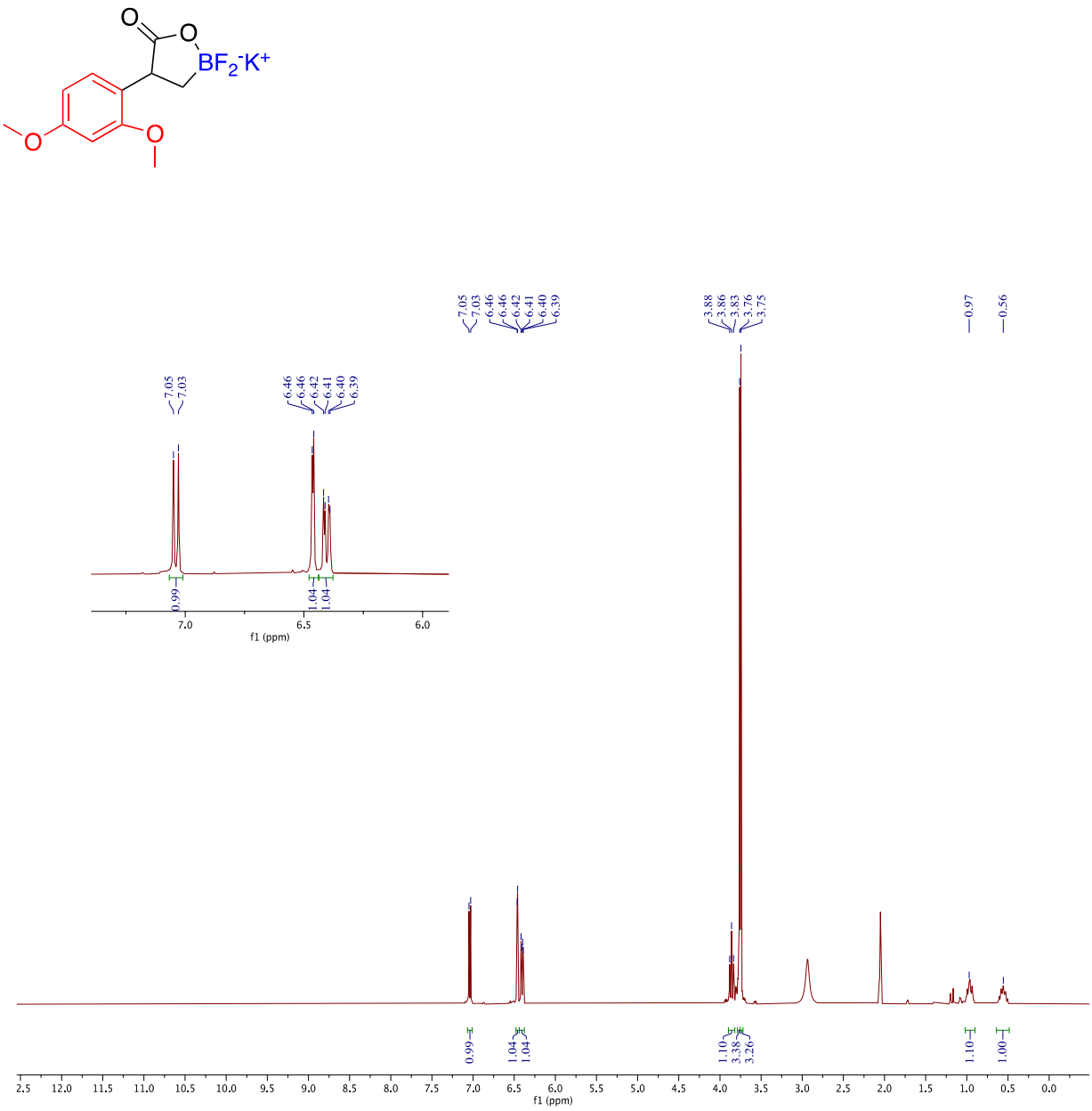

Figure A-82. ^{1}H NMR Spectrum of 2j in Acetone-d_6.

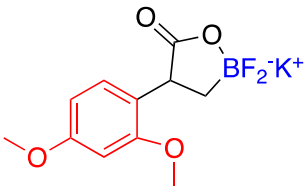

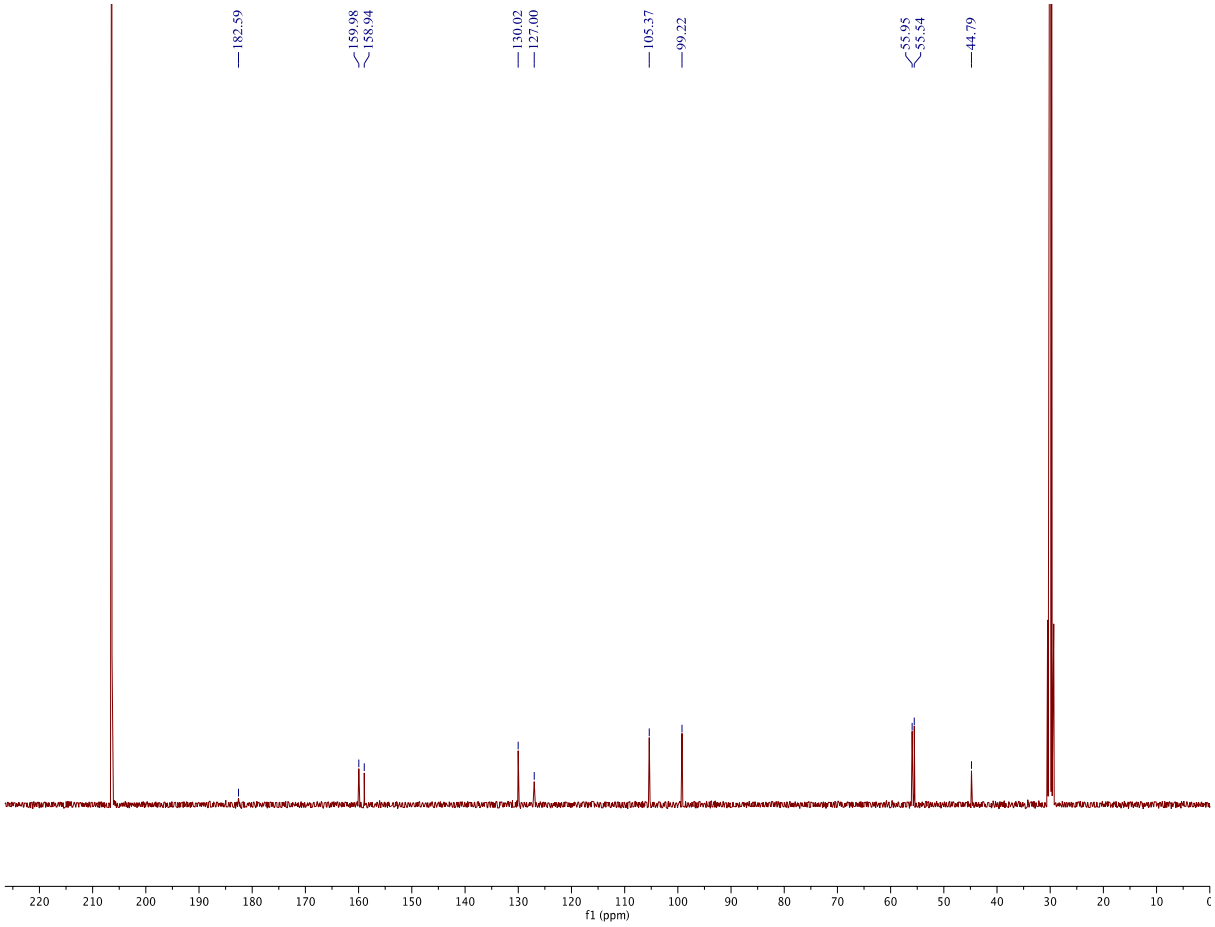

Figure A-83. ^{13}C NMR Spectrum of 2j in Acetone-d_6.

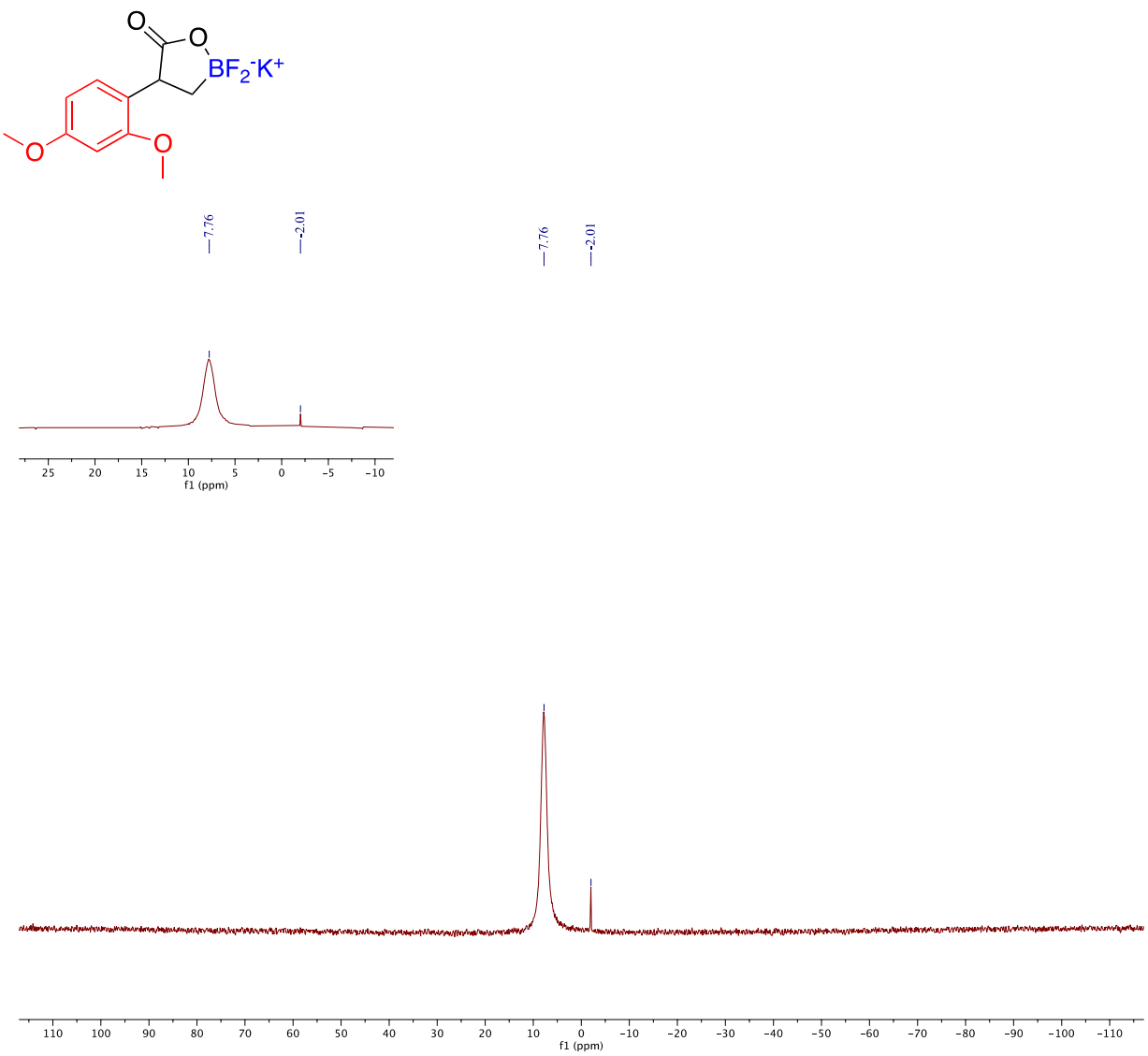

Figure A-84. ^{11}B NMR Spectrum of 2j in Acetone-d_6.

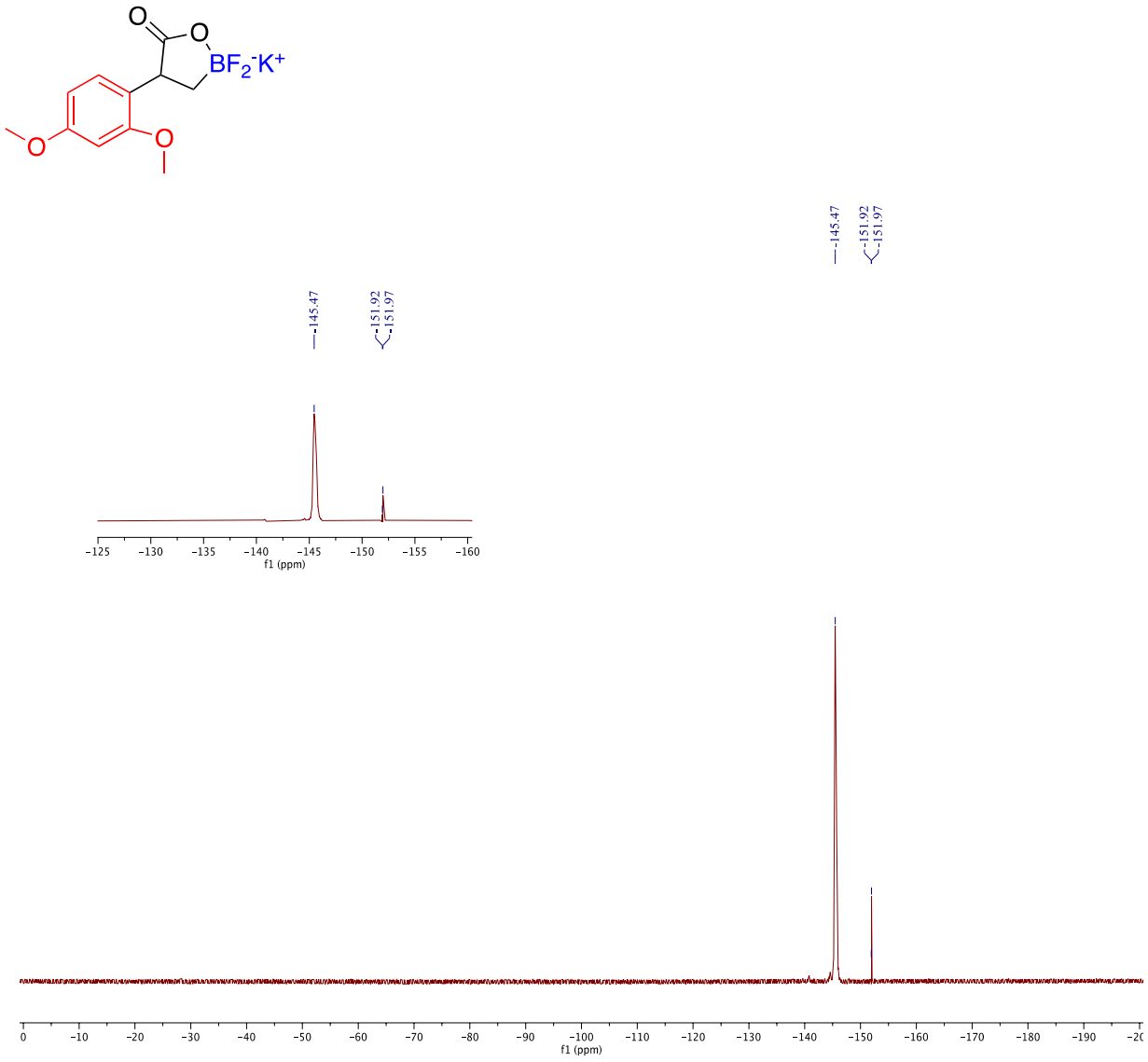

Figure A-85. ^{19}F NMR Spectrum of 2j in Acetone-d_6.

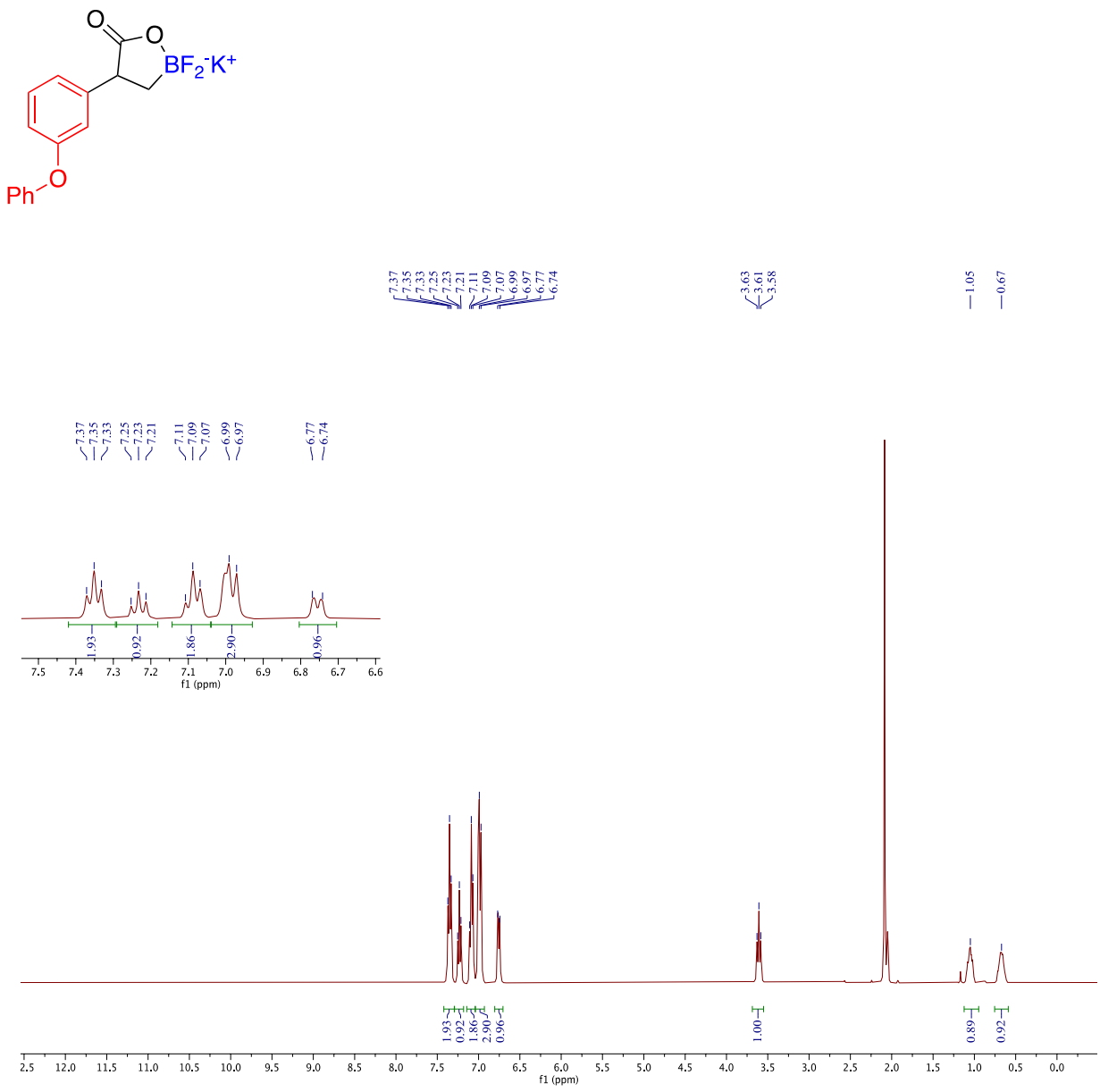

Figure A-86. ^{1}H NMR Spectrum of 2k in Acetone-d_6.

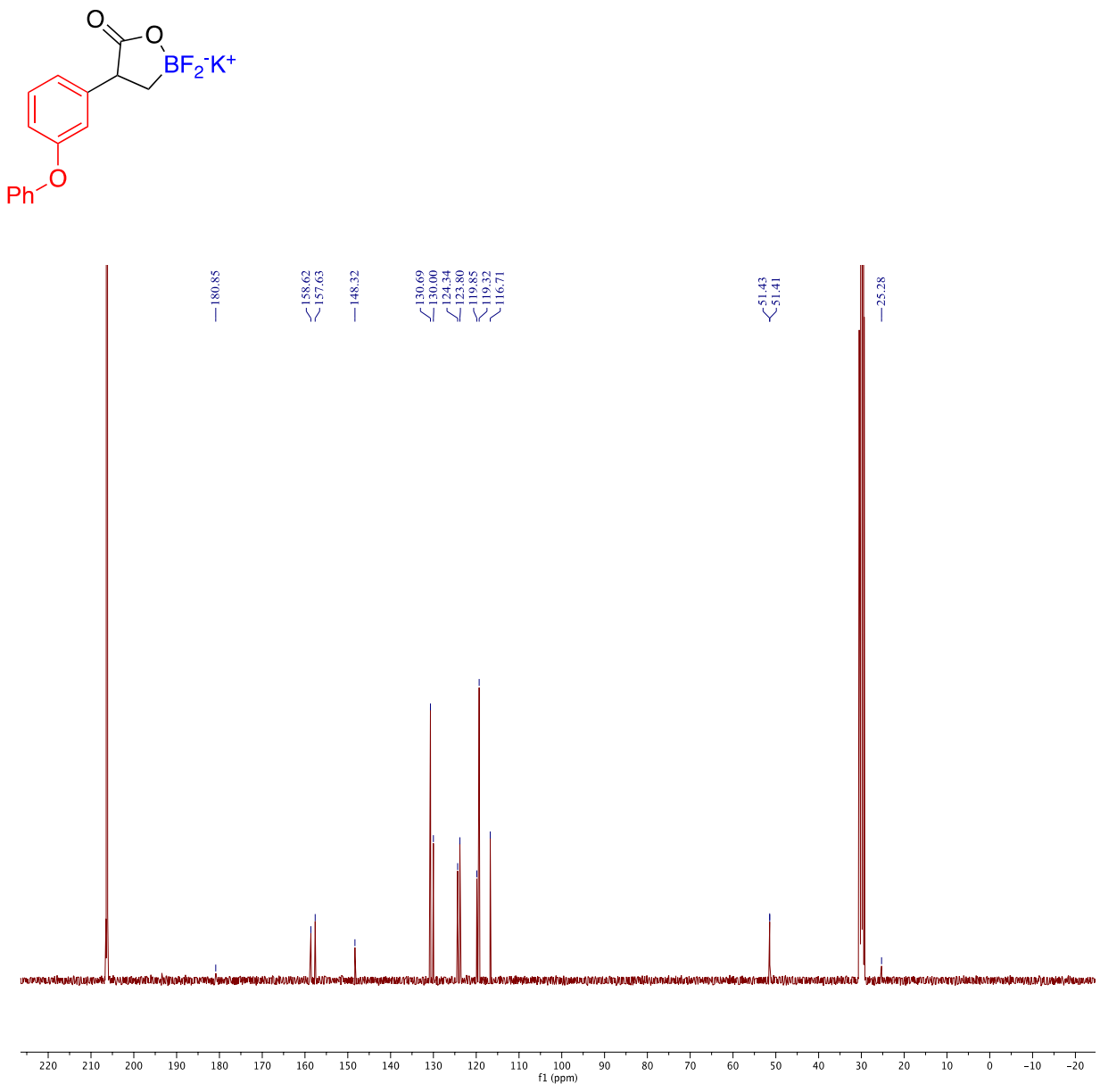

Figure A-87. ^{13}C NMR Spectrum of 2k in Acetone-d_6.

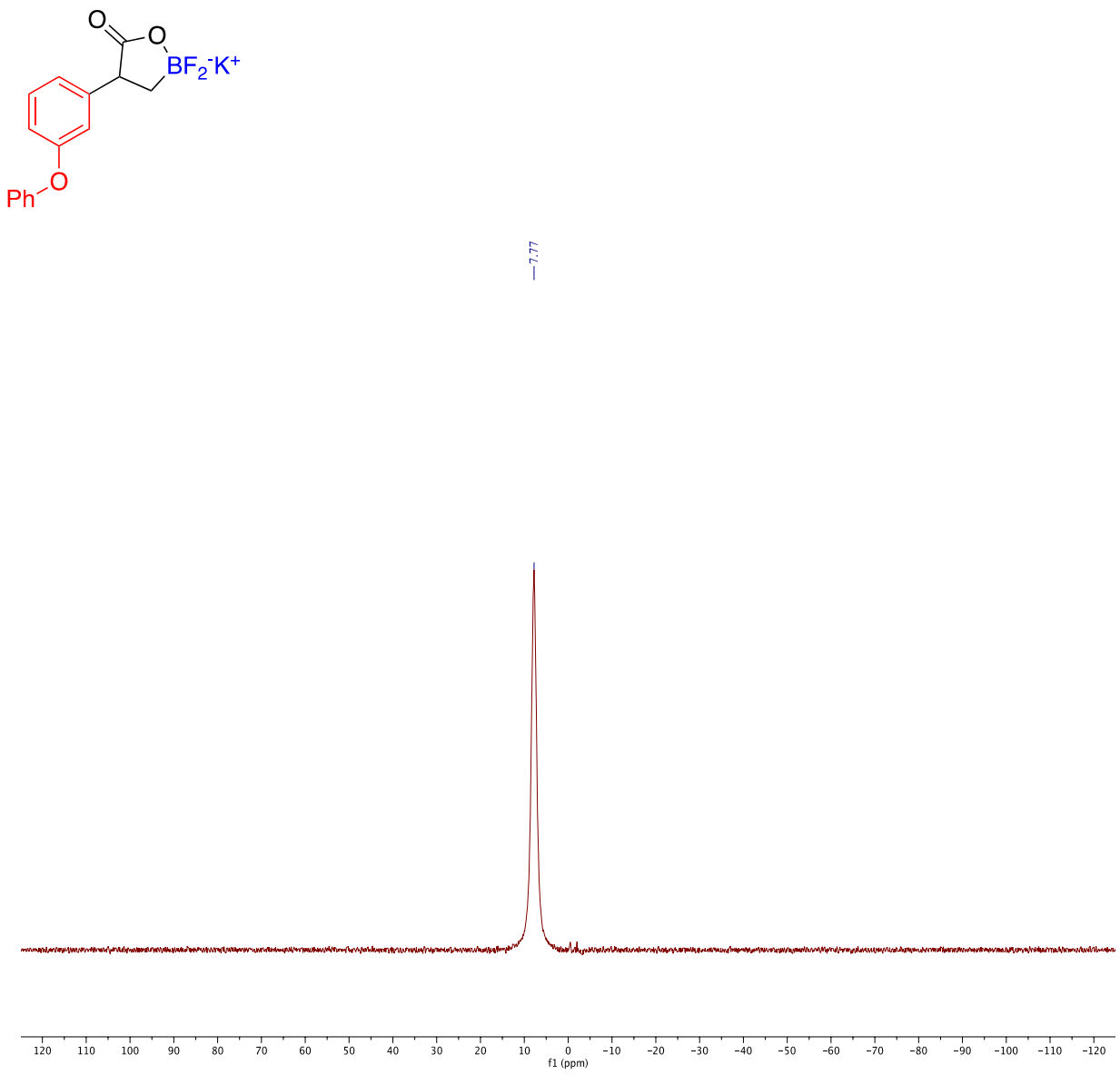

Figure A-88. ^{11}B NMR Spectrum of 2k in Acetone-d_6.

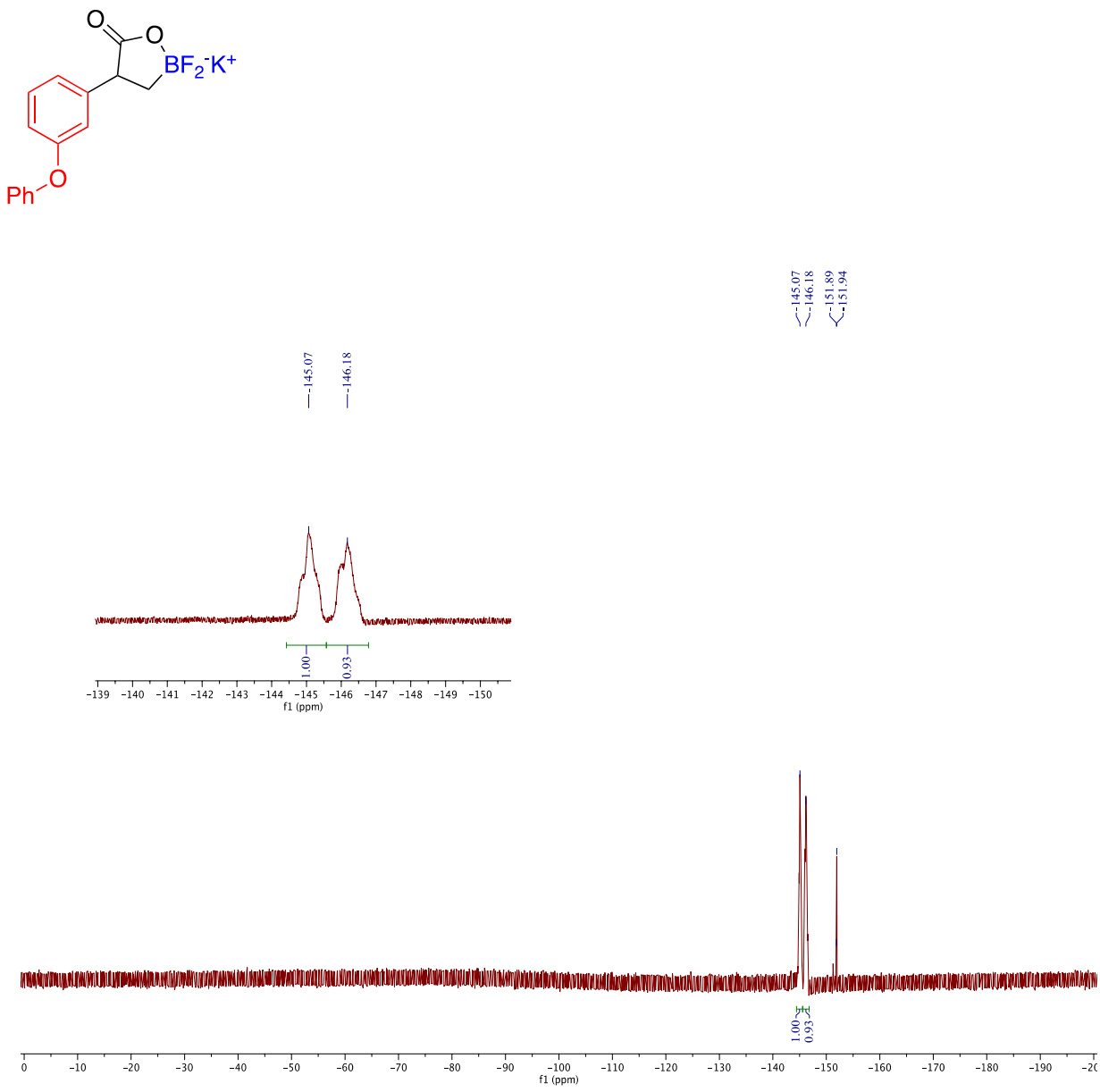

Figure A-89. ^{19}F NMR Spectrum of 2k in Acetone-d_6.

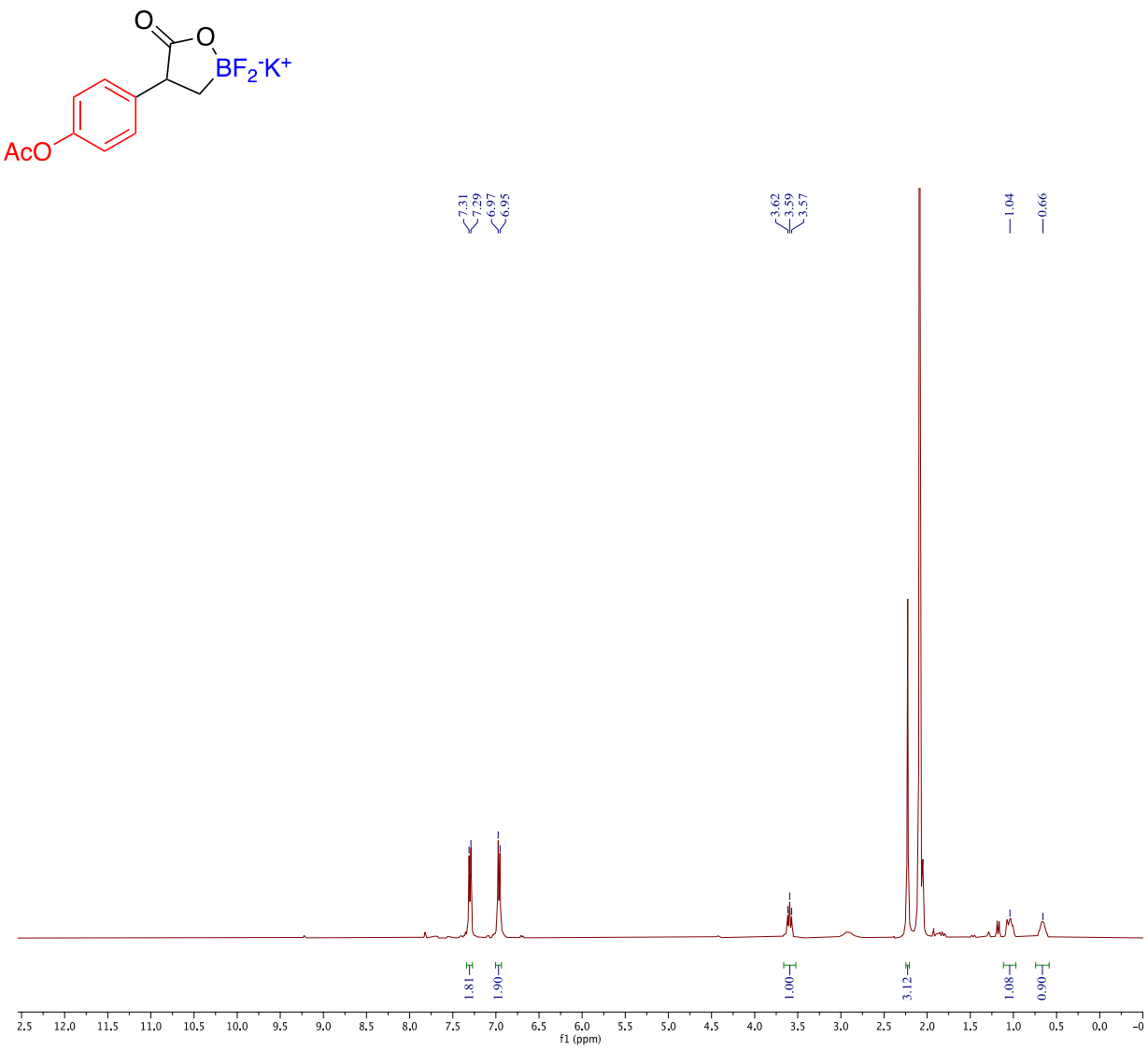

Figure A-90. ^{1}H NMR Spectrum of 2l in Acetone-d_6.

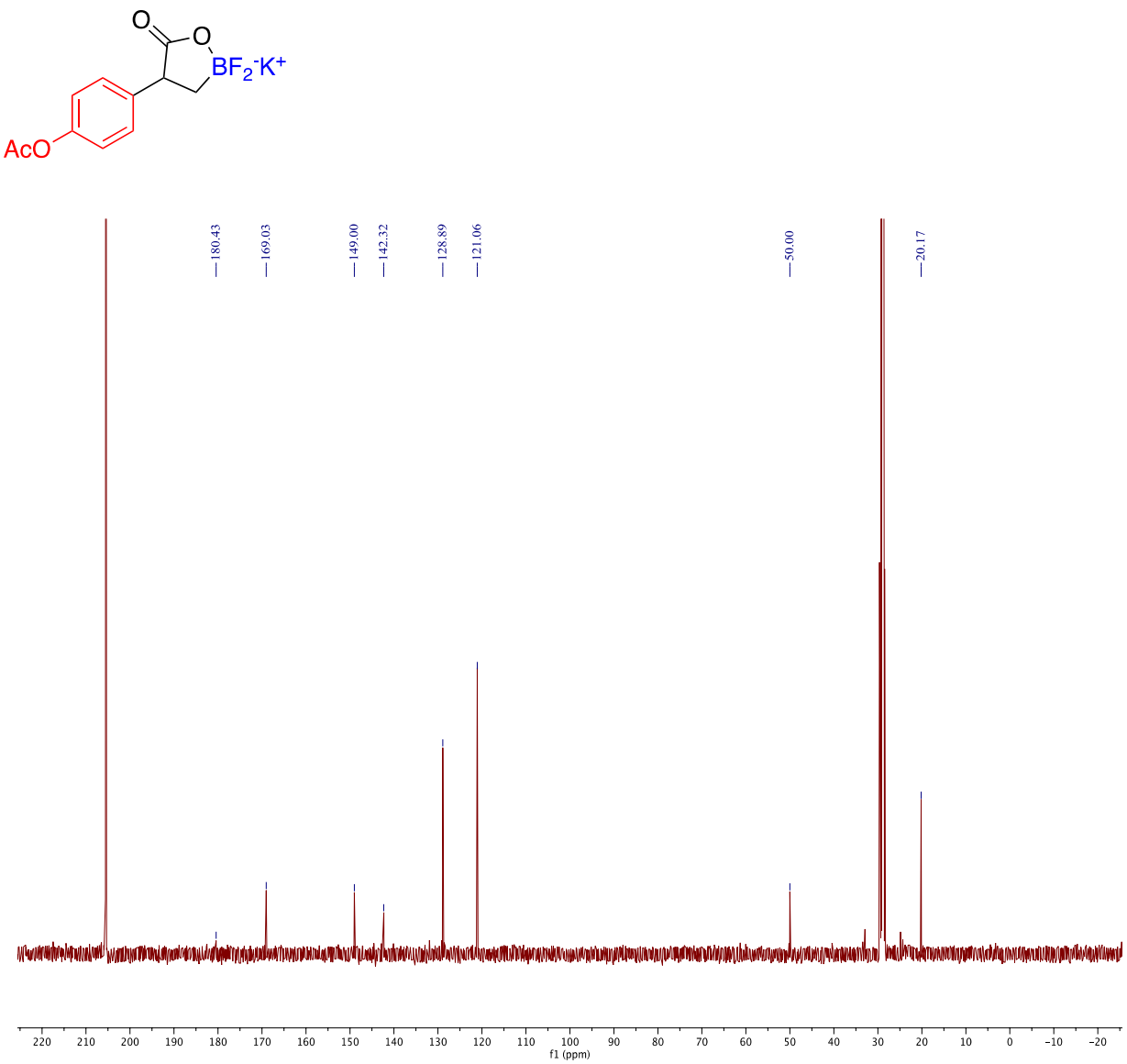

Figure A-91. ^{13}C NMR Spectrum of 2l in Acetone-d_6.

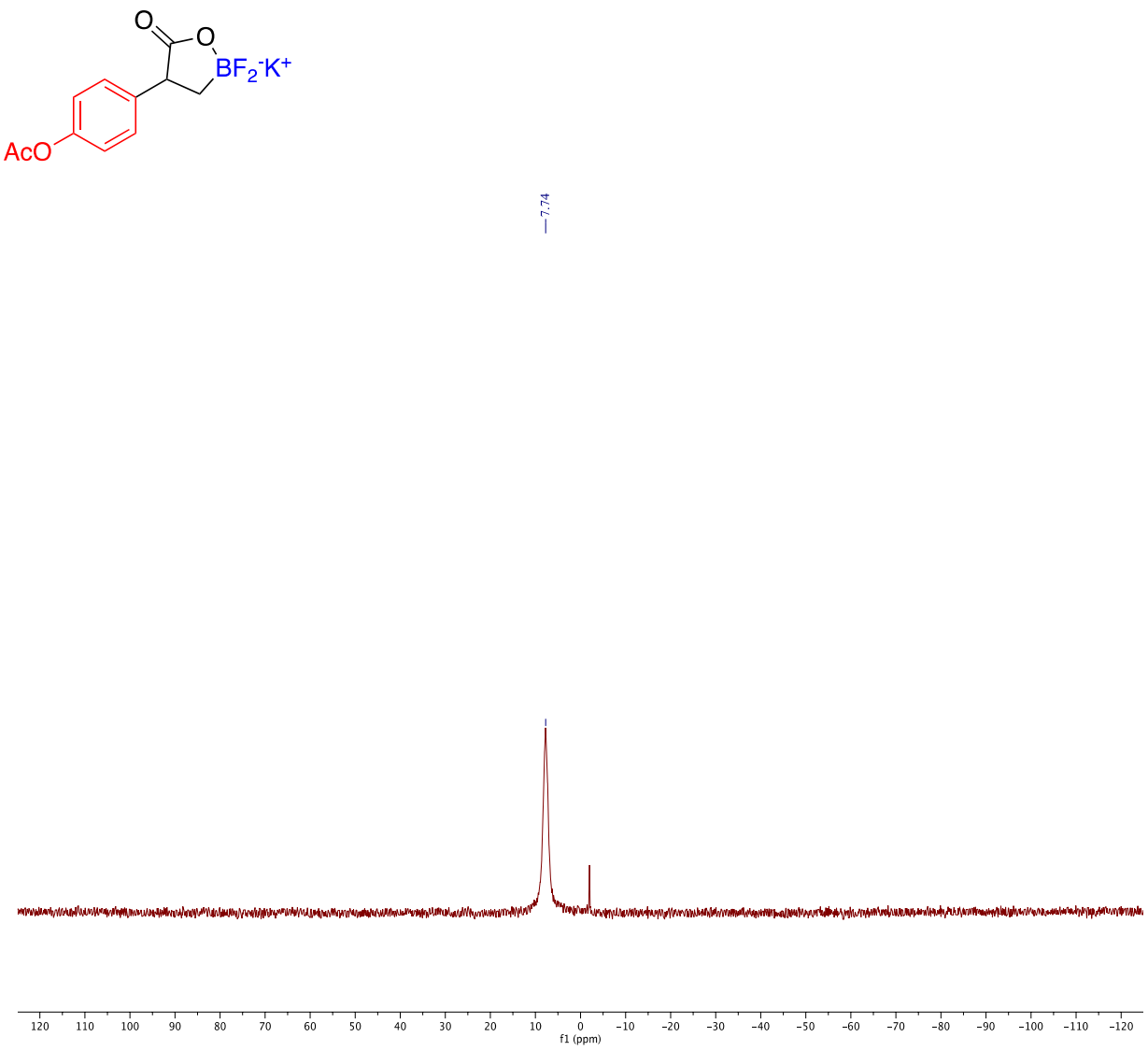

Figure A-92. ^{11}B NMR Spectrum of 2l in Acetone-d_6.

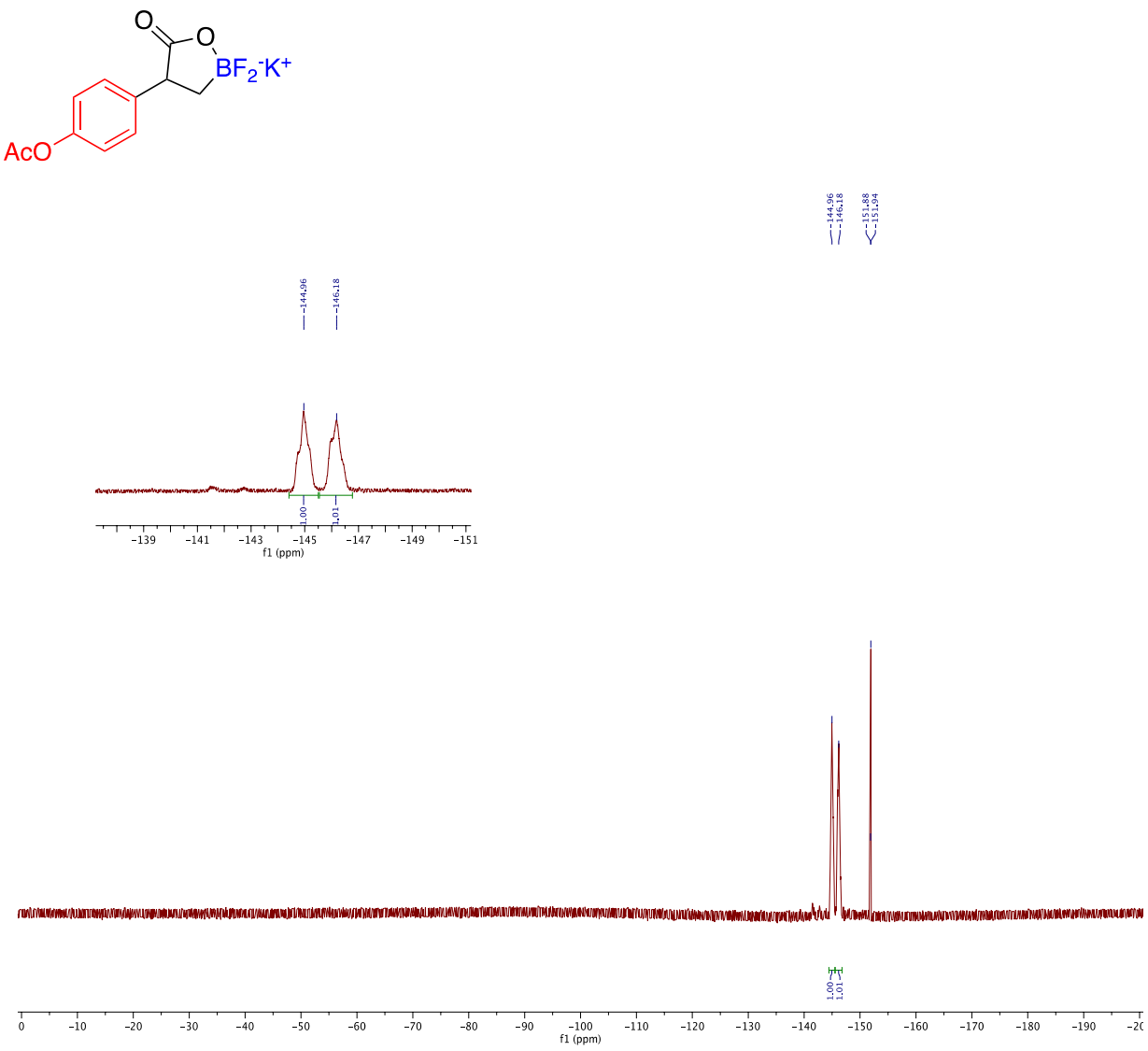

Figure A-93. ^{19}F NMR Spectrum of 2l in Acetone-d_6.

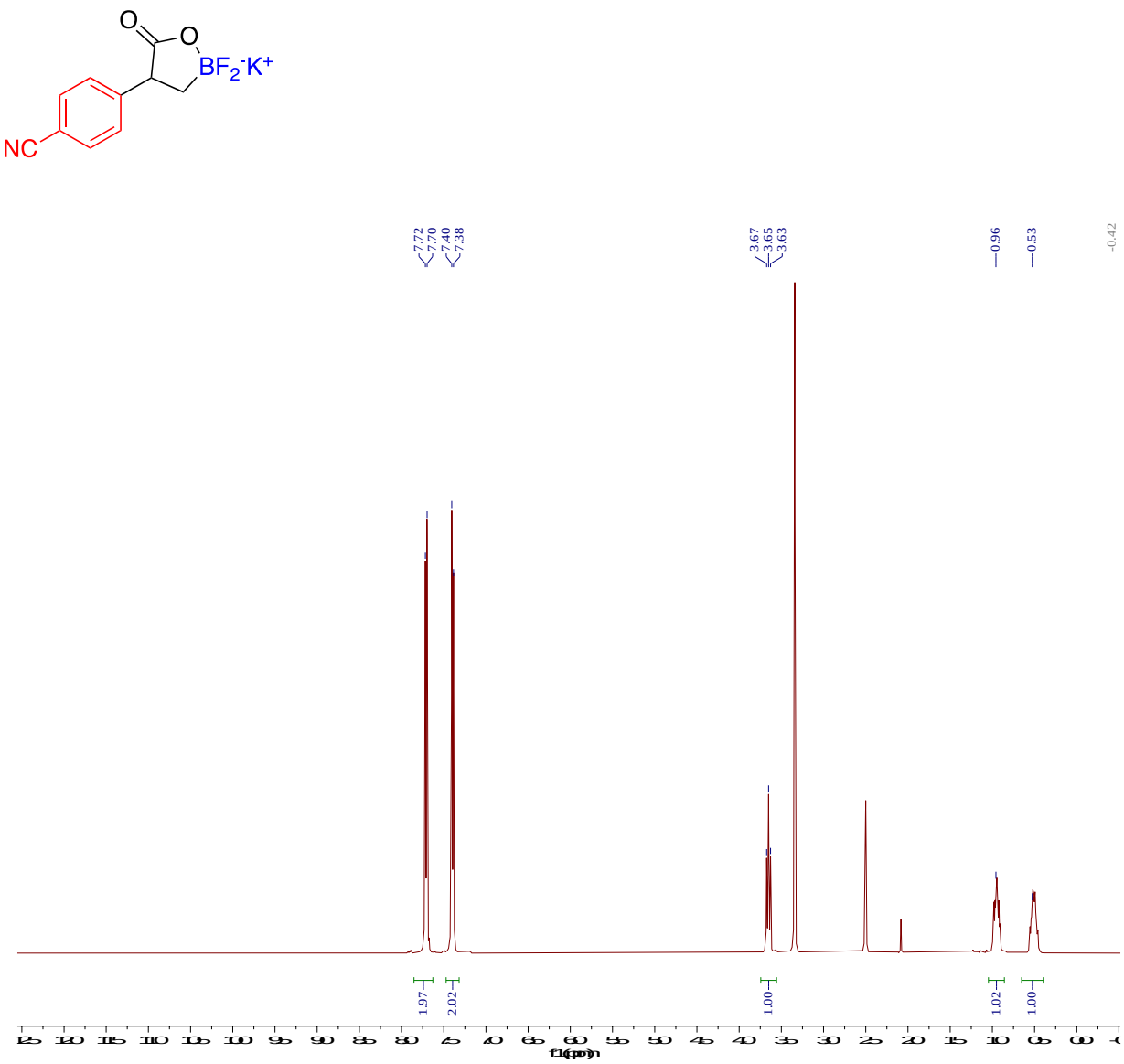

Figure A-94. ^{1}H NMR Spectrum of 2m in Acetone-d_6.

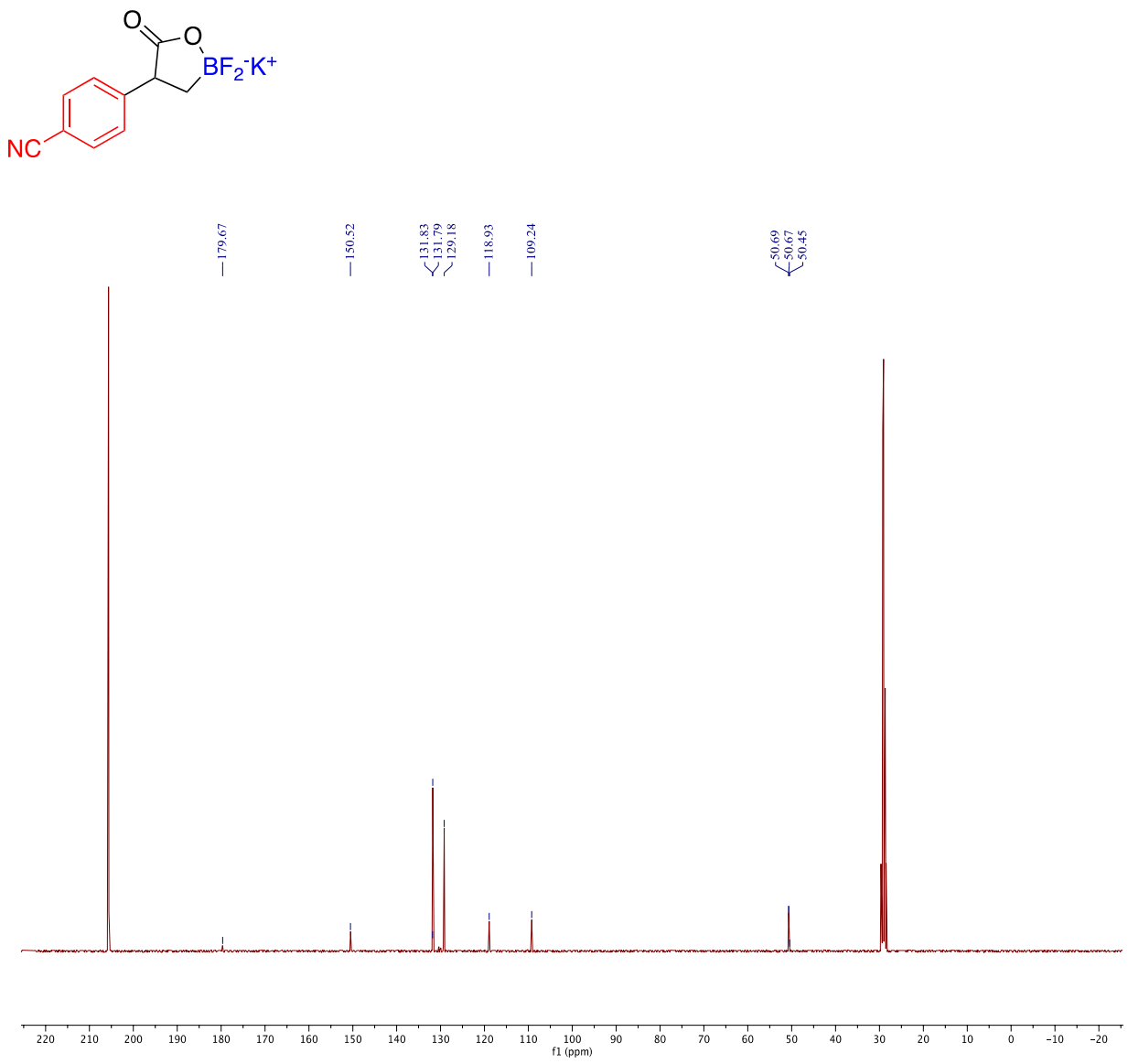

Figure A-95. ^{13}C NMR Spectrum of 2m in Acetone-d_6.

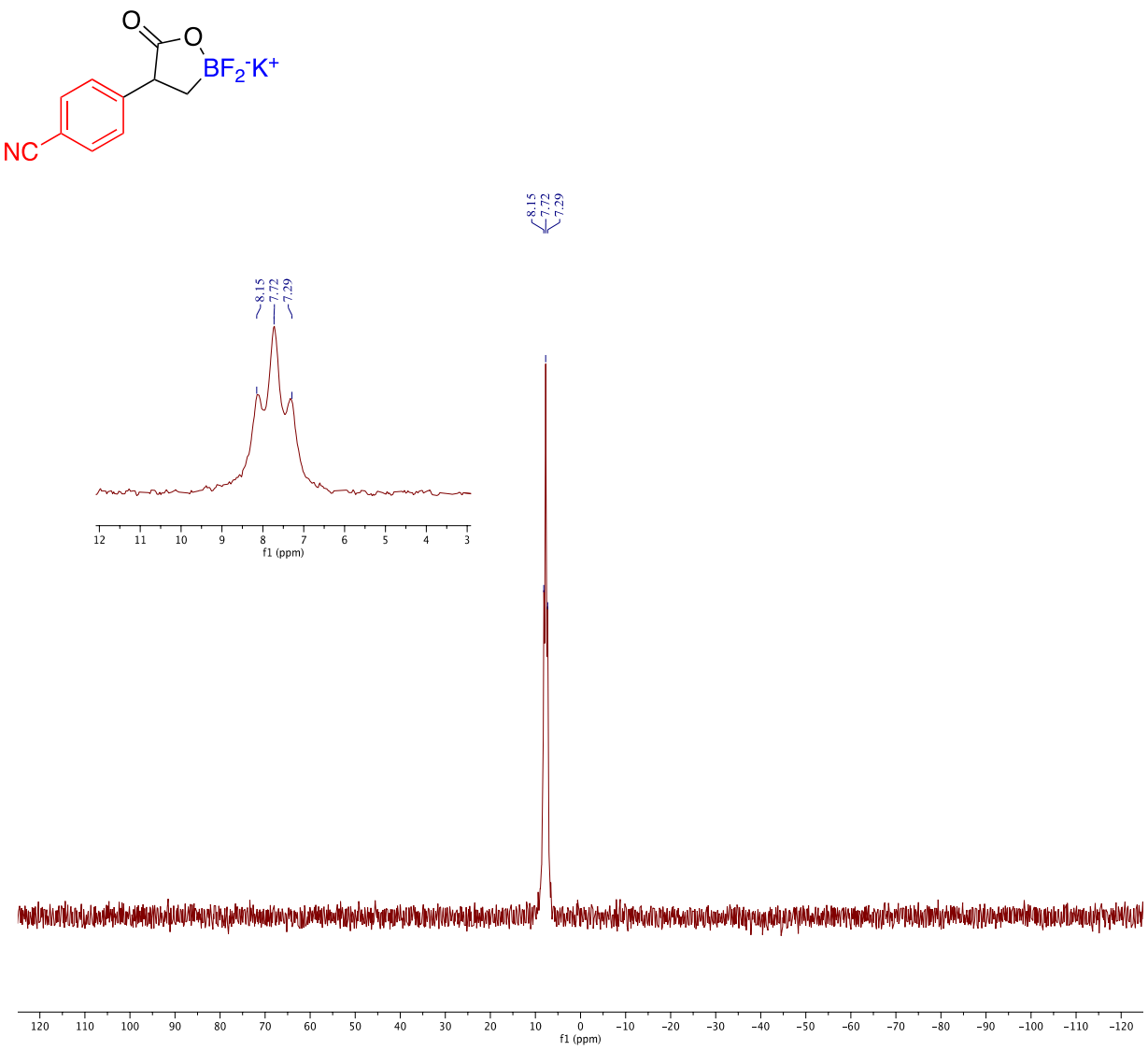

Figure A-96. ^{11}B NMR Spectrum of 2m in Acetone-d_6.

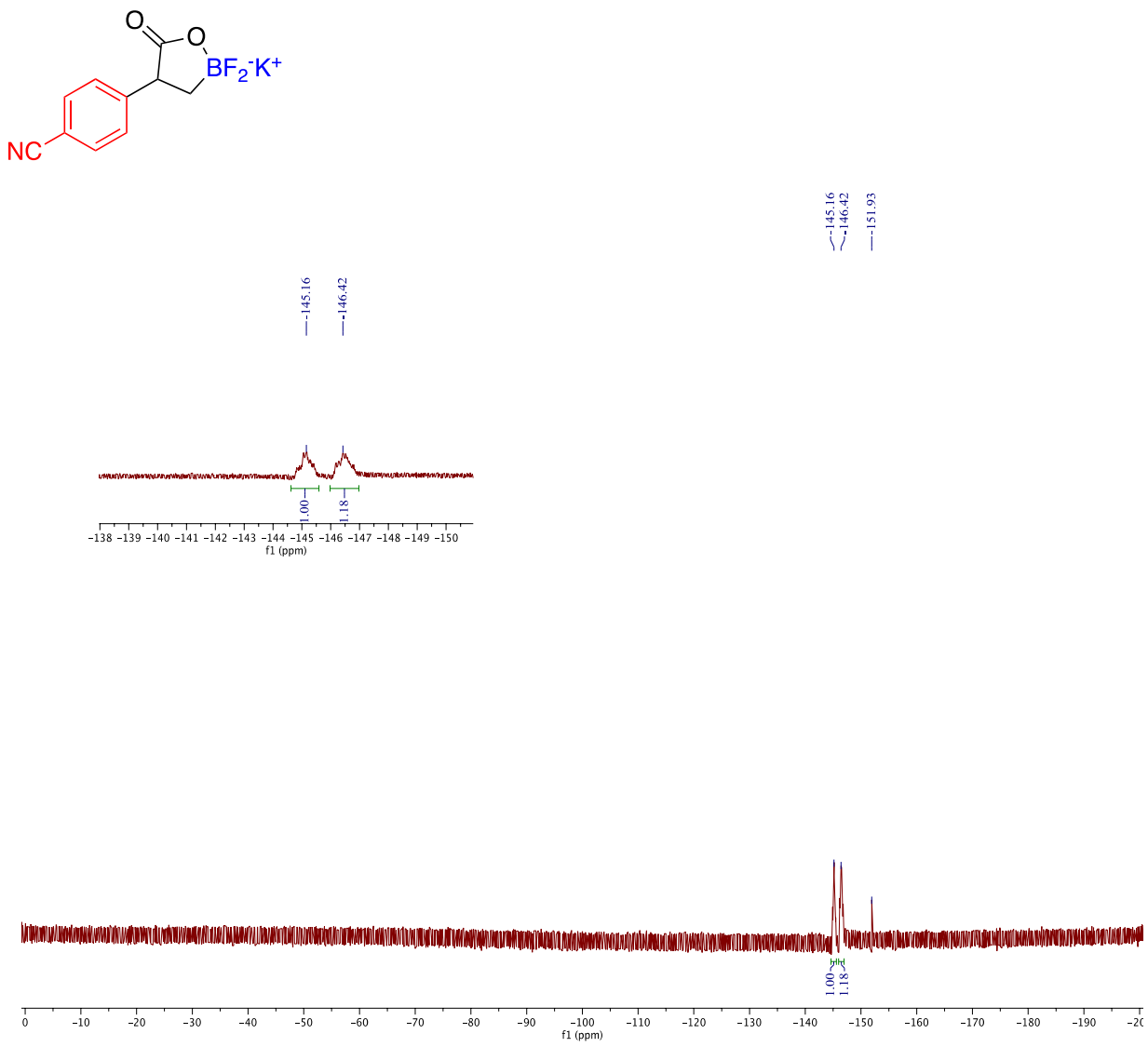

Figure A-97. ^{19}F NMR Spectrum of 2m in Acetone-d_6.

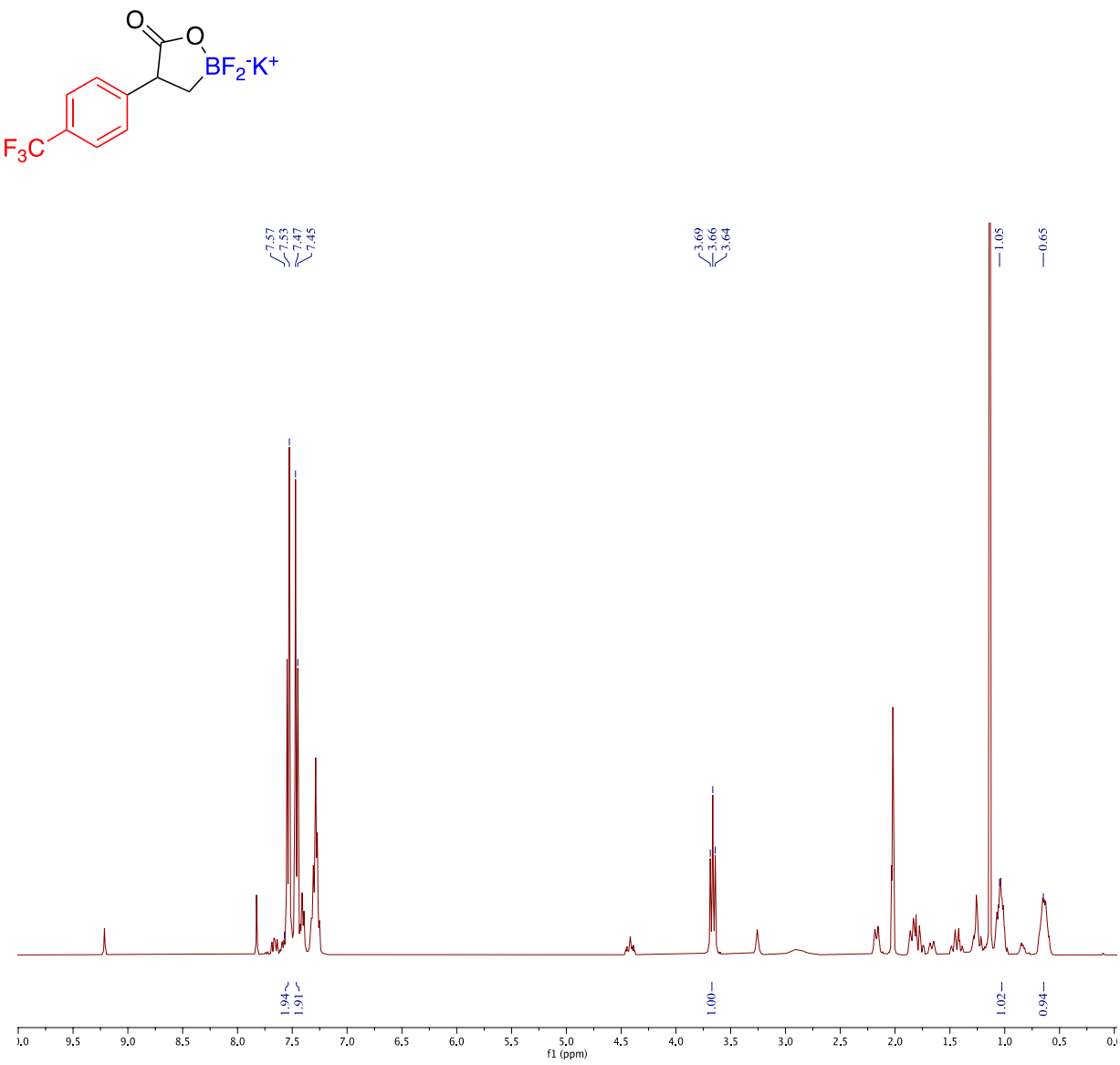

Figure A-98. ^{1}H NMR Spectrum of 2n in Acetone-d_6.

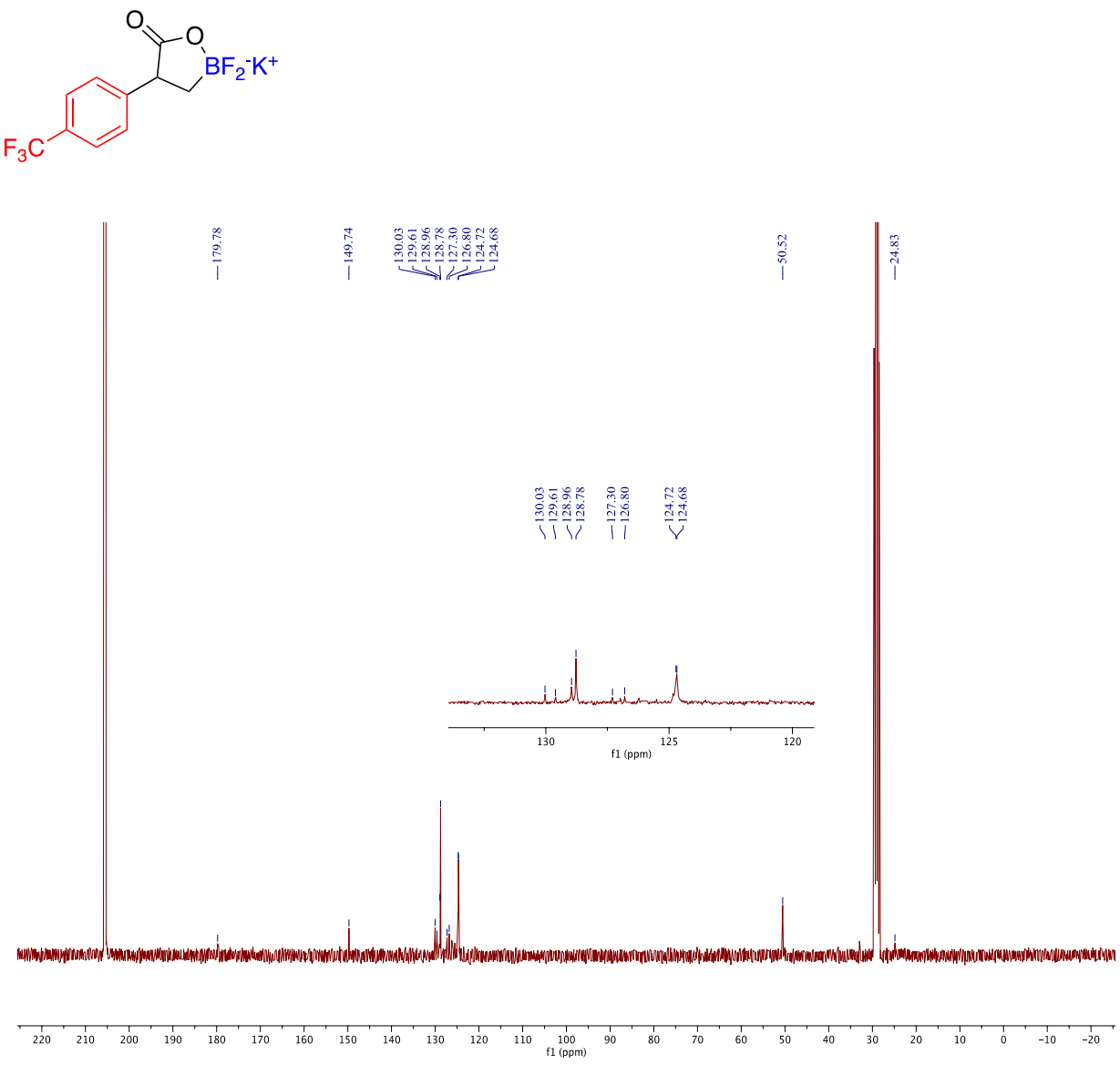

Figure A-99. ^{13}C NMR Spectrum of 2n in Acetone-d_6.

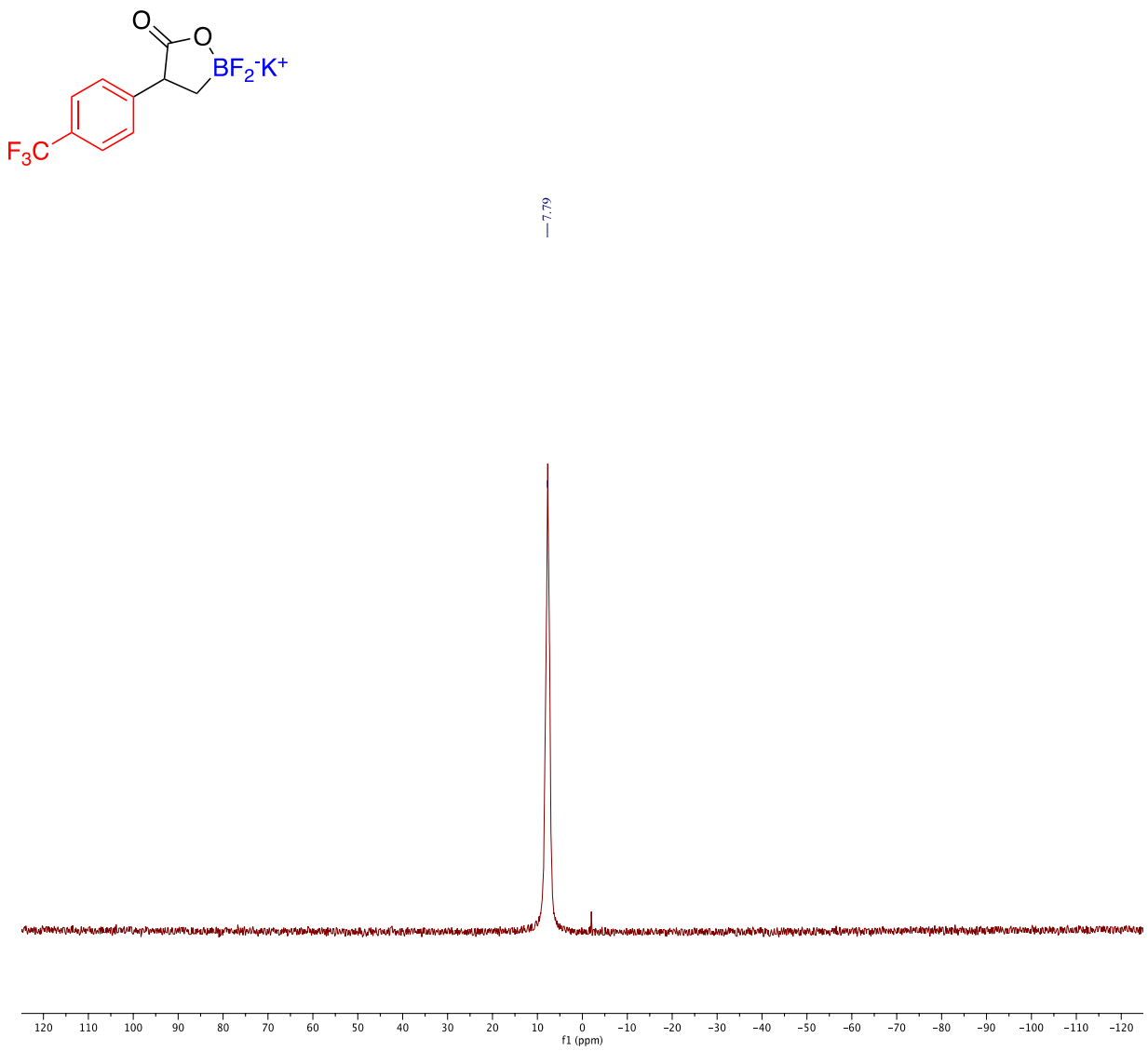

Figure A-100. ^{11}B NMR Spectrum of 2n in Acetone-d_6.

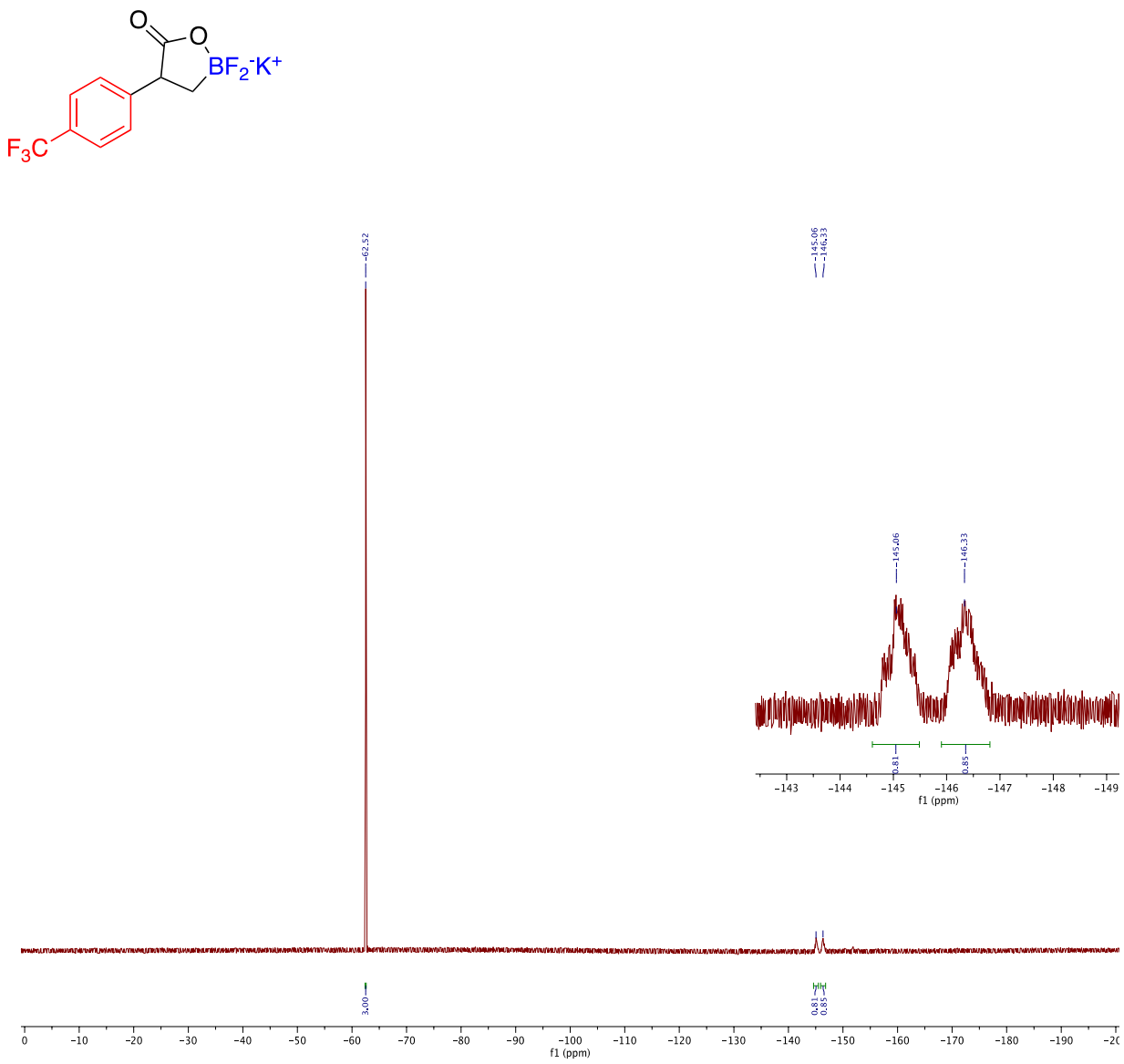

Figure A-101. ^{19}F NMR Spectrum of 2n in Acetone-d_6.

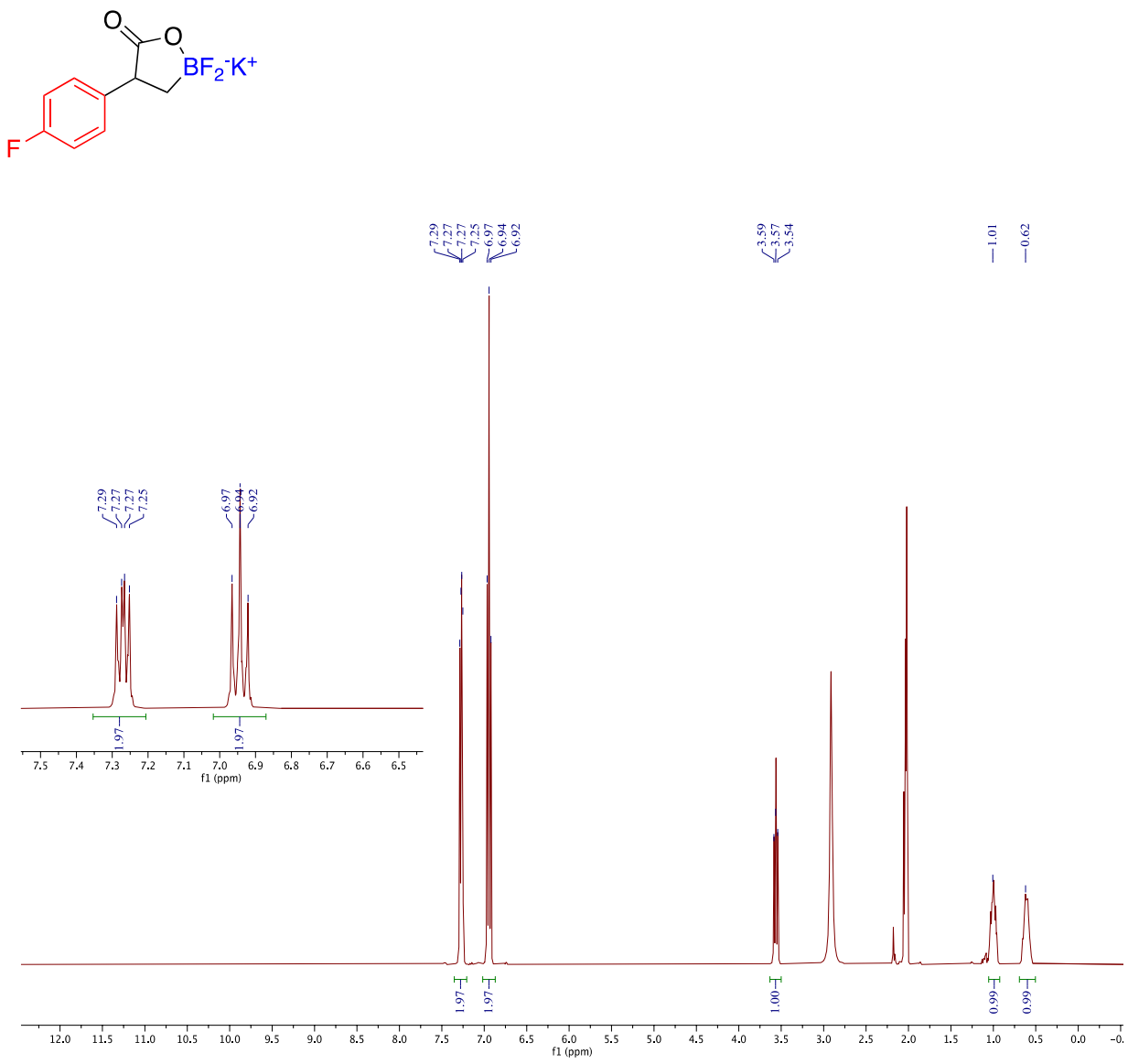

Figure A-102. ^{1}H NMR Spectrum of 2o in Acetone-d_6.

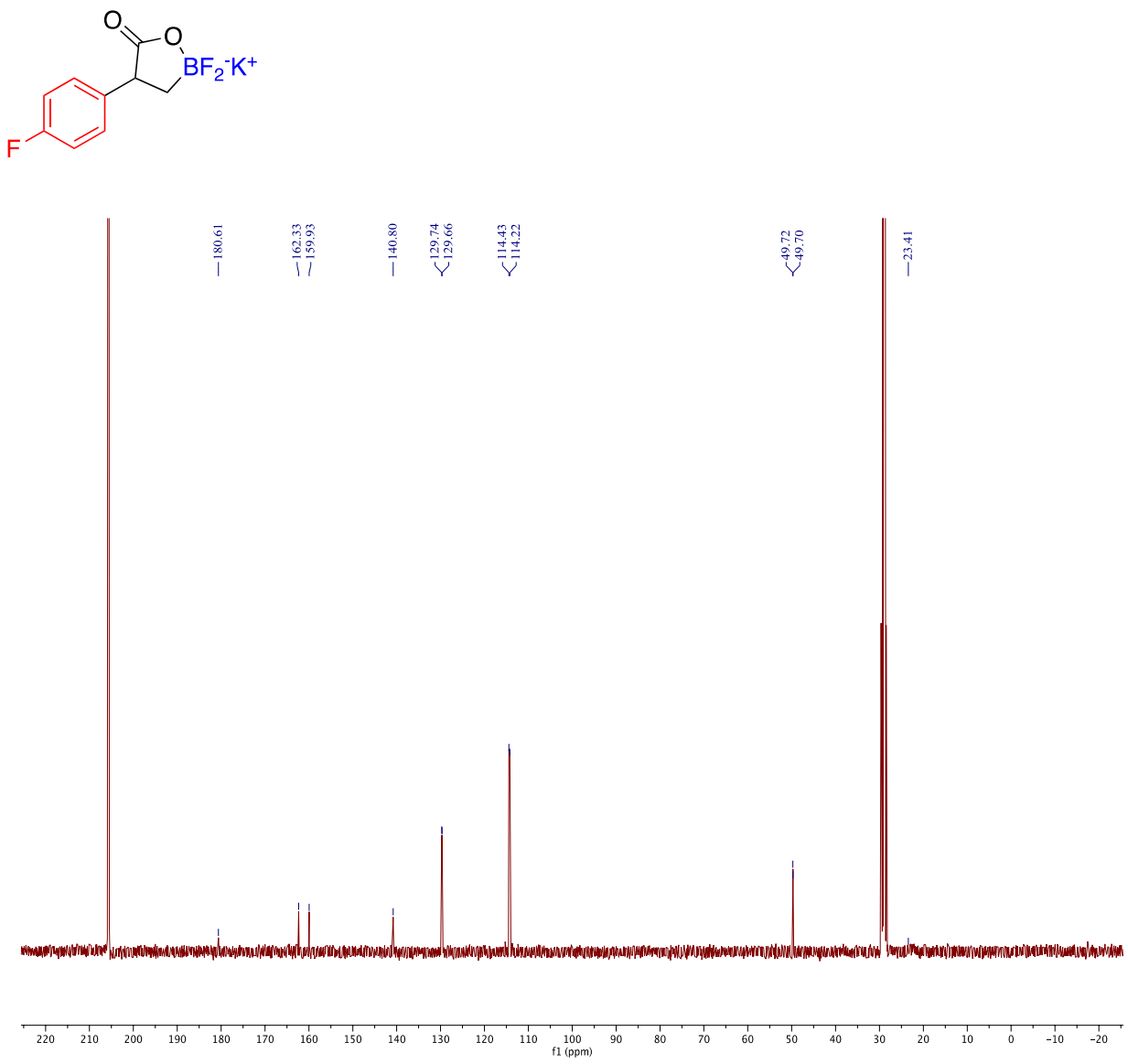

Figure A-103. ^{13}C NMR Spectrum of 2o in Acetone-d_6.

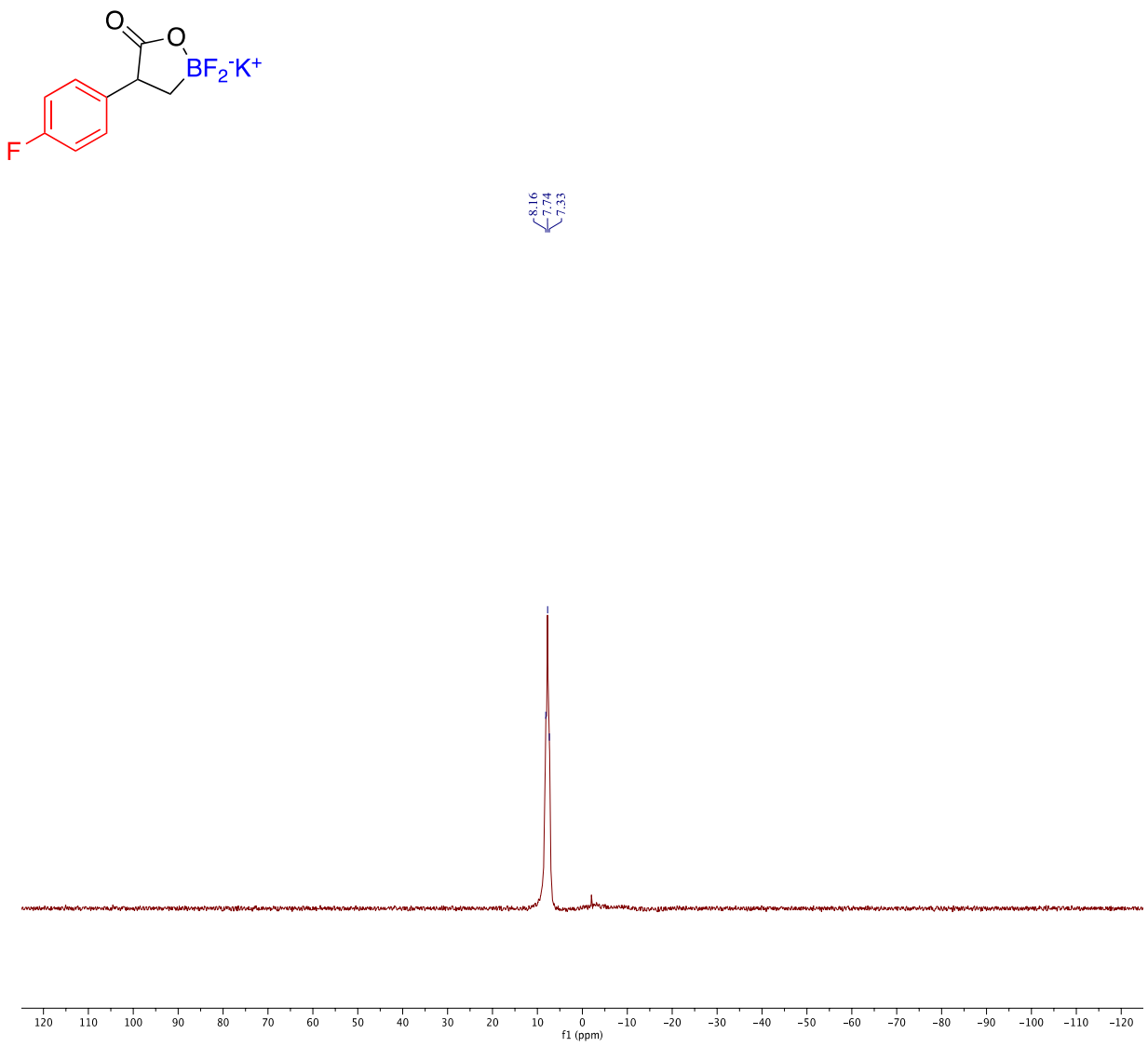

Figure A-104. ^{11}B NMR Spectrum of 2o in Acetone-d_6.

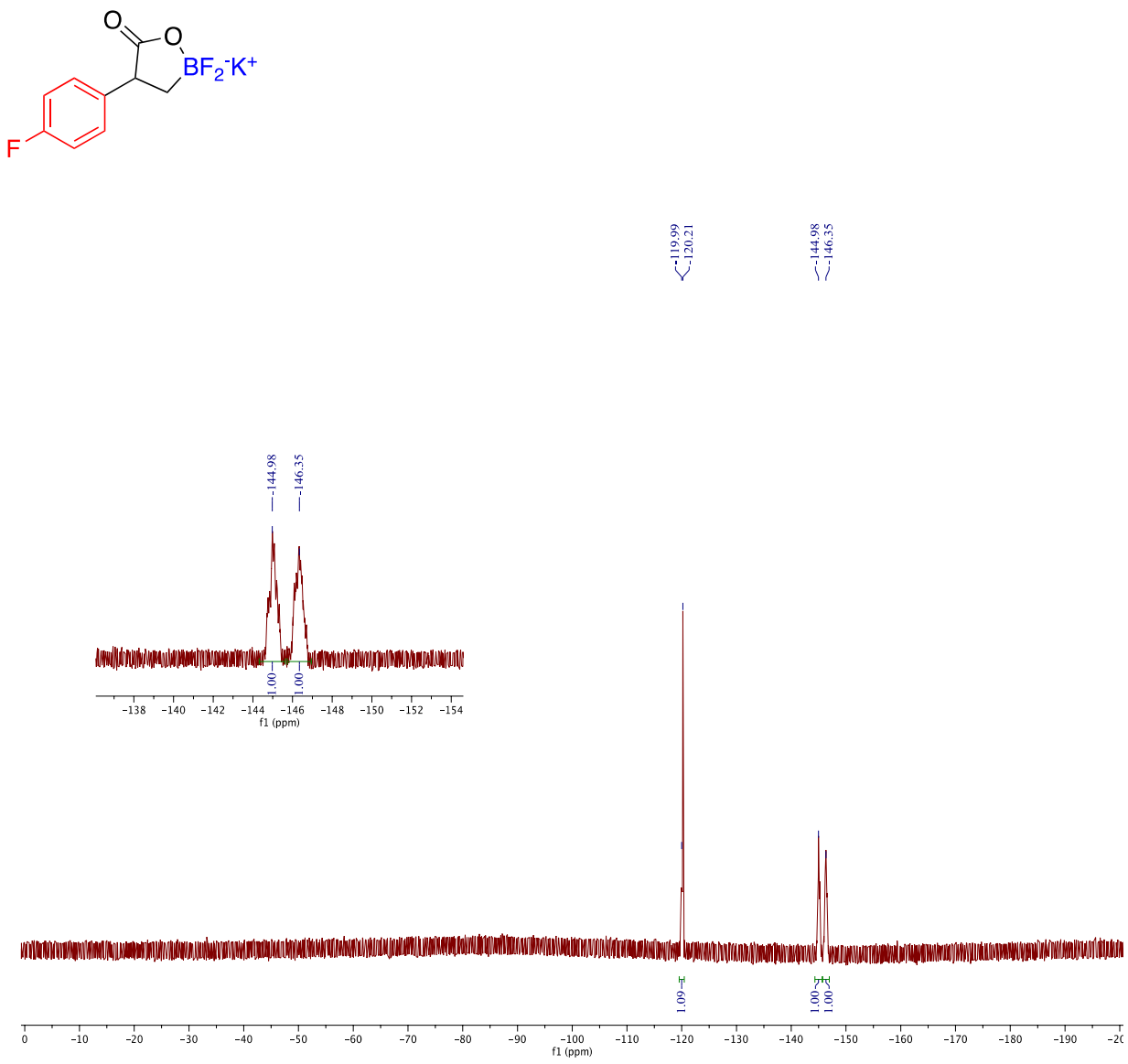

Figure A-105. ^{19}F NMR Spectrum of 2o in Acetone-d_6.

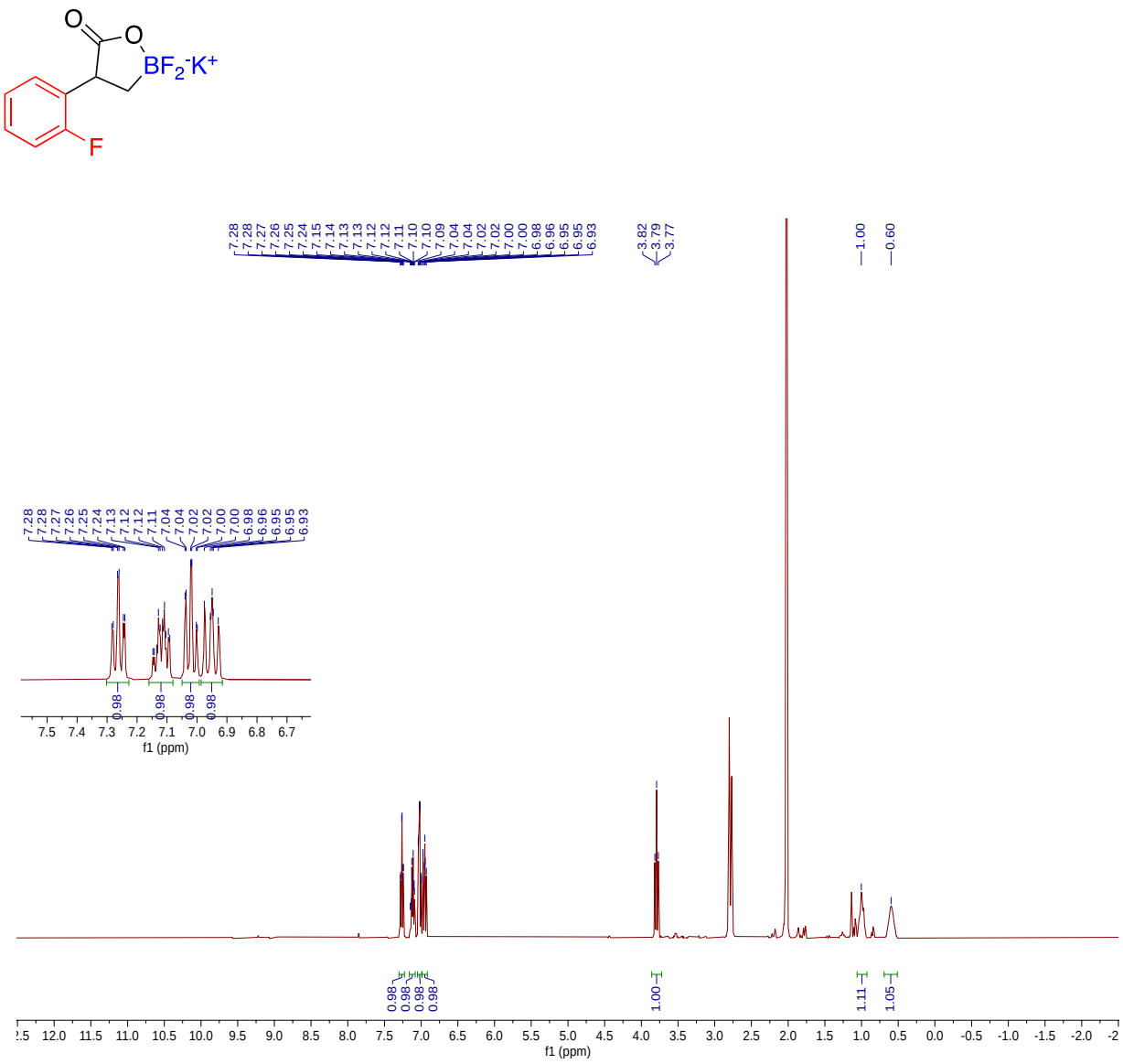

Figure A-106. ^{11}H NMR Spectrum of 2p in Acetone-d$_6$.

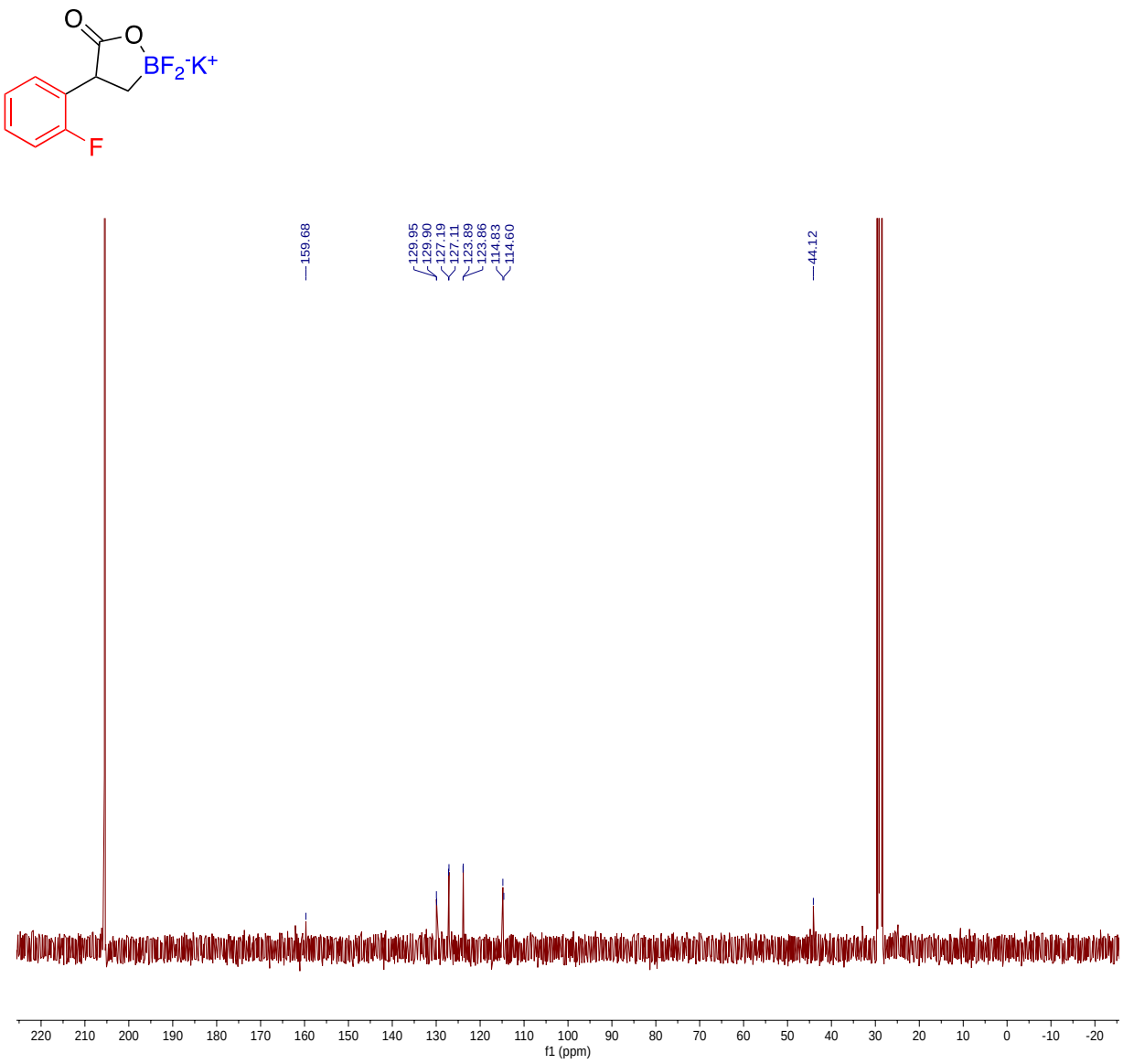

Figure A-107. ^{13}C NMR Spectrum of 2p in Acetone-d_6.

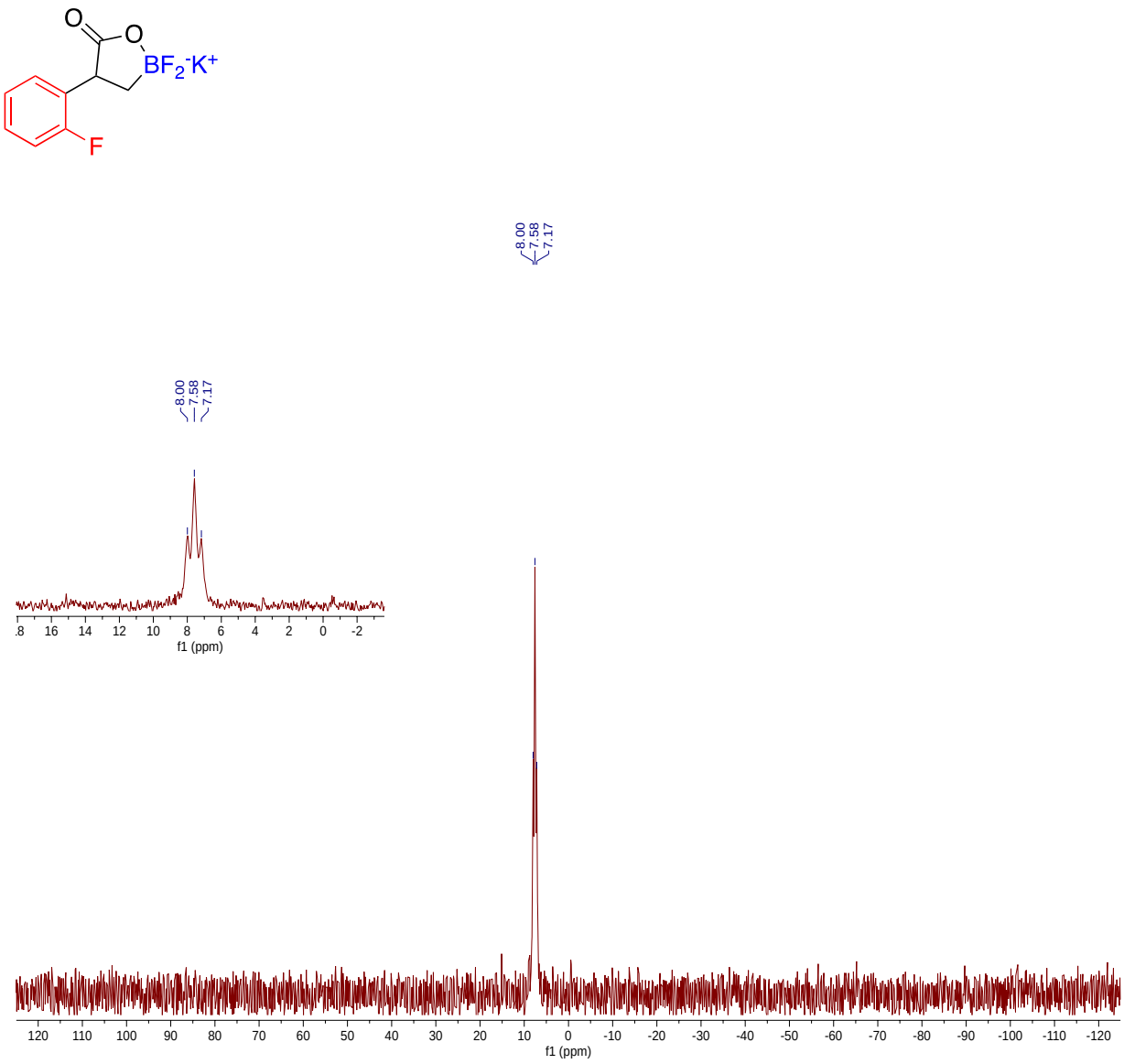

Figure A-108. ^{11}B NMR Spectrum of 2p in Acetone-d_6.

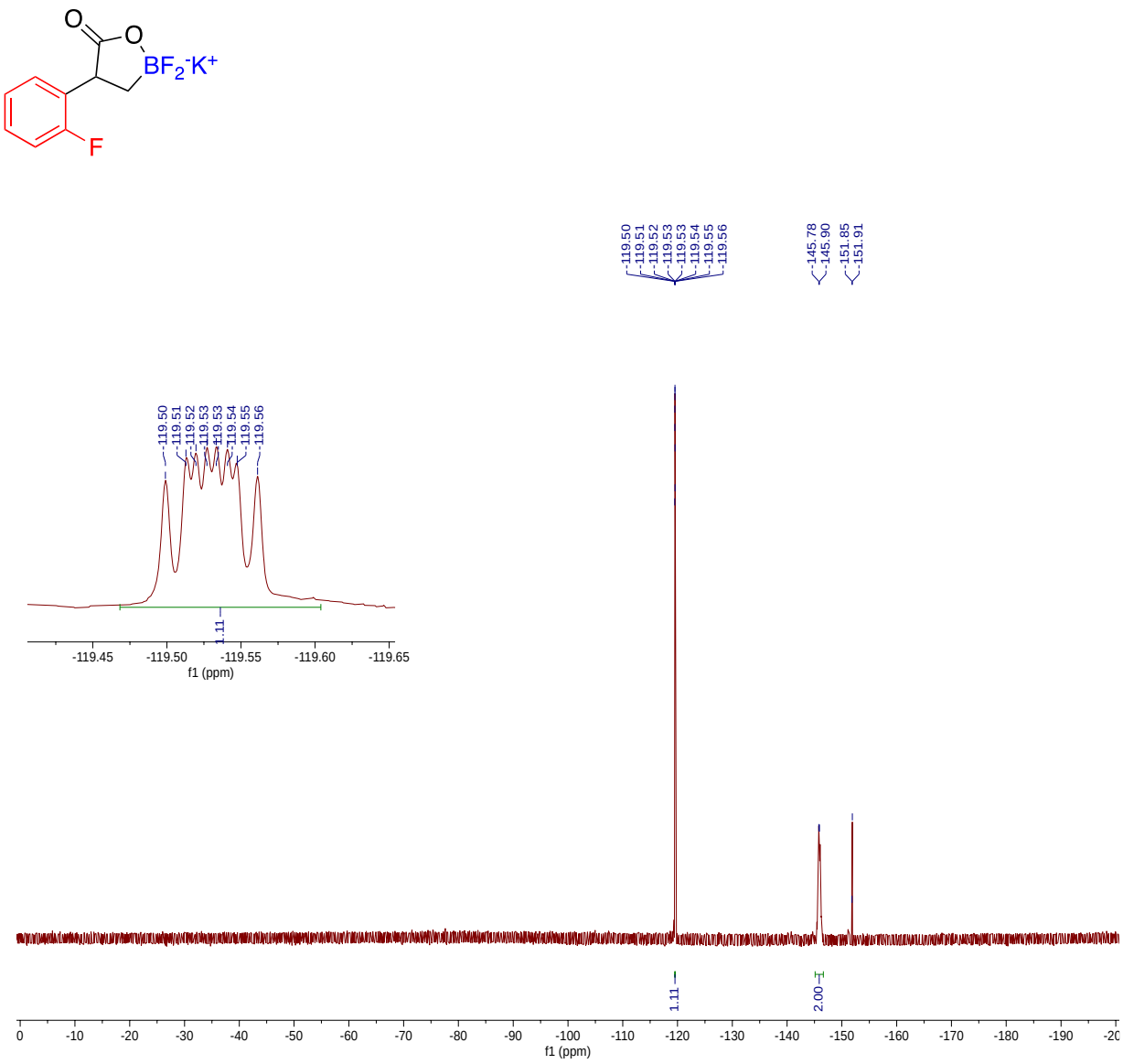

Figure A-109. ^{19}F NMR Spectrum of 2p in Acetone-d_6.

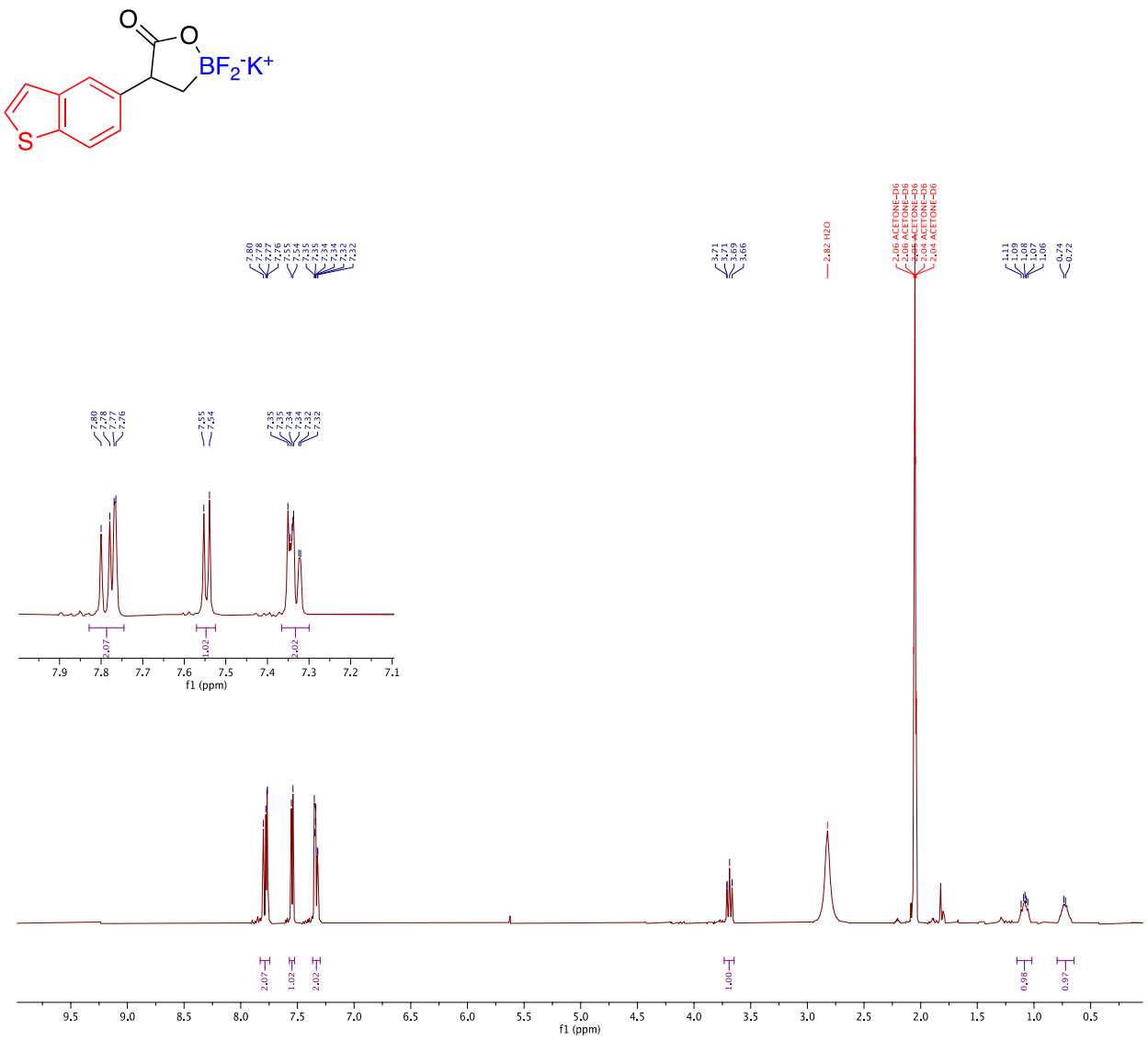

Figure A-110. ^{1}H NMR Spectrum of 2q in Acetone-d_6.

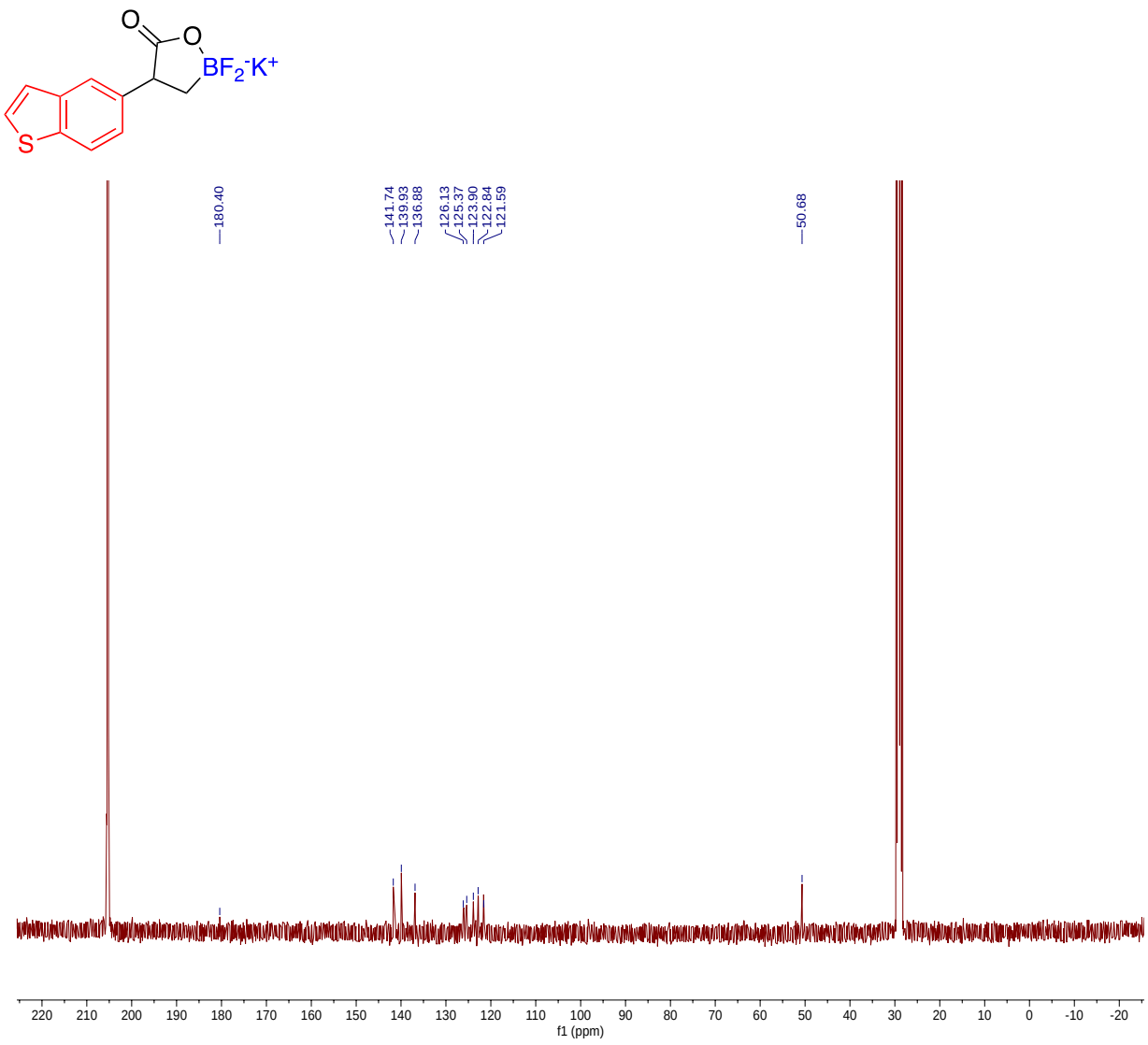

Figure A-111. ^{13}C NMR Spectrum of 2q in Acetone-d_6.

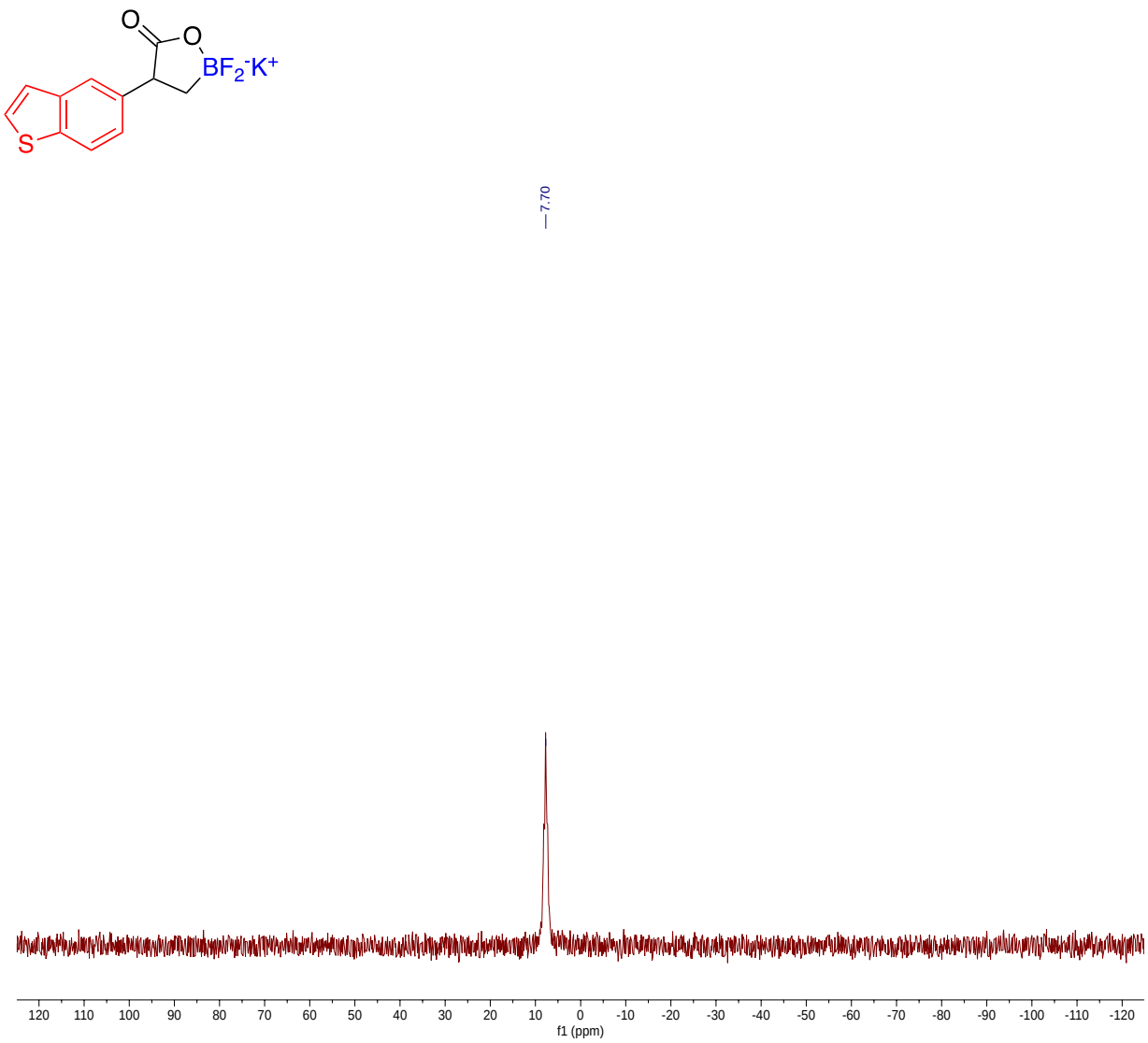

Figure A-112. ^{11}B NMR Spectrum of 2q in Acetone-d_6.

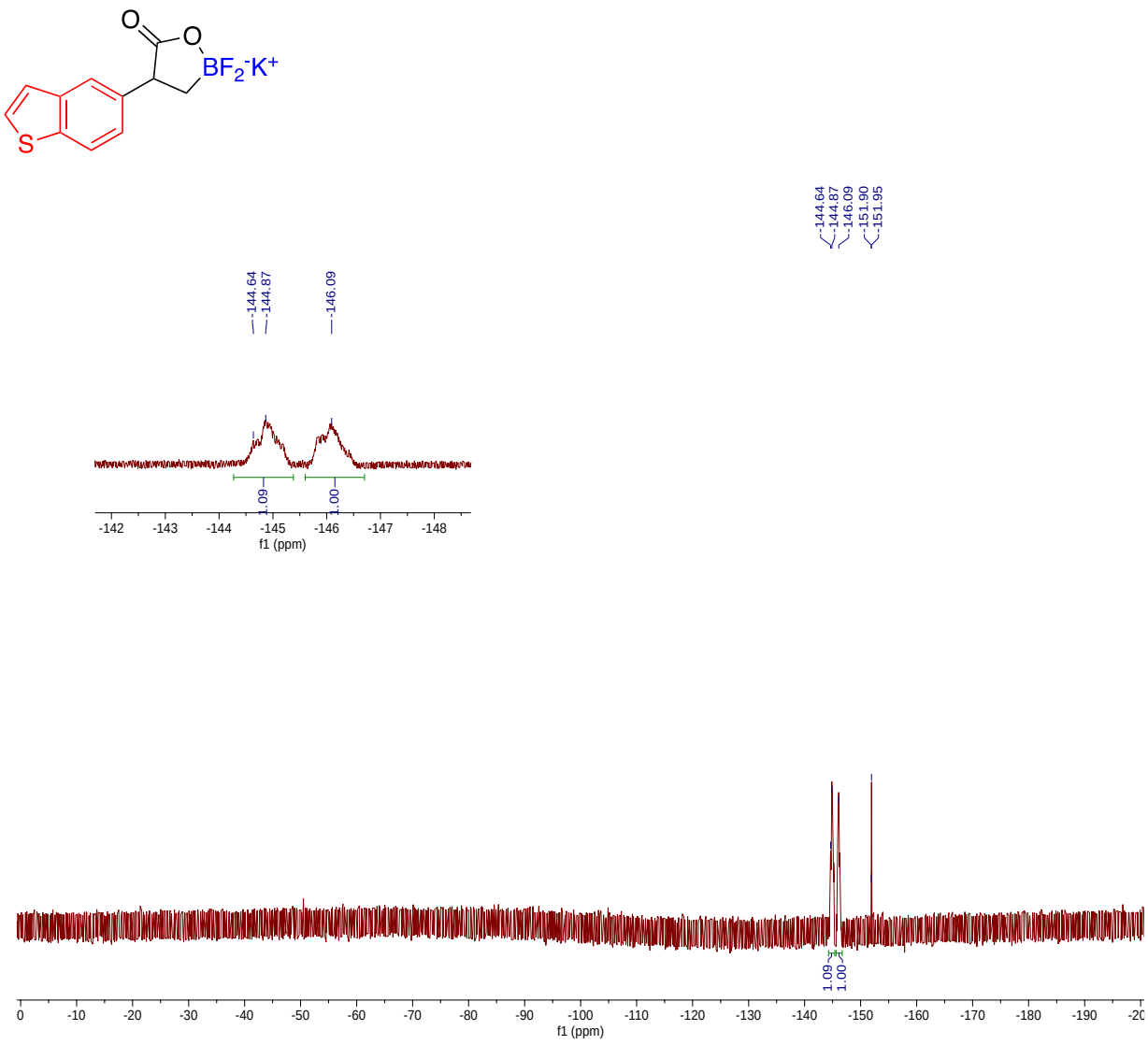

Figure A-113. ^{19}F NMR Spectrum of 2q in Acetone-d_6.

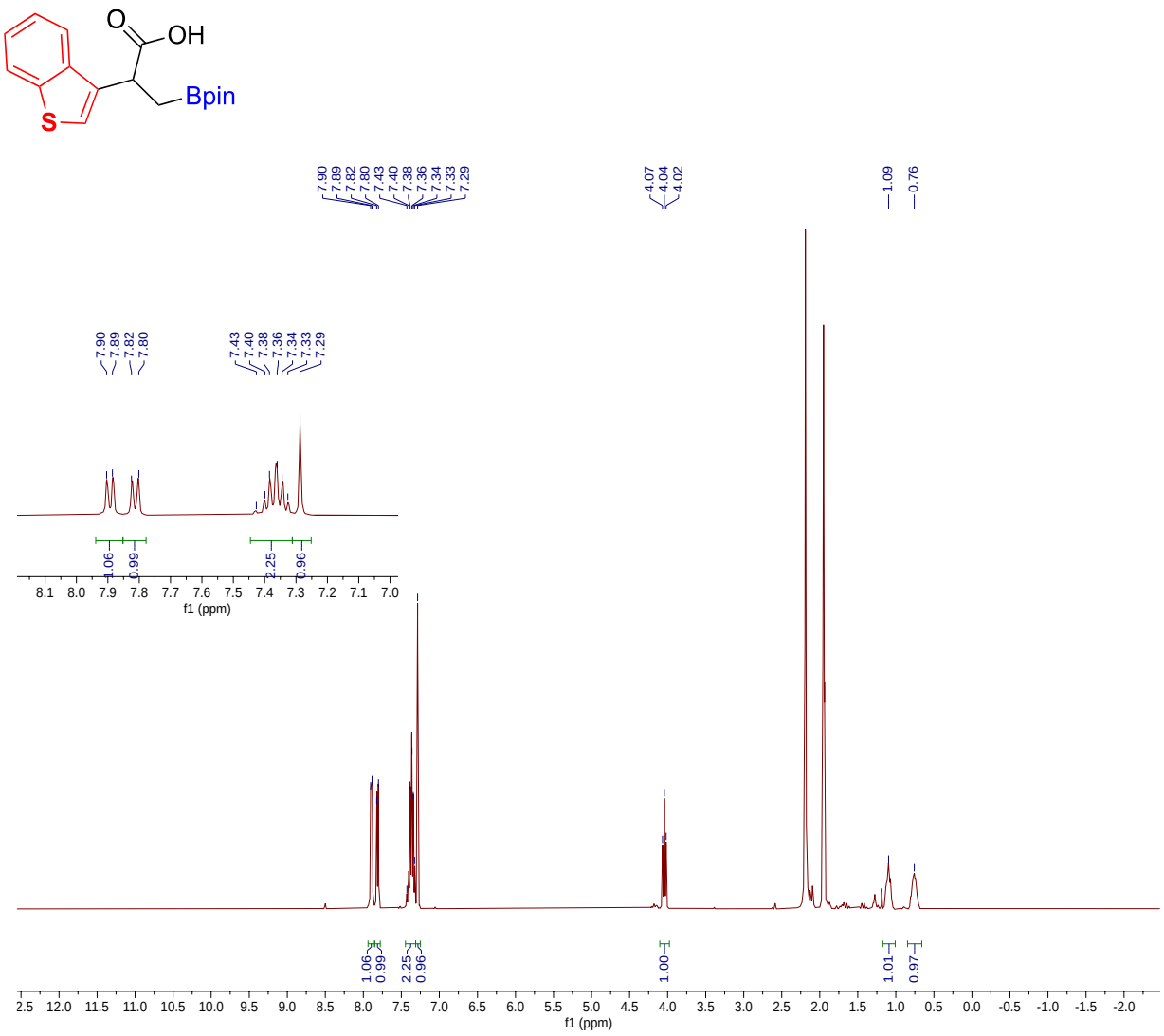

Figure A-114. ^{1}H NMR Spectrum of 2r in DMSO-d_6.

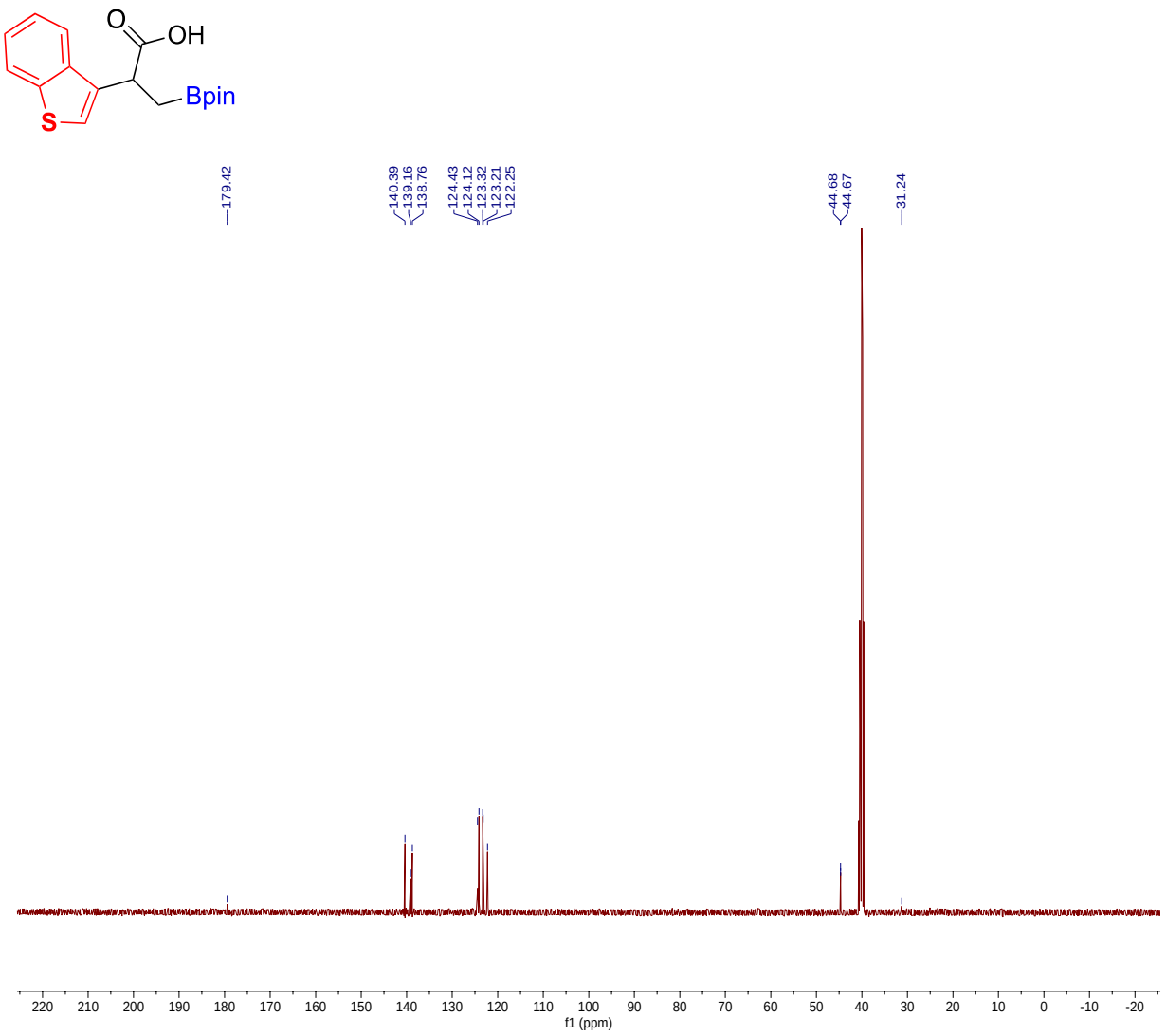

Figure A-115. ^{13}C NMR Spectrum of 2r in DMSO-d$_6$.

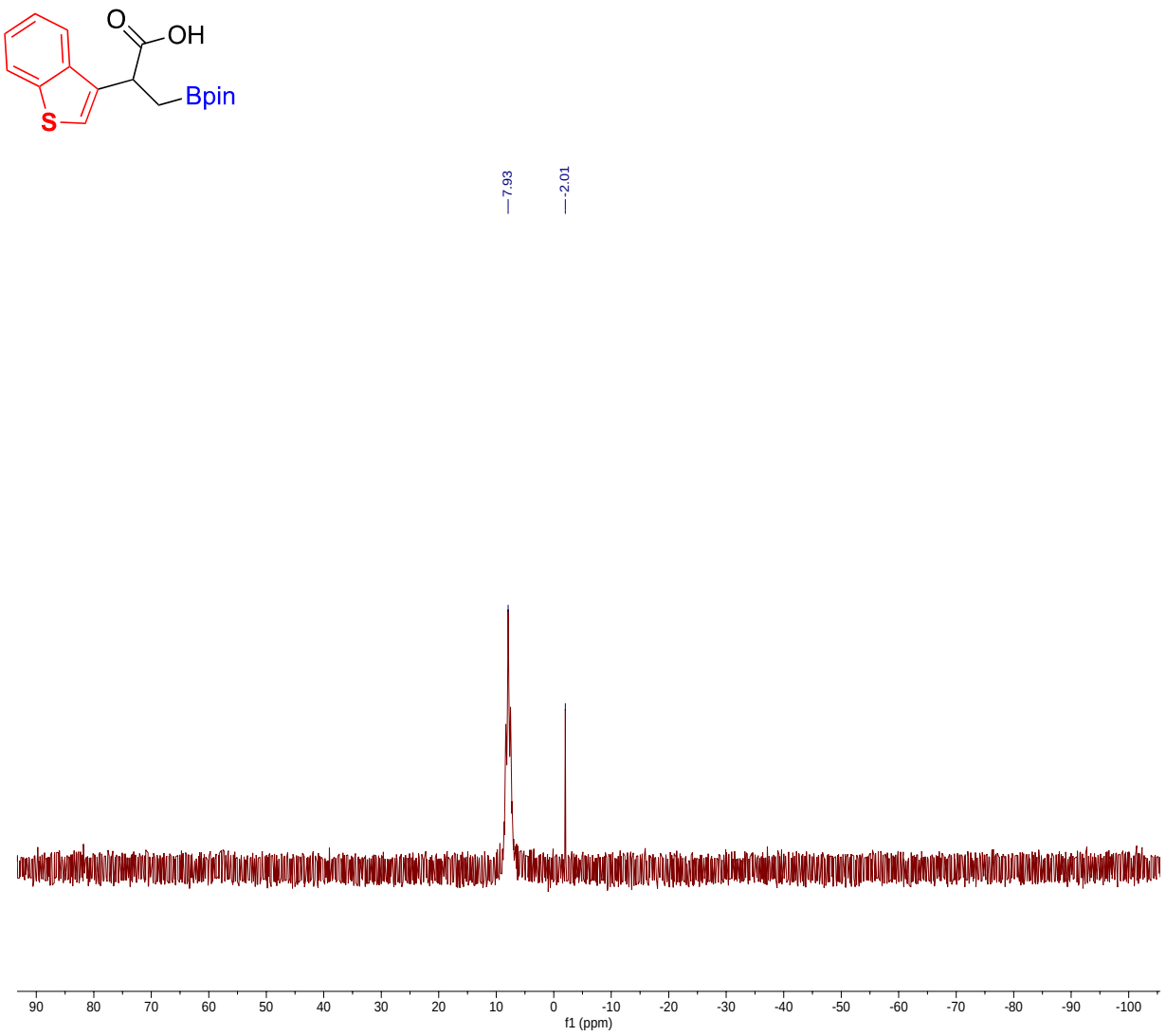

Figure A-116. ^{11}B NMR Spectrum of 2r in DMSO-d_6.

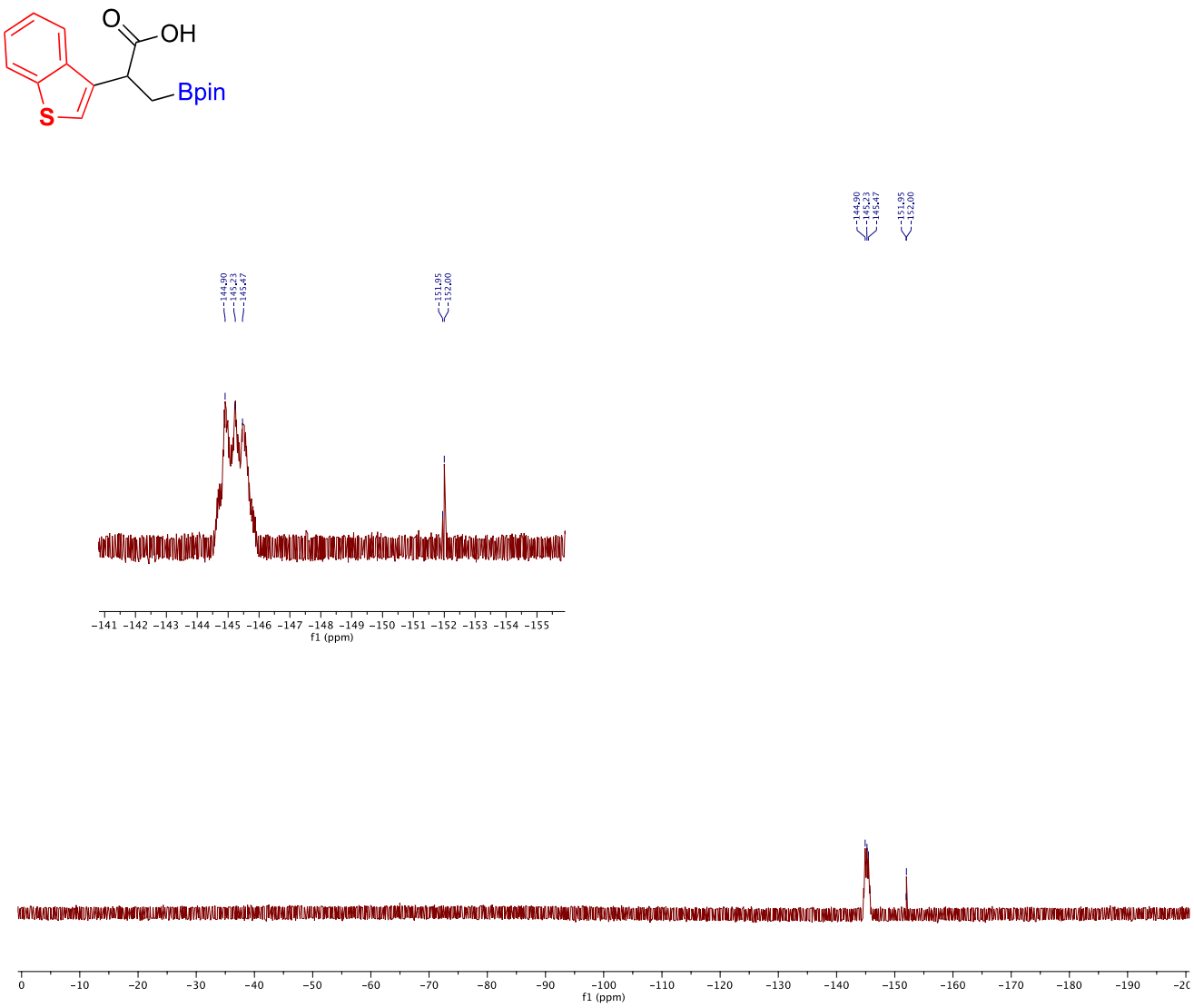

Figure A-117. ^{19}F NMR Spectrum of 2r in DMSO-d_6.

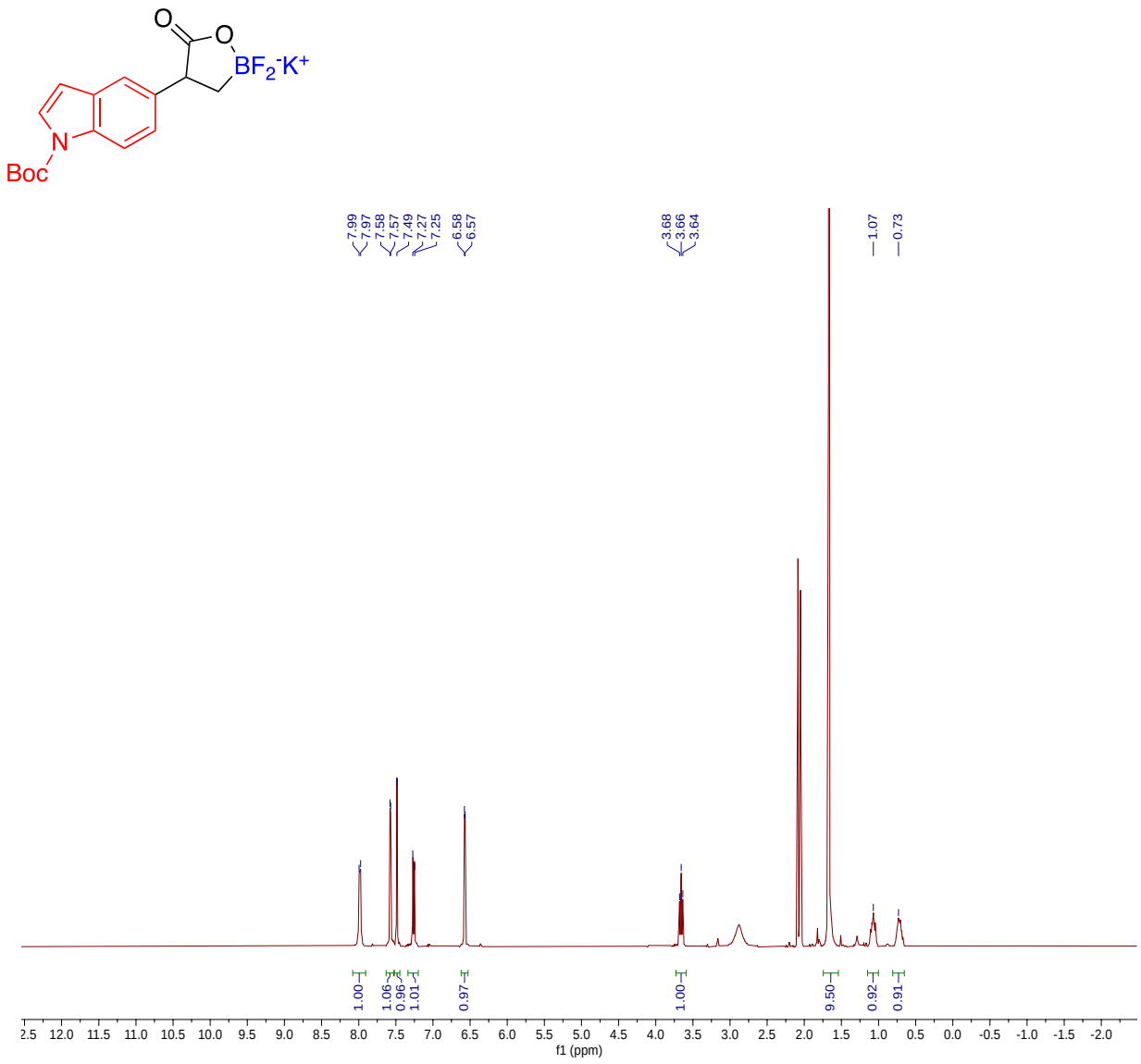

Figure A-118. ^{1}H NMR Spectrum of 2s in Acetone-d_6.

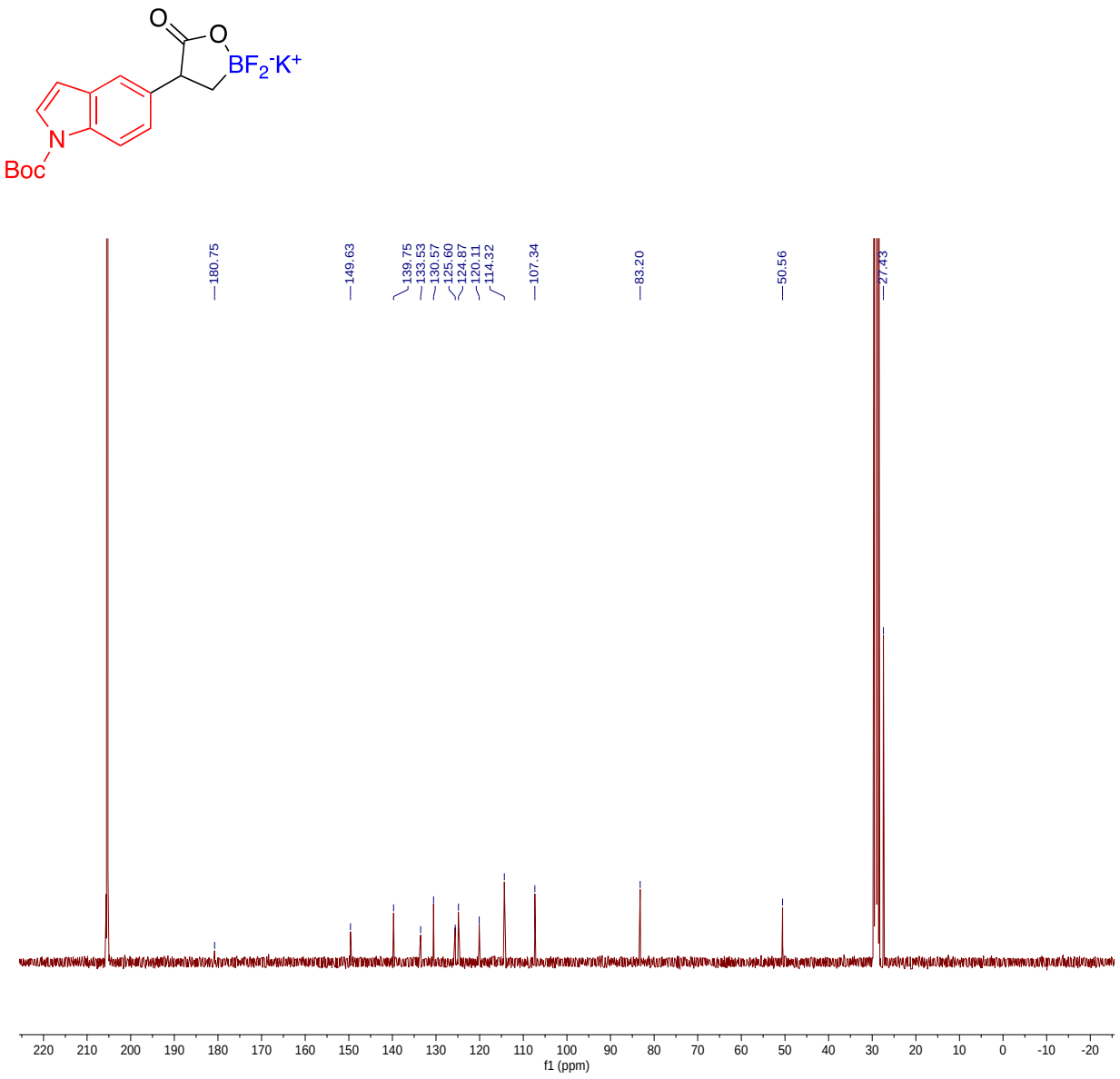

Figure A-119. ^{13}C NMR Spectrum of 2s in Acetone-d_6.

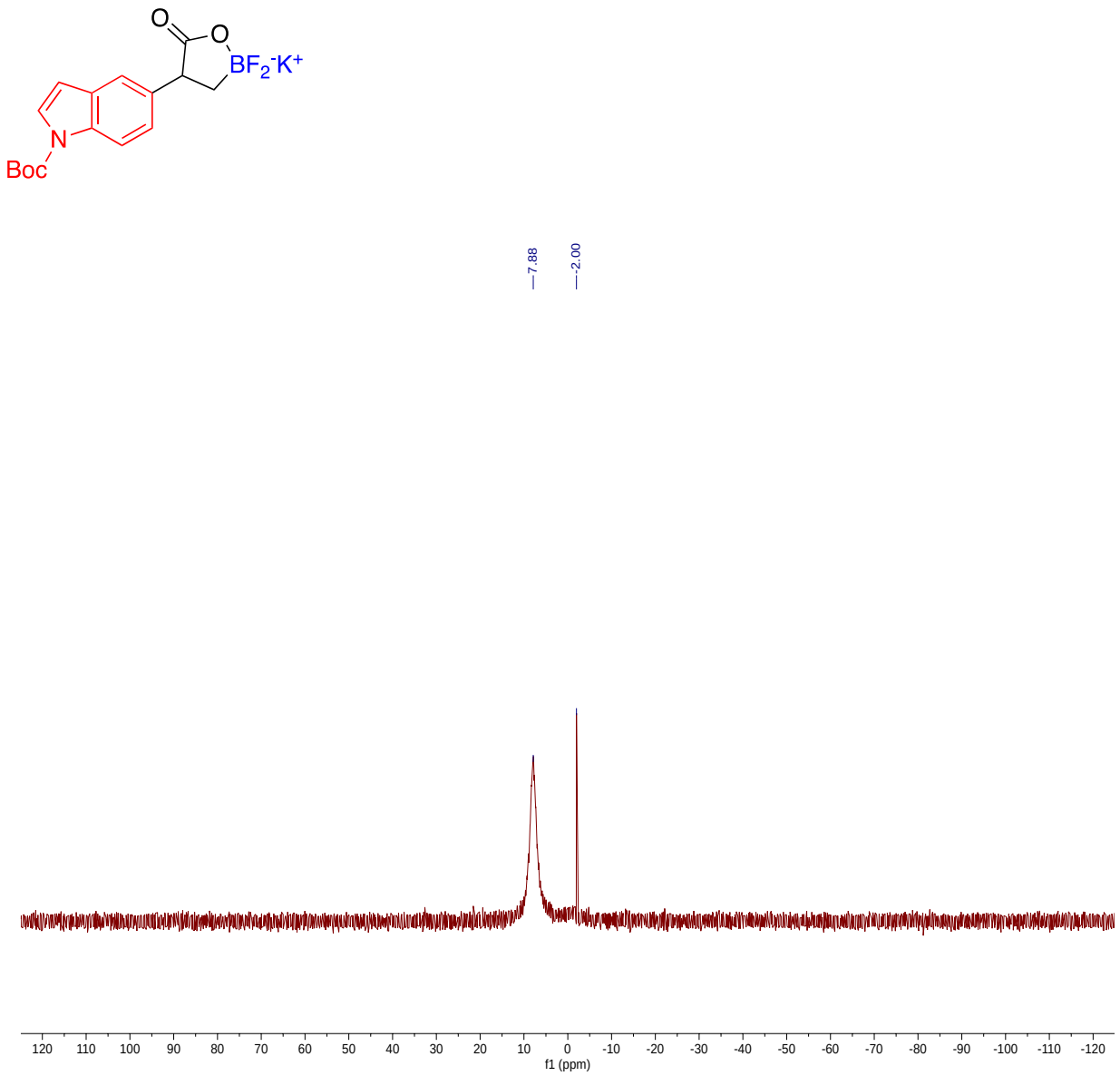

Figure A-120. ^{11}B NMR Spectrum of 2s in Acetone-d_6.

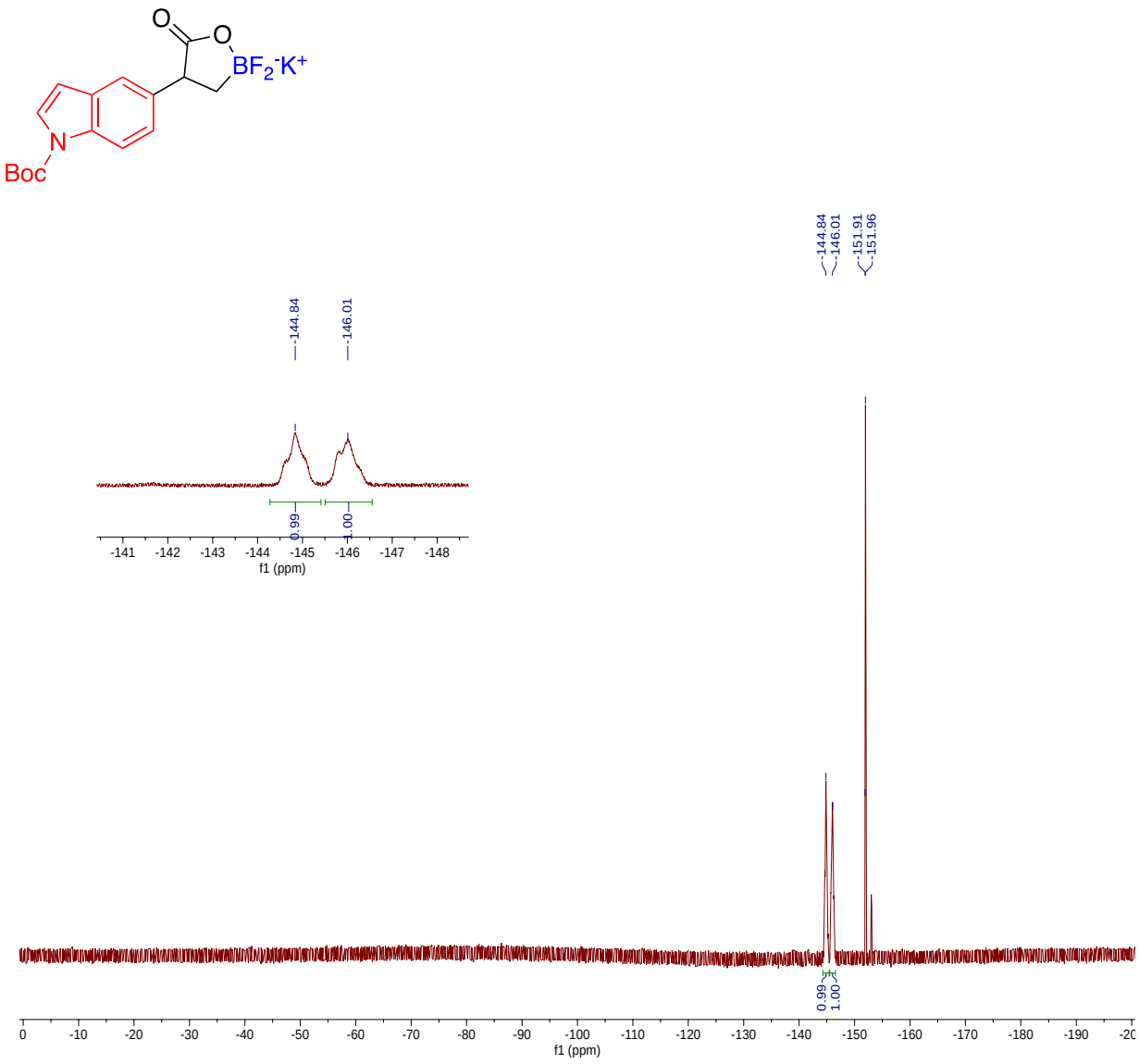

Figure A-121. ^{19}F NMR Spectrum of 2s in Acetone-d_6.

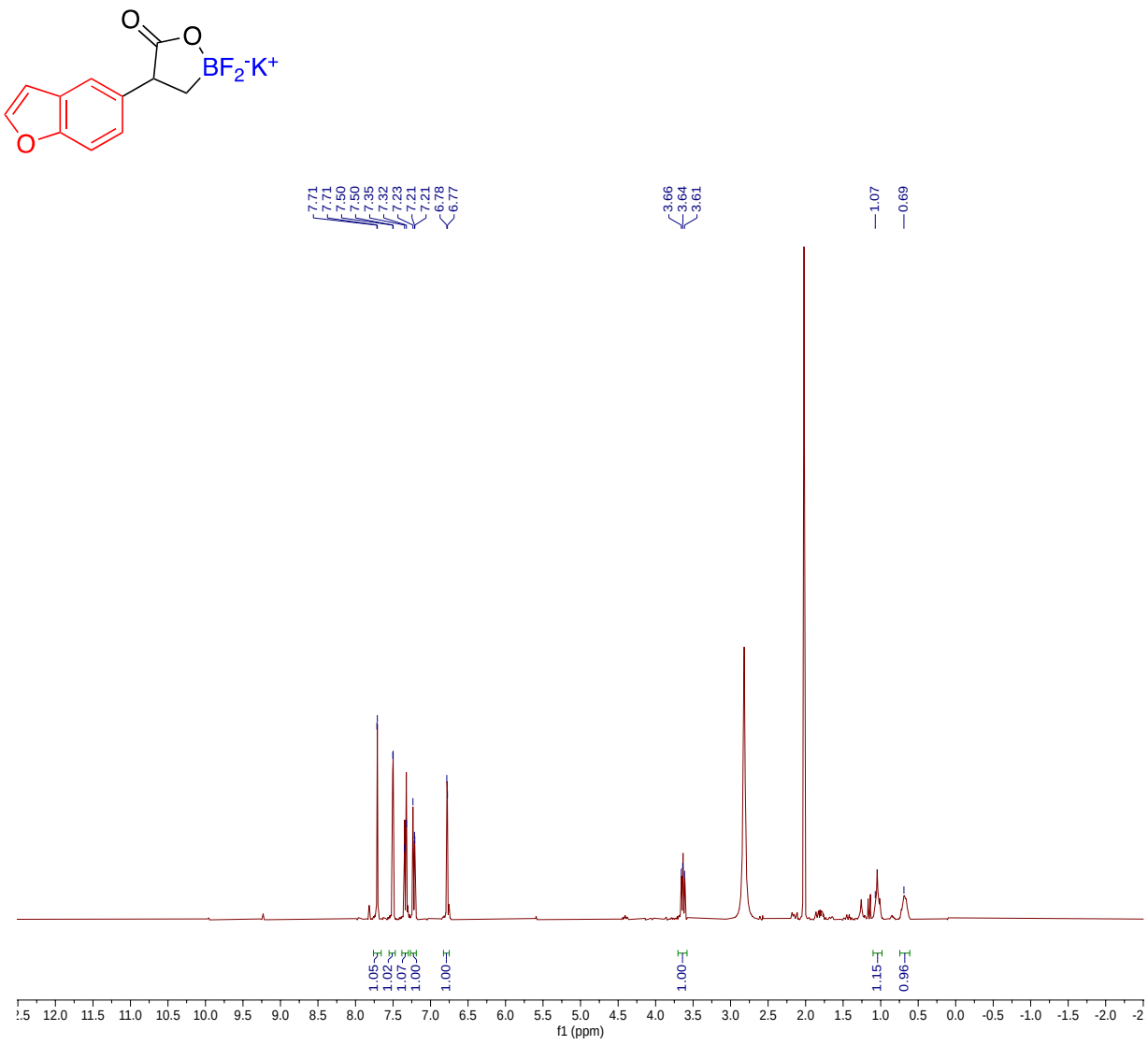

Figure A-122. ^{1}H NMR Spectrum of 2t in Acetone-d_6.

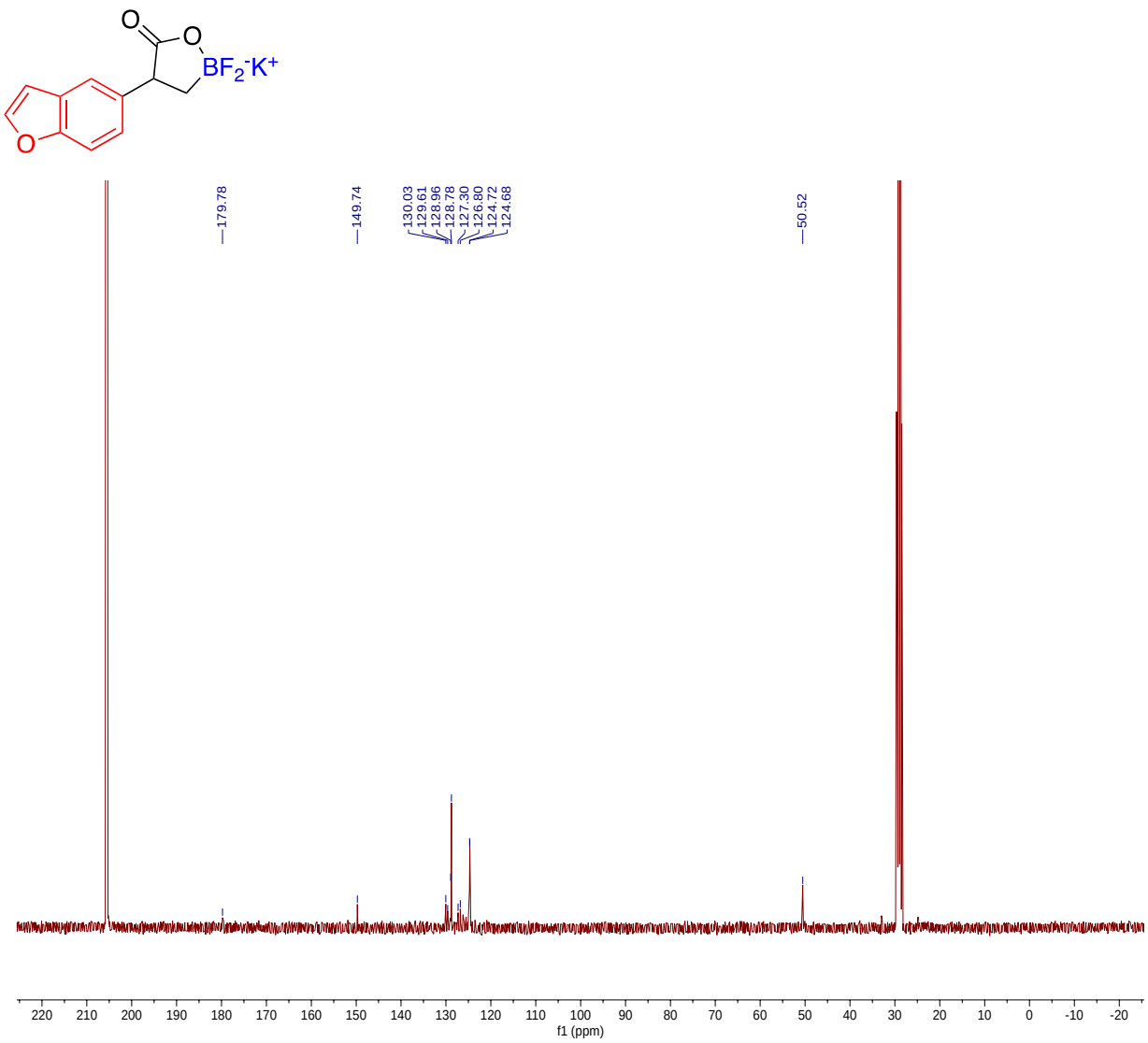

Figure A-123. ^{13}C NMR Spectrum of 2t in Acetone-d_6.

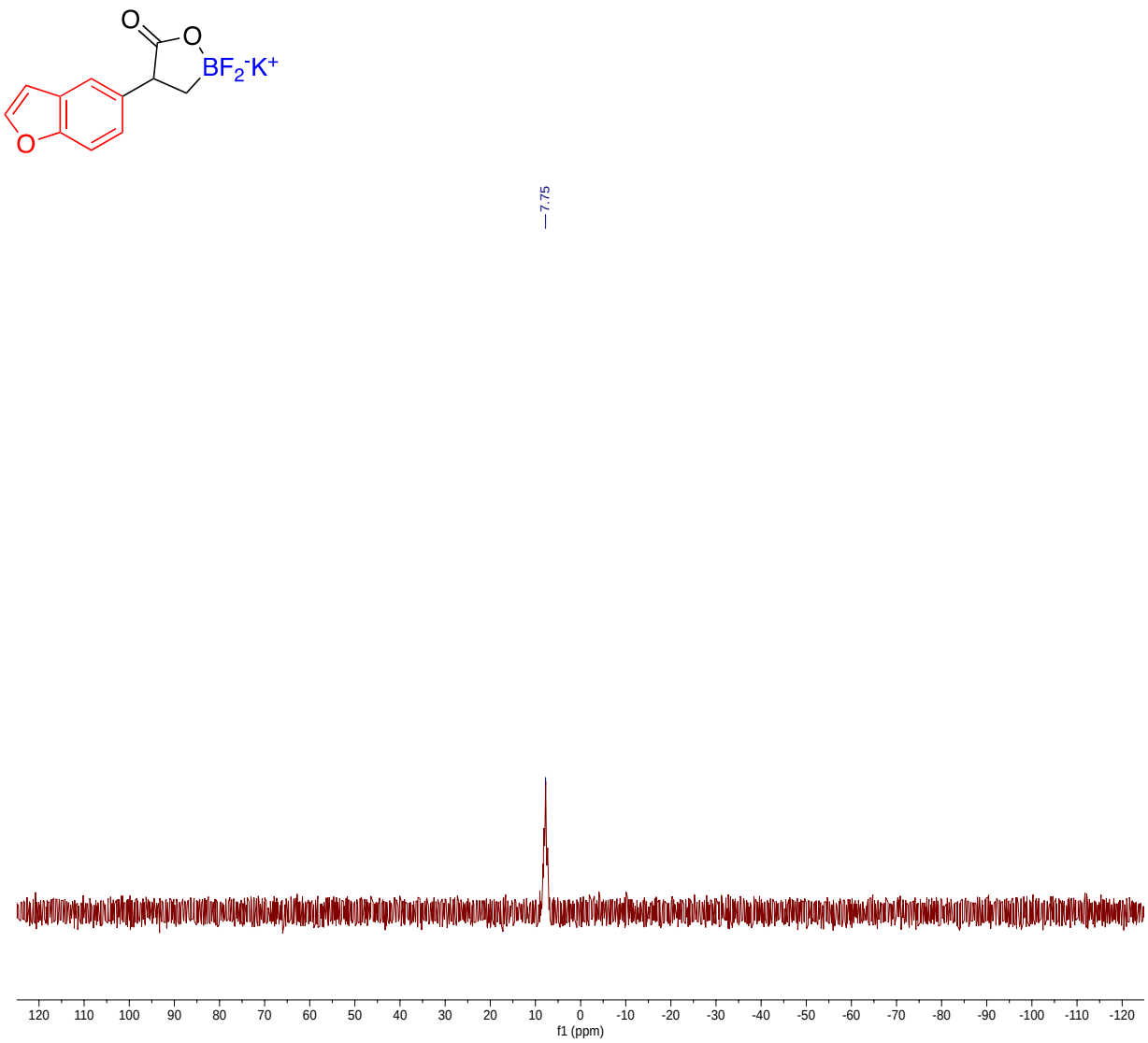

Figure A-124. ^{11}B NMR Spectrum of 2t in Acetone-d_6.

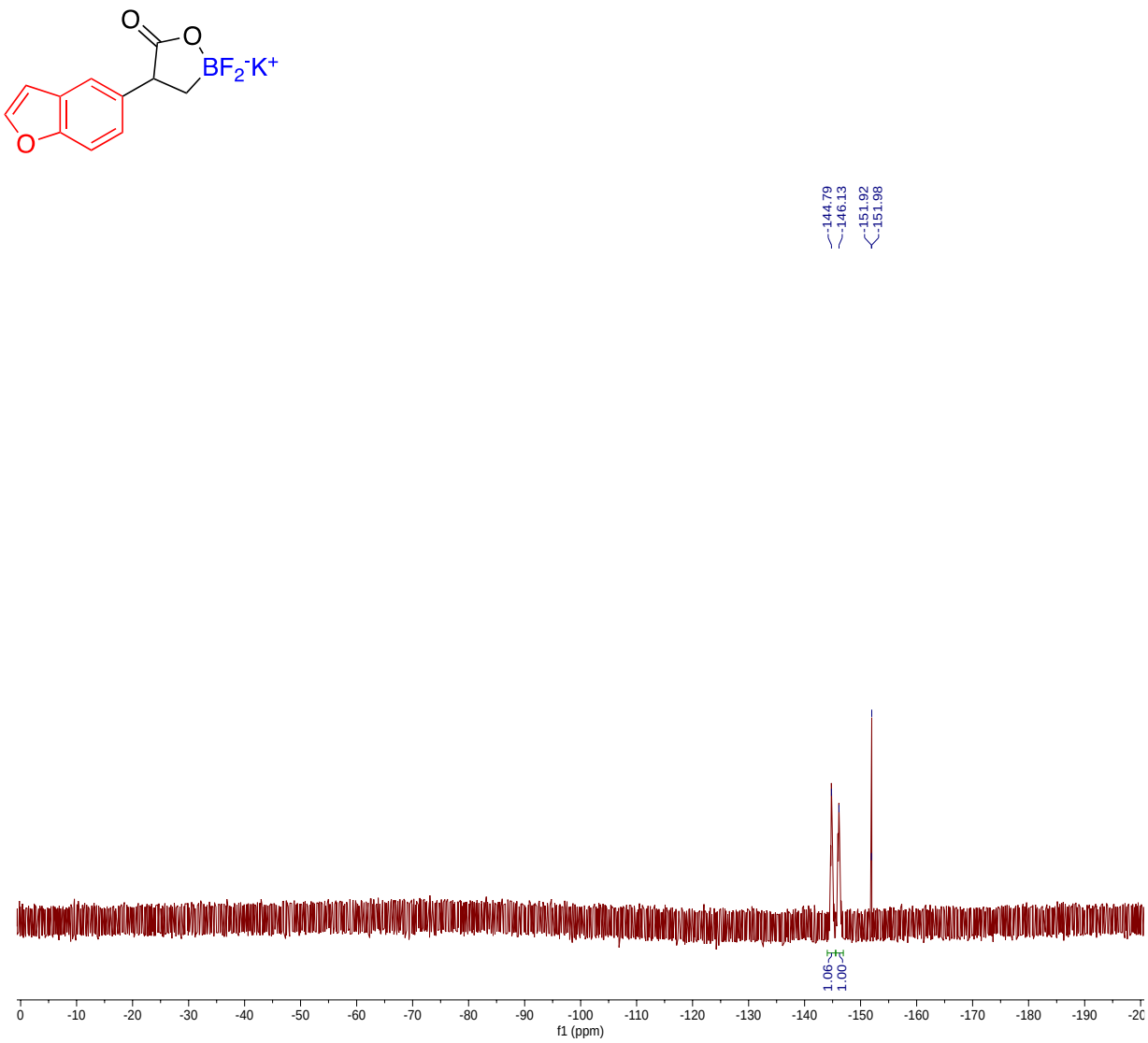

Figure A-125. ^{19}F NMR Spectrum of 2t in Acetone-d_6.

Equilibrium Data and ^{1}H, ^{13}C,^{11}B NMR Spectra-Compounds in Chapter V

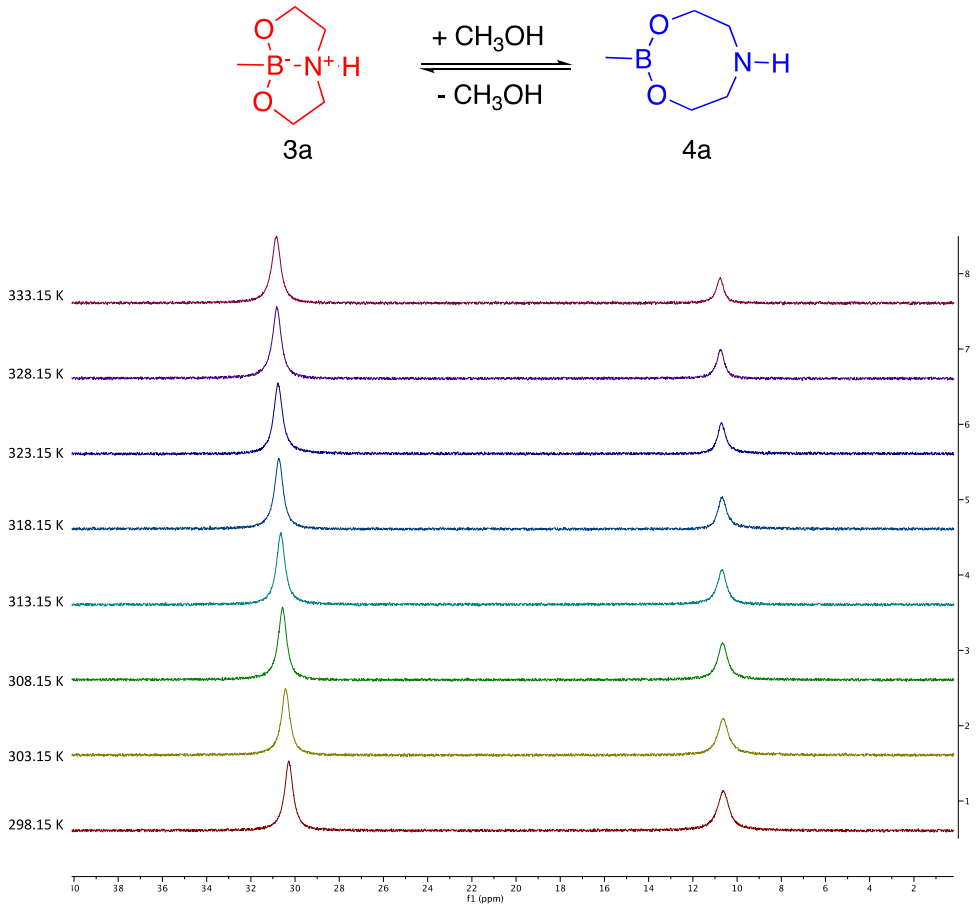

Figure A-126. VT-^{11}B NMR experimental data collected from 298.15 K to 333.15 K in CD_3OD-d4 *f*or the dynamic equilibrium between **3a** and **4a.**

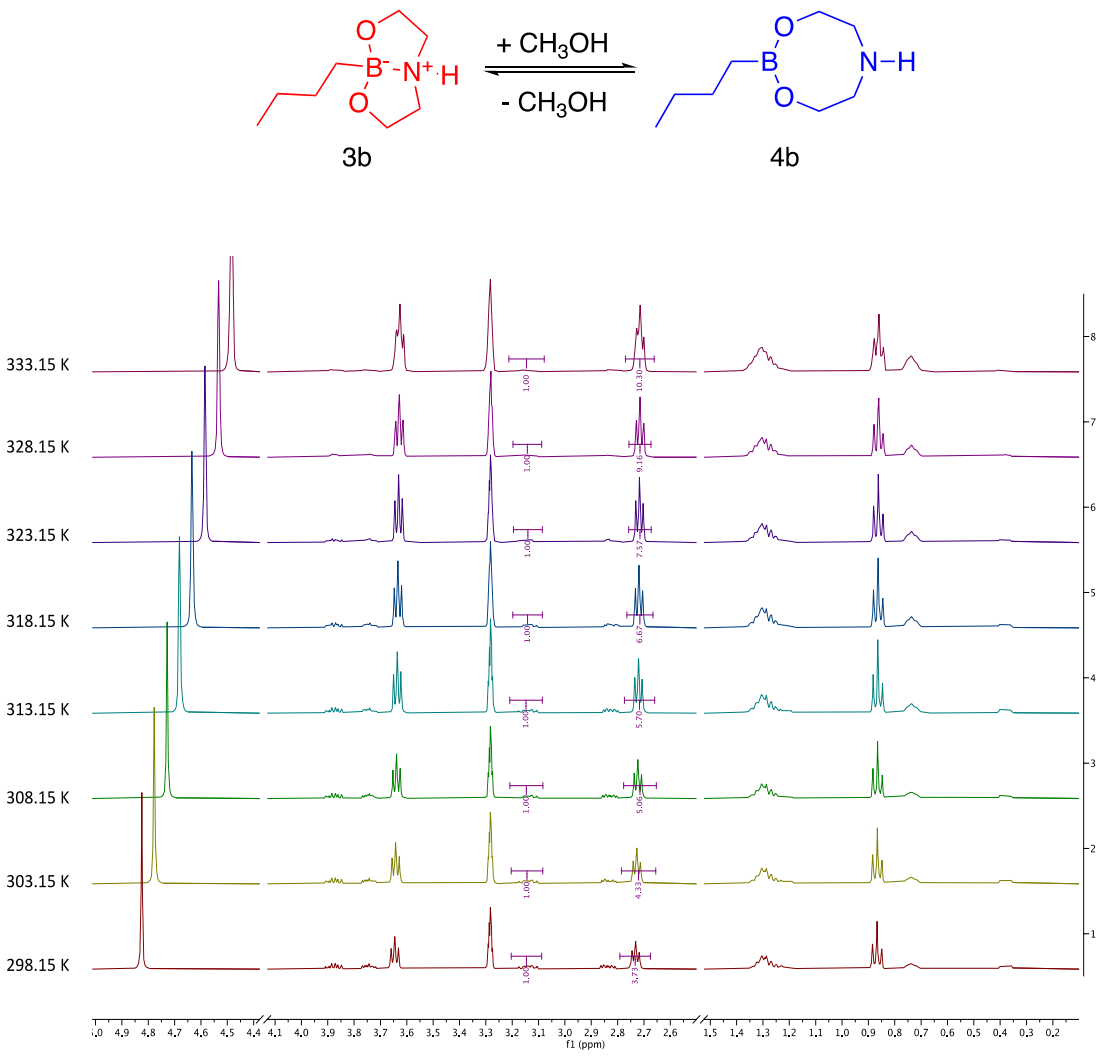

Figure A-127. VT-^{11}B NMR experimental data collected from 298.15 K to 333.15 K in CD_3OD-d4 *f*or the dynamic equilibrium between **3b** and **4b.**

Table A.1. Dynamic equilibria data for **3b** and **4b** in CD_3OD-d4 at different temperatures.

Temperature (K)	1/K x10^{-3}	Equilibrium ratio of [3,3,0] bicyclic ring structure (**3a**)	Equilibrium ratio of 8 membered ring structure (**4a**)	K_{eq}	ln K_{eq}
298.15	3.35	0.50	0.93	1.87	0.62
303.15	3.30	0.50	1.08	2.17	0.77
308.15	3.25	0.50	1.27	2.53	0.93
313.15	3.19	0.50	1.43	2.85	1.05
318.15	3.14	0.50	1.67	3.34	1.20
323.15	3.09	0.50	1.89	3.79	1.33
328.15	3.05	0.50	2.29	4.58	1.52
333.15	3.00	0.50	2.58	5.15	1.64

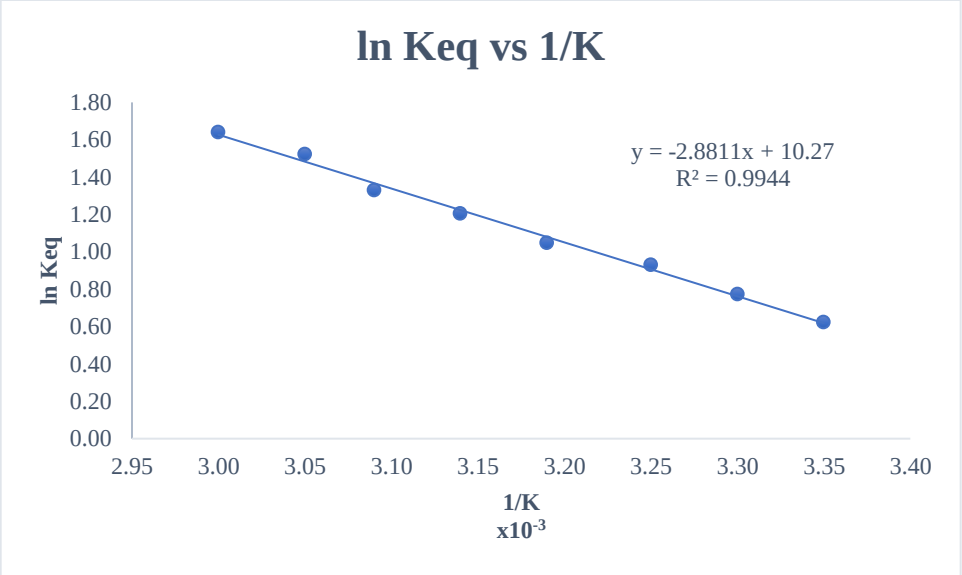

Figure A-128. Van't Hoff plot of ln K_{eq} vs. 1/T for equilibrium constants obtained for dynamic equilibria between **3a** and **4a** by VT ^{1}H NMR experiments at temperatures between 298.15 K to 333.15 K in CD_3OD-d4.

<u>$\Delta H°$ calculated using gradient</u>

$-\frac{\Delta H°}{R}$ = -2.8811

R = 1.987 cal K^{-1} mol^{-1}

$\Delta H°$ = 5.72 kcal mol^{-1}

<u>$\Delta S°$ calculated using intercept</u>

$\frac{\Delta S°}{R}$ = 10.27

R = 1.987 cal K^{-1} mol^{-1}

$\Delta S°$ = 20.4 cal K^{-1} mol^{-1}

<u>$\Delta G°$ calculated at 298.15,</u>

$\Delta G° = \Delta H° - T\Delta S$

$\Delta G°$ = - 356 cal mol^{-1}

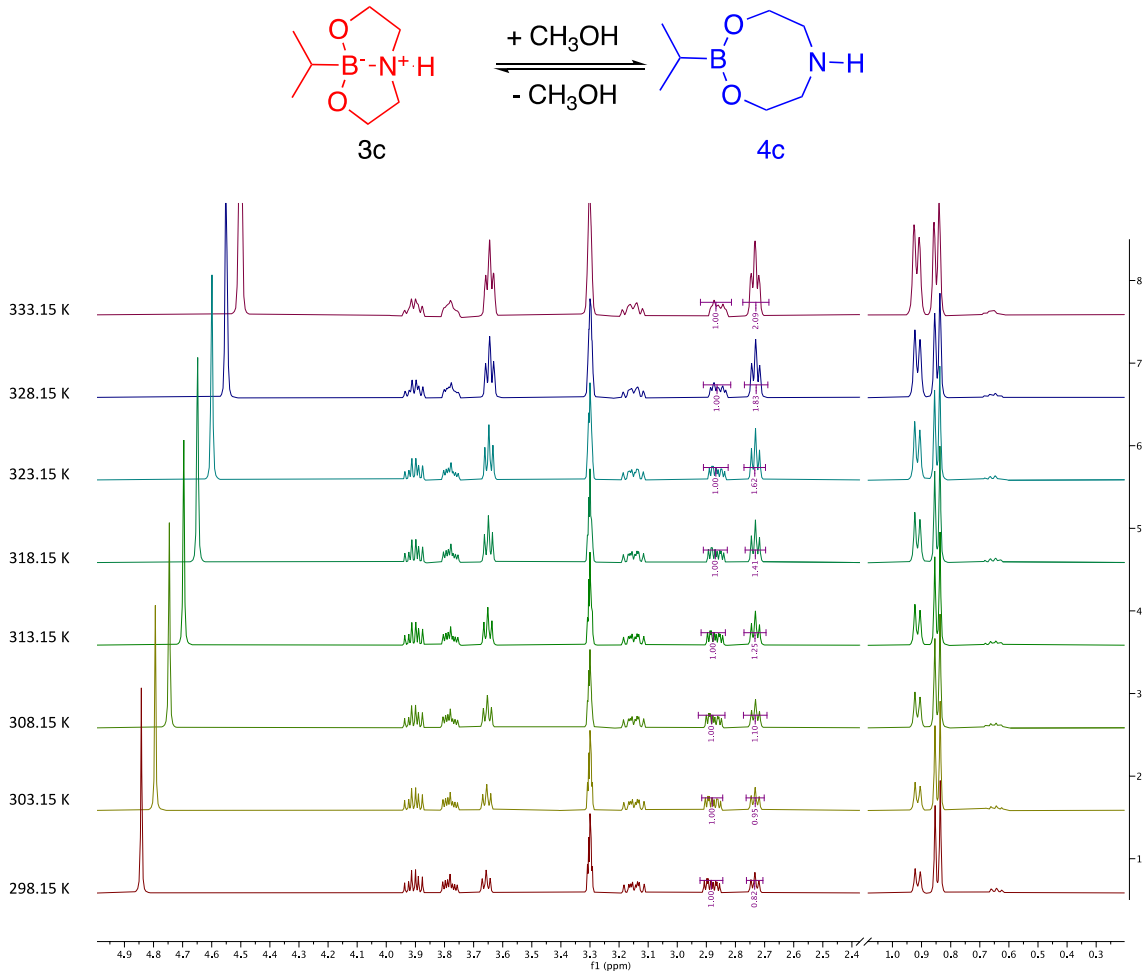

Figure A-129. VT-^{1}H NMR experimental data collected from 298.15 K to 333.15 K in CD_3OD-d4 *f*or the dynamic equilibrium between **3c** and **4c.**

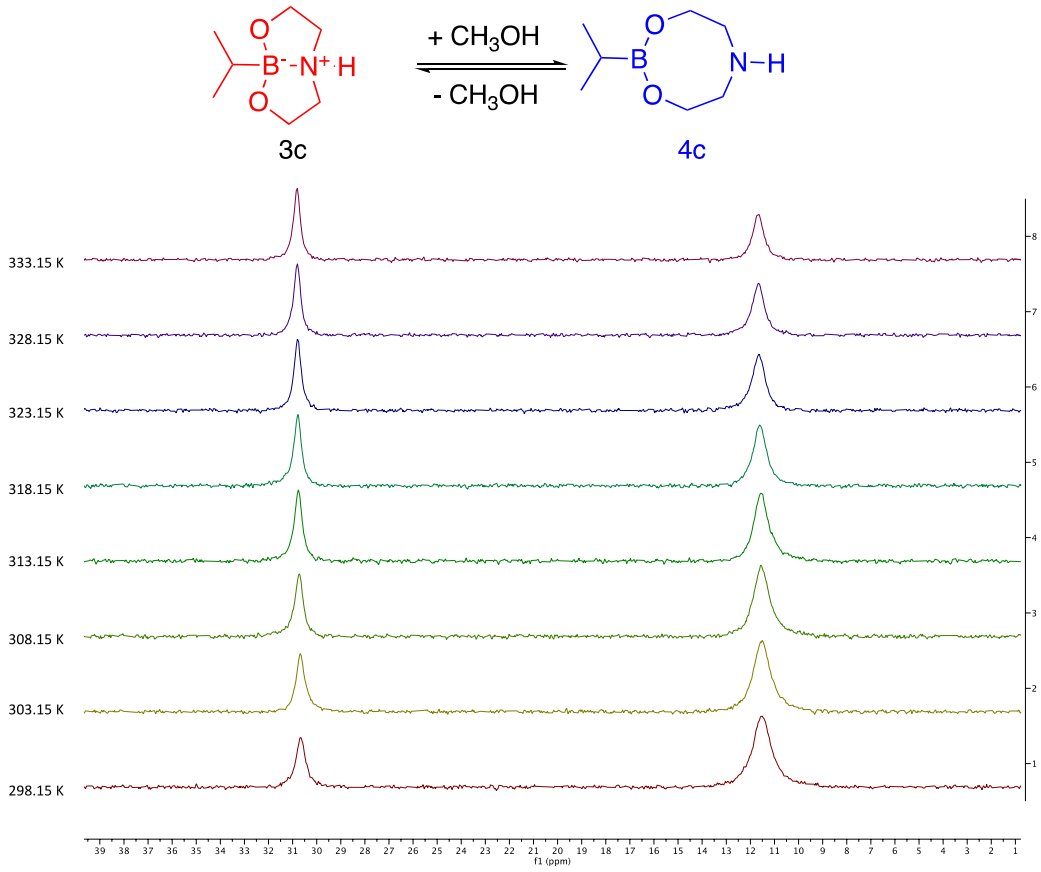

Figure A-130. VT-^{11}B NMR experimental data collected from 298.15 K to 333.15 K in CD_3OD-d4 *f*or the dynamic equilibrium between **3c** and **4c.**

Table A.2 Dynamic equilibria data for **3c** and **4c** in CD_3OD-d4 at different temperatures.

Temperature (K)	1/K $x10^{-3}$	Equilibrium ratio of [3,3,0] bicyclic ring structure (**3a**)	Equilibrium ratio of 8 membered ring structure (**4a**)	K_{eq}	ln K_{eq}
298.15	3.35	0.50	0.21	0.41	-0.89
303.15	3.30	0.50	0.24	0.48	-0.74
308.15	3.25	0.50	0.28	0.55	-0.60
313.15	3.19	0.50	0.31	0.63	-0.47
318.15	3.14	0.50	0.35	0.71	-0.35
323.15	3.09	0.50	0.41	0.81	-0.21
328.15	3.05	0.50	0.46	0.92	-0.09
333.15	3.00	0.50	0.52	1.05	0.04

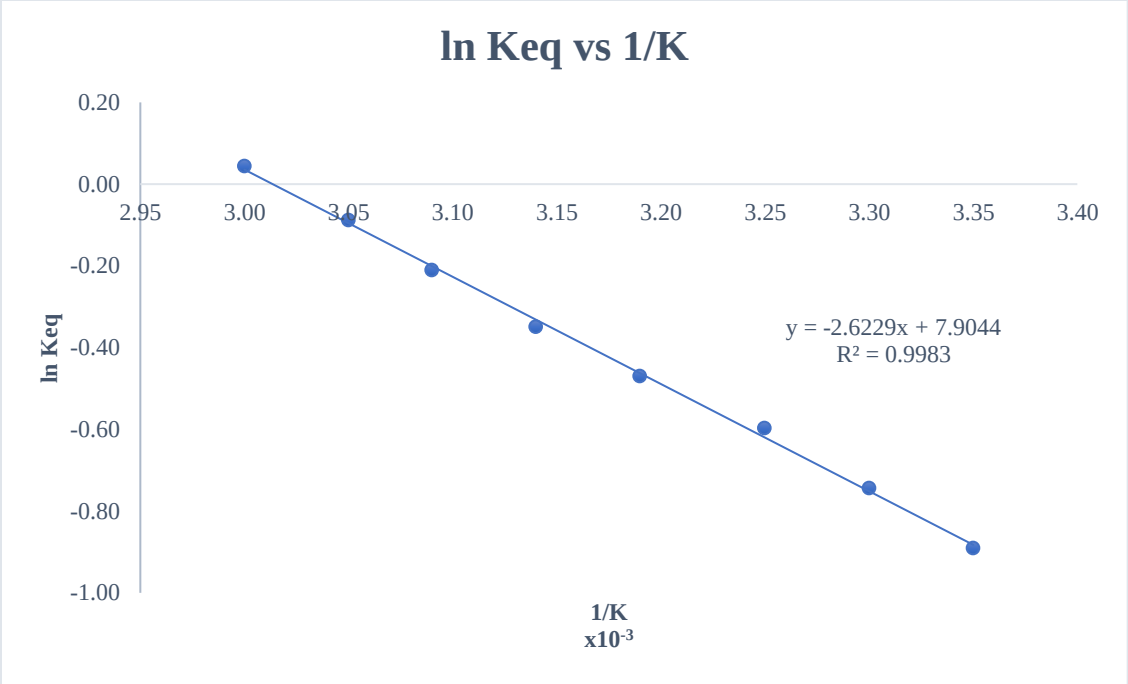

Figure A-131. Van't Hoff plot of ln K_{eq} vs. 1/T for equilibrium constants obtained for dynamic equilibria between **3c** and **4c** by VT ^{1}H NMR experiments at temperatures between 298.15 K to 333.15 K in CD_3OD-d4.

<u>$\Delta H°$ calculated using gradient</u>

$-\frac{\Delta H°}{R}$ = -2.6229

R = 1.987 cal K^{-1} mol^{-1}

$\Delta H°$ = 5.21 kcal mol^{-1}

<u>$\Delta S°$ calculated using intercept</u>

$\frac{\Delta S°}{R}$ = 7.9044

R = 1.987 cal K^{-1} mol^{-1}

$\Delta S°$ = 15.9 cal K^{-1} mol^{-1}

<u>$\Delta G°$ calculated at 298.15,</u>

$\Delta G° = \Delta H° - T\Delta S$

$\Delta G° =$ 531 cal mol^{-1}

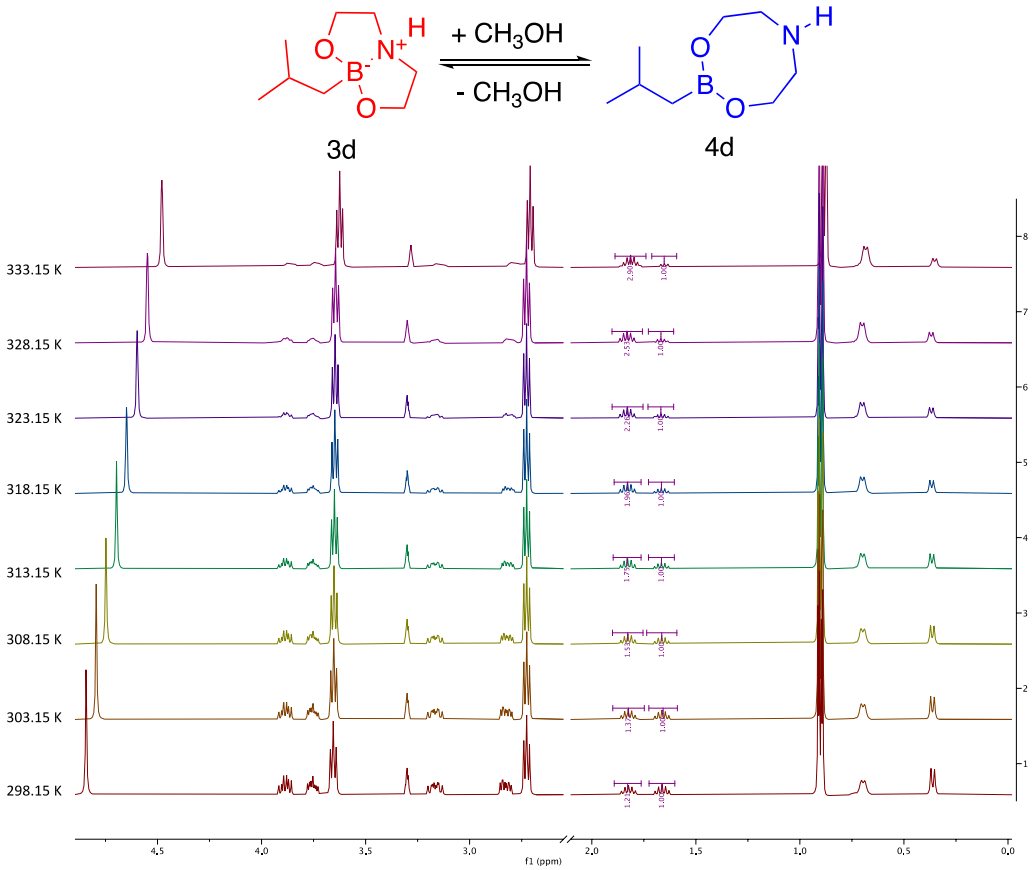

Figure A-132. VT-^{1}H NMR experimental data collected from 298.15 K to 333.15 K in CD_3OD-d4 *f*or the dynamic equilibrium between **3d** and **4d.**

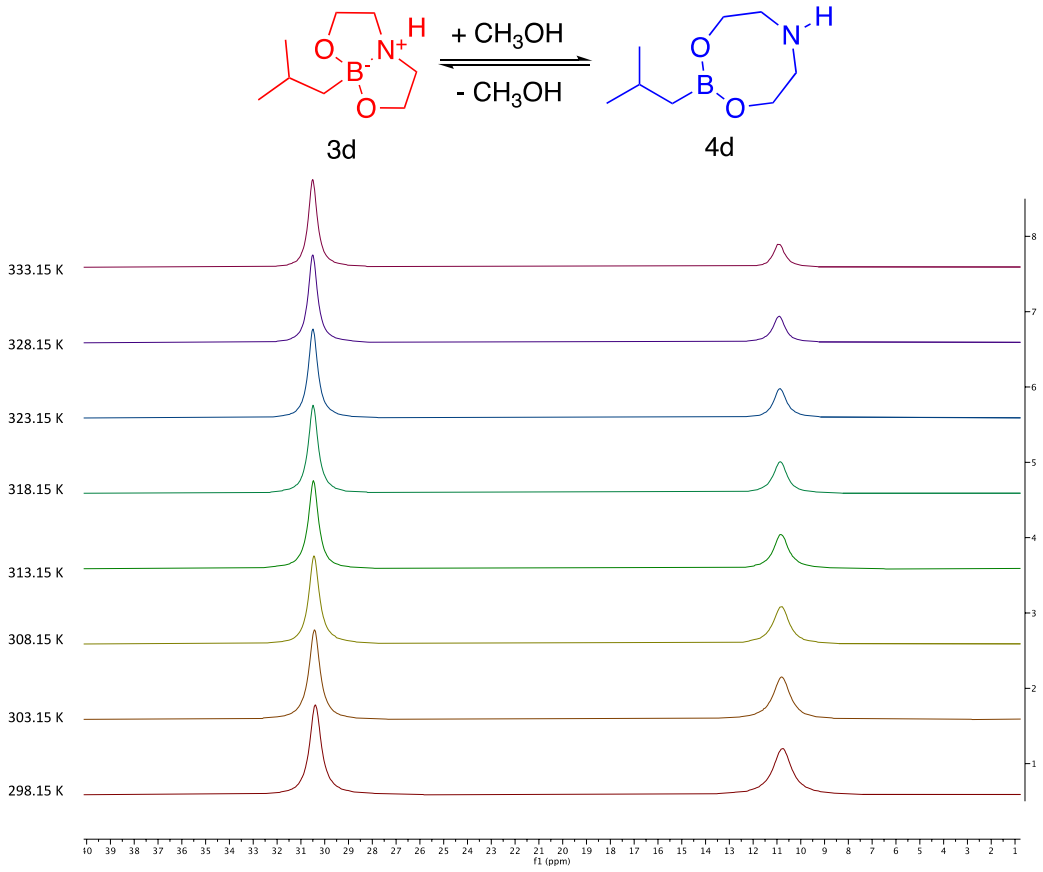

Figure A-133. VT-^{11}B NMR experimental data collected from 298.15 K to 333.15 K in CD_3OD-d4 *f*or the dynamic equilibrium between **3d** and **4d.**

Table A.3 Dynamic equilibria data for **3d** and **4d** in CD_3OD-d4 at different temperatures.

Temperature (K)	1/K x10^{-3}	Equilibrium ratio of [3,3,0] bicyclic ring structure (**3a**)	Equilibrium ratio of 8 membered ring structure (**4a**)	K_{eq}	ln K_{eq}
298.15	3.35	1.00	1.21	1.21	0.19
303.15	3.30	1.00	1.37	1.37	0.31
308.15	3.25	1.00	1.53	1.53	0.43
313.15	3.19	1.00	1.75	1.75	0.56
318.15	3.14	1.00	1.96	1.96	0.67
323.15	3.09	1.00	2.26	2.26	0.82
328.15	3.05	1.00	2.53	2.53	0.93
333.15	3.00	1.00	2.90	2.90	1.06

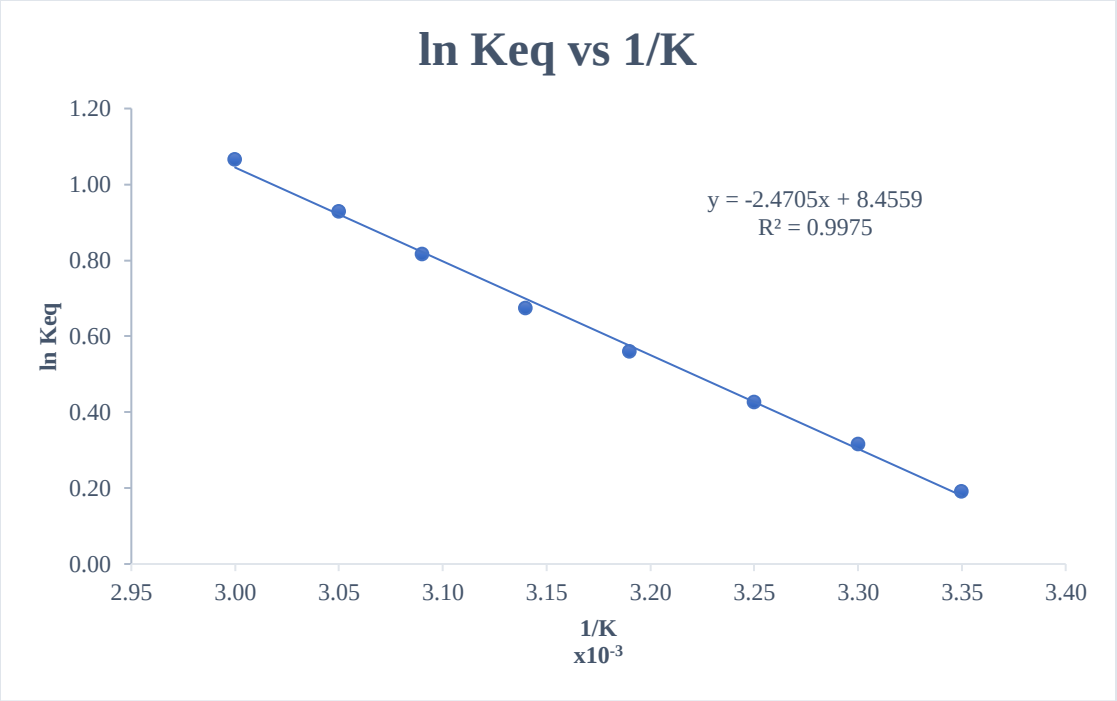

Figure A-134. Van't Hoff plot of ln K_{eq} vs. 1/T for equilibrium constants obtained for dynamic equilibria between **3d** and **4d** by VT ^{1}H NMR experiments at temperatures between 298.15 K to 333.15 K in CD_3OD-d4.

<u>$\Delta H°$ calculated using gradient</u>

$-\frac{\Delta H°}{R}$ = -2.4705

R = 1.987 cal K^{-1} mol^{-1}

$\Delta H°$ = 4.91 kcal mol^{-1}

<u>$\Delta S°$ calculated using intercept</u>

$\frac{\Delta S°}{R}$ = 8.4559

R = 1.987 cal K^{-1} mol^{-1}

$\Delta S°$ = 16.8 cal K^{-1} mol^{-1}

<u>$\Delta G°$ calculated at 298.15,</u>

$\Delta G° = \Delta H° - T\Delta S$

$\Delta G° = 101$ cal mol^{-1}

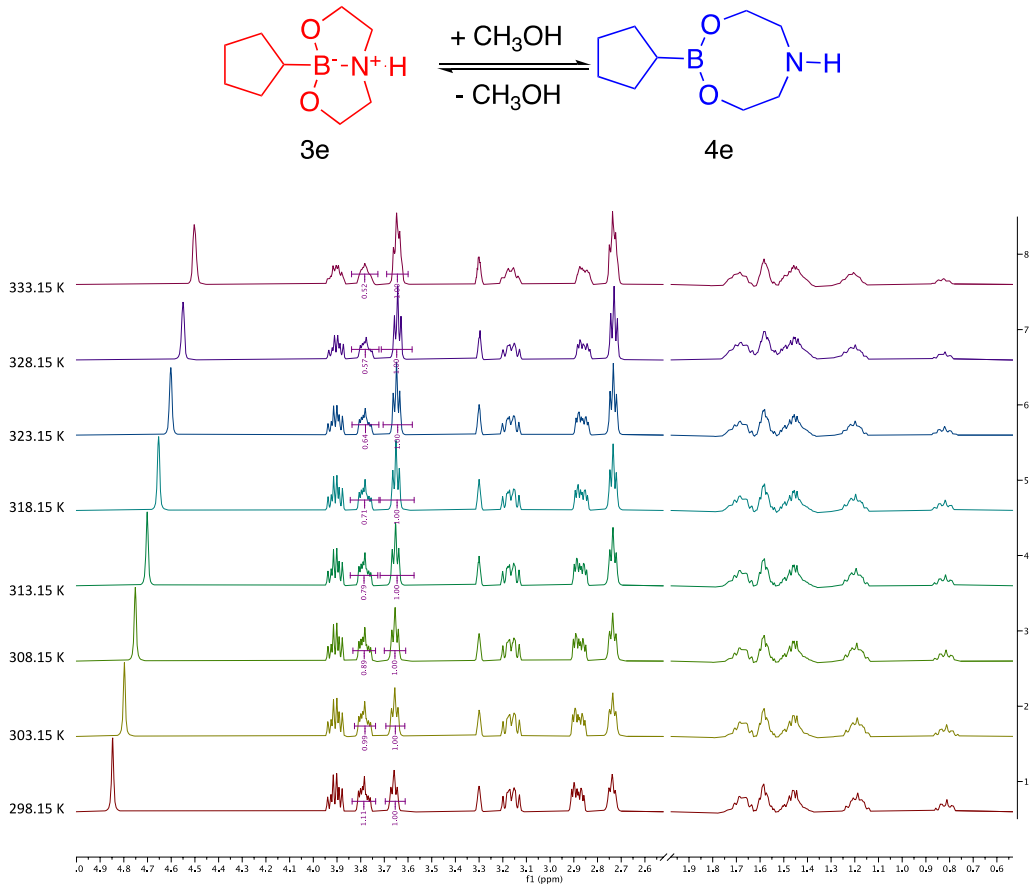

Figure A-135. VT-^{1}H NMR experimental data collected from 298.15 K to 333.15 K in CD_3OD-d4 *f*or the dynamic equilibrium between **3e** and **4e.**

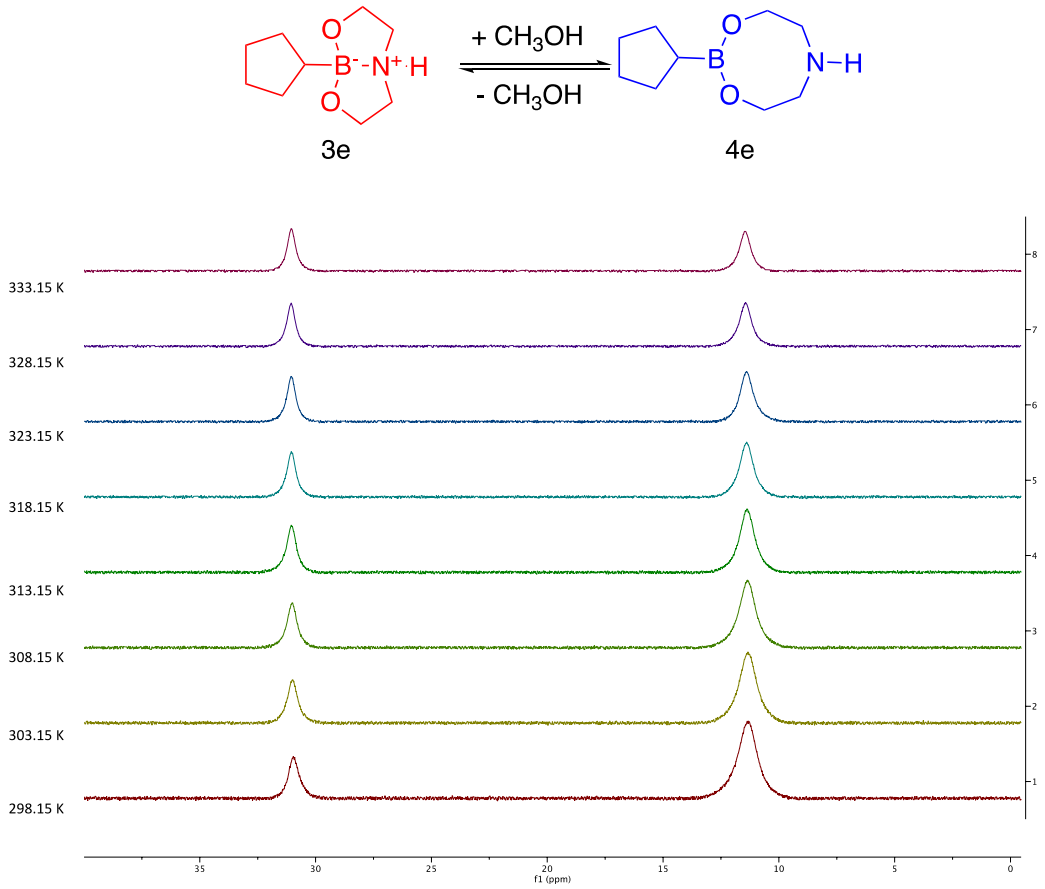

Figure A-136. VT-^{11}B NMR experimental data collected from 298.15 K to 333.15 K in CD_3OD-d4 for the dynamic equilibrium between **3e** and **4e.**

Table A.4 Dynamic equilibria data for **3e** and **4e** in CD_3OD-d4 at different temperatures.

Temperature (K)	1/K x10^{-3}	Equilibrium ratio of [3,3,0] bicyclic ring structure (**3e**)	Equilibrium ratio of 8 membered ring structure (**4e**)	K_{eq}	ln K_{eq}
298.15	3.35	0.56	0.25	0.45	-0.80
303.15	3.30	0.50	0.25	0.51	-0.68
308.15	3.25	0.45	0.25	0.56	-0.58
313.15	3.19	0.40	0.25	0.63	-0.46
318.15	3.14	0.36	0.25	0.70	-0.35
323.15	3.09	0.32	0.25	0.78	-0.25
328.15	3.05	0.29	0.25	0.88	-0.13
333.15	3.00	0.26	0.25	0.96	-0.04

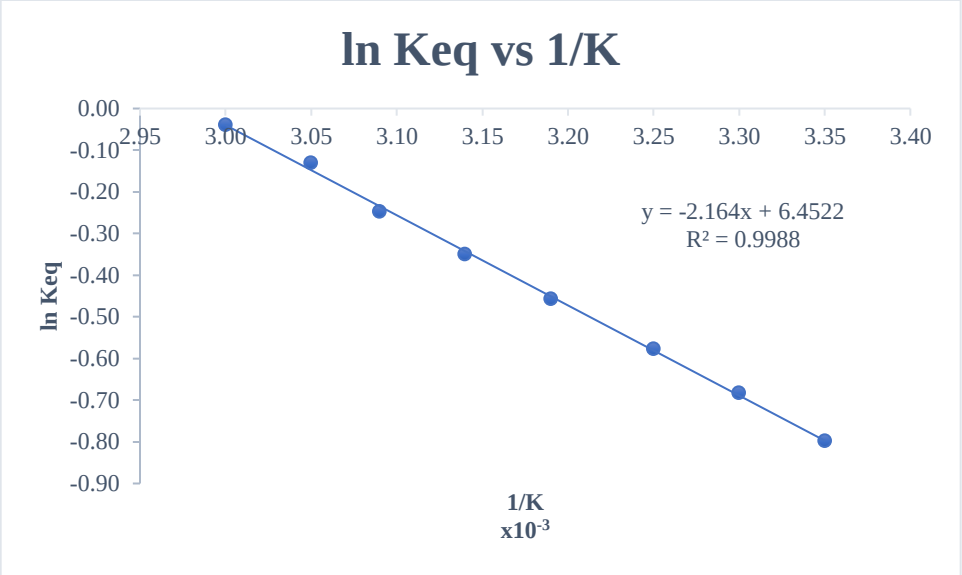

Figure A-137. Van't Hoff plot of ln K_{eq} vs. 1/T for equilibrium constants obtained for dynamic equilibria between **3e** and **4e** by VT ^{1}H NMR experiments at temperatures between 298.15 K to 333.15 K in CD_3OD-d4.

<u>$\Delta H°$ calculated using gradient</u>

$-\frac{\Delta H°}{R}$ = -2.164

R = 1.987 cal K^{-1} mol^{-1}

$\Delta H°$ = 4.30 kcal mol^{-1}

<u>$\Delta S°$ calculated using intercept</u>

$\frac{\Delta S°}{R}$ = 6.4522

R = 1.987 cal K^{-1} mol^{-1}

$\Delta S°$ = 12.8 cal K^{-1} mol^{-1}

<u>$\Delta G°$ calculated at 298.15,</u>

$\Delta G° = \Delta H° - T\Delta S$

$\Delta G° = 479$ cal mol^{-1}

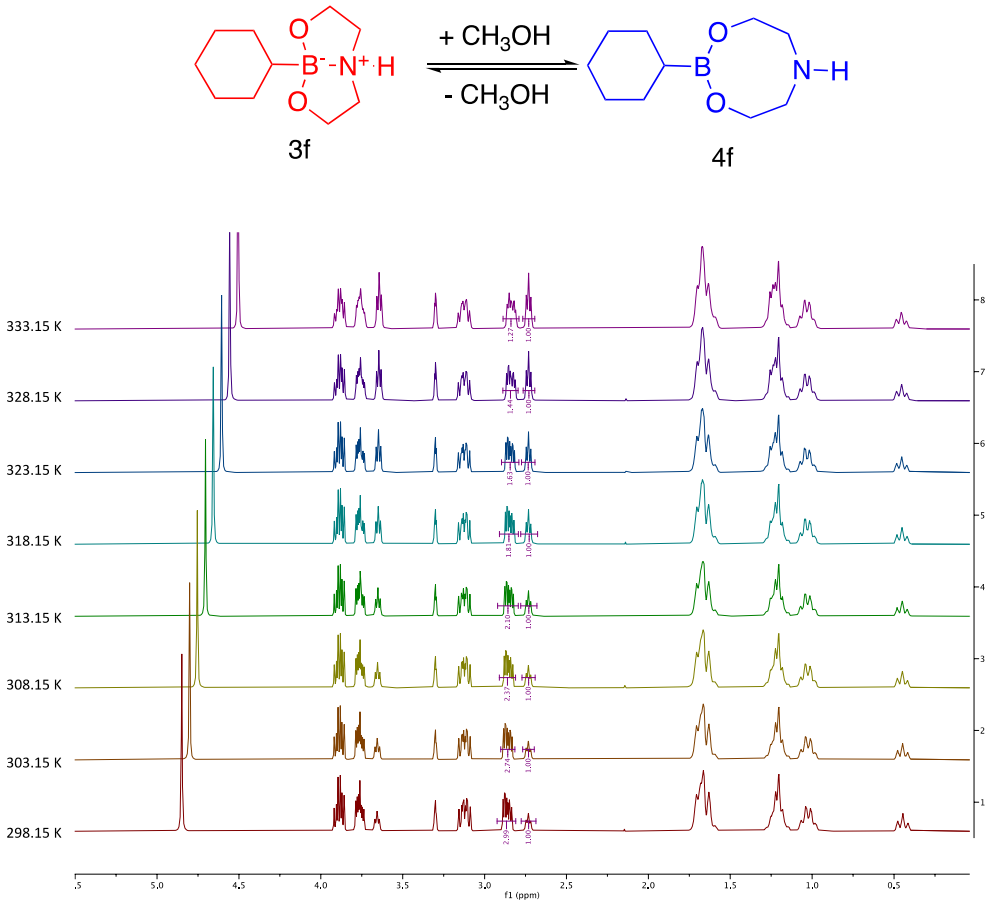

Figure A-138. VT-^{1}H NMR experimental data collected from 298.15 K to 333.15 K in CD_3OD-d4 *f*or the dynamic equilibrium between **3f** and **4f.**

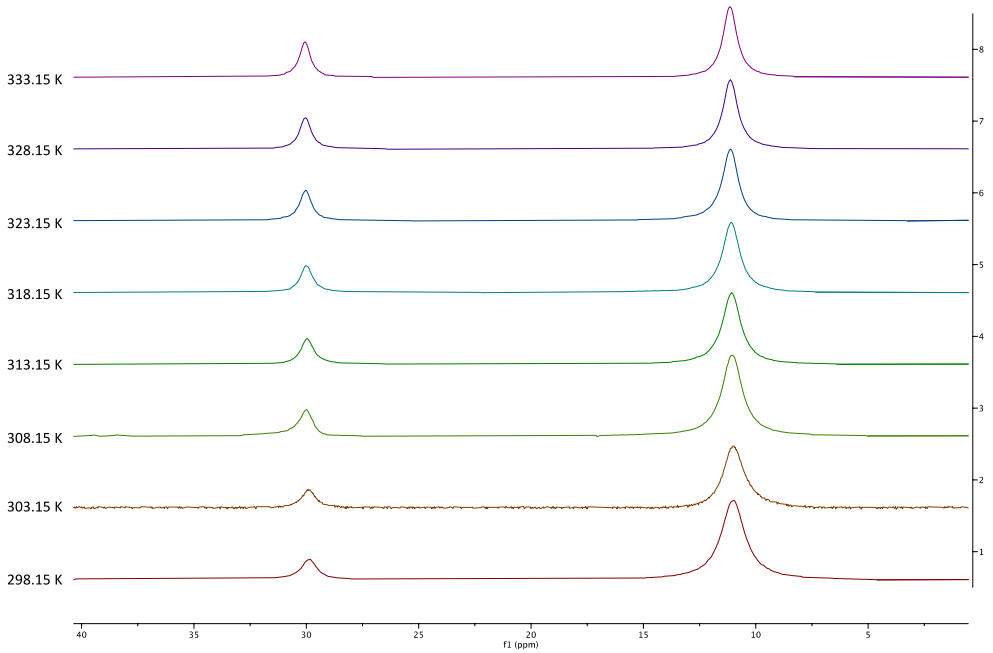

Figure A-139. VT-^{1}H NMR experimental data collected from 298.15 K to 333.15 K in CD_3OD-d4 *f*or the dynamic equilibrium between **3f** and **4f.**

Table A.5 Dynamic equilibria data for **3f** and **4f** in CD_3OD-d4 at different temperatures.

Temperature (K)	1/K x10^{-3}	Equilibrium ratio of [3,3,0] bicyclic ring structure (**3f**)	Equilibrium ratio of 8 membered ring structure (**4f**)	K_{eq}	ln K_{eq}
298.15	3.35	1.50	0.25	0.17	-1.79
303.15	3.30	1.37	0.25	0.18	-1.70
308.15	3.25	1.19	0.25	0.21	-1.56
313.15	3.19	1.05	0.25	0.24	-1.44
318.15	3.14	0.91	0.25	0.28	-1.29
323.15	3.09	0.82	0.25	0.31	-1.18
328.15	3.05	0.72	0.25	0.35	-1.06
333.15	3.00	0.64	0.25	0.39	-0.93

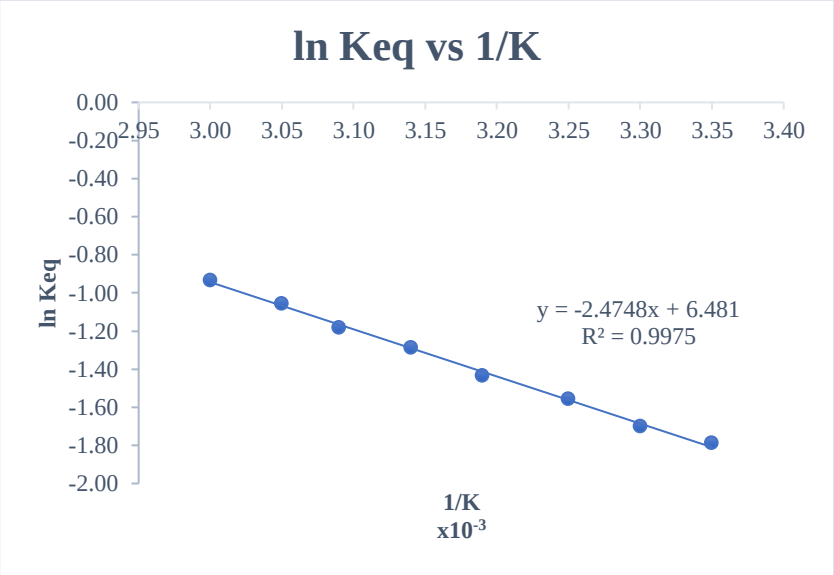

Figure A-140. Van't Hoff plot of ln K_{eq} vs. 1/T for equilibrium constants obtained for dynamic equilibria between **3f** and **4f** by VT ^{1}H NMR experiments at temperatures between 298.15 K to 333.15 K in CD_3OD-d4.

<u>$\Delta H°$ calculated using gradient</u>

$-\frac{\Delta H°}{R}$ = -2.4748

R = 1.987 cal K^{-1} mol^{-1}

$\Delta H°$ = 4.92 kcal mol^{-1}

<u>$\Delta S°$ calculated using intercept</u>

$\frac{\Delta S°}{R}$ = 6.481

R = 1.987 cal K^{-1} mol^{-1}

$\Delta S°$ = 12.9 cal K^{-1} mol^{-1}

<u>$\Delta G°$ calculated at 298.15,</u>

$\Delta G° = \Delta H° - T\Delta S$

$\Delta G° = 1078$ cal mol^{-1}

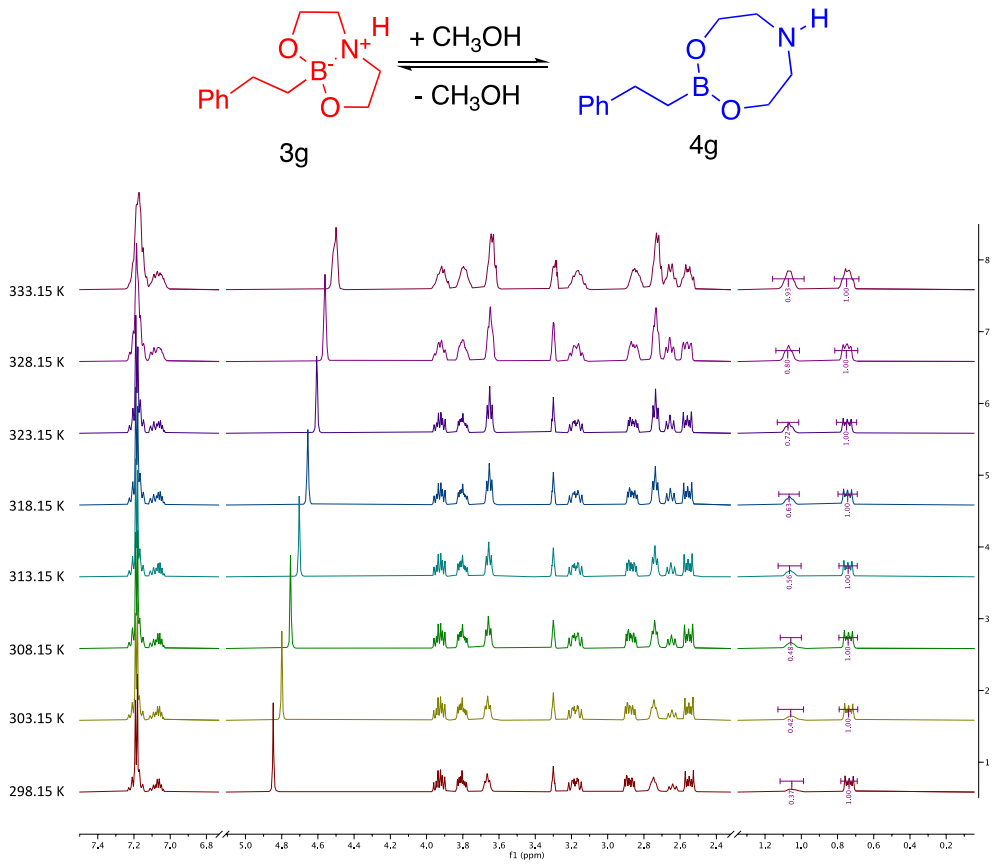

Figure A-150. VT-^{1}H NMR experimental data collected from 298.15 K to 333.15 K in CD_3OD-d4 *f*or the dynamic equilibrium between **3g** and **4g.**

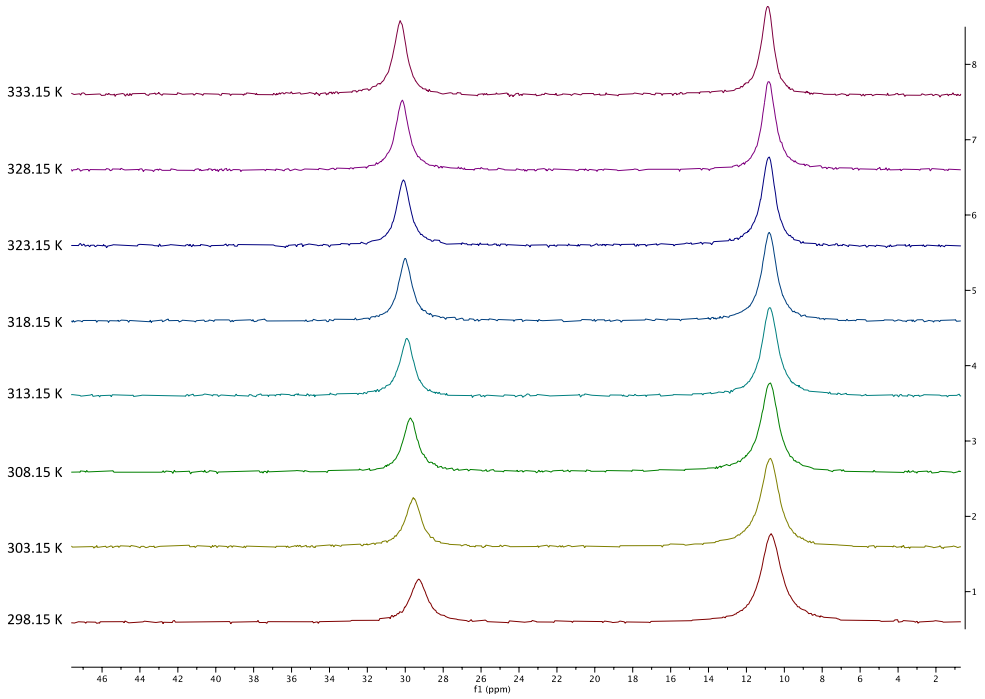

Figure A-151. VT-^{11}B NMR experimental data collected from 298.15 K to 333.15 K in CD_3OD-d4 *f*or the dynamic equilibrium between **3g** and **4g.**

Table A.2 Dynamic equilibria data for **3g** and **4g** in CD_3OD-d4 at different temperatures.

Temperature (K)	1/K $x10^{-3}$	Equilibrium ratio of [3,3,0] bicyclic ring structure (**3f**)	Equilibrium ratio of 8 membered ring structure (**4f**)	K_{eq}	ln K_{eq}
298.15	3.35	1.00	0.37	0.37	-0.99
303.15	3.30	1.00	0.42	0.42	-0.87
308.15	3.25	1.00	0.48	0.48	-0.73
313.15	3.19	1.00	0.56	0.56	-0.58
318.15	3.14	1.00	0.63	0.63	-0.46
323.15	3.09	1.00	0.72	0.72	-0.33
328.15	3.05	1.00	0.80	0.80	-0.22
333.15	3.00	1.00	0.93	0.93	-0.07

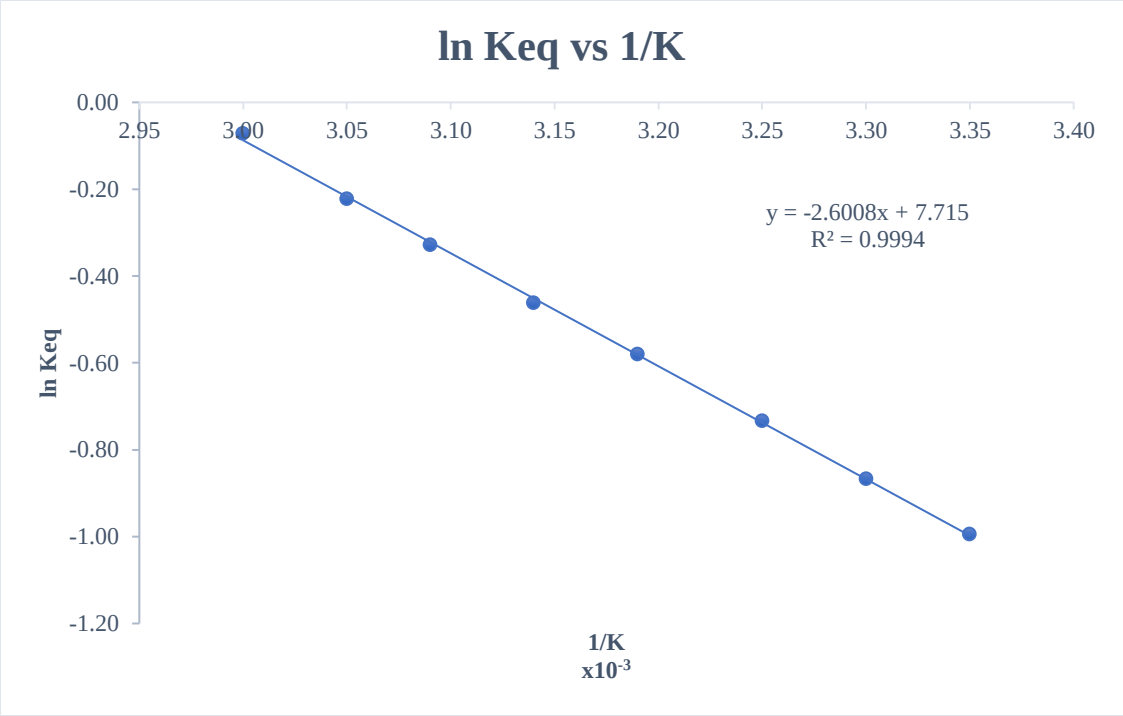

Figure A-152. Van't Hoff plot of ln K_{eq} vs. 1/T for equilibrium constants obtained for dynamic equilibria between **3g** and **4g** by VT ^{1}H NMR experiments at temperatures between 298.15 K to 333.15 K in CD_3OD-d4.

<u>$\Delta H°$ calculated using gradient</u>

$-\frac{\Delta H°}{R}$ = -2.6008

R = 1.987 cal K^{-1} mol^{-1}

$\Delta H°$ = 5.17 kcal mol^{-1}

<u>$\Delta S°$ calculated using intercept</u>

$\frac{\Delta S°}{R}$ = 7.715

R = 1.987 cal K^{-1} mol^{-1}

$\Delta S°$ = 15.3 cal K^{-1} mol^{-1}

<u>$\Delta G°$ calculated at 298.15,</u>

$\Delta G° = \Delta H° - T\Delta S$

$\Delta G° = 597$ cal mol^{-1}

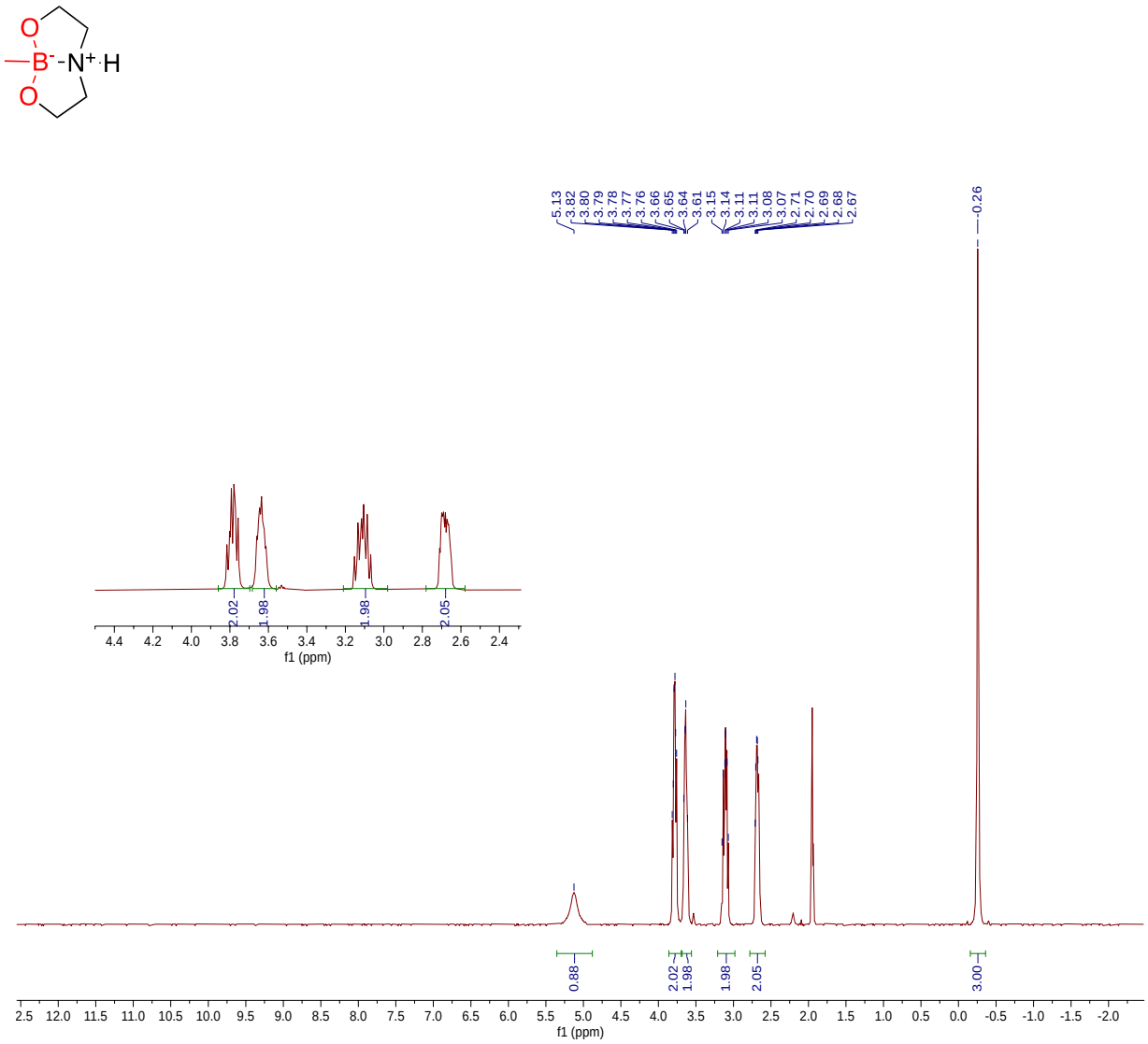

Figure A-153. ^{1}H NMR Spectrum of 3a in CD_3CN.

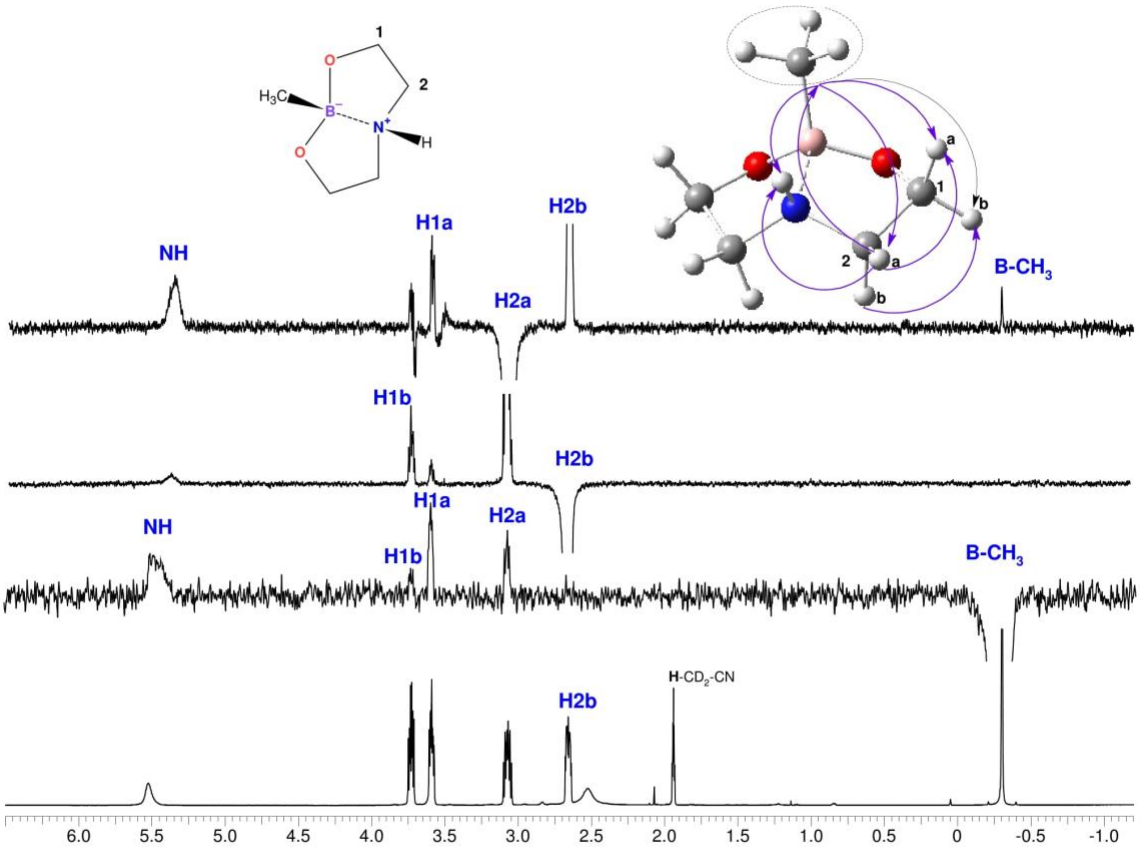

Figure A-154. NOESY 1D Spectrum of 3a in CD_3CN.

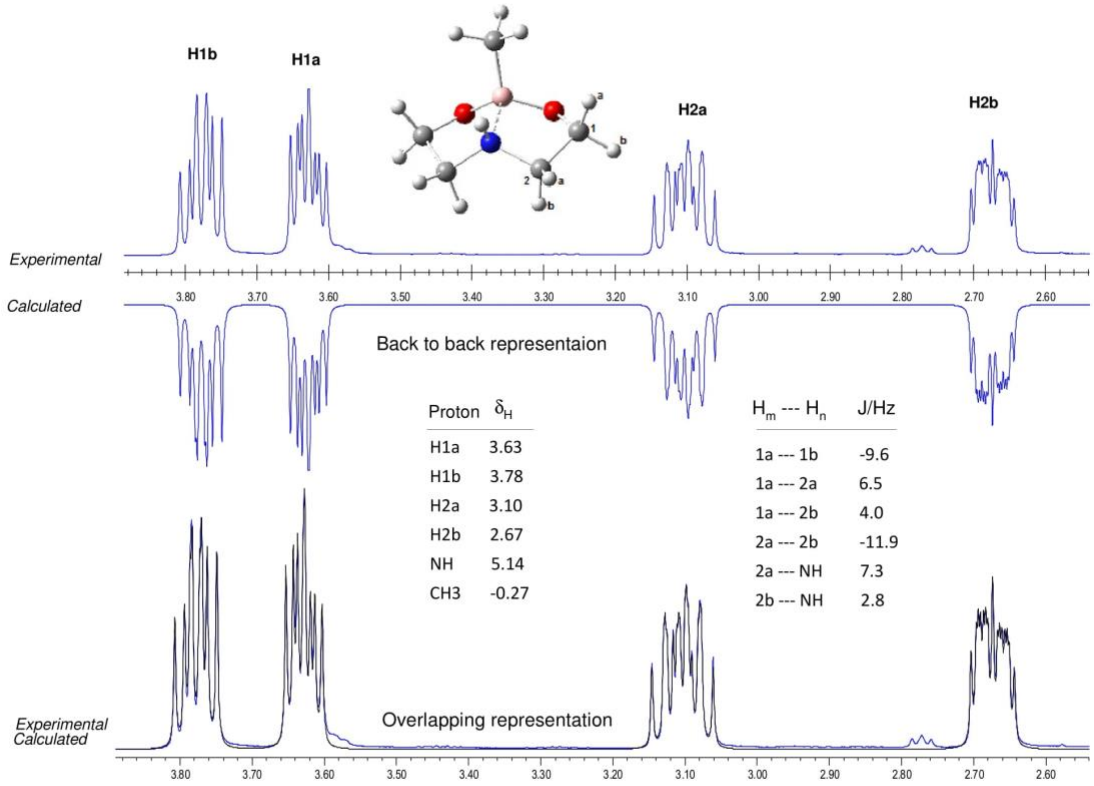

Figure A-155. Overlapping representation of experimental and calculated ^{1}H spectra of 3a in CD_3CN.

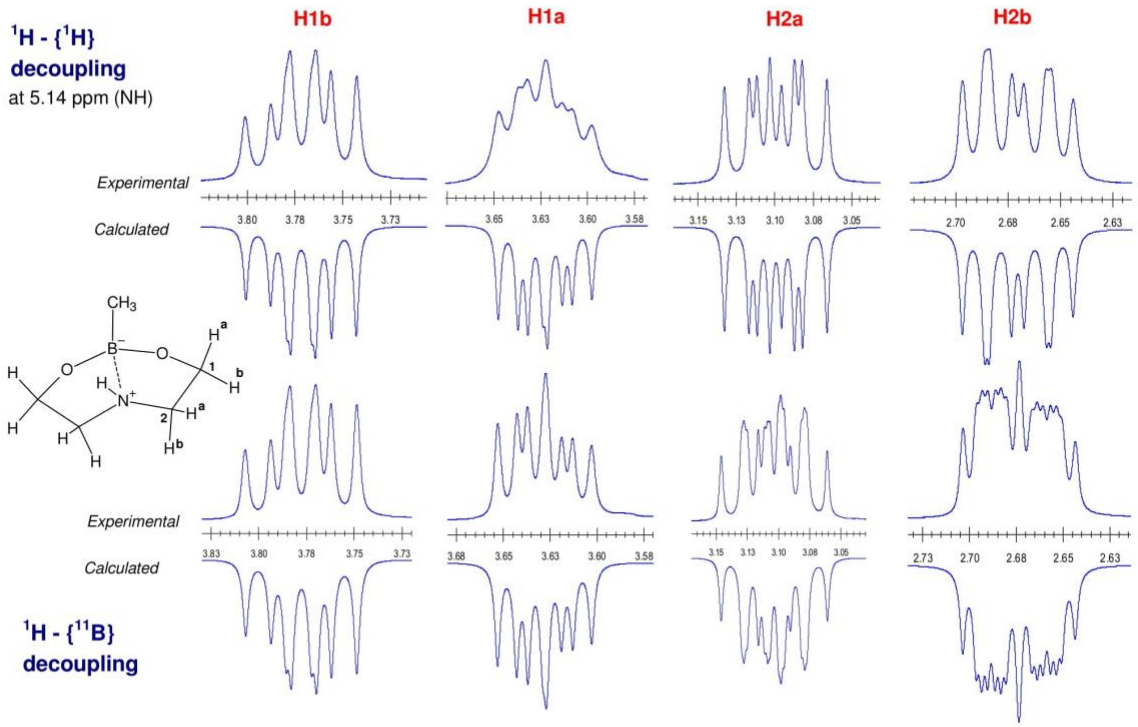

Figure A-156. Overlapping representation of experimental and calculated ^{1}H spectra for ^{1}H-{^{1}H-NH} decoupling at 5.14 ppm and ^{1}H-{^{11}B}of 3a in CD_3CN.

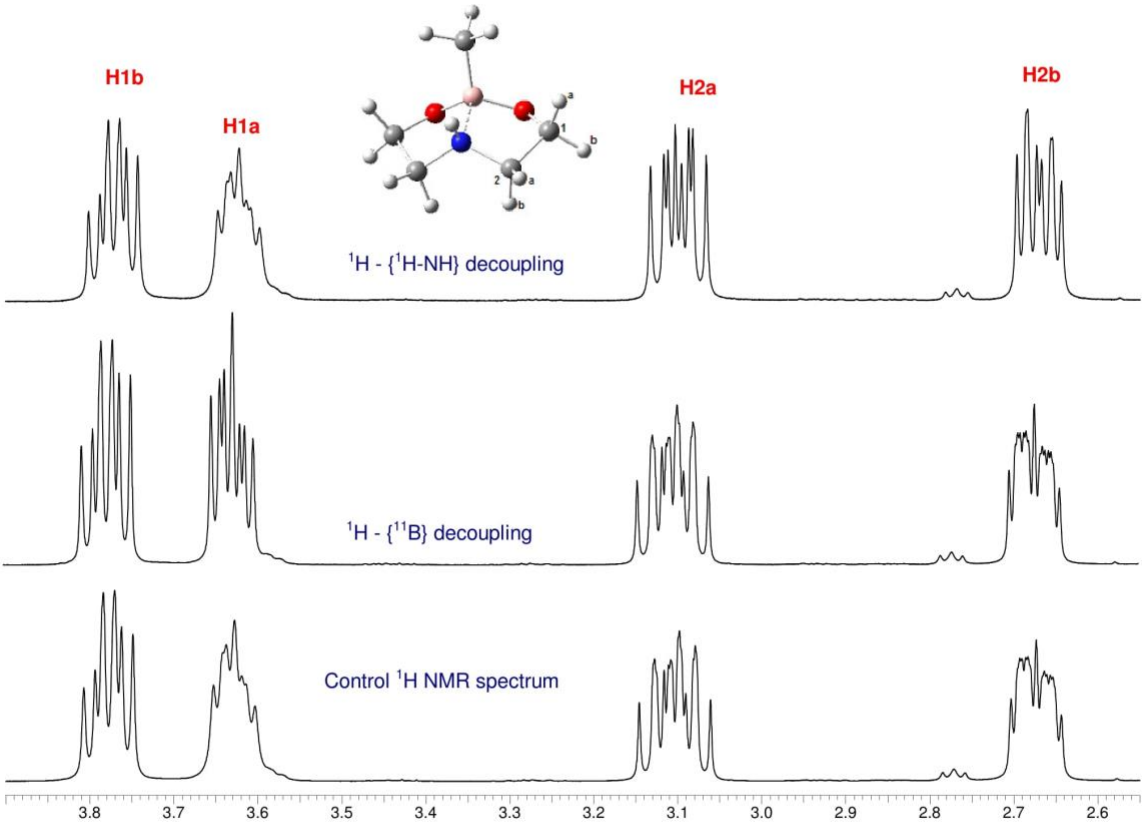

Figure A-157. Overlapping representation of experimental ^{1}H spectra for ^{1}H-{^{1}H-NH} decoupling at 5.14 ppm and ^{1}H-{^{11}B} of 3a in CD_3CN.

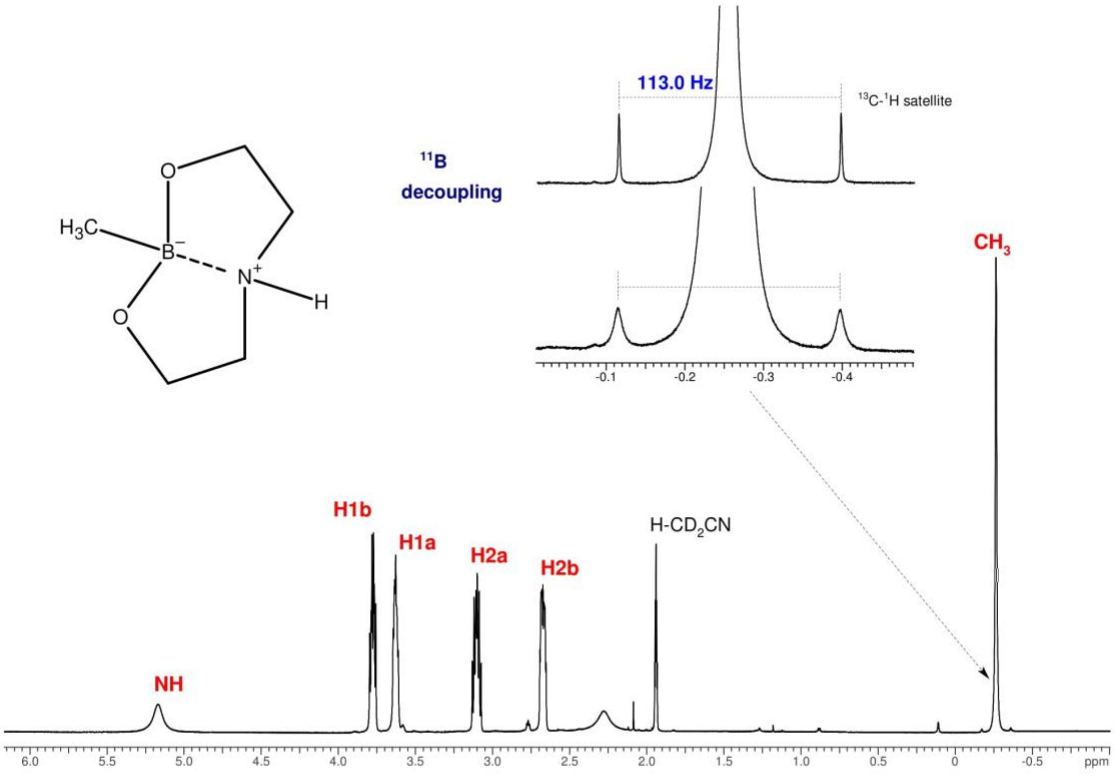

Figure A-158. ^{11}B decoupled ^{1}H NMR spectra of 3a in CD_3CN.

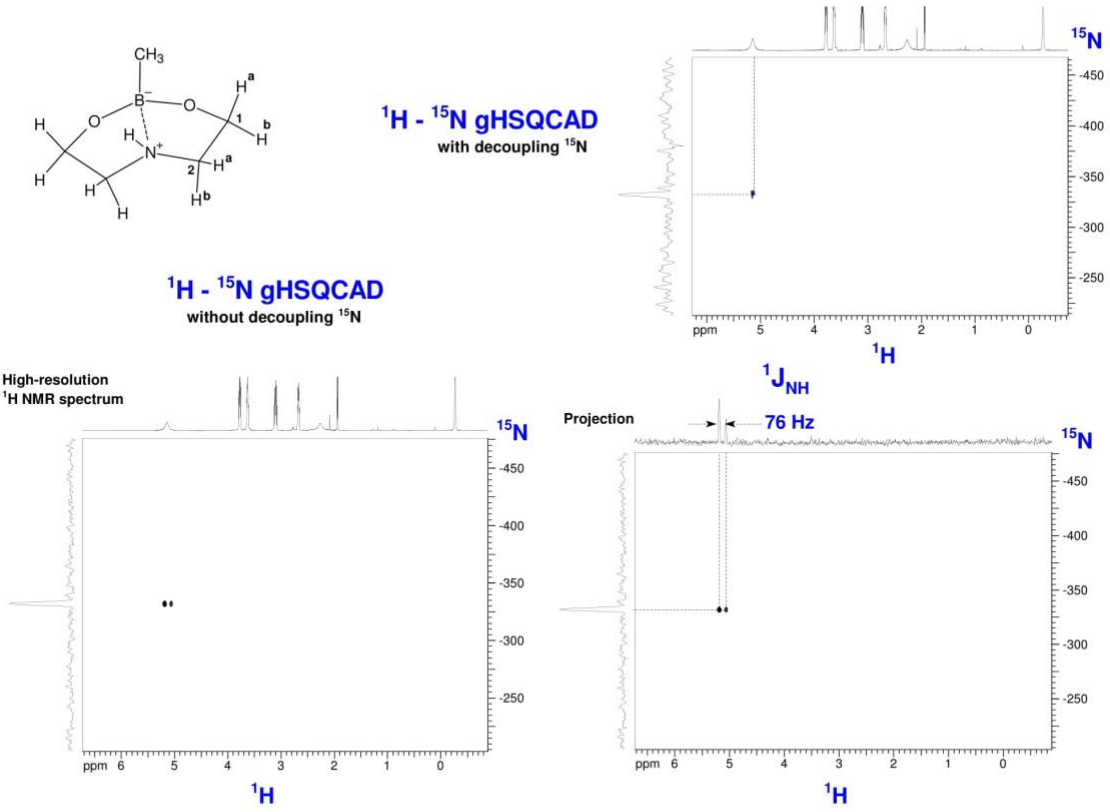

Figure A-159. ^{1}H-^{15}N gHSQCAD spectrums of 3a in CD_3CN with and without decoupling of ^{15}N
.

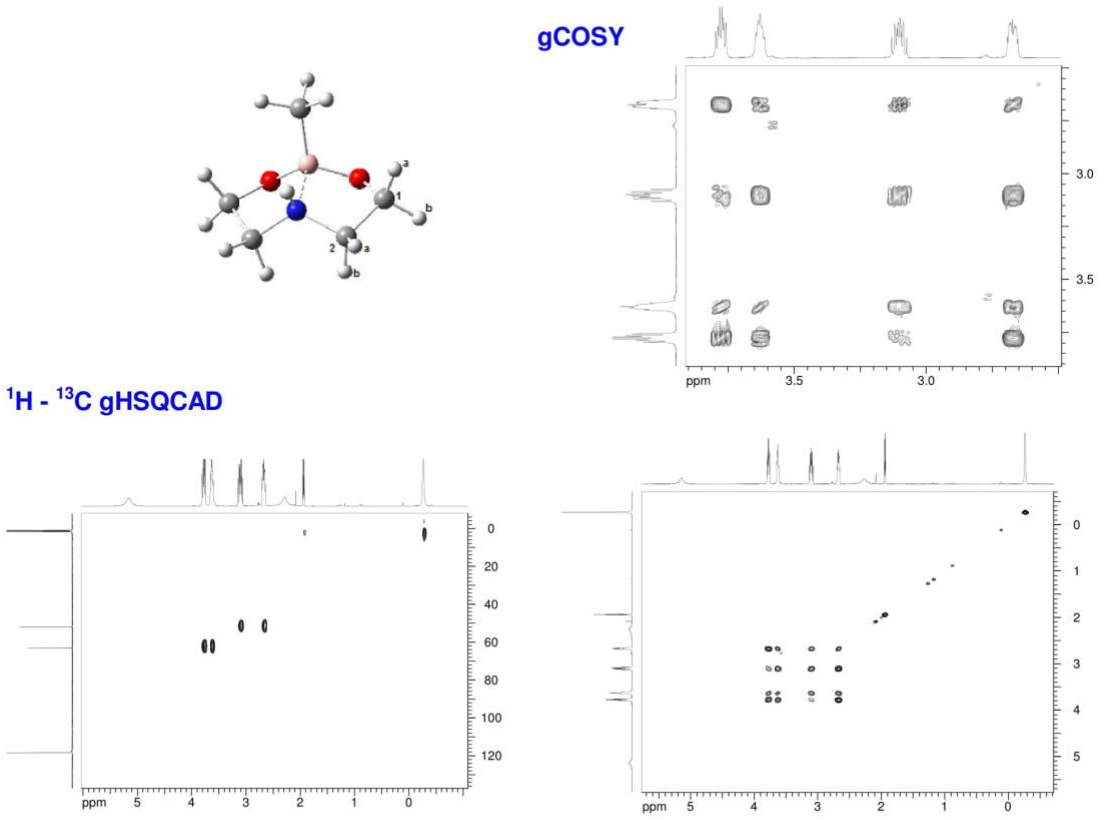

Figure A-160. ^{1}H-^{1}H gCOSY spectrum and ^{1}H-^{13}C gHSQCAD spectrum of 3a in CD_3CN.

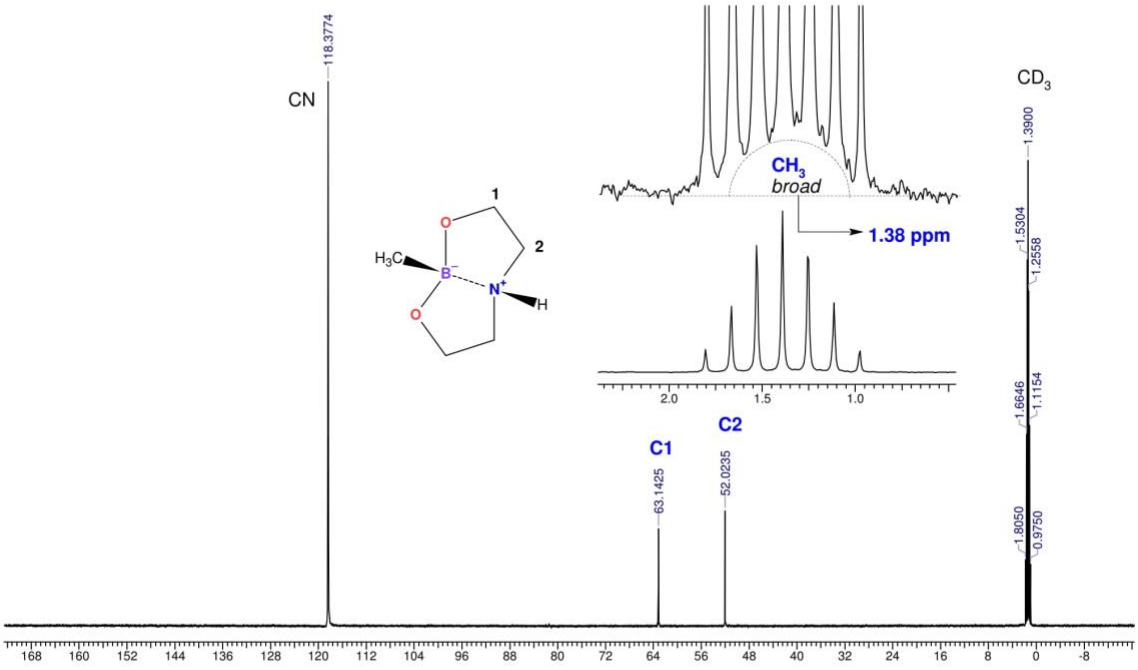

Figure A-161. ^{13}C NMR Spectrum of 3a in CD_3CN.

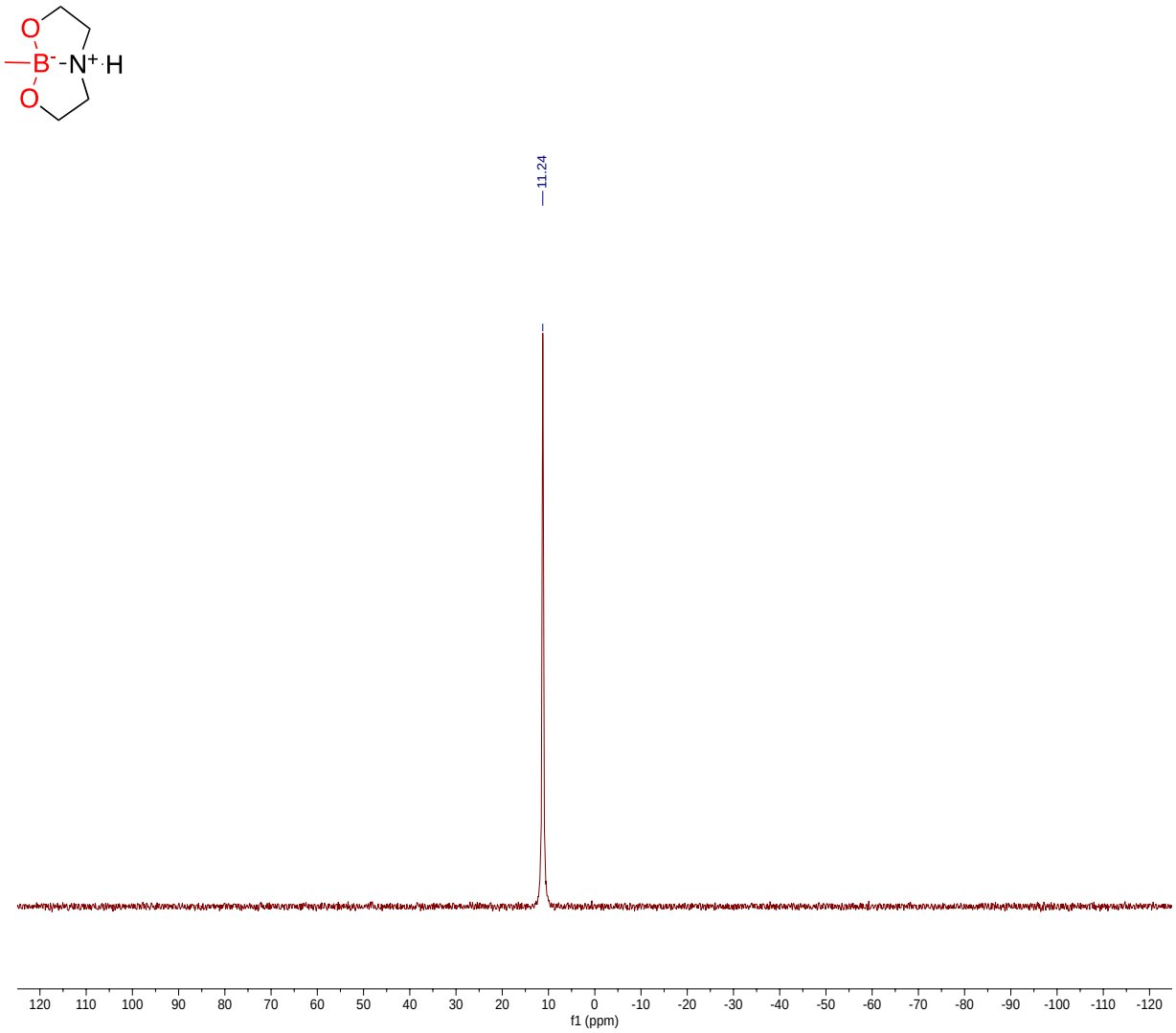

Figure A-162. ^{11}B NMR Spectrum of 3a in CD_3CN.

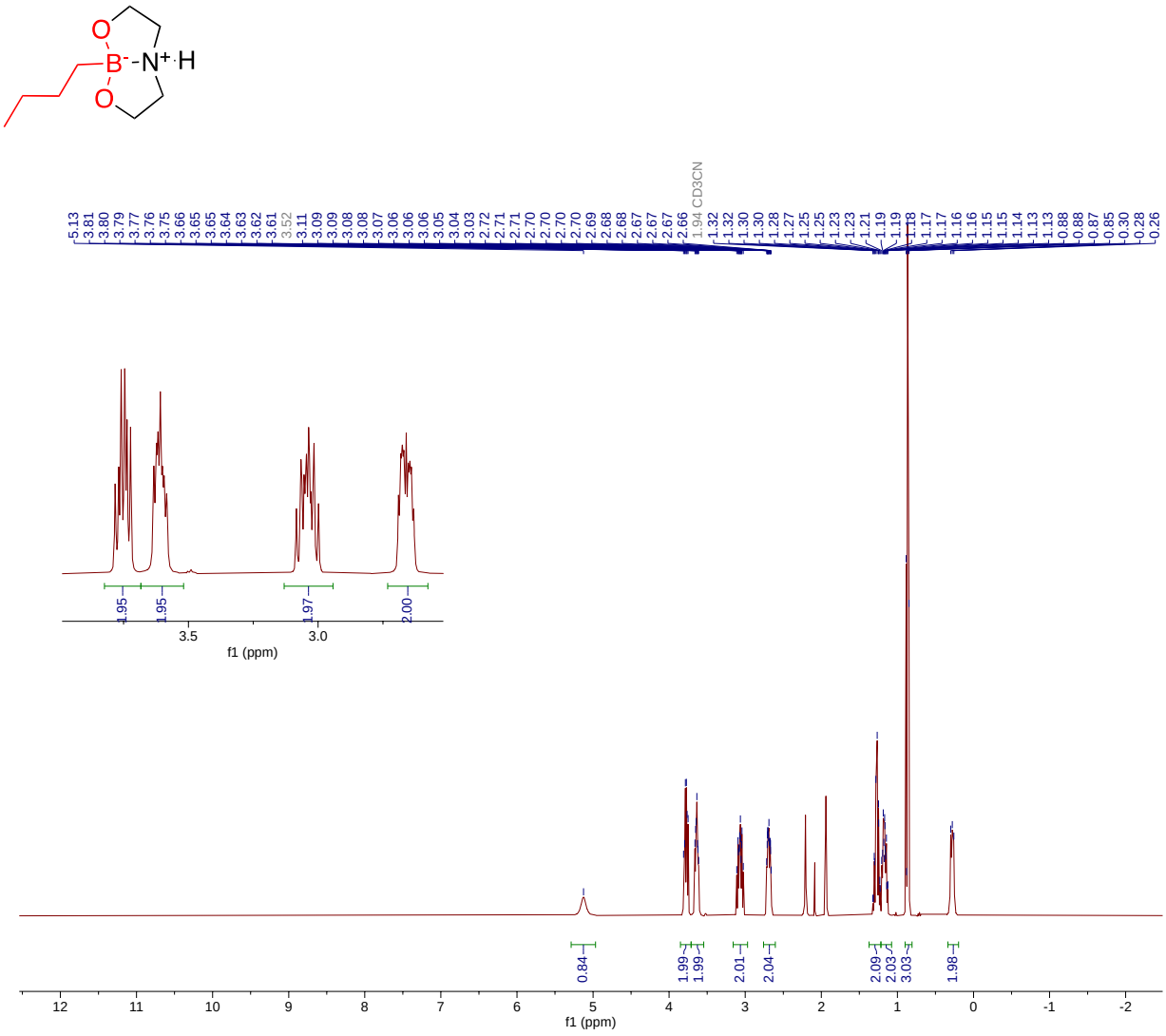

Figure A-163. ^{1}H NMR Spectrum of 3b in CD_3CN.

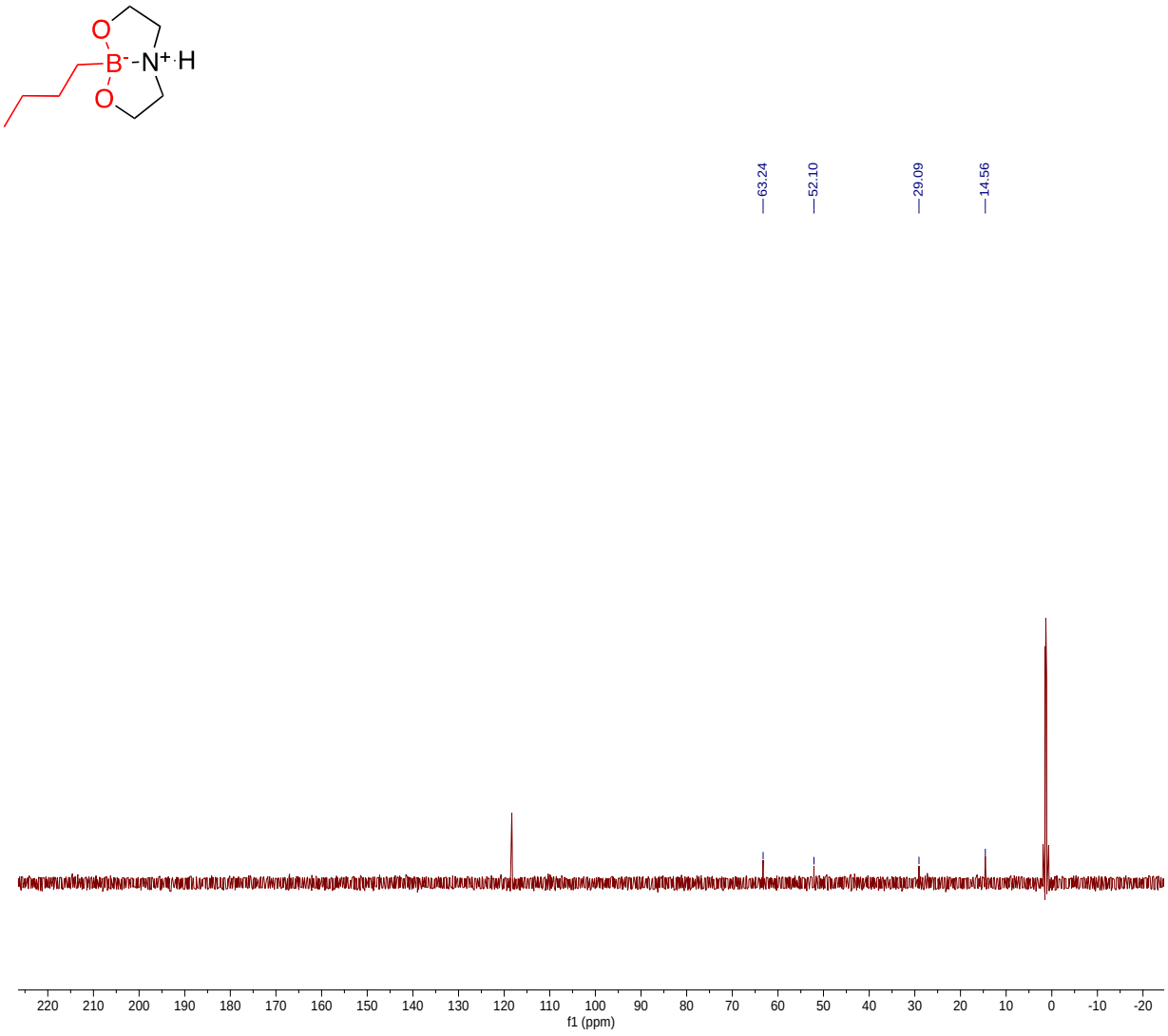

Figure A-164. ^{13}C NMR Spectrum of 3b in CD_3CN.

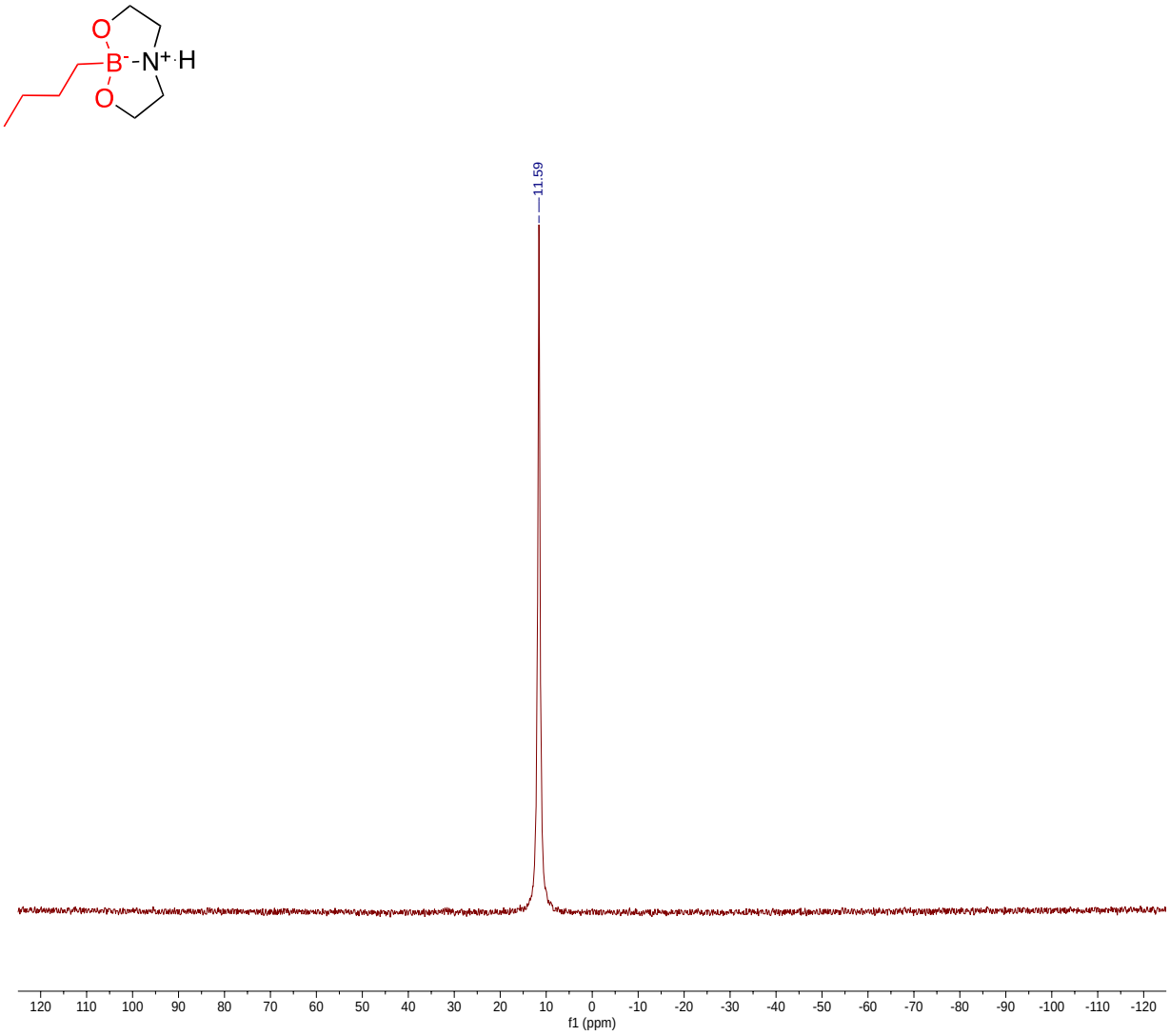

Figure A-165. ^{11}B NMR Spectrum of 3b in CD_3CN.

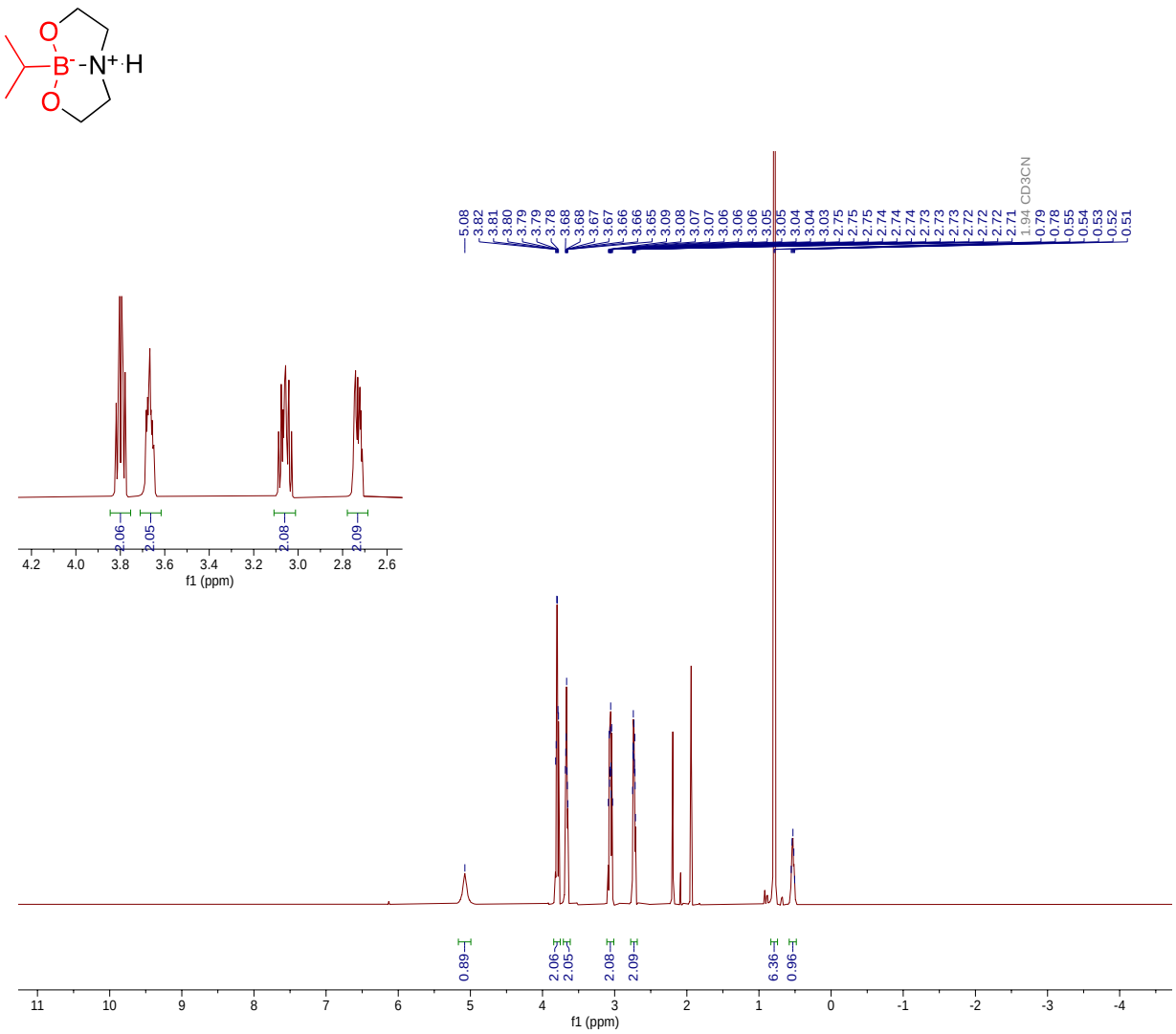

Figure A-170. ^{1}H NMR Spectrum of 3c in CD_3CN.

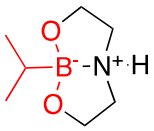

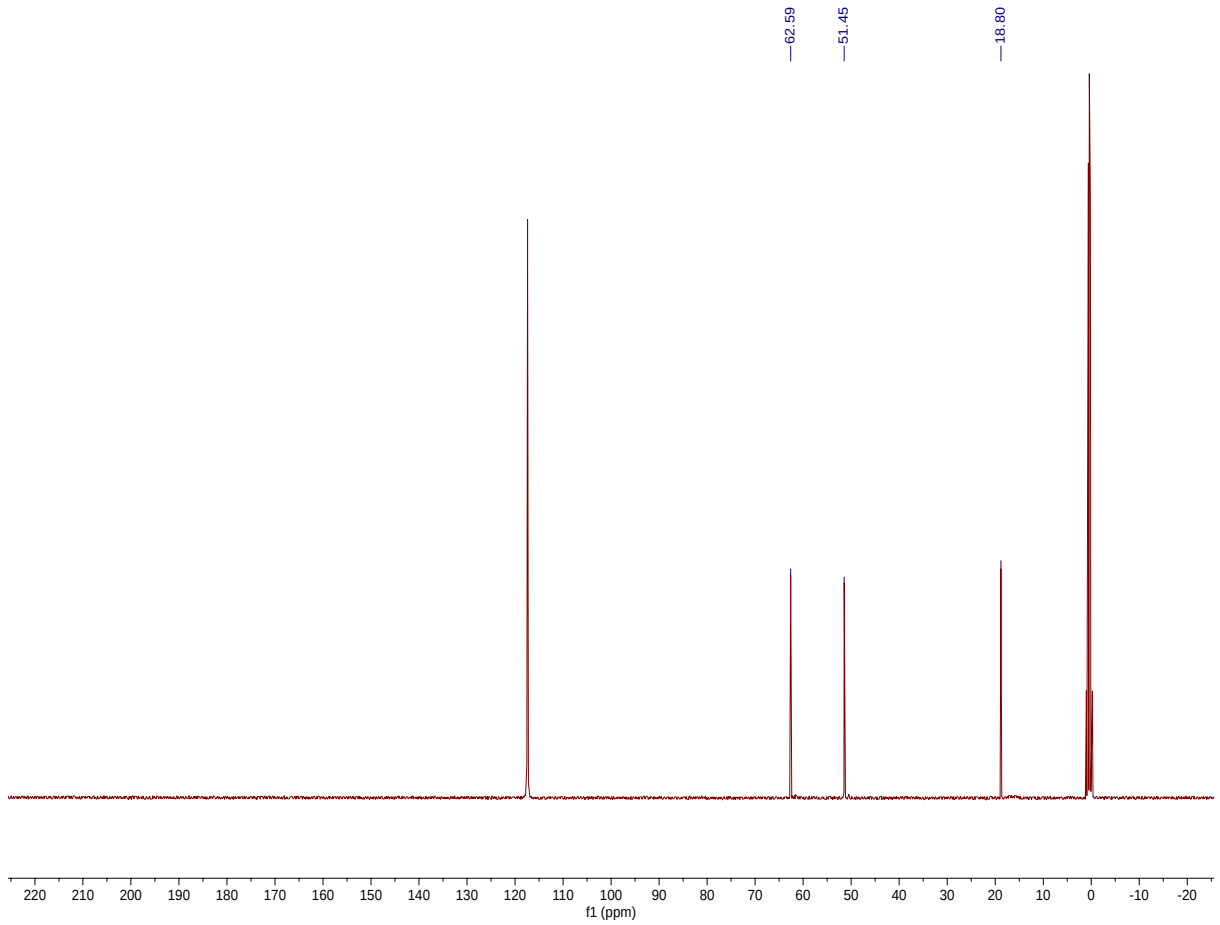

Figure A-171. ^{13}C NMR Spectrum of 3c in CD_3CN.

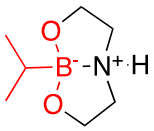

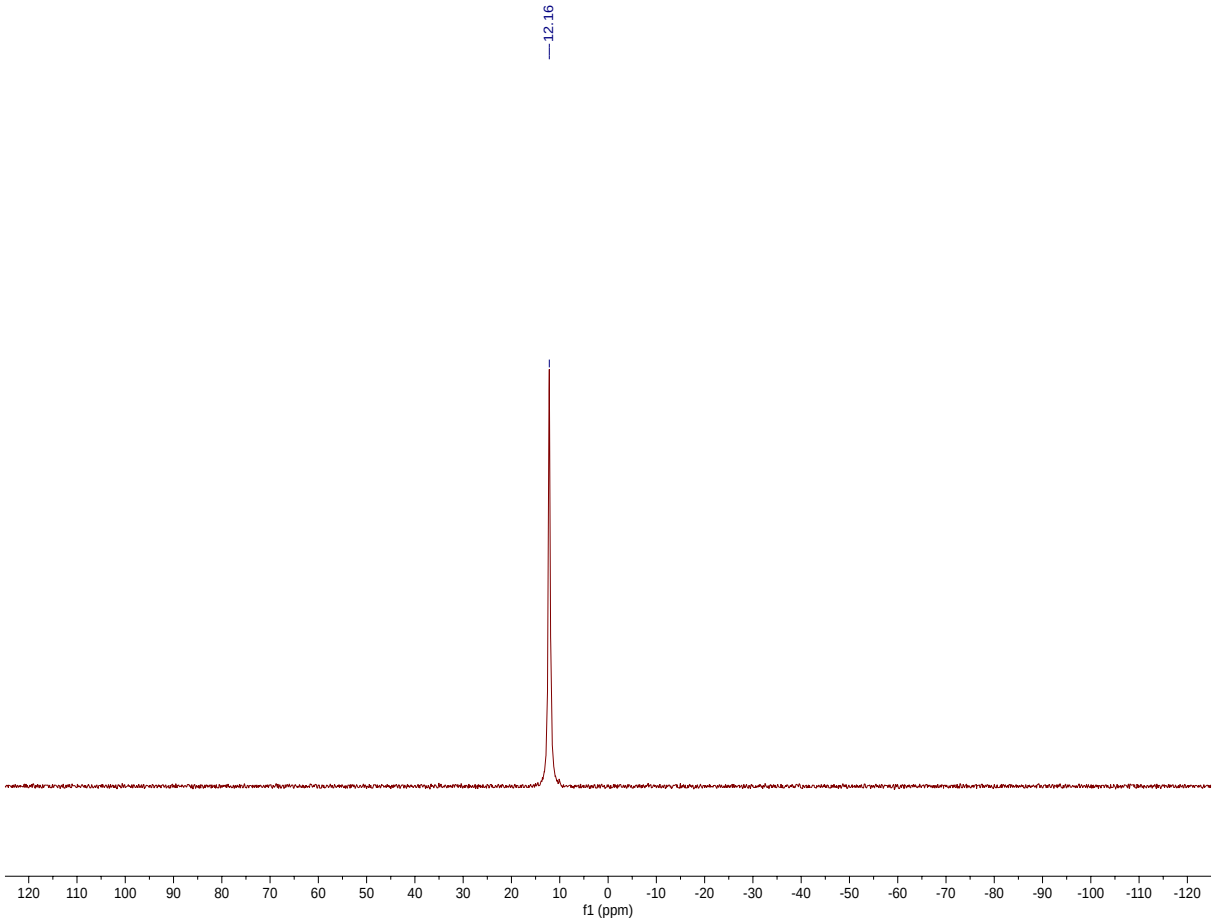

Figure A-172. ^{11}B NMR Spectrum of 3c in CD_3CN.

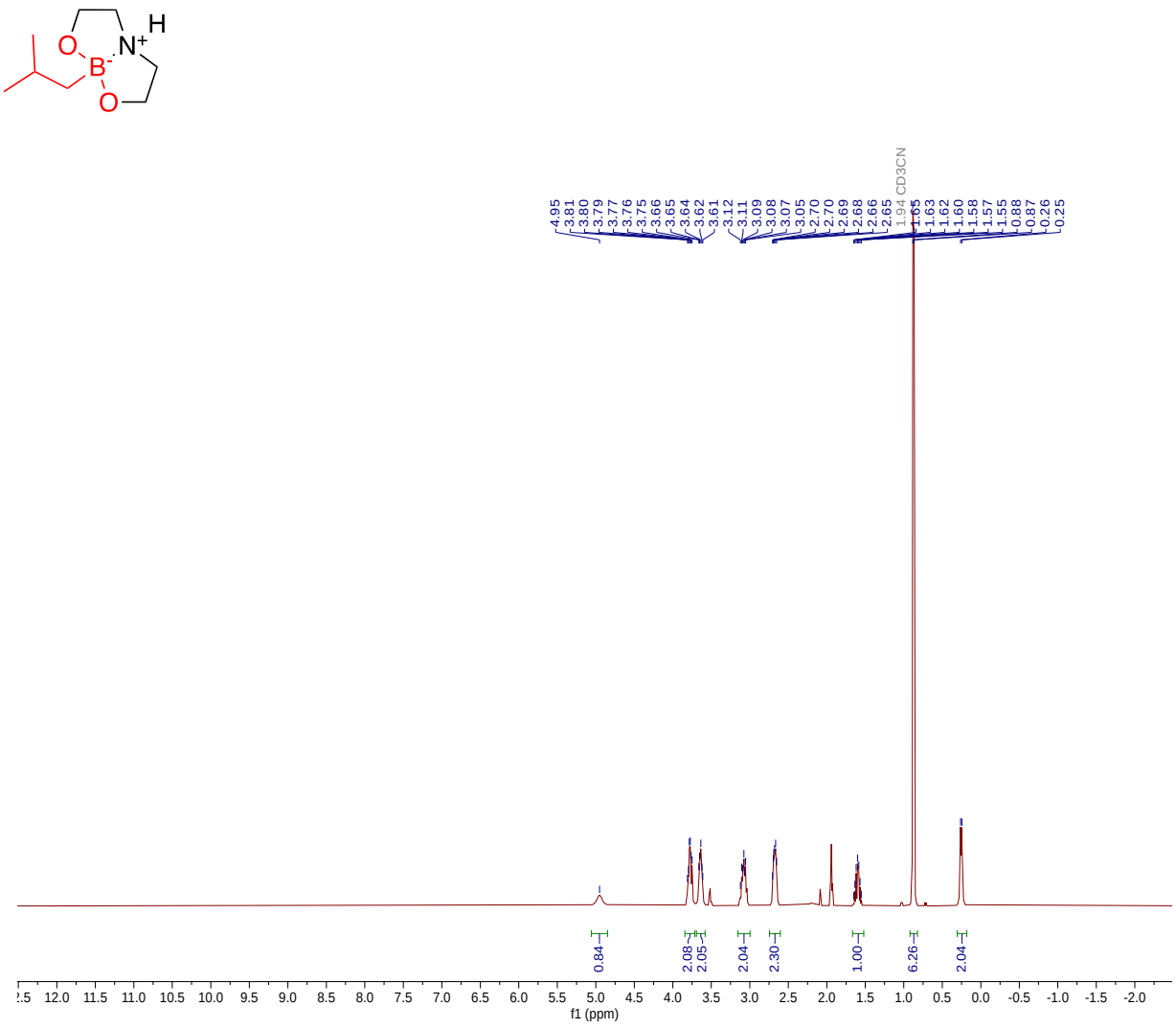

Figure A-173. ^{1}H NMR Spectrum of 3d in CD_3CN.

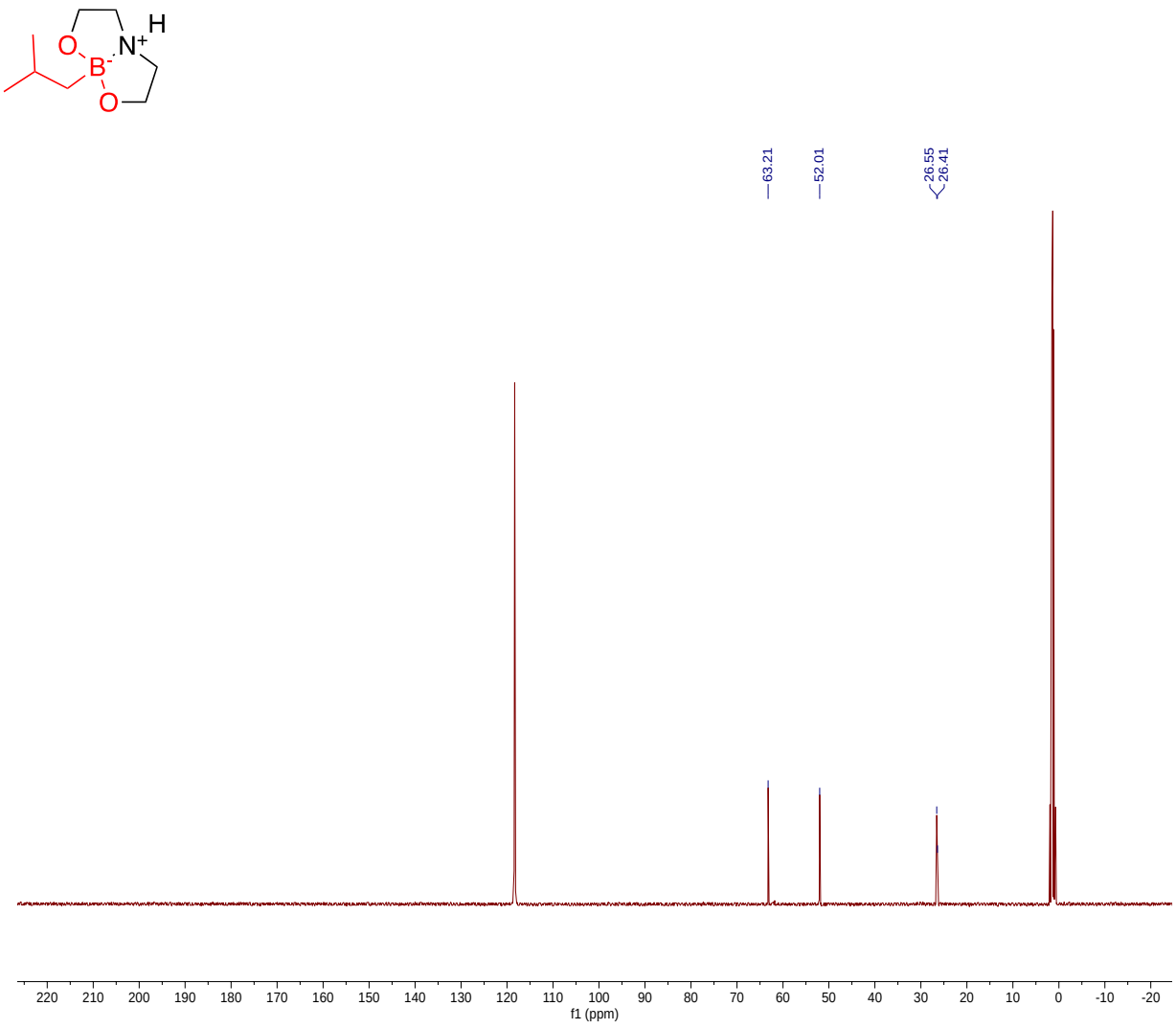

Figure A-174. ^{13}C NMR Spectrum of 3d in CD_3CN.

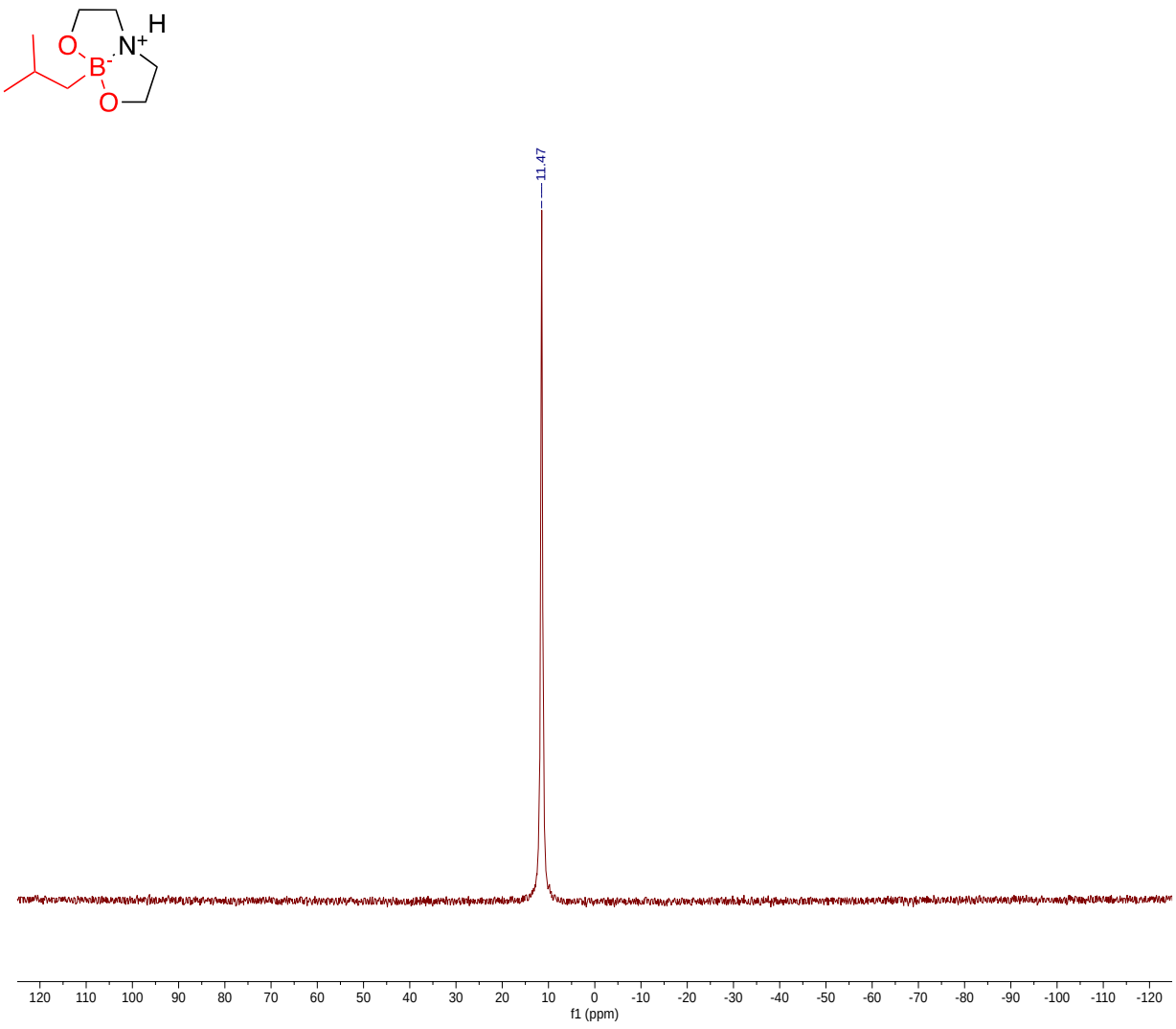

Figure A-175. ^{11}B NMR Spectrum of 3d in CD_3CN.

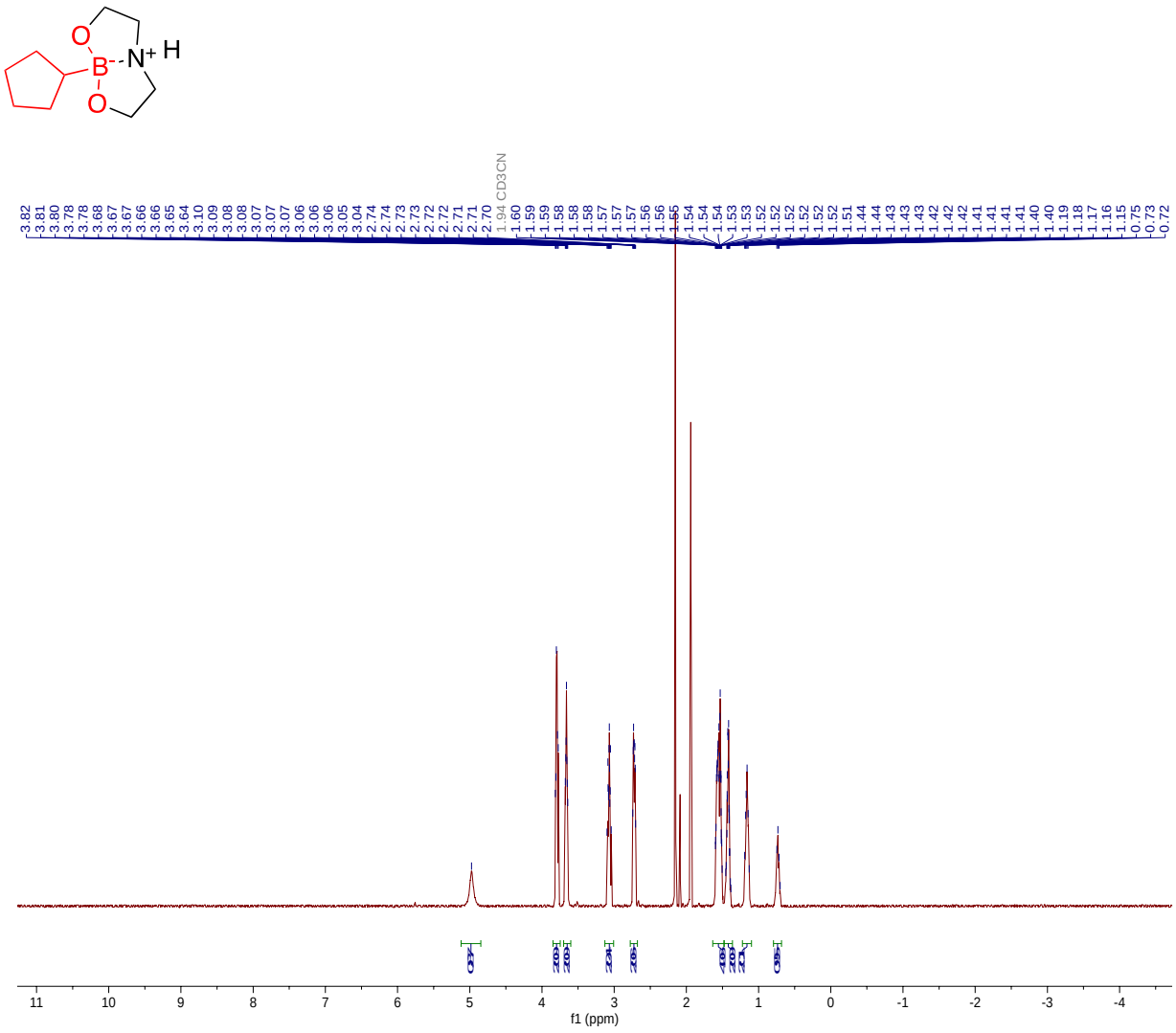

Figure A-176. ^{1}H NMR Spectrum of 3e in CD_3CN.

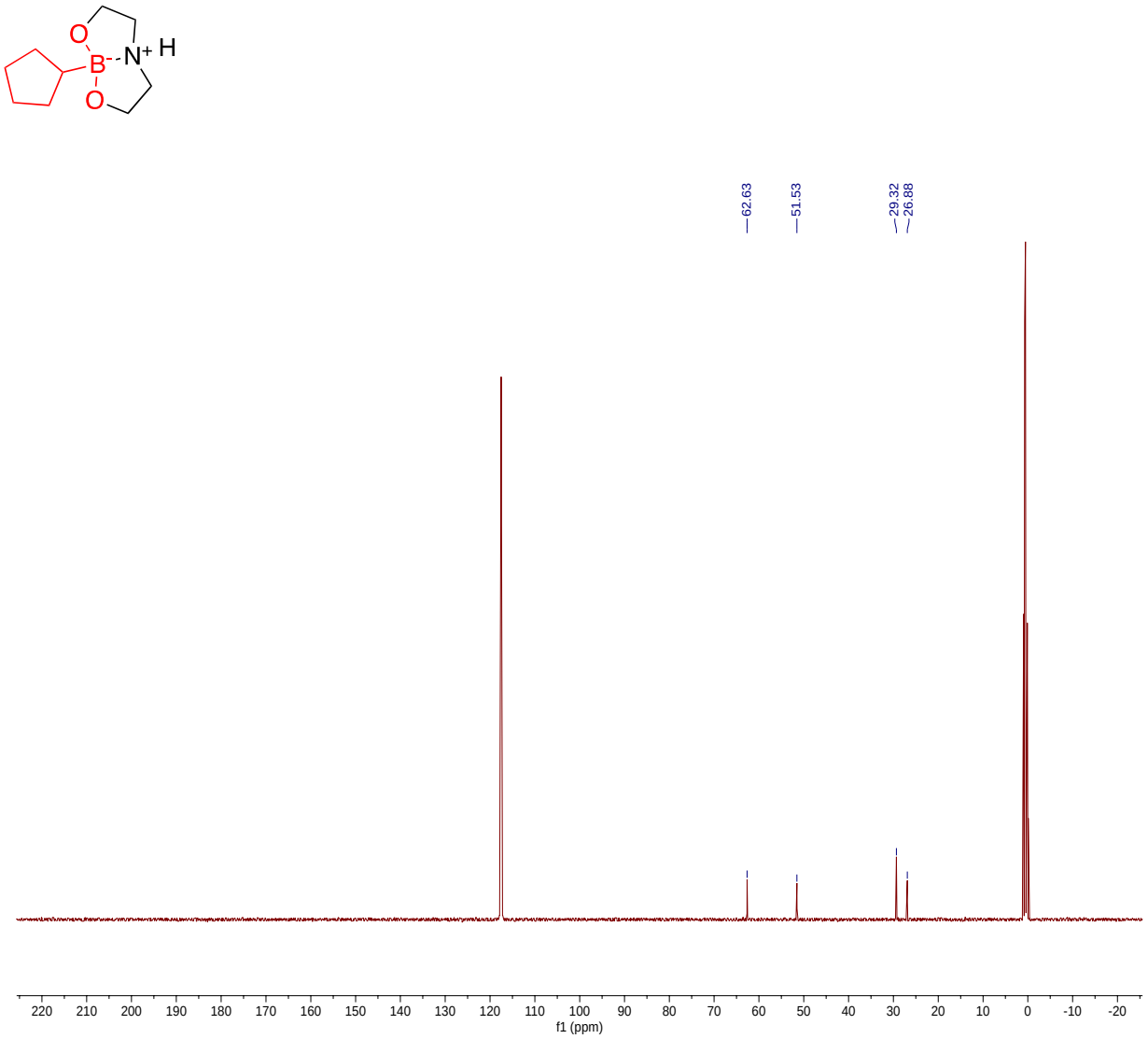

Figure A-177. ^{13}C NMR Spectrum of 3e in CD_3CN.

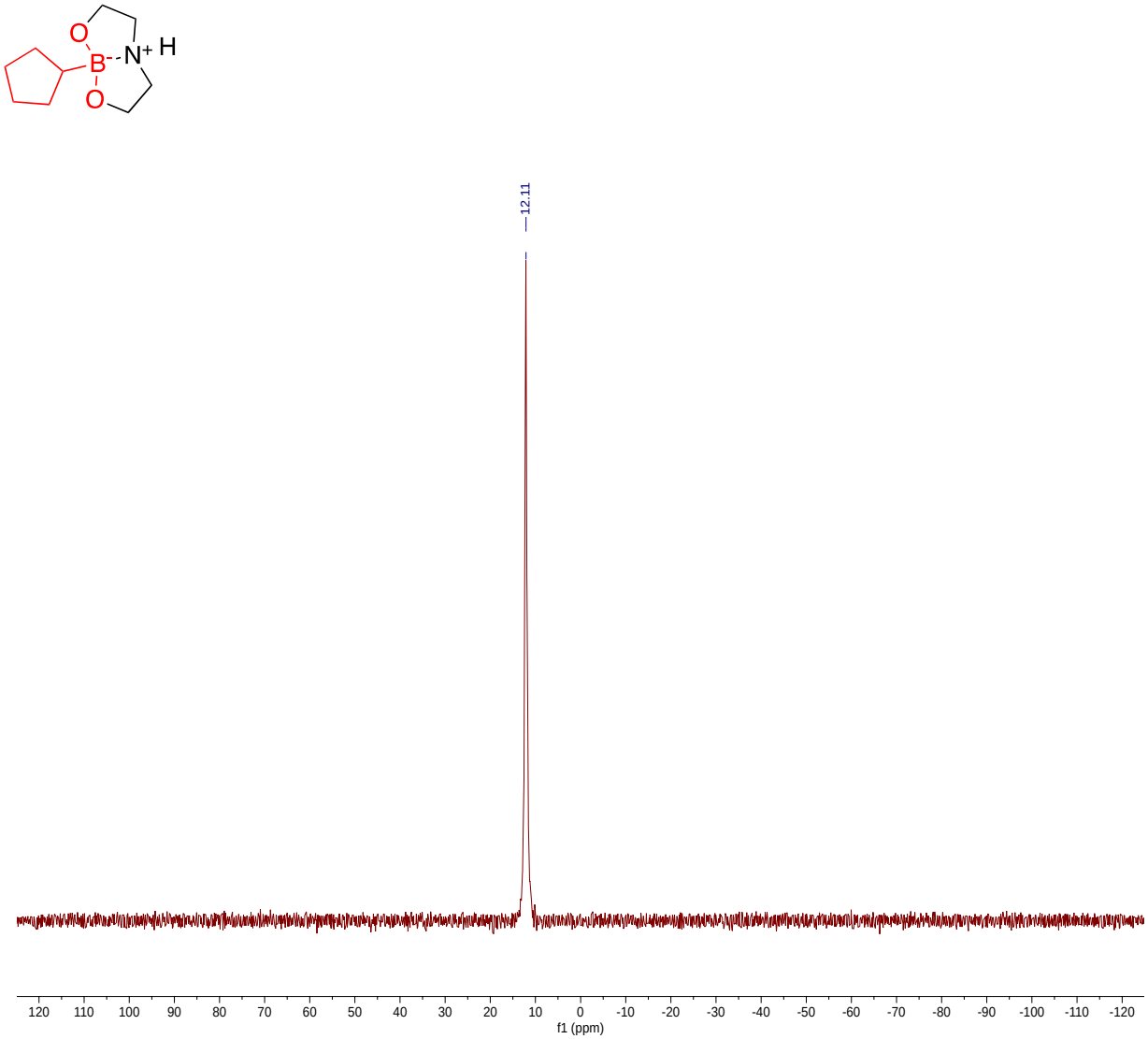

Figure A-178. ^{11}B NMR Spectrum of 3e in CD_3CN.

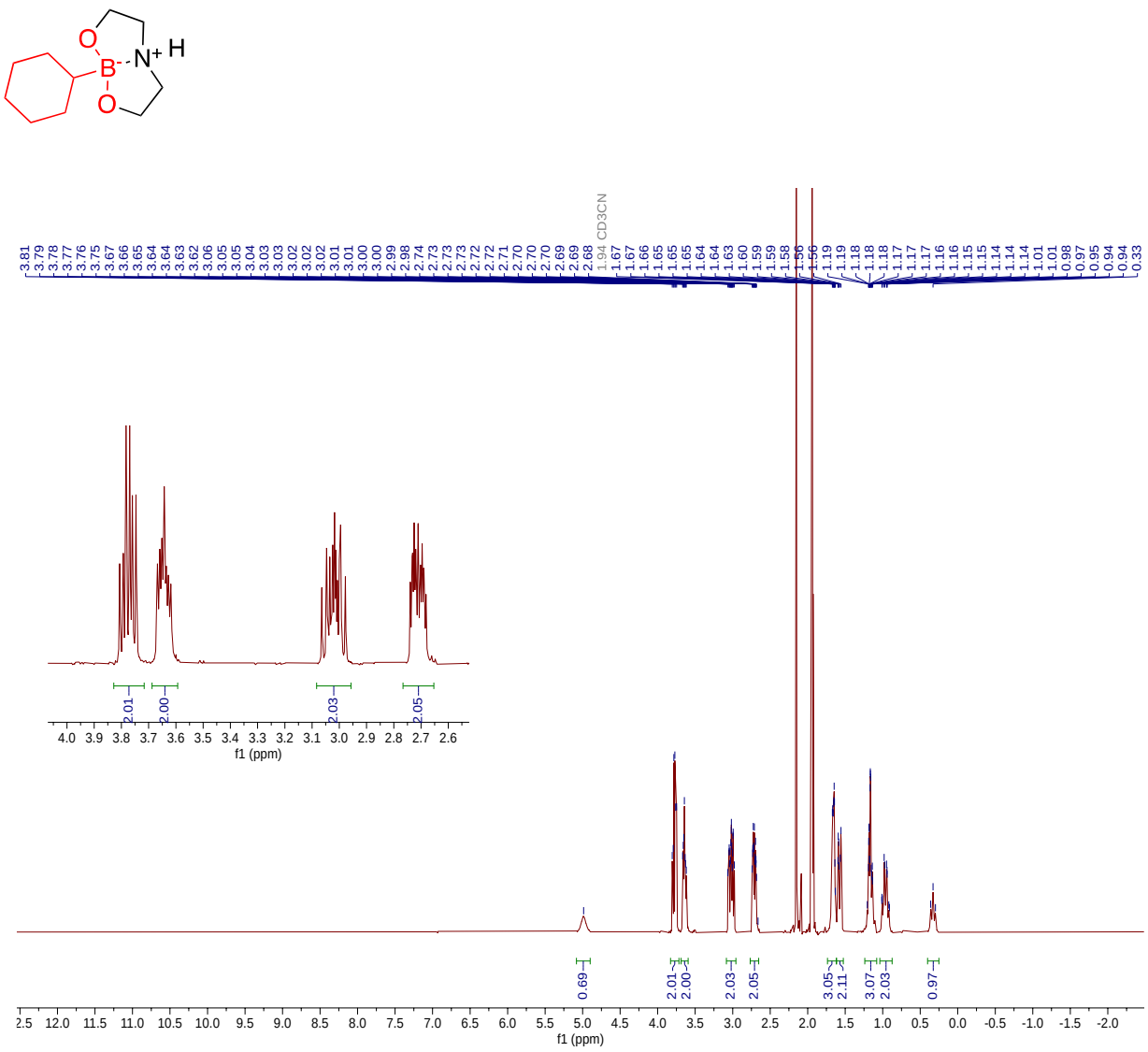

Figure A-179. ^{1}H NMR Spectrum of 3f in CD_3CN.

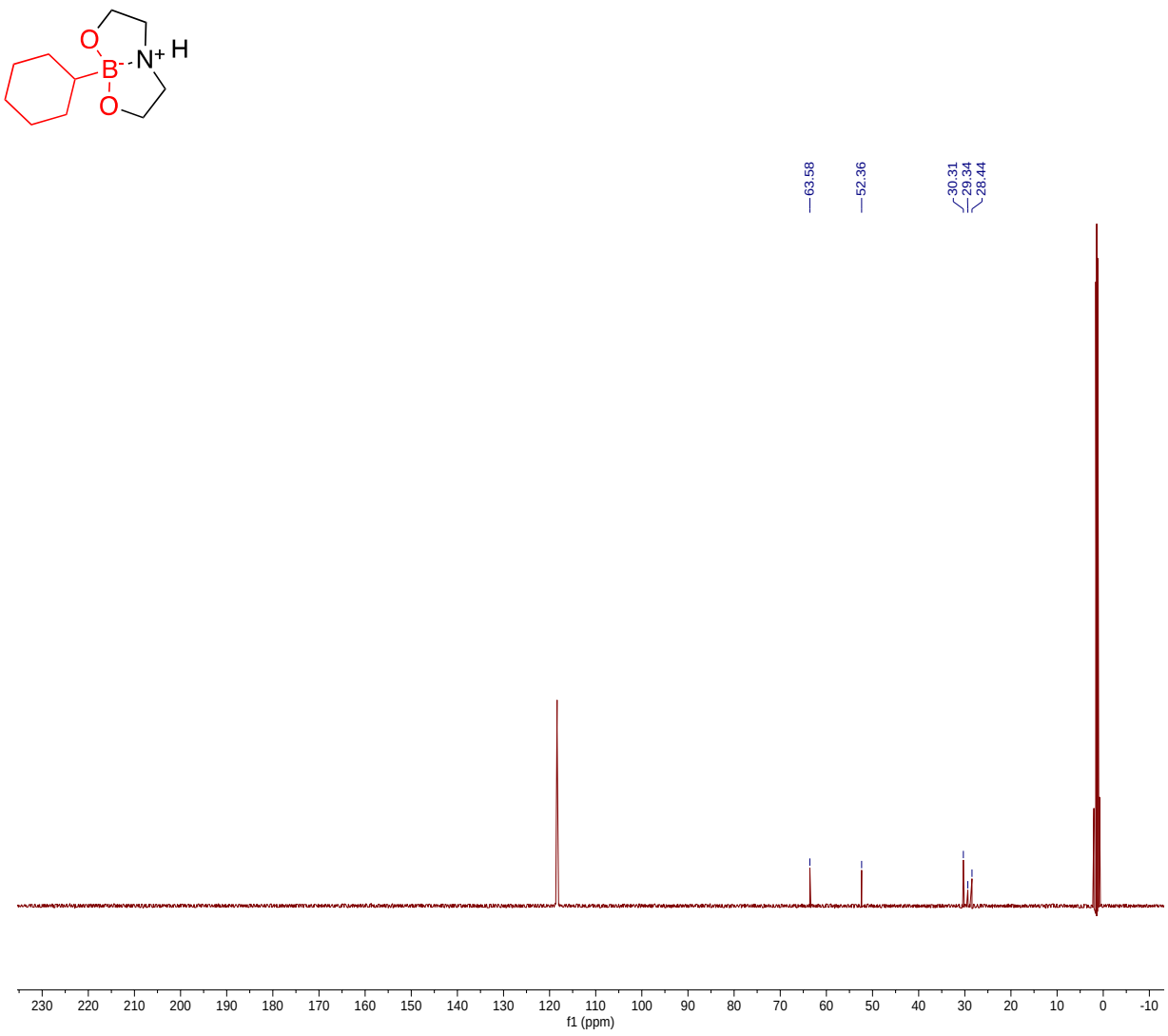

Figure A-180. ^{13}C NMR Spectrum of 3f in CD_3CN.

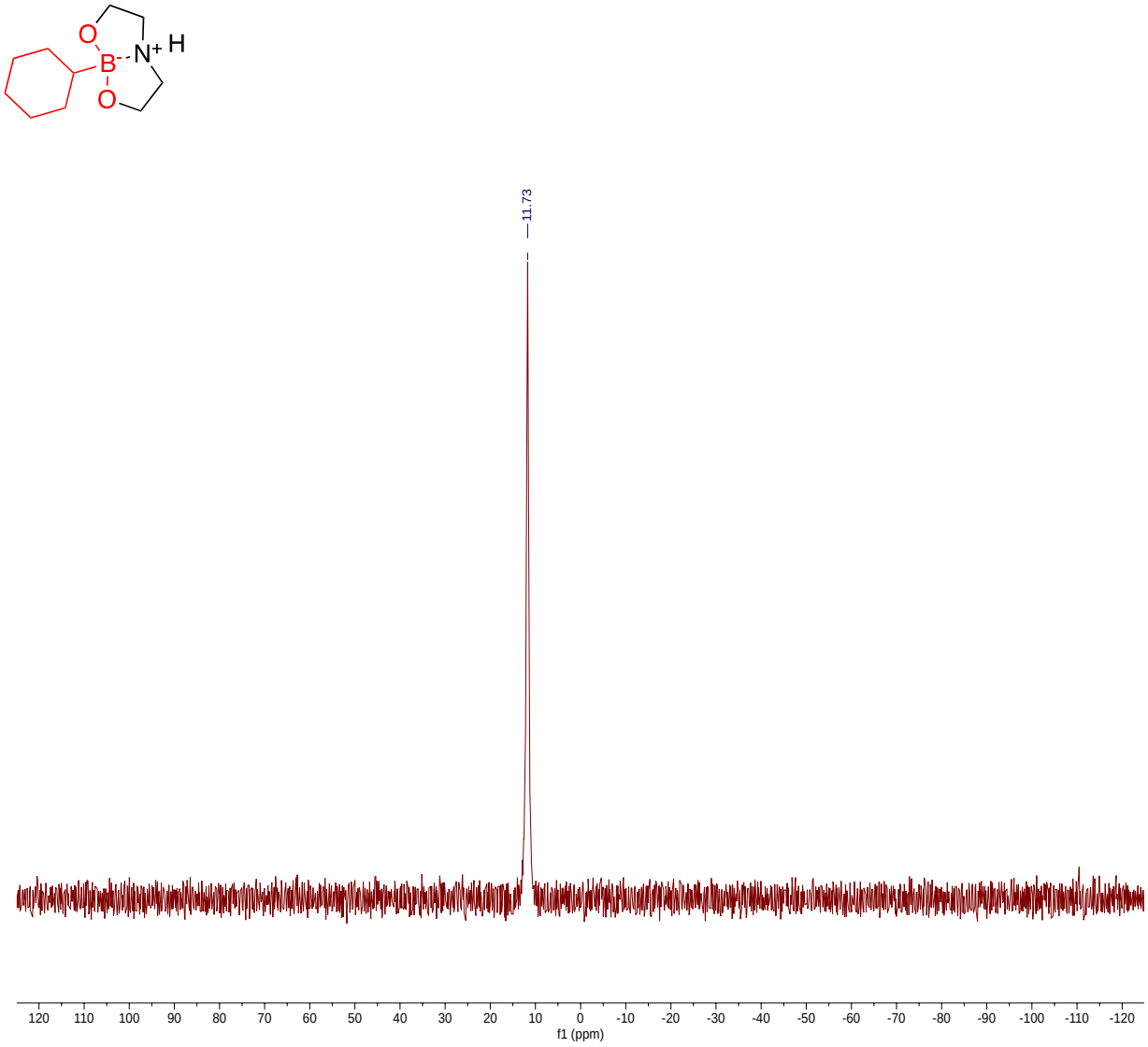

Figure A-181. ^{11}B NMR Spectrum of 3f in CD_3CN.

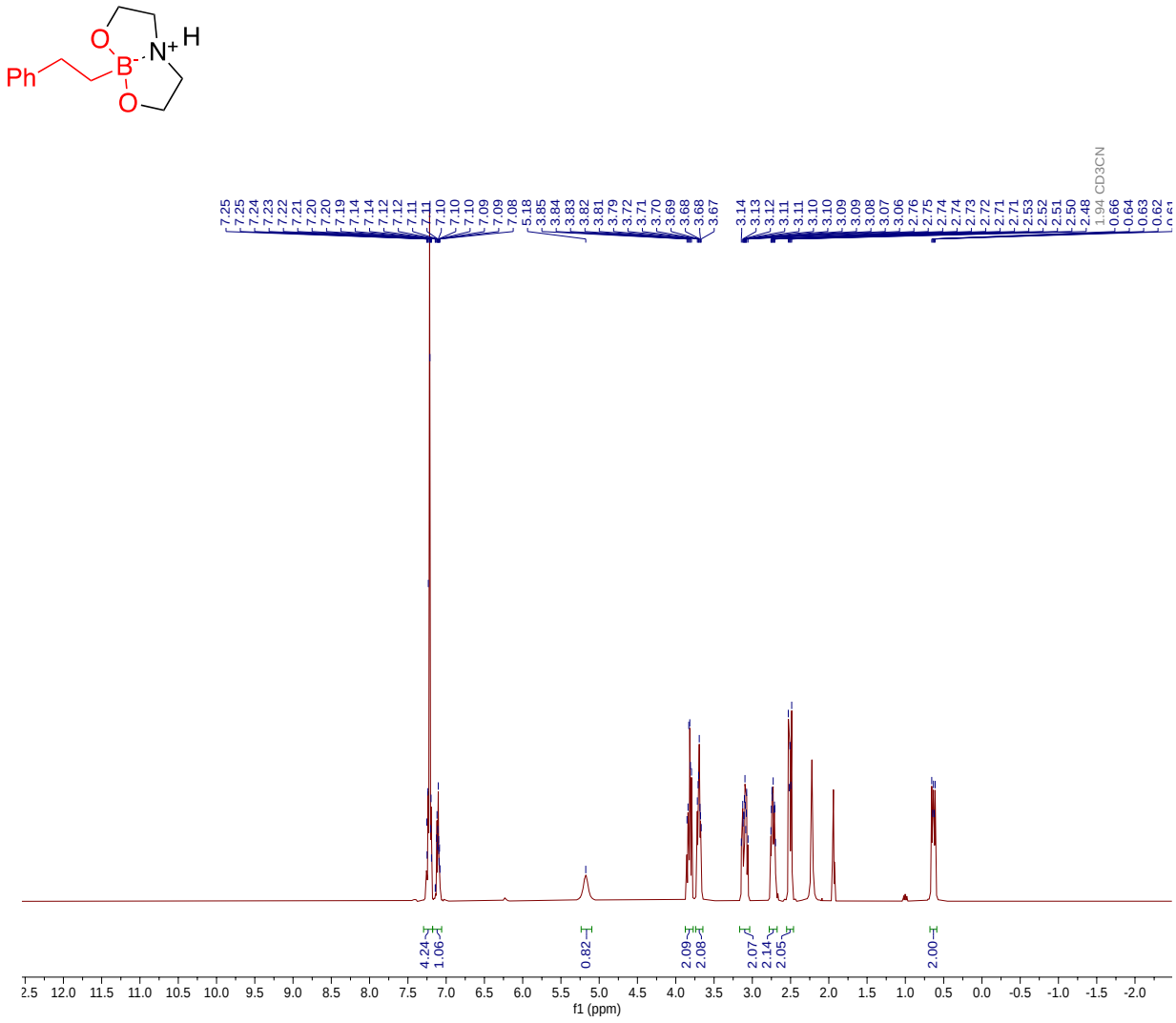

Figure A-182. ^{1}H NMR Spectrum of 3g in CD_3CN.

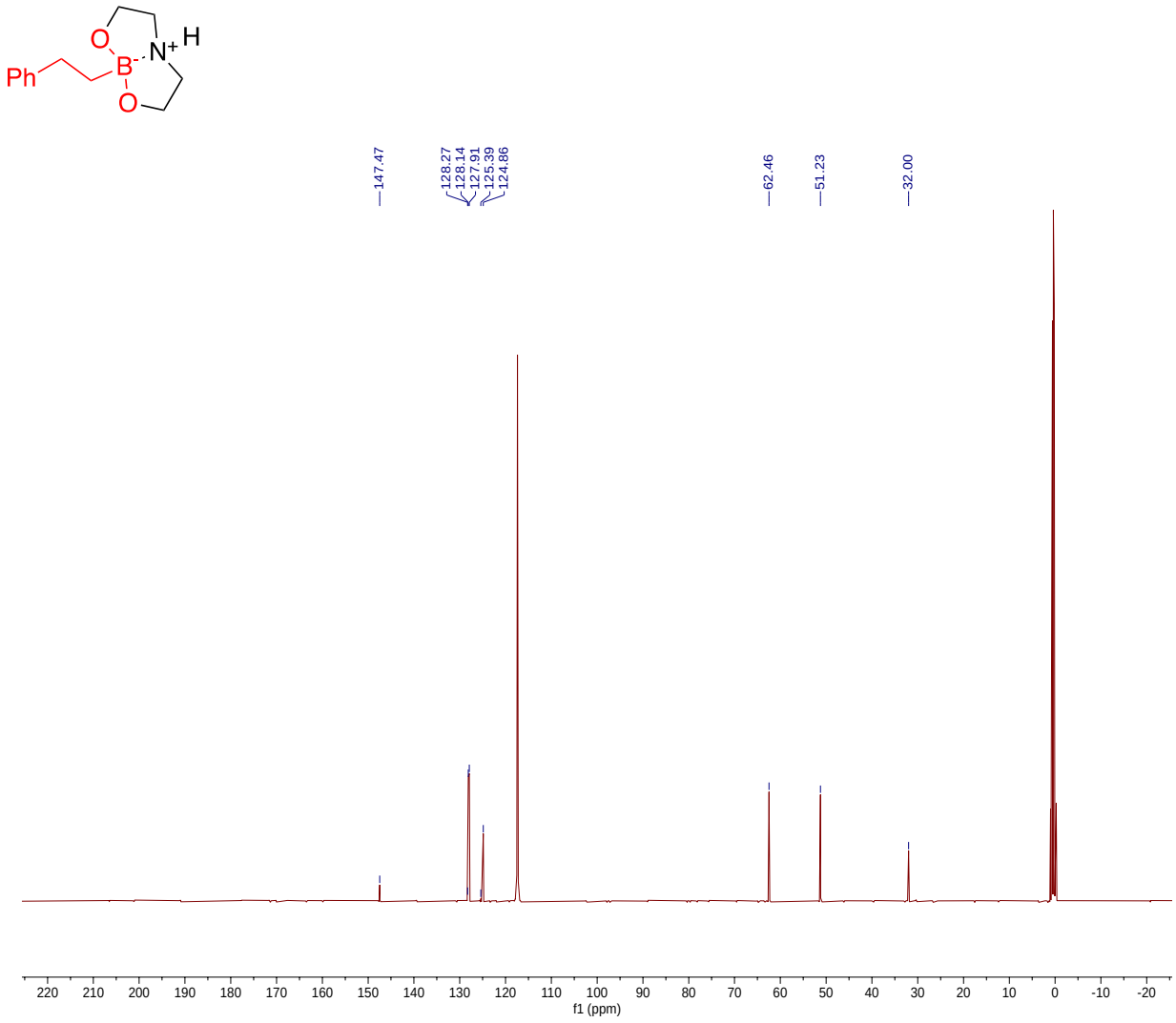

Figure A-183. ^{13}C NMR Spectrum of 3g in CD_3CN.

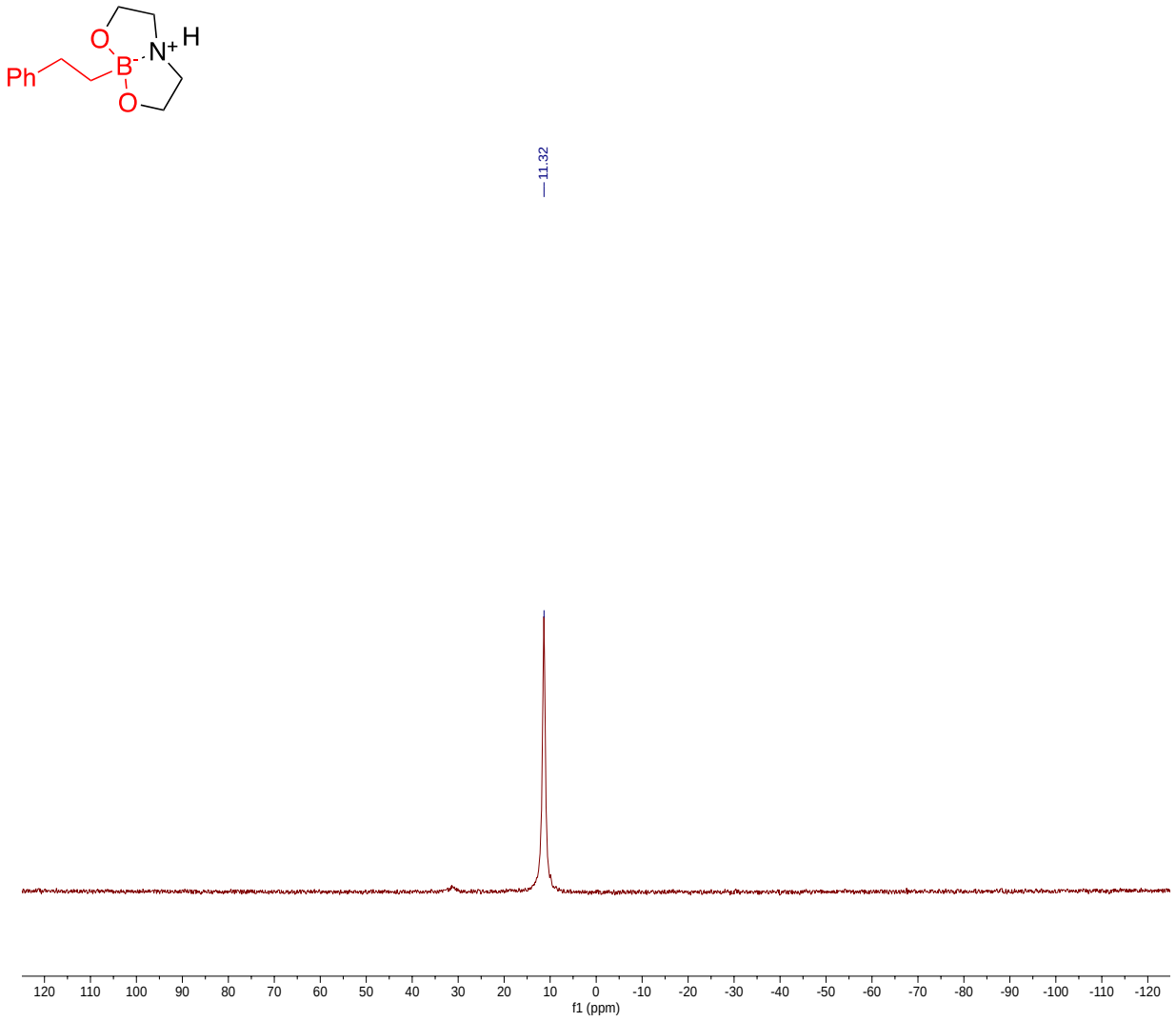

Figure A-184. ^{11}B NMR Spectrum of 3g in CD_3CN.

Appendix II X-Ray Crystallographic Data

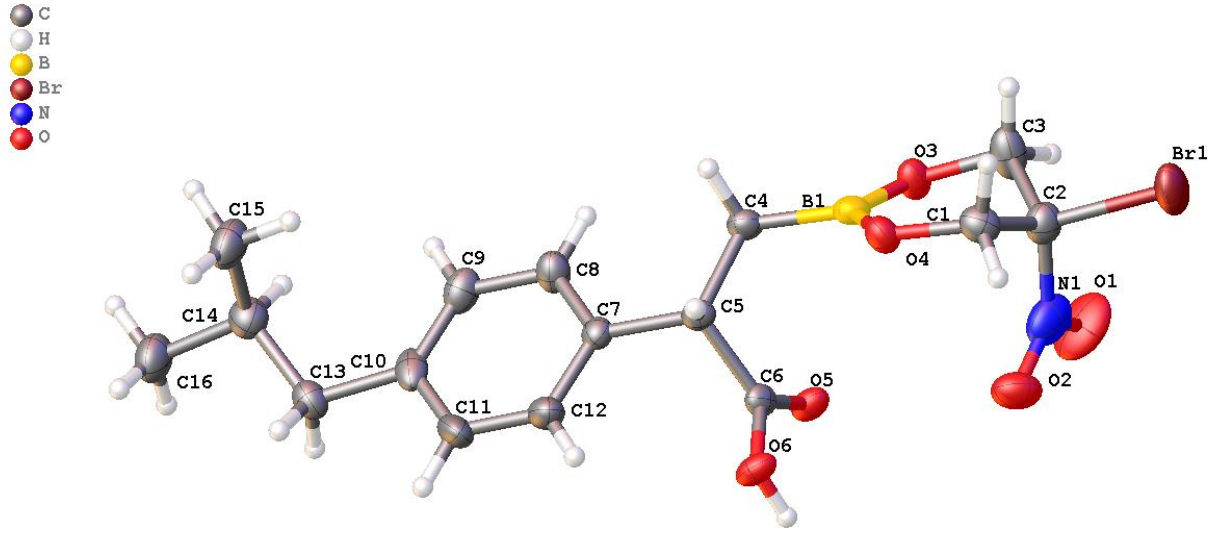

Figure A189. The asymmetric unit of **$C_{16}H_{21}BBrNO_6$** including all disordered components. All non-hydrogen atoms are drawn as 50% thermal probability ellipsoids. All hydrogen atoms are omitted for clarity.

Description of the X-ray structural analysis of $C_{16}H_{21}BBrNO_6$

A colorless block-shaped crystal measuring approximately 0.3 mm x 0.2 mm x 0.1 mm was selected under polybutene oil using a MiTeGen Micromount and mounted at 100(1) K to a D8-Venture diffractometer equipped with a Mo sealed tube X-ray source, a Triumph monochromator, and a Photon 2 CMOS area detector. The unit cell was determined from reflections harvested with a signal to noise ratio (I/σ) of at least 10 from a series of 2 ω scans of 6° with 0.5° frames using APEX3.[1] The data were collected to a resolution of 0.8 Å using 6 ω 1 φ scans.

The data were integrated using SAINT and corrected for absorption using SADABS.[2] The systematic absences and E-statistics of the data were uniquely consistent with the space group $P2_1/c$. The structure was solved using the intrinsic phasing routine of SHELXT.[3] The non-hydrogen atoms were located from a Fourier difference map of the electron density and anisotropically refined using the least-squares algorithm of SHELXL.[4] The hydrogen atoms were then placed in calculated positions and refined with riding thermal parameters.

The asymmetric unit (Figure 1) consists of the molecule shown in Figure 2. The isobutyl group is disordered over 2 positions (major component: 62.6(10)%). The Br and NO_2 are also positionally disordered over two positions (major component: 90.2(3)%). Thermal parameter and geometry restraints were used to ensure a chemically reasonable and computationally stable refinement.

The final structure consisted of 285 parameters refined against 3448 independent reflections, giving refinement residuals of R_1 = 0.0663 (based off F^2 for $I > 2\sigma$) and wR_2 = 0.1472 (based of F^2 for all reflections). The final difference Fourier map was featureless.

1. Bruker-AXS (2016). APEX 3 version 2016.9-0. Madison, Wisconsin, USA

2. (a) Bruker-AXS (2015). *SAINT V8.37A.* Madison, Wisconsin, USA. (b) Bruker-AXS (2014). *SADABS*, Madison, Wisconsin, USA.

3. Sheldrick, G. M., *Acta Crystallogr. A* **2015**, A71, 3-8.

4. (a) Sheldrick, G. M., *Acta Crystallogr. C* **2015**, C71, 3-8.; (b) Dolomanov, O. V.; Bourhis, L. J.; Gildea, R. J.; Howard, J. A. K.; Puschmann, H., *J. Appl. Crystallogr.* **2009**, *42*, 339-341.

Table 1 Crystal data and structure refinement for $C_{16}H_{21}BBrNO_6$.

Identification code	bp83-a
Empirical formula	$C_{16}H_{21}BBrNO_6$
Formula weight	414.06
Temperature/K	100.0
Crystal system	monoclinic
Space group	$P2_1/c$
a/Å	15.0011(5)
b/Å	13.4984(5)
c/Å	9.1329(3)
α/°	90
β/°	102.251(2)
γ/°	90
Volume/Å^3	1807.21(11)
Z	4
ρ_{calc}g/cm^3	1.522
μ/mm^{-1}	2.306
F(000)	848.0
Crystal size/mm^3	0.3 × 0.2 × 0.1
Radiation	MoKα (λ = 0.71073)
2Θ range for data collection/°	5.472 to 51.462
Index ranges	$-18 \leq h \leq 18$, $-16 \leq k \leq 16$, $-11 \leq l \leq 11$
Reflections collected	55837
Independent reflections	3448 [R_{int} = 0.0922, R_{sigma} = 0.0320]
Data/restraints/parameters	3448/348/285
Goodness-of-fit on F^2	1.167
Final R indexes [I>=2σ (I)]	R_1 = 0.0663, wR_2 = 0.1408
Final R indexes [all data]	R_1 = 0.0814, wR_2 = 0.1472
Largest diff. peak/hole / e Å^{-3}	0.75/-0.73

Table 2 Fractional Atomic Coordinates ($\times 10^4$) and Equivalent Isotropic Displacement Parameters ($Å^2 \times 10^3$) for $C_{16}H_{21}BBrNO_6$. U_{eq} is defined as 1/3 of the trace of the orthogonalised U_{IJ} tensor.

Atom	*x*	*y*	*z*	U(eq)
O3	4095(2)	7630(2)	1457(4)	31.2(8)
O4	4899(2)	6300(2)	603(4)	29.9(8)
O5	5061(2)	6163(2)	4515(4)	27.7(7)
O6	6000(2)	4951(2)	4144(4)	29.5(8)
C1	4111(3)	5959(4)	-470(5)	32.1(11)
C2	3264(3)	6340(4)	-25(6)	34.0(12)
C3	3319(4)	7443(4)	281(7)	39.9(13)
C4	5762(3)	7434(3)	2635(5)	26.0(10)
C5	6339(3)	6576(3)	3424(5)	22.6(9)
C6	5734(3)	5880(3)	4077(5)	23.2(10)
C7	7137(3)	6910(3)	4682(5)	23.3(10)
C8	7313(3)	7895(4)	5023(6)	31.9(11)
C9	8036(3)	8173(4)	6169(6)	34.3(12)
C10	8607(3)	7493(5)	7000(5)	35.4(13)
C11	8433(4)	6504(5)	6656(6)	43.1(14)
C12	7715(3)	6221(4)	5519(6)	34.9(12)
B1	4884(4)	7117(4)	1485(6)	26.7(12)
Br1	2212.4(5)	6069.6(5)	-1613.6(8)	46.7(2)
O1	2540(4)	6200(4)	2042(6)	68.0(16)
O2	3562(3)	5063(3)	1805(5)	44.4(11)
N1	3100(4)	5832(5)	1360(9)	52(2)
C13	9438(6)	7674(7)	8276(11)	31.3(18)
C14	9860(6)	8693(6)	8242(9)	37.5(18)
C15	10259(8)	8851(9)	6839(12)	46(3)
C16	10608(7)	8833(8)	9660(11)	46(2)
Br1A	3027(10)	5539(11)	1707(16)	82(4)
O1A	1672(8)	6250(30)	-1000(40)	64(8)
O2A	2580(20)	5510(30)	-2280(30)	62(8)
N1A	2453(13)	6100(20)	-1265(19)	64(9)
C13A	9286(9)	8031(14)	8280(19)	36(2)
C14A	10191(8)	8269(11)	7874(14)	38(2)
C15A	10087(14)	9116(16)	6710(20)	45(4)
C16A	10900(10)	8566(14)	9276(17)	48(3)

Table 3 Anisotropic Displacement Parameters ($Å^2×10^3$) for $C_{16}H_{21}BBrNO_6$. The Anisotropic displacement factor exponent takes the form: $-2\pi^2[h^2a^{*2}U_{11}+2hka^*b^*U_{12}+\ldots]$.

Atom	U_{11}	U_{22}	U_{33}	U_{23}	U_{13}	U_{12}
O3	29.3(18)	24.2(18)	35.8(19)	-5.7(15)	-2.8(15)	0.2(14)
O4	28.6(17)	27.5(18)	30.1(18)	0.3(14)	-1.4(14)	2.7(14)
O5	28.5(17)	18.9(16)	37.8(19)	0.8(14)	11.6(15)	-2.0(14)
O6	32.6(18)	19.2(17)	40(2)	1.8(14)	16.0(15)	-2.7(14)
C1	38(3)	30(3)	28(2)	-1(2)	6(2)	3(2)
C2	32(3)	32(3)	37(3)	-5(2)	4(2)	-3(2)
C3	31(3)	36(3)	48(3)	-16(3)	-2(2)	6(2)
C4	29(2)	21(2)	27(2)	2.7(19)	5(2)	0.3(19)
C5	25(2)	20(2)	23(2)	0.2(18)	6.5(18)	0.4(18)
C6	27(2)	21(2)	19(2)	-2.9(18)	-0.6(18)	-3.6(18)
C7	22(2)	26(2)	23(2)	1.0(19)	5.3(18)	-3.2(19)
C8	27(2)	29(3)	37(3)	-5(2)	2(2)	1(2)
C9	32(3)	35(3)	37(3)	-11(2)	10(2)	-7(2)
C10	25(3)	61(4)	20(2)	4(2)	6(2)	-11(2)
C11	30(3)	49(3)	44(3)	24(3)	-5(2)	-2(2)
C12	30(3)	30(3)	42(3)	12(2)	2(2)	-2(2)
B1	33(3)	22(3)	25(3)	5(2)	4(2)	-2(2)
Br1	36.1(4)	40.6(4)	53.9(4)	-9.4(3)	-11.6(3)	-3.8(3)
O1	58(3)	78(4)	85(4)	-22(3)	52(3)	-13(3)
O2	60(3)	30(2)	42(2)	5.5(19)	8(2)	-1(2)
N1	58(4)	50(4)	46(4)	-13(3)	8(3)	-24(3)
C13	28(3)	37(4)	28(3)	1(3)	2(3)	3(3)
C14	35(3)	42(4)	35(3)	1(3)	7(3)	-3(3)
C15	41(5)	53(6)	42(5)	-9(4)	6(4)	-19(5)
C16	40(4)	54(5)	42(4)	-5(4)	1(4)	-15(4)
C13A	36(4)	43(4)	33(4)	12(4)	16(4)	9(4)
C14A	36(4)	45(4)	37(4)	11(4)	17(4)	12(4)
C15A	42(7)	51(7)	49(7)	30(6)	22(6)	11(6)
C16A	46(6)	55(6)	50(6)	14(5)	25(5)	16(5)

Table 4 Bond Lengths for $C_{16}H_{21}BBrNO_6$.

Atom	Atom	Length/Å	Atom	Atom	Length/Å
O3	C3	1.429(6)	C7	C12	1.387(7)
O3	B1	1.367(7)	C8	C9	1.390(7)
O4	C1	1.442(6)	C9	C10	1.370(8)
O4	B1	1.369(6)	C10	C11	1.384(8)
O5	C6	1.222(6)	C10	C13	1.535(10)
O6	C6	1.314(5)	C10	C13A	1.558(18)
C1	C2	1.504(7)	C11	C12	1.382(7)
C2	C3	1.513(7)	O1	N1	1.250(7)
C2	Br1	1.938(5)	O2	N1	1.266(7)
C2	N1	1.505(10)	C13	C14	1.517(10)
C2	Br1A	2.010(14)	C14	C15	1.540(11)
C2	N1A	1.511(13)	C14	C16	1.535(10)
C4	C5	1.530(6)	O1A	N1A	1.263(9)
C4	B1	1.560(7)	O2A	N1A	1.262(9)
C5	C6	1.514(6)	C13A	C14A	1.516(11)
C5	C7	1.541(6)	C14A	C15A	1.546(13)
C7	C8	1.377(7)	C14A	C16A	1.534(12)

Table 5 Bond Angles for $C_{16}H_{21}BBrNO_6$.

Atom	Atom	Atom	Angle/°	Atom	Atom	Atom	Angle/°
B1	O3	C3	119.2(4)	C10	C9	C8	122.2(5)
B1	O4	C1	122.9(4)	C9	C10	C11	117.1(5)
O4	C1	C2	109.0(4)	C9	C10	C13	128.7(6)
C1	C2	C3	111.7(4)	C9	C10	C13A	109.6(8)
C1	C2	Br1	109.5(3)	C11	C10	C13	114.2(6)
C1	C2	N1	111.7(4)	C11	C10	C13A	133.0(8)
C1	C2	Br1A	109.2(5)	C12	C11	C10	121.1(5)
C1	C2	N1A	108.4(10)	C11	C12	C7	121.7(5)
C3	C2	Br1	109.1(3)	O3	B1	O4	121.3(4)
C3	C2	Br1A	113.3(6)	O3	B1	C4	118.5(4)
N1	C2	C3	107.8(5)	O4	B1	C4	120.0(4)
N1	C2	Br1	106.9(4)	O1	N1	C2	119.0(6)
N1A	C2	C3	110.8(12)	O1	N1	O2	123.1(8)
N1A	C2	Br1A	103.0(9)	O2	N1	C2	117.8(5)
O3	C3	C2	108.5(4)	C14	C13	C10	113.8(7)
C5	C4	B1	114.9(4)	C13	C14	C15	112.3(8)
C4	C5	C7	113.7(4)	C13	C14	C16	109.1(7)
C6	C5	C4	109.2(4)	C16	C14	C15	110.0(7)
C6	C5	C7	108.8(4)	O1A	N1A	C2	116.9(9)
O5	C6	O6	123.1(4)	O2A	N1A	C2	117.6(10)
O5	C6	C5	122.7(4)	O2A	N1A	O1A	122.2(14)
O6	C6	C5	114.2(4)	C14A	C13A	C10	113.0(12)
C8	C7	C5	122.2(4)	C13A	C14A	C15A	111.0(11)
C8	C7	C12	117.1(4)	C13A	C14A	C16A	110.4(10)
C12	C7	C5	120.8(4)	C16A	C14A	C15A	109.3(11)
C7	C8	C9	120.8(5)				

Table 6 Torsion Angles for $C_{16}H_{21}BBrNO_6$.

A	B	C	D	Angle/°	A	B	C	D	Angle/°
O4	C1	C2	C3	50.0(6)	C7	C8	C9	C10	0.5(8)
O4	C1	C2	Br1	171.0(3)	C8	C7	C12	C11	0.6(8)
O4	C1	C2	N1	-70.8(5)	C8	C9	C10	C11	-0.3(8)
O4	C1	C2	Br1A	-76.2(6)	C8	C9	C10	C13	179.0(6)
O4	C1	C2	N1A	172.3(12)	C8	C9	C10	C13A	-174.8(7)
C1	O4	B1	O3	3.7(7)	C9	C10	C11	C12	0.3(8)
C1	O4	B1	C4	179.3(4)	C9	C10	C13	C14	-23.0(11)
C1	C2	C3	O3	-59.0(6)	C9	C10	C13A	C14A	-95.3(12)
C1	C2	N1	O1	165.4(6)	C10	C11	C12	C7	-0.5(9)
C1	C2	N1	O2	-12.3(7)	C10	C13	C14	C15	-64.3(11)
C1	C2	N1A	O1A	171(3)	C10	C13	C14	C16	173.5(8)
C1	C2	N1A	O2A	11(3)	C10	C13A	C14A	C15A	72.0(18)
C3	O3	B1	O4	-13.0(7)	C10	C13A	C14A	C16A	-166.6(12)
C3	O3	B1	C4	171.4(4)	C11	C10	C13	C14	156.4(7)
C3	C2	N1	O1	42.3(7)	C11	C10	C13A	C14A	91.5(13)
C3	C2	N1	O2	-135.4(5)	C12	C7	C8	C9	-0.6(7)
C3	C2	N1A	O1A	-66(3)	B1	O3	C3	C2	39.7(7)
C3	C2	N1A	O2A	134(3)	B1	O4	C1	C2	-22.7(6)
C4	C5	C6	O5	-30.7(6)	B1	C4	C5	C6	-51.4(5)
C4	C5	C6	O6	149.8(4)	B1	C4	C5	C7	-173.1(4)
C4	C5	C7	C8	-1.3(6)	Br1	C2	C3	O3	179.8(3)
C4	C5	C7	C12	179.1(4)	Br1	C2	N1	O1	-74.8(6)
C5	C4	B1	O3	138.0(4)	Br1	C2	N1	O2	107.4(5)
C5	C4	B1	O4	-37.8(6)	N1	C2	C3	O3	64.0(6)
C5	C7	C8	C9	179.8(4)	C13	C10	C11	C12	-179.1(6)
C5	C7	C12	C11	-179.8(5)	Br1A	C2	C3	O3	64.9(7)
C6	C5	C7	C8	-123.3(5)	Br1A	C2	N1A	O1A	55(3)
C6	C5	C7	C12	57.1(6)	Br1A	C2	N1A	O2A	-104(3)
C7	C5	C6	O5	93.9(5)	N1A	C2	C3	O3	-180.0(10)
C7	C5	C6	O6	-85.5(5)	C13A	C10	C11	C12	173.2(8)

Table 7 Hydrogen Atom Coordinates (Å×10^4) and Isotropic Displacement Parameters (Å^2×10^3) for $C_{16}H_{21}BBrNO_6$.

Atom	*x*	*y*	*z*	U(eq)
H6	5675.58	4616.71	4607.11	44
H1A	4102.12	5225.77	-494.93	39
H1B	4136.14	6202.97	-1482.59	39
H3A	3379.43	7805.8	-635.3	48
H3B	2757.29	7671.91	581.09	48
H4A	6145.4	7837.91	2105.6	31
H4B	5581.29	7860.02	3404.62	31
H5	6594.76	6204.02	2660.31	27
H8	6934.62	8389.46	4468.48	38
H9	8137.48	8857.44	6383.4	41
H11	8813.22	6010.9	7211.85	52
H12	7615.79	5535.81	5305.67	42
H13A	9251.49	7588.51	9244.86	38
H13B	9906.79	7166.87	8220.76	38
H14	9375.46	9201.59	8242.99	45
H15A	10768.88	8393.56	6862.51	68
H15B	10476.36	9535.03	6821.74	68
H15C	9785.53	8726.28	5939.02	68
H16A	10348.32	8733.05	10547.71	70
H16B	10857.14	9504.51	9674.65	70
H16C	11096.12	8349.42	9664.58	70
H13C	9003.62	8655.02	8527.88	43
H13D	9397.48	7607.51	9185.51	43
H14A	10413.99	7663.69	7429.91	45
H15D	9681.09	8902.68	5778.21	68
H15E	10686.09	9284.38	6515.76	68
H15F	9826.53	9699.47	7105.27	68
H16D	10938.56	8048.03	10039.01	73
H16E	10716.73	9191.88	9669.25	73
H16F	11496.4	8647.47	9015.34	73

Table 8 Atomic Occupancy for $C_{16}H_{21}BBrNO_6$.

Atom	*Occupancy*	Atom	*Occupancy*	Atom	*Occupancy*
Br1	0.902(3)	O1	0.902(3)	O2	0.902(3)
N1	0.902(3)	C13	0.626(10)	H13A	0.626(10)
H13B	0.626(10)	C14	0.626(10)	H14	0.626(10)
C15	0.626(10)	H15A	0.626(10)	H15B	0.626(10)
H15C	0.626(10)	C16	0.626(10)	H16A	0.626(10)
H16B	0.626(10)	H16C	0.626(10)	Br1A	0.098(3)
O1A	0.098(3)	O2A	0.098(3)	N1A	0.098(3)
C13A	0.374(10)	H13C	0.374(10)	H13D	0.374(10)
C14A	0.374(10)	H14A	0.374(10)	C15A	0.374(10)
H15D	0.374(10)	H15E	0.374(10)	H15F	0.374(10)
C16A	0.374(10)	H16D	0.374(10)	H16E	0.374(10)
H16F	0.374(10)				

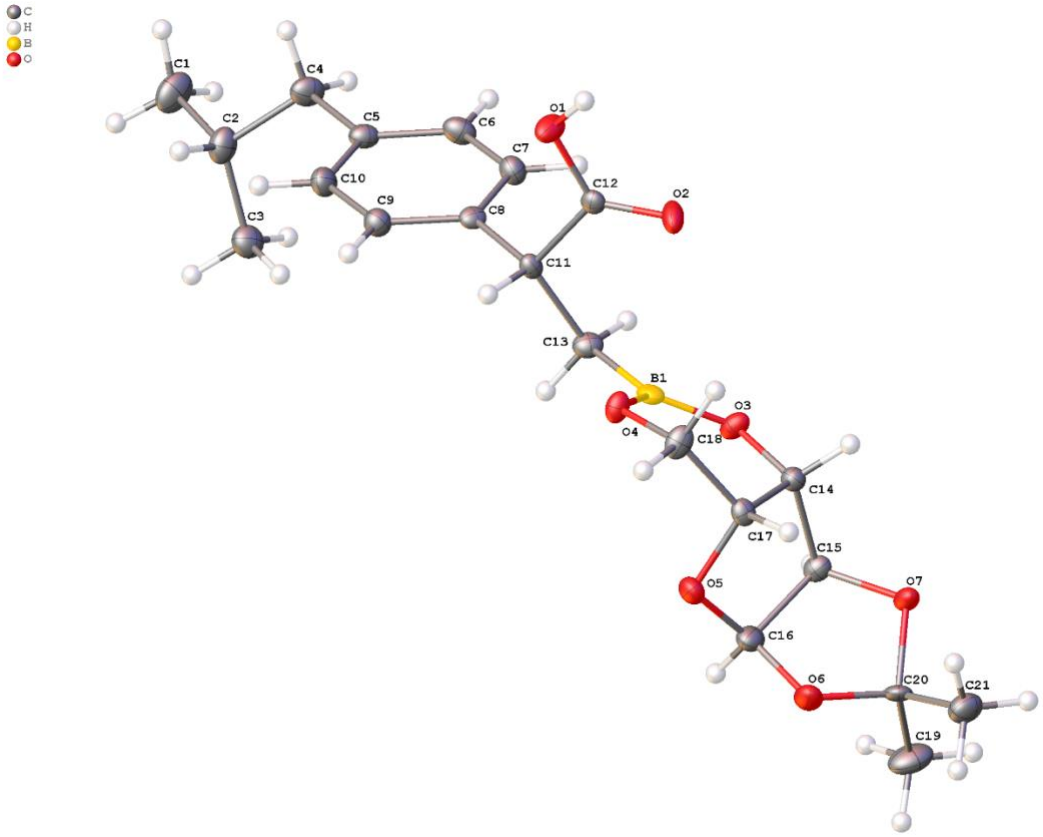

Figure A190. The asymmetric unit of $C_{21}H_{29}BO_7$. All non-hydrogen atoms are drawn as 50% thermal probability ellipsoids.

Description of the X-ray structural analysis of $C_{21}H_{29}BO_7$

A colorless plate-shaped crystal measuring approximately 0.1 mm x 0.1 mm x 0.1 mm was selected under polybutene oil using a MiTeGen Micromount and mounted at 100(1) K to a D8-Venture diffractometer equipped with a Mo sealed tube X-ray source, a Triumph monochromator, and a Photon 2 CMOS area detector. The unit cell was determined from reflections harvested with a signal to noise ratio (I/σ) of at least 10 from a series of 2 ω scans of 6° with 0.5° frames using APEX3.[1] The data were collected to a resolution of 0.8 Å using 1 φ scans.

The data were integrated using SAINT and corrected for absorption using SADABS.[2] The systematic absences and E-statistics of the data were consistent with the space group $P2_12_12_1$. The structure was solved using the intrinsic phasing routine of SHELXT.[3] The non-hydrogen atoms were located from a Fourier difference map of the electron density and anisotropically refined using the least-squares algorithm of SHELXL.[4] The hydrogen atoms were then placed in calculated positions and refined with riding thermal parameters.

The asymmetric unit consists of the molecule shown in Figure 1. While the compound crystallizes in a chiral space group, the anomalous dispersion of these light atoms is not sufficient to distinguish between the two enantiomeric pairs of compounds.

The final structure consisted of 267 parameters refined against 4290 independent reflections, giving refinement residuals of R_1 = 0.0444 (based off F^2 for $I > 2\sigma$) and wR_2 = 0.0914 (based of F^2 for all reflections). The final difference Fourier map was featureless.

References

1. Bruker-AXS (2016). APEX 3 version 2016.9-0. Madison, Wisconsin, USA

2. (a) Bruker-AXS (2015). *SAINT V8.37A.* Madison, Wisconsin, USA. (b) Bruker-AXS (2014). *SADABS*, Madison, Wisconsin, USA.

3. Sheldrick, G. M., *Acta Crystallogr. A* **2015**, A71, 3-8.

4. (a) Sheldrick, G. M., *Acta Crystallogr. C* **2015**, C71, 3-8.; (b) Dolomanov, O. V.; Bourhis, L. J.; Gildea, R. J.; Howard, J. A. K.; Puschmann, H., *J. Appl. Crystallogr.* **2009**, *42*, 339-341.

Table 1 Crystal data and structure refinement for $C_{21}H_{29}BO_7$.

Identification code	bp85
Empirical formula	$C_{21}H_{29}BO_7$
Formula weight	404.25
Temperature/K	100.00
Crystal system	orthorhombic
Space group	$P2_12_12_1$
a/Å	6.0732(2)
b/Å	9.4197(2)
c/Å	36.5711(12)
α/°	90
β/°	90
γ/°	90
Volume/Å^3	2092.15(11)
Z	4
ρ_{calc}g/cm^3	1.283
μ/mm^{-1}	0.094
F(000)	864.0
Crystal size/mm^3	0.15 × 0.1 × 0.1
Radiation	MoKα (λ = 0.71073)
2Θ range for data collection/°	4.466 to 52.812
Index ranges	$-7 \leq h \leq 7$, $-11 \leq k \leq 11$, $-45 \leq l \leq 45$
Reflections collected	25566
Independent reflections	4290 [R_{int} = 0.0721, R_{sigma} = 0.0444]
Data/restraints/parameters	4290/0/332
Goodness-of-fit on F^2	1.038
Final R indexes [I>=2σ (I)]	R_1 = 0.0444, wR_2 = 0.0869
Final R indexes [all data]	R_1 = 0.0566, wR_2 = 0.0914
Largest diff. peak/hole / e Å^{-3}	0.22/-0.23
Flack parameter	0.0(5)

Table 2 Fractional Atomic Coordinates (×10^4) and Equivalent Isotropic Displacement Parameters (Å^2×10^3) for $C_{21}H_{29}BO_7$. U_{eq} is defined as 1/3 of the trace of the orthogonalised U_{IJ} tensor.

Atom	*x*	*y*	*z*	U(eq)
O1	-23(4)	1810(2)	6221.8(5)	21.6(5)
O2	1035(4)	2062(2)	5643.4(6)	22.0(5)
O3	2584(3)	4498(2)	5044.7(5)	17.3(4)
O4	-786(3)	4808(2)	5380.5(5)	16.6(4)
O5	-517(3)	6626(2)	4749.0(5)	20.1(5)
O6	199(4)	7131(2)	4143.0(6)	24.9(5)
O7	2547(3)	5300(2)	4083.6(5)	19.1(4)
C1	8670(6)	5769(4)	7897.0(10)	31.5(8)
C2	7119(5)	5832(4)	7565.7(8)	23.6(7)
C3	7875(5)	6990(4)	7303.4(9)	23.9(7)
C4	7031(5)	4376(3)	7379.2(9)	22.8(7)
C5	5592(5)	4281(3)	7041.4(8)	17.3(6)
C6	6267(5)	3475(3)	6742.1(9)	20.3(7)
C7	4990(5)	3365(3)	6431.0(8)	18.3(6)
C8	2960(4)	4061(3)	6404.8(8)	13.9(6)
C9	2256(5)	4851(3)	6703.2(8)	18.0(6)
C10	3554(5)	4955(3)	7018.4(8)	20.6(7)
C11	1614(4)	4016(3)	6055.1(7)	13.2(6)
C12	900(4)	2532(3)	5948.2(7)	13.2(6)
C13	2790(5)	4729(3)	5731.6(8)	17.7(6)
C14	1538(4)	4555(3)	4694.9(8)	14.8(6)
C15	2665(5)	5682(3)	4462.7(8)	16.4(6)
C16	1134(5)	6978(3)	4499.0(8)	20.6(6)
C17	-807(4)	5102(3)	4722.0(8)	14.6(6)
C18	-2017(5)	4569(4)	5051.3(8)	19.1(6)
C19	3419(7)	7493(4)	3766.7(11)	34.2(8)
C20	1611(5)	6489(3)	3886.5(8)	16.7(6)
C21	256(6)	5917(4)	3575.1(9)	26.7(7)
B1	1449(5)	4653(3)	5365.7(9)	15.2(6)

Table 3 Anisotropic Displacement Parameters (Å^2×10^3) for $C_{21}H_{29}BO_7$. The Anisotropic displacement factor exponent takes the form: $-2\pi^2[h^2a^{*2}U_{11}+2hka^*b^*U_{12}+\ldots]$.

Atom	U_{11}	U_{22}	U_{33}	U_{23}	U_{13}	U_{12}
O1	30.6(12)	18.7(11)	15.6(10)	-0.1(8)	-1.6(9)	-11.4(9)
O2	29.4(12)	17.2(11)	19.5(12)	-6.8(9)	9.3(9)	-5.6(9)
O3	13.5(9)	24.1(11)	14.2(10)	4.0(8)	-0.8(8)	1.5(8)
O4	13.0(10)	24.1(11)	12.6(10)	-3.3(8)	-1.1(8)	-1.1(8)
O5	24.7(11)	15.8(10)	20.0(11)	-1.2(8)	2.3(9)	5.6(9)
O6	35.6(13)	20.5(11)	18.8(11)	3.6(8)	0.8(10)	13.2(10)
O7	24.6(11)	18.7(10)	14.0(10)	3.9(8)	2.4(9)	8.8(9)
C1	31(2)	43(2)	20.8(18)	-2.3(16)	-8.1(15)	-7.9(17)
C2	21.4(16)	31.2(17)	18.1(16)	-5.0(13)	-3.1(13)	-1.7(13)

Table 3 Anisotropic Displacement Parameters ($Å^2×10^3$) for $C_{21}H_{29}BO_7$. The Anisotropic displacement factor exponent takes the form: $-2\pi^2[h^2a^{*2}U_{11}+2hka^*b^*U_{12}+\ldots]$.

Atom	U_{11}	U_{22}	U_{33}	U_{23}	U_{13}	U_{12}
C3	25.5(17)	22.9(17)	23.4(17)	-2.8(13)	-4.8(14)	-3.6(14)
C4	24.9(16)	22.6(16)	21.1(16)	2.3(13)	-9.5(13)	-2.1(13)
C5	19.1(15)	14.8(14)	18.0(14)	1.9(11)	-4.3(12)	-2.6(11)
C6	17.8(16)	17.0(15)	26.1(17)	1.2(13)	-4.8(13)	0.8(12)
C7	18.3(15)	17.3(14)	19.5(15)	-2.7(12)	-1.2(13)	0.9(12)
C8	14.9(14)	11.7(13)	15.1(14)	0.8(11)	-2.4(11)	-5.0(11)
C9	18.1(15)	17.8(14)	18.1(15)	-1.2(12)	-1.4(12)	-0.5(12)
C10	25.8(16)	18.1(16)	17.7(16)	-3.0(12)	-2.7(13)	0.6(12)
C11	12.8(13)	13.2(13)	13.5(14)	-2.1(11)	-3.2(11)	1.5(11)
C12	10.6(13)	13.9(13)	15.0(14)	0.6(11)	-0.9(11)	3.6(10)
C13	15.5(14)	17.5(15)	20.0(15)	2.7(12)	-1.8(12)	-3.8(12)
C14	16.0(13)	13.9(14)	14.6(14)	-0.1(11)	-0.7(11)	0.7(11)
C15	13.2(14)	19.8(15)	16.1(14)	2.2(11)	0.0(12)	0.3(11)
C16	29.5(16)	13.9(14)	18.3(15)	0.2(12)	-0.3(13)	-3.2(12)
C17	12.9(13)	15.3(14)	15.7(13)	-3.2(11)	-3.0(11)	-0.9(10)
C18	12.6(14)	28.9(17)	15.6(15)	-1.7(13)	-2.5(11)	-2.9(12)
C19	38(2)	34(2)	31(2)	13.8(17)	-2.7(17)	-14.1(17)
C20	22.5(15)	11.3(13)	16.3(15)	6.5(11)	-0.4(12)	3.0(11)
C21	35.1(19)	25.9(17)	19.2(16)	3.1(13)	-4.6(15)	-2.7(16)
B1	17.0(15)	9.7(14)	18.8(16)	3.2(13)	1.6(13)	-0.7(12)

Table 4 Bond Lengths for $C_{21}H_{29}BO_7$.

Atom	Atom	Length/Å	Atom	Atom	Length/Å
O1	C12	1.333(3)	C5	C6	1.393(4)
O2	C12	1.202(3)	C5	C10	1.394(4)
O3	C14	1.429(3)	C6	C7	1.381(4)
O3	B1	1.369(4)	C7	C8	1.400(4)
O4	C18	1.435(3)	C8	C9	1.388(4)
O4	B1	1.366(4)	C8	C11	1.518(4)
O5	C16	1.397(4)	C9	C10	1.400(4)
O5	C17	1.449(3)	C11	C12	1.515(4)
O6	C16	1.428(4)	C11	C13	1.536(4)
O6	C20	1.408(4)	C13	B1	1.568(4)
O7	C15	1.434(3)	C14	C15	1.522(4)
O7	C20	1.448(3)	C14	C17	1.518(4)
C1	C2	1.536(4)	C15	C16	1.540(4)
C2	C3	1.524(5)	C17	C18	1.498(4)
C2	C4	1.532(4)	C19	C20	1.514(4)
C4	C5	1.516(4)	C20	C21	1.505(4)

Table 5 Bond Angles for b $C_{21}H_{29}BO_7$.

Atom	Atom	Atom	Angle/°	Atom	Atom	Atom	Angle/°
B1	O3	C14	122.6(2)	O2	C12	C11	124.0(3)
B1	O4	C18	117.9(2)	C11	C13	B1	113.3(2)
C16	O5	C17	106.1(2)	O3	C14	C15	109.0(2)
C20	O6	C16	108.8(2)	O3	C14	C17	111.8(2)
C15	O7	C20	107.9(2)	C17	C14	C15	102.8(2)
C3	C2	C1	109.8(3)	O7	C15	C14	110.0(2)
C3	C2	C4	111.8(3)	O7	C15	C16	104.6(2)
C4	C2	C1	109.7(3)	C14	C15	C16	103.5(2)
C5	C4	C2	115.8(3)	O5	C16	O6	109.6(2)
C6	C5	C4	120.2(3)	O5	C16	C15	107.5(2)
C10	C5	C4	122.3(3)	O6	C16	C15	104.0(2)
C10	C5	C6	117.5(3)	O5	C17	C14	103.1(2)
C7	C6	C5	121.5(3)	O5	C17	C18	109.7(2)
C6	C7	C8	121.1(3)	C18	C17	C14	113.5(2)
C7	C8	C11	121.2(3)	O4	C18	C17	111.5(2)
C9	C8	C7	117.9(3)	O6	C20	O7	103.9(2)
C9	C8	C11	120.8(3)	O6	C20	C19	111.5(3)
C8	C9	C10	120.8(3)	O6	C20	C21	109.0(3)
C5	C10	C9	121.2(3)	O7	C20	C19	110.0(3)
C8	C11	C13	112.7(2)	O7	C20	C21	108.3(2)
C12	C11	C8	113.4(2)	C21	C20	C19	113.7(3)
C12	C11	C13	109.8(2)	O3	B1	C13	118.3(2)
O1	C12	C11	113.4(2)	O4	B1	O3	123.1(3)
O2	C12	O1	122.4(2)	O4	B1	C13	118.5(3)

Table 6 Torsion Angles for $C_{21}H_{29}BO_7$.

A	B	C	D	Angle/°	A	B	C	D	Angle/°
O3	C14	C15	O7	149.6(2)	C13	C11	C12	O1	176.3(2)
O3	C14	C15	C16	-99.1(2)	C13	C11	C12	O2	-7.4(4)
O3	C14	C17	O5	79.7(3)	C14	O3	B1	O4	3.2(4)
O3	C14	C17	C18	-38.9(3)	C14	O3	B1	C13	-173.8(3)
O5	C17	C18	O4	-62.9(3)	C14	C15	C16	O5	4.8(3)
O7	C15	C16	O5	120.0(2)	C14	C15	C16	O6	-111.4(2)
O7	C15	C16	O6	3.8(3)	C14	C17	C18	O4	51.9(3)
C1	C2	C4	C5	-178.8(3)	C15	O7	C20	O6	-30.6(3)
C2	C4	C5	C6	141.3(3)	C15	O7	C20	C19	88.8(3)
C2	C4	C5	C10	-40.0(4)	C15	O7	C20	C21	-146.4(2)
C3	C2	C4	C5	-56.7(4)	C15	C14	C17	O5	-37.1(3)
C4	C5	C6	C7	179.8(3)	C15	C14	C17	C18	-155.7(2)
C4	C5	C10	C9	180.0(3)	C16	O5	C17	C14	41.7(3)
C5	C6	C7	C8	-0.1(5)	C16	O5	C17	C18	162.9(2)

Table 6 Torsion Angles for $C_{21}H_{29}BO_7$.

A	B	C	D	Angle/°	A	B	C	D	Angle/°
C6	C5	C10	C9	-1.3(4)	C16	O6	C20	O7	33.6(3)
C6	C7	C8	C9	-0.8(4)	C16	O6	C20	C19	-84.8(3)
C6	C7	C8	C11	176.3(3)	C16	O6	C20	C21	148.9(2)
C7	C8	C9	C10	0.6(4)	C17	O5	C16	O6	83.4(3)
C7	C8	C11	C12	62.0(3)	C17	O5	C16	C15	-29.0(3)
C7	C8	C11	C13	-63.5(3)	C17	C14	C15	O7	-91.6(2)
C8	C9	C10	C5	0.5(5)	C17	C14	C15	C16	19.7(3)
C8	C11	C12	O1	49.2(3)	C18	O4	B1	O3	10.3(4)
C8	C11	C12	O2	-134.4(3)	C18	O4	B1	C13	-172.7(3)
C8	C11	C13	B1	178.4(2)	C20	O6	C16	O5	-138.0(2)
C9	C8	C11	C12	-121.0(3)	C20	O6	C16	C15	-23.3(3)
C9	C8	C11	C13	113.5(3)	C20	O7	C15	C14	126.8(2)
C10	C5	C6	C7	1.1(4)	C20	O7	C15	C16	16.2(3)
C11	C8	C9	C10	-176.5(3)	B1	O3	C14	C15	124.8(3)
C11	C13	B1	O3	-144.7(3)	B1	O3	C14	C17	11.9(3)
C11	C13	B1	O4	38.2(4)	B1	O4	C18	C17	-37.2(4)
C12	C11	C13	B1	51.0(3)					

Table 7 Hydrogen Atom Coordinates (Å×10^4) and Isotropic Displacement Parameters (Å^2×10^3) for b $C_{21}H_{29}BO_7$.

Atom	*x*	*y*	*z*	U(eq)
H1	-646.77	1082.73	6138.49	32
H1A	8570(70)	6650(50)	8041(11)	47
H1B	10230(70)	5580(40)	7820(11)	47
H1C	8340(70)	4910(50)	8069(11)	47
H2	5550(60)	6090(40)	7666(9)	28
H3A	6940(60)	7060(40)	7078(11)	36
H3B	9430(70)	6840(40)	7228(10)	36
H3C	7900(60)	7950(40)	7445(10)	36
H4A	8700(60)	4130(40)	7314(9)	27
H4B	6460(60)	3660(40)	7547(10)	27
H6	7740(60)	3010(40)	6755(9)	24
H7	5470(50)	2830(30)	6224(9)	22
H9	760(50)	5350(30)	6702(8)	22
H10	2990(50)	5490(40)	7230(9)	25
H11	241.68	4572.88	6101.83	16
H13A	4240(50)	4320(30)	5713(9)	21
H13B	3110(50)	5780(40)	5800(9)	21
H14	1582.43	3607.94	4571.51	18
H15	4203.27	5885.47	4545.04	20
H16	1958.54	7847.98	4575.44	25
H17	-1641.15	4860.68	4494.58	18
H18A	-3420(50)	5080(40)	5088(9)	23

Table 7 Hydrogen Atom Coordinates (Å×10^4) and Isotropic Displacement Parameters (Å^2×10^3) for b $C_{21}H_{29}BO_7$.

Atom	*x*	*y*	*z*	U(eq)
H18B	−2240(50)	3530(40)	5017(9)	23
H19A	4480(70)	7020(50)	3581(12)	51
H19B	4350(70)	7800(50)	3984(12)	51
H19C	2740(70)	8290(50)	3635(12)	51
H21A	−940(60)	5260(40)	3682(10)	40
H21B	1230(60)	5440(40)	3397(10)	40
H21C	−400(70)	6720(40)	3460(10)	40

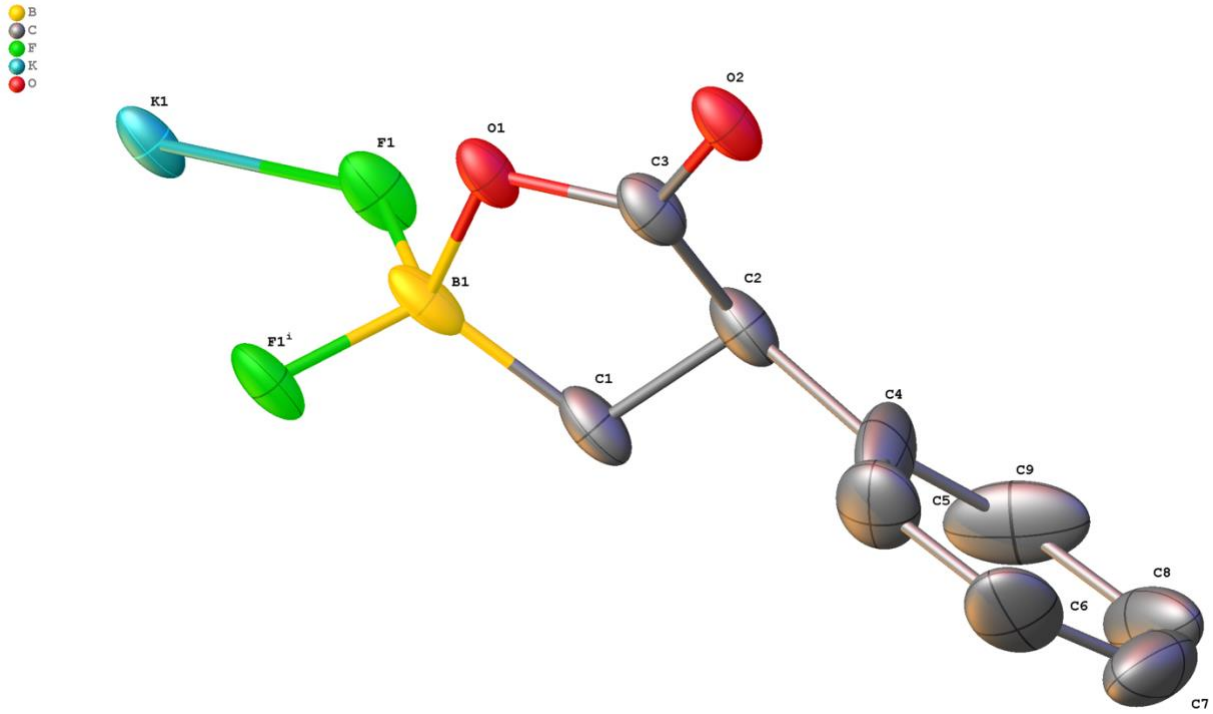

Figure A191. The asymmetric unit of **$C_9H_8BF_2KO_2$**. All non-hydrogen atoms are drawn as 50% thermal probability ellipsoids.

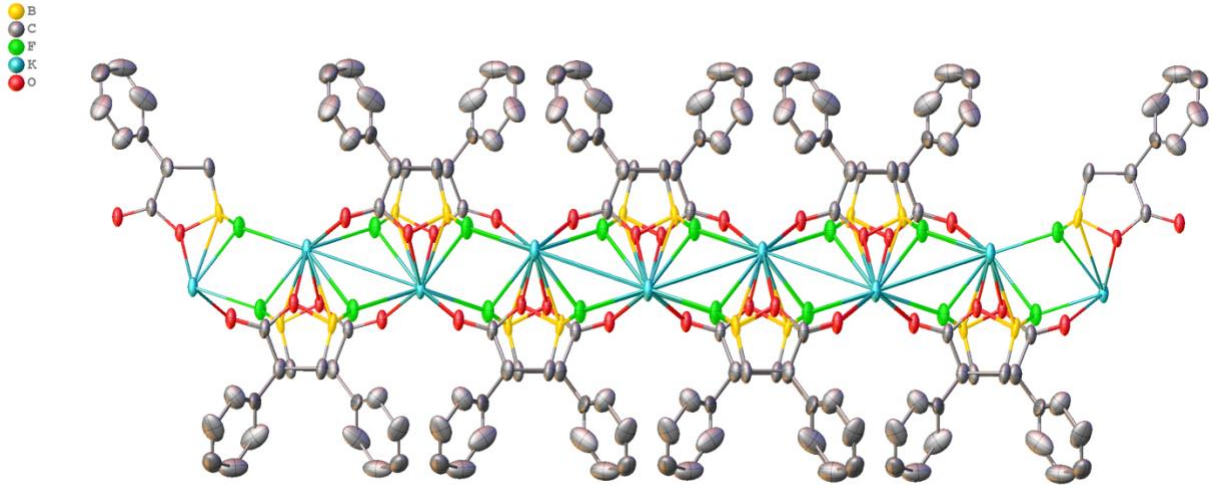

Figure A192. The polymeric structure of **$C_9H_8BF_2KO_2$**. All non-hydrogen atoms are drawn as 50% thermal probability ellipsoids. All hydrogen-atoms are omitted for clarity.

Description of the X-ray structural analysis of $C_9H_8BF_2KO_2$

A colorless plate-shaped crystal measuring 0.487 mm x 0.237 mm x 0.046 mm was selected under polybutene oil using a MiTeGen Micromount and mounted at 100(1) K to a D8-Venture diffractometer equipped with a Mo sealed tube X-ray source, a Triumph monochromator, and a Photon 2 CMOS area detector. The unit cell was determined from reflections harvested with a signal to noise ratio (I/σ) of at least 10 from a series of 2 ω scans of 6° with 0.5° frames using APEX3.[1] The data were collected to a resolution of 0.75 Å using 6 ω scans.

The data were integrated using SAINT and corrected for absorption using SADABS.[2] The systematic absences and E-statistics of the data were consistent with the space group *Pbcm*. The structure was solved using the intrinsic phasing routine of SHELXT.[3] The non-hydrogen atoms were located from a Fourier difference map of the electron density and anisotropically refined using the least-squares algorithm of SHELXL.[4] The hydrogen atoms were then placed in calculated positions and refined with riding thermal parameters.

The asymmetric unit consists of one half of the monomeric unit $C_9H_8BF_2KO_2$ (Figure 1), which resides on a crystallographic mirror plane. The compound is a 2-D polymer as shown in Figure 2. The phenyl ring was disordered over two symmetry independent positions (total occupancy: 68(2)%, 32(2)%). Geometry and thermal parameter restraints were used to ensure a chemically reasonable and computationally stable refinement. The minor component was refined isotropically.

The final structure consisted of 136 parameters refined against 1364 independent reflections, giving refinement residuals of R_1 = 0.0633 (based off F^2 for $I > 2\sigma$) and wR_2 = 0.1273 (based of F^2 for all reflections). The final difference Fourier map was featureless.

1. Bruker-AXS (2016). APEX 3 version 2016.9-0. Madison, Wisconsin, USA

2. (a) Bruker-AXS (2015). *SAINT V8.37A.* Madison, Wisconsin, USA. (b) Bruker-AXS (2014). *SADABS*, Madison, Wisconsin, USA.

3. Sheldrick, G. M., *Acta Crystallogr. A* **2015**, A71, 3-8.

4. (a) Sheldrick, G. M., *Acta Crystallogr. C* **2015**, C71, 3-8.; (b) Dolomanov, O. V.; Bourhis, L. J.; Gildea, R. J.; Howard, J. A. K.; Puschmann, H., *J. Appl. Crystallogr.* **2009**, *42*, 339-341.

Table 1 Crystal data and structure refinement for $C_9H_8BF_2KO_2$.

Identification code	bp87-a_a
Empirical formula	$C_9H_8BF_2KO_2$
Formula weight	236.06
Temperature/K	100.0
Crystal system	orthorhombic
Space group	Pbcm
a/Å	15.0608(6)
b/Å	7.8779(3)
c/Å	8.6470(3)
α/°	90
β/°	90
γ/°	90
Volume/Å^3	1025.94(7)
Z	4
ρ_{calc}g/cm^3	1.528
μ/mm^{-1}	0.520
F(000)	480.0
Crystal size/mm^3	0.487 × 0.237 × 0.046
Radiation	MoKα (λ = 0.71073)
2Θ range for data collection/°	5.836 to 56.638
Index ranges	-20 ≤ h ≤ 20, -10 ≤ k ≤ 10, -11 ≤ l ≤ 11
Reflections collected	21629
Independent reflections	1364 [R_{int} = 0.0864, R_{sigma} = 0.0313]
Data/restraints/parameters	1364/12/136
Goodness-of-fit on F^2	1.214
Final R indexes [I>=2σ (I)]	R_1 = 0.0633, wR_2 = 0.1230
Final R indexes [all data]	R_1 = 0.0771, wR_2 = 0.1273
Largest diff. peak/hole / e Å^{-3}	0.36/-0.59

Table 2 Fractional Atomic Coordinates (×10^4) and Equivalent Isotropic Displacement Parameters (Å^2×10^3) for $C_9H_8BF_2KO_2$. U_{eq} is defined as 1/3 of of the trace of the orthogonalised U_{IJ} tensor.

Atom	*x*	*y*	*z*	U(eq)
K1	9561.3(7)	7500	5000	24.9(2)
F1	9050.1(15)	4526(2)	6178(2)	30.7(5)
O1	9188(2)	1929(4)	7500	23.7(7)
O2	8834(2)	-817(4)	7500	27.5(8)
C1	7695(4)	3191(7)	7550(70)	32(2)
C3	8609(4)	670(6)	7500	27.4(10)
B1	8729(4)	3645(6)	7500	26.2(12)
C2	7691(5)	1341(8)	6996(8)	32.2(16)
C4	6935(11)	270(30)	7780(130)	54(15)
C5	7034(11)	-630(20)	9163(17)	46(4)
C6	6327(11)	-1567(18)	9711(18)	58(5)

C7	5532(10)	−1607(18)	8980(30)	58(6)
C8	5414(11)	−670(50)	7670(50)	61(12)
C9	6122(12)	270(30)	7170(20)	67(8)
C4A	6920(30)	200(100)	7500(170)	60(30)
C5A	6890(30)	−970(70)	8710(70)	86(19)
C6A	6130(30)	−1890(60)	8950(80)	102(19)
C7A	5360(30)	−1550(60)	8180(80)	90(30)
C8A	5380(20)	−460(60)	6960(70)	60(20)
C9A	6160(20)	370(40)	6710(50)	38(9)

Table 3 Anisotropic Displacement Parameters ($Å^2×10^3$) for $C_9H_8BF_2KO_2$. The Anisotropic displacement factor exponent takes the form: $-2\pi^2[h^2a^{*2}U_{11}+2hka^*b^*U_{12}+\ldots]$.

Atom	U_{11}	U_{22}	U_{33}	U_{23}	U_{13}	U_{12}
K1	50.5(6)	13.1(4)	11.0(4)	0.6(4)	0	0
F1	58.3(13)	18.3(9)	15.3(8)	4.4(7)	0.0(9)	−0.3(9)
O1	41.1(19)	12.7(13)	17.3(14)	0	0	−1.4(13)
O2	49(2)	14.5(14)	18.6(15)	0	0	0.2(14)
C1	53(3)	17(2)	25(6)	−5(11)	−5(12)	5(2)
C3	44(3)	15(2)	23(2)	0	0	1(2)
B1	53(4)	10(2)	15(2)	0	0	8(2)
C2	49(4)	22(3)	25(3)	−7(2)	−5(3)	1(3)
C4	35(11)	19(7)	110(50)	−18(13)	−3(10)	−5(4)
C5	61(9)	56(9)	21(6)	−1(6)	4(6)	−14(7)
C6	81(11)	60(9)	31(9)	−1(6)	30(7)	−23(8)
C7	44(9)	46(8)	85(15)	−6(8)	29(9)	−8(7)
C8	39(8)	110(20)	30(20)	−30(30)	−4(9)	5(8)
C9	76(12)	99(13)	26(15)	26(9)	13(7)	35(9)

Table 4 Bond Lengths for $C_9H_8BF_2KO_2$.

Atom	Atom	Length/Å	Atom	Atom	Length/Å
K1	$K1^1$	4.1547(7)	C1	B1	1.599(9)
K1	$K1^2$	4.1547(7)	C1	C2	1.54(2)
K1	F1	2.6679(18)	C3	C2	1.543(8)
K1	$F1^3$	2.6678(18)	C2	C4	1.57(4)
K1	$F1^2$	2.821(2)	C4	C5	1.40(10)
K1	$F1^4$	2.821(2)	C4	C9	1.33(5)
K1	$O1^5$	2.902(2)	C5	C6	1.381(16)
K1	$O1^2$	2.902(2)	C6	C7	1.35(2)
K1	$O2^6$	2.762(2)	C7	C8	1.36(3)
K1	$O2^7$	2.762(2)	C8	C9	1.365(18)
K1	$B1^5$	3.481(5)	C4A	C5A	1.40(10)
K1	$B1^2$	3.481(5)	C4A	C9A	1.33(5)

F1	B1	1.423(4)	C5A	C6A	1.383(18)
O1	C3	1.321(6)	C6A	C7A	1.36(2)
O1	B1	1.518(6)	C7A	C8A	1.36(3)
O2	C3	1.219(5)	C8A	C9A	1.362(19)

[1]2-X,2-Y,1-Z; [2]2-X,1-Y,1-Z; [3]+X,3/2-Y,1-Z; [4]2-X,1/2+Y,+Z; [5]2-X,1/2+Y,3/2-Z; [6]+X,1+Y,+Z; [7]+X,1/2-Y,-1/2+Z

Table 5 Bond Angles for $C_9H_8BF_2KO_2$.

Atom	Atom	Atom	Angle/°	Atom	Atom	Atom	Angle/°
K1[1]	K1	K1[2]	142.91(6)	O2[6]	K1	B1[5]	71.51(10)
F1	K1	K1[1]	157.56(4)	O2[7]	K1	B1[2]	71.51(10)
F1[3]	K1	K1[2]	157.56(4)	O2[6]	K1	B1[2]	154.64(12)
F1	K1	K1[2]	42.21(4)	O2[7]	K1	B1[5]	154.64(12)
F1[4]	K1	K1[2]	107.50(6)	B1[2]	K1	K1[1]	90.59(9)
F1[2]	K1	K1[1]	107.50(6)	B1[5]	K1	K1[1]	61.26(8)
F1[2]	K1	K1[2]	39.44(4)	B1[5]	K1	K1[2]	90.59(9)
F1[3]	K1	K1[1]	42.21(4)	B1[2]	K1	K1[2]	61.26(8)
F1[4]	K1	K1[1]	39.44(4)	B1[5]	K1	B1[2]	84.58(15)
F1[3]	K1	F1[2]	124.96(6)	K1	F1	K1[2]	98.35(6)
F1	K1	F1[4]	124.96(6)	B1	F1	K1[2]	105.4(2)
F1	K1	F1[2]	81.65(7)	B1	F1	K1	146.5(2)
F1[4]	K1	F1[2]	84.32(9)	K1[8]	O1	K1[2]	96.30(11)
F1[3]	K1	F1[4]	81.65(7)	C3	O1	K1[2]	123.02(13)
F1[3]	K1	F1	146.45(10)	C3	O1	K1[8]	123.02(13)
F1[4]	K1	O1[2]	72.55(7)	C3	O1	B1	111.6(4)
F1[3]	K1	O1[2]	76.52(7)	B1	O1	K1[8]	99.07(18)
F1	K1	O1[2]	127.42(7)	B1	O1	K1[2]	99.07(18)
F1[2]	K1	O1[2]	48.53(7)	K1[9]	O2	K1[10]	102.99(11)
F1[3]	K1	O1[5]	127.42(7)	C3	O2	K1[10]	124.84(11)
F1	K1	O1[5]	76.52(7)	C3	O2	K1[9]	124.84(11)
F1[2]	K1	O1[5]	72.55(7)	C2	C1	B1	101.9(11)
F1[4]	K1	O1[5]	48.53(7)	O1	C3	C2	109.5(4)
F1	K1	O2[6]	90.48(7)	O2	C3	O1	122.5(5)
F1[3]	K1	O2[7]	90.48(7)	O2	C3	C2	125.3(5)
F1	K1	O2[7]	76.28(7)	K1[8]	B1	K1[2]	76.78(13)
F1[3]	K1	O2[6]	76.28(7)	F1[11]	B1	K1[2]	112.0(3)
F1[4]	K1	B1[5]	23.20(8)	F1[11]	B1	K1[8]	51.38(19)
F1[3]	K1	B1[2]	101.77(8)	F1	B1	K1[8]	112.0(3)
F1	K1	B1[5]	101.77(8)	F1	B1	K1[2]	51.38(19)
F1	K1	B1[2]	102.89(9)	F1	B1	F1[11]	107.0(4)
F1[2]	K1	B1[5]	79.77(10)	F1	B1	O1	106.2(3)
F1[2]	K1	B1[2]	23.20(8)	F1[11]	B1	O1	106.2(3)
F1[4]	K1	B1[2]	79.77(10)	F1	B1	C1	117.7(19)

F1[3]	K1	B1[5]	102.89(9)	F1[11]	B1	C1	114.6(19)
O1[5]	K1	K1[2]	69.31(6)	O1	B1	K1[8]	55.41(16)
O1[2]	K1	K1[1]	69.31(6)	O1	B1	K1[2]	55.41(16)
O1[5]	K1	K1[1]	86.59(6)	O1	B1	C1	104.2(4)
O1[2]	K1	K1[2]	86.59(6)	C1	B1	K1[8]	130.1(18)
O1[5]	K1	O1[2]	99.08(11)	C1	B1	K1[2]	132.9(18)
O1[2]	K1	B1[2]	25.51(9)	C1	C2	C3	103.5(9)
O1[2]	K1	B1[5]	86.70(9)	C1	C2	C4	112(3)
O1[5]	K1	B1[2]	86.70(9)	C3	C2	C4	110(2)
O1[5]	K1	B1[5]	25.51(9)	C5	C4	C2	124(4)
O2[7]	K1	K1[2]	70.79(6)	C9	C4	C2	120(6)
O2[7]	K1	K1[1]	125.53(5)	C9	C4	C5	116(3)
O2[6]	K1	K1[2]	125.53(5)	C6	C5	C4	118.9(15)
O2[6]	K1	K1[1]	70.79(6)	C7	C6	C5	122.3(14)
O2[6]	K1	F1[2]	147.99(8)	C6	C7	C8	119.3(13)
O2[7]	K1	F1[2]	74.92(8)	C7	C8	C9	117(2)
O2[6]	K1	F1[4]	74.92(8)	C4	C9	C8	126(4)
O2[7]	K1	F1[4]	147.99(8)	C9A	C4A	C5A	116(3)
O2[6]	K1	O1[5]	75.44(8)	C6A	C5A	C4A	118.7(19)
O2[6]	K1	O1[2]	139.98(9)	C7A	C6A	C5A	122.1(18)
O2[7]	K1	O1[5]	139.98(9)	C6A	C7A	C8A	119.2(18)
O2[7]	K1	O1[2]	75.44(8)	C7A	C8A	C9A	117(2)
O2[7]	K1	O2[6]	133.29(15)	C4A	C9A	C8A	127(4)

[1]2-X,2-Y,1-Z; [2]2-X,1-Y,1-Z; [3]+X,3/2-Y,1-Z; [4]2-X,1/2+Y,+Z; [5]2-X,1/2+Y,3/2-Z; [6]+X,1+Y,+Z; [7]+X,1/2-Y,-1/2+Z; [8]2-X,1-Y,1/2+Z; [9]+X,-1+Y,+Z; [10]+X,-1+Y,3/2-Z; [11]+X,+Y,3/2-Z

Table 6 Hydrogen Atom Coordinates (Å×10^4) and Isotropic Displacement Parameters (Å^2×10^3) for $C_9H_8BF_2KO_2$.

Atom	*x*	*y*	*z*	U(eq)
H1A	7455.42	3289.25	8617.61	38
H1B	7347.5	3931.27	6854.46	38
H2	7633.33	1296.1	5845.07	39
H5	7578.44	-591.49	9716.61	55
H6	6400.63	-2207.35	10632.77	69
H7	5061.33	-2283.79	9373.37	70
H8	4864.27	-662.82	7134.89	73
H9	6024.64	983.78	6307.62	81
H5A	7396.58	-1122.02	9360.18	103
H6A	6132.4	-2790.92	9683.25	123
H7A	4820.58	-2067.09	8488.26	113
H8A	4878.54	-285.96	6320.45	71
H9A	6167.64	1166.4	5879.32	45

Table 7 Atomic Occupancy for $C_9H_8BF_2KO_2$.

Atom	*Occupancy*	Atom	*Occupancy*	Atom	*Occupancy*

C1	0.5	H1A	0.5	H1B	0.5
C2	0.5	H2	0.5	C4	0.34(2)
C5	0.34(2)	H5	0.34(2)	C6	0.34(2)
H6	0.34(2)	C7	0.34(2)	H7	0.34(2)
C8	0.34(2)	H8	0.34(2)	C9	0.34(2)
H9	0.34(2)	C4A	0.16(2)	C5A	0.16(2)
H5A	0.16(2)	C6A	0.16(2)	H6A	0.16(2)
C7A	0.16(2)	H7A	0.16(2)	C8A	0.16(2)
H8A	0.16(2)	C9A	0.16(2)	H9A	0.16(2)

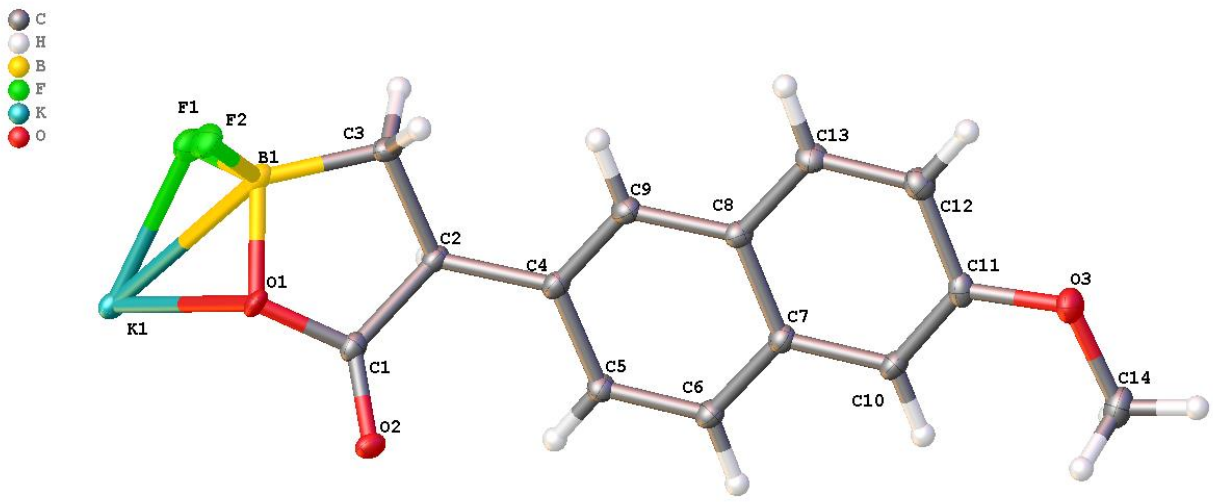

Figure A193. The asymmetric unit of **$C_{14}H_{12}BF_2KO$** including all disordered components. All non-hydrogen atoms are drawn as 50% thermal probability ellipsoids.

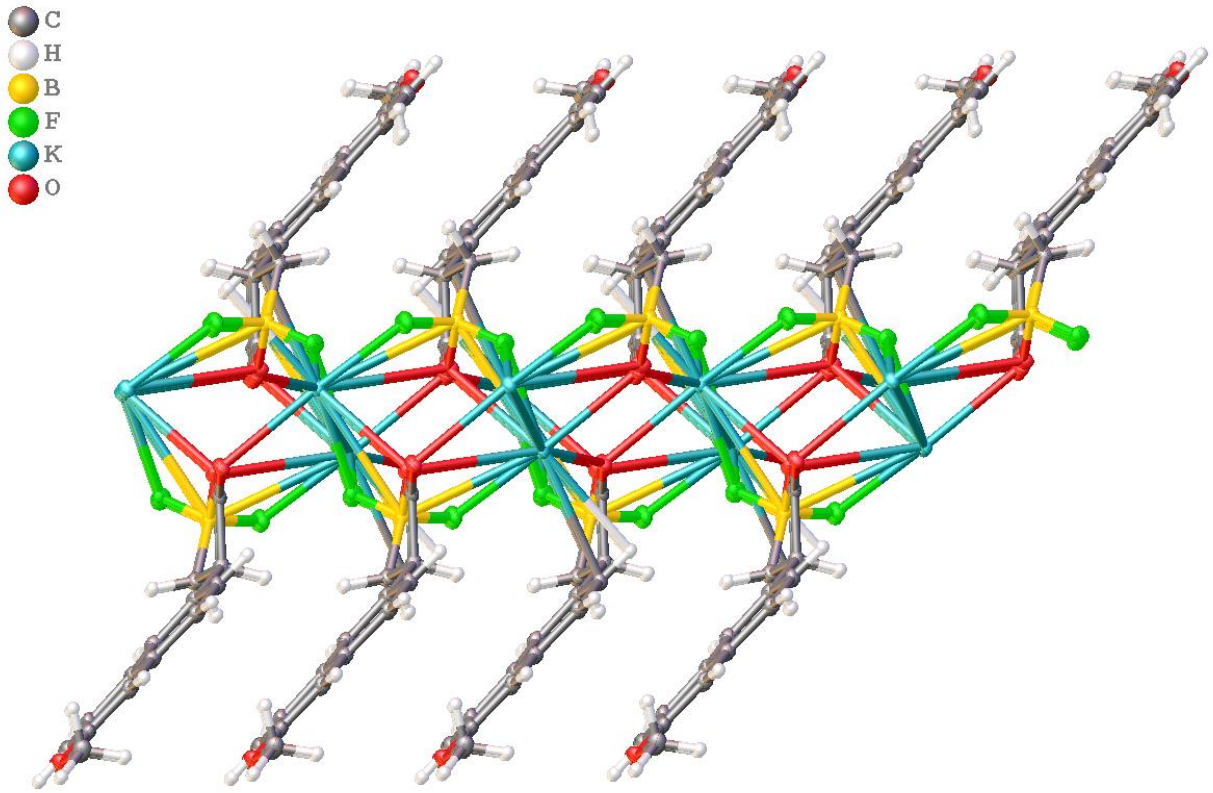

Figure A194. The polymer of **$C_{14}H_{12}BF_2KO_3$**. All non-hydrogen atoms are drawn as 50% thermal probability ellipsoids.

Description of the X-ray structural analysis of $C_{14}H_{12}BF_2KO_3$

A colorless block-shaped crystal measuring approximately 0.3 mm x 0.2 mm x 0.1 mm was selected under polybutene oil using a MiTeGen Micromount and mounted at 100(1) K to a D8-Venture diffractometer equipped with a Mo sealed tube X-ray source, a Triumph monochromator, and a Photon 2 CMOS area detector. The unit cell was determined from reflections harvested with a signal to noise ratio (I/σ) of at least 10 from a series of 2 ω scans of 6° with 0.5° frames using APEX3.[1] The data were collected to a resolution of 0.8 Å using 6 ω 1 φ scans.

The data were integrated using SAINT and corrected for absorption using SADABS.[2] The systematic absences and E-statistics of the data were uniquely consistent with the space group $P2_1/c$. The structure was solved using the intrinsic phasing routine of SHELXT.[3] The non-hydrogen atoms were located from a Fourier difference map of the electron density and anisotropically refined using the least-squares algorithm of SHELXL.[4] The hydrogen atoms were then placed in calculated positions and refined with riding thermal parameters.

The asymmetric unit consists of the monomeric unit shown in Figure 1. The monomers are connected via the K^+ ion into a 2-D polymer (Figure 2).

The final structure consisted of 192 parameters refined against 4009 independent reflections, giving refinement residuals of R_1 = 0.0709 (based off F^2 for $I > 2\sigma$) and wR_2 = 0.1697 (based of F^2 for all reflections). The final difference Fourier map was featureless.

1. Bruker-AXS (2016). APEX 3 version 2016.9-0. Madison, Wisconsin, USA

2. (a) Bruker-AXS (2015). *SAINT V8.37A.* Madison, Wisconsin, USA. (b) Bruker-AXS (2014). *SADABS*, Madison, Wisconsin, USA.

3. Sheldrick, G. M., *Acta Crystallogr. A* **2015**, A71, 3-8.

4. (a) Sheldrick, G. M., *Acta Crystallogr. C* **2015**, C71, 3-8.; (b) Dolomanov, O. V.; Bourhis, L. J.; Gildea, R. J.; Howard, J. A. K.; Puschmann, H., *J. Appl. Crystallogr.* **2009**, *42*, 339-341.

Table 1 Crystal data and structure refinement for $C_{14}H_{12}BF_2KO_3$.

Identification code	bp82
Empirical formula	$C_{14}H_{12}BF_2KO_3$
Formula weight	316.15
Temperature/K	100.00
Crystal system	monoclinic
Space group	$P2_1/c$
a/Å	6.9603(5)
b/Å	5.4664(4)
c/Å	34.611(2)
α/°	90
β/°	94.124(2)
γ/°	90
Volume/Å^3	1313.45(16)
Z	4
ρ_{calc}g/cm^3	1.599
μ/mm^{-1}	0.434
F(000)	648.0
Crystal size/mm^3	0.42 × 0.231 × 0.048
Radiation	MoKα (λ = 0.71073)
2Θ range for data collection/°	5.868 to 61.082
Index ranges	$-9 \le h \le 9$, $-7 \le k \le 7$, $-49 \le l \le 49$
Reflections collected	28145
Independent reflections	4009 [R_{int} = 0.0484, R_{sigma} = 0.0303]
Data/restraints/parameters	4009/0/192
Goodness-of-fit on F^2	1.182
Final R indexes [I>=2σ (I)]	R_1 = 0.0709, wR_2 = 0.1689
Final R indexes [all data]	R_1 = 0.0716, wR_2 = 0.1697
Largest diff. peak/hole / e Å^{-3}	0.67/-0.55

Table 2 Fractional Atomic Coordinates (×10^4) and Equivalent Isotropic Displacement Parameters (Å^2×10^3) for $C_{14}H_{12}BF_2KO_3$. U_{eq} is defined as 1/3 of the trace of the orthogonalised U_{IJ} tensor.

Atom	*x*	*y*	*z*	U(eq)
K1	-2296.6(10)	8478.5(15)	5210.1(2)	14.12(15)
F1	-1354(3)	4621(5)	5632.7(7)	18.8(5)
F2	555(3)	1413(4)	5483.8(6)	18.0(4)
O1	1534(4)	5377(5)	5331.6(7)	15.3(5)
O2	3974(4)	7967(5)	5295.8(7)	15.0(5)
O3	12884(4)	7640(6)	7210.3(8)	19.5(6)
C1	2933(5)	6761(7)	5491.3(10)	13.1(6)
C2	2944(5)	6714(6)	5935.6(10)	12.6(6)
C3	1902(5)	4304(7)	6022.7(10)	14.1(6)
C4	4908(5)	7219(7)	6145.1(10)	13.8(6)
C5	5921(5)	9392(7)	6057.7(10)	13.5(6)

Table 2 Fractional Atomic Coordinates ($\times 10^4$) and Equivalent Isotropic Displacement Parameters ($Å^2 \times 10^3$) for $C_{14}H_{12}BF_2KO_3$. U_{eq} is defined as 1/3 of the trace of the orthogonalised U_{IJ} tensor.

Atom	*x*	*y*	*z*	U(eq)
C6	7676(5)	9947(7)	6244.0(10)	14.1(6)
C7	8532(5)	8384(7)	6535.5(10)	13.3(6)
C8	7501(5)	6257(6)	6634.9(10)	12.3(6)
C9	5695(5)	5728(7)	6434.8(10)	14.6(6)
C10	10357(5)	8912(6)	6727.7(10)	14.0(6)
C11	11128(5)	7362(7)	7009.3(10)	14.8(6)
C12	10087(5)	5265(7)	7117.2(10)	16.7(7)
C13	8323(5)	4736(7)	6934.8(10)	15.3(6)
C14	13956(5)	9786(8)	7130.9(12)	21.0(8)
B1	570(5)	3868(7)	5630.3(11)	12.9(7)

Table 3 Anisotropic Displacement Parameters ($Å^2 \times 10^3$) for $C_{14}H_{12}BF_2KO_3$. The Anisotropic displacement factor exponent takes the form: $-2\pi^2[h^2a^{*2}U_{11}+2hka^*b^*U_{12}+\ldots]$.

Atom	U_{11}	U_{22}	U_{33}	U_{23}	U_{13}	U_{12}
K1	9.5(3)	15.4(3)	17.4(3)	2.4(3)	0.9(2)	-1.5(3)
F1	11.3(9)	21.2(11)	23.7(11)	3.7(9)	1.1(8)	0.7(9)
F2	18.7(10)	13.0(9)	21.9(10)	-1.8(9)	-0.9(8)	-3.9(9)
O1	10.2(10)	19.9(13)	15.7(11)	1.0(10)	-1.1(8)	-7.6(10)
O2	9.9(10)	17.5(13)	17.6(11)	5.0(9)	1.3(9)	-1.9(9)
O3	14.8(12)	23.7(14)	19.3(12)	2.3(11)	-4.0(10)	-1.7(11)
C1	9.3(13)	13.0(15)	16.8(14)	-0.2(12)	-0.1(11)	-0.1(12)
C2	9.9(13)	11.8(14)	16.0(14)	1.1(12)	0.5(11)	-2.0(12)
C3	12.8(14)	13.7(15)	15.9(15)	3.3(12)	2.2(11)	-1.5(12)
C4	11.5(14)	15.3(15)	14.7(14)	0.0(12)	1.4(11)	-2.2(12)
C5	13.1(14)	12.1(14)	15.1(14)	1.6(12)	-0.7(11)	-0.1(12)
C6	13.8(15)	12.6(14)	15.8(14)	-0.3(12)	1.0(12)	-2.0(12)
C7	12.8(14)	12.6(14)	14.4(14)	-0.8(12)	0.1(11)	-1.7(12)
C8	11.3(14)	11.5(14)	14.3(14)	0.8(12)	1.4(11)	0.6(12)
C9	15.6(15)	13.6(15)	14.6(14)	0.5(12)	0.9(12)	-2.9(12)
C10	11.3(14)	13.5(15)	17.3(15)	-0.8(12)	1.3(11)	-2.4(12)
C11	12.4(15)	17.9(16)	13.9(14)	-3.3(13)	-0.9(11)	2.4(12)
C12	16.5(16)	17.2(16)	16.4(15)	1.2(13)	0.3(12)	2.0(13)
C13	17.2(16)	11.2(15)	17.5(15)	1.6(12)	0.4(12)	0.4(13)
C14	15.0(16)	22.5(19)	24.9(18)	-4.3(15)	-2.8(14)	-1.4(14)
B1	9.7(15)	12.8(17)	16.3(16)	-2.2(13)	2.4(12)	-1.6(12)

Table 4 Bond Lengths for b $C_{14}H_{12}BF_2KO_3$.

Atom	Atom	Length/Å	Atom	Atom	Length/Å
K1	K1[1]	3.9714(15)	O3	C11	1.371(4)
K1	K1[2]	4.2728(15)	O3	C14	1.428(5)
K1	F1	2.623(2)	C1	C2	1.538(5)
K1	F2[3]	2.672(2)	C2	C3	1.544(5)
K1	F2[4]	2.767(2)	C2	C4	1.525(5)
K1	O1	3.162(3)	C3	B1	1.606(5)
K1	O1[4]	2.895(3)	C4	C5	1.425(5)
K1	O2[5]	2.648(3)	C4	C9	1.375(5)
K1	O2[1]	2.813(3)	C5	C6	1.373(5)
K1	C5[5]	3.304(4)	C6	C7	1.420(5)
K1	B1	3.469(4)	C7	C8	1.421(5)
K1	B1[4]	3.472(4)	C7	C10	1.421(5)
F1	B1	1.402(4)	C8	C9	1.421(5)
F2	B1	1.435(4)	C8	C13	1.418(5)
O1	C1	1.322(4)	C10	C11	1.371(5)
O1	B1	1.516(5)	C11	C12	1.420(5)
O2	C1	1.220(4)	C12	C13	1.370(5)

[1]-X,2-Y,1-Z; [2]-1-X,2-Y,1-Z; [3]+X,1+Y,+Z; [4]-X,1-Y,1-Z; [5]-1+X,+Y,+Z

Table 5 Bond Angles for $C_{14}H_{12}BF_2KO_3$.

Atom	Atom	Atom	Angle/°	Atom	Atom	Atom	Angle/°
K1[1]	K1	K1[2]	115.14(4)	B1	K1	K1[2]	153.08(7)
F1	K1	K1[1]	111.42(6)	B1[3]	K1	K1[1]	60.77(7)
F1	K1	K1[2]	132.98(6)	B1	K1	K1[1]	90.22(7)
F1	K1	F2[3]	113.18(8)	B1[3]	K1	K1[2]	102.01(7)
F1	K1	F2[4]	97.77(7)	B1	K1	B1[3]	81.93(10)
F1	K1	O1[3]	74.08(8)	B1	F1	K1	115.7(2)
F1	K1	O1	47.16(7)	K1[6]	F2	K1[3]	93.78(7)
F1	K1	O2[5]	93.47(8)	B1	F2	K1[3]	107.11(19)
F1	K1	O2[1]	168.14(8)	B1	F2	K1[6]	132.3(2)
F1	K1	C5[5]	73.82(8)	K1[3]	O1	K1	119.75(8)
F1	K1	B1[3]	94.73(9)	C1	O1	K1[3]	121.6(2)
F1	K1	B1	21.36(8)	C1	O1	K1	109.7(2)
F2[4]	K1	K1[1]	44.05(5)	C1	O1	B1	112.0(3)
F2[4]	K1	K1[2]	120.04(6)	B1	O1	K1[3]	99.0(2)
F2[3]	K1	K1[2]	97.25(5)	B1	O1	K1	88.40(18)
F2[3]	K1	K1[1]	42.17(5)	K1[7]	O2	K1[1]	102.92(8)
F2[4]	K1	F2[3]	86.22(7)	C1	O2	K1[7]	138.2(2)
F2[3]	K1	O1	73.09(7)	C1	O2	K1[1]	118.8(2)
F2[4]	K1	O1[3]	120.03(7)	C11	O3	C14	116.9(3)
F2[3]	K1	O1[3]	48.82(7)	O1	C1	C2	111.1(3)
F2[4]	K1	O1	71.15(7)	O2	C1	O1	121.8(3)
F2[4]	K1	O2[1]	94.04(8)	O2	C1	C2	127.1(3)

Table 5 Bond Angles for $C_{14}H_{12}BF_2KO_3$.

Atom	Atom	Atom	Angle/°	Atom	Atom	Atom	Angle/°
F2[3]	K1	O2[1]	68.47(7)	C1	C2	C3	103.9(3)
F2[4]	K1	C5[5]	84.92(8)	C4	C2	C1	114.4(3)
F2[3]	K1	C5[5]	169.43(9)	C4	C2	C3	118.6(3)
F2[3]	K1	B1[3]	23.26(8)	C2	C3	B1	102.2(3)
F2[4]	K1	B1	84.10(8)	C5	C4	C2	119.3(3)
F2[3]	K1	B1	96.02(8)	C9	C4	C2	122.4(3)
F2[4]	K1	B1[3]	103.05(8)	C9	C4	C5	118.1(3)
O1[3]	K1	K1[1]	82.99(6)	C4	C5	K1[7]	106.6(2)
O1[3]	K1	K1[2]	105.12(6)	C6	C5	K1[7]	94.1(2)
O1	K1	K1[1]	65.16(5)	C6	C5	C4	121.4(3)
O1	K1	K1[2]	165.36(6)	C5	C6	C7	120.9(3)
O1[3]	K1	O1	60.25(8)	C6	C7	C8	118.1(3)
O1[3]	K1	C5[5]	141.54(9)	C6	C7	C10	121.7(3)
O1	K1	C5[5]	109.26(8)	C8	C7	C10	120.2(3)
O1[3]	K1	B1	67.41(8)	C7	C8	C9	119.5(3)
O1[3]	K1	B1[3]	25.56(8)	C13	C8	C7	118.2(3)
O1	K1	B1[3]	64.78(8)	C13	C8	C9	122.3(3)
O1	K1	B1	25.91(8)	C4	C9	C8	121.8(3)
O2[5]	K1	K1[1]	155.03(7)	C11	C10	C7	119.9(3)
O2[1]	K1	K1[2]	37.17(5)	O3	C11	C10	125.5(4)
O2[5]	K1	K1[2]	39.91(6)	O3	C11	C12	114.2(3)
O2[1]	K1	K1[1]	77.98(6)	C10	C11	C12	120.3(3)
O2[5]	K1	F2[4]	137.12(8)	C13	C12	C11	120.4(3)
O2[5]	K1	F2[3]	126.40(8)	C12	C13	C8	121.0(3)
O2[1]	K1	O1	139.60(8)	K1	B1	K1[3]	98.08(10)
O2[5]	K1	O1	138.79(8)	F1	B1	K1	42.96(16)
O2[1]	K1	O1[3]	100.78(8)	F1	B1	K1[3]	120.1(2)
O2[5]	K1	O1[3]	102.85(8)	F1	B1	F2	107.1(3)
O2[5]	K1	O2[1]	77.08(8)	F1	B1	O1	108.3(3)
O2[1]	K1	C5[5]	106.42(8)	F1	B1	C3	116.4(3)
O2[5]	K1	C5[5]	58.86(8)	F2	B1	K1	122.8(2)
O2[5]	K1	B1[3]	117.11(9)	F2	B1	K1[3]	49.63(15)
O2[1]	K1	B1[3]	83.50(9)	F2	B1	O1	105.1(3)
O2[5]	K1	B1	114.53(9)	F2	B1	C3	115.3(3)
O2[1]	K1	B1	164.48(9)	O1	B1	K1[3]	55.44(16)
C5[5]	K1	K1[2]	82.27(6)	O1	B1	K1	65.69(17)
C5[5]	K1	K1[1]	128.71(7)	O1	B1	C3	103.8(3)
C5[5]	K1	B1[3]	167.00(10)	C3	B1	K1[3]	123.4(2)
C5[5]	K1	B1	88.80(9)	C3	B1	K1	121.8(2)

[1]-X,2-Y,1-Z; [2]-1-X,2-Y,1-Z; [3]-X,1-Y,1-Z; [4]+X,1+Y,+Z; [5]-1+X,+Y,+Z; [6]+X,-1+Y,+Z; [7]1+X,+Y,+Z

Table 6 Torsion Angles for $C_{14}H_{12}BF_2KO_3$.

A	B	C	D	Angle/°	A	B	C	D	Angle/°
K1	F1	B1	K1[1]	-67.4(3)	C1	O1	B1	C3	-8.3(4)
K1	F1	B1	F2	-120.1(2)	C1	C2	C3	B1	-25.6(3)
K1	F1	B1	O1	-7.3(3)	C1	C2	C4	C5	54.5(4)
K1	F1	B1	C3	109.2(3)	C1	C2	C4	C9	-129.7(4)
K1[1]	F2	B1	K1	70.8(2)	C2	C3	B1	K1[1]	78.7(3)
K1[2]	F2	B1	K1[1]	-111.9(2)	C2	C3	B1	K1	-48.6(3)
K1[2]	F2	B1	K1	-41.1(3)	C2	C3	B1	F1	-97.8(3)
K1[2]	F2	B1	F1	3.4(4)	C2	C3	B1	F2	135.5(3)
K1[1]	F2	B1	F1	115.3(2)	C2	C3	B1	O1	21.1(3)
K1[2]	F2	B1	O1	-111.7(3)	C2	C4	C5	K1[4]	-75.6(3)
K1[1]	F2	B1	O1	0.3(3)	C2	C4	C5	C6	178.8(3)
K1[2]	F2	B1	C3	134.7(2)	C2	C4	C9	C8	-178.2(3)
K1[1]	F2	B1	C3	-113.4(3)	C3	C2	C4	C5	177.7(3)
K1	O1	C1	O2	-89.2(3)	C3	C2	C4	C9	-6.5(5)
K1[1]	O1	C1	O2	57.8(4)	C4	C2	C3	B1	-153.8(3)
K1[1]	O1	C1	C2	-125.3(2)	C4	C5	C6	C7	-0.9(5)
K1	O1	C1	C2	87.7(3)	C5	C4	C9	C8	-2.4(5)
K1[1]	O1	B1	K1	−119.88(10)	C5	C6	C7	C8	-1.4(5)
K1	O1	B1	K1[1]	119.88(10)	C5	C6	C7	C10	179.2(3)
K1	O1	B1	F1	5.4(2)	C6	C7	C8	C9	1.7(5)
K1[1]	O1	B1	F1	-114.4(2)	C6	C7	C8	C13	-177.9(3)
K1	O1	B1	F2	119.6(2)	C6	C7	C10	C11	179.6(3)
K1[1]	O1	B1	F2	-0.3(3)	C7	C8	C9	C4	0.1(5)
K1	O1	B1	C3	-118.9(2)	C7	C8	C13	C12	-1.7(5)
K1[1]	O1	B1	C3	121.2(2)	C7	C10	C11	O3	178.7(3)
K1[3]	O2	C1	O1	59.5(4)	C7	C10	C11	C12	-1.7(5)
K1[4]	O2	C1	O1	-124.3(3)	C8	C7	C10	C11	0.1(5)
K1[4]	O2	C1	C2	59.4(5)	C9	C4	C5	K1[4]	108.5(3)
K1[3]	O2	C1	C2	-116.9(3)	C9	C4	C5	C6	2.8(5)
K1[4]	C5	C6	C7	-113.2(3)	C9	C8	C13	C12	178.6(3)
O1	C1	C2	C3	22.7(4)	C10	C7	C8	C9	-178.8(3)
O1	C1	C2	C4	153.6(3)	C10	C7	C8	C13	1.6(5)
O2	C1	C2	C3	-160.6(3)	C10	C11	C12	C13	1.6(5)
O2	C1	C2	C4	-29.8(5)	C11	C12	C13	C8	0.2(5)
O3	C11	C12	C13	-178.8(3)	C13	C8	C9	C4	179.8(3)
C1	O1	B1	K1	110.6(3)	C14	O3	C11	C10	3.0(5)
C1	O1	B1	K1[1]	-129.5(3)	C14	O3	C11	C12	-176.6(3)
C1	O1	B1	F1	116.1(3)	B1	O1	C1	O2	174.4(3)
C1	O1	B1	F2	-129.7(3)	B1	O1	C1	C2	-8.8(4)

[1]-X,1-Y,1-Z; [2]+X,-1+Y,+Z; [3]-X,2-Y,1-Z; [4]1+X,+Y,+Z

Table 7 Hydrogen Atom Coordinates (Å×10^4) and Isotropic Displacement Parameters (Å^2×10^3) for $C_{14}H_{12}BF_2KO_3$.

Atom	*x*	*y*	*z*	U(eq)
H2	2076.78	8069.17	6009.03	15
H3A	1115.83	4482.74	6248.26	17
H3B	2828.9	2946.14	6071.8	17
H5	5370.17	10481.06	5866.48	16
H6	8326.06	11397.44	6176.9	17
H9	5012.38	4305.3	6503.02	17
H10	11042.9	10336.17	6661.22	17
H12	10616.11	4222.12	7317.09	20
H13	7640.4	3330.73	7010.43	18
H14A	14281.15	9762.04	6860.09	32
H14B	15141.85	9829.67	7301.35	32
H14C	13179.32	11239.13	7176.61	32

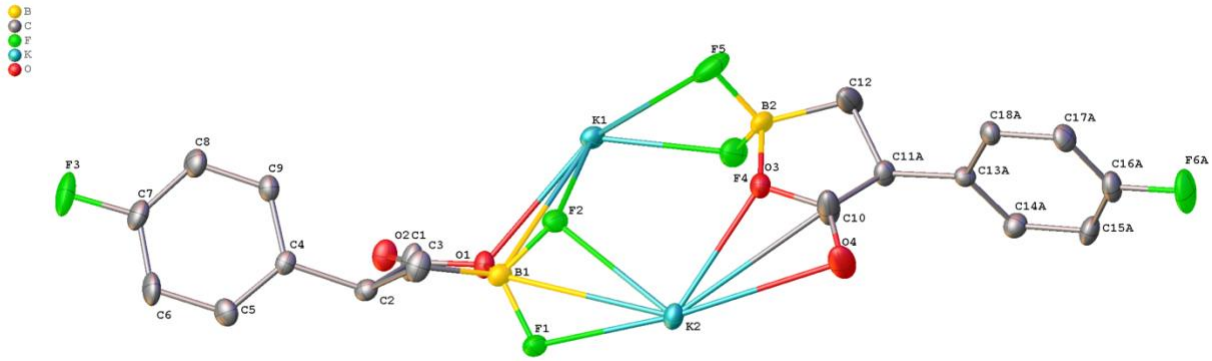

Figure A196. The polymer of **$C_{14}H_{12}BF_2KO_3$.** All non-hydrogen atoms are drawn as 50% thermal probability ellipsoids.

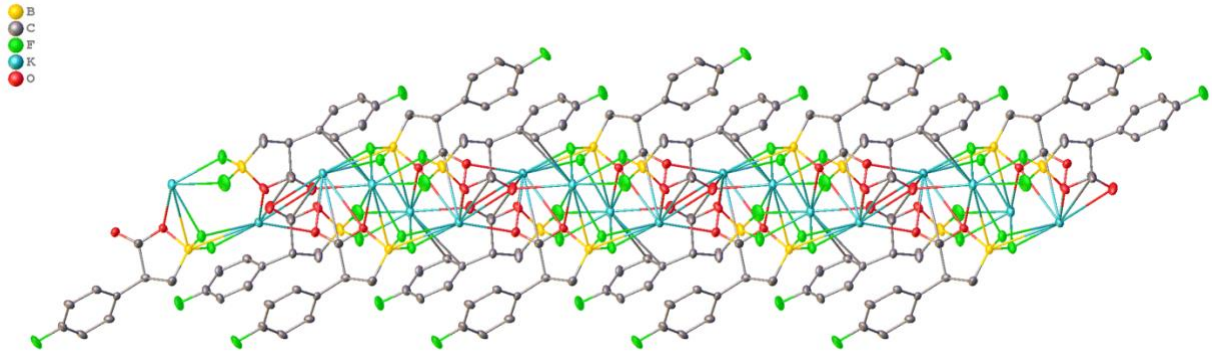

Figure A197. The polymer of **$C_9H_7BO_2F_3K$**. All non-hydrogen atoms are drawn as 50% thermal probability ellipsoids.

Description of the X-ray structural analysis of $C_9H_7BO_2F_3K$

A colorless plate-shaped crystal measuring 0.25 mm x 0.24 mm x 0.044 mm was selected under polybutene oil using a MiTeGen Micromount and mounted at 100(1) K to a D8-Venture diffractometer equipped with a Mo sealed tube X-ray source, a Triumph monochromator, and a Photon 2 CMOS area detector. The unit cell was determined from reflections harvested with a signal to noise ratio (I/σ) of at least 10 from a series of 2 ω scans of 6° with 0.5° frames using APEX3.[1] The data were collected to a resolution of 0.75 Å using 6 ω and 1 φ scans.

The data were integrated using SAINT and corrected for absorption using SADABS.[2] The systematic absences and E-statistics of the data were consistent with the space group $P\bar{1}$. The structure was solved using the intrinsic phasing routine of SHELXT.[3] The non-hydrogen atoms were located from a Fourier difference map of the electron density and anisotropically refined using the least-squares algorithm of SHELXL.[4] The hydrogen atoms were then placed in calculated positions and refined with riding thermal parameters.

The asymmetric unit consists of a dimeric pair of the monomeric unit $C_9H_7BO_2F_3K$ (Figure 1). The compound is a 2-D polymer as shown in Figure 2. The two 4-fluoro phenyl rings were each disordered over two positions (major component occupancies 63.8(6)%, 54.5(6)%) Geometry and thermal parameter restraints were used to ensure a chemically reasonable and computationally stable refinement.

The final structure consisted of 435 parameters refined against 5113 independent reflections, giving refinement residuals of R_1 = 0.0587 (based off F^2 for $I > 2\sigma$) and wR_2 = 0.1065 (based of F^2 for all reflections). The final difference Fourier map was featureless.

1. Bruker-AXS (2016). APEX 3 version 2016.9-0. Madison, Wisconsin, USA

2. (a) Bruker-AXS (2015). *SAINT V8.37A.* Madison, Wisconsin, USA. (b) Bruker-AXS (2014). *SADABS*, Madison, Wisconsin, USA.

3. Sheldrick, G. M., *Acta Crystallogr. A* **2015**, A71, 3-8.

4. (a) Sheldrick, G. M., *Acta Crystallogr. C* **2015**, C71, 3-8.; (b) Dolomanov, O. V.; Bourhis, L. J.; Gildea, R. J.; Howard, J. A. K.; Puschmann, H., *J. Appl. Crystallogr.* **2009**, *42*, 339-341.

Table 1 Crystal data and structure refinement for $C_9H_7BO_2F_3K$.

Identification code	bp86_0m
Empirical formula	$C_9H_7BO_2F_3K$
Formula weight	254.06
Temperature/K	100.0
Crystal system	triclinic
Space group	P-1
a/Å	8.8835(3)
b/Å	9.4413(3)
c/Å	12.9922(4)
α/°	71.0780(10)
β/°	89.5090(10)
γ/°	86.2670(10)
Volume/Å^3	1028.52(6)
Z	4
ρ_{calc}g/cm^3	1.641
μ/mm^{-1}	0.538
F(000)	512.0
Crystal size/mm^3	0.25 × 0.24 × 0.044
Radiation	MoKα (λ = 0.71073)
2Θ range for data collection/°	4.596 to 56.58
Index ranges	-11 ≤ h ≤ 11, -12 ≤ k ≤ 12, -17 ≤ l ≤ 17
Reflections collected	45499
Independent reflections	5113 [R_{int} = 0.0339, R_{sigma} = 0.0193]
Data/restraints/parameters	5113/402/435
Goodness-of-fit on F^2	1.307
Final R indexes [I>=2σ (I)]	R_1 = 0.0587, wR_2 = 0.1050
Final R indexes [all data]	R_1 = 0.0628, wR_2 = 0.1065
Largest diff. peak/hole / e Å^{-3}	0.48/-0.45

Table 2 Fractional Atomic Coordinates (×10^4) and Equivalent Isotropic Displacement Parameters (Å^2×10^3) for $C_9H_7BO_2F_3K$. U_{eq} is defined as 1/3 of of the trace of the orthogonalised U_{IJ} tensor.

Atom	*x*	*y*	*z*	U(eq)
K1	4044.1(6)	7919.0(6)	4514.2(5)	21.19(12)
K2	8410.9(6)	5339.6(6)	5888.6(4)	20.18(12)
F1	6053.6(16)	3821.8(16)	6787.2(13)	23.3(3)
F2	5559.1(16)	6318.5(16)	6379.8(12)	22.1(3)
F4	6548.5(17)	8586.3(19)	3518.2(15)	31.4(4)
F5	6662(2)	10199(2)	4458.7(17)	45.0(5)
O1	3639.0(19)	4867(2)	6092.4(13)	19.2(3)
O2	1250(2)	4281(2)	6232.4(14)	24.0(4)
O3	8654(2)	8348(2)	4664.7(15)	23.1(4)
O4	11049(2)	7523(2)	4665.9(17)	35.5(5)
C1	2420(3)	4432(4)	6642(2)	28.1(6)
C3	4127(3)	4624(3)	8001(2)	23.7(5)

C10	9993(3)	8397(4)	4241(2)	35.1(7)
C12	8592(3)	10409(3)	2936(3)	32.8(7)
B1	4925(3)	4917(3)	6846(2)	18.7(5)
B2	7522(3)	9446(3)	3866(3)	25.1(6)
F3	-2618(5)	3580(6)	10197(4)	41.1(11)
F6A	15517(4)	11047(6)	1208(4)	44.3(12)
C2	2782(4)	3735(4)	7880(3)	16.8(9)
C4	1368(5)	3728(7)	8535(4)	15.1(9)
C5	1006(6)	2433(7)	9358(4)	21.9(11)
C6	-339(8)	2390(11)	9924(7)	26.5(14)
C7	-1316(14)	3660(10)	9641(11)	23.1(15)
C8	-1000(10)	4981(11)	8840(7)	24.0(15)
C9	361(7)	4994(7)	8305(5)	19.0(12)
C11A	9870(5)	9303(5)	3004(4)	19.1(11)
C13A	11395(8)	9799(8)	2543(6)	14.5(12)
C14A	12079(11)	9140(12)	1830(7)	20.7(16)
C15A	13472(10)	9552(11)	1385(9)	23.1(18)
C16A	14163(16)	10626(11)	1670(10)	25(2)
C17A	13535(9)	11304(10)	2363(7)	22.0(15)
C18A	12142(9)	10880(8)	2811(6)	18.4(13)
F3A	-2442(10)	2845(10)	10317(7)	42.1(19)
F6	15473(5)	10298(7)	996(4)	35.6(12)
C2A	2511(7)	5043(8)	7679(5)	18.1(15)
C4A	1223(10)	4429(12)	8438(7)	15.6(14)
C5A	1292(11)	2995(12)	9164(9)	21.7(17)
C6A	91(14)	2440(20)	9807(13)	25(2)
C7A	-1180(30)	3330(20)	9710(20)	25(2)
C8A	-1300(19)	4760(20)	9026(13)	24(2)
C9A	-109(14)	5323(14)	8369(10)	22.3(19)
C11	10147(5)	10083(5)	3416(4)	14.0(11)
C13	11563(10)	10166(9)	2749(6)	14.4(14)
C14	11795(13)	9249(14)	2092(8)	18(2)
C15	13091(13)	9287(14)	1494(11)	21.8(19)
C16	14170(20)	10261(14)	1542(11)	21(2)
C17	14002(11)	11188(12)	2178(9)	22.0(17)
C18	12683(10)	11126(10)	2772(7)	17.9(15)

Table 3 Anisotropic Displacement Parameters ($Å^2×10^3$) for $C_9H_7BO_2F_3K$. The Anisotropic displacement factor exponent takes the form: $-2\pi^2[h^2a^{*2}U_{11}+2hka^*b^*U_{12}+\ldots]$.

Atom	U_{11}	U_{22}	U_{33}	U_{23}	U_{13}	U_{12}
K1	15.2(2)	19.8(3)	27.6(3)	-6.8(2)	0.4(2)	1.35(19)
K2	15.3(2)	24.6(3)	19.8(3)	-6.0(2)	3.57(19)	-1.68(19)
F1	17.7(7)	18.3(7)	32.0(8)	-6.2(6)	3.7(6)	1.6(6)
F2	17.7(7)	18.3(7)	31.4(8)	-9.4(6)	0.9(6)	-2.3(5)
F4	17.1(7)	30.4(9)	45.5(10)	-10.4(8)	2.5(7)	-2.9(6)

F5	34.4(10)	45.4(11)	61.6(13)	-29.4(10)	8.1(9)	13.6(8)
O1	16.9(8)	25.1(9)	16.6(8)	-7.6(7)	2.6(6)	-4.3(7)
O2	17.0(8)	35.3(10)	20.0(9)	-9.0(8)	-2.4(7)	-3.4(7)
O3	20.3(9)	21.5(9)	25.1(9)	-4.4(7)	7.7(7)	-2.1(7)
O4	19.0(9)	36.4(11)	35.5(11)	9.2(9)	-3.3(8)	2.3(8)
C1	17.0(12)	51.5(18)	17.1(12)	-12.2(12)	1.1(9)	-5.5(11)
C3	17.7(12)	36.6(15)	19.6(12)	-12.7(11)	-1.8(9)	-3.0(10)
C10	19.3(13)	42.1(17)	28.2(14)	9.3(13)	3.4(11)	2.5(12)
C12	16.2(12)	24.6(14)	45.4(17)	4.7(12)	2.2(11)	1.5(10)
B1	14.5(12)	19.6(13)	22.7(13)	-8.3(11)	-1.2(10)	0.6(10)
B2	16.7(13)	19.8(14)	36.1(17)	-6.3(12)	7.7(12)	2.4(10)
F3	27.7(18)	67(3)	36(2)	-25(2)	19.8(15)	-15(2)
F6A	19.8(16)	60(3)	46(2)	-5(2)	11.2(15)	-17.6(18)
C2	18.9(18)	18.2(18)	14.3(17)	-7.0(13)	-0.5(13)	1.0(13)
C4	12.7(17)	21(2)	13.9(19)	-8(2)	-1.1(14)	-1.8(19)
C5	25(2)	24(3)	15(2)	-4(2)	0.2(18)	-3(2)
C6	27(3)	36(2)	18(2)	-8.9(19)	11(2)	-10(3)
C7	19(3)	34(4)	20(3)	-14(3)	6(2)	-3(3)
C8	26(4)	29(3)	17(3)	-8(2)	6(2)	-2(2)
C9	19(3)	23(3)	15.7(18)	-6.0(19)	3(2)	-5(2)
C11A	12.9(19)	22(2)	20(2)	-4.1(17)	-0.3(16)	-2.6(16)
C13A	13(2)	14(3)	18(3)	-5.8(19)	-1.1(19)	-2(2)
C14A	19(4)	23(2)	23(4)	-10(3)	2(3)	-3(2)
C15A	15(4)	32(4)	22(3)	-9(3)	6(3)	-1(3)
C16A	16(2)	31(4)	23(3)	-2(3)	3(3)	-6(4)
C17A	16(4)	23(2)	27(3)	-8(2)	1(3)	-8(3)
C18A	18(3)	19(3)	16(2)	-3(2)	2(3)	-2(3)
F3A	32(3)	59(5)	33(3)	-10(4)	13(2)	-16(4)
F6	25(2)	47(3)	35(2)	-11(2)	12.1(16)	-9(2)
C2A	15(3)	23(3)	20(3)	-12(2)	4(2)	0(2)
C4A	15(3)	18(3)	16(3)	-9(3)	2(2)	0(3)
C5A	19(3)	22(4)	19(4)	-2(3)	2(3)	4(3)
C6A	22(4)	28(3)	21(4)	-3(3)	5(4)	-2(4)
C7A	24(4)	35(5)	16(3)	-7(4)	9(3)	-8(4)
C8A	23(5)	35(5)	18(4)	-13(4)	7(4)	-5(4)
C9A	22(5)	26(4)	19(3)	-8(3)	0(4)	-1(3)
C11	14(2)	10(2)	16(2)	-0.8(17)	-3.1(17)	1.8(16)
C13	18(3)	11(3)	15(3)	-5(2)	-1(2)	-3(3)
C14	16(4)	20(3)	18(4)	-5(3)	0(3)	-4(3)
C15	20(4)	25(4)	21(4)	-8(3)	2(4)	-6(3)
C16	16(3)	29(4)	18(3)	-7(3)	4(2)	0(4)
C17	12(4)	26(3)	26(4)	-6(3)	8(3)	-6(3)
C18	13(4)	16(3)	25(3)	-6(2)	3(3)	-4(3)

Table 4 Bond Lengths for $C_9H_7BO_2F_3K$.

Atom	Atom	Length/Å	Atom	Atom	Length/Å
K1	F1[1]	2.7186(16)	C3	C2A	1.490(7)
K1	F2	2.7176(16)	C10	C11A	1.557(5)
K1	F4	2.5740(17)	C10	C11	1.619(5)
K1	F5	3.255(2)	C12	B2	1.603(4)
K1	F5[2]	2.5906(19)	C12	C11A	1.475(5)
K1	O1	2.9878(18)	C12	C11	1.492(5)
K1	O4[3]	2.707(2)	F3	C7	1.352(14)
K1	B1	3.465(3)	F6A	C16A	1.364(14)
K1	C13A[3]	3.444(6)	C2	C4	1.510(6)
K1	C18A[3]	3.317(7)	C4	C5	1.393(7)
K1	C13[3]	3.308(8)	C4	C9	1.397(7)
K1	C18[3]	3.298(8)	C5	C6	1.393(7)
K2	F1	2.6581(15)	C6	C7	1.382(12)
K2	F2	2.7802(15)	C7	C8	1.384(11)
K2	O1[1]	3.2297(18)	C8	C9	1.388(9)
K2	O2[4]	2.6385(19)	C11A	C13A	1.517(8)
K2	O2[1]	2.6780(18)	C13A	C14A	1.389(8)
K2	O3	2.7906(19)	C13A	C18A	1.388(8)
K2	O4[5]	3.024(2)	C14A	C15A	1.386(10)
K2	O4	3.272(2)	C15A	C16A	1.367(13)
K2	C1[1]	3.311(3)	C16A	C17A	1.361(12)
K2	C10	3.371(3)	C17A	C18A	1.390(9)
K2	B1	3.327(3)	F3A	C7A	1.39(3)
K2	C9A[4]	3.486(12)	F6	C16	1.351(18)
F1	B1	1.412(3)	C2A	C4A	1.521(10)
F2	B1	1.416(3)	C4A	C5A	1.374(12)
F4	B2	1.395(4)	C4A	C9A	1.394(12)
F5	B2	1.399(3)	C5A	C6A	1.373(14)
O1	C1	1.306(3)	C6A	C7A	1.34(2)
O1	B1	1.524(3)	C7A	C8A	1.35(2)
O2	C1	1.209(3)	C8A	C9A	1.377(15)
O3	C10	1.304(3)	C11	C13	1.513(10)
O3	B2	1.532(4)	C13	C14	1.405(11)
O4	C10	1.216(3)	C13	C18	1.396(9)
C1	C2	1.554(4)	C14	C15	1.379(12)
C1	C2A	1.633(7)	C15	C16	1.384(16)
C3	B1	1.602(4)	C16	C17	1.385(13)
C3	C2	1.541(4)	C17	C18	1.392(10)

[1]1-X,1-Y,1-Z; [2]1-X,2-Y,1-Z; [3]-1+X,+Y,+Z; [4]1+X,+Y,+Z; [5]2-X,1-Y,1-Z

Table 5 Bond Angles for $C_9H_7BO_2F_3K$.

Atom	Atom	Atom	Angle/°	Atom	Atom	Atom	Angle/°
F1[1]	K1	F5	124.83(5)	B1	F2	K1	109.87(13)
F1[1]	K1	O1	76.87(5)	B1	F2	K2	99.74(13)
F1[1]	K1	B1	94.11(6)	B2	F4	K1	119.25(16)
F1[1]	K1	C13A[2]	75.86(13)	K1[3]	F5	K1	113.55(6)
F1[1]	K1	C18A[2]	95.54(14)	B2	F5	K1	87.07(16)
F1[1]	K1	C13[2]	84.26(16)	B2	F5	K1[3]	159.35(18)
F1[1]	K1	C18[2]	98.77(18)	K1	O1	K2[1]	81.28(4)
F2	K1	F1[1]	108.56(5)	C1	O1	K1	125.93(17)
F2	K1	F5	80.65(5)	C1	O1	K2[1]	82.01(14)
F2	K1	O1	48.60(4)	C1	O1	B1	110.97(19)
F2	K1	B1	22.61(5)	B1	O1	K1	94.78(13)
F2	K1	C13A[2]	166.45(13)	B1	O1	K2[1]	165.81(14)
F2	K1	C18A[2]	155.90(14)	K2[2]	O2	K2[1]	90.78(6)
F2	K1	C13[2]	163.28(16)	C1	O2	K2[2]	142.65(19)
F2	K1	C18[2]	151.36(18)	C1	O2	K2[1]	111.10(16)
F4	K1	F1[1]	81.53(5)	C10	O3	K2	104.92(17)
F4	K1	F2	90.80(5)	C10	O3	B2	110.7(2)
F4	K1	F5[3]	109.36(6)	B2	O3	K2	129.63(15)
F4	K1	F5	43.42(5)	K1[5]	O4	K2[4]	89.86(6)
F4	K1	O1	121.61(5)	K1[5]	O4	K2	146.28(7)
F4	K1	O4[2]	155.53(6)	K2[4]	O4	K2	73.79(5)
F4	K1	B1	106.18(6)	C10	O4	K1[5]	129.40(19)
F4	K1	C13A[2]	102.60(12)	C10	O4	K2[4]	119.3(2)
F4	K1	C18A[2]	93.00(15)	C10	O4	K2	84.04(17)
F4	K1	C13[2]	101.94(15)	O1	C1	K2[1]	74.99(13)
F4	K1	C18[2]	84.78(17)	O1	C1	C2	111.1(2)
F5[3]	K1	F1[1]	163.23(6)	O1	C1	C2A	104.6(3)
F5[3]	K1	F2	84.55(6)	O2	C1	K2[1]	48.99(13)
F5[3]	K1	F5	66.45(6)	O2	C1	O1	123.8(2)
F5[3]	K1	O1	106.23(6)	O2	C1	C2	123.3(3)
F5[3]	K1	O4[2]	82.67(7)	O2	C1	C2A	123.8(3)
F5[3]	K1	B1	94.89(7)	C2	C1	K2[1]	160.0(2)
F5	K1	B1	103.21(6)	C2	C3	B1	101.6(2)
F5	K1	C13A[2]	107.70(12)	C2A	C3	B1	102.2(3)
F5[3]	K1	C13A[2]	89.06(14)	O3	C10	K2	53.13(14)
F5[3]	K1	C18A[2]	71.74(14)	O3	C10	C11A	109.2(3)
F5	K1	C18A[2]	85.84(15)	O3	C10	C11	107.6(3)
F5	K1	C13[2]	101.12(16)	O4	C10	K2	74.93(17)
F5[3]	K1	C13[2]	81.05(16)	O4	C10	O3	123.3(3)
F5[3]	K1	C18[2]	70.45(18)	O4	C10	C11A	124.3(3)
F5	K1	C18[2]	76.74(17)	O4	C10	C11	124.8(3)
O1	K1	F5	129.11(5)	C11A	C10	K2	134.8(2)
O1	K1	B1	26.00(5)	C11	C10	K2	160.0(2)

O1	K1	C13A[2]	122.84(12)	C11A	C12	B2	100.9(3)
O1	K1	C18A[2]	142.19(15)	C11	C12	B2	105.4(3)
O1	K1	C13[2]	128.38(16)	K2	B1	K1	82.92(6)
O1	K1	C18[2]	151.50(17)	F1	B1	K1	118.36(16)
O4[2]	K1	F1[1]	82.69(6)	F1	B1	K2	50.35(11)
O4[2]	K1	F2	111.97(6)	F1	B1	F2	105.8(2)
O4[2]	K1	F5	145.74(6)	F1	B1	O1	106.9(2)
O4[2]	K1	O1	72.25(5)	F1	B1	C3	116.1(2)
O4[2]	K1	B1	93.49(6)	F2	B1	K1	47.52(11)
O4[2]	K1	C13A[2]	55.20(12)	F2	B1	K2	55.45(11)
O4[2]	K1	C18A[2]	70.04(15)	F2	B1	O1	106.7(2)
O4[2]	K1	C13[2]	57.82(16)	F2	B1	C3	117.2(2)
O4[2]	K1	C18[2]	79.27(17)	O1	B1	K1	59.22(11)
C13A[2]	K1	B1	147.71(13)	O1	B1	K2	119.53(15)
C18A[2]	K1	B1	159.61(15)	O1	B1	C3	103.40(19)
C18A[2]	K1	C13A[2]	23.60(14)	C3	B1	K1	125.57(16)
C13[2]	K1	B1	151.28(16)	C3	B1	K2	136.94(16)
C18[2]	K1	B1	164.25(17)	F4	B2	K1	40.25(11)
F1	K2	F2	48.95(4)	F4	B2	F5	107.1(2)
F1	K2	O1[1]	73.52(5)	F4	B2	O3	107.0(2)
F1	K2	O2[1]	114.65(5)	F4	B2	C12	114.4(3)
F1	K2	O3	131.78(5)	F5	B2	K1	69.24(14)
F1	K2	O4[4]	77.93(5)	F5	B2	O3	107.0(2)
F1	K2	O4	173.72(5)	F5	B2	C12	117.9(2)
F1	K2	C1[1]	95.88(6)	O3	B2	K1	105.38(15)
F1	K2	C10	152.74(6)	O3	B2	C12	102.6(2)
F1	K2	B1	24.15(6)	C12	B2	K1	147.2(2)
F1	K2	C9A[5]	93.9(2)	C3	C2	C1	101.4(3)
F2	K2	O1[1]	77.48(4)	C4	C2	C1	110.5(3)
F2	K2	O3	84.42(5)	C4	C2	C3	121.1(3)
F2	K2	O4[4]	122.00(5)	C5	C4	C2	120.6(5)
F2	K2	O4	125.22(5)	C5	C4	C9	118.2(5)
F2	K2	C1[1]	96.13(6)	C9	C4	C2	121.1(5)
F2	K2	C10	106.37(6)	C4	C5	C6	121.0(6)
F2	K2	B1	24.81(6)	C7	C6	C5	118.4(10)
F2	K2	C9A[5]	91.8(2)	F3	C7	C6	117.1(9)
O1[1]	K2	O4	103.70(5)	F3	C7	C8	120.0(8)
O1[1]	K2	C1[1]	22.99(5)	C6	C7	C8	122.9(12)
O1[1]	K2	C10	91.29(6)	C7	C8	C9	117.2(11)
O1[1]	K2	B1	74.32(6)	C4	C9	K2[2]	107.9(3)
O1[1]	K2	C9A[5]	167.0(2)	C8	C9	K2[2]	90.1(5)
O2[5]	K2	F1	124.73(6)	C8	C9	C4	122.2(7)
O2[1]	K2	F2	113.11(5)	C12	C11A	C10	103.5(3)
O2[5]	K2	F2	157.57(5)	C12	C11A	C13A	120.9(4)
O2[1]	K2	O1[1]	42.86(5)	C13A	C11A	C10	111.3(4)

O2[5]	K2	O1[1]	123.61(5)	C11A	C13A	K1[5]	106.6(3)
O2[5]	K2	O2[1]	89.22(6)	C14A	C13A	K1[5]	89.9(5)
O2[5]	K2	O3	103.01(6)	C14A	C13A	C11A	118.8(7)
O2[1]	K2	O3	68.06(6)	C18A	C13A	K1[5]	73.1(4)
O2[1]	K2	O4	64.08(6)	C18A	C13A	C11A	122.6(7)
O2[1]	K2	O4[4]	64.88(6)	C18A	C13A	C14A	118.5(8)
O2[5]	K2	O4[4]	68.36(6)	C15A	C14A	C13A	121.2(11)
O2[5]	K2	O4	61.53(5)	C16A	C15A	C14A	118.2(12)
O2[5]	K2	C1[1]	106.22(6)	F6A	C16A	C15A	117.7(10)
O2[1]	K2	C1[1]	19.92(6)	C17A	C16A	F6A	119.6(9)
O2[5]	K2	C10	82.52(7)	C17A	C16A	C15A	122.7(13)
O2[1]	K2	C10	59.52(7)	C16A	C17A	K1[5]	89.9(6)
O2[1]	K2	B1	116.73(6)	C16A	C17A	C18A	118.8(9)
O2[5]	K2	B1	144.71(7)	C18A	C17A	K1[5]	70.8(4)
O2[5]	K2	C9A[5]	66.2(2)	C13A	C18A	K1[5]	83.3(4)
O2[1]	K2	C9A[5]	150.1(2)	C13A	C18A	C17A	120.5(7)
O3	K2	O1[1]	86.47(5)	C17A	C18A	K1[5]	85.9(4)
O3	K2	O4	41.97(5)	C3	C2A	C1	100.1(4)
O3	K2	O4[4]	132.08(6)	C3	C2A	C4A	122.7(6)
O3	K2	C1[1]	74.86(7)	C4A	C2A	C1	108.1(5)
O3	K2	C10	21.95(6)	C5A	C4A	C2A	122.6(9)
O3	K2	B1	108.62(6)	C5A	C4A	C9A	118.1(9)
O3	K2	C9A[5]	99.9(2)	C9A	C4A	C2A	119.2(10)
O4[4]	K2	O1[1]	65.01(5)	C6A	C5A	C4A	121.6(10)
O4[4]	K2	O4	106.21(5)	C7A	C6A	C5A	118.3(17)
O4	K2	C1[1]	82.01(6)	C6A	C7A	F3A	121.6(15)
O4[4]	K2	C1[1]	63.99(7)	C6A	C7A	C8A	123(2)
O4[4]	K2	C10	116.57(7)	C8A	C7A	F3A	115.6(18)
O4	K2	C10	21.02(6)	C7A	C8A	C9A	119(2)
O4[4]	K2	B1	99.98(6)	C8A	C9A	C4A	119.7(15)
O4	K2	B1	150.01(6)	C12	C11	C10	99.8(3)
O4[4]	K2	C9A[5]	116.5(2)	C12	C11	C13	123.7(5)
O4	K2	C9A[5]	88.4(2)	C13	C11	C10	110.7(4)
C1[1]	K2	C10	73.06(8)	C14	C13	C11	120.3(9)
C1[1]	K2	B1	96.91(7)	C18	C13	C11	121.9(7)
C1[1]	K2	C9A[5]	170.0(2)	C18	C13	C14	117.8(9)
C10	K2	C9A[5]	98.9(2)	C15	C14	C13	121.2(12)
B1	K2	C10	130.44(7)	C14	C15	C16	118.8(15)
B1	K2	C9A[5]	92.9(2)	F6	C16	C15	120.6(10)
K2	F1	K1[1]	97.86(5)	F6	C16	C17	116.7(13)
B1	F1	K1[1]	125.58(14)	C15	C16	C17	122.6(16)
B1	F1	K2	105.51(14)	C16	C17	C18	117.3(13)
K1	F2	K2	109.81(5)	C17	C18	C13	122.3(10)

[1]1-X,1-Y,1-Z; [2]-1+X,+Y,+Z; [3]1-X,2-Y,1-Z; [4]2-X,1-Y,1-Z; [5]1+X,+Y,+Z

Table 6 Torsion Angles for $C_9H_7BO_2F_3K$.

A	B	C	D	Angle/°	A	B	C	D	Angle/°
K1[1]	F1	B1	K1	-60.9(2)	C3	C2	C4	C9	72.2(5)
K1[1]	F1	B1	K2	111.90(15)	C3	C2A	C4A	C5A	-35.0(11)
K1[1]	F1	B1	F2	110.74(17)	C3	C2A	C4A	C9A	147.9(8)
K1[1]	F1	B1	O1	2.8(3)	C10	O3	B2	K1	152.0(2)
K1[1]	F1	B1	C3	117.47(19)	C10	O3	B2	F4	110.0(3)
K1	F2	B1	K2	115.32(10)	C10	O3	B2	F5	-135.5(3)
K1	F2	B1	F1	114.23(16)	C10	O3	B2	C12	-10.7(3)
K1	F2	B1	O1	0.6(2)	C10	C11A	C13A	K1[3]	10.9(5)
K1	F2	B1	C3	114.62(19)	C10	C11A	C13A	C14A	110.2(7)
K1	F4	B2	F5	-20.6(3)	C10	C11A	C13A	C18A	-69.3(7)
K1	F4	B2	O3	93.92(19)	C10	C11	C13	K1[3]	-38.0(5)
K1	F4	B2	C12	153.16(16)	C10	C11	C13	C14	58.1(8)
K1[2]	F5	B2	K1	176.8(5)	C10	C11	C13	C18	-121.1(7)
K1	F5	B2	F4	14.04(19)	C12	C11A	C13A	K1[3]	132.6(3)
K1[2]	F5	B2	F4	-169.2(4)	C12	C11A	C13A	C14A	-128.1(6)
K1	F5	B2	O3	100.40(18)	C12	C11A	C13A	C18A	52.4(7)
K1[2]	F5	B2	O3	76.4(6)	C12	C11	C13	K1[3]	-156.2(4)
K1[2]	F5	B2	C12	-38.5(7)	C12	C11	C13	C14	-60.1(9)
K1	F5	B2	C12	144.7(2)	C12	C11	C13	C18	120.7(7)
K1	O1	C1	K2[1]	73.10(13)	B1	O1	C1	K2[1]	174.07(17)
K1	O1	C1	O2	68.2(4)	B1	O1	C1	O2	-178.9(3)
K1	O1	C1	C2	-127.0(2)	B1	O1	C1	C2	-14.2(3)
K1	O1	C1	C2A	-81.6(3)	B1	O1	C1	C2A	31.2(4)
K1	O1	B1	K2	-59.86(14)	B1	C3	C2	C1	-32.5(3)
K1	O1	B1	F1	113.38(17)	B1	C3	C2	C4	-155.1(4)
K1	O1	B1	F2	-0.54(18)	B1	C3	C2A	C1	36.5(4)
K1	O1	B1	C3	123.64(16)	B1	C3	C2A	C4A	155.8(6)
K1[3]	O4	C10	K2	-175.2(2)	B2	O3	C10	K2	-143.7(2)
K1[3]	O4	C10	O3	-152.1(2)	B2	O3	C10	O4	-172.0(3)
K1[3]	O4	C10	C11A	50.4(5)	B2	O3	C10	C11A	-11.6(4)
K1[3]	O4	C10	C11	1.6(5)	B2	O3	C10	C11	30.4(4)
K1[3]	C13A	C14A	C15A	-71.0(8)	B2	C12	C11A	C10	-35.1(4)
K1[3]	C13A	C18A	C17A	81.2(6)	B2	C12	C11A	C13A	-160.5(4)
K1[3]	C17A	C18A	C13A	-79.8(5)	B2	C12	C11	C10	29.4(4)
K1[3]	C13	C14	C15	-74.5(9)	B2	C12	C11	C13	152.7(5)
K1[3]	C13	C18	C17	81.2(7)	F3	C7	C8	C9	179.5(9)
K2	F1	B1	K1	51.00(16)	F6A	C16A	C17A	K1[3]	-113.2(9)

K2	F1	B1	F2	1.2(2)	F6A	C16A	C17A	C18A	178.9(8)
K2	F1	B1	O1	114.66(16)	C2	C3	B1	K1	87.4(2)
K2	F1	B1	C3	−130.62(18)	C2	C3	B1	K2	−149.7(2)
K2	F2	B1	K1	−115.32(10)	C2	C3	B1	F1	−90.8(3)
K2	F2	B1	F1	−1.08(19)	C2	C3	B1	F2	142.9(2)
K2	F2	B1	O1	−114.69(15)	C2	C3	B1	O1	25.9(3)
K2	F2	B1	C3	130.07(19)	C2	C4	C5	C6	−176.2(6)
K2[1]	O1	C1	O2	−4.9(3)	C2	C4	C9	K2[4]	73.2(5)
K2[1]	O1	C1	C2	159.9(2)	C2	C4	C9	C8	175.1(6)
K2[1]	O1	C1	C2A	−154.7(3)	C4	C5	C6	C7	0.6(12)
K2[1]	O1	B1	K1	73.2(6)	C5	C4	C9	K2[4]	−104.3(4)
K2[1]	O1	B1	K2	13.3(7)	C5	C4	C9	C8	−2.4(9)
K2[1]	O1	B1	F1	−40.2(7)	C5	C6	C7	F3	179.4(8)
K2[1]	O1	B1	F2	72.6(6)	C5	C6	C7	C8	−1.5(16)
K2[1]	O1	B1	C3	−163.2(5)	C6	C7	C8	C9	0.5(16)
K2[4]	O2	C1	K2[1]	−122.0(3)	C7	C8	C9	K2[4]	112.8(9)
K2[4]	O2	C1	O1	−115.8(3)	C7	C8	C9	C4	1.5(12)
K2[1]	O2	C1	O1	6.2(4)	C9	C4	C5	C6	1.3(8)
K2[4]	O2	C1	C2	81.3(4)	C11A	C12	B2	K1	−119.1(3)
K2[1]	O2	C1	C2	−156.7(2)	C11A	C12	B2	F4	−86.5(3)
K2[1]	O2	C1	C2A	150.5(3)	C11A	C12	B2	F5	146.2(3)
K2[4]	O2	C1	C2A	28.5(5)	C11A	C12	B2	O3	29.0(3)
K2	O3	C10	O4	−28.3(4)	C11A	C13A	C14A	C15A	180.0(7)
K2	O3	C10	C11A	132.2(3)	C11A	C13A	C18A	K1[3]	99.2(5)
K2	O3	C10	C11	174.2(2)	C11A	C13A	C18A	C17A	−179.7(6)
K2	O3	B2	K1	19.9(2)	C13A	C14A	C15A	C16A	0.2(13)
K2	O3	B2	F4	−22.1(3)	C14A	C13A	C18A	K1[3]	−80.4(6)
K2	O3	B2	F5	92.4(2)	C14A	C13A	C18A	C17A	0.8(9)
K2	O3	B2	C12	−142.82(18)	C14A	C15A	C16A	F6A	−178.6(9)
K2[5]	O4	C10	K2	67.65(12)	C14A	C15A	C16A	C17A	−0.3(15)
K2[5]	O4	C10	O3	90.8(4)	C15A	C16A	C17A	K1[3]	68.6(10)
K2	O4	C10	O3	23.1(3)	C15A	C16A	C17A	C18A	0.7(14)
K2[5]	O4	C10	C11A	−66.7(4)	C16A	C17A	C18A	K1[3]	78.8(7)
K2	O4	C10	C11A	−134.4(4)	C16A	C17A	C18A	C13A	−0.9(11)
K2	O4	C10	C11	176.8(4)	C18A	C13A	C14A	C15A	−0.5(11)
K2[5]	O4	C10	C11	−115.5(4)	F3A	C7A	C8A	C9A	−178.4(17)
K2[1]	C1	C2	C3	135.1(5)	F6	C16	C17	C18	−178.0(9)
K2[1]	C1	C2	C4	−95.2(6)	C2A	C3	B1	K1	40.4(4)
K2[1]	C1	C2A	C3	−129.8(5)	C2A	C3	B1	K2	163.3(3)
K2[1]	C1	C2A	C4A	100.7(8)	C2A	C3	B1	F1	−137.8(3)
K2	C10	C11A	C12	88.1(4)	C2A	C3	B1	F2	95.9(3)
K2	C10	C11A	C13A	−140.5(4)	C2A	C3	B1	O1	−21.2(4)

K2	C10	C11	C12	-24.7(9)	C2A	C4A	C5A	C6A	-177.0(11)
K2	C10	C11	C13	-156.6(7)	C2A	C4A	C9A	K2[4]	70.7(8)
O1	C1	C2	C3	30.9(3)	C2A	C4A	C9A	C8A	177.7(11)
O1	C1	C2	C4	160.6(3)	C4A	C5A	C6A	C7A	0(2)
O1	C1	C2A	C3	-44.1(4)	C5A	C4A	C9A	K2[4]	-106.6(8)
O1	C1	C2A	C4A	-173.5(5)	C5A	C4A	C9A	C8A	0.4(17)
O2	C1	C2	C3	-164.3(3)	C5A	C6A	C7A	F3A	179.1(17)
O2	C1	C2	C4	-34.6(5)	C5A	C6A	C7A	C8A	-2(3)
O2	C1	C2A	C3	166.0(3)	C6A	C7A	C8A	C9A	3(3)
O2	C1	C2A	C4A	36.6(7)	C7A	C8A	C9A	K2[4]	106.5(18)
O3	C10	C11A	C12	31.4(4)	C7A	C8A	C9A	C4A	-2(2)
O3	C10	C11A	C13A	162.8(4)	C9A	C4A	C5A	C6A	0.2(16)
O3	C10	C11	C12	-38.5(4)	C11	C12	B2	K1	-162.9(3)
O3	C10	C11	C13	-170.4(5)	C11	C12	B2	F4	-130.3(3)
O4	C10	C11A	C12	-168.4(3)	C11	C12	B2	F5	102.5(3)
O4	C10	C11A	C13A	-37.0(6)	C11	C12	B2	O3	-14.8(3)
O4	C10	C11	C12	164.4(4)	C11	C13	C14	C15	-178.7(8)
O4	C10	C11	C13	32.5(6)	C11	C13	C18	K1[3]	97.6(6)
C1	O1	B1	K1	-131.5(2)	C11	C13	C18	C17	178.7(7)
C1	O1	B1	K2	168.64(18)	C13	C14	C15	C16	-0.6(15)
C1	O1	B1	F1	115.1(2)	C14	C13	C18	K1[3]	-81.6(7)
C1	O1	B1	F2	-132.0(2)	C14	C13	C18	C17	-0.4(12)
C1	O1	B1	C3	-7.9(3)	C14	C15	C16	F6	177.9(10)
C1	C2	C4	C5	131.5(4)	C14	C15	C16	C17	0.8(18)
C1	C2	C4	C9	-46.0(5)	C15	C16	C17	C18	-0.8(17)
C1	C2A	C4A	C5A	80.4(9)	C16	C17	C18	K1[3]	76.0(9)
C1	C2A	C4A	C9A	-96.8(9)	C16	C17	C18	C13	0.6(13)
C3	C2	C4	C5	-110.4(5)	C18	C13	C14	C15	0.5(13)

[1]1-X,1-Y,1-Z; [2]1-X,2-Y,1-Z; [3]1+X,+Y,+Z; [4]-1+X,+Y,+Z; [5]2-X,1-Y,1-Z

Table 7 Hydrogen Atom Coordinates (Å×10[4]) and Isotropic Displacement Parameters (Å[2]×10[3]) for $C_9H_7BO_2F_3K$

Atom	*x*	*y*	*z*	U(eq)
H3AA	4808.46	4027.8	8606.6	28
H3AB	3783.92	5578.33	8118.38	28
H3BC	4277.44	3559.14	8459.85	28
H3BD	4510.8	5266.61	8396.12	28
H12C	8536.59	10105.25	2276.8	39
H12D	8289.8	11493.58	2736.53	39
H12A	8090.19	10733.03	2211.63	39
H12B	8913.76	11300.53	3097.03	39
H2	3164.5	2668.7	8021.72	20
H5	1685.41	1567.18	9537.28	26

H6	-579.4	1508.82	10489.65	32
H8	-1685.36	5843.22	8663.96	29
H9	616.02	5893.93	7763.84	23
H11A	9536.87	8600.26	2630.31	23
H14A	11583.27	8393.33	1643.37	25
H15A	13933.65	9100.85	896.19	28
H17A	14040.83	12054.62	2538.27	26
H18A	11698.23	11333.61	3305.19	22
H2A	2362.46	6162.49	7405.37	22
H5A	2193.27	2373.07	9222.29	26
H6A	155.25	1449.28	10309.39	30
H8A	-2202.21	5367.48	8999.16	29
H9A	-194.41	6316.7	7871.39	27
H11	10255.76	10745.51	3871.95	17
H14	11046	8591.78	2058.46	22
H15	13242.76	8655.08	1057.97	26
H17	14759.9	11839.82	2206.62	26
H18	12540.32	11758.17	3208.43	22

Table 8 Atomic Occupancy for $C_9H_7BO_2F_3K$.

Atom	*Occupancy*	Atom	*Occupancy*	Atom	*Occupancy*
H3AA	0.638(6)	H3AB	0.638(6)	H3BC	0.362(6)
H3BD	0.362(6)	H12C	0.455(6)	H12D	0.455(6)
H12A	0.545(6)	H12B	0.545(6)	F3	0.638(6)
F6A	0.545(6)	C2	0.638(6)	H2	0.638(6)
C4	0.638(6)	C5	0.638(6)	H5	0.638(6)
C6	0.638(6)	H6	0.638(6)	C7	0.638(6)
C8	0.638(6)	H8	0.638(6)	C9	0.638(6)
H9	0.638(6)	C11A	0.545(6)	H11A	0.545(6)
C13A	0.545(6)	C14A	0.545(6)	H14A	0.545(6)
C15A	0.545(6)	H15A	0.545(6)	C16A	0.545(6)
C17A	0.545(6)	H17A	0.545(6)	C18A	0.545(6)
H18A	0.545(6)	F3A	0.362(6)	F6	0.455(6)
C2A	0.362(6)	H2A	0.362(6)	C4A	0.362(6)
C5A	0.362(6)	H5A	0.362(6)	C6A	0.362(6)
H6A	0.362(6)	C7A	0.362(6)	C8A	0.362(6)
H8A	0.362(6)	C9A	0.362(6)	H9A	0.362(6)
C11	0.455(6)	H11	0.455(6)	C13	0.455(6)
C14	0.455(6)	H14	0.455(6)	C15	0.455(6)
H15	0.455(6)	C16	0.455(6)	C17	0.455(6)
H17	0.455(6)	C18	0.455(6)	H18	0.455(6)

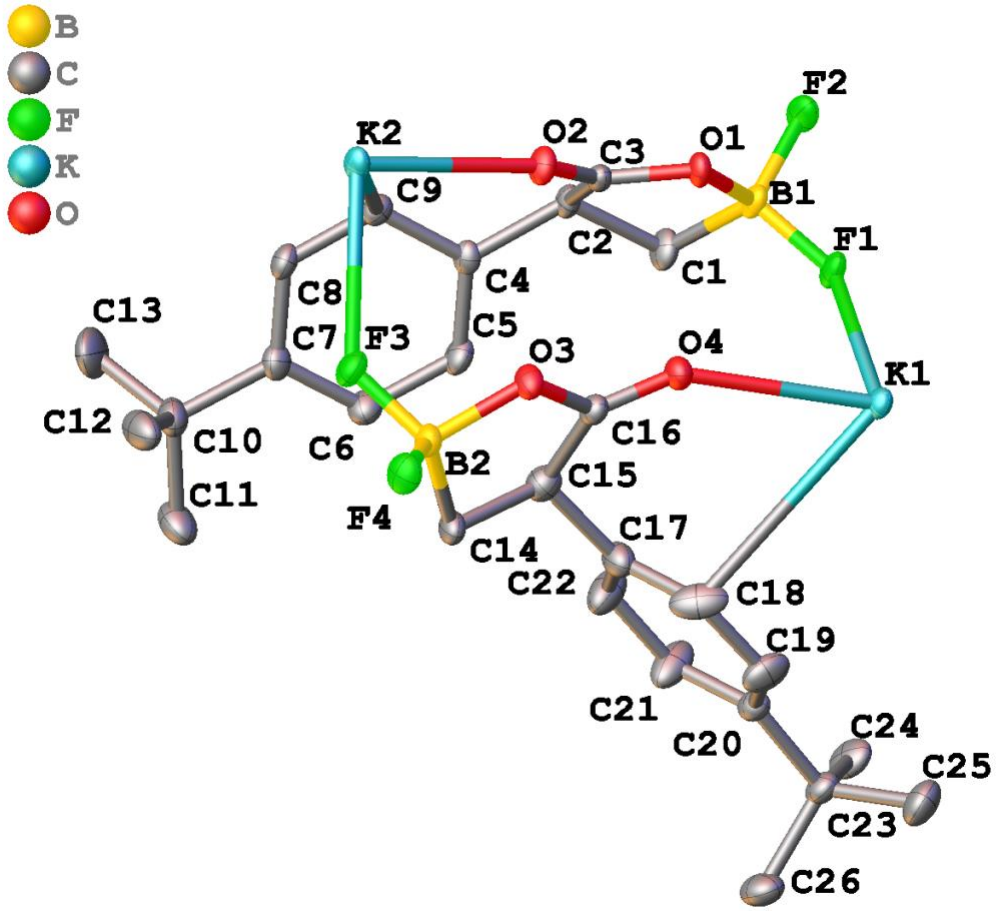

Figure A198. The asymmetric unit of $\mathbf{C_{26}H_{32}B_2F_4K_2O_4}$. All non-hydrogen atoms are drawn as 50% thermal probability ellipsoids. All hydrogen atoms are omitted for clarity.

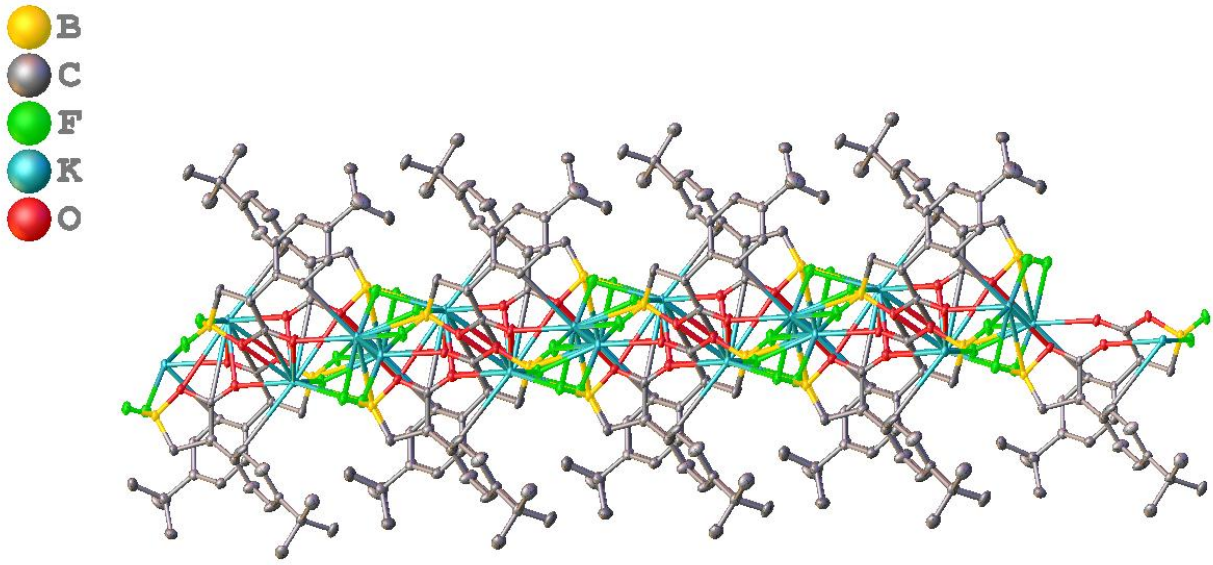

Figure A199. The polymer of **$C_{26}H_{32}B_2F_4K_2O_4$**. All non-hydrogen atoms are drawn as 50% thermal probability ellipsoids. All hydrogen atoms are omitted for clarity.

Description of the X-ray structural analysis of $C_{26}H_{32}B_2F_4K_2O_4$

A colorless block-shaped crystal measuring approximately 0.3 mm x 0.2 mm x 0.1 mm was selected under polybutene oil using a MiTeGen Micromount and mounted at 100(1) K to a D8-Venture diffractometer equipped with a Mo sealed tube X-ray source, a Triumph monochromator, and a Photon 2 CMOS area detector. The unit cell was determined from reflections harvested with a signal to noise ratio (I/σ) of at least 10 from a series of 2 ω scans of 6° with 0.5° frames using APEX3.[1] The data were collected to a resolution of 0.8 Å using 6 ω 1 φ scans.

The data were integrated using SAINT and corrected for absorption using SADABS.[2] The E-statistics of the data were consistent with the space group $P\bar{1}$. The structure was solved using the intrinsic phasing routine of SHELXT.[3] The non-hydrogen atoms were located from a Fourier difference map of the electron density and anisotropically refined using the least-squares algorithm of SHELXL.[4] The hydrogen atoms were then placed in calculated positions and refined with riding thermal parameters.

The asymmetric unit consists of the dimeric unit shown in Figure 1. These are connected to form a coordination polymer through the K^+ ions of the structure. (Figure 2).

The final structure consisted of 349 parameters refined against 5850 independent reflections, giving refinement residuals of R_1 = 0.0448 (based off F^2 for $I > 2\sigma$) and wR_2 = 0.1046 (based of F^2 for all reflections). The final difference Fourier map was featureless.

1. Bruker-AXS (2016). APEX 3 version 2016.9-0. Madison, Wisconsin, USA
2. (a) Bruker-AXS (2015). *SAINT V8.37A.* Madison, Wisconsin, USA. (b) Bruker-AXS (2014). *SADABS*, Madison, Wisconsin, USA.
3. Sheldrick, G. M., *Acta Crystallogr. A* **2015**, A71, 3-8.
4. (a) Sheldrick, G. M., *Acta Crystallogr. C* **2015**, C71, 3-8.; (b) Dolomanov, O. V.; Bourhis, L. J.; Gildea, R. J.; Howard, J. A. K.; Puschmann, H., *J. Appl. Crystallogr.* **2009**, *42*, 339-341.

Table 1 Crystal data and structure refinement for $C_{26}H_{32}B_2F_4K_2O_4$

Identification code	bp80
Empirical formula	$C_{26}H_{32}B_2F_4K_2O_4$
Formula weight	584.33
Temperature/K	100.0
Crystal system	triclinic
Space group	P-1
a/Å	9.3615(2)
b/Å	10.0975(3)
c/Å	16.3289(4)
α/°	91.1418(16)
β/°	93.4906(16)
γ/°	111.7333(14)
Volume/Å^3	1429.65(6)
Z	2
ρ_{calc}g/cm^3	1.357
μ/mm^{-1}	0.387
F(000)	608.0
Crystal size/mm^3	0.3 × 0.2 × 0.1
Radiation	MoKα (λ = 0.71073)
2Θ range for data collection/°	4.916 to 52.83
Index ranges	-11 ≤ h ≤ 11, -12 ≤ k ≤ 12, -20 ≤ l ≤ 20
Reflections collected	44032
Independent reflections	5850 [R_{int} = 0.0564, R_{sigma} = 0.0321]
Data/restraints/parameters	5850/0/349
Goodness-of-fit on F^2	1.069
Final R indexes [I>=2σ (I)]	R_1 = 0.0448, wR_2 = 0.0991
Final R indexes [all data]	R_1 = 0.0571, wR_2 = 0.1046
Largest diff. peak/hole / e Å^{-3}	1.13/-0.32

Table 2 Fractional Atomic Coordinates (×10^4) and Equivalent Isotropic Displacement Parameters (Å^2×10^3) for $C_{26}H_{32}B_2F_4K_2O_4$. U_{eq} is defined as 1/3 of of the trace of the orthogonalised U_{IJ} tensor.

Atom	*x*	*y*	*z*	U(eq)
K1	6351.2(5)	4336.8(5)	9217.0(3)	16.92(12)
K2	504.4(5)	7754.0(5)	9777.8(3)	17.32(12)
F1	7608.7(14)	7208.9(14)	9191.5(9)	23.2(3)
F2	8424.1(15)	9462.6(15)	9737.0(10)	27.0(3)
F3	-590.5(15)	5507.7(14)	8674.7(9)	23.9(3)
F4	-1457.2(15)	3113.5(15)	8773.8(9)	25.3(3)
O1	5817.3(17)	7969.4(16)	9817.4(10)	17.8(3)
O2	3436.1(17)	7939.3(17)	9778.8(10)	20.1(3)
O3	1148.9(17)	4455.1(18)	9172.9(10)	20.3(4)
O4	3642.9(18)	4802.3(17)	9185.6(10)	20.8(4)
C1	6535(3)	8892(3)	8461.8(16)	23.6(5)
C2	5181(2)	9243(2)	8747.9(14)	17.7(5)
C3	4686(2)	8312(2)	9489.7(14)	15.3(4)
C4	3841(2)	9103(2)	8142.0(14)	16.5(5)
C5	3702(3)	8539(3)	7348.3(15)	22.3(5)
C6	2420(3)	8375(3)	6813.9(15)	24.1(5)
C7	1231(3)	8765(2)	7057.0(15)	20.5(5)
C8	1394(3)	9369(2)	7850.3(14)	19.2(5)
C9	2676(3)	9553(2)	8378.2(14)	17.8(5)
C10	-227(3)	8548(3)	6499.4(16)	27.4(6)
C11	-143(3)	7977(3)	5635.8(16)	35.8(7)
C12	-1614(3)	7461(3)	6887.2(18)	36.2(7)
C13	-456(4)	9970(4)	6433(2)	47.9(8)
C14	471(3)	4155(3)	7688.3(15)	21.5(5)
C15	2220(3)	4830(3)	7886.8(15)	24.4(5)
C16	2436(2)	4655(2)	8809.2(14)	17.6(5)
C17	3211(3)	4272(3)	7384.9(15)	25.2(5)
C18	3513(3)	3067(3)	7588.2(17)	35.1(7)
C19	4407(3)	2560(3)	7109.5(17)	31.3(6)
C20	5009(3)	3228(2)	6401.9(15)	19.9(5)
C21	4667(4)	4415(3)	6203.7(17)	37.0(7)
C22	3816(4)	4949(3)	6688.1(17)	36.5(7)
C23	5925(3)	2667(3)	5833.2(16)	23.1(5)
C24	7313(3)	3894(3)	5548.7(18)	31.4(6)
C25	6521(3)	1616(3)	6263.5(19)	36.9(7)
C26	4846(3)	1898(3)	5076.1(17)	32.9(6)
B1	7177(3)	8401(3)	9287.6(18)	19.0(5)
B2	-191(3)	4302(3)	8550.3(17)	18.8(5)

Table 3 Anisotropic Displacement Parameters (Å²×10³) for $C_{26}H_{32}B_2F_4K_2O_4$. The Anisotropic displacement factor exponent takes the form: $-2\pi^2[h^2a^{*2}U_{11}+2hka^*b^*U_{12}+\ldots]$.

Atom	U_{11}	U_{22}	U_{33}	U_{23}	U_{13}	U_{12}
K1	12.0(2)	18.4(2)	21.6(3)	0.11(18)	3.95(18)	6.75(18)
K2	9.0(2)	16.6(2)	25.2(3)	1.33(19)	1.39(18)	3.35(17)
F1	13.3(6)	19.9(7)	38.7(8)	-3.6(6)	1.2(6)	9.3(5)
F2	12.0(6)	22.3(7)	43.6(9)	-7.5(6)	-2.2(6)	3.8(5)
F3	21.7(7)	24.9(7)	29.7(8)	-1.2(6)	5.1(6)	13.8(6)
F4	16.4(7)	26.1(7)	32.6(8)	3.9(6)	6.6(6)	6.0(6)
O1	10.1(7)	20.1(8)	24.3(9)	2.0(6)	0.5(6)	6.9(6)
O2	13.1(8)	25.3(8)	24.3(9)	5.7(7)	6.9(6)	9.0(7)
O3	15.3(8)	30.5(9)	17.6(8)	1.3(7)	4.0(6)	10.8(7)
O4	14.4(8)	25.5(9)	23.0(9)	-1.9(7)	-0.1(6)	8.6(7)
C1	14.6(11)	32.3(13)	27.8(13)	5.5(10)	8.1(9)	11.9(10)
C2	12.2(10)	18.9(11)	23.4(12)	1.3(9)	3.0(9)	7.2(9)
C3	11.2(10)	14.9(10)	20.0(11)	-2.8(8)	-0.6(8)	5.3(8)
C4	10.9(10)	16.2(10)	21.6(12)	4.6(9)	3.7(8)	3.7(8)
C5	19.3(11)	28.3(12)	24.6(13)	2.4(10)	6.7(9)	14.1(10)
C6	24.6(12)	30.6(13)	20.1(12)	0.2(10)	4.6(10)	13.5(10)
C7	19.2(11)	22.2(11)	22.3(12)	5.4(9)	1.9(9)	10.0(9)
C8	17.9(11)	21.2(11)	23.0(12)	3.7(9)	5.2(9)	11.7(9)
C9	19.1(11)	17.1(11)	18.8(11)	2.2(9)	4.4(9)	7.9(9)
C10	23.7(12)	38.5(15)	25.0(13)	-0.7(11)	-1.7(10)	17.9(11)
C11	28.7(14)	58.6(19)	21.9(14)	-2.0(13)	-2.1(11)	19.1(13)
C12	19.3(13)	55.1(18)	33.4(15)	-11.8(13)	-0.6(11)	14.2(12)
C13	55(2)	57(2)	45.2(19)	0.5(15)	-17.0(15)	39.7(17)
C14	16.2(11)	31.2(13)	20.7(12)	-1.9(10)	0.6(9)	13.1(10)
C15	24.0(12)	24.4(12)	26.1(13)	1.1(10)	5.5(10)	9.9(10)
C16	13.4(10)	19.4(11)	20.6(12)	-0.9(9)	4.0(9)	6.5(9)
C17	18.4(11)	35.3(14)	22.8(13)	-3.7(10)	0.8(9)	11.3(10)
C18	42.5(16)	26.5(13)	27.4(14)	-0.6(11)	21.3(12)	-0.5(12)
C19	44.4(16)	19.6(12)	33.7(15)	4.8(11)	13.9(12)	14.3(12)
C20	16.9(11)	21.8(11)	20.8(12)	-2.3(9)	3.3(9)	6.9(9)
C21	55.9(19)	49.0(17)	23.5(14)	11.3(12)	17.1(13)	37.2(15)
C22	50.7(18)	47.7(17)	27.3(15)	7.5(12)	10.6(13)	35.7(15)
C23	21.6(12)	24.0(12)	26.8(13)	-3.5(10)	4.8(10)	11.8(10)
C24	24.0(13)	34.4(14)	38.0(16)	-3.0(12)	15.1(11)	11.8(11)
C25	39.2(16)	37.4(16)	44.7(18)	1.3(13)	6.9(13)	26.1(13)
C26	31.7(14)	34.0(15)	32.9(15)	-11.0(12)	4.4(12)	12.4(12)
B1	10.4(11)	17.6(12)	30.1(15)	-1.7(10)	4.1(10)	6.1(10)
B2	13.3(12)	21.3(13)	22.6(14)	-0.6(10)	1.2(10)	7.4(10)

Table 4 Bond Lengths for b $C_{26}H_{32}B_2F_4K_2O_4$.

Atom	Atom	Length/Å	Atom	Atom	Length/Å
K1	F1	2.6983(14)	O3	B2	1.525(3)
K1	F3[1]	2.8675(14)	O4	C16	1.210(3)
K1	F4[1]	2.8777(15)	C1	C2	1.532(3)
K1	O1[2]	3.0107(16)	C1	B1	1.604(4)
K1	O2[2]	2.9085(17)	C2	C3	1.535(3)
K1	O3[2]	3.2994(17)	C2	C4	1.511(3)
K1	O4[2]	2.7319(17)	C4	C5	1.384(3)
K1	O4	2.7422(16)	C4	C9	1.399(3)
K1	C3[2]	3.333(2)	C5	C6	1.396(3)
K1	C16[2]	3.359(2)	C6	C7	1.387(3)
K1	C18	3.501(3)	C7	C8	1.396(3)
K1	B2[1]	3.490(3)	C7	C10	1.536(3)
K2	F1[3]	2.6694(14)	C8	C9	1.386(3)
K2	F2[3]	3.0415(15)	C10	C11	1.530(4)
K2	F2[4]	2.6944(15)	C10	C12	1.538(4)
K2	F3	2.7074(15)	C10	C13	1.534(4)
K2	F4[5]	2.7497(15)	C14	C15	1.533(3)
K2	O2	2.6807(16)	C14	B2	1.598(4)
K2	O3[5]	2.8680(17)	C15	C16	1.530(3)
K2	C9	3.264(2)	C15	C17	1.520(4)
K2	B1[3]	3.464(3)	C17	C18	1.390(4)
K2	B2[5]	3.424(3)	C17	C22	1.380(4)
F1	B1	1.413(3)	C18	C19	1.398(4)
F2	B1	1.410(3)	C19	C20	1.391(3)
F3	B2	1.415(3)	C20	C21	1.390(4)
F4	B2	1.413(3)	C20	C23	1.535(3)
O1	C3	1.318(3)	C21	C22	1.388(4)
O1	B1	1.515(3)	C23	C24	1.531(3)
O2	C3	1.217(3)	C23	C25	1.534(4)
O3	C16	1.325(3)	C23	C26	1.543(4)

[1]1+X,+Y,+Z; [2]1-X,1-Y,2-Z; [3]-1+X,+Y,+Z; [4]1-X,2-Y,2-Z; [5]-X,1-Y,2-Z

Table 5 Bond Angles for $C_{26}H_{32}B_2F_4K_2O_4$.

Atom	Atom	Atom	Angle/˚	Atom	Atom	Atom	Angle/˚
F1	K1	F3[1]	64.19(4)	O3[5]	K2	C9	163.73(5)
F1	K1	F4[1]	110.38(4)	O3[5]	K2	B1[3]	90.08(6)
F1	K1	O1[2]	140.02(5)	O3[5]	K2	B2[5]	26.19(5)
F1	K1	O2[2]	139.02(5)	C9	K2	K1[3]	123.06(4)
F1	K1	O3[2]	71.64(4)	C9	K2	K1[2]	97.65(4)
F1	K1	O4	83.02(5)	C9	K2	B1[3]	100.13(6)
F1	K1	O4[2]	76.69(5)	C9	K2	B2[5]	147.46(6)
F1	K1	C3[2]	141.70(5)	B1[3]	K2	K1[3]	60.33(4)
F1	K1	C16[2]	76.75(5)	B1[3]	K2	K1[2]	160.73(5)

F1	K1	C18	108.43(6)	B2[5]	K2	K1[3]	76.96(4)
F1	K1	B2[1]	87.31(5)	B2[5]	K2	K1[2]	50.39(4)
F3[1]	K1	F4[1]	46.33(4)	B2[5]	K2	B1[3]	112.38(6)
F3[1]	K1	O1[2]	144.93(4)	K2[1]	F1	K1	101.85(5)
F3[1]	K1	O2[2]	101.09(4)	B1	F1	K1	139.43(13)
F3[1]	K1	O3[2]	70.72(4)	B1	F1	K2[1]	112.38(12)
F3[1]	K1	C3[2]	122.03(5)	K2[4]	F2	K2[1]	121.67(5)
F3[1]	K1	C16[2]	93.17(5)	B1	F2	K2[1]	95.06(13)
F3[1]	K1	C18	112.76(5)	B1	F2	K2[4]	141.98(14)
F3[1]	K1	B2[1]	23.17(5)	K2	F3	K1[3]	96.71(4)
F4[1]	K1	O1[2]	102.46(4)	B2	F3	K1[3]	103.95(12)
F4[1]	K1	O2[2]	63.69(4)	B2	F3	K2	132.19(13)
F4[1]	K1	O3[2]	81.56(4)	K2[5]	F4	K1[3]	105.11(5)
F4[1]	K1	C3[2]	83.55(5)	B2	F4	K1[3]	103.54(13)
F4[1]	K1	C16[2]	100.56(5)	B2	F4	K2[5]	106.18(13)
F4[1]	K1	C18	101.75(6)	C3	O1	K1[2]	92.20(12)
F4[1]	K1	B2[1]	23.17(5)	C3	O1	B1	111.44(18)
O1[2]	K1	O3[2]	91.89(4)	B1	O1	K1[2]	146.85(13)
O1[2]	K1	C3[2]	23.28(5)	K2	O2	K1[2]	106.09(5)
O1[2]	K1	C16[2]	75.35(5)	C3	O2	K1[2]	99.47(13)
O1[2]	K1	C18	85.79(5)	C3	O2	K2	152.63(15)
O1[2]	K1	B2[1]	124.40(5)	K2[5]	O3	K1[2]	84.71(4)
O2[2]	K1	O1[2]	43.91(4)	C16	O3	K1[2]	81.04(12)
O2[2]	K1	O3[2]	67.39(4)	C16	O3	K2[5]	129.88(14)
O2[2]	K1	C3[2]	21.12(5)	C16	O3	B2	111.59(18)
O2[2]	K1	C16[2]	65.67(5)	B2	O3	K1[2]	159.68(14)
O2[2]	K1	C18	112.47(6)	B2	O3	K2[5]	97.69(12)
O2[2]	K1	B2[1]	82.41(5)	K1[2]	O4	K1	101.20(5)
O3[2]	K1	C3[2]	75.70(5)	C16	O4	K1[2]	110.84(14)
O3[2]	K1	C16[2]	22.94(5)	C16	O4	K1	147.27(15)
O3[2]	K1	C18	176.29(5)	C2	C1	B1	102.61(19)
O3[2]	K1	B2[1]	75.39(5)	C1	C2	C3	103.45(18)
O4	K1	F3[1]	141.62(5)	C4	C2	C1	119.6(2)
O4[2]	K1	F3[1]	110.09(5)	C4	C2	C3	112.71(18)
O4	K1	F4[1]	158.90(5)	O1	C3	K1[2]	64.52(11)
O4[2]	K1	F4[1]	119.38(5)	O1	C3	C2	111.66(18)
O4[2]	K1	O1[2]	67.48(5)	O2	C3	K1[2]	59.41(12)
O4	K1	O1[2]	73.40(5)	O2	C3	O1	121.7(2)
O4	K1	O2[2]	117.04(5)	O2	C3	C2	126.6(2)
O4[2]	K1	O2[2]	73.33(5)	C2	C3	K1[2]	165.81(15)
O4[2]	K1	O3[2]	42.04(4)	C5	C4	C2	122.8(2)
O4	K1	O3[2]	118.86(5)	C5	C4	C9	117.4(2)
O4[2]	K1	O4	78.80(5)	C9	C4	C2	119.8(2)
O4	K1	C3[2]	95.94(5)	C4	C5	C6	121.3(2)
O4[2]	K1	C3[2]	65.66(5)	C7	C6	C5	121.4(2)
O4[2]	K1	C16[2]	19.68(5)	C6	C7	C8	117.1(2)
O4	K1	C16[2]	98.34(5)	C6	C7	C10	123.0(2)
O4	K1	C18	57.68(6)	C8	C7	C10	119.9(2)
O4[2]	K1	C18	134.25(6)	C9	C8	C7	121.6(2)

O4[2]	K1	B2[1]	117.40(6)	C4	C9	K2	117.02(14)
O4	K1	B2[1]	158.65(6)	C8	C9	K2	91.30(14)
C3[2]	K1	C16[2]	65.48(5)	C8	C9	C4	121.0(2)
C3[2]	K1	C18	102.89(6)	C7	C10	C12	108.3(2)
C3[2]	K1	B2[1]	103.38(6)	C11	C10	C7	112.2(2)
C16[2]	K1	C18	153.38(6)	C11	C10	C12	108.5(2)
C16[2]	K1	B2[1]	97.89(6)	C11	C10	C13	108.9(2)
B2[1]	K1	C18	108.31(6)	C13	C10	C7	109.6(2)
K1[3]	K2	K1[2]	103.398(13)	C13	C10	C12	109.4(2)
F1[3]	K2	K1[2]	142.69(3)	C15	C14	B2	102.71(19)
F1[3]	K2	K1[3]	39.32(3)	C16	C15	C14	104.32(19)
F1[3]	K2	F2[4]	104.06(4)	C17	C15	C14	116.9(2)
F1[3]	K2	F2[3]	46.04(4)	C17	C15	C16	112.9(2)
F1[3]	K2	F3	66.81(4)	O3	C16	K1[2]	76.02(12)
F1[3]	K2	F4[5]	127.28(5)	O3	C16	C15	111.26(19)
F1[3]	K2	O2	157.97(5)	O4	C16	K1[2]	49.48(12)
F1[3]	K2	O3[5]	79.48(4)	O4	C16	O3	122.9(2)
F1[3]	K2	C9	105.54(5)	O4	C16	C15	125.5(2)
F1[3]	K2	B1[3]	22.17(5)	C15	C16	K1[2]	157.24(15)
F1[3]	K2	B2[5]	105.19(5)	C18	C17	C15	122.4(2)
F2[4]	K2	K1[2]	110.72(3)	C22	C17	C15	119.9(2)
F2[3]	K2	K1[2]	159.61(3)	C22	C17	C18	117.6(2)
F2[4]	K2	K1[3]	140.36(3)	C17	C18	K1	102.98(17)
F2[3]	K2	K1[3]	82.85(3)	C17	C18	C19	121.4(2)
F2[4]	K2	F2[3]	58.33(5)	C19	C18	K1	94.31(19)
F2[4]	K2	F3	155.25(5)	C20	C19	C18	121.3(2)
F2[4]	K2	F4[5]	94.66(5)	C19	C20	C23	123.2(2)
F2[4]	K2	O3[5]	122.18(5)	C21	C20	C19	116.2(2)
F2[3]	K2	C9	94.87(5)	C21	C20	C23	120.6(2)
F2[4]	K2	C9	72.22(5)	C22	C21	C20	122.8(3)
F2[3]	K2	B1[3]	23.93(5)	C17	C22	C21	120.6(3)
F2[4]	K2	B1[3]	81.93(5)	C20	C23	C26	108.1(2)
F2[3]	K2	B2[5]	114.23(6)	C24	C23	C20	110.9(2)
F2[4]	K2	B2[5]	110.04(6)	C24	C23	C25	108.1(2)
F3	K2	K1[2]	85.69(3)	C24	C23	C26	109.0(2)
F3	K2	K1[3]	43.11(3)	C25	C23	C20	111.6(2)
F3	K2	F2[3]	110.89(4)	C25	C23	C26	109.1(2)
F3	K2	F4[5]	109.21(5)	F1	B1	K2[1]	45.45(9)
F3	K2	O3[5]	80.00(5)	F1	B1	O1	107.45(19)
F3	K2	C9	87.72(5)	F1	B1	C1	115.4(2)
F3	K2	B1[3]	87.67(5)	F2	B1	K2[1]	61.02(11)
F3	K2	B2[5]	94.68(6)	F2	B1	F1	106.30(18)
F4[5]	K2	K1[2]	38.44(3)	F2	B1	O1	107.5(2)
F4[5]	K2	K1[3]	99.93(3)	F2	B1	C1	116.0(2)
F4[5]	K2	F2[3]	121.79(5)	O1	B1	K2[1]	123.24(15)
F4[5]	K2	O3[5]	49.46(4)	O1	B1	C1	103.67(18)
F4[5]	K2	C9	127.14(5)	C1	B1	K2[1]	132.20(15)
F4[5]	K2	B1[3]	129.23(6)	K2[5]	B2	K1[3]	80.53(6)
F4[5]	K2	B2[5]	23.34(5)	F3	B2	K1[3]	52.88(10)

O2	K2	K1[2]	38.71(3)	F3	B2	K2[5]	114.52(15)
O2	K2	K1[3]	131.38(4)	F3	B2	O3	107.14(19)
O2	K2	F2[3]	144.39(5)	F3	B2	C14	116.4(2)
O2	K2	F2[4]	88.26(5)	F4	B2	K1[3]	53.29(10)
O2	K2	F3	94.40(5)	F4	B2	K2[5]	50.48(10)
O2	K2	F4[5]	68.41(5)	F4	B2	F3	106.15(19)
O2	K2	O3[5]	109.61(5)	F4	B2	O3	106.39(19)
O2	K2	C9	60.43(5)	F4	B2	C14	116.5(2)
O2	K2	B1[3]	160.27(6)	O3	B2	K1[3]	120.05(15)
O2	K2	B2[5]	87.04(6)	O3	B2	K2[5]	56.12(10)
O3[5]	K2	K1[2]	70.97(3)	O3	B2	C14	103.46(18)
O3[5]	K2	K1[3]	52.03(3)	C14	B2	K1[3]	136.48(15)
O3[5]	K2	F2[3]	99.45(4)	C14	B2	K2[5]	128.90(16)

[1]1+X,+Y,+Z; [2]1-X,1-Y,2-Z; [3]-1+X,+Y,+Z; [4]1-X,2-Y,2-Z; [5]-X,1-Y,2-Z

Table 6 Torsion Angles for $C_{26}H_{32}B_2F_4K_2O_4$.

A	B	C	D	Angle/˚	A	B	C	D	Angle/˚
K1	F1	B1	K2[1]	145.4(2)	C3	O1	B1	K2[1]	-178.86(14)
K1	F1	B1	F2	140.39(15)	C3	O1	B1	F1	-131.17(19)
K1	F1	B1	O1	25.6(3)	C3	O1	B1	F2	114.8(2)
K1	F1	B1	C1	-89.5(3)	C3	O1	B1	C1	-8.5(2)
K1[2]	F3	B2	K2[3]	-55.11(13)	C3	C2	C4	C5	-115.5(2)
K1[2]	F3	B2	F4	-1.70(19)	C3	C2	C4	C9	64.4(3)
K1[2]	F3	B2	O3	-115.08(15)	C4	C2	C3	K1[4]	82.2(6)
K1[2]	F3	B2	C14	129.79(17)	C4	C2	C3	O1	153.70(19)
K1[2]	F4	B2	K2[3]	110.44(9)	C4	C2	C3	O2	-28.2(3)
K1[2]	F4	B2	F3	1.69(19)	C4	C5	C6	C7	-0.3(4)
K1[2]	F4	B2	O3	115.58(15)	C5	C4	C9	K2	113.0(2)
K1[2]	F4	B2	C14	-129.70(17)	C5	C4	C9	C8	3.4(3)
K1[4]	O1	C3	O2	16.8(2)	C5	C6	C7	C8	1.9(4)
K1[4]	O1	C3	C2	-165.08(15)	C5	C6	C7	C10	-177.6(2)
K1[4]	O1	B1	K2[1]	-46.3(3)	C6	C7	C8	C9	-1.0(3)
K1[4]	O1	B1	F1	1.4(4)	C6	C7	C10	C11	-4.7(3)
K1[4]	O1	B1	F2	-112.6(2)	C6	C7	C10	C12	114.9(3)
K1[4]	O1	B1	C1	124.1(2)	C6	C7	C10	C13	-125.8(3)
K1[4]	O2	C3	O1	-17.6(2)	C7	C8	C9	K2	-124.7(2)
K1[4]	O2	C3	C2	164.5(2)	C7	C8	C9	C4	-1.7(3)
K1[4]	O3	C16	O4	16.6(2)	C8	C7	C10	C11	175.8(2)
K1[4]	O3	C16	C15	-157.34(18)	C8	C7	C10	C12	-64.6(3)
K1[4]	O3	B2	K1[2]	-43.7(4)	C8	C7	C10	C13	54.7(3)
K1[4]	O3	B2	K2[3]	-95.5(4)	C9	C4	C5	C6	-2.4(3)
K1[4]	O3	B2	F3	12.9(5)	C10	C7	C8	C9	178.6(2)
K1[4]	O3	B2	F4	-100.3(4)	C14	C15	C16	K1[4]	-125.7(3)
K1[4]	O3	B2	C14	136.3(3)	C14	C15	C16	O3	-20.8(3)
K1	O4	C16	K1[4]	167.6(3)	C14	C15	C16	O4	165.5(2)
K1[4]	O4	C16	O3	-21.4(3)	C14	C15	C17	C18	-84.8(3)
K1	O4	C16	O3	146.2(2)	C14	C15	C17	C22	93.6(3)
K1[4]	O4	C16	C15	151.67(19)	C15	C14	B2	K1[2]	158.05(18)

K1	O4	C16	C15	-40.7(4)	C15	C14	B2	K2[3]	-79.1(2)
K1	C18	C19	C20	-109.2(3)	C15	C14	B2	F3	95.2(2)
K2[1]	F1	B1	F2	-5.0(2)	C15	C14	B2	F4	-138.3(2)
K2[1]	F1	B1	O1	-119.78(14)	C15	C14	B2	O3	-22.0(2)
K2[1]	F1	B1	C1	125.14(16)	C15	C17	C18	K1	-77.7(2)
K2[5]	F2	B1	K2[1]	165.7(2)	C15	C17	C18	C19	178.9(3)
K2[5]	F2	B1	F1	169.76(13)	C15	C17	C22	C21	-177.2(3)
K2[1]	F2	B1	F1	4.05(18)	C16	O3	B2	K1[2]	-169.61(14)
K2[1]	F2	B1	O1	118.86(15)	C16	O3	B2	K2[3]	138.53(18)
K2[5]	F2	B1	O1	-75.4(3)	C16	O3	B2	F3	-113.1(2)
K2[1]	F2	B1	C1	-125.75(18)	C16	O3	B2	F4	133.74(19)
K2[5]	F2	B1	C1	40.0(3)	C16	O3	B2	C14	10.4(2)
K2	F3	B2	K1[2]	112.80(16)	C16	C15	C17	C18	36.2(3)
K2	F3	B2	K2[3]	57.7(2)	C16	C15	C17	C22	-145.4(2)
K2	F3	B2	F4	111.10(17)	C17	C15	C16	K1[4]	106.4(4)
K2	F3	B2	O3	-2.3(3)	C17	C15	C16	O3	-148.7(2)
K2	F3	B2	C14	-117.40(19)	C17	C15	C16	O4	37.5(3)
K2[3]	F4	B2	K1[2]	-110.44(9)	C17	C18	C19	C20	-1.1(4)
K2[3]	F4	B2	F3	-108.74(15)	C18	C17	C22	C21	1.3(4)
K2[3]	F4	B2	O3	5.1(2)	C18	C19	C20	C21	-0.1(4)
K2[3]	F4	B2	C14	119.87(18)	C18	C19	C20	C23	-176.7(2)
K2	O2	C3	K1[4]	-159.0(4)	C19	C20	C21	C22	1.9(4)
K2	O2	C3	O1	-176.6(2)	C19	C20	C23	C24	-138.5(3)
K2	O2	C3	C2	5.5(5)	C19	C20	C23	C25	-18.0(3)
K2[3]	O3	C16	K1[4]	-75.33(13)	C19	C20	C23	C26	102.0(3)
K2[3]	O3	C16	O4	-58.7(3)	C20	C21	C22	C17	-2.6(5)
K2[3]	O3	C16	C15	127.33(17)	C21	C20	C23	C24	45.0(3)
K2[3]	O3	B2	K1[2]	51.87(14)	C21	C20	C23	C25	165.5(3)
K2[3]	O3	B2	F3	108.42(16)	C21	C20	C23	C26	-74.5(3)
K2[3]	O3	B2	F4	-4.78(18)	C22	C17	C18	K1	103.9(2)
K2[3]	O3	B2	C14	-128.11(15)	C22	C17	C18	C19	0.5(4)
C1	C2	C3	K1[4]	-48.4(6)	C23	C20	C21	C22	178.7(3)
C1	C2	C3	O1	23.1(2)	B1	O1	C3	K1[4]	156.25(17)
C1	C2	C3	O2	-158.8(2)	B1	O1	C3	O2	173.0(2)
C1	C2	C4	C5	6.3(3)	B1	O1	C3	C2	-8.8(2)
C1	C2	C4	C9	-173.8(2)	B1	C1	C2	C3	-26.0(2)
C2	C1	B1	K2[1]	-169.22(15)	B1	C1	C2	C4	-152.3(2)
C2	C1	B1	F1	138.9(2)	B2	O3	C16	K1[4]	163.46(16)
C2	C1	B1	F2	-95.8(2)	B2	O3	C16	O4	-179.9(2)
C2	C1	B1	O1	21.7(2)	B2	O3	C16	C15	6.1(3)
C2	C4	C5	C6	177.5(2)	B2	C14	C15	C16	25.2(2)
C2	C4	C9	K2	-66.9(2)	B2	C14	C15	C17	150.7(2)
C2	C4	C9	C8	-176.6(2)					

[1]1+X,+Y,+Z; [2]-1+X,+Y,+Z; [3]-X,1-Y,2-Z; [4]1-X,1-Y,2-Z; [5]1-X,2-Y,2-Z

Table 7 Hydrogen Atom Coordinates (Å×10^4) and Isotropic Displacement Parameters (Å^2×10^3) for $C_{26}H_{32}B_2F_4K_2O_4$.

Atom	*x*	*y*	*z*	U(eq)
H1A	7329.55	9741.2	8249.28	28
H1B	6184.33	8113.45	8030.57	28
H2	5616.59	10257.2	8964.74	21
H5	4495.12	8257.4	7163.52	27
H6	2360.72	7988.07	6272.08	29
H8	607.23	9660.93	8032.65	23
H9	2764.77	9991.85	8908.83	21
H11A	755.45	8644.84	5386.46	54
H11B	-1082.88	7875.94	5298.35	54
H11C	-47.78	7045	5669.46	54
H12A	-1488.89	6540.24	6909.56	54
H12B	-2563.9	7344.39	6554.54	54
H12C	-1674.64	7804.13	7444.75	54
H13A	-602.64	10302.67	6978.38	72
H13B	-1367.49	9836.55	6062.86	72
H13C	454.4	10680.33	6216.64	72
H14A	147.73	3141.82	7499.25	26
H14B	127.18	4678.7	7262.68	26
H15	2545.77	5875.54	7799.23	29
H18	3103.62	2576.89	8062.39	42
H19	4608.23	1743.37	7270.48	38
H21	5030.83	4882.18	5715.61	44
H22	3648.65	5786.97	6538.55	44
H24A	6954.48	4558.9	5250.45	47
H24B	7878.31	3511.71	5185.92	47
H24C	7994.93	4397.39	6027.6	47
H25A	7137.61	2074.34	6769.88	55
H25B	7160.7	1331.36	5898.5	55
H25C	5644.78	769.22	6396.94	55
H26A	3954.64	1109.78	5253.84	49
H26B	5405.53	1521.58	4706.44	49
H26C	4491.44	2574.2	4787.14	49